Substitution Effects in Binary Intermetallic Compounds:

Investigations in the System Alkali and Alkaline-Earth Metal – Tin and Alkaline-Earth Metal – Bismuth

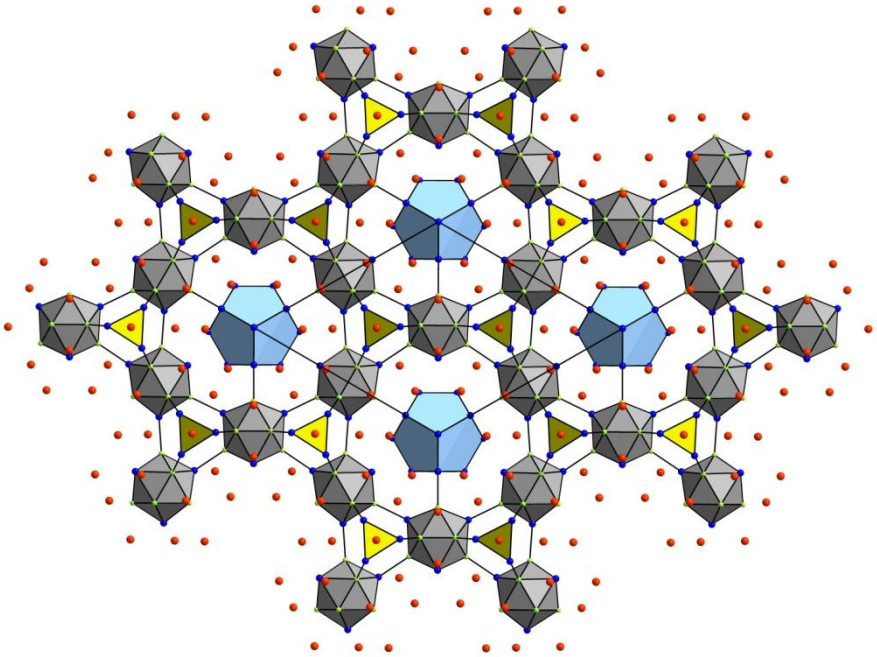

Sung-Jin Kim

Technische Universität München

Lehrstuhl für Anorganische Chemie

mit Schwerpunkt Neue Materialien

November 2007

Technische Universität München

Lehrstuhl für Anorganische Chemie mit Schwerpunkt Neue Materialien

Substitution Effects in Binary Intermetallic Compounds: Investigations in the System Alkali and Alkaline-Earth Metal – Tin and Alkaline-Earth Metal – Bismuth

Sung-Jin Kim

Vollständiger Abdruck der von der Fakultät für Chemie der Technischen Universität München zur Erlangung des akademischen Grades eines

Doktors der Naturwissenschaften

genehmigten Dissertation.

Vorsitzende: Univ.-Prof. Dr. Sevil Weinkauf

Prüfer der Dissertation:

1. Univ.-Prof. Dr. Thomas Fässler
2. Univ.-Prof. Dr. Ulrich K. Heiz
3. Univ.-Prof. Dr. Klaus Köhler

Die Dissertation wurde am 05.11.2007 bei der Technischen Universität München eingereicht und durch die Fakultät für Chemie am 06.12.2007 angenommen.

Acknowledgments

- To my supervisor Prof. Dr. Thomas F. Fässler for accepting me as a PhD student, the interesting topic, valuable advices, patience, and guidance in difficult situations.
- Dr.-Ing. Stephan D. Hoffmann, for introducing me to single-crystal X-ray diffraction techniques as well as for the valuable discussions, SQUID measurements, and advices in every respect.
- I am particularly indebted to Dr. Siméon Ponou, for introducing me to the 'Endless Wonders' of Zintl chemistry and fruitful discussions.
- Dr. Martin Schreyer, for introducing me to powder X-ray diffraction methods.
- Dr. Florian Kraus, for the Gaussian calculations and general advices.
- Prof. Dr. R. Niewa, for the discussions of DTA experiments.
- Ingrid Werner, for helping out with the EDX measurements.
- Dr. Matthias Opel (Walther-Meissner-Institut, TU-München) and Dipl.-Chem. Bele Boeddinghaus for the SQUID measurements.
- Special thanks go to M. Sc. Andreas Kaltzoglou, Dipl.-Chem. Annette Spiekermann, and Dipl.-Chem. Saskia Stegmaier for reading and correcting the manuscript.
- Dipl.-Chem. Annette Spiekermann, for solution experiments with my compounds.
- M. Sc. Andreas Kaltzoglou, for the time in the ‚Praktikum für Lebensmittelchemiker' and many discussions.
- To all other co-workers during my time in Prof. Fässler's group: Sebastian Baer (my 'Knecht'), Dr. Frank Dubois, M. Sc. Magreth A. Fredricks, Dr. Viktor Hlukhyy (for his experimental advices), M. Sc. Florian Kiefer, Ursula Madan-Singh, Dipl.-Chem. Sandra Scharfe, Dipl.-Chem. Lisa Siggelkow, Dr. Jian-Qiang Wang, and Dr. Li Yong.
- Finally, my parents deserve my deepest gratitude for their eternal understanding, support, and lenience.

Table of Contents

List of Abbreviations

2b-, 3b-, 4b-	two-bonded, three-bonded, four-bonded
A	Alkali Metal (element of group 1)
ADP	Anisotropic Displacement Parameter
Ae	Alkaline Earth Metal (element of group 2)
AIM	Atoms In Molecules
at%	Atomic Composition / %
bcc	Body Centered Cubic
CCD	Charge Coupled Device
CN	Coordination Number
COHP	Crystal Orbital Hamilton Population
DOS	Density of States
DTA	Differential Thermal Analysis
EDX	Energy Dispersive X-ray Analysis
EH	Extended-Hückel
ELF	Electron Localization Function
emf	Electromotive Force
hcp	Hexagonal Close Packed
HOMO	Highest Occupied Molecular Orbital
ICDD	International Center for Diffraction Data
ICOHP	Integrated Crystal Orbital Hamilton Population
ICSD	Inorganic Crystal Structure Database
IDOS	Integrated Density of States
LCAO	Linear Combination of Atomic Orbitals
LMTO	Linear Muffin Tin Orbital
LUMO	Lowest Unoccupied Molecular Orbital
MO	Molecular Orbital
NBO	Natural Bond Orbital Analysis
Occ.	Occupancy
PBO	Pauling Bond Order
pDOS	Projected Density of States
Pn	Pnictogen (element of group 15)
RE	Rare Earth Metal
SQUID	Superconducting Quantum Interference Device
TE	Thermoelectric
Tr	Triel (element of group 13)
Tt	Tetrel (element of group 14)
VE	Valence Electron(s)
VEC	Valence Electron Concentration
X	Halogenide (element of group 17)

1 General Introduction

The fascination for solid state chemistry and the more applied field of material science not only arises from the structural diversity and the curiosity driven research but also from the often exciting physical properties of the compounds. In general solid state chemistry is truly interdisciplinary as it borders solid state physics, crystallography, quantum theory, metal science and inorganic chemistry. Outstanding technological advances of the 20th and 21st century are based on fundamental research of solid state chemistry. For instance insulators with designed properties such as dielectric ceramics, novel ionic conductors, magnetic intermetallics and oxides for data storage, advanced nitrides for electro optical applications, high strength superalloys, superconductors, metallic glasses, fuel cells, or hydrogen storage reflect the importance of solid states.[1]

'Designing' new compounds with new physical properties means understanding why a structure is formed and this in turn involves the investigation of the main driving forces, the electronic factor, the packing efficiency, and the Madelung energy. Whereas most of the elemental structures of metals are rather simple (the majority adopts simple packings of atoms, such as the cubic close packing, the hexagonal close packing, or the body centered cubic structure), the outcome of the combination of just two different metals is difficult to predict. One may obtain a solid solution based on one of the simple close packings or very complex, ordered structures with more than thousand atoms in the unit cell ($NaCd_2$, β-Mg_2Al_3),[2] or even quasi crystals with no 3D periodicity at all (Mn–Al).[3] Such examples show that chemical bonding among inorganic solids can be very diverse and in fact is least understood for intermetallics. Thus, the surprising behavior of metallic elements when forming a compound requires a better understanding of the interplay between the structure stabilizing factors.

In solid state chemistry several rules and schemes for describing and sorting structures have been elaborated. For characterization of ionic structures the principles of Laves[4, 5] together with the Goldschmidt,[6] Grimm-Sommerfeld,[7] Fajans,[8-10] and Pauling[11] rules are worthy for rationalization. Sorting and predicting solid state phases can be done in Van Arkel-Ketelaar's triangle,[12-14] Mooser-Pearson plots,[15] Phillips-van Vechten plots,[16] and Pettifor structure maps.[17, 18] More specific families were worked out by categorizing fractions of intermetallics.

The most important involve the Frank-Kasper[19, 20] phases and the related Laves and *σ*-phases. Electronic factors are considered to be dominant in brass type Hume-Rothery[21] and Zintl phases.

1.1 Classes of intermetallic Compounds

Despite the models mentioned above, the classification of intermetallic systems as a whole is difficult. The fluent transition between metallic and semiconducting properties, as well as the many different bonding types that are often present simultaneously, together with the myriads of evolved different structures, stoichiometries, and different magnetic behaviors, make a clear separation almost impossible. Whereas structuring the huge amounts of intermetallic compounds can be done very generally in terms of bonding characteristics, as they occur in *d*–*d*, *d*–*p*, and *s*–*p* bonded systems,[22] the term ‘metallic bond’ should be used cautiously.[23]

d–d(f) bonded Intermetallic compounds involving just transition metals are important due to their mechanical, chemical, and physical properties. The *d*–*d* orbital interactions involve *σ*, *π*, and *δ* types of orbital overlap, with *σ* overlap the greatest and *δ* overlap the lowest. Various transition metal Laves phases have interesting magnetic properties (superconducting HfV_2, C15 Laves type[24]) or are hydrogen storage materials (ZrV_2).[25] Intermetallics between rare-earth and transition metals are noteworthy due to their magnetic properties (e.g. $SmCo_5$).[26]

d–p bonded These intermetallics display magnetic, superconducting, mechanical, and structural properties. The electronic states near E_F are dominated by the *d* orbitals of the transition metal. The electronic structures arise from the expansion of the transition metal lattice due to the insertion of the *p* element; and the interaction between the valence *d* bands on the transition metal with the *sp* bands of the main group element. Good metallic conductors exist which are often excellent superconductors (A15 phases, e.g. Nb_3Sn[27]). On the *p* metal rich side the compounds become narrow-gap semiconductors with thermoelectric properties, e.g. $CoSb_3$ [28] (cubic skutterudite structure), and the Half-Heusler[29] phases.

s–p bonded This bonding is present between electropositive A, Ae, RE metals and *p* block metals. Late ‘transition metals’ with core-like, filled *d* orbitals, such as Zn, Cd, or Hg can be counted in as well. The difference in electronegativity is large enough to (formally) transfer all electrons from the active metal to the *p* block element, which leads to the formation of polymeric anions.

Apart from this, other aspects, such as stoichiometries, driven from structural, Madelung energies and packing efficiency, can lead to deviations from electron precise compounds. Then other bonding models, such as Wade's rules or hypervalent bonding have to be introduced and the structures become metallic conductors, which are either electron deficient (empty bonding states) or electron rich, with extra electrons (filled conduction band). Of course, in electron precise compounds, structure motifs can be based on electron deficiency. This interplay between different bonding types evolving into a huge variety of structures is what contributes to the fascination for this class of intermetallics. However, between Zintl phases and polar intermetallics no clear separation exists. For example in NaTl,[30] which is often referred to as a typical Zintl phase, the structure is formed from two interpenetrating diamond structures (Na and Tl). Each Tl atom is tetrahedrally coordinated with other Tl atoms, with a Tl–Tl (3.24 Å) separation shorter than in metallic hcp *α*-Tl (3.42 Å, CN 12) or bcc *β*-Tl (3.36 Å, CN 8). Zintl considered NaTl as $Na^{+}Tl^{-}$, with Tl^{1-} present not as a simple anion but in an extended 3D anionic framework, like the four valence electron elements C or Si. Nevertheless, NaTl is a metallic conductor[31, 32] because the interaction between two Tl atoms is not strong enough to open a bonding-antibonding gap at the Fermi level.

As the present thesis investigates *s*–*p* bonded intermetallics, the characteristics of electron precise classical Zintl phases, non-classical, metallic Zintl phases, and polar intermetallic compounds are briefly described in the next section.

1.1.1 Zintl Phases

Classical Zintl Phases with Main Group Elements According to the Zintl concept[30, 33-36] a complete charge transfer from the electropositive (active) metal, such as alkali, alkaline earth or rare earth atoms to the more electronegative elements leads to the development of covalent, localized, and directional 2*c*-2*e* bonds or lone pairs. Such anions can either be isolated (clusters, chains) or polymeric (2D layers, 3D networks), and homo- or heteroatomic. The connectivity of the as formed polyanions can then be explained by the (8–N) rule and often structures of the corresponding pseudoelement are adopted. However, which kind of anionic substructure is formed depends not only on the number of electrons available for bonding but also on the type of cation that is present.

The term Zintl ion dates back to the observation that some post-transition elements could be reduced in liquid ammonia by alkali metals by Johannis in 1891.[37, 38] The characteristic blue solution of Na turned green in the presence of excess Pb. $NaPb_4$ and $NaPb_2$ were precipitated from this solution. Zintl published results on potentiometric titrations of sodium solutions in liquid ammonia by salts of post transition elements (e.g. Sn, Pb, Sb, Bi) which lead to identification of numerous homoatomic polyanions. In the case of Pb the potentiometric and conductimetric titrations referred to the reaction $(4+2x)Na + xPbI_2 \rightarrow Na_4Pb_x + (2x)NaI$. However, despite this example, Zintl phases not necessarily dissolve in polar solvents, since this might only depend on the right choice of the solvent.

Another very illustrating example are the $AeSi_2$ phases (Ae = Ca, Sr, Ba). The Ae metal donates its two valence electrons and forms Si^-, which becomes a pseudoelement with five VE and three bonds to neighboring Si^-. However, the resulting anionic substructure cannot be foretold. $CaSi_2$[39] contains 2D corrugated layers of hexagons, which are reminiscent of gray arsenic. In $BaSi_2$[40] white phosphorus like $\{Si_4\}^{4-}$ tetrahedra are formed and finally in $SrSi_2$[41] the Si atoms form a three dimensional network with trigonal planar coordinated three bonded Si, which has no correspondence to an element structure of the pnictide group. This example shows that the role of the active metal is more than just providing electrons.

In Zintl phases the electronic states (bonding and nonbonding), that are localized at the anionic part, are fully occupied and lead to a gap opening, the cationic states are usually well above the Fermi level (Figure 1.1). As a first extension of the Zintl concept, lithium rich silicides show significant lithium contributions in the occupied orbitals.[42]

Summarizing, Zintl phases are salt like valence compounds (without a homogeneity range), closed shell, semiconducting, diamagnetic (or weakly temperature independent paramagnetic, RE containing Zintl phases are paramagnetic), and are electronically intermediate to insulating salts and pure intermetallics, which are electronic conductors. In addition to the often neglected size effects of the cations, another major point of criticism of the Zintl concept is the assumption of complete charge transfer from the cations to the anions.

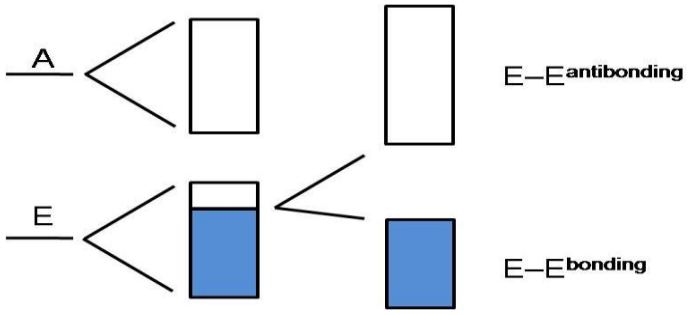

***Figure 1.1*. Schematic band diagram for a binary Zintl phase AE.[43] Blue areas represent occupied (filled) bands. Left: Cations (A) fill the E states to an extent not sufficient to achieve a closed shell, so E-E bonding occurs (right). Orbitals near the top of the E band are pushed upwards in energy due to antibonding combinations.**

Non-classical Zintl Phases If the polyanions are deltahedral clusters the simple (8–N) rule cannot be applied. These clusters mark the transition to polar intermetallic compounds where polyanionic bonding cannot be described by classical valence rules. These phases can be explained by extending the Zintl concept by Wade's rules. The term 'cluster' designates aggregates of at least three metal atoms forming three metal-metal bonds (metal triangle) and can figuratively be understood as frozen oxidation states of elements.[44] Understanding of the chemical bonds within deltahedral clusters was promoted in the early 1950s by crystallographic studies and semi-empirical molecular orbital calculations. Using the MO-LCAO method, Longuet-Higgins analyzed the stability of a regular boron icosahedron and also predicted the existence of the $\{B_{12}H_{12}\}^{2-}$ boron hydride.[45, 46] Bonding therein cannot be described in terms of localized covalent bonds, meaning there are not enough electrons to form classical 2*c*-2*e* bonds along each edge of the polyhedron. Results of MO calculations indicate that the icosahedron is stabilized with 26 skeletal electrons, while 24 *exo*-electrons are involved in B-H *exo*-bonding, so the polyhedral electron count is 50 for the icosahedron. These findings feature the polyhedral skeleton electron pair theory that was later developed by Wade,[47, 48] Mingos,[49] Williams,[50] and Rudolph.[51] A molecular orbital diagram for octahedral *closo*-$\{B_6H_6\}^{2-}$ is given in Figure 1.2. A graph theory derived approach was reported by King and describes the bonding topology of metal clusters by a graph in which the vertices correspond to atoms or orbitals participating in the relevant bonding and the edges correspond to bonding relationships.[52-56] Recently, Jemmis et al.[57-59] have extended Wade's rules to explain the electronic requirements of condensed polyhedral boranes.

In their *mno* rule *m* + *n* + *o* electrons pairs are necessary for a multideltahedral borane system to be stable, with *m* the number of polyhedra, *n* the number of vertices, and *o* the number of single vertex sharing connections. The applicability of this rule has been demonstrated for a variety of boranes and more recently for {(19b)-Ga_{11}} in $Li_9K_3Ga_{28.8}$,[60, 61] {$Ga_{11}LiGa_{11}$} in Li_5Ga_9,[62] and {$(Ga,Zn)_{29}$} in $Li_{38}Zn_{34}Ga_{66.9}$.[63] Of course Wade's rules are a special case of the *mno* rule, with *m* = 1 and *o* = 0 (see Chapter 4.6).

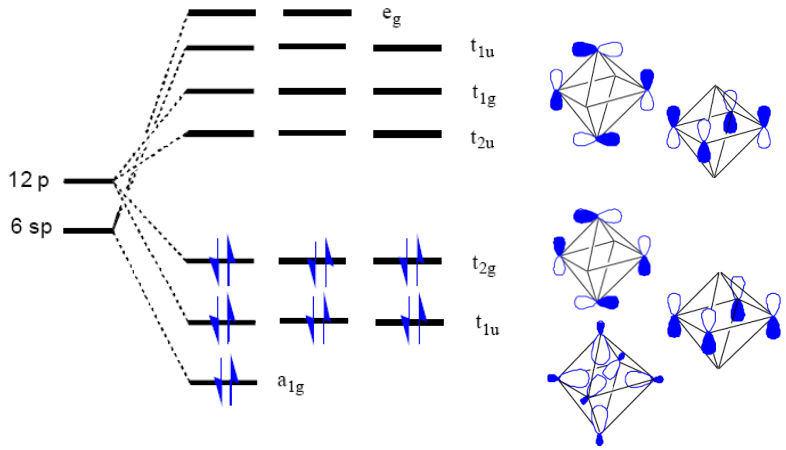

***Figure 1.2*. MO diagram of *closo*-$\{B_6H_6\}^{2-}$ adapted from ref. [64]. The 14 skeletal electrons occupy all seven bonding molecular orbitals. Each B atoms is *sp* hybridized. The outwards pointing *sp* hybrids (not shown) are used to bond the H atoms and lie at lower energies. In the t_{1u} orbital the two inward pointing *sp* atomic orbitals are not shown.**

The term ***Metallic Zintl phase*** is not being used uniformly. In general in such metallic salts, the connectivity of the atoms forming the anionic substructure can be well rationalized by the (8–N) rule. However, on the one hand few extra electrons are present that occupy the conduction band. Those extra electrons are often delocalized across the whole anion or in cation–anion bonding states. The appropriate term 'submerged continent' by Nesper[42] can be understood as polyanions buried in a sea of electrons. Prominent examples are the phases A_5Pn_4 (A = K, Rb, Cs; Pn = As, Sb, Bi),[65] K_3Bi_2,[66] $Ba_7Ga_4Sb_9$,[67] $Ba_3Sn_4As_6$.[68] On the other hand metallic conduction can also be obtained by electron deficiency in polar intermetallics at the Zintl boundary, such as Sr_3In_5,[69] leading to an open and incompletely filled valence band. However, for both cases a gap in the proximity of E_F in the DOS should be present.

1.1.2 Polar Intermetallics

In contrast to Zintl phases polar intermetallics are metallic conductors. The structures can be explained by the (8–N) or by Wade's rules but additional contacts, such as metallic electrons (with coordination numbers of the constituting atoms exceeding four) or bonding cation–anion interactions, are often present. Additionally, in order to explain some puzzling bonding situations, new models such as fractional bonds[70, 71] and hypervalent multicenter bonding were introduced. In this context, many polyanionic networks built up by heavy *p*-block elements show an unusual local coordination e.g. linear chains, 2D square nets, and several atom wide ribbons constructed from the latter. Such hypervalent geometries have been reviewed by Hoffmann et al. for electron rich Sb. The connection to the bonding in hypervalent molecules[72, 73] can be understood in similar terms as the relation between the Zintl concept and the octet rule for molecules.

Many polar intermetallics consist of 3D networks of deltahedral clusters. For example the unit cell of KGa_3[74] contains two $\{Ga_8\}$ clusters (triangle dodecahedra) and four isolated (4b)-Ga atoms. The clusters are *exo*-bonded; four bonds are established to neighboring clusters and four bonds to the (4b)-Ga atoms. The clusters are of *closo*-type and according to Wade's rules require 18 electrons for skeletal bonding. Considering the eight *exo*-bonds the clusters have to be formulated as $\{Ga_8\}^{2-}$, the bridging Ga atoms as Ga^{1-}, which results in $(K^+)_3(Ga_8)^{2-}Ga^-$. Although the compound is electronically balanced it is a poor metallic conductor. This difference arises from the weaker interactions within the polyanionic units between metallic *p* block elements compared to the more electronegative semi/metametals in the Zintl phases. Additionally multicenter bonding creates smaller bonding-antibonding orbital splitting compared to regular 2*c*-2*e* bonding. However, many exceptions exist, where calculations of fused and linked deltahedral clusters indeed lead to the opening of a considerable band gap.[75] In general, the electronic structure of polar intermetallics is very similar to that of Zintl phases. The main difference is the weaker bonding within the anionic substructure, which does not lead to an opening of a band gap at the Fermi level. Furthermore, in polar intermetallics the cation states start to significantly contribute to the occupied bands and in phases with deviations from the optimum electron count other factors, such as size and packing effects become more and more important for the stabilization of the structure..

1.2 The Element Sn in intermetallic Compounds

The tetrel elements (C, Si, Ge, Sn, Pb) show the biggest diversity among each other in terms of chemical and physical properties compared to the other groups of the periodic system. The line separating the *p* block elements in metals and non metals crosses this group right in the middle meaning a strong increase of metallic character from C to Pb. Sn in particular is interesting due to its unique physical and chemical properties. First of all the metametal Sn exists in two modifications, gray *α*-Sn and white *β*-Sn. Under standard conditions the tetragonal metallic *β*-form (space group $I4_1/amd$, ρ = 7.29 g·cm^{-3}, *d*(Sn–Sn) = 3.02, 3.18 Å) exists with metallic luster. At 13.2 °C the phase transition takes place through a symmetry relation to the semimetallic *α*-modification with cubic diamond structure (space group $Fd\bar{3}m$, ρ = 5.77 g·cm^{-3}, *d*(Sn-Sn) = 2.81 Å). This transition is known as tin pest and can destroy a metallic work piece at low temperatures. A peculiar noise, the tin cry, can be noticed when bending a tin bar. This is caused from friction of crystallites in the *β*-modification, which also reflects the high ductility and softness of this metal. For technical applications tin is alloyed with other metals e.g. Cu–Sn bronzes, or in britannia metal as Sn–Sb–Cu. In intermetallic compounds with alkali, alkaline earth, (rare earth and actinoids) the low melting point (231 °C), high boiling point (2687 °C), and good wettability for many metals are a big advantage for syntheses. Tin flux techniques are also used. Besides the self-flux technique for the growth of Sn rich stannides, liquid tin is widely used for the growth of other crystals. Jolibois used liquid tin for the growth of NiP_3 crystals.[76] Silica tubes, ceramic (Al_2O_3, ZrO_2), Nb and Ta crucibles are suitable containers for tin flux reactions, although unwanted Nb_3Sn can form at ~1000 °C. The excess tin can easily be removed with hydrochloric acid, provided that the binary or ternary target compound is stable under these conditions. Two compounds of this thesis, Na_2ZnSn_5 (Chapter 4.2) and $Sr_3Sn_{4-x}Bi_{1+x}$ (Chapter 5.2), were prepared under Sn flux conditions. A more detailed overview on the tin flux technique is provided in ref. [77].

Due to the ability to establish covalent and/or metallic bonds tin containing intermetallics show a great structural diversity, especially in combination with alkali and alkaline-earth metals. Therefore tin is the ideal element for studying structure–property relationships in electron-precise Zintl phases as well as their structural and chemical bond changes by partial substitution of atoms.

A detailed review on the synthesized A/Ae stannides, transition metal stannides, rare earth based ternary stannides, and uranium and thorium based stannides would go beyond this thesis and are competently covered by Fässler[78, 79], Pöttgen[80], and Evans.[81] A short overview of the binary Na stannides is provided in Chapter 4.1.

To outline a few technical applications the binary transition metal stannides such as Ni_3Sn_4, Cu_6Sn_5, AuSn, FeSn and Ni_3Sn_2[82, 83] are listed.[80] They are used at the interface between solder and contacts of electronic devices.[84, 85] In former times cans were coated with tin to prevent corrosion. Nowadays such coatings consist of polymers. Transition metal stannides are also important catalytical active materials in heterogenous catalysis.[86-88] Pt_3Sn and Pt_2Sn have been discussed for surface alloys[89] and model systems for cyclohexane to benzene conversion.[88] Co/Sn and Ru/Sn catalysts are used for large scale production of fatty alcohols.[90] Another important field of tin based intermetallic compounds and alloys is represented by new anode materials for lithium ion batteries, since such materials exhibit high specific capacities. In this context Cu_6Sn_5 has widely been studied.[91-93] The Mn-based stannides, such as $TiMnSn_4$, are interesting magnetic materials.[94] ZrNiSn adopts the Half-Heusler structure and $ZrNi_2Sn$ crystallizes in the Heusler structure. ZrNiSn and related materials have been reinvestigated for their thermoelectric properties.[95-97]

1.3 References

[1] R. Dronskowski, *Computational Chemistry of Solid State Materials, Wiley-VCH* **2005**.
[2] S. Samson, *Acta Crystallogr.* **1965**, *19*, 401.
[3] D. Shechtman, I. Blech, D. Gratias, J. W. Cahn, *Phys. Rev. Lett.* **1984**, *53*, 1951.
[4] F. Laves, H. Witte, *Metallwirtschaft* **1935**, *14*, 645.
[5] F. Laves, H. Witte, *Metallwirtschaft* **1936**, *15*, 840.
[6] V. M. Goldschmidt, *J. Chem. Soc. (London)* **1937**, *140*, 655.
[7] H. G. Grimm, A. Sommerfeld, *Z. Phys.* **1926**, *36*, 36.
[8] K. Fajans, *Z. Phys.* **1915**, *16*, 456.
[9] K. Fajans, *Z. Phys.* **1924**, *25*, 596.
[10] K. Fajans, H. G. Grimm, *Z. Phys.* **1920**, *2*, 299.
[11] L. Pauling, *J. Am. Chem. Soc.* **1929**, *51*, 1010.
[12] L. C. Allen, J. F. Capitani, G. A. Kolks, G. D. Sproul, *J. Mol. Struct.* **1993**, *300*, 647.
[13] J. A. A. Ketelaar, *Chemical Constitution, An Introduction to the Theory of the Chemical Bond, 2nd Ed., Elsevier, New York* **1958**.
[14] A. E. van Arkel, *Molecules and Crystals in Inorganic Chemistry, New York* **1956**.
[15] E. Mooser, *Acta Crystallogr.* **1959**, *12*, 1015.
[16] J. C. Phillips, J. A. van Vechten, *Phys. Rev. Lett.* **1969**, *22*, 705.
[17] D. G. Pettifor, *Solid State Commun.* **1984**, *51*, 31.
[18] D. G. Pettifor, *Solid State Phys.* **1986**, *19*, 285.
[19] F. C. Frank, J. S. Kasper, *Acta Crystallogr.* **1958**, *11*, 184.
[20] F. C. Frank, J. S. Kasper, *Acta Crystallogr.* **1959**, *12*, 483.

[21] W. Hume-Rothery, *J. Inst. Met.* **1926**, *35*, 295.
[22] O. Gourdon, D. Gout, G. J. Miller, *Encyclopedia of Condensed Matter Physics* **2005**, 409.
[23] W. P. Anderson, J. K. Burdett, P. T. Czech, *J. Am. Chem. Soc.* **1994**, *116*, 8808.
[24] V. A. Finkel, E. A. Pushkarev, *Z. Phys.* **1985**, *60*, 387.
[25] V. A. Finkel, E. A. Pushkarev, *Metallofizika* **1973**, *46*, 90.
[26] K. H. J. Buschow, A. S. van der Goot, *J. Less -Comm. Met.* **1968**, *14*, 323.
[27] P. Mueller, *Z. Metallkunde* **1977**, *68*, 421.
[28] A. Kjekshus, T. Rakke, *Acta Chem. Scan.* **1974**, *28*, 99.
[29] F. Heusler, *Verhandl. d. Deutsch. Physik* **1903**, *5*, 219.
[30] E. Zintl, W. Dullenkopf, *Z. Phys. Chem.* **1932**, *B 16*, 195.
[31] N. E. Christensen, *Phys. Rev.* **1985**, *32 B*, 207.
[32] P. C. Schmidt, *Struct. Bonding* **1987**, *65*, 91.
[33] E. Zintl, G. Brauer, *Z. Phys. Chem.* **1933**, *B 29*, 245.
[34] E. Zintl, J. Gobeau, W. Dullenkopf, *J. Phys. Chem.* **1931**, *A 154*, 1.
[35] E. Zintl, A. Harder, *J. Phys. Chem.* **1931**, *A 154*, 47.
[36] E. Zintl, H. Kaiser, *Z. Anorg. Allg. Chem.* **1933**, *211*, 113.
[37] A. Johannis, *C. R. Hebd. Seances Acad. Sci.* **1891**, *113*, 795.
[38] A. Johannis, *C. R. Hebd. Seances Acad. Sci.* **1892**, *114*, 587.
[39] J. Boehm, O. Hassel, *Z. Anorg. Allg. Chem.* **1927**, *160*, 152.
[40] K. H. Janzon, H. Schäfer, A. Weiss, *Z. Anorg. Allg. Chem.* **1970**, *372*, 87.
[41] K. H. Janzon, H. Schäfer, A. Weiss, *Angew. Chem.* **1965**, *77*, 258.
[42] R. Nesper, *Prog. Solid State Chem* **1990**, *20*, 1.
[43] S. M. Kauzlarich, *Ed., Chemistry, Structure and Bonding of Zintl Phases and Ions, VCH* **1996**, 62.
[44] H. G. von Schnering, *Angew. Chem.* **1981**, *93*, 44.
[45] H. C. Longuet-Higgins, M. d. V. Roberts, *Proc. Roy. Soc.* **1954**, *A 224*, 336.
[46] H. C. Longuet-Higgins, M. d. V. Roberts, *Proc. Roy. Soc.* **1955**, *A 230*, 110.
[47] K. Wade, *J. Chem. Soc. D* **1971**, 792.
[48] K. Wade, *Adv. Inorg. Chem. Radiochem.* **1976**, *18*, 1.
[49] D. M. P. Mingos, *Nature Phys. Chem.* **1972**, *236*, 99.
[50] R. E. Williams, *Inorg. Chem.* **1971**, *10*, 210.
[51] R. W. Rudolph, *Acc. Chem. Res.* **1976**, *9*, 446.
[52] R. B. King, *Inorg. Chim. Acta* **1982**, *57*, 79.
[53] R. B. King, *Chemical Applications of Topology and Graph Theory; King, R. B., Ed. Elsevier, Amsterdam* **1983**, 99.
[54] R. B. King, *J. Math. Chem.* **1987**, *1*, 249.
[55] R. B. King, *Inorg. Chem.* **1988**, *27*, 1941.
[56] R. B. King, D. H. Rouvray, *J. Am. Chem. Soc.* **1977**, *99*, 7834.
[57] M. M. Balakrishnarajan, E. D. Jemmis, *J. Am. Chem. Soc.* **2000**, *122*, 4516.
[58] E. D. Jemmis, M. M. Balakrishnarajan, P. D. Pancharatna, *J. Am. Chem. Soc.* **2001**, *123*, 4313.
[59] E. D. Jemmis, M. M. Balakrishnarajan, P. D. Pancharatna, *Chem. Rev.* **2002**, *102*, 93.
[60] C. Belin, *J. Solid State Chem.* **1983**, *50*, 225.
[61] M. Charbonnel, A. Marteghetti, C. Belin, *Inorg. Chem.* **2000**, *39*, 1684.
[62] M. Tillard-Charbonnel, N. Chouaibi, C. Belin, J. Lapasset, *Eur. J. Sol. State Inorg. Chem.* **1992**, *29*, 347.
[63] E. D. Jemmis, M. M. Balkarishnarajan, *J. Am. Chem. Soc.* **2001**, *123*, 4324.
[64] U. Müller, *Anorganische Strukturchemie, Teubner Stuttgart* **1996**.
[65] F. Gascoin, S. C. Sevov, *Inorg. Chem.* **2001**, *40*, 5177.
[66] F. Gascoin, S. C. Sevov, *J. Am. Chem. Soc.* **2000**, *122*, 10251.
[67] P. Alemany, M. Llunell, E. Canadell, *Inorg. Chem.* **2006**, *45*, 7235.
[68] R. Lam, A. Mar, *Solid State Sci.* **2001**, *3*, 503.
[69] D. K. Seo, J. D. Corbett, *J. Am. Chem. Soc.* **2001**, *123*, 4512.

[70] R. E. Rundle, *J. Am. Chem. Soc.* **1947**, *69*, 1327.
[71] R. E. Rundle, *J. Chem. Phys.* **1949**, *17*, 671.
[72] G. A. Papoian, R. Hoffmann, *Angew. Chem.* **2000**, *112*, 2500.
[73] G. A. Papoian, R. Hoffmann, *J. Am. Chem. Soc.* **2001**, *123*, 6600.
[74] C. Belin, R. G. Ling, *C. R. Acad. Sci. Ser. B* **1982**, *294*, 1083.
[75] J. Burdett, E. Canadell, *J. Am. Chem. Soc.* **1990**, *112*, 7207.
[76] P. Jolibois, *C. R. Hebd. Seances Acad. Sci.* **1910**, *150*, 106.
[77] M. G. Kanatzidis, R. Pöttgen, W. Jeitschko, *Angew. Chem.* **2005**, *117*, 7156.
[78] T. F. Fässler, *Z. Anorg. Allg. Chem.* **2006**, *632*, 1125.
[79] T. F. Fässler, S. Hoffmann, *Z. Kristallogr.* **1999**, *214*, 722.
[80] R. Pöttgen, *Z. Naturforsch.* **2006**, *61 B*, 677.
[81] C. J. Evans, *The Tin Handbook, Tin Handbook 3rd Ed., Hüthig, Heidelberg* **1994**.
[82] Y. C. Hsu, Y. M. Huang, C. Chen, H. Wang, *J. Alloys Compd.* **2006**, in press.
[83] C. Luef, A. Paul, H. Flandorfer, A. Kodentsov, H. Ipser, *J. Alloys Compd.* **2005**, *391*, 67.
[84] G. Gosh, *J. Electr. Mater.* **1999**, *28*, 1238.
[85] G. Y. Li, Y. C. Chan, *Journal of Electronic Packaging* **2002**, *124*, 305.
[86] T. F. Fässler, *225th ACS National meeting, New Orleans, LA, Abstract INOR-093* **2003**.
[87] M. Rehbein, R. D. Fischer, M. Epple, *Thermochim. Acta* **2002**, *382*, 143.
[88] C. Xu, Y. L. Tsai, B. E. Koel, *J. Phys. Chem.* **1994**, *98*, 585.
[89] M. T. Paffett, R. G. Windham, *Surf. Sci.* **1989**, *208*, 34.
[90] Y. Pouilloux, F. Autin, A. Piccirilli, C. Guimon, J. Barrault, *Appl. Catal. A: General* **1998**, *169*, 65.
[91] K. D. Kepler, J. T. Vaughey, M. M. Thackeray, *Electrochem. Solid-State Lett.* **1999**, *2*, 307.
[92] D. Larcher, L. Y. Beaulieu, D. D. MacNeil, J. R. Dahn, *J. Electrochem. Soc.* **2000**, *147*, 1658.
[93] M. M. Thackeray, J. T. Vaughey, A. J. Kahaian, K. D. Kepler, R. Benedek, *Electrochem. Commun.* **1999**, *1*, 111.
[94] A. V. Tkachuk, L. G. Akselrud, Y. V. Stadnyk, O. I. Bodak, *J. Alloys Compd.* **2000**, *312*, 284.
[95] S. Katsuyama, H. Matsushima, M. Ito, *J. Alloys Compd.* **2004**, *385*, 232.
[96] J. Tobola, J. Pierre, S. Kaprzyk, R. V. Skolozdra, M. A. Kouacou, *J. Magn. Mater.* **1996**, *159*, 192.
[97] C. Uher, J. Yang, S. Hu, D. T. Morelli, G. P. Meisner, *Phys. Rev.* **1999**, *59 B*, 8615.

2 Scope and Outline of this Work

"...It is the wonder and excitement of finding the unprecedented and unimaginable that makes the research enjoyable, even exhilarating, and worthwhile."

J. D. Corbett, *Inorg. Chem.* **2000**, *39*, 5178.

The present thesis aims to investigate electronic effects and stability ranges of Zintl phases and borderline intermetallic phases. Transitions from electron balanced Zintl phases to pure intermetallics are almost continuous in terms of chemical bonding and electronic properties and have many unprecedented structures to offer at their borderline. The applied strategies were either tuning the valence electron concentration (VEC) by successive partial substitution with electron richer or electron poorer elements, or keeping the VEC constant and studying the size and polarizing effects of the electropositive metal. In this context a series of new ternary and binary phases have been discovered. The obtained compounds were characterized by X-ray diffraction methods, EDX, DTA, and SQUID measurements. The electronic structures were calculated, whenever possible.

Firstly, partial Zn for Sn substitutions in the Sn-rich binary system Na_xSn_y ($x < y$) were performed (Chapter 4) in order to study the impact of the electronic factor. At the same time these reactions represented the exploration of the *hitherto* unreported ternary intermetallic compounds in the system Na–Zn–Sn. The Zn for Sn substitution decreases the valence electron concentration in the Sn network and at balanced Zn : Sn ratio this should result in electron deficient structure elements reminiscent of pure triel binaries. At unbalanced ratios, meaning VEC < 4 or ≥ 4, typical electron deficient or structures reminiscent of the electron rich stannides were expected. Therefore, this system was explored also by changing the Na ratio and, with K, offering a second kind of cation. Apart from the rich structure chemistry the nature of Zn–Sn interactions was investigated.

Secondly, in the metallic Zintl phase Sr_3Sn_5 partial substitutions by electron richer Bi and electron poorer Tr (Tr = In, Tl) was studied (Chapter 5.2 and 5.3). The idea was to introduce a triggering factor that changes the electronic fluctuations in the Zintl polyanion $\{Sn_5\}^{6-}$. Whereas in the experiments with In and Tl formation of closed shell compounds by removing electrons from destabilizing states was anticipated, the Bi substitution was carried out in order to combine the covalent nature of Sn with the special metallic property of Bi.

Thirdly, the partial cation for cation substitutions in the phases Sr_2Bi_3 and Sr_3Sn_5 (Chapter 5.1 and 5.4) aimed to investigate the often neglected size and bonding effects of the electropositive metal and their effects on the material's properties. Stepwise Ba substitution in Sr_2Bi_3 was carried out in order to study changes in the anionic substructure and the structure-property relationship. This systematic work also aimed to clarify the puzzling bonding situation within the Bi framework. In the Na for Sr substitution of Sr_3Sn_5 the phase was allowed to optimize lattice packing by offering two kinds of cations. Such attempts have proven to result in new covalent Sn substructures.

Lastly, some fully substituted binary 'end members', which were not known before, became accessible (Chapters 6.2 and 6.3). In this context also the importance of flux conditions, such as Tl flux, for the formation of new binaries (Chapter 6.1), was observed.

In Figure 2.1 all substitution experiments, as covered in this thesis, with corresponding starting stoichiometries and outcomes are comprised.

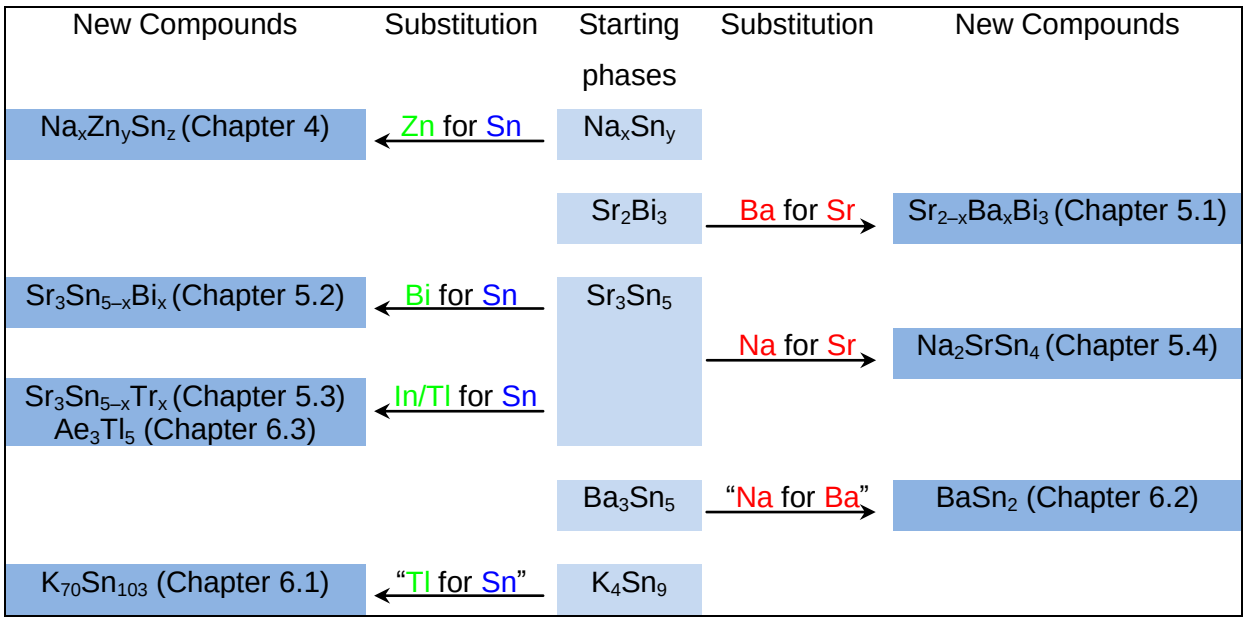

***Figure 2.1*. Overview of the experiments and results covered by this thesis.**

3 Experimental and Analytical Methods

3.1 Synthesis

All chemicals used in the syntheses were commercially obtained and stored in an Ar (4.6, Fa. Messer Griesheim) filled glovebox (H_2O and O_2 levels < 0.1 ppm; MB 20 G, MBraun). Some data are given in Table 3.1. The alkali metals were washed in hexane, put into a Schlenk tube and dried under vacuum. As for Zn, the element was purified by distilling commercially obtained pieces in an evacuated silica ampoule at 600 °C for 12 hours. Further details of this procedure can be found in the literature.[1] Before usage, all metals were freed from surface oxide layers with a knife or a wire cutter.

Table 3.1: **Starting chemicals, their purities, source, shape, and hazard symbols.**

Element	Purity	Manufacturer	Shape	Hazard symbol
Na	99%	Merck	rod under paraffin oil	F, C
K	99%	Merck	rod under paraffin oil	F, C
Ca	99.5%	Riedel-de-haän	chips	F
Sr	98+%	Chempur	pieces	F, Xi
Ba	99.3%	Chempur	rod	F, Xi
Zn	99.99%	Merck	rod	F, N
In	99.99%	Aldrich	granules	F
Tl	99.95%	ABCR	granules	T+, N
Sn	99.99%	Merck	granules	-

Due to their chemical resistivity, high melting points, and reluctance to undergo reactions with the relevant elements used in this work, welded niobium and tantalum ampoules were used as reaction containers. The crucible material is dependent on the elements used for synthesis. Stable binary Nb or Ta compounds have to be checked in the phase diagrams before carrying out a synthesis. For instance, Ta can react with Ge, Nb can react with Zn, and little amounts of Nb_3Sn can form by reaction of the crucible material with elemental Sn. Additionally, the size of the crucible may also affect the success of a reaction. For instance, elements with low melting and boiling points have high vapor pressures and can cause bursting if the volume of the ampoule is too small. For preparation of the crucibles, pieces were cut from commercially obtained Nb/Ta tubings (2000 × 10 mm, wall thickness 0.5 mm, Plansee), and closed by arc welding (W electrode, Lorch Handy S 200, Schweissinverter) at one side under lowered inert gas (Ar) pressure (dried 4.6 Ar over BTS catalyst, P_2O_5, and silica gel) in a custom designed welding chamber.

After ultrasonication in 6 molar HNO_3 and detergent they were dried and stored in a drying oven (Binder).

For synthesis, the as prepared crucibles were transferred into the glovebox and loaded with the elements. The ampoules were sealed by arc welding. This time the crucible holder, a Cu block, was cooled with H_2O to prevent prior reactions or even evaporation of the elements. Subsequently, the ampoules were weighted, which is especially necessary when doing multiple syntheses and to investigate loss of material by leaking or burst crucibles. In a typical heating procedure the as set ampoules were transferred into a silica tube (melting point ~1200 °C) which was alternately evacuated (down to 2×10^{-2} mbar), flooded with Ar (three times), and placed into a tubular oven (HTM Reetz GmbH, Berlin; Model: LOBA 1200-400-600; T_{max}: 1200 °C; interior diameter: 45 mm, length 300 mm, length of uniform temperature zone: 200 mm) which is equipped with a temperature regulator (Eurotherm Deutschland GmbH). Then a temperature profile could be applied to the reaction mixtures. After the reaction, the crucibles were opened in the glovebox and the products stored there in glass bottles. Further details about the handling of inert crucibles materials have been summarized by Corbett.[2]

An alternative preparation method, e.g. for $Sr_3Sn_{3.36}Bi_{1.64(3)}$ (see Chapter 5.2), was applied when handling a flux system. In this case the elements were filled into a stainless steel ampoule which already contained coarse glass pieces and a glass wool (acting as a filter) plug. Afterwards, the container was placed into a muffle furnace (M110, Heraeus) with the reacting metals at the bottom. After reaction, the flux metal was removed by centrifuging the hot steel crucible upside down in a centrifuge (Model: Heraeus Megafuge 1.0) at 3000 rpm for several minutes. In general, the applied temperature profile (which can include quenching to various temperatures e.g. room temperature, ice water, or liquid nitrogen, slow cooling rates, multiple heating/cooling cycles, and long annealing periods) is strongly dependent on the elements reacting, possibly formed byproducts, and the nature of the target compound. Therefore, it is essential to accommodate the temperature treatments to results from X-ray diffraction experiments and thermal analyses.

3.2 X-ray Diffraction Experiments

X-rays are generated by accelerating electrons, emitted from a heated cathode (W), in vacuum at high voltage (~50 kV) targeting a cooled anti-cathode (which can also be a rotating anode) made of different elements (Cu, Mo, Ag, etc). The emitted spectrum consists of the Bremsstrahlung (caused by loss of E_{kin} of the electrons) and characteristic peaks, such as Mo-$K_{\alpha1}$ and Mo-$K_{\alpha2}$. Thus, the spectrum has to be monochromated first and then focused, via a collimator, onto the sample. When these X-rays interfere with the crystalline sample, which is either a powder (many small single-crystals) or a single-crystal, a diffraction pattern, i.e. a picture of the reciprocal space is generated. The latter is related to the real space by a Fourier transformation. In a typical X-ray experiment of a powder or a single-crystal, two kinds of information are collected: the position and the intensity of reflections. Based on the prominent Bragg equation the positions of reflections (angles) are determined by the corresponding net-planes distances in the crystal(s). The conjugated complex product of the structure factor (F_{hkl}) determines the reflection intensity. It is calculated from diffraction factors f_j of single atoms in the unit cell and their positions.

3.2.1 Powder X-ray Diffraction

The outcome of all reactions was monitored by powder X-ray diffraction measurements on a STOE STADI P (Fa. STOE, Darmstadt) which was operating at 30 mA / 50 kV with Ge monochromated Cu-$K_{\alpha1}$ (λ = 1.54056 Å) radiation. All measurements were carried out at room temperature. For data collection two types of detectors were installed. An image plate detector was used for good diffracting samples and short measuring times (up to 120 min). The majority of the samples was analyzed with a linear PSD detector with higher angular resolution and intensity. The powder diagrams were usually collected over a 2θ range of 10° - 80° with step widths of 1.5° and lasted for 3 to 20 h. Powder samples could be prepared either on transmission sample holders by fixing the finely ground sample on Scotch tape or in capillaries and measuring in Debye-Scherrer mode. Since all compounds reported in this thesis are sensitive to air the latter technique was applied throughout. For preparation of capillary samples the solids were ground in an agate mortar to a homogeneous powder. Too much pressure must not be used when grinding since it can decrease the crystal size. For highly absorbing samples the powder was diluted with dried silica powder and in all cases diamond powder (~25 µm) was added as

an internal standard. The powder was then filled into a capillary (Hilgenberg, external diameter 0.3 mm, wall thickness 0.01 mm, length 80 mm), which was afterwards sealed with a hot tungsten wire. Before starting a full measurement, a short measurement (~10 min) was carried out in order to check for acceptable intensities. When measuring highly absorbing samples this pre-measurement should at least show the diamond reflections to ensure sufficient dilution. The obtained powder diagrams were indexed and compared with either calculated diagrams from single-crystal structure solutions or with relevant structures from databases, such as ICSD[3] or ICDD. The latter is implemented in the STOE software WINXPOW.[4]

3.2.2 Single-Crystal X-ray Diffraction

Structure determinations of new compounds were carried out on single-crystals. They were selected and checked for singularity under the microscope. Intergrown crystals were separated by breaking off small pieces. The crystals were fixed on glass capillaries with silicon grease and inserted into bigger capillaries (0.3 mm MARK-Röhrchen, Hilgenberg) which were subsequently sealed with a hot tungsten wire (MaxWax, Waxpen). Data collections were carried out on a STOE IPDS II equipped with an image plate detector (diameter: 340 mm, $2\theta_{max}$: 77°) and an Enraf Nonius κ-CCD, both at the window of a rotating anode (Nonius, FR591). Most crystals were measured on an Oxford Xcalibur3 diffractometer which was equipped with a CCD detector and operated with graphite monochromated Mo-K_α radiation (λ = 0.71073 Å) at 40 mA / 50 kV. Absorption corrections were either performed empirically[5] or numerically.[6, 7]

The structures were solved by direct or *Patterson* methods and refined on F^2 with the software SHELXTL.[8] Graphical presentations of the crystal structures were generated with the program Diamond3.[9] Some important definitions and equations used for crystallography are given in Table 3.2 and are explained in the following. From structure solution only a partial set of atoms in the unit cell is generated. Difference maps help to reveal positive peaks where an insufficient amount of electron density has been included (missing atoms) and negative holes where too much electron density (a too heavy atom) has been included in the model. Structure refinements are usually based on the least squares method and on the structure factors F or the intensities F^2. Whereas for refinements based on F weak data is problematic, refinements based on F^2 can utilize all data.

The weights w used in least square refinement represent the relative influence an observation should have on the results. Weights include the term representing the statistical error of the measured data. Additionally, systematic errors, such as improper absorption correction or secondary extinction problems are present. In the weighting scheme used in SHELXL[8, 10-13] the values a and b are chosen to give even distribution of the variances across all groups of data based on the relative intensities. To judge how well the model fits the observed data the discrepancy factors R_1 and wR_2 are calculated. wR_2 is a weighted R factor based on all data. The R_1 factor is based on F. The goodness of fit shows how reliable the standard deviations of the positional and displacement parameters of the atoms really are. Standard deviations of the atomic parameters should be multiplied by the GooF to give more realistic values. The GooF is strongly influenced by the weighting scheme, thus the latter is modified to force the GooF to have a value near one. Upon refinement many other factors, such as large correlations, constraints (that can be explicitly set parameters e.g. *exyz*, *eadp*, which are not refined or can be related to other variables and are not allowed to refine independently), restrains (additional information e.g. equalizing bond lengths), oscillation/damping, and anomalous scattering have to be considered. A common problem in structure refinement is the presence of atomic disorder (vacancies, mixed occupancies, discrete positional disorder e.g. split positions, continuous positional disorder), twinning/drilling formation, and modulated structures.

Table 3.2: **Important equations and definitions used for structure solution and refinement.[14, 15]**

Electron density	$\rho_{XYZ} = \frac{1}{V}\sum_{hkl} F_{hkl} \cdot \exp\left(-i2\pi\left(hX + kY + lZ\right)\right); h,k,l$ Miller indices
Structure factor	$F_{hkl} = \int_{cell} \rho_{XYZ} \cdot \exp\left(2\pi i\left(hx + ky + lz\right)\right)dV$; h,k,l Miller indices $F_c = \sum_i f_i\left[\cos 2\pi\left(hx_i + ky_i + lz_i\right) + i\sin 2\pi\left(hx_i + ky_i + lz_i\right)\right]$; h,k,l Miller indices
Error	$\Delta_1 = \left\|\|F_o\| - \|F_c\|\right\|$ (based on Structure factors) and $\Delta_2 = \left\|F_o^2 - F_c^2\right\|$ (based on intensities) F_o: measured structure amplitude F_c: calculated structure amplitude
Goodness of Fit	$S = \sqrt{\frac{\sum_{hkl} w\Delta_2^2}{m-n}}$ m: number of reflections; n: number of parameters

R_{int} and R_σ	$R_{\text{int}} = \frac{\sum_{hkl} F_o^2 - \overline{F_o^2}}{\sum_{hkl} F_o^2}$; $R_\sigma = \frac{\sum_{hkl} \sigma(F_o^2)}{\sum_{hkl} F_o^2}$
Conventional *R*-value and weighted *R*-value	$R_1 = \frac{\sum_{hkl} w\Delta_1}{\sum_{hkl} \lvert F_o \rvert}$; $wR_2 = \sqrt{\frac{\sum_{hkl} w\Delta_2^2}{\sum_{hkl} w\left(F_o^2\right)^2}} = \sqrt{\frac{\sum_{hkl} w\left(F_0^2 - F_c^2\right)}{\sum_{hkl} w\left(F_o^2\right)^2}}$
Weighting	$w = \frac{1}{\sigma^2\left(F_o^2\right) + \left(a \cdot P\right)^2 + bP}$; $P = \frac{1}{3}\max\left(0, F_o^2\right) + \frac{2}{3}F_c^2$
Isotropic displacement parameter U / Å^2	$f'(\Theta) = f(\Theta) \cdot \exp\left(-\frac{8\pi^2 U \sin^2\Theta}{\lambda^2}\right)$; f' corrected atomic scattering factor, considering atomic vibrations; Debye-Waller-Factor $B = U \cdot 8\pi^2$
Anisotropic displacement parameter (*l* Å^2) $f'(\Theta) = f(\Theta) \cdot \exp\left(-2\pi^2(U_{11}h^2a^{*2} + U_{22}k^2b^{*2} + U_{33}l^2c^{*2} + 2U_{23}klb^*c^* + 2U_{13}hla^*c^* + 2U_{12}hka^*b^*\right)$ h,k,l Miller indices; *a**, *b**, *c** reciprocal lattice vectors	

3.3 SEM and EDX

Energy dispersive X-ray analyses (EDX) were carried out on a JEOL 5900 LV scanning electron microscope with a Si(Li) detector. By interference of an electron beam with matter different information, such as secondary electrons, backscattered electrons, or X-rays, can be detected. Based on the breakthrough invention of E. Ruska (Nobel Prize 1986) the SEM (Scanning Electron Microscope) uses the interference of electrons with matter to generate a picture. The sample is scanned by highly energetic electrons (in vacuum), which are focused through magnetic lenses. Secondary electrons are emitted, some of which can leave the sample and are collected by a positively charged detector, which then generates a picture. The more secondary electrons are detected, the brighter the picture. The sample penetration of primary electrons (with E = 1 - 50 keV) scales with their energy: 0.1 - 10 µm. Due to *Coulomb* interactions the primary electrons can repulse bonded electrons from the samples atoms (secondary electrons). However, the latter kind of electrons have much lower kinetic energies (10^3 - 10^4 times lower) compared to the primary electrons (due to the short time for the *Coulomb* repulsion) so only secondary electrons that are near the surface (1 - 10 nm) can leave the sample and be detected. The contrast of the sample is caused by the surface topology. Areas with slopes, edges etc. exposed to the same electron beam have a bigger surface and

volume from which secondary electrons can be emitted. Additionally, the fast primary electrons generate X-rays. The energy of the emitted X-ray beam is the same as the energy difference of the shells involved in the electron-hole recombination. As this radiation is characteristic for each element the qualitative sample composition can be determined. The X-rays are collected and sorted by intensity and energy. The primary electrons experience *Coulomb* interactions with the positively charged nuclei, while traveling through the sample. In addition to the signals mentioned before they can be backscattered. As the energies of the backscattered electrons depend on the elements present a distribution of elements in the sample can be generated. Detection limits range from 10^{-10} to 10^{-14} g for elements with $Z \geq 6$ and characteristic X-ray spectra of lighter elements are absorbed by the window material covering the detector.

Practically, crystallites were selected in the glovebox and fixed on a carbon pad on a cylindrical Al-sample holder. Non-conducting samples have to be coated first (Au or graphite). If the flow of electrons is hindered, the samples will be charged resulting in unemployable pictures. During transfer into the microscope's chamber the samples were shortly exposed to air. For EDX, standard measurement times were 5 min for acceptable statistics and the operating voltage was 20 kV.

3.4 DTA

Several techniques (DTA, DSC, DIL, TG, EGA, etc.) are comprised by the term thermal analysis in material science. DTA[16] (Differential Thermal Analysis) involves heating and cooling of a sample and an inert reference under controlled identical conditions. Any temperature difference (exothermic or endothermic signals) between sample and reference is recorded (as changes in voltage between two thermoelements) and plotted against temperature or time. Therefore, detection of melting/crystallization behavior, purity, reaction heats, identification, and thermal stability is possible. The area under the DTA peak corresponds to enthalpy changes. The machine used was a DSC 404 C (Netzsch).

For DTA experiments, ~80 mg of a ground sample were sealed into a specific Nb crucible. During sealing cooling is essential to prevent material evaporation and unwanted reactions, e.g. decomposition. Both, the filled crucible and the empty reference Nb crucible were then placed onto temperature sensors (thermo elements).

After three cycles of evacuation and purging with Ar, the sample is exposed to a temperature program that is running under a constant Ar (50 ml·min^{-1}) flow. Programs used usually consist of two equivalent cycles of heating, cooling (±10 K·min^{-1}), and isothermal segments. It should be noted that different heating/cooling gradients can lead to changes in resolution of the signal. Many other effects, such as chemical reactions, dissolving/crystallization processes, phase transitions, sample mass, particle size, sample density, and/or a combination of these may influence the measurement. Whereas for known binary phases the melting points can be assigned due to their position in the phase diagrams, for new systems absolute conclusions have to be coupled with other methods, such as multi-temperature experiments.

3.5 Magnetic Measurements (SQUID)

A SQUID (Superconducting Quantum Interference Device) is used to measure very small magnetic fields (fluxes) down to flux densities of 10^{-14} T and magnetic susceptibility.[17, 18] Therefore magnetic behaviors, such as different forms of paramagnetism, diamagnetism, superconductive transitions, magnetic couplings, and field/temperature dependencies of a sample can be determined. For tracking down superconductive phases low external fields should be applied (10 - 20 G). The measurements were performed on a MPMS XL (Quantum Design) magnetometer with a temperature range of 1.7 - 400 K and magnetic field ranges up to 5 T. In the glovebox approximately 20 mg of the pure sample were tightly sealed into a gelatin capsule and fixed in the center of a straw. Before measuring, the remanent field of the sample chamber was checked with a Hall probe and compensated with a polarized field. For superconductive transitions the sample was cooled in the absence of a magnetic field and then heated (shielding) and cooled (Meissner) with an external field. If possible the sample was checked for decomposition via powder X-ray diffraction afterwards.

3.6 Computational Methods

Electronic structure calculations, i.e. all band structure, DOS, and COHP calculations were carried out by using the TB-LMTO-ASA (Tight-Binding-Linear-Muffin-Tin-Orbital-Atomic-Sphere Approximation) method in the software package LMTO 47c.[19]

In the LMTO approach, the density functional theory (instead of conducting the variational procedure from multi Slater determinants, DFT uses a functional of the electron density) is used with exchange and correlation treated at a local level within the local density approximation (LDA).[20] Within the atomic sphere approximation (ASA), the atomic potential used in the Schrödinger equation is not the true crystal potential but rather an approximation and various corrections for the neglect of interstitial atoms are applied. The unit cell is filled with small overlapping atomic spheres and the spheres' total volume equals the unit cell volume (*Wiegner-Seitz* Spheres). The radii of the WS spheres were obtained under the requirement that the overlapping potential is the best achievable approximation to the full potential and were automatically determined by the software. The potentials of the WS spheres are considered to be spherical (Muffin-tin-orbitals) and are constant upon a certain radius (muffin-tin-zero). When asking for the electronic structure in a crystal whose unit cell is separated in muffin tin spheres terms have to be added to the partial wave of the radial Schrödinger equation in order to fulfill continuous conditions at the spheres boundaries. Hence, the MTOs (muffin-tin-orbitals) result. If the interstitial space between the spheres is small the *tails* of the MTO are constant. By this ASA approximation and the use of modified Bessel and Neumann functions augmented MTOs are produced. To minimize overlapping, and achieve space filling, the voids are filled with empty spheres (ES). Maximum overlap should not be too large, since the error in the kinetic energy introduced by the combined correction is proportional to the fourth power of the relative sphere overlap. The optimal positions and radii for the ES were also determined automatically according to the described method.[21] Basis sets for the atoms were automatically generated and were adjusted (used, downfolded, or deactivated). The *Löwdin* downfolding technique[22, 23] allows the derivation of few-orbital Hamiltonians by keeping only the relevant degrees of freedom and integrating out the irrelevant. The *k* space integrations were performed by the tetrahedron method.[21] For bonding analysis the energy contributions of all electronic states for selected bonds were calculated by the COHP (Crystal Orbital *Hamilton* Population) method.[24] Whereas COOP (Crystal Orbital Overlap Population) partitions the band structure into states, COHP partitions them by energy. Integration over all filled states gives ICOHP values which measure relative bond strengths. In all analyses negative COHP and ICOHP values indicate bonding interactions.

The corresponding term derived from COOP is called MOP (*Mulliken* overlap populations).[25] The Electron Localization Function (ELF)[26-30] was used to locate bonding or electron lone pairs and was first introduced by Becke and Edgecombe. The ELF can be derived from the electron density by comparing the local Pauli repulsion with that in a uniform electron gas at a given point in the compound. It can have values between 0 and 1. High ELF values mean high localization of electrons with antiparallel spins meaning high probability to find paired electrons at a given point, which perfectly reflects the Lewis model of bonding and non bonding electron pairs. However, this localization is high but not perfect, due to Heisenberg's relation. This is the case for core shells, covalent (single, double, triple) bonds and electron lone pairs. High variances (σ^2) of the ELF mean high delocalization, which is found in bonds of higher orders. The ELF always reflects the symmetry of a given molecule. For visualization the ELF can be graphically presented as 2D slices through the structure or by displaying isosurfaces of a certain ELF value. The ELF was calculated using the wavefunction obtained from a calculation with the Gaussian03[31] software with the TOPMOD program package.[32] Visualization was done by use of the programs GaussView[33] (for molecular orbitals) and MOLEKEL (for ELF).[34] Further computational methods, such as NBO (natural bond orbital)[35-37] and AIM (atoms in molecules),[38, 39] both aiming for the charge assignment of atoms, were used also with the wavefunction obtained from Gaussian03.

For tight-binding semiempirical Extended-Hückel band structure calculations of parts of extended networks the software package MEHMACC was used.[40, 41] The programs allow self consistent charge iteration calculations for the determination of H_{ii} (= orbital energies) parameters, DOS calculations, atomic orbital popuplations (AOPOP), overlap populations (OVLPOP), and representation of ELF. The extended Hückel method (EHM) has proved successful for the study of molecules which are too large to be treated by more precise methods. It gives approximate molecular orbitals, orbital energies, and can be used to calculate 'anionic parts' of a structure.

3.7 References

[1] G. Brauer, *Handbuch der präparativen anorganischen Chemie, Ferdinand Enke Verlag, Stuttgart, Germany* **1952**.
[2] J. D. Corbett, *Inorg. Synth.* **1983**, *22*, 15.
[3] ICSD/Retrieve, *Version 1.4.1, FIZ Karlsruhe* **2005**.
[4] STOE/WinXPOW, *Version 2.08, STOE & Cie GmbH, Darmstadt* **2003**.
[5] Scale3/ABSPACK, *CrysAlis RED, Oxford Diffraction Ltd., Version 1.171.32* **2007**.
[6] X-RED, *STOE Data Reduction Program, STOE&Cie GmbH, Darmstadt* **2001**.
[7] X-Shape, *STOE & Cie GmbH: Crystal optimization program for numerical absorption correction, based on the program HABITUS by W. Herrendorf and H. Bärnighausen, Karlsruhe **1993**,Gieben, **1996**, Darmstadt, **1997**.*
[8] SHELXTL, *Bruker Analytical X-ray instruments: Madison, WI* **1998**.
[9] K. Brandenburg, *Diamond, Version 3.1e, Crystal Impact GbR, Bonn* **2007**.
[10] G. Sheldrick, *Acta Crystallogr.* **1990**, *46 A*, 467.
[11] G. Sheldrick, *SHELXS-97, Program for the Solution of Crystal Structures, Universität Göttingen* **1997**.
[12] G. Sheldrick, *SHELXL-97, Program for the Refinement of Crystal Structures, Universität Göttingen* **1997**.
[13] G. Sheldrick, *SHELXTL Reference Manual, Bruker-AXS, Inc., Madison, WI* **1997**.
[14] W. Massa, *Crystal Structure Determination, Teubner 3rd Ed.* **2002**.
[15] W. Clegg, *Crystal Structure Determination, Oxford Science Publications* **1998**.
[16] M. I. Pope, M. J. Judd, *Differential Thermal Analysis, London, Heyden* **1977**.
[17] H. Lueken, *Magnetochemie, Teubner Studienbücher* **1999**.
[18] M. McElfresh, *Fundamentals of Magnetism and Magnetic Measurements, Quantum Design* **1994**.
[19] R. W. Tank, O. Jepsen, A. Burkhardt, O. K. Andersen, *TB-LMTO-ASA 4.7; Max-Planck-Institut für Festkörperforschung, Stuttgart, Germany* **1998**.
[20] U. v. Barth, L. Hedin, *J. Phys. Chem.* **1972**, *5*, 1629.
[21] P. E. Blöchl, O. Jepsen, O. K. Andersen, *Phys. Rev.* **1994**, *49 B*, 16223.
[22] O. K. Andersen, *Phys. Rev.* **1975**, *12 B*, 3060.
[23] O. K. Andersen, O. Jepsen, *Phys. Rev. Lett.* **1984**, *53*, 2571.
[24] P. E. Blöchl, R. Dronskowski, *J. Phys. Chem.* **1993**, *97*, 8617.
[25] R. S. Mulliken, *J. Chem. Phys.* **1955**, *23*, 2343.
[26] A. D. Becke, K. E. Edgecombe, *J. Chem. Phys.* **1990**, *92*, 5397.
[27] T. F. Fässler, A. Savin, *Chemie in unserer Zeit* **1997**, *3*, 110.
[28] A. Savin, R. Nesper, S. Wengert, T. F. Fässler, *Angew. Chem.* **1997**, *109*, 1892.
[29] T. F. Fässler, *Chem. Soc. Rev.* **2003**, *32*, 80.
[30] B. Silvi, A. Savin, *Nature* **1994**, *371*, 683.
[31] M. J. Frisch, G. W. Trucks, H. B. Schlegel, G. E. Scuseria, M. A. Robb, J. R. Cheeseman, J. J. A. Montgomery, T. Vreven, K. N. Kudin, J. C. Burant, J. M. Millam, S. S. Iyengar, J. Tomasi, V. Barone, B. Mennucci, M. Cossi, G. Scalmani, N. Rega, G. A. Petersson, H. Nakatsuji, M. Hada, M. Ehara, K. Toyota, R. Fukuda, J. Hasegawa, M. Ishida, T. Nakajima, Y. Honda, O. Kitao, H. Nakai, M. Klene, X. Li, J. E. Knox, H. P. Hratchian, J. B. Cross, V. Bakken, C. Adamo, J. Jaramillo, R. Gomperts, R. E. Stratmann, O. Yazyev, A. J. Austin, R. Cammi, C. Pomelli, J. W. Ochterski, P. Y. Ayala, K. Morokuma, G. A. Voth, P. Salvador, J. J. Dannenberg, V. G. Zakrzewski, S. Dapprich, A. D. Daniels, M. C. Strain, O. Farkas, D. K. Malick, A. D. Rabuck, K. Raghavachari, J. B. Foresman, J. V. Ortiz, Q. Cui, A. G. Baboul, S. Clifford, J. Cioslowski, B. B. Stefanov, G. Liu, A. Liashenko, P. Piskorz, I. Komaromi, R. L. Martin, D. J. Fox, T. Keith, M. A. Al-Laham, C. Y. Peng, A. Nanayakkara, M. Challacombe, P. M. W. Gill, B. Johnson, W. Chen, M. W. Wong, C. Gonzalez, J. A. Pople, , *Gaussian 03, Revision D.01, Gaussian, Inc., Wallingford CT* **2004**.
[32] S. Noury, X. Krokidis, F. Fuster, B. Silvi, *Computers & Chemistry* **1999**, *23*, 597.

[33] GaussView, V 4.1, R. Dennington, T. Keith, J. Millam, K. Eppinnett, W. L. Hovell, R. Gilliland, Semicham, Inc., Shawnee Mission, KS, **2003**.
[34] P. Flükiger, H. P. Lüthi, S. Portman, J. Weber, *Molekel 4.0, Manno (Switzerland), Swiss Center for Scientific Computing* **2000**.
[35] J. P. Foster, F. Weinhold, *J. Am. Chem. Soc.* **1980**, *102*, 7211.
[36] A. E. Reed, F. Weinhold, *J. Chem. Phys.* **1983**, *78*, 4066.
[37] A. E. Reed, R. B. Weinstock, F. Weinhold, *J. Chem. Phys.* **1985**, *83*, 735.
[38] R. F. W. Bader, *An Introduction to the Electronic Structure of Atoms and Molecules, Clarke, Toronto* **1970**.
[39] R. F. W. Bader, *Atoms in Molecules (Oxford, New York)* **1994**.
[40] U. Häussermann, R. Nesper, S. Wengert, T. F. Fässler, *Program MEHMACC: modified version of the QCPE program EHMACC, ETH Zürich: Zürich* **1994**.
[41] M. H. Whangbo, M. Evain, T. Hughbanka, M. Kertesz, S. Wijeyesekera, C. Wilker, C. Zheng, R. Hoffmann, *Program EHMACC. Quantum Chemistry Program Exchange* **1988**, *571*.

4 Substitution Effects in the Binary System Na–Sn with Zn

4.1 Introduction

As mentioned in Chapter 1.2 the element tin shows the exceptional property to undergo metallic and covalent bonding at ambient conditions. This feature is adopted in intermetallic compounds with alkali and alkaline earth stannides. By variation of number and type of the counter ions, e.g. by mixing A/A', A/Ae, Ae/Ae', A/RE,or Ae/RE, many different stannide substructures with new interesting structural and bonding properties have been synthesized.

Recalling the past, a wide range of remarkable structure and bonding motifs can be found on the tin-rich side of the binary phases in the system Na_xSn_y ($x \leq y$) as shown in Figure 4.1. Therefore, they represent very suitable starting points for systematic investigations of substitution reactions. In *β*-NaSn[1] isolated Sn tetrahedra are present (*α*-NaSn is a rotor phase). All Sn atoms are 3-bonded and the bonding can be explained by Wade's rules[2, 3] deriving the tetrahedron from a *closo*-trigonal bipyramid, and hence a *nido*-cluster with (2n + 4, n = 4) 12 cluster electrons is formed. However, the simple (8–N) rule also works efficiently and is consistent with white phosphorus (pseudoatom concept) in this case. The next two - Sn-richer - phases, Na_7Sn_{12}[4] ($^2_\infty[Sn_2]^{1-}$) and $NaSn_2$[5] ($\{Sn_8\}^{4-}$), both exhibit separated 2D slabs of 3b- and 4b-Sn atoms. Whereas Na_5Sn_{13}[6] ($^2_\infty[Sn_{12}]^{7-}$) can still qualify as a Zintl phase, the tin-richest compound $NaSn_5$[7] contains 4b- and formally 5b-Sn atoms, a remarkable coexistence of structure motifs of *α*- and *β*-Sn in one single phase.

Alloys between Zn and Sn are widely used for refining steel surfaces by electrochemical deposition of Sn/Zn alloys.[8, 9] This binary system owns a rich tradition in fundamental and applied research. Up to now only the liquid phase and the solubility of Sn in pure hexagonal Zn and also of Zn in pure body centered tetragonal *β*-Sn has been analyzed. No experimental evidences for stable solid phases, either as an intermetallic compound or as intermetallic solutions with wider homogeneity ranges even at high pressures have been found. It seems that Zn and Sn (Pettifor[10, 11] chemical scales 1.44 and 1.84, respectively) 'cannot get along with each other' on the atomic scale. With respect to that the access to stable binaries between Zn and Sn by controlled decomposition (recently, Guloy et al. reported a new Ge modification obtained from oxidation of binary germanides[12]) of ternary phases but also with respect to investigate the interesting structural and electronical

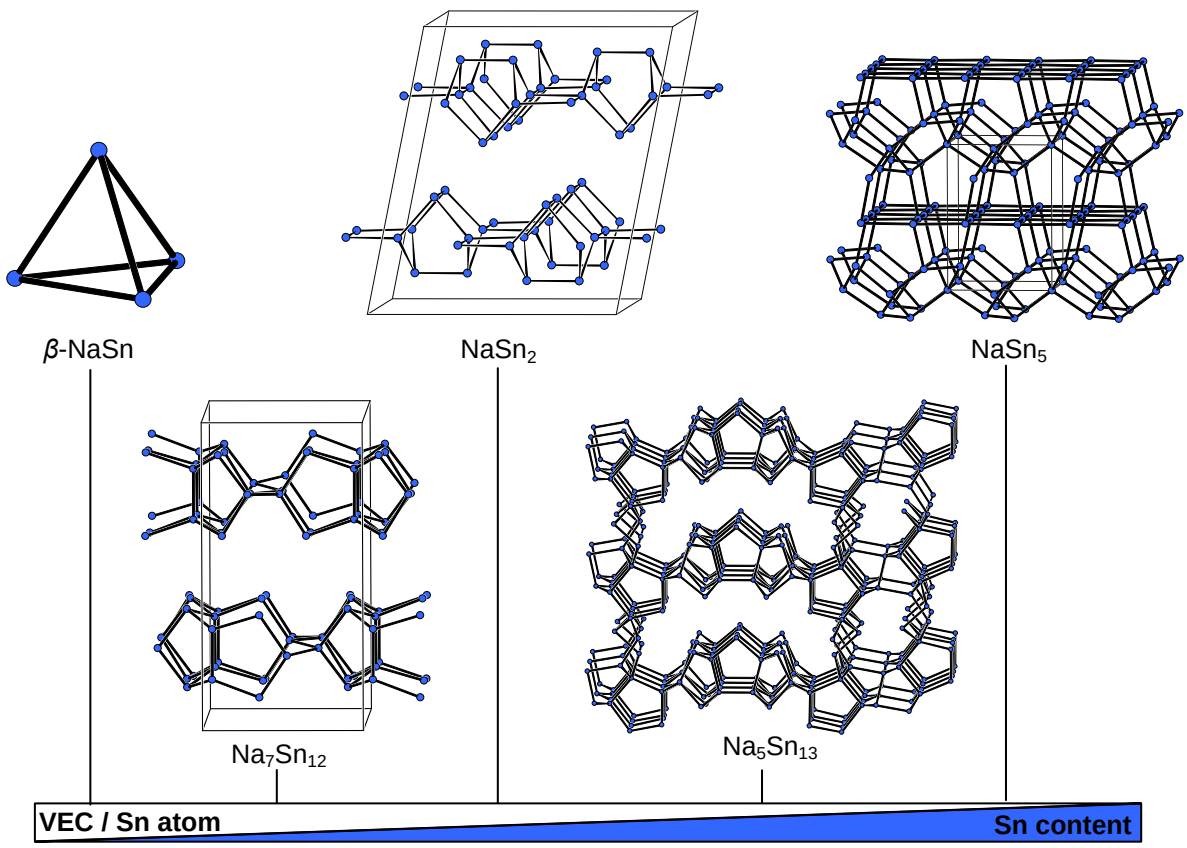

***Figure 4.1*. Tin substructures of the binary phases Na_xSn_y ($x \leq y$). From left to right: *β*-NaSn, Na_7Sn_{12}, $NaSn_2$, Na_5Sn_{13}, $NaSn_5$. With increasing Sn content the VEC per Sn atom drops and the average connectivity per Sn atom increases.**

changes, the substitution effects of Zn in Na stannides are a fruitful subject of research.

Whereas some ternary compounds A–M–Tt (M = Zn, Cd; Tt = Ge, Sn, Pb) have already been reported (Table 4.1), the ternary system Na–Zn–Sn has not been explored yet and with Zn and Sn only the compound Li_2ZnSn[13] exists. With Ae metals 3D networks have been found in compounds such as $BaZn_2Sn_2$[14] ($CaBe_2Ge_2$-type, a structural variant of $BaAl_4$) and AeZnSn[15] (Ae = Sr, Ba; AlB_2-type). Icosahedra made of Zn and Sn have only been reported in a few cases with transition metals e.g. $Mo_7Zn_{40}Sn_{12}$.[16]

The non scientific term ‘design’ of compounds has always been a topic of debate.[17] Due to very sophisticated and elaborated synthesis methods, at least in organic and organometallic chemistry this term might be applied. In classical solid state syntheses this concept is harder to realize.

Here, the chemist has to face many obstacles, such as closed reaction containers, crystal quality, intrinsic disorder, purification, relatively low heats of formation, or the preferred formation of thermodynamically favoured binaries. In most classical cases the reactions are carried out by varying stoichiometries and temperatures. Hence rather than designing new compounds, the herein reported new phases where discovered by looking for chemical analogies and applying appropriate reaction conditions.

***Table 4.1*: The *hitherto* known A–M–Tt (A = Li, Na, K, Cs; M = Zn, Cd; Tt = Ge, Sn, Pb) compounds.**

germanides	stannides	plumbides
$Li_{1.08}Zn_{0.92}Ge$[18]	Li_2ZnSn[13]	Li_2CdPb[19]
Li_2ZnGe[20]	Na_2CdSn[21]	K_6CdPb_8[22]
Li_2CdGe[23]	$Na_{49}Cd_{58.34}Sn_{37.69}$[24]	K_2CdPb[25]
Na_2ZnGe[26]		Na_2CdPb[21]
Cs_6ZnGe_8[27]		$Na_{13}Cd_{20.09}Pb_{6.91}$[28]

This chapter includes the description of the *hitherto* found ternary compounds in the system Na–Zn–Sn. Due to the relativlely low melting points of the participating elements and the formation of a simple eutectic system between Sn and Zn (eutectic mixture with 85.1% Sn and m_p = 198.5 °C) all preparations were carried out at relatively low temperatures (< 600 °C), minimizing feasibilities of damaging the ampoule material or protective tubings. As for Zn, some binary phases with Nb exist; therefore most experiments were carried out in Ta ampoules (at higher temperatures the ternary compounds and Zn have been detected to react with the Nb crucible). The two most common stable unwanted byproducts of the elements under investigation have been experienced to be *β*-NaSn and $NaZn_{13}$. These phases could be partially avoided by faster cooling rates and variations of the loading stoichiometries. The two metametals Zn and Sn have higher electronegativities compared to normal metals and they are of similar magnitudes ($\chi_{Pauling/Allred}$(Sn) = 1.96 / 1.7; $\chi_{Pauling/Allred}$(Zn) = 1.65 / 1.7), which is yet another advantage for successful syntheses of new ternary systems.

4.2 Na_2ZnSn_5 and $NaZn_{0.3}Sn_{2.7(1)}$ - Open Framework Phases with Zeolite-like Structures

The here presented Sn-richest phases $Na_2Zn_xSn_{6-x}$ (x = 1.0 and 0.6) within the ternary phase system can be derived from the tin-richest pure binary $NaSn_5$. Although the compounds are related to the framework structures found in $NaGaSn_5$[29] and $NaTrSn_2$[30, 31] (Tr = Ga, In), for x = 1, the current all metal framework made of tetrahedra represents a new structure type and does not have an analogue among oxides.[32] The anionic framework in $Na_2Zn_{0.6}Sn_{5.4(2)}$ (= $NaZn_{0.3}Sn_{2.7(1)}$) is similar to that in $NaGaSn_2$.

4.2.1 Synthesis and Characterization

Synthesis The compound Na_2ZnSn_5 (**1**) was obtained as a pure phase by direct reaction of the pure elements in a tin flux. Under inert gas conditions the elements were weighted in tantalum ampoules in the ratio Na : Zn : Sn = 2 : 1 : 20 and heated to 500 °C. After cooling (2 $K \cdot min^{-1}$) to 350 °C and annealing for seven days the crystals of the compound were isolated from the surface of the excess tin block. The synthesis succeeded from a total chemical loading of 1.381 g, with m(Na) = 0.026 g, m(Zn) = 0.036 g, and m(Sn) = 1.319 g. The product is highly crystalline and shows metallic luster. Efforts to synthesize the compound by use of a centrifugation technique (Chapter 3.1) to remove the tin flux led to bigger crystals. Reaction of stoichiometric amounts of the elements also resulted in the formation of the phase with similar composition but lower average quality of the single-crystals. The compound $NaZn_{0.3}Sn_{2.7(1)}$ (**2**) was first obtained by a stepwise increase of the Na content of the reaction mixture that lead to the discovery of Na_2ZnSn_5, mentioned above, from Na : Zn : Sn = 2 : 2 : 20 to 7 : 2 : 20 and applying the same reaction conditions. From the latter loading almost single phase $NaZn_{0.3}Sn_{2.7(1)}$ was obtained and the synthesis was carried out in Ta ampoules with total loading mass of 1.666 g, with m(Na) = 0.101 g, m(Zn) = 0.082 g, and m(Sn) = 1.484 g. The block shaped crystals exhibit metallic luster. As described below, this phase, together with elemental Sn, can also be obtained by quenching a sample containing an almost pure phase of Na_2ZnSn_5 (with minor amounts of elemental Sn) from 500 °C in liquid nitrogen.

EDX Analyses The elemental analysis of different crystallites of Na_2ZnSn_5 proved the presence of all three elements with atomic ratios of Na : Zn : Sn = 27(2) : 10(4) : 63(3)% (calculated: Na: 25; Zn: 12.5; Sn: 62.5 at%). EDX measurements of $NaZn_{0.3}Sn_{2.7(1)}$ showed compostions with very low Zn contents. For both compounds the quantifications were hampered by overlapping peaks from Na and Zn series.

Thermal Behavior For the thermal behavior of Na_2ZnSn_5 the product of a slightly tin-rich reaction with Na : Zn : Sn = 2 : 1 : 6, (reacted at 500 °C, Na_2ZnSn_5 and little amounts of excess Sn were detected in powder XRD measurements), was heated in a sealed Nb crucible under continuous Ar flow from room temperature to 800 °C at a rate of 10 $K \cdot min^{-1}$ and cooled down to 100 °C at the same rate. Isothermal dwelling times were 10 min and two loops were recorded. As shown in Figure 4.2 the heating and cooling curves show a minor peak at ~ 215 °C, indicating the presence of a solid solution between Zn and Sn as an admixture. On heating, at 360.7 °C (onset) a broad endothermal signal appears, which consists of at least three individual signals. The cooling curves do not show a significant hysteresis and the heating and cooling is perfectly reversible. A powder diffractogram recorded after the DTA measurement revealed no changes in composition of the sample. The splitted signal in the heating loop can be associated with the presence of a series of peritectic points (meaning decompositions into liquids and other phases with different composition), while the rather sharp peak in the cooling curves hint for an oversaturated melt and spontaneous crystallization of the compound. Annealing experiments at 350 °C, with higher yields and crystallinity, compared to samples obtained from higher temperatures, leads to the assignement of the melting point of Na_2ZnSn_5 to be in the range of 350 - 360 °C. For thermal behavior of $NaZn_{0.3}Sn_{2.7(1)}$ 80 mg of a quenched sample of Na_2ZnSn_5 (from 500 °C), which contained a mixture of $NaZn_{0.3}Sn_{2.7(1)}$ and elemental Sn, were heated to 600 °C. Two loops with isothermal dwelling times of 10 min (at 600 and 100 °C) were recorded. Heating rates were 10 $K \cdot min^{-1}$. The shape and characteristics (Figure 4.3) are very similar to the DTA experiment of Na_2ZnSn_5 (Figure 4.2). However, the onsets and cooling-end temperatures are slightly shifted towards lower values. The broad signal hints for a phase width of phases with similar compositons. The signal at ~ 350 °C can be assigned to the melting of the phase, since experiments on stoichiometric loaded samples show better results when annealed in that temperature region.

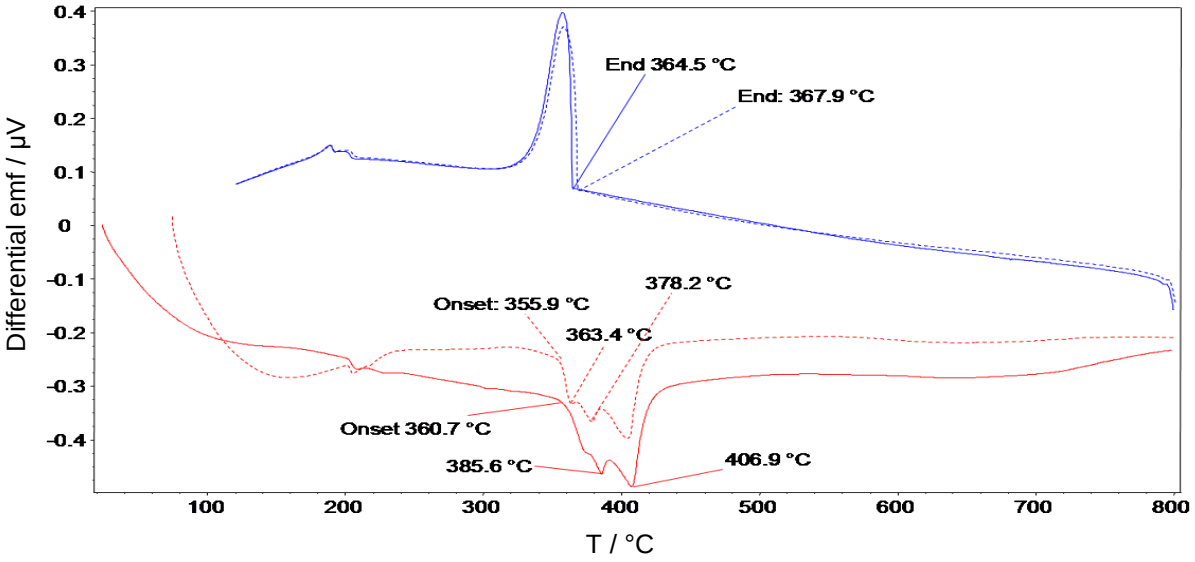

Figure 4.2. **DTA curves of the product of a reaction with Na : Zn : Sn = 2 : 1 : 5 at 500 °C. Heating curves (red), cooling curves (blue), 2nd cycle (dashed line).**

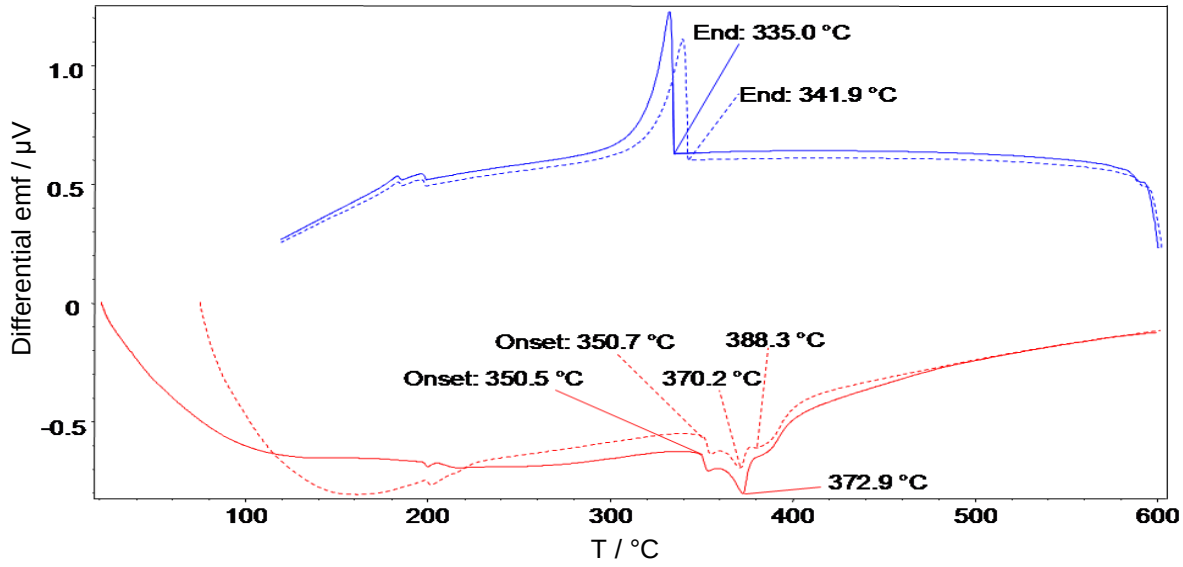

Figure 4.3. **DTA curves of a sample containing $NaZn_{0.3}Sn_{2.7(1)}$ and Sn. Heating curves (red), cooling curves (blue), 2nd cycle (dashed line).**

Powder X-ray Diffraction Measurements The diffraction data for the isolated phase Na_2ZnSn_5 (from loading Na : Zn : Sn = 2 : 1 : 20) proved the formation of the compound as an almost single phase with few weak unindexed reflections (Figure 4.4) in the range $2\theta > 50°$. These reflections may originate from a byproduct containing Sn. The measurement was carried out in Debye-Scherrer mode and lasted for 18 h. The highest quality powder diagram for $NaZn_{0.3}Sn_{2.7(1)}$ was obtained from a quenched sample (see synthesis section). As shown in Figure 4.5, elemental Sn is formed as a byproduct.

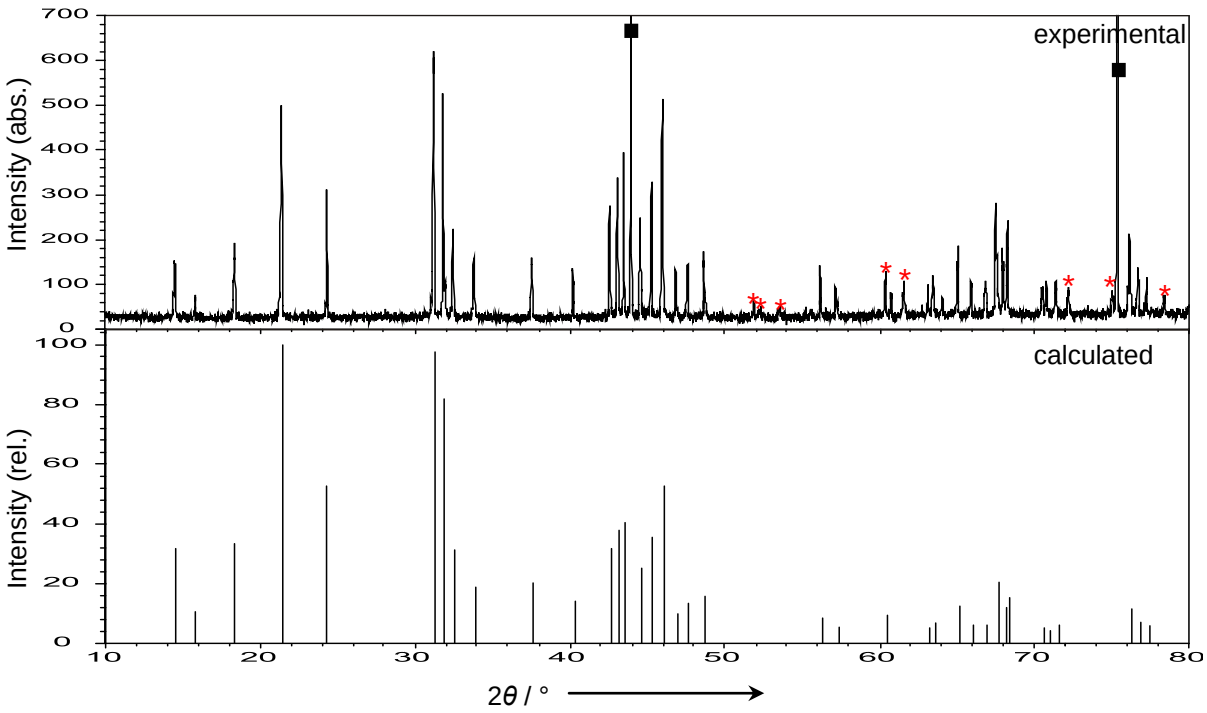

***Figure 4.4*. Experimental powder diagram (top) from sample loading Na : Zn : Sn = 2 : 1 : 20 and simulated powder diagram (bottom) of Na_2ZnSn_5. Reflections from diamond (internal standard) are labeled with a square. Unindexed reflections are marked with a red star.**

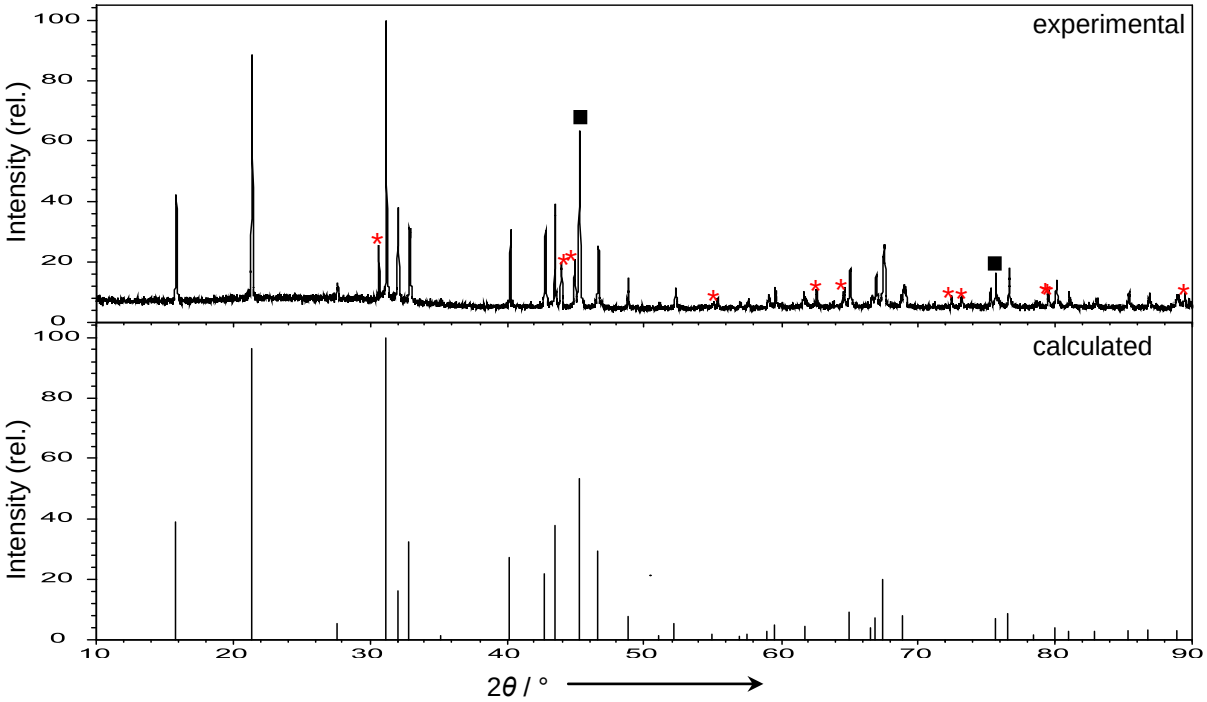

***Figure 4.5*. Experimental powder diamgram (top) from the quenched sample loaded as Na : Zn : Sn = 2 : 1 : 5 and simulated powder diagram (bottom) of $NaZn_{0.3}Sn_{2.7(1)}$. Reflections from diamond (internal standard) are labeled with a square. Reflections from *β*-Sn are marked with a red star.**

4.2.2 Crystal Structure Determination and Description of Na_2ZnSn_5 and $NaZn_{0.3}Sn_{2.7(1)}$

Structure Determination Single block shaped crystals of both phases were fixed with silicon grease and sealed in a capillary in the glovebox. Data collections took place on an Oxford Xcalibur3 diffractometer and involved four sets of ω scans (–41° to +63° for φ = 0°, +90°, +180°, +270°), with θ = +30°, detector distance 50 mm, exposure time 15 s/frame, and scan width 2°/frame. After an empirical absorption correction the structures for **1** and **2** were solved with direct methods in the acentric tetragonal space group *I*–42*d* and the orthorhombic space group $C222_1$, respectively. The space groups were assigned on the basis of systematic absences and the statistical analyses of the intensity distributions. During the refinement of **1** the model including four independent atomic sites significantly converged by setting the occupancy factor for Na to 0.5 and refining all atoms anisotropically. Refinements in the lower symmetry space groups *Fdd*2 and *I*4 did not show any improvement and led to slightly worse final residuals (R_1 / wR_2 (all data) = 0.029 / 0.062 and 0.025 / 0.060, respectively). Therefore the solution in the highest symmetry was chosen. The space group for **2** had to be chosen from a variety of orthorhombic and trigonal space groups, including $P2_12_12_1$ and $P3_11_2$, which led to somewhat higher residual electron densities and two Sn positions of same multiplicity, from which just one was slightly mixed occupied and made no chemical sense. The solution in $C222_1$ showed the lowest residuals with two statistically occupied M = Zn / Sn sites. However, similar to **1** the Na position is strongly displaced. In the final refinement cycles for the resulting composition $NaZn_{0.3}Sn_{2.7(1)}$ the occupancy factor for the split position (50 : 50) of Na was fixed to 0.5. This resulted in negligible changes in the occupancies of the two M sites. The presence of any superstructure or incommensurate structure, which might generate the unusual displacements and occupancy factors, was not indicated by the observation of additional or irregular Bragg reflections or satellites. No phase width could be observed as single-crystals obtained from stochiometric loadings ranging from Na : Zn : Sn = 2 : 2 : 20 to 7 : 2 : 20 result in the same Sn : Zn occupancies on the 4*b* and 8*c* sites with respect to standard deviations. Table 4.2 shows selected crystallographic and refinement data of the two compounds. Tables 4.3 and 4.4 contain atomic positions, displacement parameters. Interatomic distances up to 4 Å are listed in Table 8.1 (see Appendix).

***Table 4.2*: Selected crystallographic and refinement data for Na_2ZnSn_5 and $NaZn_{0.3}Sn_{2.7(1)}$.**

Empirical formula	**Na_2ZnSn_5 (1)**	**$NaZn_{0.3}Sn_{2.7(1)}$ (2)**
Formula weight / g·mol^{-1}	704.80	365.20
Temperature / K	293(2)	293(2)
Crystal size / mm^3	0.05 × 0.05 × 0.05	0.03 × 0.03 × 0.03
Crystal color; shape	Silvery; Block	
Diffractometer	Oxford Xcalibur3 (CCD)	
Crystal system	Tetragonal	Orthorhombic
Space group	I–4_2d (No. 122)	$C222_1$ (No. 20)
Unit cell parameters / Å	a = 6.313(2)	a = 6.459(2)
	c = 22.329(9)	b =11.177(3)
		c = 6.240(1)
Unit cell volume / Å^3; Z	889.9(5); 4	450.4(2); 4
ρ_{calc} / g·cm^{-3}	5.26	5.39
μ / mm^{-1} (Mo K_α)	16.47	16.32
Absorption correction	empirical	empirical
F(000)	1208	623
Θ range / °	3.35 - 27.99	3.64 - 27.82
Index range	$-7 \le h \le 8$; $-8 \le k \le 7$	$-8 \le h \le 5$; $-14 \le k \le 14$
	$-28 \le l \le 29$	$-8 \le l \le 8$
Data completeness / %	99.5	100
Integrated reflections	3271 (R_σ = 0.017)	3204 (R_σ = 0.014)
Independent reflections	541 (R_{int} = 0.029)	542 (R_{int} = 0.026)
Refinement method	Full-matrix least-squares on F^2 (SHELXTL)	
Parameters	24	36
Goodness of fit on F^2	1.190	1.164
Observed reflections [$I > 2\sigma(I)$]	484	514
R_1 / wR_2 [$I > 2\sigma(I)$]	0.022 / 0.053	0.017 / 0.039
R_1 / wR_2 (all data)	0.025 / 0.055	0.019 / 0.039
Weighting scheme*	a = 0.034; b = 0	a = 0.021; b = 1.756
Extinction coefficient	0.0116(4)	0.0268(13)
Residual map / e$^-$·Å^{-3}	+0.94 [1.02 Å from Sn2]	+0.71 [0.95 Å from Zn2]
	–1.70 [0.53 Å from Zn]	–0.64 [0.76 Å from Zn1]

*) $w = 1 / [\sigma^2(F_o^2) + (aP)^2 + bP]$, where $P = (F_o^2 + 2F_c^2) / 3$

***Table 4.3*: Atomic coordinates and equivalent isotropic displacement parameters for Na_2ZnSn_5 and $NaZn_{0.3}Sn_{2.7(1)}$.**

Atom	**Wyck.**	**Occ. ≠ 1**	***x***	***y***	***z***	**U_{eq} / Å^2**
			Na_2ZnSn_5 (1)			
Sn1	16*e*		0.6678(1)	0.1579(1)	0.0653(1)	0.016(1)
Sn2	4*b*		½	½	0	0.015(2)
Zn	4*a*		0	0	0	0.019(1)
Na	16*e*	0.5	0.1530(10)	0.2892(15)	0.1083(4)	0.057(4)
			$NaZn_{0.3}Sn_{2.7(1)}$ (2)			
M1 = Sn1 / Zn1	4*b*	0.92 / 0.08(3)	0	0.7358(1)	¾	0.025(1)
M2 = Sn2 / Zn2	8*c*	0.90 / 0.10(6)	0.3538(1)	0.6179(1)	0.9167(1)	0.025(1)
Na_a*	8*c*	0.25	0.9682(80)	0.5933(20)	0.2053(40)	0.113(30)
Na_b*	8*c*	0.25	0.1548(20)	0.5465(20)	0.4272(40)	0.067(7)

*) split position (50% : 50%)

***Table 4.4*: Anisotropic thermal displacement parameters (*l* Å^2) for Na_2ZnSn_5 and $NaZn_{0.3}Sn_{2.7(1)}$.**

Atom	U_{11}	U_{22}	U_{33}	U_{23}	U_{13}	U_{12}
			Na_2ZnSn_5 (1)			
Sn1	0.017(1)	0.016(1)	0.016(1)	0	0	0
Sn2	0.016(1)	0.016(1)	0.013(1)	0	0	0
Zn	0.019(1)	0.019(1)	0.017(1)	0	0	0
Na	0.032(3)	0.056(7)	0.08(1)	–0.046(6)	0.013(3)	–0.007(4)
			$NaZn_{0.3}Sn_{2.7(1)}$ (2)			
M1	0.023(1)	0.025(1)	0.027(1)	0	–0.004(1)	0
M2	0.025(1)	0.024(1)	0.027(1)	0.004(1)	–0.002(1)	0
Na_a*	0.18(5)	0.07(1)	0.09(4)	0.06(2)	0.11(4)	0.09(3)
Na_b*	0.040(7)	0.09(1)	0.07(1)	–0.061(9)	0.019(8)	–0.024(6)

*) split position (50% : 50%)

Structure Description of Na_2ZnSn_5 The compound crystallizes in a new structure type. The anionic network is exclusively made up of tetrahedrally coordinated 4b-atoms Sn1, Sn2, and Zn with bonding angles of 106.4 and 115.7° in the {Zn[Sn1]$_4$}, 99.7° to 129.3° in the {Sn1[(Sn1)$_2$(Sn2)Zn]}, and 105.6° and 117.5° in the {Sn2[Sn1]$_4$} tetrahedra. The projection of the unit cell (Figure 4.6) shows that the structure realizes in an open framework arrangement. The structure's main building motifs are twisted {Sn2(Sn1)$_4$} pentagons and boat-like {(Sn1)$_3$Sn2Zn} pentagons. This linking of five-membered ring units is quite common in alkali tetrelides (e.g. $NaSn_2$, $NaSn_5$, Na_7Sn_{12}) and is reminiscent of purple phosphorus. As outlined in Figure 4.6b the latter pentagons form $(5^4)(5^3)_4(5^4)$[33] nets (Schläfli symbols denote types and numbers of polygons around a net point) in the (001) plane resulting in corrugated layers that are stacked along [001] in a *AA'A''A'''* sequence. Whereas a similar stacking of those layers can be easily assessed for **2** (see below), it is rather complex for **1** and involves translational and rotational symmetry operations. In Figure 4.6c the the as stacked layers are shown in different colors. The outcome of this stacking are layers of 6-member helical channels that are stacked *ABAB* along [001]. Similar corrugated nets are found in $NaSn_5$ and can be described as condensed fragments of a pentagonal dodecahedron. The 12 atoms (2 Zn and 10 Sn) of one such tub-like half shell (indicated in Figure 4.6b) are arranged in four boat-like {(Sn1)$_3$Sn2Zn} pentagons with five shared edges and three such tubs are interconnected by one twisted {Sn2(Sn1)$_4$} pentagon (Figure 4.7). The outcome is a porous structure with two atom wide walls. The as generated helical pores (6 atoms per turn) are not symmetric and have different diameters of 3.4 - 5.6 Å (smaller and bigger diameters, calculated from pore surface atom centers). Comparable values can be found for the channels in $K_8Ga_8Sn_{38}$[34, 35] (5.24 - 6.02 Å), $NaGaSn_2$ (6.01 - 6.12 Å), and $NaInSn_2$ (6.3 - 6.4 Å).

The whole alignment is reminiscent of the helical porous structures found in $NaTrSn_2$ (Tr = Ga, In)[30, 31] but the structure's porosity topology is decidedly different, since along [001] the rows of channels are no longer 'condensed' but separated from each other. Homoatomic bond lengths Sn1–Sn1 and Sn1–Sn2 range from 2.908(1) to 2.813(1) Å, respectively and are in good agreement with values for covalent single bonds found in *α*-Sn (2.80 Å), $NaSn_2$ (2.83 - 2.98 Å), or $NaSn_5$ (2.86 - 2.89 Å). The heteroatomic Sn1–Zn bond (2.742(1) Å) is comparable to *inter*- and *exo*-cluster separations found in $Na_{29}Zn_{24}Sn_{32}$ (2.724(1) - 2.914(1) Å, see Chapter 4.4) and formally reflects a single bond interaction as it is in the same range as the sum of the single bond covalent radii of the elements.[36, 37] A point of interest is the site preference of Zn atoms. In the present structure Zn and Sn atoms, are distributed to the positions of the three dimensional network.[38] Since all network atoms are formally four-bonded the method of 'topological charge stabilization'[39] based on electronegativity (electronegativer elements prefer positions with higher electron density) is not applicable. Apparently Zn avoids the 16*e* (Sn1) site that would put three Zn atoms next to each other but prefers the 4*a* position which is well separated and surrounded only by Sn (Figure 4.6b). This is consistent with a high site energy neighboring 4b-Zn^{2-} (or Zn^{2+} when treating Zn as a typical cation) would experience due to electrostatic repulsion, whereas the placement into a tetrahedral lone pair cage of Sn is a more desirable coordination. Besides, the number of heteroatomic contacts is maximized.

Another structural feature is the significant disorder with large thermal displacement parameters of Na atoms that are located inside the channels of the anionic framework. Such displacement is common among clathrate-like frameworks and has its origin in the cavity sizes that are too big for the guest cations. Here, the sodium atoms are distributed to equal amounts (50%) around a screw axis and are significantly dispositioned from the channel centers (which lie at y = 0 along *a* and at y = 0.5 along *b*). The thermal ellipsoids are elongated along [201] and [–201]. In Figure 4.7b the coordination environments of Na atoms are depicted with the cation displaced from the pore's center. The red lines indicate the shorter Na–Sn and Na–Zn separations ranging from 3.10 to 3.31 Å, whereas the dashed red lines mark the longer contacts ranging from 3.49 to 3.57 Å. In the pore, up to 3.6 Å, six Na–Sn distances (3.10(1) to 3.525(7) Å) with an average of 3.36 Å are present, whereas the two Na–Zn contacts (3.18(1) and 3.57(1) Å), have an average of 3.38 Å.

These values are not significantly different but regarding distances up to 4 Å the average Na–Zn separation of 3.38 Å is considerably larger than 3.11 Å for the average Na–Sn contact. Thus, it can be concluded that Na is off-centered in the pores in order to be closer to the more electronegative Sn. A hypothetically ordered Na position would follow the pore walls in a zigzag alignment.

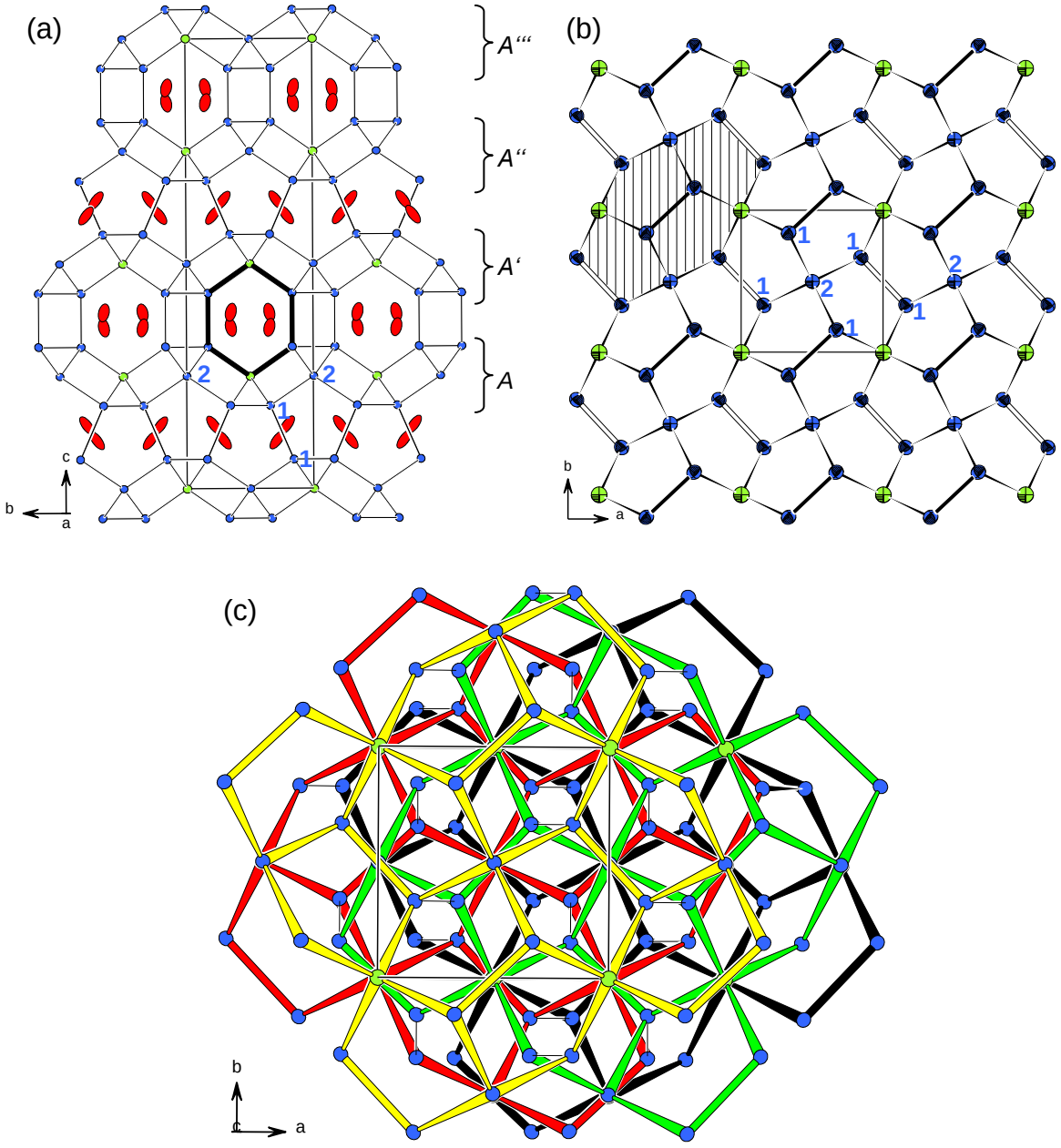

***Figure 4.6*. Structural details of Na_2ZnSn_5. (a) Unit cell projection along [100]. A helical chain is indicated with thick lines (all atoms at 50%). (b) Projection of a single layer along [001]. Thick lines mark Sn1-Sn1 bonds located up (black) and below (white) a hypothetical square planar layer of Zn and Sn2 atoms at *z* = 0 (90% probability). One tub like half shell is indicated. Na (red), Zn (green), Sn (blue). (c) Projection along [001] emphasizing the stacking of the layer motif according to the sequence *AA'A''A'''*. The corresponding layers are outlined with black, red, green, and yellow lines, respectively.**

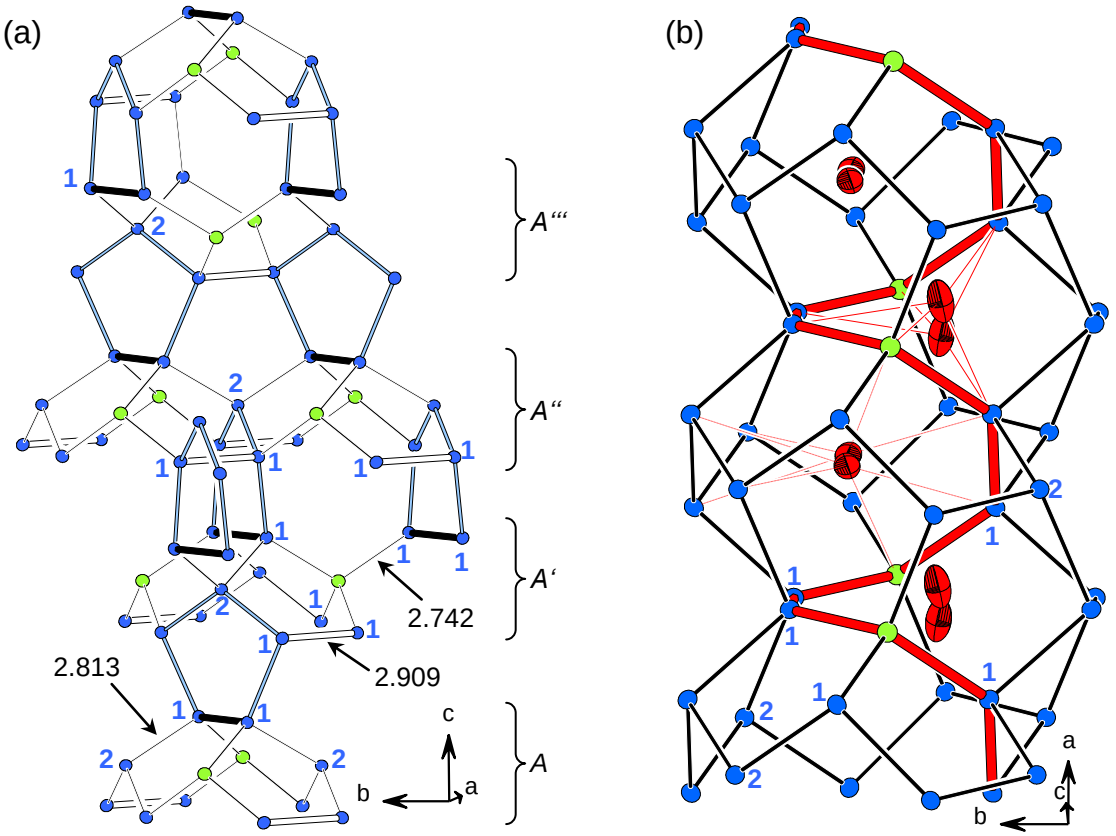

***Figure 4.7*. (a) A more detailed view of the anionic network with twisted Sn pentagons (light blue lines) interconnecting the corrugated layers made of tub-like half shells. Sn1–Sn1 bonds are emphasized by thick filled and empty lines. (b) Na disposition and displacement inside a framework channel. For the upper Na atoms Na–Sn and Na–Zn distances are given only between 3.10 - 3.31 Å (thin red lines), for the lower, interactions between 3.49 - 3.57Å (dotted red lines) are drawn. One helical channel is indicated with thick red lines. Thermal ellipsoids with 50% probability. Na (red), Zn (green), and Sn (blue).**

Structure Description of $NaZn_{0.3}Sn_{2.7(1)}$ The structural arrangement of $NaZn_{0.3}Sn_{2.7(1)}$ is the same as reported for $NaTrSn_2$ (Tr = In, Ga) by Blase and Corbett, respectively. The unit cell (Figure 4.8a) shows the 3D network of 4b-atoms. The network atoms Zn and Sn show no site preference and the atomic positions are statistically occupied (8% Zn on 4*b* and 10% Zn on 8*c*, respectively). The structure in a view down the *c*-axis is built of helical chains of six atoms per turn that are composed of the tetrahedrally-coordinated M (= Zn/Sn) atoms with pore diameters ranging from 5.2 to 5.3 Å. In contrast to Na_2ZnSn_5 and due to symmetry these channels run only along one axis. The splitted Na atoms, Na_a and Na_b have comparable average distances of 3.27 and 3.31 Å to the next nearest M atoms. Distortions in the framework result in interbond angles from 105.7° to 124.6°. The helical chains run parallel to the *c*-axis and enclose the sodium cations.

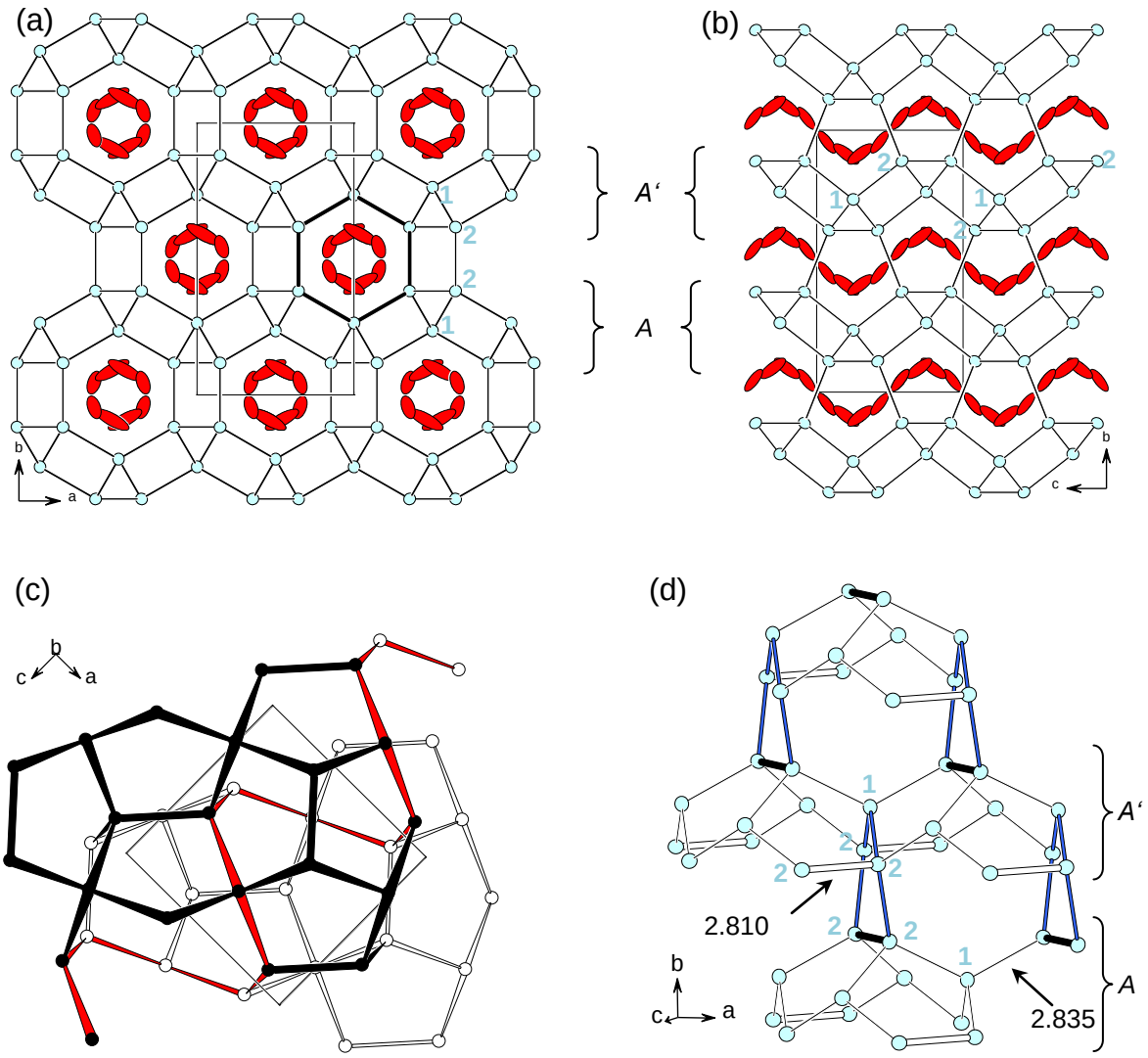

***Figure 4.8*. The structure of $NaZn_{0.3}Sn_{2.7(1)}$ (a) Projection along [001]. (b) Projection along [100]. Both Na split positions are shown. The six member helical chain is emphasized. Thermal ellipsoids are drawn with 50% probability. (c) Schematic representation of two layers at *y* = 0.76 (open lines, empty atoms, layer *A*) and 0.24 (filled lines, filled atoms, layer *A*'). One helical channel is indicated with thick red lines. (d) More detailed view on two adjacent layers emphasizing on the interconnection of the tub-like half shells that are interconnected by pentagons (blue lines). Thick lines denote M2–M2 bonds. In all pictures except for (c): Mixed occupied sites M = Zn / Sn (light blue), and Na (red).**

Two vertices of each layer are associated with one channel while the other two bonds connect it to two adjacent helices. This results in the above described layered structure that is crosslinked along the long *b*-axis. Figure 4.8c is a view of two adjacent layers along *b*. The layers are composed of tetrahedrally coordinated atoms with all M1 atoms four-bonded within the layer while the M2 sites on the surfaces of each layer are three bonded within the layer and form a fourth bond to an M2 atom on the adjoining layer above or below.

The sequence of the layers can be assessed by a translation of the layers along *a* with *a*/2 which leads to the stacking sequence *AA*'*AA*' (Figures 4ba and 4.8b). This construction results in channels along the *c*-axis (Figure 4.8a) and a network of five membered, twisted pentagons interconnecting the layers along [100]. In the anionic framework bond lengths range from *d*(M1–M2) = 2.809(1) Å, *d*(M2–M2) = 2.834(1) Å, to *d*(M1–M2) = 2.835(1) Å and lie between the shortest and longest Sn–Sn contacts in the ordered compound **1**. Similar to **2** in this compound the most important feature seems to be the formation of the tetrahedra network which leaves the sodium atoms in a less than ideal position. Following the spiral like channels the ~ 50% : 50% split cations are dispositioned in a helical assembly along [100] from the projected channel center.

4.2.3 Electronic Structure of Na_2ZnSn_5

The electronic structure of Na_2ZnSn_5 was calculated by lowering the system's symmetry into the orthorhombic space group *Fdd*2 (No. 43). The space groups *I*–42*d* and *Fdd*2 have no direct group-subgroup relation but the overall composition and atomic connectivities are equivalent. The structure refinement in *Fdd*2 is of comparable quality (R_{int} = 0.026; R_1 = 0.029; wR_2 = 0.062 (all data)). Due to the throughout mixed occupied network sites no comparable calculations could be carried out for **2**.

In the new space group the Na position is fully occupied and an additional Sn position is created by the transformation of 16*e* to 16*b* (× 2). Compared to the true space group (*I*–42*d*), symmetry directions in the band structure change, due to different directions of the reciprocal lattice vectors. Nevertheless, a qualitative analysis of the interatomic bonding is possible. The band structure, together with DOS projections, as calculated from the LMTO program (4096 *k* points), are shown in Figure 4.9. DOS projections for all three elements are given in Figure 4.10. A gap is discerned at the Fermi level and qualifies the compound as a semiconductor with a calculated energy gap of ~ 0.5 eV. The detached valence band between –3 eV and the Fermi level consists mainly of Sn-5*p* bonding states and few contributions from Na-3*s*/3*p* and Zn-*p* states. The DOS projections clearly indicate segregation of the bands for each of the elements. Sn-*s* orbitals are confined in the area of –10 to –5 eV. Some orbital mixing can be observed from –5.5 to –3.5 eV.

A similar situation is found for Zn. The core like *d* orbitals are completely filled and separated at lower energies at ~ –8 eV. They do not take part in the bonding but show an antibonding interaction with Sn-*s* bands. The Zn-*p* and Zn-*s* contributions are filled and mainly found in the valence band and in the region from –4.5 to –3 eV, respectively. No such clear separation is revealed for Na, for which the *s* and *p* bands decidedly mix but are barely populated. Since the contributions of the elements to the total DOS reflect the composition of the compound it can still be concluded that Zn-*p* Sn-*p* mixing, i.e. covalent bonding between these two elements, is present. To compare interactions between atoms –COHP analyses were evaluated (for all bonds up to 4 Å). They revelead strong bonding character for Sn–Sn bonds. An overall bonding character is also present for Zn–Sn and Na–Sn with no unoccupied bonding or antibonding states left above E_F. All bonds are optimized. The covalent bonding between the network-atoms is quantified by –ICOHP populations. All calculated values are listed in Table 4.5.

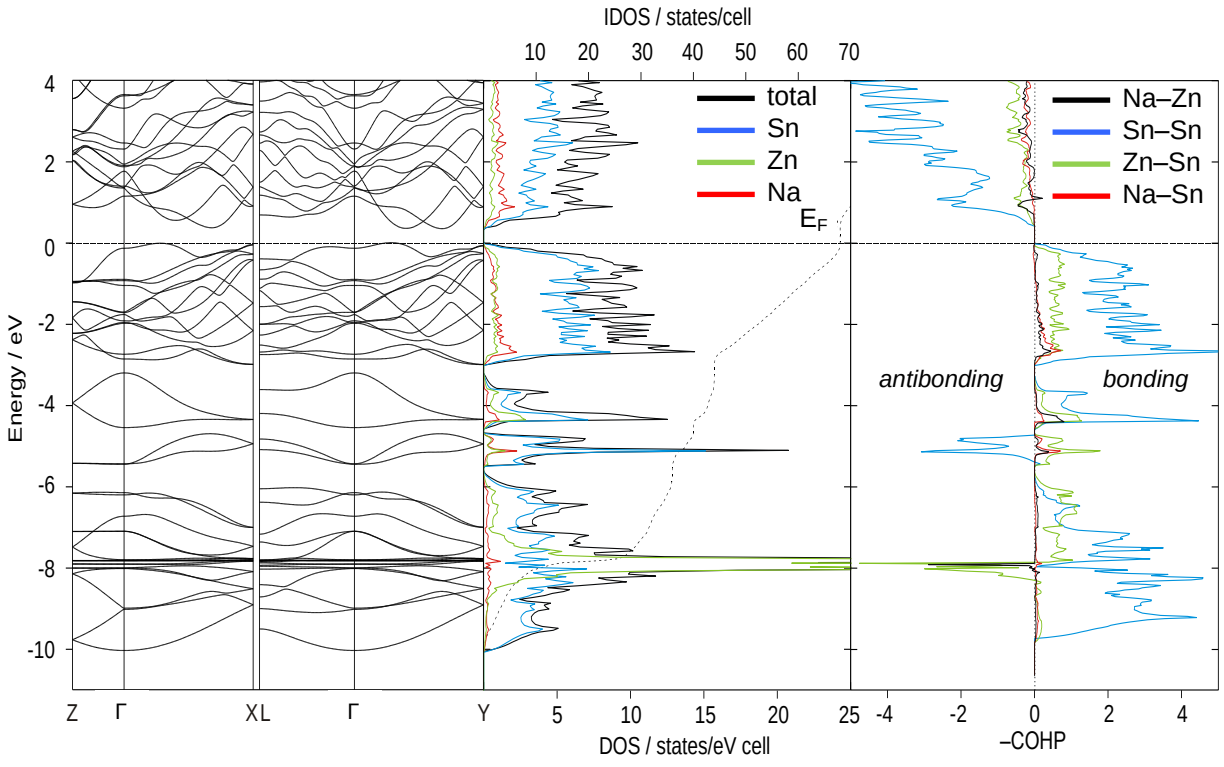

Figure 4.9. **Band structure (left) and DOS (center) for Na_2ZnSn_5. Sn (blue), Zn (green), Na (red). The –COHP diagrams (right) show the sum of all Sn–Sn (blue), Zn–Sn (green), Na–Sn (red), and Na–Zn (black) interactions (≤ 4 Å).**

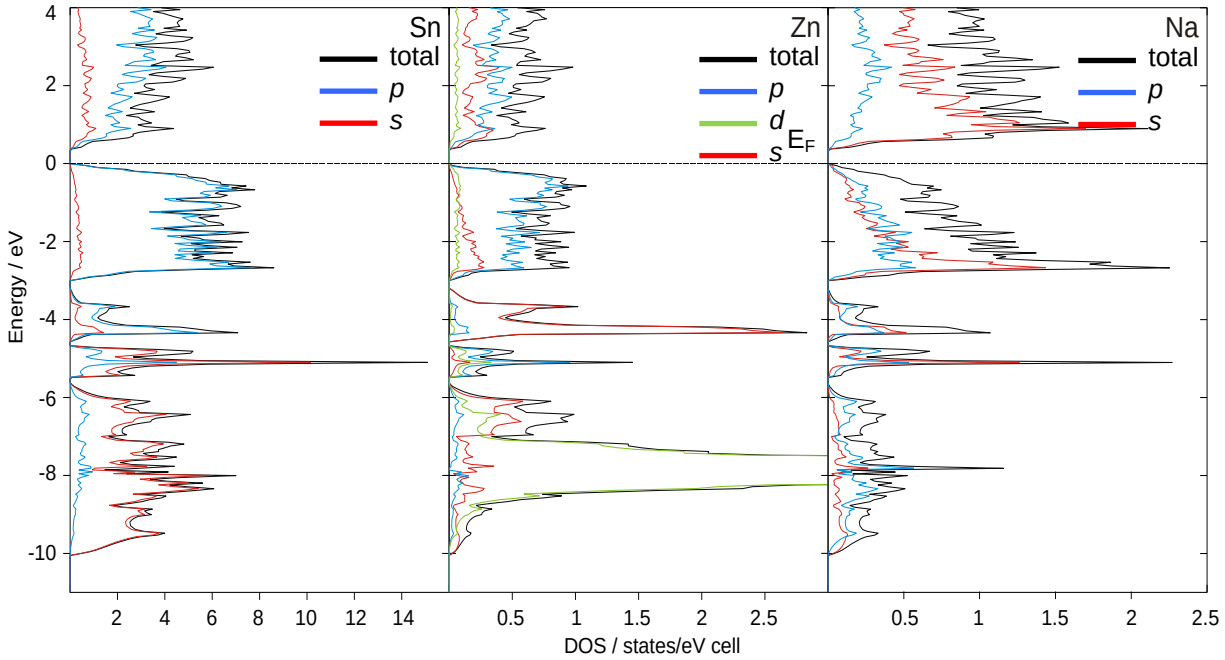

***Figure 4.10*. Projected DOS diagrams for Sn (left), Zn (center), and Na (right) in Na_2ZnSn_5 (space group *Fdd*2). Orbital contributions: *p* (blue), *s* (red), and *d* (green).**

As expected from interatomic distances the Sn–Sn bonds have bond energies ranging from 2.05 to 2.42 eV/bond, values that are typical for covalently bonded Sn atoms. The Zn–Sn bonds are slightly weaker (1.72 eV/bond) but much stronger than expected for a purely ionic interaction. Thus, as also revealed from the DOS diagrams, this contact has covalent character. Compared to that the Na–Zn and Na–Sn interactions (0.12 eV/bond, 0.14 eV/bond, respectively) are much smaller and suggest rather ionic bonding.

***Table 4.5*: –ICOHP values for selected interatomic contacts in Na_2ZnSn_5 (space group *Fdd*2). Energies are given in eV/bond.**

interaction		*d* / Å	–ICOHP (at E_F)	–ICOHP (max.)
Sn1	Sn2	2.814(1)	2.42	2.42
Sn1	Sn3	2.813(1)	2.42	2.42
Sn2	Sn3	2.908(2)	2.05	2.05
Zn	Sn	2.741(1)	1.72	1.72
Na	Sn	3.427(2)	0.14	0.15
Na	Zn	3.338(1) - 3.362(1)	0.12	0.12

4.2.4 Discussion

Applying Zintl's electron counting scheme, Na_2ZnSn_5 (**1**) can be rationalized as $(Na^+)_2(4b\text{-}Zn^{2-})(4b\text{-}Sn^0)_5$ or, taking into account the more classical role of Zn as a cation, $(Na^+)_2(Zn^{2+})(3b\text{-}Sn1^{1-})_4(4b\text{-}Sn2^0)$.

With respect to the –ICOHP values between Zn–Sn bonds the latter formula seems less appropriate. The presented compound is a new Zintl phase with a narrow band gap and a framework of throughout four-bonded framework atoms which is reflected in the VEC/M that equals four. The Zn–Sn distance of 2.742(1) Å is only slightly larger than the sum of Pauling's covalent radii[36, 37] for single bonds: r(Sn) + r(Zn) = 1.399 Å + 1.249 Å = 2.648 Å. However, the comparable values of –ICOHP bond strengths point to covalent interactions between these elements.

The reason for the throughout statistically occupied framework sites in $NaZn_{0.3}Sn_{2.7(1)}$ can be attributed to the system's electron need of the same four valence electrons per atom. Using the Zintl concept, the structure of $NaZn_{0.3}Sn_{2.7(1)}$ can be rationalized as $Na^{+}(4b\text{-}Zn^{2-})_{0.3}(4b\text{-}Sn^{0})_{2.7}$ and a slight average electron excess of 0.40 per formula unit is calculated. Fixing the occupancy factors to a hypothetical electron balanced compound would result in '$NaZn_{0.5}Sn_{2.5}$', which indeed has the same stoichiometry as **1**. With respect to the high standard deviatons this suggest the possible formation of a polymorph, or phases with slightly different colorings (phase widths), which was also indicated by DTA measurements.

As mentioned before, the present corrugated layers of 5-member rings are found in related structures such as in $NaGaSn_2$ or $NaSn_5$. Figure 4.11 depicts the differences of these structures. The anionic frameworks of **2**, $NaGaSn_2$, $NaInSn_2$, and $NaGaSn_5$[29] (the latter one could not be reproduced in the reported stochiometry by Corbett[31]) are isotypic and feature the described corrugated layers (with completely disordered *p* elements) connected in one crystallographic direction in a *AA'AA'* stacking sequence. $NaSn_5$ contains equivalent homoatomic layers that are separated by planar square (4^4) nets which are reminiscent of *β*-Sn. The different stacking of the puckered layers (compared to $NaGaSn_2$) in compound **1** is a direct result of the coloring. The term 'coloring' refers to the 'four-color problem' in mathematics, where the original basic problem is 'to find the smallest number of colors necessary to color the countries of any map so that each two countries with a common border have different colors.' In Na_2ZnSn_5 the Zn atoms try to maximize homoatomic distances and do not take part in the interconnection of the layers. With respect to the stacking sequence of the corrugated layers this is the lowest energetic configuration. Within the layers each pentagon involves only one Zn atom (with *d*(Zn–Zn) > 6.3 Å).

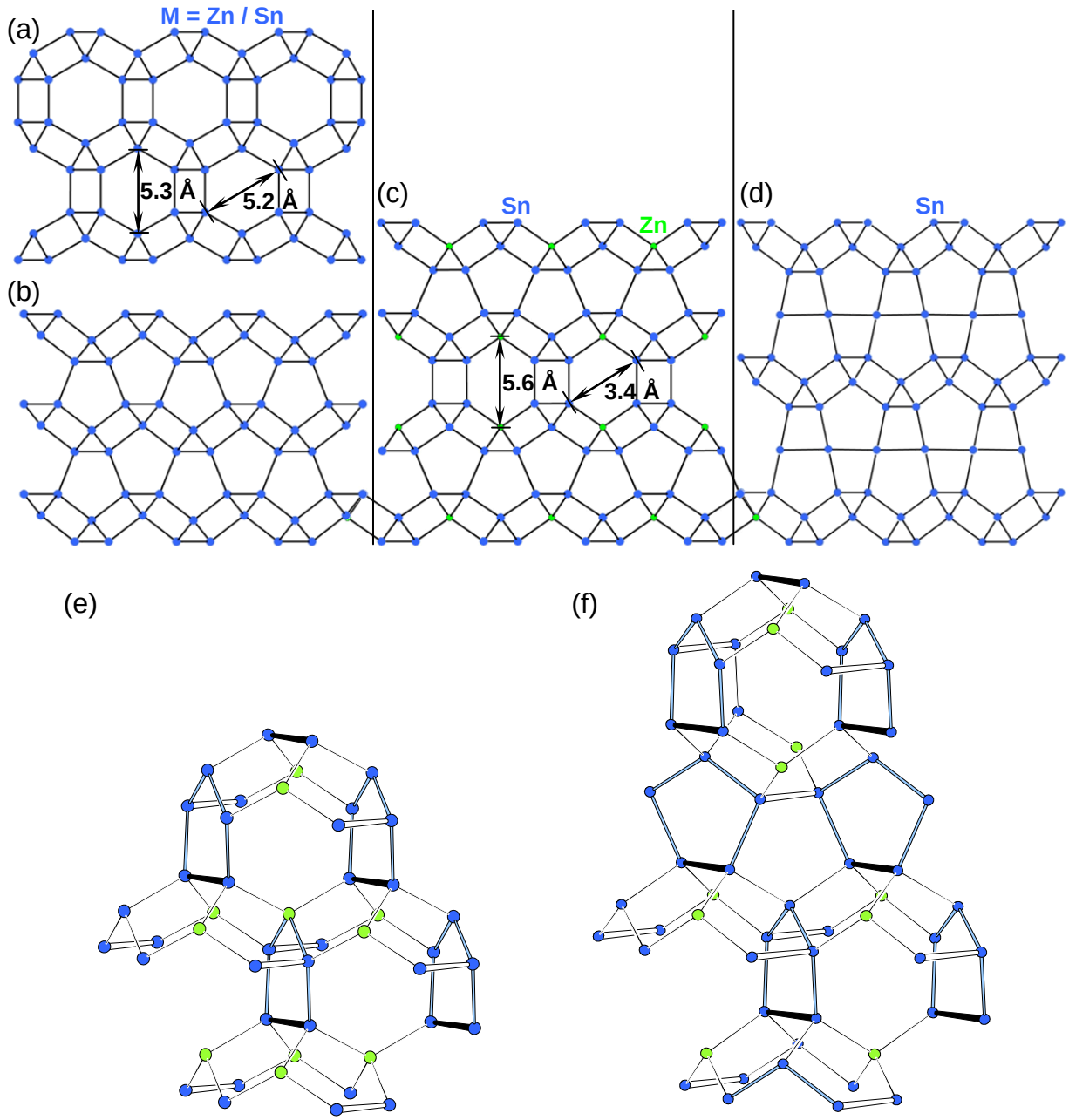

***Figure 4.11*. (a) to (d) Related structures containing the same corrugated layers of pentagons made of 4b-atoms: (a) and (b) two projections of $NaZn_{0.3}Sn_{2.7(1)}$ ($NaGaSn_2$, $NaInSn_2$). (c) Na_2ZnSn_5, and (d) $NaSn_5$. Pore diameters are shown for $NaZn_{0.3}Sn_{2.7(1)}$ and Na_2ZnSn_5. (e) Ordered network of hypothetical '$NaZnSn_2$'. (f) Ordered network of compound 1. Sn (blue), Zn (green). In (a) and (b) the M = Zn / Sn atoms are blue.**

An ordered network for the hypothetical structure of '$NaZnSn_2$'. (with 100% Zn and 100% Sn of M1 and M2 site, respectively, see Figure 4.11e) would result in pentagons including two Zn atoms and shorter Zn–Zn separations of ~ 4.5 Å. However, this is considerably larger than twice the van der Waals radius for Zn but with respect to the resulting low average VEC/M (3.67), with respect to a valence compound with VEC = 4, for this structure, i.e. this layer stacking, throughout mixed occupied framework atoms with overall less Zn content are expected.

Unfortunately, due to symmetry problems no band structure calculation for the two hypothetical phases 'NaZnSn_2' or 'NaSn_3 (both M sites occupied with 100% Sn)' could be carried out in order to see if the mixed site occupancies stem from non-optimized bonding situations. Regarding the ordered atomic sites of Na_2ZnSn_5 structure selection must also be intimately related to lattice effects. This is reflected in averagely larger and more balanced pore diameters (Figure 4.11a to 4.11c) for **2**, whereas for **1** the pores are less symmetric, with the larger values (5.6 Å, along *c*) calculated for the diameters involving Zn–Zn separations. Hence, in the latter case the atomic ordering takes place by doubling one cell parameter. On the bottom line the atomic positions in the disordered network of **2** are more 'alike' in terms of coordination and cation-anion separations. The driving force for both compounds is the formation of the 3D network and leaves behind the Na cations in a less favorable situation. The poor environment is reflected in the large corresponding thermal ellipsoids, in the occupancies refined, and dispositions. Such disposition and displacement of the atoms has been reported to be typical for tunnel-like structures with small cations, such as $K_{0.4}Cd_2$[40], K-Au-In networks,[41] and the hollandite type compounds.[42] The Na atoms in **1** and **2** show significant disposition from the (helical not cylindrical) channel centers. The cations favor the movement further from the channel centers and closer to one pore wall in order to maintain proper bonding distances to the framework and maximize the number of close neighbours. This is obvious in the larger pores of $NaInSn_2$, where the cations are significantly more off-centered. Similar observations have been made in other systems, such as in $CaNa[La_9I_{16}N_4]$[43] where changes in either the cation or the framework result in a shift of the cation positions within a structurally unchanged channel.

The described microporous intermetallic phases **1** and **2** are also closely related to the *cP*54 clathrates with group 14 elements where the cations are trapped in cages rather than in tunnels. Since one of the most intensively studied solids are the inorganic open and closed framework structures, the two compounds presented here can be seen in the context of new materials with promising chemical and physical properties. The predominant class of framework materials with three dimensional crystalline structures studied *hitherto* were the aluminosilicate zeolites of general formula $A_{x/n}[Si_{1-x}Al_xO_2]\cdot mH_2O$.

They exhibit great stability, thus they are widely utilized in the fields of catalysis, separations, or ion exchange. By expanding the syntheses to as many as 25 elements of the *p*-block and the transition series as major components new frameworks in the realm of phosphates, oxyfluorides, nitrides, sulfides, and coordination compounds have been found.[44] Closed framework compounds often feature guests encaged in a host structure. Intermetallic compounds with open/closed frameworks made of tetrels have attracted attention mainly because of their unique structures. Recently the interest in these compounds with rigid covalent networks has shifted towards their potential for optics, thermal conductivity, and superconductivity.

To date at least two types of Zintl phases have been synthesized that are isostructural with microporous oxide framework structures and show the result of the chemical reduction of the diamond structure in order to create four-bonded networks: Clathrate-I derivatives with the general formula $A_{8-x}T_{46-y}$ (A = Na - Cs, Ba, T = group 13 - 15 element mixtures)[45] in which the framework T positions are those of Al and Si in sodalite, and the clathrate-II type compounds Cs_7Si_{136} and Na_xSi_{136}[46] ($3 < x < 11$) wherein the framework is isotypic with the tetrahedral centers in the aluminosilicate ZSM-39.[32] They are reminiscent of the analogous isomorphus gas and liquid hydrates $G_8(H_2O)_{46}$ or $G_8G_{16}(H_2O)_{136}$ (G = Cl_2, Xe, CH_4, etc.). In general, the four clathrates with tetrel frameworks known so far are clathrate-I (A_8Tt_{46}), clathrate-II ($A_{24}Tt_{136}$), clathrate-III ($A_{30}Tt_{172}$) and chiral clathrate ($A_{32}Tt_{100}$).[47] These materials have the ability to cloak ‘rattling’ and displaced A/Ae cations that effectively scatter heat-carrying phonons within the cages formed by the framework. In that cases the cations do not exhibit large relative displacement parameter ratios due to the more spherical environment in such cages made of pentagon dodecahedra or tetrakaidecahedra (although these cages are not perfectly spherical).

However, structures with host frameworks in which the guest species is not entirely encapsulated in closed cages, but rather in tunnel or helical like networks are less common.The present two clathrate-like compounds with their heavy structural cation disorder might exhibit similar interesting physical properties, such as effective dampening of heat carrying phonons, and might qualify as ‘Phonon-Glass and Electron Crystal’ with interesting thermoelectric properties. Ion conducting properties may also be present.

4.3 $Na_5Zn_{2+x}Sn_{10-x}$ (x = 0.28) - An Intermediate Phase between the *α*-Sn and Half-Heusler Structure

The compound presented in this chapter is comparably Sn rich as the phases discussed in the last subchapter. Again the VEC per framework atom here is high enough to generate a novel network structure made of exclusively four bonded atoms that can be traced back to precendents of simple four bonded systems.

4.3.1 Synthesis and Characterization

Synthesis This compound was first found as single-crystals in a synthetic attempt that aimed to investigate the substitution of Na by Ca in the quaternary system Ca–Na–Zn–Sn. The product of a sample loaded as Na : Ca : Zn : Sn = 4 : 3 : 3 : 9 resulted into a mixture of *β*-NaSn, CaZnSn and $Na_5Zn_{2.28}Sn_{9.72(2)}$. Later the compound could also be found as a byproduct, together with Na_2ZnSn_5 (Chapter 4.2), in a synthetic approach with loading ratio Na : Zn : Sn = 5 : 2.35 : 9.65. An almost pure phase was accidently produced (see powder diagram below) when trying to prepare a pure phase of Na_6ZnSn_2 (Chapter 4.7), with ratios Na : Zn : Sn = 6 : 1 : 2, by quenching the hot ampoule (500 °C) in liquid nitrogen and subsequent annealing at 350 °C for seven days. In this experiments Ta ampoules served as reaction containers and the total chemical loading of 1.075 g consisted of m(Na) = 0.469 g, m(Zn) = 0.131 g, and m(Sn) = 0.475 g. The target compound crystallizes in form of silvery block shape crystals that are air and moisture sensitive at room temperature. The Hg analogue, $Na_5Hg_{2+x}Sn_{10-x}$ (x = 0.39), was obtained by use of a Sn flux and stoichiometric amounts of Hg and Na.[48]

EDX Analysis The bulk purities of selected single-crystals were independently confirmed from EDX analysis; indicating the presence of only Na, Sn and Zn elements. No other element could be detected. Average detected ratio: Na : Zn : Sn = 25(3) : 13(4) : 62(3) at%; calculated ratio: Na : Zn : Sn = 29.4 : 13.5 : 57.1 at%.

Powder X-ray Diffraction The measurements were carried out in capillaries in Debye-Scherrer mode and lastet for 16 h (1.5° step width). The product was finely ground in an agate mortar, diluted with diamond powder and filled into a glass capillary which was in turn sealed using a red-hot platinum wire.

The experimental diagram together with the calculated diagram from single-crystal refinement data are shown in Figure 4.12. The picture shows the formation of the target compound as a nearly pure phase, with no reflections from binary Na phases, as one would expect from the loading stoichiometry. Some reflections that could not be assigned are marked with a red star. During quenching (the crucible was dropped into a metal bucket that was filled with liquid nitrogen) the excess elements might have been accumulated at one side of the crucible, which was removed upon opening.

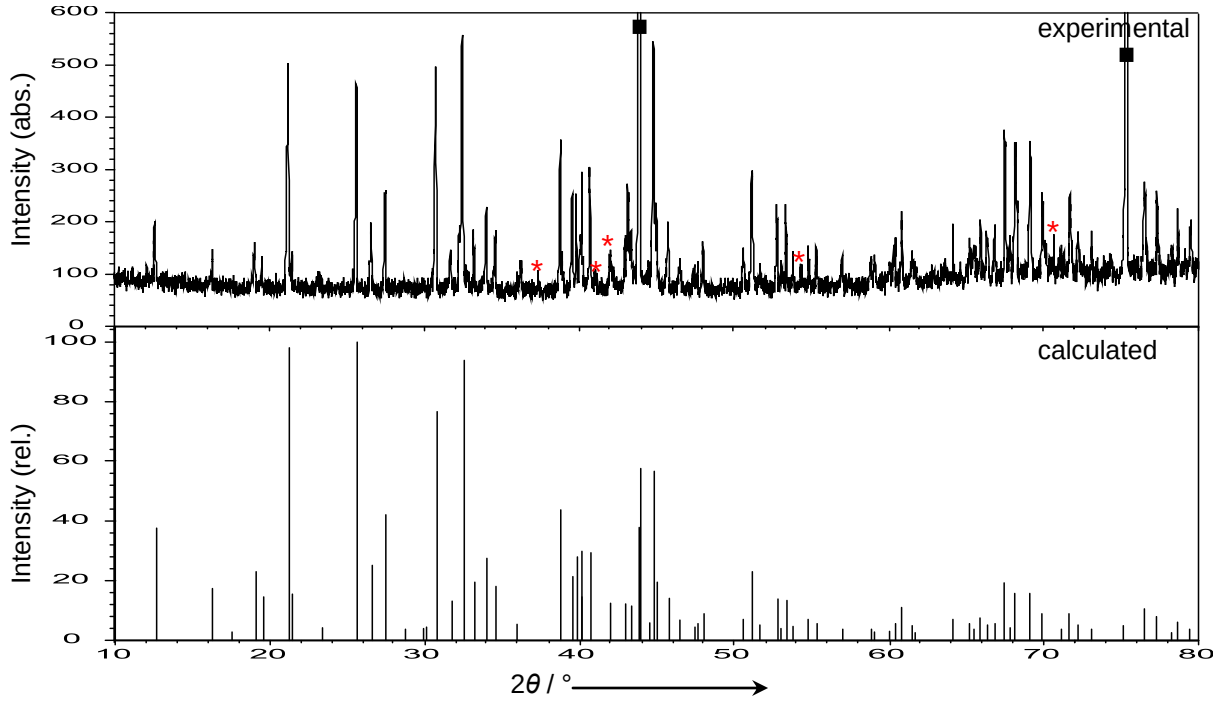

***Figure 4.12*. Experimental powder diagram (top) from a quenched sample with loading Na : Zn : Sn = 6 : 1 : 2 and calculated powder diagram (bottom) of $Na_5Zn_{2.28}Sn_{9.72(2)}$. Reflections from diamond (internal standard) are labeled with a square. Unindexed reflections are labeled with a red star.**

4.3.2 Crystal Structure Determination and Description

Structure Determination A single-crystal was selected in an argon-filled glovebox and mounted in a glass capillary which was subsequently sealed to prevent contact with air. Several crystals were first checked for singularity and the best crystal was used for full data collection at room temperature. The data was collected on the Oxford Xcalibur3 diffractometer. Four series with a total of 776 frames were collected with an exposure time of 20 s each and a crystal-detector distance of 50 mm. The reflections were collected over the range 2θ = 55.5° and corrected for absorption (empirical) using the program CrysAlis RED (Oxford Diffraction Ltd).

The phase $Na_5Zn_{2+x}Sn_{10-x}$ (x = 0.28(2)) crystallizes in the space group *Pbcn* (No. 60, Z = 4) with a = 12.772(1) Å, b = 10.804(1) Å, and c = 12.777(1) Å. Structure refinements in tetragonal space groups, including non-centrosymmetric $P\text{–}42_1m$ (No. 113), led to comparable final residuals, but resulted in statistically occupied anion positions distributed only in one of two chemical equivalent polyhedral layers and were therefore not considered. Relevant crystallographic and refinement details are listed in Table 4.6, Table 4.7, and Table 4.8 contain the atomic positions and equivalent displacement parameters. In Table 8.2 (see Appendix) interatomic distances (≤ 4 Å) are given.

***Table 4.6*: Selected crystallographic and refinement data for $Na_5Zn_{2.28}Sn_{9.72(2)}$.**

Empirical formula	**$Na_5Zn_{2.28}Sn_{9.72(2)}$**
Formula weight / g·mol^{-1}	1417.66
Temperature / K	293(2) K
Crystal size / mm^3	0.10 × 0.10 × 0.10
Crystal color; shape	Silvery metallic; Block
Diffractometer	Oxford Xcalibur3 (CCD)
Crystal system	Orthorhombic
Space group	*Pbcn* (No. 60)
Unit cell parameters / Å	a = 12.772(1); b = 10.804(1) c = 12.777(1)
Unit cell volume / Å^3; Z	1763.1(2); 4
ρ_{calc} / g·cm^{-3}	5.34
μ / mm^{-1} (Mo K_α)	16.64
Absorption correction	empirical
F(000)	2438
Θ range / °	2.94 - 27.81
Index range	$-16 \le h \le 13$; $-14 \le k \le 14$; $-16 \le l \le 16$
Data completeness / %	100
Integrated reflections	24268 (R_σ = 0.020)
Independent reflections	2083(R_{int} = 0.036)
Refinement method	Full-matrix least-squares on F^2 (SHELXTL)
Parameters	89
Goodness of fit on F^2	1.218
Observed reflections [$I > 2\sigma(I)$]	1593
R_1 / wR_2 [$I > 2\sigma(I)$]	0.035 / 0.069
R_1 / wR_2 (all data)	0.048 / 0.072
Weighting scheme[a]	a = 0.005; b = 56.701
Extinction coefficient	0.00058(3)
Residual map / e$^-$·Å^{-3}	+1.63 [0.62 Å from Zn1] / –1.14 [0.74 Å from Sn1]

[a] $w = 1 / [\sigma^2(F_o^2) + (aP)^2 + bP]$, where $P = (F_o^2 + 2F_c^2) / 3$

***Table 4.7*: Atomic coordinates and equivalent isotropic displacement parameters for $Na_5Zn_{2.28}Sn_{9.72(2)}$.**

Atom	Wyck.	Occ. ≠ 1	*x*	*y*	*z*	U_{eq} / Å^2
Sn1	8*d*		0.6789(1)	0.1461(1)	0.5725(1)	0.023(1)
Sn2	8*d*		0.9163(1)	0.9215(1)	0.3316(1)	0.018(1)
M = Sn / Zn	8*d*	0.86 / 0.14(1)	0.5809(1)	0.9303(1)	0.6666(1)	0.020(1)
Sn3	8*d*		0.7733(1)	0.2600(1)	0.7529(1)	0.020(1)
Sn4	8*d*		0.4952(1)	0.2487(1)	0.4770(1)	0.020(1)
Zn1	8*d*		0.8361(1)	0.1420(1)	0.4153(1)	0.019(1)
Na1	8*d*		0.8614(4)	0.9560(5)	0.6001(4)	0.035(1)
Na2	8*d*		0.6540(4)	0.9503(5)	0.3928(4)	0.039(1)
Na3	4*c*		0	0.7472(8)	¾	0.040(2)

***Table 4.8*: Anisotropic thermal displacement (/ Å^2) parameters for $Na_5Zn_{2.28}Sn_{9.72(2)}$.**

Atom	U_{11}	U_{22}	U_{33}	U_{23}	U_{13}	U_{12}
Sn1	0.019(1)	0.021(1)	0.018(1)	0	0	0
Sn2	0.018(1)	0.019(1)	0.017(1)	0	0	0
M = Sn / Zn	0.020(1)	0.019(1)	0.020(1)	0	0	0
Sn3	0.024(1)	0.022(1)	0.024(1)	–0.003(1)	–0.003(1)	0.002(1)
Sn4	0.019(1)	0.023(1)	0.019(1)	0	0	0
Zn1	0.020(1)	0.016(1)	0.020(1)	0.002(1)	–0.007(1)	–0.003(1)
Na1	0.040(3)	0.032(3)	0.044(3)	–0.007(2)	–0.005(2)	–0.002(2)
Na2	0.037(3)	0.031(3)	0.037(3)	0.002(2)	–0.008(3)	0.006(2)
Na3	0.035(3)	0.053(4)	0.032(3)	0	0.002(4)	0

Structure Description The structure contains nine independent atomic sites, one of which is occupied by Zn, five by Sn, and one is statistically occupied by Zn and Sn (~ 14% Zn). The cations are distributed among three Na sites from which one is at a special position (Na3 at site 4*c*). The novel framework can be viewed as built from covalently bonded Sn and Zn atoms, which are embedded in distorted tetrahedral coordinations.

As depicted in Figure 4.14a the major structure motif are interconnected realgar like cages which results in a complex 3D network structure. The eight atom realgar like entity can be seen as the outcome of two trigonal prisms being face fused (see inset). The unit consist of four Sn atoms $(Sn3)_2(Sn4)_2$ in the common face of the trigonal prisms, a $(Sn2)_2$ dumbbell, and a M_2 dumbbell on each of the opposite sides. The longest homoatomic Sn–Sn contact is found between the equatorial Sn2 atoms (*d*(Sn2–Sn2) = 2.986(1) Å), and between the mixed M sites (*d*(M–M) = 2.969(1) Å). The cluster is *exo*-bonded at each vertex to atoms of Sn1Zn1 dumbbells that bridge the cluster units. The shortest *exo*-bonds range from *d*(Sn3–Zn1) = 2.717(1) to *d*(Sn4–Zn1) = 2.723(1) Å. Interestingly the M–Sn1 *exo*-bonds (2.907(1) Å) are longer than the longest homoatomic *exo*-bond: *d*(Sn3–Sn1) = 2.877(1) Å. Similar homoatomic realgar units made of Sn are found in the Zintl phase $NaSn_2$.

The *exo*-bonds of {Sn_8} units in $NaSn_2$ are slightly longer with 2.93 and 2.95 Å. As indicated in the unit cell projection the clusters in the present compound are aligned in layers along the (010) plane and are stacked in a *AA'AA'* sequence along [010].

As a result of the distortion of the tetrahedral coordinations, the pure Sn–Sn bond lengths (Table 8.2) range from *d*(Sn2–Sn4) = 2.865(1) Å to *d*(Sn2–Sn2) = 2.986(1) Å in agreement with those found in many Na–Sn binary systems, in which Sn–Sn bond lengths are generally longer than the ideal 2.810 Å in *α*-Sn. The {Zn1(Sn1Sn2Sn3Sn4)} tetrahedron is also distorted with Zn–Sn distances ranging from 2.717(1) to 2.840(1) Å. So the Zn–Sn bond lengths compare well with the sum of the covalent radii of the atoms (1.40 Å + 1.33 Å = 2.73 Å).

From a topological point of view the structure of $Na_5Zn_{2.28(2)}Sn_{9.72(2)}$ is built up by two fundamental structural features: the realgar-like {Sn_8} unit and the {Zn1–Sn1} dumbbell fragment (Figure 4.14) that are interconnected in the (010) plane to form a sheet with [ZnSn] : [Sn_8] ratio of 2 : 1. The simple *AA'AA'* stacking allows the anionic sheets further connections in the [010] direction that results in a 3D anionic framework in which no direct connection is observed between two equivalent units.

The larger voids of the 3D framework are occupied by Na cations (Figure 4.15a and 4.17c). The three crystallographically different Na cations have distinct coordination environments, as shown in Figure 4.16. The shortest interaction distances (< 4 Å) between Na cations and the polyanionic framework are between 3.116(5) Å and 3.692(5) Å. The three Na positions are embedded in cage or ring like coordination environments, to which no regular polyhedron can be assigned (Figure 4.16). They form 2D networks along the (010) plane that consist of interconnected larger Na3-centered {$(Na1)_2(Na2)_2$} tetrahedra (Figure 4.16c) centered by Na3 (site 4*c*). Each such tetrahedron is nested between six realgar-like cages in an octahedral fashion (Figure 4.17c). The {$ZnSn_4$} tetrehedron represents a fragment of a hypothetical half-Heusler structure AZnSn, whereas the {Sn_6M_2} unit may be viewed as a fragment of the *α*-Sn structure.

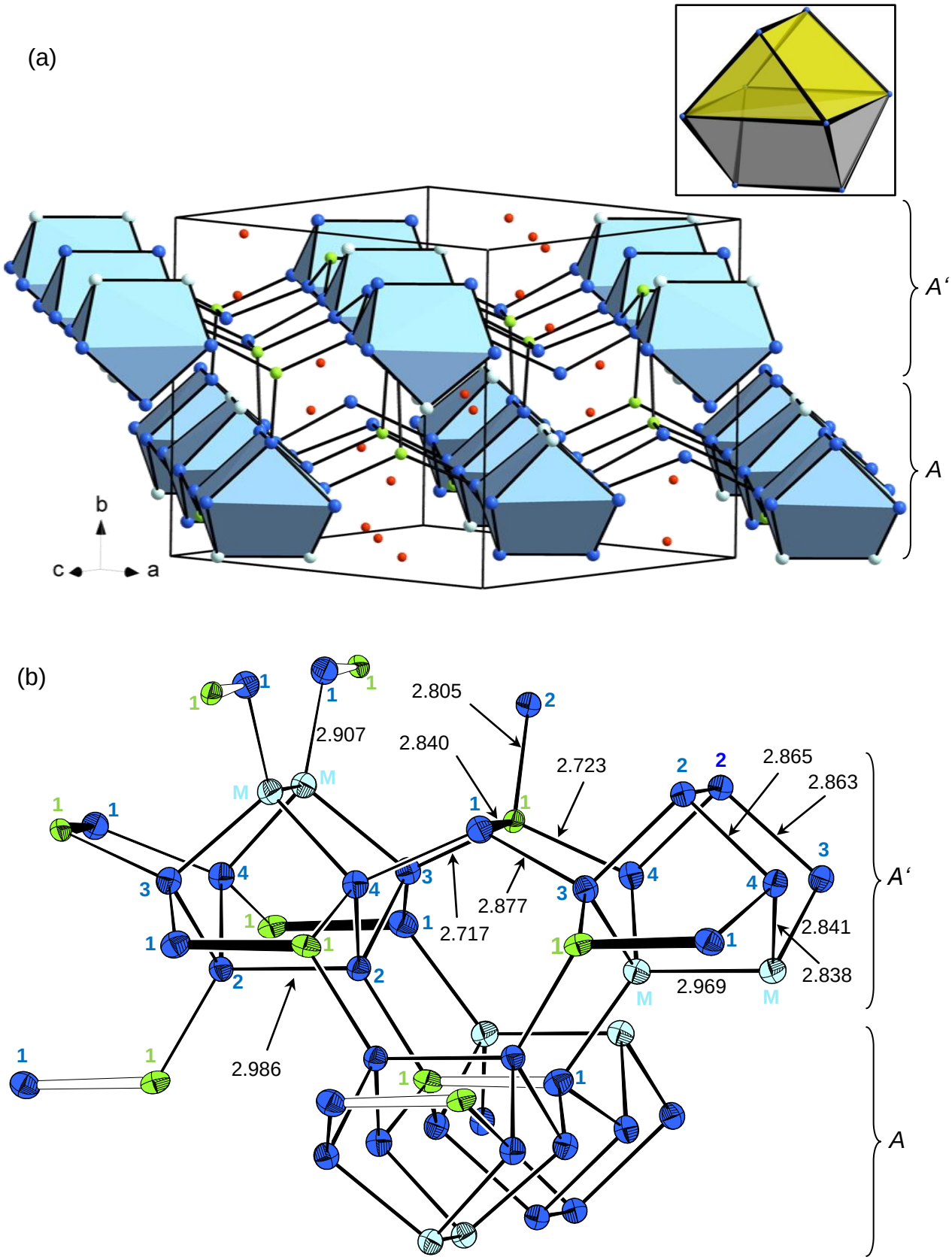

***Figure 4.14*. (a) Polyhedral representation of the unit cell of $Na_5Zn_{2.28}Sn_{9.72(2)}$, the inset shows a realgar cage that can be reagarded as made of two fused trigonal prisms. (b) Connectivity of the realgar-like units in $Na_5Zn_{2.28}Sn_{9.72(2)}$ (90% level). The interbridging Sn1–Zn1 dumbbells are drawn with black thick lines (white thick lines denote dumbbells of adjacent realgar layers). Na (blue), Zn (green), M = Zn / Sn (light blue).**

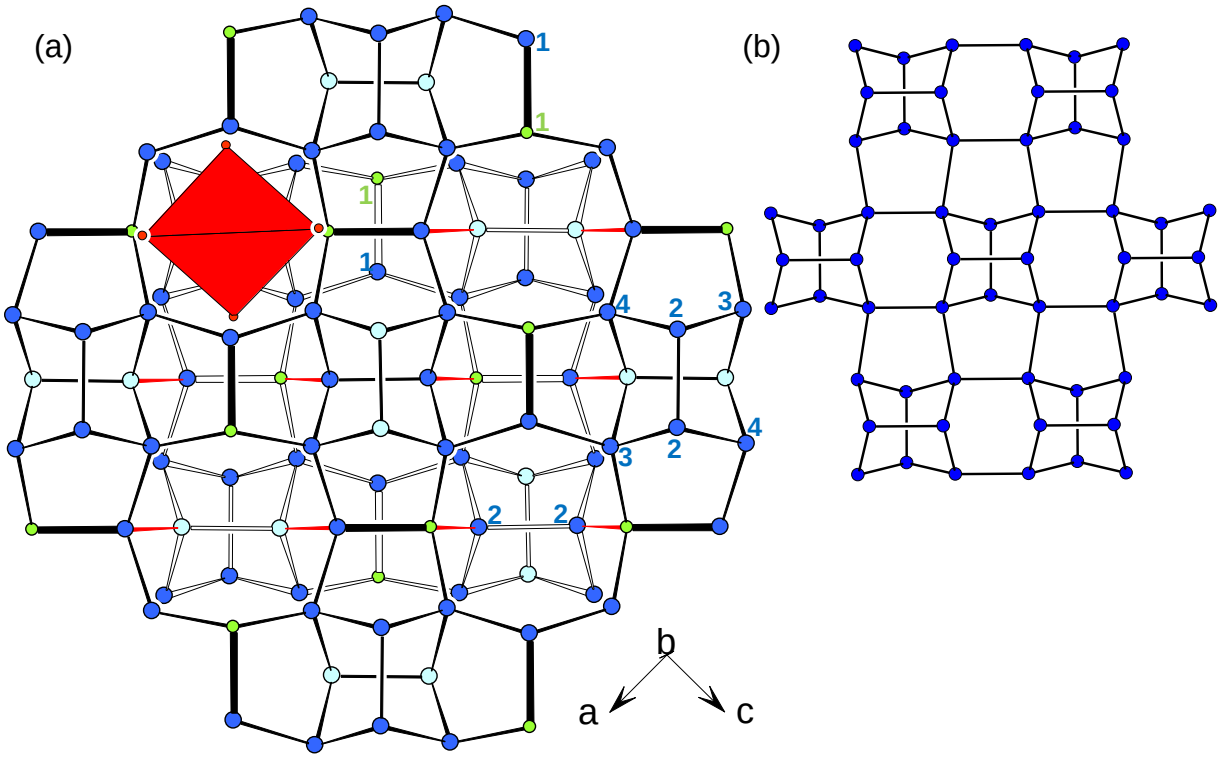

***Figure 4.15*. (a) [010] view of two anionic layers at *z* = ¾ (filled lines) and *z* = ¼ (empty lines) in $Na_5Zn_{2.28}Sn_{9.72(2)}$. Thick lines indicate Sn1-Zn1 dumbbells and red lines mark interlayer contacts, one embedded {$NaNa_4$} tetrahedron is shown. (b) Single layer of interconnected realgar-like {Sn_8} polyhedra in $NaSn_2$. All Na atoms are omitted; Zn (green), Sn (blue), M (light blue).**

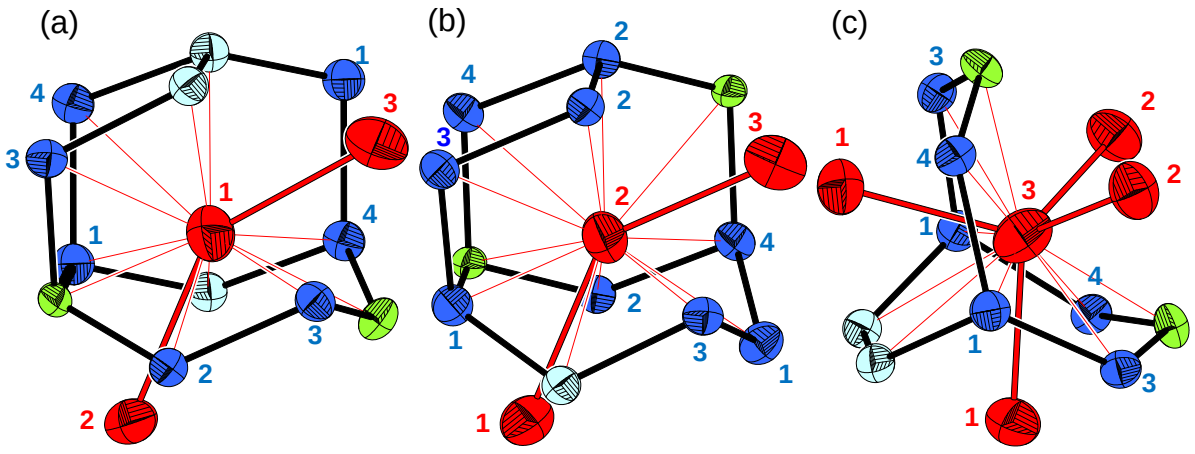

***Figure 4.16*. Coordination environment up to 4 Å of the three Na sites in $Na_5Zn_{2.28}Sn_{9.72(2)}$: (a) Na1, (b) Na2, (c) Na3. Na (red), Zn (green), Sn (blue), M = Zn / Sn (light blue). All thermal ellipsoids are at 90% probability level.**

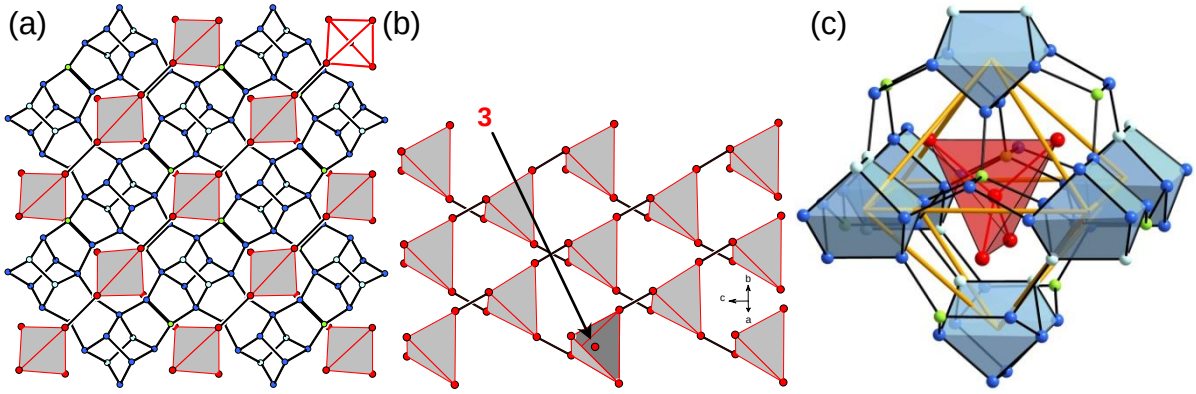

***Figure 4.17*. Sublattices in $Na_5Zn_{2.28}Sn_{9.72(2)}$.(a) Overlay of cationic and anionic network in an off-[010] projection. (b) Framework of {Na_4} tetrahedra. (c) One {Na_4} tetrahedron is octahedrally coordinated with six realgar like units. Na (red), Zn (green), Sn (blue), M = Zn / Sn (light blue).**

4.3.3 Electronic Structure

Band structure, DOS, and COHP calculations were carried out under the assumption of a fully ordered phase, with a lower Zn content and the formula '$Na_5Zn_2Sn_{10}$', corresponding to $Na_5Zn_{2+x}Sn_{10-x}$ (x = 0) with five (Sn1 to Sn5) Sn positions. The calculated density of states (DOS) is plotted in Figure 4.18a, where the Fermi level crosses a relatively high band, close to a very narrow gap at –0.32 eV below E_F. The lower region in the band structure shows strongly localized states (very sharp spikes) essentially of Zn-3*d* orbital character. Because all five Zn-3*d* block bands of $Na_5M_{2+x}Sn_{10-x}$ (M = Zn, Hg) are completely filled (Figure 4.19b), the *d*-electron count of d^{10} is assumed and, as they lie well below the Fermi level, they may be regarded as "pseudocore" electrons. As a result, each M atom of $Na_5M_{2+x}Sn_{10-x}$ has the electron configuration $3d^{10}4s^24p^2$ for Zn (and $5d^{10}6s^26p^2$ for Hg). Thus, the 18-electron rule is reduced to the octet rule for $Na_5Zn_{2+x}Sn_{10-x}$, and each Zn atom may be regarded as a 'pseudo'-main-group element with four valence electrons leading to the *s*- and *p*-electron counts of ns^2np^2. In terms of the ionic electron counting, this configuration is equivalent to a formally four bonded Zn^{2-} ion so that the charge assignment of $(Na^+)_5(Zn^{2-})_{2+x}(Sn^0)_{10-x}$ is appropriate for $Na_5Zn_{2+x}Sn_{10-x}$. The Sn-*s* orbitals are clearly separated at –11 to –5 eV and the valence band mainly consists of Sn-*p* orbitals. Some *sp* mixing is observed at a local maximum at ~ –4.5 eV and the lower lying *s* band. A first sign for covalent interactions between Zn and Sn is revealed in the significant mixing of *p*-contributions with Sn-*p* in the valence band and in the sharp band at ~ –4.5 eV. The relative contributions indicate a Zn–Sn bond which is polarized towards Sn.

The integration of the DOS (IDOS, dashed line in Figure 4.18b) indicates that the electron count at the Fermi level is 276 electrons/cell (for x = 0) and 272 electron/cell at the gap (marked with a red line in Figure 4.18) where it corresponds exactly to the electron count for the charge balanced phase according to the Zintl concept, i.e. x = 0.5.

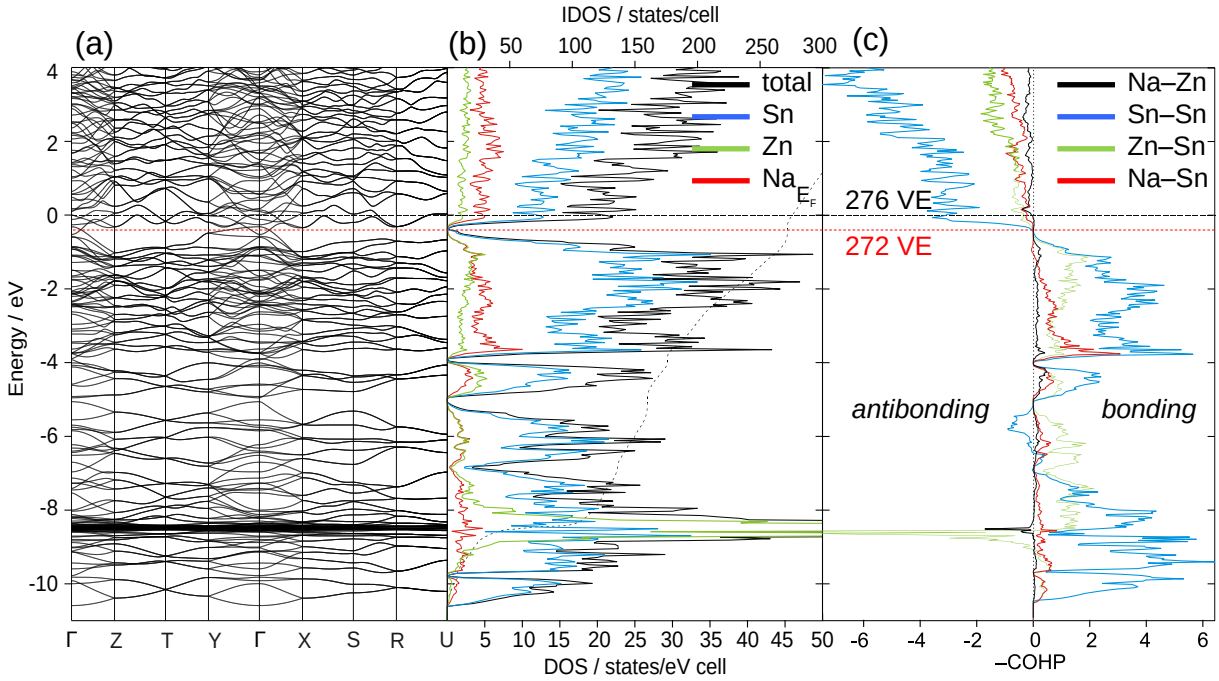

***Figure 4.18*. (a) Band structure, (b) DOS projections: total (black), Sn (blue), Zn (green), Na (red), and (c) –COHP curves, Sn–Sn (blue), Zn–Sn (green), Na–Sn (red), Na–Zn (black), for $Na_5Zn_{2+x}Sn_{10-x}$ (x = 0). The Fermi level for the charge balanced compound with x = 0.5 is shown with dashed red lines.**

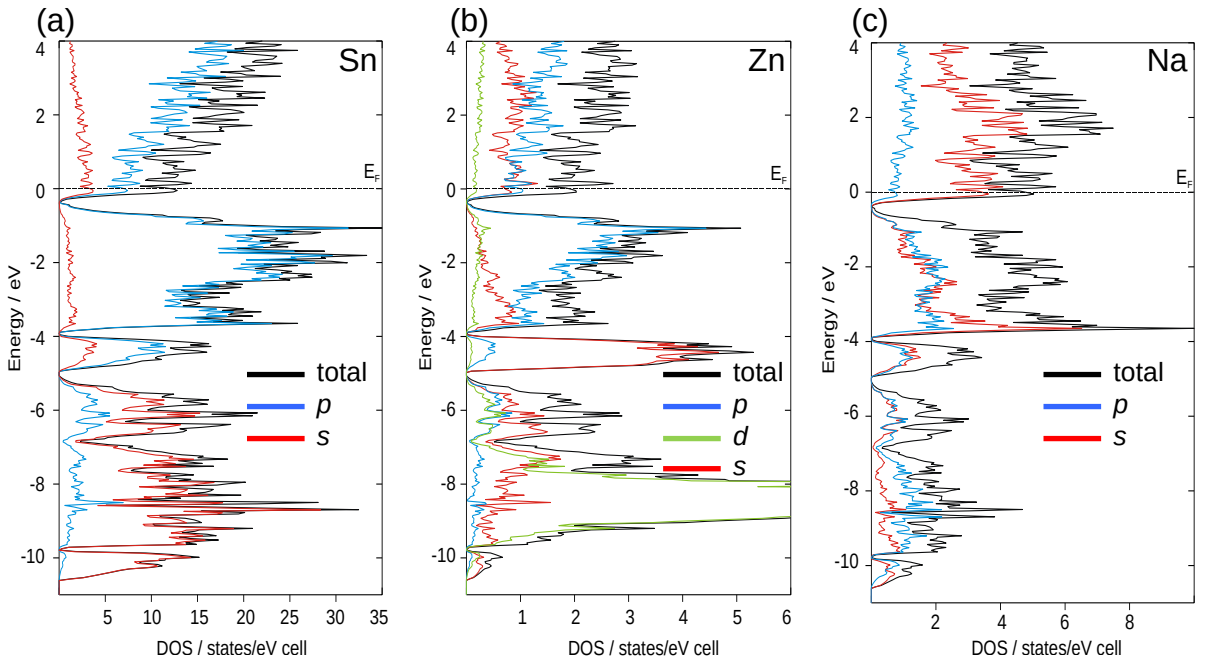

***Figure 4.19*. DOS projections of (a) Sn, (b) Zn, and (c) Na for $Na_5Zn_{2+x}Sn_{10-x}$ (x = 0). Total DOS (black), *s* states (red), *p* states (blue), and *d* contributions (green).**

***Table 4.9*: –ICOHP values for selected interatomic contacts in hypothetical '$Na_5Zn_2Sn_{10}$'. Energies are given in eV/bond.**

interaction	*d* /Å	–ICOHP (at E_F)	–ICOHP (max.)
Sn Sn	2.838 - 2.986	2.05	2.13
Sn Zn	2.717 - 2.840	1.71	1.74
Na Sn	< 3.8	0.18	0.18
Na Zn	< 3.5	0.19	0.19

Therefore, the Zn for Sn partial substitution occurs at one atomic position to optimize the electron count of the compound. Within the rigid band the electronic structure of the phase $Na_5Sn_{10-x}Zn_{2+x}$ ($x \leq 0.5$) typically corresponds to doped narrow band-gap semiconductors or semimetals, therefore meeting an important requirement of thermoelectric (TE) materials. The slight deviation from the optimum electron count which is observed on refinement for both phases $Na_5(Zn,Hg)_{2+x}Sn_{10-x}$ may allow the control of the carrier concentration which is critical in TE material as their performance is highly sensitive to it. Furthermore, the –COHP diagram (Figure 4.18c) indicated that the Sn–Sn and Zn–Sn interactions are overall bonding, with weak repulsive interactions between Zn-*d* and Sn-*s* orbitals. All Sn and Zn levels above the gap are antibonding, meaning that both Sn–Sn and Sn–Zn interactions are optimized at the gap. The strong covalent-type bonding within the polyanionic framework is evidenced by the integrated crystal orbital Hamiltonian population (–ICOHP). The maximum value of the –ICOHP is achieved at –0.32 eV below E_F corresponding to about 2.13 eV/bond for the Sn–Sn interaction and 1.74 eV/bond for the Zn–Sn. Thus, the strong covalent Sn–Sn and Sn–Zn bonds are the backbone of the polyanionic framework and will be the key factor governing the structure and the properties of these phases. The cation–anion interactions, though important in many other compounds,[49-51] are also optimized but are a magnitude smaller than the Sn–Sn and Sn–Zn bonds. Therefore their part in bonding is mainly ionic.

4.3.4 Discussion

The most common crystal structure adopted by many commercial semiconductors is the diamond lattice where each atom undergoes strong covalent interactions with four adjacent atoms which together result in a tetrahedron. For instance, elemental Si, Ge (and *α*-Sn) are archetypal band-gapped compounds with a diamond lattice. Moreover, the isoelectronic group III - V binary phases are the most frequently used semiconductors, and of these GaAs is the most important commercially. Their crystal structures are similar to the diamond lattice where each atom is still four-coordinated,

but they are bonded to unlike atoms. This structure is refered to as the zinc blende lattice, named after zinc blende ZnS. The structure of the Zintl compound NaTl is based on the diamond lattice of Tl^{1-} anions with a $(ns)^2(np)^2$ configuration as in C or Si and is filled with interstitial Na^+. Hence, the NaTl structure is the simplest filled-variant of the diamond structure. The closely related half-Heusler compounds (AME, e.g. MgAgAs,[52] see Figure 4.20) consist of an electropositive metal A, a late transition metal M and a heavy maingroup atom E of group 14 or 15. The atoms M and E form a zinc blende lattice, which becomes a diamond lattice if M = E. The atoms A occupy half of the 10-coordinated voids (AM_4 tetrahedra and AE_6 octahedra) of the structure. Hence the half-Heusler structure is the cation-stuffed version of the zinc blende structure. It was found that the 18-electron half-Heusler (18e-HH) compounds also represent an interesting family of semiconductors and the most promising classes of thermoelectric materials.[53, 54] The electronic structure of a 18e-HH compound AME is described by the charge assignment $A^{n+}(ME)^{n-}$, where *n* is the number of valence electrons donated from A according to the Zintl concept. Qualitatively, the semiconducting property of most 18e-HH compounds has been understood by noting that the 18-electron count around M implies a closed-shell electron configuration (i.e. $d^{10} + s^2 + p^6$).

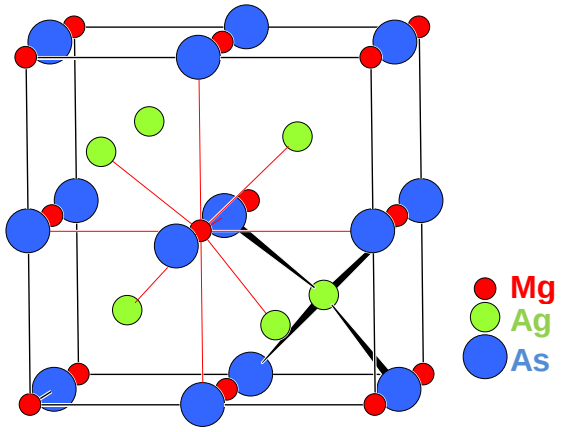

***Figure 4.20*. Unit cell of the half-Heusler phase MgAgAs.**

Furthermore, in several phases of the alkali metal tin systems, the anionic tin substructures feature structural motifs with varying dimensionality that can be viewed as fragments of the *α*-Sn structure. In Li_5NaSn_4,[55] a two dimensional partial structure of *α*-Sn is clearly visible.

In the Sn-rich region where the charge transfer from the electropositive *s*-block metal to Sn, according to Zintl concept, is not sufficient to allow the Sn anions to achieve the octet as isolated species, the Sn atoms are forced to form bonds to each other, resulting in polyanionic networks with various connectivity and bond types as shown in Chapter 4.2. The group 14 clathrates with zeolite-like structure represent another class of filled tetrahedral semiconducting compounds which are structurally more complex. In the type I clathrate, the framework of four coordinated tetrel elements may be substituted by an electron poorer atom like a triel (group 13) or a late transition (mainly group 11 or 12) metal to fulfill the electronic requirement of closed-shell compounds. Similarly, the electron short chiral clathrate $K_{6+x}Sn_{25}$ could be stabilized by atoms of electron richer Bi in $K_6Sn_{23}Bi_2$.[56] Nevertheless, in the chemistry of group 14 elements in their negative oxidation state, compounds which may be structurally rationalized as intermediates between unfilled and filled diamond-type structures are rather rare.

Assuming charge transfer from Na to the anionic network of Sn and Zn according to the Zintl concept, one can write $Na_5Zn_{2+x}Sn_{10-x}$ as $5Na^+(4b\text{-}Zn^{2-})_{2+x}(4b\text{-}Sn^0)_{10-x}$. Thus, the charge is balanced if x = 0.5 and the compound will formally correspond to an electron precise Zintl phase where all Sn atoms are neutral, whereas the Zn atoms have a formal charge of 2–. A formal ionic description including Zn^{2+} cations is rather complicated to formulate. However, the presence of the mixed occupied position and the comparable –ICOHP values for Sn–Sn and Sn–Zn interactions rather point into the direction of covalently bonded Zn.

In the hypothetical phase $Na_5Zn_2Sn_{10}$ (x = 0) without mixed occupied positions, there is one extra electron for a charge balanced Zintl phase including tetrahedrally coordinated Zn atoms. This explains why one Sn position is partially substituted by the electron poorer Zn with the refined x value (0.28(2)) roughly close to the expected value for the charge optimization. Nevertheless, the refined value is significantly smaller than the Zintl limit. Higher Zn or Hg atom content in the solid solutions, although possible, could not be confirmed experimentally and quantitative EDX analyses were hampered by the extreme air-sensitivity of the crystals. It is worth noting that the substituted Sn position corresponds to the only one without any direct contact to a Zn atom. This indicates that the system is trying to avoid any direct Zn–Zn interaction, because their negative charge will lead to a strong electrostatic repulsion as illustrated also by the unusual long M–M bond length.

Thus, the anionic substructure of $Na_5Zn_{2+x}Sn_{10-x}$ can be partitioned into fragments 2× $\{Zn–Sn\}^{2-}$ and realgar-like units $\{Zn_xSn_{8-x}\}^{2x-}$, where the partial substitution of Zn for Sn stems from only one additional Na atom in the structure. The hypothetical phase 'Na_2ZnSn' (formulation A_2ME) has one extra electropositive metal (A) with respect to the regular half-Heusler structure (AME) meaning that there will not be enough room available for all A type atoms. Therefore, the combination of diamond like *α*-Sn and half-Heusler structures or, in other words, of diamond and unfilled diamond-type structures occurs likely to accommodate the abundance of Na^+ cations.

4.4 $Na_{29}Zn_{24}Sn_{32}$ - A Zintl Phase with a New Type of Sn Polyhedron

The ternary compound discussed in this subchapter has an almost balanced Zn/Sn stoichiometry thus the VEC per atom is close to that of elements of the triel group, such as indium or gallium. This Zn : Sn ratio marks the transition point from covalently bonded frameworks to networks of electron conserving clusters.

4.4.1 Synthesis and Characterization

Synthesis For the synthesis of $Na_{29}Zn_{24}Sn_{32}$, stoichiometric amounts of the pure elements (freshly distilled zinc, see Chapter 3.1) were loaded into a tantalum ampoule in an Ar-filled glovebox. After sealing the ampoule, the sample was heated to 450 °C at a rate of 2 $K \cdot min^{-1}$ and then slowly cooled to room temperature with a rate of 0.1 $K \cdot min^{-1}$. Annealing at 350 °C for four weeks resulted in higher crystallinity and higher yields. The product contained the air-sensitive target compound as a highly crystalline powder, together with lighter crystals of other phases. The crystals of $Na_{29}Zn_{24}Sn_{32}$ are dark silvery with metallic luster and have block shape. The phase was prepared from a loading with Na : Zn : Sn = 29 : 24 : 32 and a total loading mass of 1.509 g, with m(Na) = 0.167 g, m(Zn) = 0.392 g, and m(Sn) = 0.950 g.

Powder X-ray Diffraction The measurement was carried out in a capillary by finely grinding the powder and diluting with diamond powder in the glovebox. The measurement was carried out in Debye-Scherrer mode with 2.5° step width and a total measuring time of 16 h. The diffractogram (Figure 4.21) indicates the presence of the target compound as the main phase and small amounts of byproducts (se below), marked with red stars. The intense reflection triplett at 2θ ~ 34.2, 34.4, and 34.6°, originating from (330), (322), (303) net planes, is a good ‘fingerprint’ for the detection of this phase.

Thermal Analysis The thermal behavior was investigated by sealing 150 mg of the reaction product of a stoichiometric loading (obtained from a sample that was slowly cooled from 450 °C to room temperature) into Nb crucibles and running two loops of heating to 650 °C and cooling to 100 °C, both with gradients of 10 $K \cdot min^{-1}$. The endothermal signal in the heating curve (Figure 4.22, red line) is very broad and ranges from 394.3 (393.7)°C (onsets) to 485.9 °C (peak). The corresponding and further signals appear in the cooling loops starting at 460.9 (448.1)°C (cooling-end). The presence of additional

signals is consistent with the phase mixture that was detected in the powder X-ray diagram that originated from compounds with similar crystallographic compositions (see Chapter 4.5 and 4.6). The first onset temperature can be assigned to the melting of $Na_{29}Zn_{24}Sn_{32}$ since annealing experiments at and above 350 °C using stoichiometric amounts of the elements resulted in different yields and crystallinity.

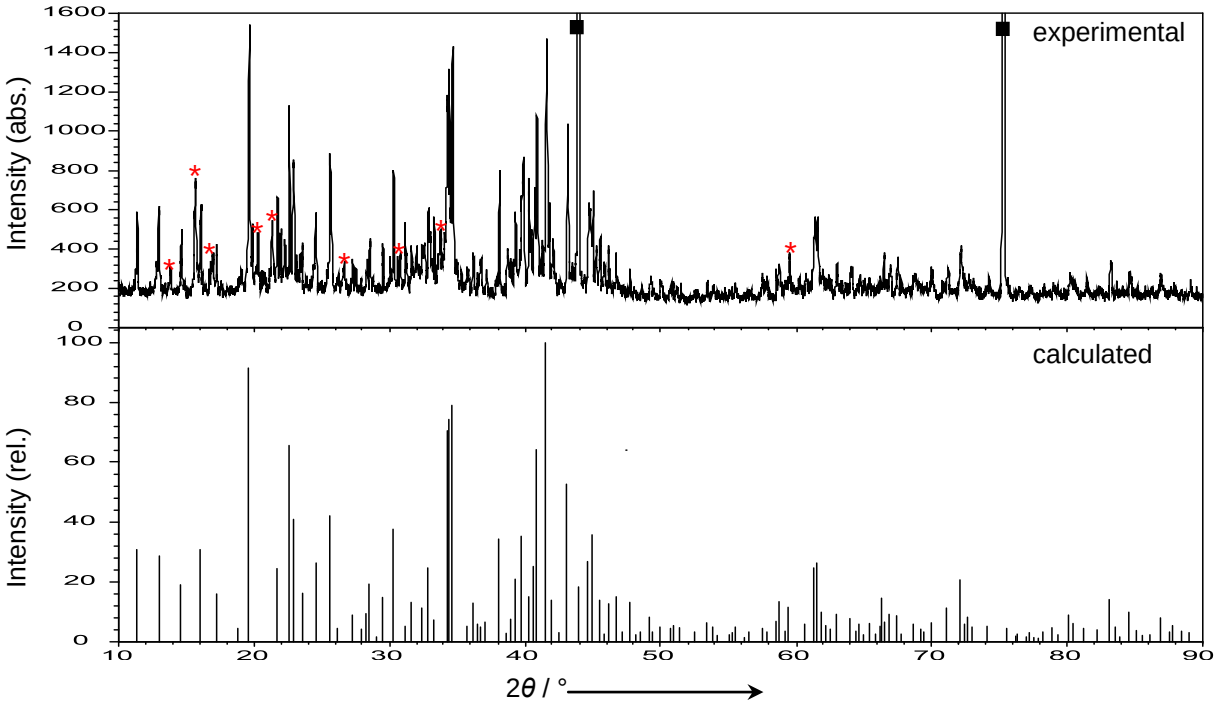

***Figure 4.21*. Experimental powder diagram (top) from the product of stoichiometric loading Na : Zn : Sn = 29 : 24 : 32 and simulated powder diagram (bottom) of $Na_{29}Zn_{24}Sn_{32}$. Reflections from diamond (internal standard) are labeled with a square. Most intense reflections from byproducts are marked with a red star.**

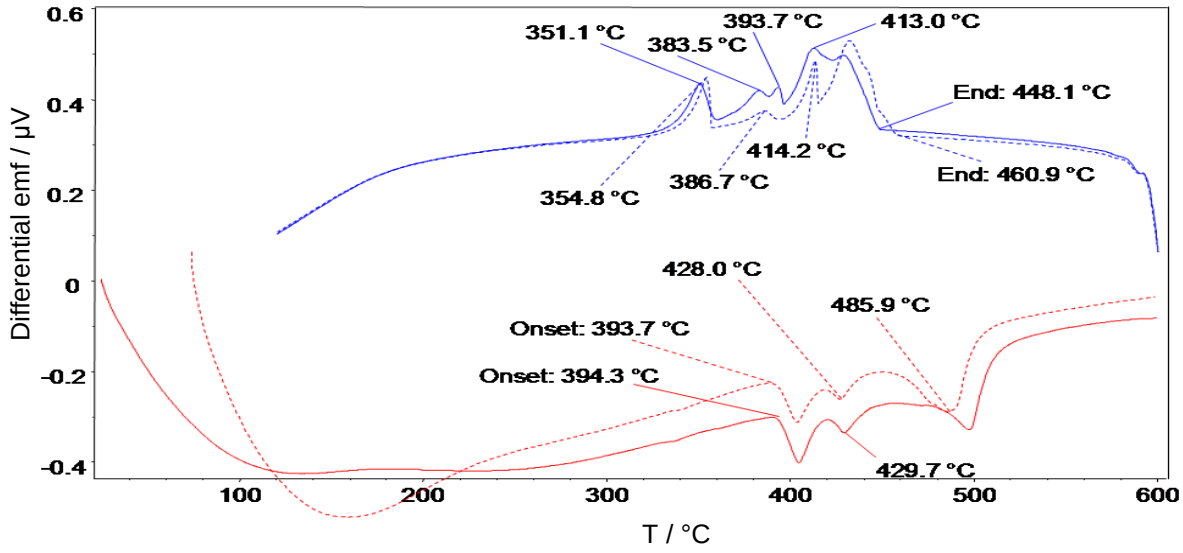

***Figure 4.22*. DTA curves of the product of a reaction with Na : Zn : Sn = 29 : 24 : 32 at 500 °C. Heating curve (red), cooling curve (blue), 2nd loop (dashed line).**

4.4.2 Crystal Structure Determination and Description

Structure Determination A dark silvery, block-shaped single-crystal of $Na_{29}Zn_{24}Sn_{32}$ was inserted and sealed in a glass capillary (0.3 mm diameter) in an argon-filled glovebox. The data collection (776 frames) involved four sets of ω scans (–41° - +63° for different φ positions: 0°, +90°, +180°, +270°) and a φ scan (0° - 360° with θ = +30°) with scan width 1°/frame and exposure time 10 s/frame. The crystal structure was solved using direct methods and refined on F^2 by full-matrix least-squares methods, with anisotropic displacement parameters for all atoms. Of all the possible space groups that fulfilled the systematic extinction conditions, only *P*–62*m* produced a successful model. No further symmetry elements were found (checked with the PLATON/ADDSYM routine[57]). Thus, the structure was refined in this non-centrosymmetric space group. Testings for twin and 'drilling' formation by lowering the symmetry to orthorhombic *Amm*2 involving unit cell transformations (to a = 9.462, b = 27.214, c = 15.710 Å) resulted in the same structures and same connectivities. Therefore, the solution in the space group with highest symmetry was chosen. The Flack parameter of 0.01(3) indicates that the absolute structure is correct (a value of 0.5 would be expected for a racemic twin or if a center of inversion was present).

Despite a well-converged refinement (R_1 = 0.029 (all data)), a residual electron-density peak (~ 4.5 $e^{-}\cdot Å^{-3}$) remained near the three-bonded Sn6 site. Furthermore, the anisotropic displacement parameters of Sn6 (U_{iso} = 0.0281(2) $Å^2$) were slightly bigger than those of the other tin positions. Therefore, a split model was introduced for the Sn6 site. Attempts to refine the residual electron-density peak as a partially occupied sodium or oxygen site did not result in a satisfying model, for geometric, electronic, and chemical reasons. In the split model, the occupancy of the original Sn6a site refined to 92.4(2) %; in the final refinement, the occupancy of Sn6a was fixed at 92% and that of the new Sn6b site at 8 %. The isotropic displacement parameter of the sites refined to U_{iso} = 0.0238(2) $Å^2$. Additional Bragg reflections indicative for the presence of a superstructure or incommensurable structure were not observed. Tables 4.10 to 4.12 contain relevant crystallographic data and in Table 8.3 (see Appendix) interatomic distances (≤ 4 Å) are listed.

***Table 4.10*: Selected crystallographic and refinement data for $Na_{29}Zn_{24}Sn_{32}$.**

Empirical formula	**$Na_{29}Zn_{24}Sn_{32}$**
Formula weight / g·mol^{-1}	6033.67
Temperature / K	293(2)
Crystal size / mm^3	0.10 × 0.10 × 0.10
Crystal color; shape	dark metallic; Block
Diffractometer	Oxford Xcalibur3 (CCD)
Crystal system	Hexagonal
Space group	*P*–62*m* (No. 189)
Unit cell parameters / Å	*a* = 15.712(1); *c* = 9.462(1)
Unit cell volume / Å^3; *Z*	2022.9(2); 1
ρ_{calc} / g·cm^{-3}	4.95
μ / mm^{-1} (Mo K_α)	16.78
Absorption correction	empirical
F(000)	2639
Θ range / °	2.99 - 27.79
Index range	–10 ≤ *h* ≤ 10; 0 ≤ *k* ≤ 20; 0 ≤ *l* ≤ 12
Data completeness / %	99.6
Integrated reflections	15973 (R_σ = 0.018)
Independent reflections	1801 (R_{int} = 0.039)
Refinement method	Full-matrix least-squares on F^2 (SHELXTL)
Parameters	86
Goodness of fit on F^2	1.092
Observed reflections [$I > 2\sigma(I)$]	1660
R_1 / wR_2 [$I > 2\sigma(I)$]	0.024 / 0.059
R_1 / wR_2 (all data)	0.027 / 0.058
Weighting scheme[a]	a = 0.036; b = 5.080
Extinction coefficient	0.00217(8)
Residual map / e$^-$·Å^{-3}	+2.09 [0.85 Å from Sn6b]
	–2.17 [0.08 Å from Sn6b]

[a] $w = 1 / [\sigma^2(F_o^2) + (aP)^2 + bP]$, where $P = (F_o^2 + 2F_c^2) / 3$

***Table 4.11*: Atomic coordinates and equivalent isotropic displacement parameters for $Na_{29}Zn_{24}Sn_{32}$. *) split position**

Atom	**Wyck.**	**Occ. ≠ 1**	***x***	***y***	***z***	**U_{eq} / Å^2**
Sn1	6*j*		0.6079(1)	0.4025(1)	0.0000(1)	0.012(1)
Sn2	6*k*		0.6787(1)	0.5136(1)	0.5000(1)	0.011(1)
Sn3	6*i*		0.3588(1)	0.3588(1)	0.3395(1)	0.013(1)
Sn4	2*e*		1.0000(1)	1.0000(1)	0.3476(1)	0.019(1)
Sn5	6*i*		0.8239(1)	0.8239(1)	0.2268(1)	0.022(1)
Zn1	6*i*		0.6532(1)	0.6532(1)	0.3472(1)	0.016(1)
Zn2	6*k*		0.5002(1)	0.3450(1)	0.5000(1)	0.015(1)
Zn3	12*l*		0.5602(1)	0.4638(1)	0.2543(1)	0.015(1)
Na1	4*h*		0.6667(1)	0.3333(1)	0.3066(5)	0.020(1)
Na2	12*l*		0.7916(2)	0.5733(2)	0.1984(3)	0.021(1)
Na3	6*k*		0.7357(3)	0.8761(4)	0.5000(1)	0.032(1)
Na4	3*f*		0.6338(4)	0.6338(4)	0.0000(1)	0.027(1)
Na5	3*f*		0.3901(4)	0.3901(4)	0.0000(1)	0.026(1)
Na6	1*a*		1.0000(1)	1.0000(1)	0.0000(1)	0.019(1)
Sn6a*	6*j*	0.92	0.8962(1)	0.7541(1)	0.0000(1)	0.024(1)
Sn6b*	6*i*	0.08	0.2147(6)	0.2147(6)	0.1451(11)	0.024(1)

***Table 4.12*: Anisotropic thermal displacement parameters (*l* Å^2) for $Na_{29}Zn_{24}Sn_{32}$.**

Atom	U_{11}	U_{22}	U_{33}	U_{23}	U_{13}	U_{12}
Sn1	0.014(1)	0.014(1)	0.011(1)	0	0	0.009(1)
Sn2	0.011(1)	0.012(1)	0.011(1)	0	0	0.007(1)
Sn3	0.014(1)	0.014(1)	0.013(1)	0	0	0.008(1)
Sn4	0.020(1)	0.020(1)	0.017(1)	0	0	0.010(1)
Sn5	0.021(1)	0.021(1)	0.017(1)	0.002(1)	0.002(1)	0.005(1)
Zn1	0.016(1)	0.016(1)	0.018(1)	0	0	0.009(1)
Zn2	0.014(1)	0.014(1)	0.017(1)	0	0	0.008(1)
Zn3	0.015(1)	0.017(1)	0.015(1)	0	0	0.009(1)
Na1	0.018(1)	0.018(1)	0.022(2)	0	0	0.009(1)
Na2	0.019(1)	0.024(1)	0.019(1)	0.003(1)	0	0.010(1)
Na3	0.034(3)	0.028(3)	0.038(2)	0	0	0.020(2)
Na4	0.026(2)	0.026(2)	0.031(4)	0	0	0.015(3)
Na5	0.033(3)	0.033(3)	0.016(3)	0	0	0.018(3)
Na6	0.018(3)	0.018(3)	0.019(4)	0	0	0.009(1)
Sn6a	0.024(1)	0.017(1)	0.023(1)	0	0	0.005(1)
Sn6b	0.024(1)	0.017(1)	0.023(1)	0	0	0.005(1)

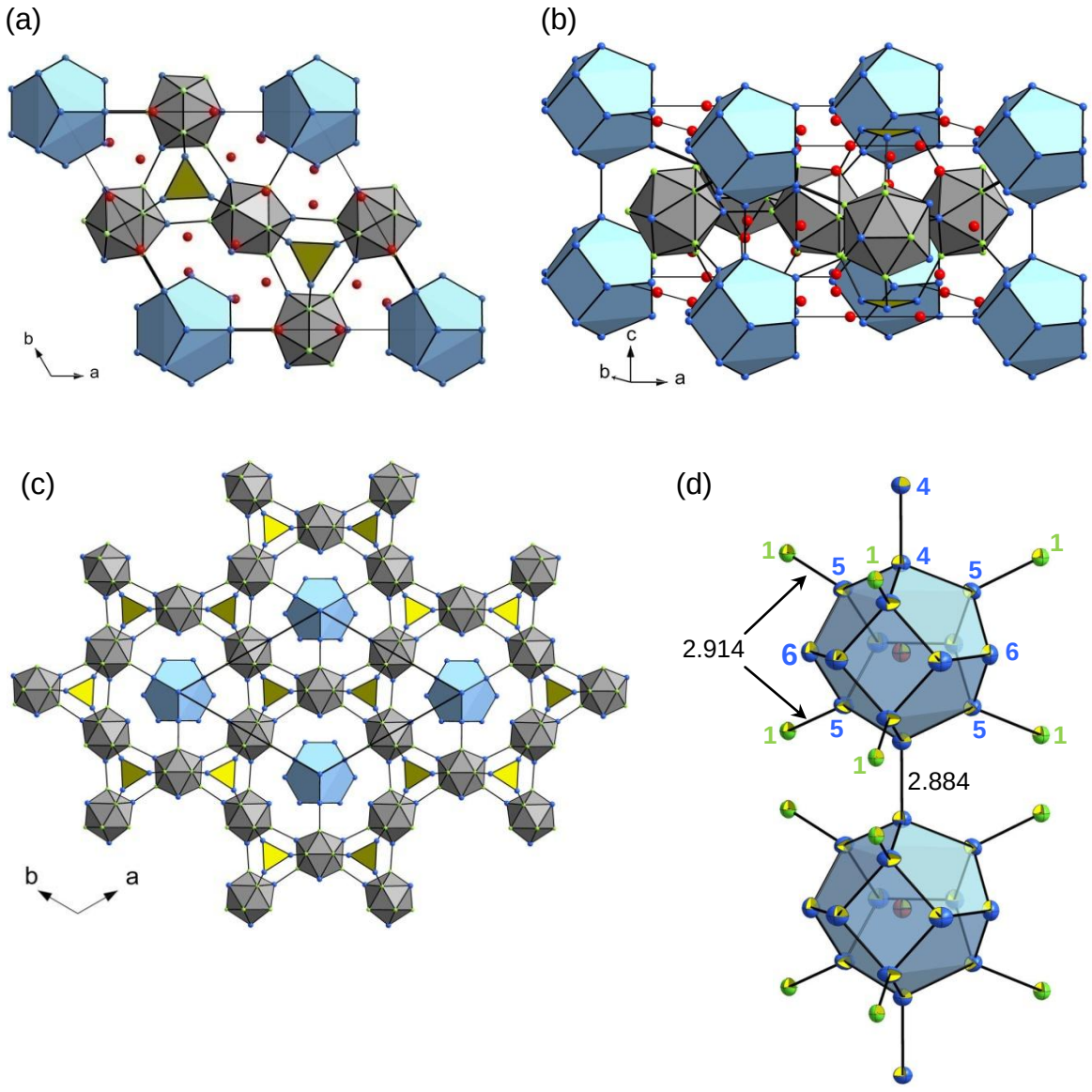

***Figure 4.23*. For figure captions see next page.**

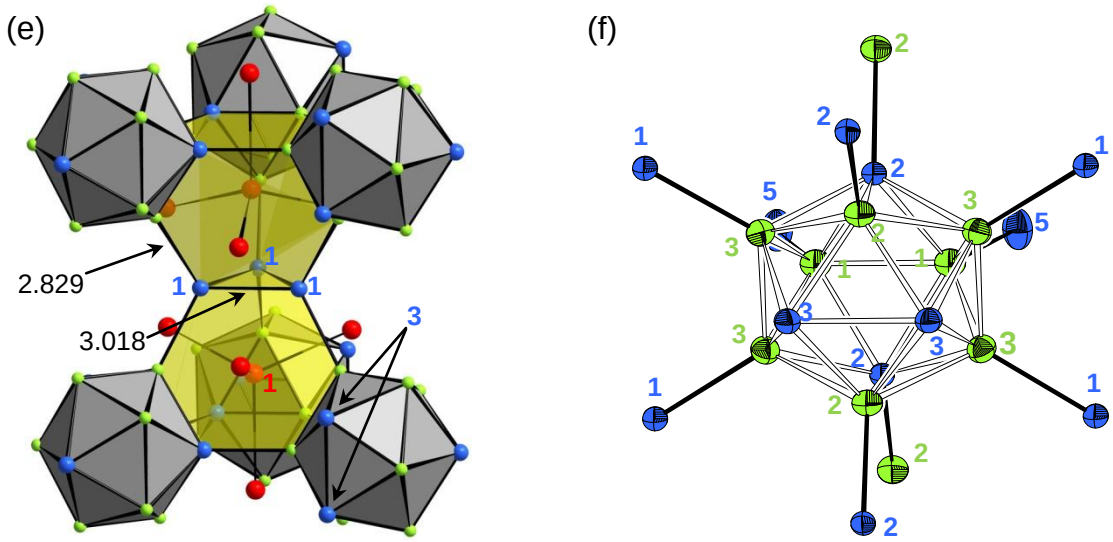

***Figure 4.23, continued*. The structure of $Na_{29}Zn_{24}Sn_{32}$. (a) The unit cell in projection along the *c*-axis, highlighting the $\{Zn_8Sn_4\}$ icosahedra (gray), $\{Sn_{14}\}$ polyhedra (blue), and $\{Sn_3\}$ triangles (yellow). (b) The unit cell in projection perpendicular to the *c*-axis, showing how the $\{Sn_3\}$ triangles bridge the $\{Zn_8Sn_4\}$ icosahedra. (c) The Kagomé net of $\{Zn_8Sn_4\}$ icosahedra parallel to the (001) plane, as well as the embedded $\{Sn_{14}\}$ polyhedra. (d) The linear chain of $\{Sn_{14}\}$ polyhedra along the *c*-axis; displacement ellipsoids are set at 90% probability. (e) The interconnection of the truncated tetrahedra (yellow) and the $\{Zn_8Sn_4\}$ icosahedra along *c* direction. (f) 10-fold *exo*-bonded $\{Zn_8Sn_4\}$ icosahedron (atoms drawn at 90% probability level). In all pictures Na (red), Zn (green), Sn (blue).**

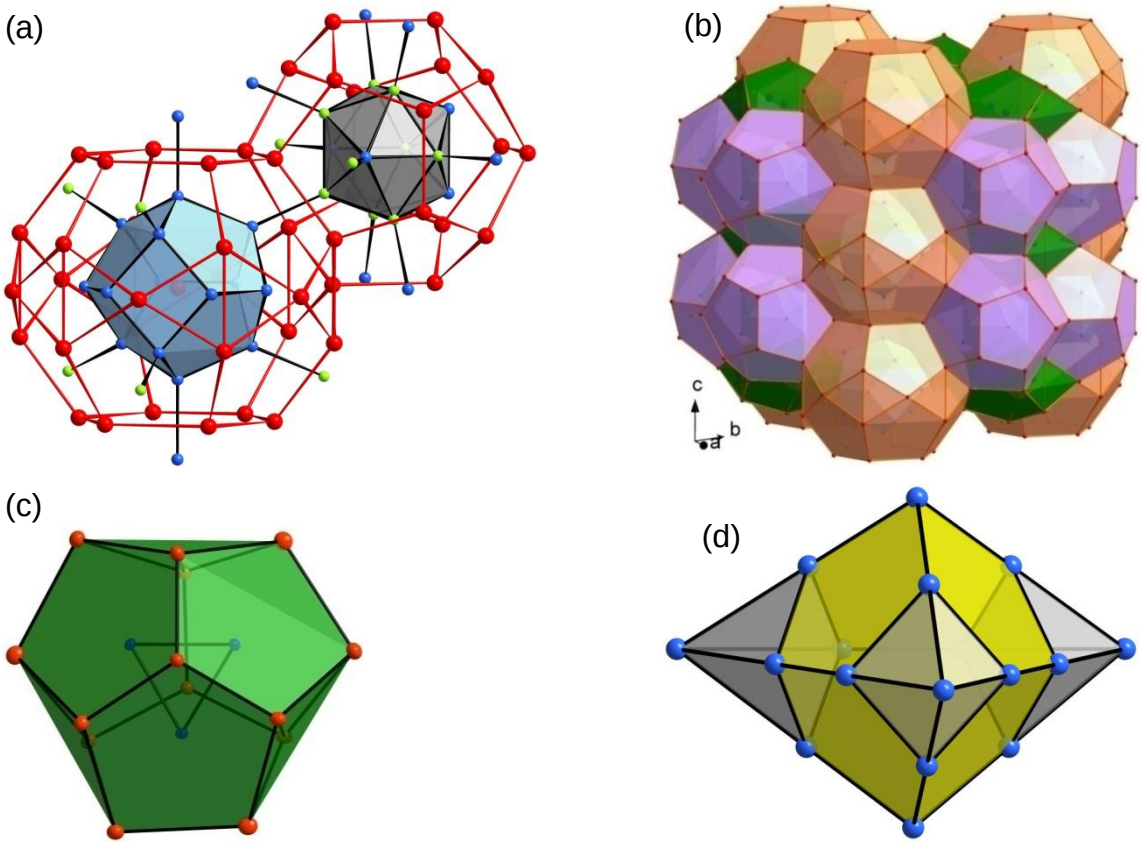

***Figure 4.24*: Na substructures in $Na_{29}Zn_{24}Sn_{32}$: (a) A pair of interconnected $\{Sn_{14}\}$ and $\{Zn_8Sn_4\}$ clusters with the $\{Na_{30}\}$ and $\{Na_{20}\}$ cages surrounding the. (b) The anionic substructures are completely encaged in a clathrate like cationic framework. (c) $\{Na_{14}\}$ polyhedron around the $\{Sn_3\}$ ring. (d) The $\{Sn_{14}\}$ enneahedron can be derived from a compressed trigonal bipyramid by truncating three vertices.**

Structure Description The compound crystallizes in a new structure type in the primitive hexagonal space group *P*–62*m* with cell parameters *a* = 15.712(1) Å and *c* = 9.462(1) Å. The main building units are 1D connected $\{Sn_{14}\}$ clusters, $\{Sn_3\}$ triangles, and $\{Zn_8Sn_4\}$ icosahedra. A projection of the unit cell along the *c*-axis (Figure 4.23a) illustrates the arrangement of the structural units in a three-dimensional network. The $\{Zn_8Sn_4\}$ icosahedra (gray) are assembled in a Kagomé net-like fashion (Figure 4.23c) and are interconnected by four Sn–Zn-contacts with *d*(Sn2–Zn2) = 2.724(1) Å. The Kagomé net can be regarded as a close packed layer of icosahedra with ¼ of the icosahedra missing. The atomic positions in the present icosahedra (on (3*g*)-site and (*m*2*m*)-symmetry) are well ordered, and the 30 edges are composed of 1× Sn–Sn, 18× Sn–Zn, and 11× Zn–Zn contacts. Compared to covalent 2-center-2-electron bonds the homoatomic intracluster contacts are widened, whereas the intracluster and *exo*-cluster Zn–Sn distances are of comparable lengths. The average Zn–Zn distance and the Sn–Sn distance in the $\{Zn_8Sn_4\}$ cluster are $d(Zn–Zn)_{ø}$ = 2.759 Å and $d(Sn–Sn)_{ø}$ = 3.038(1) Å. For comparison, the interatomic distance in elemental zinc is *d*(Zn–Zn) = 2.665 Å , and the average interatomic distance in the $\{Sn_{14}\}$ substructure is $d(Sn–Sn)_{ø}$ = 2.909 Å . The intracluster Zn–Sn distances are in the range of 2.729(2) to 2.856(1) Å, and the corresponding *exo*-cluster contacts range from 2.724(1) to 2.914(1) Å. The intermetallic phase $Mo_7Sn_{12}Zn_{40}$[16] contains molybdenum-centered icosahedra of composition $\{MoZn_{10}Sn_2\}$ with Zn–Sn distances similar to those in $Na_{29}Zn_{24}Sn_{32}$.

As shown in Figure 4.23b, the polyhedra of the Kagomé net are connected along *c* via Zn atoms to the Sn1 atoms of the $\{Sn_3\}$ units between these layers with *d*(Zn2–Sn1) = 2.829(1) Å. The $\{Sn_3\}$ triangular units are symmetrically aligned between the Kagomé layers and within three-membered channels with respect to the Kagomé net. Therefore, together with neighboring $\{Zn_3Sn_3\}$ hexagons, they form Na centered truncated tetrahedra and Friauf polyhedra with four additional Na atoms which cap the six-membered faces. The Friauf polyhedra are alternately stacked along [001] over shared $\{Sn1_3\}$ triangles and $\{Sn_3Zn_3\}$hexagons, thus connecting the layers of icosahedra (Figure 4.23e) in a primitive sequence such as in $CaCu_5$.

In the bigger channels of the Kagomé framework, a homoatomic Sn substructure is embedded that can be described as a linear chain of $\{Sn_{14}\}$ polyhedra, each encapsulating a Na atom (Na1) (Figure 4.23d).

As shown in Figure 4.23d and in Figure 4.26 (cluster A), this polyhedron consists of six pentagonal and three distorted square faces. The three-fold axis of rotation (D_{3h}) is equivalent with the crystallographic rotation axis. The simple polyhedron can be derived from a trigonal bipyramid by capping the three equatorial vertices and compressing the three-fold axis (Figure 4.24d). The polyhedron is not a member of the 92 Johnson polyhedra.[58] A part of the complex network structure of the intermetallic phase Ag_7Te_4[59] can be interpreted as a highly elongated variant of this body. Another figurative derivation would be from a distorted bicapped anti cuboctahedron. The faces are almost planar and have bond angles ranging from 106.1° to 109.9° for the pentagon (angular sum 538.4°) and from 84° to 96° (angular sum 360°) for the square planes. Thus, they are just slightly distorted. The Sn–Sn distances vary from 2.825(1) to 2.993(1) Å, and are in the range of covalent Sn–Sn interactions found in *α*-Sn and *β*-NaSn, respectively. Along the *c*-direction, the *enneahedra* (a nine sided polyhedron) are covalently interconnected via the shared atom (Sn4) of three pentagonal faces (*d*(Sn4–Sn4') = 2.884(2) Å) and generate a linear chain of clusters. Additionally, six other Sn-vertices (Sn5) of the polyhedron establish *exo*-bonds to the Zn1 atoms of 6 of 12 surrounding $\{Zn_8Sn_4\}$ icosahedra (*d*(Sn5–Zn1) = 2.914(1) Å). These are positioned in a hexagonal-prismatic fashion around the $\{Sn_{14}\}$ entity (Figure 4.27).

The coordination of the two cluster types by Na results in two different Na polyhedra: 20 Na atoms surmounting the deltahedral faces of the icosahedra form the dual polyhedron, a pentagondodecahedron. An icosihexahedron built by 30 Na atoms encapsulates the $\{Sn_{14}\}$ cluster and shows two hexagonal, twelve pentagonal, and twelve triangular faces. A similar cage is realized by the tetracaidecahedron, a 24-vertex polyhedron with two hexagonal and twelve pentagonal faces. It is likewise accompanied by pentagondodecahedra in the clathrate-I structures of $[Br_8(H_2O)_{46}]$[60] or K_8Tt_{46-x} (Tt = Si, Ge, Sn).[45] In the tetracaidecahedron the hexagonal faces are staggered whereas in the present icosihexahedron they are eclipsed. The $\{Na_{30}\}$ polyhedra are face fused by sharing hexagons along [001] and share pentagons with neighbouring pentagondodecahedra (Figure 4.24a). In contrast to the structure of clathrate-I, space-filling is not accomplished with the $\{Na_{20}\}$ and $\{Na_{30}\}$ polyhedra alone, but with the $\{Na_{14}\}$ cage around the $\{Sn_3\}$ rings (Figure 4.24c). The latter is the cationic equivalent of the $\{Sn_{14}\}$ enneahedron. The Na cages distinctively separate the structure into areas with homo- and heteroatomic substructures (Figure 4.24b).

4.4.3 Electronic Structure

In Figure 4.25 the DOS (density of states) obtained from an Extended Hückel calculation of the described anionic Sn–Zn sublattice is shown. By filling the electronic states successively with electrons, the Fermi level corresponding to $\{Zn_{24}Sn_{32}\}^{30-}$ lies in an energy gap of 1 eV. The Fermi level for $\{Zn_{24}Sn_{32}\}^{29-}$ is placed at ~ –7.0 eV, thus cutting through a high DOS (red line in Figure 4.25a) consisting mainly of the 3b-Sn6 (Sn6a) states of the enneahedron as outlined by the projected DOS. The presence of an energetically separated area in the DOS near the Fermi level is consistent with the case observed in K_6Sn_{25} and $K_6Bi_2Sn_{23}$.[56] There, the energetic states of sp^3 hybrid orbitals of 3-bonded Sn atoms are raised by interaction between electron lone pairs. In $Na_{29}Zn_{24}Sn_{32}$, the distances between the three-bonded Sn6 atoms of the $\{Sn_{14}\}$ unit and the Sn3 atoms of the $\{Zn_8Sn_4\}$ icosahedron are comparable to the distances between three-bonded Sn atoms in K_6Sn_{25}.

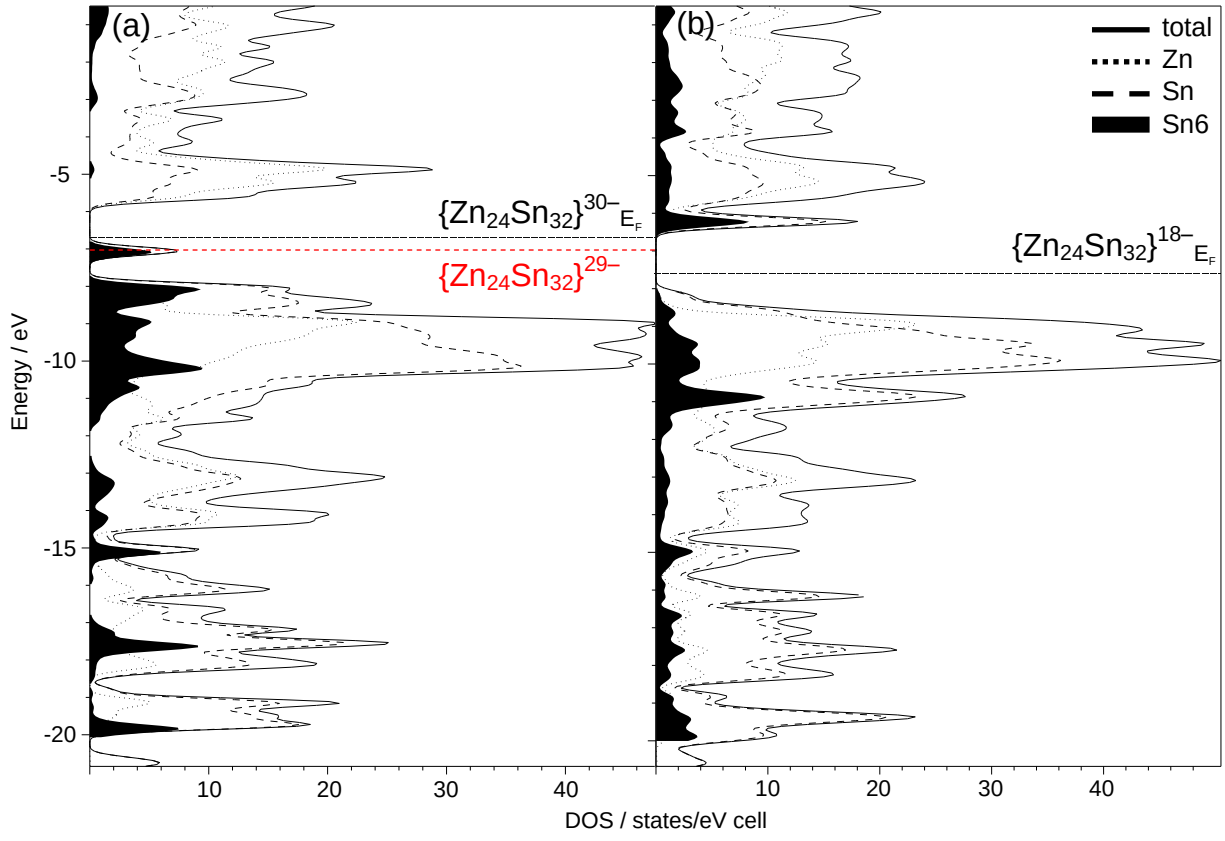

***Figure 4.25*. DOS of $Zn_{24}Sn_{32}$ models containing the two limiting isomers of the $\{Sn_{14}\}$ cluster: (a) Model containing $\{Sn_{14}\}$ clusters in which the Sn6a sites are occupied (see Figure 4.26, cluster A); the Fermi energies (E_F) for the $\{Zn_{24}Sn_{32}\}^{30-}$ substructure and for $\{Zn_{24}Sn_{32}\}^{29-}$ are indicated. (b) Model containing $\{Sn_{14}\}$ clusters in which the Sn6b sites are occuopied (see Figure 4.26, cluster C); the E_F for the $\{Zn_{24}Sn_{32}\}^{18-}$ substructure is indicated. Total DOS (line); Sn states (dashed line); Zn states (dotted line); Sn6 states (black area).**

4.4.4 Discussion

Homoatomic element clusters, such as the here presented $\{Sn_{14}\}$ species, experience growing interest as they represent suitable candidates for the research of structure-property relationships at the borderline between molecules and the solid state. Due to enhanced functionalization, bridging, coupling, and polymerization of these element-clusters in solution, they have become promising building blocks for the design of tailored nanostructures.[61, 62] Interesting parallels between ligand stabilized metal clusters that contain non-ligand bonded atoms along with metal atoms that are bonded by non-covalent interactions, so called metalloid clusters,[63-65] and interconnected clusters in intermetallic phases, such as in solid state compounds with electron poor triel block elements, exist.[66, 67] In the latter compounds, the cluster entities experience stabilization compared to the 3D-atom array, whereas the polyhedra of typically closed-packed intermetallic phases (e.g. Frank Kasper phases) are just depicted for a better topological view of the structure.[68] Solid state compounds with elements of the triel group often feature icosahedral structure motifs, such as *α*- and *β*-rhombohedral boron, metal borides, *δ*-Ga, and the extended cluster networks of alkaline metal indides and gallides. The counterpart in molecular chemistry with icosahedral $\{M_{12}\}$ units is represented by multi-atom, soluble, ligand stabilized metal clusters such as $\{Al_{77}R_{20}\}^{2-}$ (R = $N(Si(Me_3)_2)$,[69] $Al_{22}Br_{20}\cdot 12THF$,[70] and $\{Ga_{12}R_{10}\}^{2-}$ (R = fluorenyl, $C_{13}H_9$).[71] Molecular clusters with metalloid character normally do not evolve in closed-shell compounds, but the formation of electron precise clusters based on the rules by Zintl-Klemm-Busmann[72-74] and Wade[3] is common among the solid state phases mentioned earlier. Electron deficiencies in these structures are compensated for by condensation of the icosahedral units, for instance by establishing shared faces.[75-77] Among numerous homoatomic examples the boron theme can also be realized heteroatomically, such as in $K_{34}Zn_{20}In_{85}$[78] or $Na_{102}Cu_{36}Ga_{279}$[79]. Few examples exist in which icosahedral units are made even in the absence of a triel element. The combination of even amounts of group 12 and 14 elements result in an electronic setup (three valence electrons on average) that matches the valence electron configuration of the triels $(ns^2)(np^1)$. Compounds such as $Mo_7Sn_{12}Zn_{40}$,[16] $Na_{13}Cd_{20}E_7$ (E = Pb, Sn),[28] or $Na_{49}Cd_{58.34}Sn_{37.69}$[24] illustrate this principle.

As the icosahedral clusters are expected at balanced Sn–Zn ratios in $Na_{29}Zn_{24}Sn_{32}$ both building principles, covalent and electron deficient motifs, coexist - namely in the presence of covalently bonded $\{Zn_8Sn_4\}$ icosahedra and the 1D covalently bonded homoatomic $\{Sn_{14}\}$-substructure. The present arrangement of icosahedra in Kagomé nets is a common feature among phases with stoichiometries close to 1 : 2 (see Chapters 4.5 and 4.6) which is found e.g. in $Na_8K_{23}Cd_{12}In_{48}$.[80] In that structure, $\{In_{12}\}$ icosahedra are linked by $\{In_3\}$ units, resulting in a three-dimensional network. In contrast to the covalently bonded tin substructure of the present $Na_{29}Zn_{24}Sn_{32}$, in the channels of the Kagomé nets of $Na_8K_{23}Cd_{12}In_{48}$, double hexagonal antiprisms $\{Cd_{12}In_6\}$ are found, which reflect the metallic nature of that compound. Another close relative is the structure of $Na_xMg_{5-x}Ga_9$.[81] Whereas the electron deficient triel networks often feature defect clusters[82] to attain closed shell configuration the present compound offers another elegant possibility to achieve charge balance, which will be discussed in the following.

Refinement of the crystallographic data lead to a split model for the Sn6 position and an occupation for the initial Sn6 site (Sn6a) of 92 %. The effect of this disorder on the cluster structure is shown in Figure 4.26. The $\{Sn_{14}\}$ cluster of the major component **A** has three Sn6a–Sn6a contacts which are oriented parallel to the (001) plane. The ‘transition state’ with a statistical distribution of Sn6b once per cluster is shown as an overlaid model **B**. The disorder corresponds to a rotation of the Sn6a-Sn6a unit in **A** around an axis perpendicular to the bond-vector.

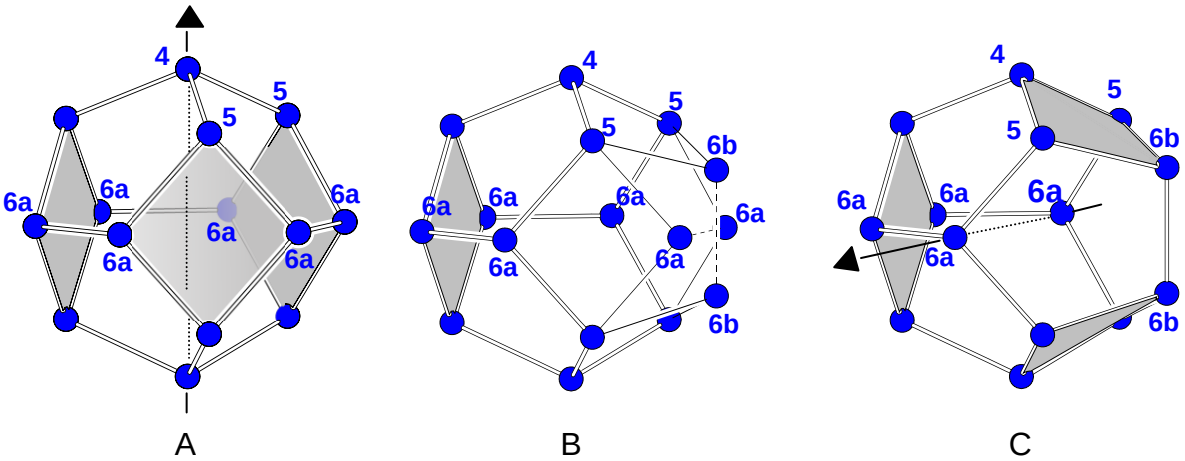

***Figure 4.26*. Disorder of the $\{Sn_{14}\}$ cluster. Cluster A corresponds to the major disorder component, in which the Sn6a sites are occupied. The rotation of one Sn6a–Sn6a unit (model B) leads to cluster C, in which one pair of Sn6b sites is occupied. Clusters A and C have the same number and types of vertices and faces, but the location of the (quasi) three-fold axis (arrow) has changed. See text for details.**

Cluster **C** shows the outcome of this rotation. Polyhedron **C** has the same number and kinds of vertices and faces as the initial cluster **A**. Again, six interconnected pentagonal faces together with distorted square planes generate an enneahedron. Here, the (quasi) three-fold rotation axis runs through opposite Sn6a atoms. The simple rotation of one of the three 3-bonded (Sn6–Sn6) units results in a topologically identical cluster and thus the process can be interpreted as a pseudorotation. However, compared to **A**, cluster **C** suffers from stronger distortion and shows longer Sn6b–Sn5 separations (3.208(6) Å). Through the quasi-rotation, additional contacts between Sn atoms can be established (Figure 4.27). The initially 3-bonded Sn6 atoms are now capable of establishing a further covalent bond to one Sn atom (formerly possessing an electron lone pair) of an adjacent icosahedron (*d*(Sn6b–Sn3) = 2.918(9) Å). Consequently, in the icosahedron all vertices exhibit *exo*-bonds.

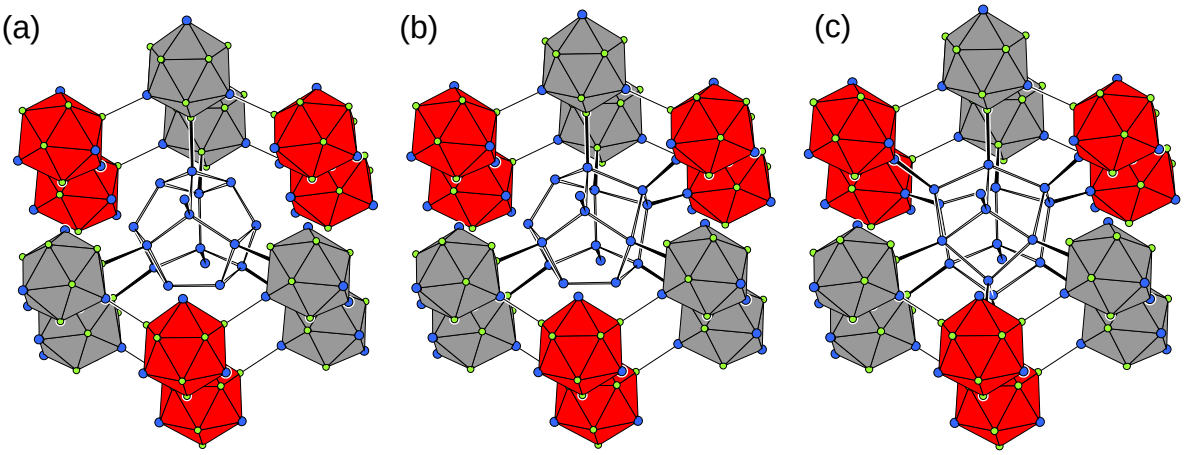

***Figure 4.27*. Isomers of the $\{Sn_{14}\}$ cluster and their interconnection with neighboring $\{Zn_8Sn_4\}$ icosahedra: (a) The major $\{Sn_{14}\}$ isomer, in which the Sn6a sites are occupied: the $\{Sn_{14}\}$ cluster is connected by the Sn5 atoms to six $\{Zn_8Sn_4\}$ icosahedra; Zn (green spheres), Sn (blue spheres). (b) An $\{Sn_{14}\}$ isomer in which one pair of Sn6a atoms is replaced by a pair of Sn6b atoms, which establish two additional bonds to Sn3 atoms of $\{Zn_8Sn_4\}$ icosahedra. (c) The $\{Sn_{14}\}$ isomer in which all the Sn6b sites are occupied: the $\{Sn_{14}\}$ cluster is connected by the Sn5 and Sn6b atoms to 12 $\{Zn_8Sn_4\}$ icosahedra.**

Based on the number of interatomic contacts, the electron count for the title compound can be rationalized as follows. The 14 Sn atoms of the enneahedron are covalently bonded among each other. Six of them (Sn5) establish *exo*-(Sn–Zn) and two (Sn4) establish *exo*-(Sn–Sn) contacts. This leads to $[(4b\text{-}Sn)_8(3b\text{-}Sn)_6]^{6-}$ for a valence compound with electron lone pairs at the 3-bonded Sn atoms.

The $\{Zn_8Sn_4\}$ polyhedron can be regarded analogously to the 26 skeletal electron cluster *closo*-$\{B_{12}H_{12}\}^{2-}$. An *exo*-bonded Zn_{exo} atom contributes one, an *exo*-bonded Sn_{exo} atom three, and a not *exo*-bonded Sn atom two electrons to the cluster skeleton. The polyhedral requirements are presumed not to be altered by Zn/Sn mixing, but only the number of electrons available. Thus, 18 (2 × 3 + 2 × 2 + 8 × 1) bonding electrons are assigned to the 10-fold *exo*-bonded $(Zn_{exo})_8(Sn_{exo})_2(Sn)_2$ icosahedron. A formal charge of 8– is needed to reach the 26 electrons of the icosahedral *closo*-cluster (2n+2 electrons for *closo*, n = 12). Assuming the slightly widened Sn1–Sn1 contacts (d(Sn1–Sn1) = 3.018(1) Å) of the $\{Sn_3\}$ unit are covalent interactions, all Sn atoms of this unit are 4-bonded which results in a formally non-charged Sn_3 ring. $\{Sn_3\}$ units with a formal charge of 2– and comparable Sn–Sn distances (d(Sn–Sn) = 3.059 Å) have been reported in $BaSn_3$. Band structure calculations demonstrated the covalent nature of the Sn–Sn bond. For compensation of the charge of 1 × $\{Sn_{14}\}^{6-}$, 3 × $\{Zn_8Sn_4\}^{8-}$, and 2 × $\{Sn_3\}^0$ per unit cell, 30 Na are required in order to transfer their valence electrons to this sublattice according to the Zintl-Klemm concept. The calculated electron number is confirmed by Extended-Hückel calculations (see Chapter 4.4.3). Assuming a statistical distribution of the Sn6b-sites only once per cluster 3 × 8% = 24 % of the polyhedra adopt shape **C**. By formation of two extra bonds, the electron requirement is reduced to such an extent that allows one to calculate an electron precise Zintl phase. Due to the additional two contacts in the isomeric structure that contains entity **C** the following electron count results. The *enneahedron* is counted as $[(4b\text{-}Sn)_{10}(3b\text{-}Sn)_4]^{4-}$ and according to 20 (= 4 × 3 + 8 × 1) bonding electrons that can be assigned to the $(Sn_{exo})_4(Zn_{exo})_8$ icosahedron. Six additional electrons are acquired for a electron precise Wade cluster. In order to compensate for the charge in the structure with 1× $\{Sn_{14}\}^{4-}$, 1 × $\{Zn_8Sn_4\}^{6-}$, 2 × $\{Zn_8Sn_4\}^{8-}$, and 2 × $\{Sn_3\}^0$, 26 Na atoms are necessary. Evaluation of the structural weighting with 76% cluster **A** and 24% cluster **C** results in an average electron demand of (0.76 × 30) + (0.24 × 26) = 29.04 electrons. This is in good agreement with the 29 Na atoms in the chemical formula determined crystallographically.

As mentioned earlier the lowering of the Fermi level by establishing these additional bonds is confirmed by EH calculations on a model that exclusively contains Sn6b sites (Figure 4.25b). Due to symmetry reasons in the unit cell, a model that contains both cluster orientations cannot be calculated.

As expected, the DOS in Figure 4.25b shows a broader band gap of ~ 2 eV and the states contributed by the electron lone pairs that lie in the proximity of the Fermi level in Figure 4.25a are now lower in energy. This result correlates with the assumption that no electron lone pairs are present in a structure containing the bonding scenario shown in Figure 4.27c. In the title compound with statistically occupied split positions the amount of 3b-Sn6 atoms is reduced to such an extent that the Fermi level lies above the states contributed by the 3-bonded atoms.

The herein presented intermetallic compound shows that the icosahedral building principle that is common among the elements of group 13 can be adopted by the combination of electron richer and electron poorer elements. The icosahedral cluster units prove to be stable entities, which lead to the formation of the $\{Sn_{14}\}$ substructure and permit an isomerization by pseudorotation of the $\{Sn_{14}\}$ polyhedra. Hence, the structure provides a neat possibility to attain a closed-shell configuration and to generate a Zintl phase.

4.5 Synthesis and Crystal Structure of $Na_{16}Zn_{13.54}Sn_{13.47(5)}$ - Icosahedral Linking through Triangular Motifs

The title compound described in this chapter is slightly Zn richer (Zn : Sn ~ 1 : 1) then $Na_{29}Zn_{24}Sn_{32}$ (Zn : Sn = 0.75 : 1) (Chapter 4.4) and possesses a rather similar structure. However, more atomic positions are mixed-occupied which indicates a great electronic flexibility of the three-dimensional network structures that contain icosahedra and covalent substructures. The balanced Zn/Sn ratio is reflected in building units that are typical for structures of electron-poor trielide networks.

4.5.1 Synthesis and Characterization

Synthesis The compound with composition $Na_{16}Zn_{13.54}Sn_{13.47(5)}$ was obtained from a solid state reaction of the elements (Zn was distilled) with Na : Zn : Sn ratio of 15 : 7 : 12 at 500 °C. However, in this mixture, $Na_{16}Zn_{13.54}Sn_{13.47(5)}$ was only found as single-crystals. Later the comound was also obtained in a reaction mixture that targeted a stoichiometric synthesis of $Na_{29}Zn_{24}Sn_{32}$ at 500 °C. Higher yields with clear presence of the compound according to the powder experiments (see below) were synthesized by the reaction of stoichiometric amounts (128 : 110 : 110) at 500 °C for 6 h, followed by quenching to room temperature and annealing at 420 °C for 30 days. Sealed Ta ampoules served as reaction containers and the total chemical loading was 1.160 g, with m(Na) = 0.147 g, m(Zn) = 0.360 g, and m(Sn) = 0.653 g.

Powder X-ray Diffraction The diffraction experiment was carried out in Debye-Scherrer mode after diluting the crystalline product (obtained from above chemical loadings) with diamond powder. The measurement ran with 1° step width and lasted for 18 h. The obtained diagram, together with a calculated pattern from the single-crystal solution of the compound is shown in Figure 4.28. The result reveals the target compound as the main phase with admixtures of β-NaSn and $NaZn_{13}$. Unmatching intensities e.g. at 2θ ~ 35° are caused by overlapping reflections. Most intense reflections from the main admixture $NaZn_{13}$ are marked with a red star.

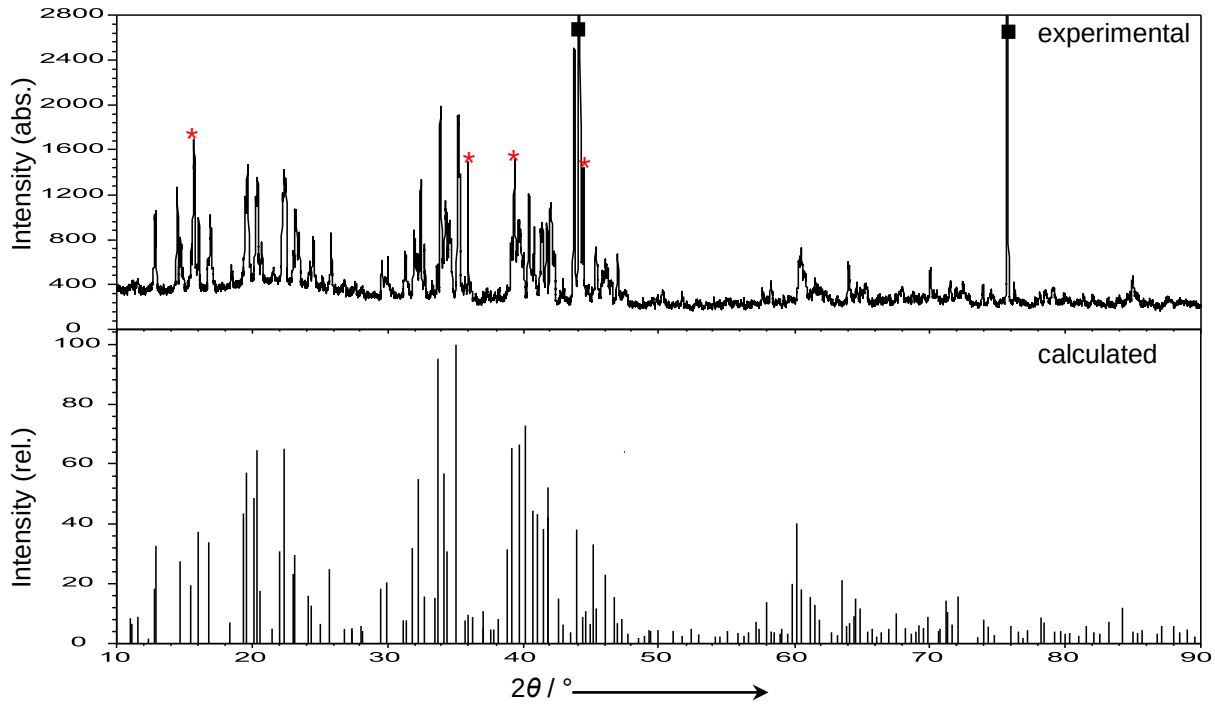

***Figure 4.28*. Experimental powder diagram (top) from a reaction of a sample loaded with Na : Zn : Sn = 128 : 110 : 110 and calculated powder diagram (bottom) of a refined crystal with composition of $Na_{16}Zn_{13.54}Sn_{13.47(5)}$. Reflections from diamond (internal standard) are labeled with a square. Red stars mark reflections of $NaZn_{13}$.**

4.5.2 Crystal Structure Determination and Description

Structure Determination Silvery block shaped crystals were sealed in capillaries and measured at room temperature on the Oxford Xcalibur3 diffractometer. The data collections for $Na_{16}Zn_{13.54}Sn_{13.47(5)}$ included 416 frames from 4 ω scans with 1°/frame scan width, detector distance 50 mm and 10 s exposure time. The indexing routine and the systematic absence conditions indicated a body-centered orthorhombic unit cell in the possible space groups *Iba*2 (non-centrosymmetric) and *Ibam* (No. 72, centrosymmetric). The latter one was chosen due to the best converging model in terms of final residuals, internal *R*-values, and residual electron density peaks. Upon refinement 10 Na, 10 Sn and 7 Zn positions could be assigned. Three Sn (Sn8 to Sn10) sites showed considerably larger displacement parameters. Therefore mixed site occupancies with Zn were introduced which led to occupancies for M = Sn / Zn: 0.48 / 0.52(1) for M8, 0.52 / 0.48(1) for M9, and 0.49 / 0.51(1) for M10. This resulted in a significant decrease of final residual electron density. The Sn7 position showed only small amounts of mixing with Zn (98% Sn) and was therefore treated as a fully occupied Sn atom. Relevant crystallographic data is comprised in Tables 4.13 to 4.15. Interatomic distances up to 4 Å are given in Table 8.4 (see Appendix).

***Table 4.13*: Selected crystallographic and refinement data for $Na_{16}Zn_{13.54}Sn_{13.47(5)}$.**

Empirical formula	**$Na_{16}Zn_{13.54}Sn_{13.47(5)}$**
Formula weight / g·mol^{-1}	5701.43
Temperature / K	293(2) K
Crystal size / mm^3	0.05 × 0.05 × 0.05
Crystal color; shape	Silvery; Block
Diffractometer	Oxford Xcalibur3 (CCD)
Crystal system	Orthorhombic
Space group	*I b a m* (No. 72)
Unit cell parameters / Å	a = 27.401(1); b = 16.100(1); c = 18.431(1)
Unit cell volume / Å^3; *Z*	8131.2(3); 8
ρ_{calc} / g·cm^{-3}	4.66
μ / mm^{-1} (Mo K_α)	16.08
Absorption correction	Empirical
F(000)	10042
Θ range / °	2.93 - 27.81
Index range	–35 ≤ *h* ≤ 22; -21 ≤ *k* ≤ 20; –24 ≤ *l* ≤ 24
Data completeness / %	99.6
Integrated reflections	30990 (R_σ = 0.035)
Independent reflections	4949 (R_{int} = 0.048)
Refinement method	Full-matrix least-squares on F^2 (SHELXTL)
Parameters	213
Goodness of fit on F^2	1.086
Observed reflections [$I > 2\sigma(I)$]	3616
R_1 / wR_2 [$I > 2\sigma(I)$]	0.033 / 0.078
R_1 / wR_2 (all data)	0.051 / 0.088
Weighting scheme[a]	a = 0.047.; b = 31.009
Extinction coefficient	0.000044(5)
Residual map / e$^-$·Å^{-3}	+1.87 [0.80 Å from Zn10] / –2.15 [0.77 Å from Sn7]

[a] $w = 1 / [\sigma^2(F_o^2) + (aP)^2 + bP]$, where $P = (F_o^2 + 2F_c^2) / 3$

***Table 4.14*: Atomic coordinates and equivalent isotropic displacement parameters for $Na_{16}Zn_{13.54}Sn_{13.47(5)}$.**

Atom	**Wyck.**	**Occ. ≠ 1**	***x***	***y***	***z***	**U_{eq} / Å^2**
Sn1	8*j*		0.1705(1)	0.1600(1)	0	0.013(1)
Sn2	8*j*		0.2561(1)	0.0909(1)	½	0.013(1)
Sn3	16*k*		0.3300(1)	0.1707(1)	0.0818(1)	0.016(1)
Sn4	8*j*		0.0800(1)	0.0996(1)	0.5000(1)	0.018(1)
Sn5	16*k*		0.8926(1)	0.3789(1)	0.3436(1)	0.018(1)
Sn6	16*k*		0.1995(1)	0.0953(1)	0.2498(1)	0.016(1)
Sn7	16*k*		0.9870(1)	0.2838(1)	0.3312(1)	0.021(1)
M8 = Sn8 / Zn8	16*k*	0.48 / 0.52(1)	0.0510(1)	0.0017(1)	0.3765(1)	0.016(1)
M9 = Sn9 / Zn9	8*f*	0.52 / 0.48(1)	0.1063(1)	0	¼	0.018(1)
M10 = Sn10 / Zn10	16*k*	0.49 / 0.51(1)	0.9784(1)	0.4280(1)	0.4238(1)	0.027(1)
Zn1	16*k*		0.2294(1)	0.1723(1)	0.1227(1)	0.015(1)
Zn2	8*j*		0.1678(1)	0.1795(1)	½	0.016(1)
Zn3	8*j*		0.2588(1)	0.0813(1)	0	0.016(1)
Zn4	16*k*		0.1803(1)	0.3077(1)	0.0772(1)	0.017(1)
Zn5	16*k*		0.2263(1)	0.1818(1)	0.3775(1)	0.016(1)
Zn6	16*k*		0.9932(1)	0.1428(1)	0.4244(1)	0.018(1)
Zn7	8*j*		0.0814(1)	0.0823(1)	0	0.016(1)
Na1	8*j*		0.0762(1)	0.2815(3)	0	0.022(1)
Na2	16*k*		0.1695(1)	0.9927(2)	0.9034(2)	0.022(1)
Na3	16*k*		0.1112(1)	0.1729(2)	0.1508(2)	0.022(1)
Na4	16*k*		0.2918(1)	0.0054(2)	0.3467(2)	0.029(1)
Na5	8*g*		0	0.1073(3)	¼	0.028(1)
Na6	16*k*		0.3056(1)	0.1968(2)	0.2538(2)	0.022(1)
Na7	16*k*		0.4222(1)	0.0768(2)	0.1798(2)	0.032(1)

Na8	8*j*	0.0581(2)	0.3041(3)	½	0.037(1)
Na9	8*j*	0.3726(2)	0.0151(3)	½	0.035(1)
Na10	16*k*	0.1019(1)	0.1892(2)	0.3418(2)	0.034(1)

***Table 4.15*: Anisotropic thermal displacement parameters (*I* Å^2) for $Na_{16}Zn_{13.54}Sn_{13.47(5)}$.**

Atom	U_{11}	U_{22}	U_{33}	U_{23}	U_{13}	U_{12}
Sn1	0.014(1)	0.013(1)	0.012(1)	0	0	0
Sn2	0.016(1)	0.012(1)	0.012(1)	0	0	0
Sn3	0.017(1)	0.016(1)	0.014(1)	0	0	0
Sn4	0.017(1)	0.019(1)	0.018(1)	0	0	–0.002(1)
Sn5	0.017(1)	0.018(1)	0.018(1)	0.002(1)	0	0
Sn6	0.021(1)	0.015(1)	0.011(1)	0	0	–0.003(1)
Sn7	0.025(1)	0.016(1)	0.021(1)	0	0.004(1)	0
M8	0.016(1)	0.016(1)	0.017(1)	0	0	0
M9	0.023(1)	0.020(1)	0.012(1)	0	0	0
M10	0.029(1)	0.018(1)	0.034(1)	0.003(1)	0.008(1)	–0.003(1)
Zn1	0.017(1)	0.016(1)	0.013(1)	0	0	–0.002(1)
Zn2	0.019(1)	0.015(1)	0.015(1)	0	0	0
Zn3	0.017(1)	0.015(1)	0.016(1)	0	0	0
Zn4	0.018(1)	0.015(1)	0.017(1)	0	0	–0.002(1)
Zn5	0.019(1)	0.016(1)	0.013(1)	0.002(1)	0	0
Zn6	0.019(1)	0.016(1)	0.017(1)	0	0)	0
Zn7	0.016(1)	0.017(1)	0.015(1)	0	0	0
Na1	0.024(2)	0.019(2)	0.023(2)	0	00	0
Na2	0.023(2)	0.021(2)	0.022(2)	0	0.002(1)	0.004(1)
Na3	0.020(2)	0.024(2)	0.022(2)	0.004(1)	0	0
Na4	0.035(2)	0.028(2)	0.024(2)	0.002(1)	0	0
Na5	0.042(3)	0.022(3)	0.020(3)	0	0	0
Na6	0.024(2)	0.021(2)	0.019(2)	0	0.004(1)	0
Na7	0.033(2)	0.028(2)	0.035(2)	–0.006(2)	0.005(2)	–0.005(2)
Na8	0.036(3)	0.027(3)	0.049(3)	0	0	0.004(2)
Na9	0.036(3)	0.039(3)	0.030(3)	0	0	–0.005(2)
Na10	0.035(2)	0.036(2)	0.031(2)	–0.005(2)	0.002(2)	–0.007(2)

Structure Description As depicted in Figure 4.29a the structure is a 3D network of two types of icosahedra (units A and B) and two triangular units C and D. Icosahedra A (gray) and B (white) are directly interlinked and form Kagomé layers (3.6.3.6 net) in the (001) plane. The layers lie at z = 0, ½ and are interlinked by triangular units C at z = ¼ and ¾. The layer stacking along c is *AA'AA'* (Figure 4.29c) meaning that in every second layer icosahedron A is inverted and icosahedron B is mirrored at (010). In a [001] projection of the unit cell the rings C lie in the smaller channels, whereas in the bigger channels of the Kagomé net strands of interconnected triangles D are embedded (Figure 4.29a).

As shown in Figure 4.29d icosahedron A is well ordered and composed of atoms Sn1 to Sn3 and Zn1 to Zn5. It lies on the (8*j*)-site and has (..*m*)-symmetry. The homoatomic intracluster distances in the icosahedron are in the range of *d*(Sn3–Sn3) = 3.016(1), *d*(Zn–Zn) = 2.644(1) - 2.845(1) Å and the heteroatomic distances vary from 2.730(1) to 2.929(1) Å. Cluster A has 10 *exo*-bonds which connect the atoms to adjoining clusters A (×2), B (×2), triangular units C (×4), and D (×2). The Sn3 atoms have no *exo*-cluster bond. All *exo*-bonds are heteroatomic and range from 2.726(1) to 2.832(1) Å. Reagarding only *exo*-contacts to cluster A, linear chains of icosahedra A are formed via Sn2–Zn3 (2.774(2) Å) along [010].

Cluster B (on (4*c*)-site with (2/*m*)-symmetry) consists of the atoms Sn4, Zn6, Zn7, and M8 (Figure 4.29e). The intracluster bonds are distributed to Zn–Zn (2.658(1), 2.787(2) Å), Zn–Sn (2.842(1), 2.930(2) Å), M–Sn (2.882(1) Å), M–Zn (2.768(1) to 2.906(1) Å), and the only M–M contact with 2.795(1) Å. These values are slightly larger than those for the corresponding *exo*-bonds. All 12 atoms of cluster B have *exo*-bonds which connect the atoms to neighboring clusters A (×4), C (×4), and D (×4) units. These bonds are formed via M8–M9 (2.780(1) Å (×4)) and Zn(Sn)–Sn(Zn) with bond lengths ranging from 2.729(1) to 2.853(1) Å. For both clusters A and B the *exo*-bonds, in average, are shorter than the corresponding multicenter intracluster bonds.

Motif C is a triatomic ring of 4b-atoms (Sn6–Sn6–M9) reminiscent of the one found in $Na_{29}Zn_{24}Sn_{32}$ (Chapter 4.4). However, due to mixed occupancy the present ring is slightly distorted with the smaller ring angle (59° ×2) at Sn6 and the larger at M9 (~ 62°). The interatomic distances in this ring are *d*(Sn6–Sn6) = 3.069(1) and *d*(M9–Sn6) = 2.978(1) Å. They are comparable to the Sn–Sn separation (3.058 Å) in cyclopropenyl like {Sn_3} in $BaSn_3$. As shown in Figure 4.29b this entity represents the shared triangular face of fused capped tetrahedra. The latter share common triangles and hexagons along [001]. Thus ring C interlinks four units A and two units B through M9–M8 (2.780(1) Å) and Sn6–Zn1, Sn6–Zn5 bonds (2.774(1), 2.832(1) Å, respectively). It is worth noting that the mixed occupied position of icosahedron B does not take part in the bonding of the Kagomé net, but is associated only with M9 of unit C.

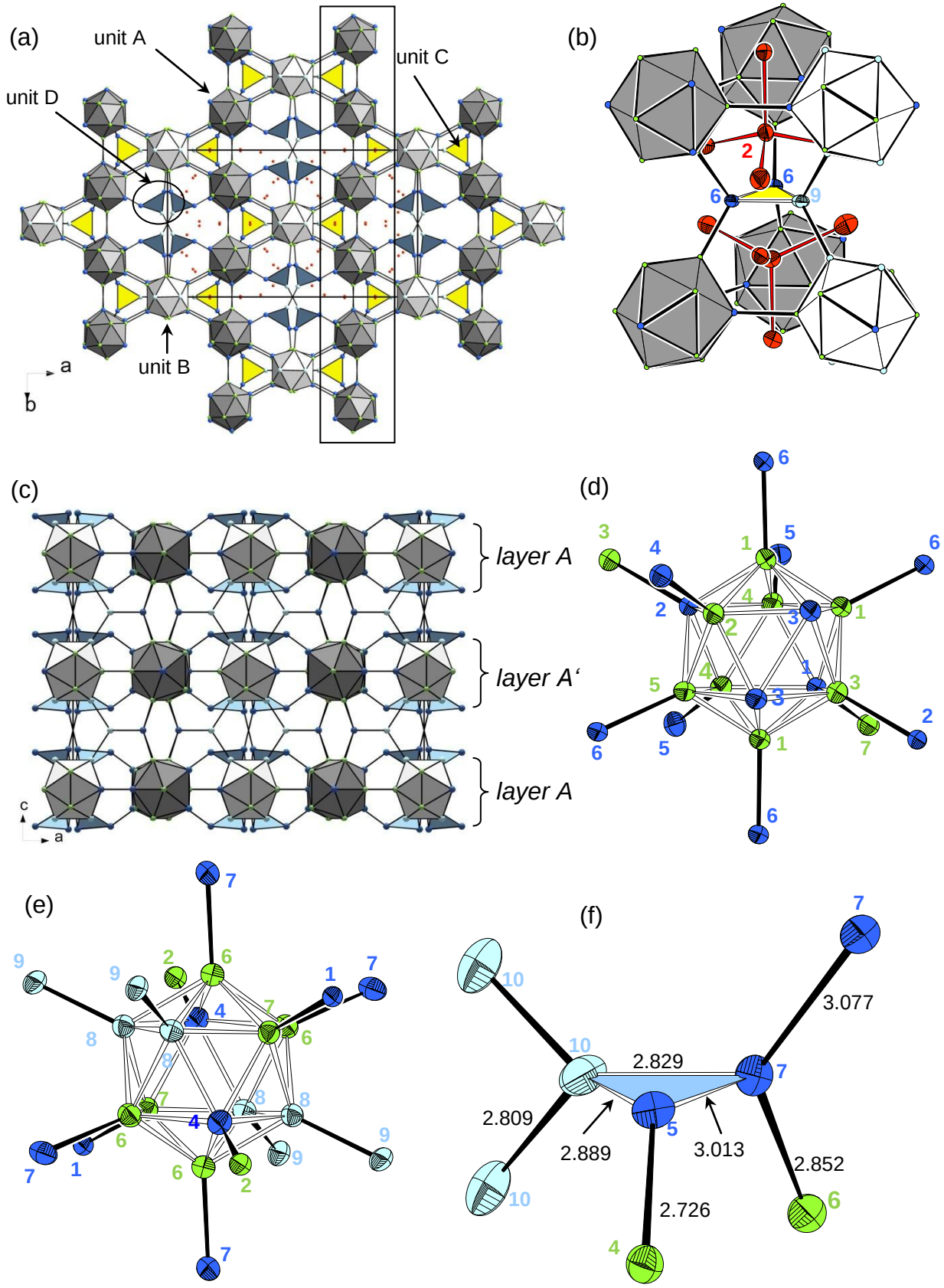

***Figure 4.29*. (a) [001]-projection of the unit cell of $Na_{16}Zn_{13.54}Sn_{13.47(5)}$. A linear chain of clusters A is indicated. (b) Ring unit C connecting four A and two B clusters forming Friauf polyhedra with the tetrahedrally coordinated Na2 in the centers. (c) [010]-view of the unit cell (Na atoms are omitted). (d) and (e) Anisotropic representations (90%) of icosahedron A and icosahedron B, respectively, (f) anisotropic representation (90%) of unit D. In all pictures: Na (red), Zn (green), Sn (blue), M = Zn / Sn (light blue), icosahedron A (dark gray), icosahedron B (white), triangular unit C (yellow), and the triangular unit D (blue).**

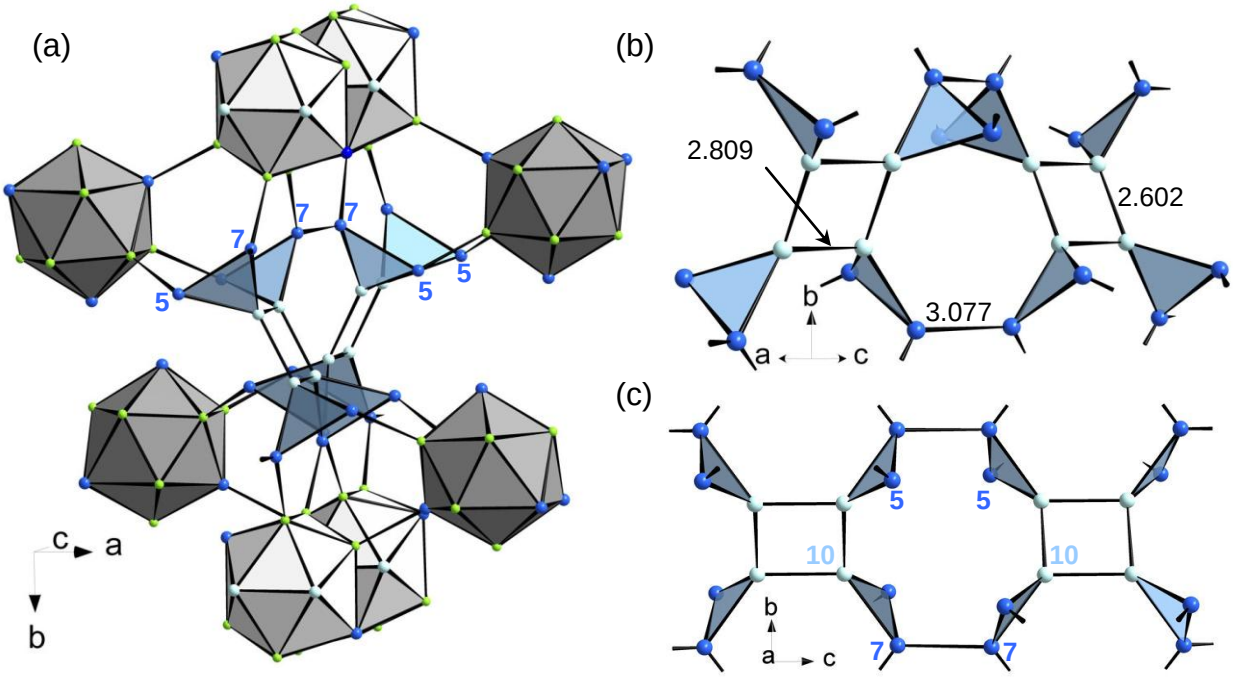

***Figure 4.30*. Connectivity of the ring unit D (a) Off [001] projection with bonded icosahedra. (b) and (c) Two further projections. Zn (green), Sn (blue), M = Zn / Sn (light blue).**

Finally, positions Sn5, Sn7, and M10 compose the three-member unit D. The M–Sn bonds (2.889(1), 2.892(1) Å) within this cluster are almost equal and slightly shorter than the intracluster Sn5-Sn7 contact (3.013(1) Å). Compared to unit C, deviations from an ideal triangle (ring angles 58.5° - 62.8°) are smaller, reflecting an almost homoatomic composition (Figure 4.29f). In contrast to C, which is exclusively composed of 4b-atoms, in ring D one vertex (Sn5) is only three bonded and binds one icosahedron A (*d*(Sn5–Zn4) = 2.726(1) Å). Atom Sn7 establishes bonds to one unit B (*d*(Sn7–Zn6) = 2.852(1) Å) and one adjoining ring D (*d*(Sn7–Sn7) = 3.077(1) Å). The remaining vertex M10 forms two M10–M10 contacts (2.602(2) and 2.809(2) Å). As indicated in Figure 4.30a two units D represent two of the four triangular faces of a truncated tetrahedron (the other triangular faces are deltahedral faces of clusters A and B). This results in pairs of directly linked stripes of truncated tetrahedra or, together with the tetraehdrally coordinated central Na1 atoms, in Friauf polyhedra along the *c*-axis. The connection between D occurs through a planar rectangular $(M10)_4$ fragment with ∠M10M10M10 angles equal to 90° resulting in quite unusual valence angles for the M10 atoms. Such a fragment is known in molecular chemistry e.g. in cyclotetrastannane $[ClSnSi(SiMe_3)_3]_4$[83] but not for Zn. Similar homonuclear ring systems can also be found in $\{Te_4\}^{4+}$ in *α*-TeI or $\{As_4\}^{4-}$ in $CoAs_3$.

Whereas the interlinking motif of unit C has been found in indium metallic phases $Na_{15}In_{27.4}$ and $Na_8K_{23}Cd_{12}In_{48}$, the arrangement of ring D in the present compound is novel.

4.5.3 Discussion

The presented compound is similar in structure to $Na_{29}Zn_{24}Sn_{32}$. However, the Zn content is higher and the formerly homoatomic covalent Sn-substructure is replaced by triangular units (which are rather typical for electron deficient bonding) that interlink the icosahedra. Therefore, a short overview into icosahedral linking in the binary triel phases is given. As pointed out by Charbonnel et al.[84] the linking of icosahedral units within structures is dependent on the number of valence electrons. In very reduced phases with high VECs and equal to the Wade polyhedral electron demand for naked clusters, the icosahedra are not linked to adjacent units. Up to now, in intermetallics no isolated icosahedron for Ga or In has been reported. When the amount of electropositive metal decreases linking between icosahedra is required to minimize the electron deficiency by establishing bonds. In cases of severe electron deficiencies, the units may condense through vertex, edge, or face sharing and form oligomeric entities. Discrete icosaehdral clusters have high charges, such as a hypothetical $\{Ga_{12}\}^{14-}$, and only few examples with discrete Tl-centered thallium icosahedra (e.g. $Na_3K_8Tl_{13}$[85]) have been found, rendering these clusters highly solvated and polarized by the alkali countercations. The simplest way to connect two icosahedra is by direct bonding between two apices. This is commonly observed in intermetallic gallides. Normally such inter icosahedral bonds are 2*c*-2*e* bonds but can also be 3*c*-2*e* like in the case of $RbGa_7$.[86] No such classical covalent bonds are present in extended structures with separated icosahedra as in $NaZn_{13}$.[87] Here the Zn centered icosahedra are directly interconnected by sharing tetrahedra. In $MoAl_{12}$[88] the units share pseudooctahedra. Linking via interstitial atoms such as in $K_6(NaCd)_2Tl_{12}Cd$[89] is another way. Finally, condensed or fused icosahedra are realized by vertex sharing (bi-icosahedra, tri-icosahedra, etc.), with very specific electronic requirements.[84, 90, 91] The sandwiched Ni ion in $Ni(C_2B_9H_{11})_2$[92] is an example for vertex sharing. While edge sharing is common for smaller polyhedra no example for non-defective edge sharing icosahedra has been reported. According to quantumchemical calculations such a regular unit would be unstable with respect to too small interatomic distances.

Oligomeric units by face fusion are realized in twinned or triply fused icosahedra, which can also form extended structures (see Chapter 4.6). A tetra-icosahedron, resulting from the fusion of four tetrahedrally arranged icosahedra only exists as a building block in tcp (tetrahedrally close-packed)-related structures of *γ*-brass type.

On the basis of the refined empirical formula and with respect to the site occupancy factors (Table 4.14) the average electron count for $Na_{16}Zn_{13.54}Sn_{13.47(5)}$ can be performed as follows. All *exo*-bonds lie well in the range of 2*c*-2*e* bonds, thus, based on the 26 cluster electrons needed for a *closo*-cluster, the 10-fold *exo*-bonded icosahedron A has to be formulated as $\{Zn_8Sn_4\}^{8-}$, and the 12-fold *exo*-bonded icosahedron B as $\{Zn_{8.09}Sn_{3.91}\}^{6.18-}$. The chain unit D, assigning a charge of –2 to a 4b-Zn and multiplying by 0.51, results in $\{Zn_{0.51}Sn_{2.49}\}^{2.02-}$. The triangular unit C is $\{Zn_{0.48}Sn_{2.52}\}^{0.96-}$. One formula unit contains two A^{8-}, one $B^{6.18-}$, two $C^{0.96-}$, and four $D^{2.02-}$ which results in a total electron demand of ~ 32.2 electrons (on the assumption of a compositon $Na_{32}Zn_{27}Sn_{27}$, which would result, when fixing the occupancies for M8 to M10 to 50%, one formula unit would need 34 electrons). As one can see the number of the crystallographically determined 32 Na atoms is very close to the calculated value, which shows again that the present disorder originates from the driving force towards the formation of a closed shell compound. Thus, the present compound can formally be considered as a Zintl phase. Longer annealing periods did not result in a ordering of the atomic positons, so that the statistical site occupancies can be assumed to be essential. It should be noted that slightly Na-richer compounds with compositions $Na_{132}Zn_{116\pm x}Sn_{100\mp x}$ (x ~ 1.0) exist, which crystallize with similar structures in the same space group *Ibam* and one additional Na position. To accommodate the 132 electrons, they are Zn-richer (the Zn-richer, the more electrons are needed), which means a higher degree of disorder is being observed, e.g. the Sn7 site in triangle D becomes considerably mixed occupied. However, the observation of the two different kinds of icosahedra, one completely ordered, whereas the other shows significant statistically occupied sites is hardly explainable. In addition the Na coordinations around the clusters are virtually the same, both are encaged in $\{Na_{20}\}$ dodecahedra. As icosahedron A $\{Zn_8Sn_4\}^{8-}$ has been also found in $Na_{29}Zn_{24}Sn_{32}$ it can be speculated that the present coloring of this unit, with equal electron contributions from both elements, is energetically favoured and tries to be attained when possible. A statistical analysis of the different kinds of icosahedra found in the course of this thesis is provided in Chapter 4.9.

4.6 Synthesis and Crystal Structures of $Na_{22}Zn_{20}Sn_{19(1)}$ and $Na_{34}Zn_{65}Sn_{40(1)}$ - Two Cluster Compounds with Structures Analogous to Gallides without an Element of Group 13

In the field of electron counting rules in infinite solids much attention has centered around the extended networks of fused boron or gallium deltahedra. In neat solid state arrays the clusters are forced to join or fuse due to lack of electrons and to build up the structure. The solid can be assembled in one dimensional ways, e.g. stripes of either vertex linked or edge, vertex, or face sharing polyhedra. In two and three dimensions the building blocks can use these connection motifs in turn, which results in an enormous variety of structures. The majority of the known examples contain frameworks made of main group atoms, especially of triel atoms. CaB_6 contains $\{B_6\}$ vertex linked octahedra and the structure of KGa_3[93] shows $\{Ga_8\}$ dodecahedra linked via Ga atom spacers. MgB_4[94] contains chains of edge fused *nido*-pentagonal bipyramids which are in turn vertex linked to each other. These examples are relatively straightfoward compared to materials examined by Belin and co-workers. For instance in $Rb_{0.6}Na_{6.25}Ga_{20.02}$[77] there are face fused icosahedral dimers of $\{Ga_{21}\}$, which are vertex linked to other such units as well as to single Ga icosahedra. This fragment is reminiscent of tetragonal *β*-boron. In $Rb_{0.6}Na_{6.25}Ga_{20.02}$ not all of the sites have an occupancy of 100%, which means that such fused polyhedra can be of *nido*-, *arachno*-, or even *hypho*-type. Electron deficiency is usually present by the formation of multicenter bonding in these clusters. However, these phases also exhibit, or closely approach, closed shell electronic configuration as a driving force for the creation of the extensive networks. These can be generated in different ways e.g. by formation of vacancies at specific cluster sites or through substitution by electron poorer elements, or (in the present work) of variable mixed occupancies of Zn and Sn. Triply-fused iosahedra are building units in *β*-rhombohedral boron and were also found for $\{(Ga/M)_{28}\}$ in $Na_{102}(MGa)_{315}$ (M = Cu, Zn)[79] and related $\{(In/Li)_{28}\}$ building blocks were discovered in $K_{34}In_{92.30}Li_{12.70}$.[95] Clusters or cages with no special symmetries are the electron precise $\{M_{15}\}$ or $\{M_{16}\}$ open spacers which are present in moderately reduced rhombohedral phases (e.g. in $Na_{22}Ga_{29}$,[96] Na_7Ga_{13},[97, 98], or $K_{21.33}In_{39.67}$[99]). The combination of those and a variety of other building motifs found in the triel chemistry indicates the optional complexity of these structures. Based on the method of moments[100] between three and four electrons per atom,

the preference for three member rings is replaced by that for six member rings. This rule, established by Burdett et al. helps to rationalize the overwhelming amount of such compounds. Two phases that have isostructural precedants among gallides are presented in the following.

4.6.1 Synthesis of $Na_{22}Zn_{20}Sn_{19(1)}$ and $Na_{34}Zn_{65}Sn_{40(1)}$

Synthesis Single-crystals of $Na_{22}Zn_{20}Sn_{19(1)}$ (**1**) and $Na_{34}Zn_{65}Sn_{40(1)}$ (**2**) were found as byproducts when reacting elemental Na : Zn : Sn in the ratio of 29 : 24 : 32 at 500 °C. The main phase of this reaction, $Na_{29}Zn_{24}Sn_{32}$, is discussed in Chapter 4.4. The thermal analysis of that mixture indicated the presence of at least two additional phases. However, accomodating stoichiometric loadings to the refined compositions of **1** and **2** did not result in higher yields. Up to now the two phases were only found as the minor product and exhibit same crystal color and shape.

4.6.2 Crystal Structure Determination of $Na_{22}Zn_{20}Sn_{19(1)}$ and $Na_{34}Zn_{65}Sn_{40(1)}$

Single-crystals were sealed into capillaries in the glovebox. X-ray data of the compounds $Na_{22}Zn_{20}Sn_{19(1)}$ (**1**) and $Na_{34}Zn_{65}Sn_{40(1)}$ (**2**) was collected on an Oxford Xcalibur3 diffractometer. For each compound 776 frames were taken in four ω and one φ scan with 20 s exposure time and 50 mm detector distance. The space group *Pnma* was assigned based on systematic absence conditions for **1**. From the 18 Sn positions 13 had to be refined considering Sn/Zn mixed occupancies (M1 to M13). The remaining five Sn (Sn14 to 18) and five Zn (Zn14 to 18) did not show noteworthy mixed occupancy. Of the 16 Na atoms only Na16 showed larger atomic thermal displacement parameters. This was ascribed to its poor coordination environment.

For **2** the structure could be successfully solved and refined in the rhombohedral space group *R*–3*m*. A solution in the other centrosymmetrical space group *R*–3 resulted in comparable final electron residuals. As the compositions of the cluster units resulted in almost the same empirical formula, the solution in the higher symmetric *R*–3*m* was chosen. Structure solution and refinement shows two Sn, four Zn, nine M sites that are statistically occupied with Sn and Zn (M2, M3, M5 to M11 with Sn occupancies ranging from 23 to 80%), and six independent Na atoms. Of the two ordered sites Sn1 and Sn4, the latter showed slightly smaller thermal parameters. Refining the two sites with equal displacement parameters lead to a slightly Zn richer overall formula and higher final residuals. Crystallographic data for **1** and **2** are shown in Table 4.16.

Atomic positions and anisotropic thermal displacement parameters are shown in Tables 4.17 to 4.20 and interatomic distances are comprised in Tables 8.5 and 8.6 (see Appendix.).

***Table 4.16*: Selected crystallographic and refinement data for $Na_{22}Zn_{20}Sn_{19(1)}$ and $Na_{34}Zn_{65}Sn_{40(1)}$.**

Empirical formula	**$Na_{22}Zn_{20}Sn_{19(1)}$ (1)**	**$Na_{34}Zn_{65}Sn_{40(1)}$ (2)**
Formula weight / g·mol^{-1}	4057.63	9764.45
Temperature / K	293(2) K	
Crystal size / mm^3	0.06 × 0.05 × 0.05	0.05 × 0.05 × 0.04
Crystal color; shape	Silvery metallic; Block	
Diffractometer	Oxford Xcalibur3 (CCD)	
Crystal system	Orthorhombic	Rhombohedral
Space group	*Pnma* (No. 62)	*R*–3*m* (No. 166)
Unit cell parameters / Å	*a* = 16.403(1)	*a* = 16.956(1)
	b = 15.598(1)	*c* = 36.861(1)
	c = 22.655(6)	
Unit cell volume / Å^3; *Z*	5796.1(1); 4	9177.6(2); 3
ρ_{calc} / g·cm^{-3}	4.65	5.30
μ / mm^{-1} (Mo K_α)	16.27	20.57
Absorption correction	empirical	empirical
F(000)	7152	12956
Θ range / °	2.95 - 27.78	3.55 - 25.30
Index range	–13 ≤ *h* ≤ 21; –20 ≤ *k* ≤ 20	–20 ≤ *h* ≤ 20; –20 ≤ *k* ≤ 20
	–29 ≤ *l* ≤ 29	–44 ≤ *l* ≤ 29
Data completeness / %	99.8	99.5
Integrated reflections	83143 (R_σ = 0.019)	29093 (R_σ = 0.013)
Independent reflections	7086 (R_{int} = 0.043)	2061 (R_{int} = 0.030)
Refinement method	Full-matrix least-squares on F^2 (SHELXTL)	
Parameters	312	139
Goodness of fit on F^2	1.132	1.310
Observed reflections [$I > 2\sigma(I)$]	5844	1912
R_1 / wR_2 [$I > 2\sigma(I)$]	0.028 / 0.065	0.043 / 0.095
R_1 / wR_2 (all data)	0.038 / 0.071	0.047 / 0.096
Weighting scheme[a]	a = 0.029;	a = 0;
	b = 52.042	b = 1739.647
Extinction coefficient	0.000136(8)	0.000046(2)
Residual map / e$^-$·Å^{-3}	+2.54 [0.82 Å from Zn10]	+1.72 [1.93 Å from Na6]
	–1.80 [0.70 Å from Zn11]	–4.27 [2.63 Å from Zn5]

[a] $w = 1 / [\sigma^2(F_o^2) + (aP)^2 + bP]$, where $P = (F_o^2 + 2F_c^2) / 3$

***Table 4.17*: Atomic coordinates and equivalent isotropic displacement parameters for $Na_{22}Zn_{20}Sn_{19(1)}$ (1).**

Atom	**Wyck.**	**Occ. ≠ 1**	***x***	***y***	***z***	U_{eq} **/ Å^2**
M1 = Sn1 / Zn1	8*d*	0.49 / 0.51(1)	0.5997(1)	0.0770(1)	0.4178(1)	0.016(1)
M2 = Sn2 / Zn2	8*d*	0.47 / 0.53(1)	0.3402(1)	0.1607(1)	0.3264(1)	0.015(1)
M3 = Sn3 / Zn3	8*d*	0.36 / 0.64(1)	0.4231(1)	0.0721(1)	0.4094(1)	0.016(1)
M4 = Sn4 / Zn4	8*d*	0.43 / 0.57(1)	0.6426(1)	–0.0733(1)	0.4741(1)	0.016(1)
M5 = Sn5 / Zn5	8*d*	0.49 / 0.51(1)	0.2139(1)	0.1488(1)	0.5561(1)	0.019(1)
M6 = Sn6 / Zn6	8*d*	0.44 / 0.56(1)	0.9275(1)	0.0582(1)	0.5609(1)	0.020(1)
M7 = Sn7 / Zn7	8*d*	0.14 / 0.86(1)	0.6390(1)	0.0767(1)	0.5443(1)	0.019(1)
M8 = Sn8 / Zn8	8*d*	0.44 / 0.56(1)	0.5035(1)	0.1643(1)	0.5033(1)	0.014(1)
M9 = Sn9 / Zn9	8*d*	0.52 / 0.48(1)	0.0698(1)	0.0902(1)	0.5081(1)	0.019(1)
M10 = Sn10 / Zn10	4*c*	0.44 / 0.56(1)	0.2161(1)	¼	0.6577(1)	0.033(1)
M11 = Sn11 / Zn11	4*c*	0.31 / 0.69(1)	0.1060(1)	¼	0.7492(1)	0.032(1)
M12 = Sn12 / Zn12	8*d*	0.66 / 0.34(1)	0.9728(1)	0.1489(1)	0.7788(1)	0.028(1)

M13 = Sn13 / Zn13	8*d*	0.71 / 0.29(1)	0.7842(1)	0.1553(1)	0.5816(1)	0.020(1)
Sn14	8*d*		0.8758(1)	0.0552(1)	0.6841(1)	0.020(1)
Sn15	4*c*		0.0987(1)	¼	0.2548(1)	0.014(1)
Sn16	4*c*		0.1242(1)	¼	0.4583(1)	0.017(1)
Sn17	8*d*		0.3364(1)	0.0946(1)	0.2069(1)	0.016(1)
Sn18	4*c*		0.3323(1)	¼	0.1308(1)	0.016(1)
Zn14	4*c*		0.1997(1)	¼	0.3514(1)	0.020(1)
Zn15	4*c*		–0.0726(1)	0.2500	0.2589(1)	0.020(1)
Zn16	8*d*		0.5100(1)	–0.0743(1)	0.3907(1)	0.014(1)
Zn17	8*d*		0.1841(1)	0.1603(1)	0.1644(1)	0.020(1)
Zn18	8*d*		0.1939(1)	0.1022(1)	0.2806(1)	0.019(1)
Na1	8*d*		0.2223(2)	0.0648(2)	0.4190(1)	0.023(1)
Na2	4*c*		0.3293(2)	¼	0.4575(2)	0.021(1)
Na3	4*c*		0.0127(2)	¼	0.1277(2)	0.023(1)
Na4	8*d*		0.0149(2)	0.0636(2)	0.2181(1)	0.027(1)
Na5	8*d*		0.3021(2)	0.0622(2)	0.0545(1)	0.031(1)
Na6	4*c*		0.6072(3)	¼	0.6143(2)	0.028(1)
Na8	4*c*		–0.0725(3)	¼	0.4944(2)	0.037(1)
Na9	4*c*		0.1847(3)	¼	0.0320(2)	0.025(1)
Na10	4*c*		0.8054(3)	¼	0.7185(2)	0.034(1)
Na11	8*d*		0.0187(2)	0.1266(2)	0.3674(1)	0.033(1)
Na12	8*d*		0.3320(2)	–0.0634(2)	0.3107(1)	0.032(1)
Na13	8*d*		0.1961(2)	–0.0565(2)	0.1744(1)	0.031(1)
Na14	4*c*		0.6111(3)	¾	0.3917(2)	0.029(1)
Na15	8*d*		0.0796(2)	0.0820(2)	0.6564(1)	0.038(1)
Na16	4*c*		–0.0242(6)	¼	0.6291(4)	0.104(3)

***Table 4.18*: Anisotropic thermal displacement parameters (*I* Å^2) for $Na_{22}Zn_{20}Sn_{19(1)}$ (1).**

Atom	U_{11}	U_{22}	U_{33}	U_{23}	U_{13}	U_{12}
M1	0.018(1)	0.014(1)	0.016(1)	0.002(1)	0.002(1)	0
M2	0.017(1)	0.014(1)	0.014(1)	0	0	0
M3	0.017(1)	0.015(1)	0.015(1)	0	0	0
M4	0.016(1)	0.014(1)	0.017(1)	0	0	0
M5	0.018(1)	0.021(1)	0.018(1)	–0.002(1)	0	0
M6	0.018(1)	0.021(1)	0.021(1)	0	0.003(1)	–0.003(1)
M7	0.020(1)	0.016(1)	0.020(1)	0	0	0
M8	0.016(1)	0.012(1)	0.015(1)	0	0	0
M9	0.017(1)	0.020(1)	0.020(1)	0	0.003(1)	0
M10	0.037(1)	0.045(1)	0.016(1)	0	0.003(1)	0
M11	0.030(1)	0.038(1)	0.029(1)	0	0.008(1)	0
M12	0.040(1)	0.023(1)	0.022(1)	0.002(1)	0.005(1)	–0.006(1)
M13	0.019(1)	0.018(1)	0.025(1)	0	0	0.002(1)
Sn14	0.025(1)	0.019(1)	0.017(1)	0	–0.002(1)	–0.004(1)
Sn15	0.013(1)	0.016(1)	0.013(1)	0	0	0
Sn16	0.019(1)	0.017(1)	0.015(1)	0	0.002(1)	0
Sn17	0.018(1)	0.015(1)	0.016(1)	0	0	0
Sn18	0.018(1)	0.017(1)	0.013(1)	0	0	0
Zn14	0.017(1)	0.028(1)	0.014(1)	0	0	0
Zn15	0.017(1)	0.024(1)	0.017(1)	0	0	0
Zn16	0.015(1)	0.012(1)	0.014(1)	0	0	0
Zn17	0.019(1)	0.021(1)	0.020(1)	0.002(1)	0	0.002(1)
Zn18	0.020(1)	0.019(1)	0.019(1)	0	0	0
Na1	0.022(1)	0.027(1)	0.019(1)	0	0.002(1)	0

Na2	0.025(1)	0.019(2)	0.019(2)	0	0	0
Na3	0.027(2)	0.018(2)	0.023(2)	0	0.002(2)	0
Na4	0.028(1)	0.027(1)	0.025(1)	–0.003(1)	–0.002(1)	0
Na5	0.035(2)	0.027(2)	0.032(2)	–0.003(1)	0	0.002(1)
Na6	0.033(2)	0.024(2)	0.027(2)	0	0	0
Na8	0.031(2)	0.032(2)	0.047(3)	0	0.008(2)	0
Na9	0.028(2)	0.024(2)	0.024(2)	0	–0.003(2)	0
Na10	0.046(3)	0.024(2)	0.033(2)	0	0	0
Na11	0.034(2)	0.038(2)	0.028(2)	–0.002(1)	–0.006(1)	0
Na12	0.033(2)	0.030(2)	0.033(2)	0.004(1)	0	0
Na13	0.032(2)	0.030(2)	0.031(2)	–0.005(1)	0	–0.002(1)
Na14	0.031(2)	0.024(2)	0.030(2)	0	0	0
Na15	0.034(2)	0.047(2)	0.032(2)	–0.005(1)	0.004(1)	–0.009(1)
Na16	0.140(8)	0.062(5)	0.110(7)	0	–0.065(6)	0

4.6.3 Crystal Structure Description and Discussion of $Na_{22}Zn_{20}Sn_{19(1)}$

The compound crystallizes in the primitive orthorhombic space group *Pnma* (No. 62), Pearson code *oP*256. It is isostructural to Na_7Ga_{13}-II and $Na_{22}Ga_{39}$[96, 98] with equivalent atomic positons but larger unit cell parameters.

The projection of the unit cell (Figure 4.31a) indicates the structure as an extended network of cluster units, namely two types of heteroatomic Zn–Sn icosahedra (clusters A and B) and a 15-atom spacer (unit C). A topologic description of the cluster arrangement can be done similarly to compound **1**. Due to the fact, that the unit cell contains icosahedra A, B and 15-atom cages in the ratio of 1 : 1 : 1, the structure can be easily understood in terms of a *Laves* phase. The structure adopts a $MgCu_2$ *Laves* type structure by hierachical cluster for atom replacement. As shown in Figure 4.31c icosahedra A (gray) and icosahedra B (white) form 3.6.3.6 Kagomé nets (close packed layers of icosahedra with ¼ of the icosahedra missing) in the (010) plane. Due to symmetry the nets are formed in two crystallographic planes. The layers are stacked in a cubic *ABCABC* sequence along [101] and are separated by 3^6 nets of icosahedron A, which form vertex sharing supertetrahedra (centered by Na3) indicated as red polyhedra in Figure 4.31b. The role of Mg is taken by a 15-atom spacers (unit C), shown in blue, which occupies the large voids. As depicted in Figure 4.31d and 4.31e these units are distributed roughly along the 3^6 nets and arranged in corrugated layers of hexagons in chair conformation, equivalent to the diamond lattice.

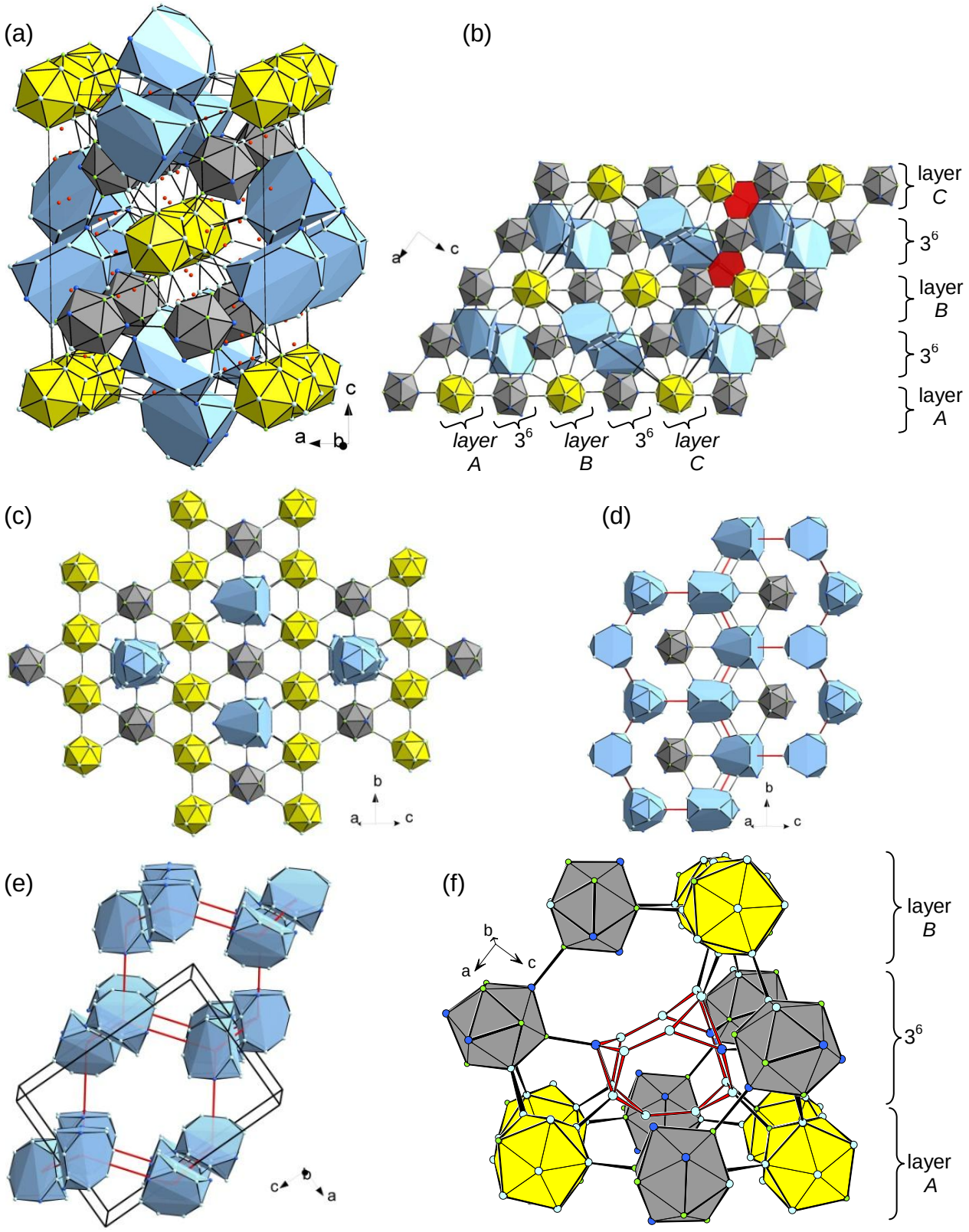

***Figure 4.31*: For figure captions see next page.**

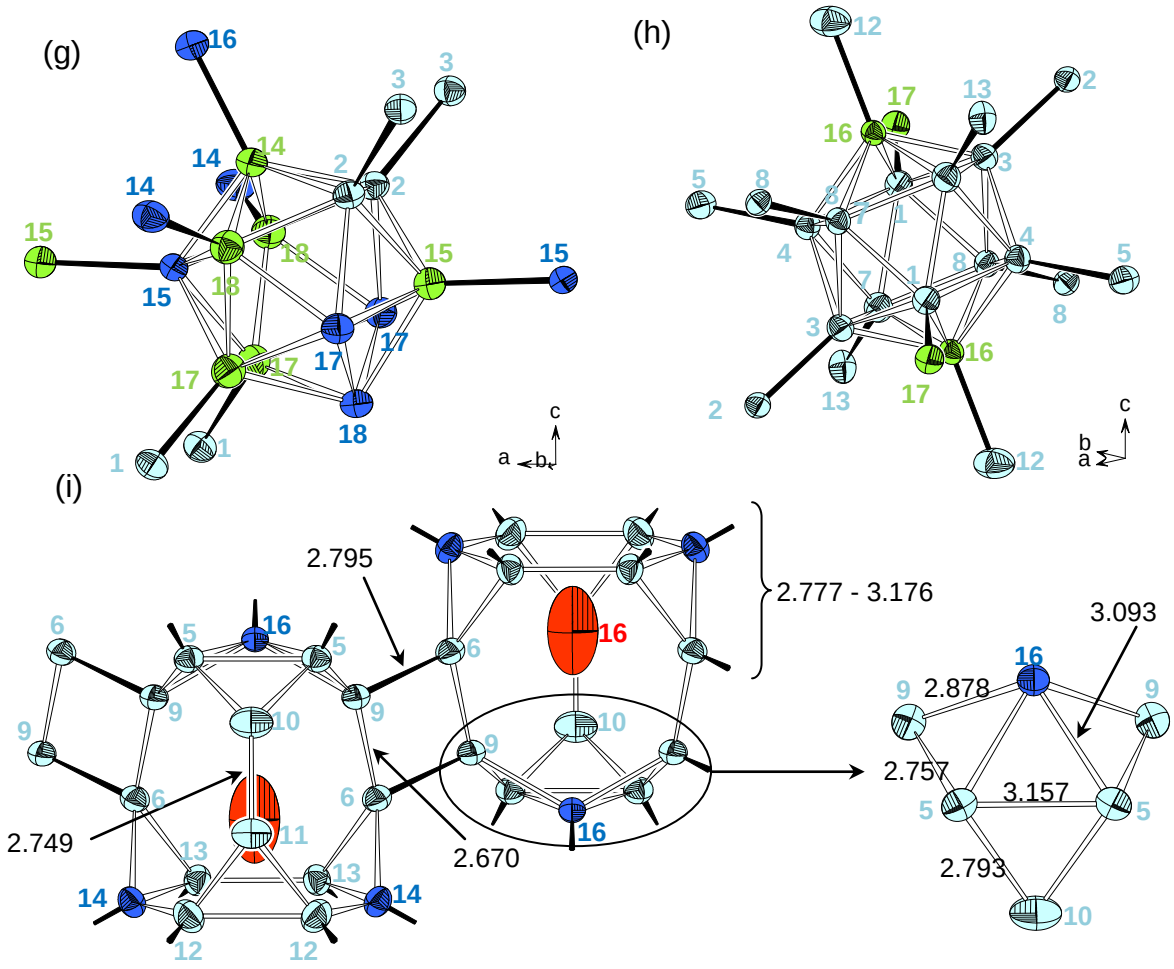

***Figure 4.31, continued*. The structure of $Na_{22}Zn_{20}Sn_{19(1)}$ (1): (a) [010] projection of the unit cell with icosahedron A (gray), B (yellow), 15-atom spacer (blue). (b) Cubic stacking of the Kagomé layers (*ABC*) in two directions. (c) A Kagomé layer in the (010) plane made of clusters A and B and embedded clusters C (clusters above and below the triangles of the Kagomé net are omitted for clarity). (d) 3^6 net of cluster A and corrugated layer of cluster C forming hexagons (indicated with red lines). (e) Diamond sublattice of the 15-atom spacer cage. (f) Truncated supertetrahedron made of twelve icosahedra around the 15-atom unit. (g) 9-fold *exo*-bonded icosahedron A. (h) 12-fold *exo*-bonded icosahedron B. (i) Two interconnected 15-atom units and a cutout fragment of this unit (right). For Figures (g) to (i) all atoms are drawn at 90% probability level. Na (red), Zn (green), Sn (blue), M (light blue).**

Due to the extended nature of the present structure the as formed diamond sublattice is not segregated from the network of icosahedra. Unit C establishes several bonds (see below) to the surrounding icosahedra and is embedded in a truncated supertetrahedron composed of six clusters A and six clusters B, respectively (Figure 4.31f). This feature is consistent with the 12(+4) coordination of Mg in $MgCu_2$.

Icosahedron A (Figure 4.31g) consists of the atoms Sn15, Sn18, Sn17 (×2), Zn14, Zn15, Zn17 (×2), Zn18 (×2), M2 (×2), and has nine *exo*-bonds. It lies on site (4*c*) and has (.*m*.)-symmetry. The intracluster bonds range from *d*(M2–Zn18) = 2.770(1) to *d*(Sn17–Sn18) = 2.976(1) Å.

They are slightly longer than the nine *exo*-bonds that are established to four type B icosahedra within one Kagomé layer with d_{exo}(Zn17–M1) = 2.660(1) Å (×2) and d_{exo}(M2–M3) = 2.701(1) Å (×2). Two further *exo*-bonds are formed to adjoining icosahedra A via Sn15–Zn15 and Zn15–Sn15 bonds of length 2.811(1) Å. Finally, three 15-atom cages are bonded via Zn18–Sn14 (*d* = 2.823(1) Å (×2)) and a Zn14–Sn16 bond of 2.720(1) Å. At Sn17 and Sn18 the icosahedron has no *exo*-bonds.

Icosahedron B consists of the atoms Zn16 (×2), M1 (×2), M3 (×2), M4 (×2), M7 (×2), and M8 (×2). It is located at 4*a* site and has (–1)-symmetry. Its intracluster bonds range from shorter M–Zn contacts (2.724(1) - 2.881(1) Å) to longer M–M bonds (2.760(1) to 2.938(1) Å). As shown in Figure 4.31h it is *exo*-bonded at each vertex that is to six 15-atom spacers via Zn16-M12 (*d* = 2.805(1) Å (×2)), M4–M5 (*d* = 2.719(1) Å (×2)), and M7–M13 (*d* = 2.808(1) Å (×2)). Furthermore, four icosahedra A are bonded with distances *d*(M3–M2) = 2.701(1) (×2) and *d*(M1–Zn17) = 2.660(1) Å (×2). Two icosahedra B with a rather short M8–M8 separation (2.674(1) Å) complete the coordination sphere of cluster B, which therefore can be interpreted as a supericosahedron. For both clusters, A and B, the average intracluster bonds are slightly longer than the *exo*-bonds, which therefore can be regarded as multicenter and 2*c*-2*e* bonds, respectively.

The interesting 15-vertex unit C that fills the structure is centered by Na19 (Figure 4.31i) and consists of M5 (×2), Sn14 (×2), M6 (×2), M9 (×2), M12 (×2), M13 (×2), M10, Sn16, and M11 atoms. It lies on 4*c* site and has (.*m*.)-symmetry. The bottom part the polyhedron consists of two (M12–M13–Sn14) and one (M11–M12–M12) triangular clusters, which are interconnected in an arrangement reminiscent of a truncated tetrahedron. The top part is composed of six atoms (M5, M9, M10, Sn16) that are arranged in four triangles, similar to a typical deltahedron. In unit C, the intracluster bonds can be divided into two groups: In the covalent part (the bottom part) the M–M bonds range from *d*(M9–M6) = 2.670(1) Å to *d*(M12–M12) = 3.156(1) Å and the M–Sn bonds are 2.916(1) to 3.176(1) Å. The top part contains M–M bonds ranging from 2.757(1) to 3.157(1) Å and M–Sn bonds from 2.878(1) to 3.093(1) Å. According to Burdett[91] multicenter bonding is associated with the inner triangle (see below). Indeed the bonds of the inner triangle are considerably longer than the ones associated with the other triangles in that part (Figure 4.31, right). However, as mentioned above some even longer contacts are present in the bottom part.

As shown in Figure 4.31d along [010] the 15-atom spacers are connected via four *exo*-bonds to two adjacent spacers with M9–M6 (×2) and M6–M9 (×2) (2.795(1) Å). Three icosahedra A are bonded via two Sn14–Zn18 and one Sn16–Zn14 bonds of lengths 2.823(1) Å and 2.720(1) Å, respectively. Finally, six icosahedra B complete the coordination via two M13–M7, two M12–Zn16, and two M5–M4 bonds of lengths 2.808(1), 2.805(1), and 2.719(1) Å, respectively. In total, 13 *exo*-bonds are developed. As indicated in Figure 4.32 , the largely opened 15-vertex cluster can be derived from a triply fused icosahedron by the removal of 13 atoms and unfolding of the resulting figure. This emphasizes the relationship to $Na_{34}Zn_{65}Sn_{40(1)}$ (see below), which also crystallizes in a $MgCu_2$ variant.

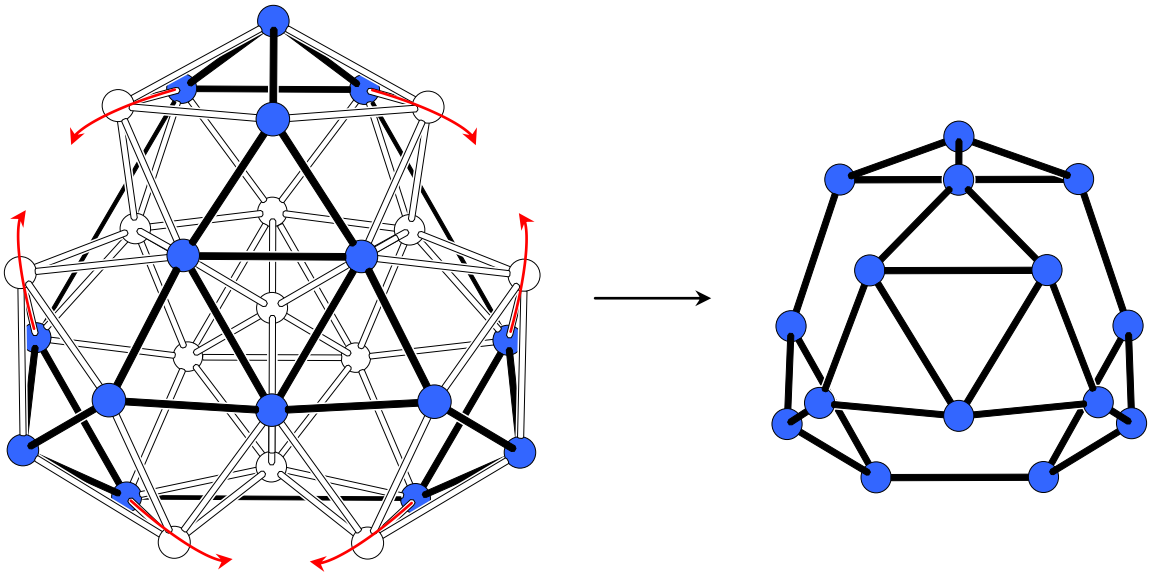

***Figure 4.32*. Transition from a triply fused icosahedron into the 15-vertex polyhedron by atom defections (empty spheres) and moving atoms (red arrows) adopted from ref. [67].**

The average electron count for this compound is difficult to assing due to the througout statistical occupancy of Zn and Sn and the unsual bonding in cluster C. Before summing up the charge for the present compound a short summary of the investigation of the 15-atom spacer is provided. Firstly, this polyhedron has been found in Na_7Ga_{13}-I (*R*–3*m*) and Na_7Ga_{13}-II (*Pnma*) by Schäfer and co workers.[97, 98] Further, it was reported in $Na_{22}Ga_{13}$ (*Pnma*) by Belin.[96] In the latter compound the bond corresponding to M10–M11 (Ga23–Ga22) is quite short (2.43 Å) and was treated as a normal 2*c*-2*e* bond (with lone pairs) by Belin et al. with 43 electrons for skeletal bonding of the $\{Ga_{15}\}$ cluster.

However, King[101] considered the Ga23–Ga22 linkage as a double bond and assigned 47 skeletal electrons. Both electron counting schemes lead to the same number of total electrons for the spacer. In Na_7Ga_{13}-I the corresponding Ga–Ga distance is normal (2.54 Å) and Schäfer distributed 44 skeletal electrons to 21× 2*c*-2*e* bonds and 1× 3*c*-2*e* bond at the very top.

To clarify the puzzling assignments the bonding situation of the 15-atom spacer was reinvestigated by Burdett with molecular orbital studies (hydrogens were used to saturate the appropriate atoms).[91] According to his calculations each of the triangular clusters at the bottom part needs three skeletal electron pairs. The net (composed of four triangles with six atoms) requires seven skeletal electron pairs. Six of them are associated with six *exo*-bonds. An extra electron pair goes into an orbital of higher energy which represents a 3*c*-2*e* bond associated with the inner triangle. Since the intertriangular bonds seem to be normal, the results suggested a total of 22 *σ*-skeletal pairs. Two low lying orbitals centered at Ga22 and Ga23 interact to produce a bonding and an antibonding combination, hence creating a Ga–Ga double bond (2*c*-4*e*) and increasing the number of skeletal electron pairs by one. Their analysis results in 44 and 46 skeletal electrons to be associated with the $\{Ga_{15}\}$ cluster in Na_7Ga_{13}-I and $Na_{22}Ga_{39}$, respectively. These numbers perfectly match Schäfer's assignment but it does not match for $Na_{22}Ga_{39}$ (there are 556 electrons per unit cell but the calculated number required is only 552, Z = 4). Therefore it was suspected that the stoichiometric formula for $Na_{22}Ga_{39}$ was incorrect. Indeed Schäfer reported a second phase Na_7Ga_{13}-II which is practically identical with $Na_{22}Ga_{39}$ except for the sodium content (both compounds crystallize in the space group *Pnma*).

For $Na_{22}Zn_{20}Sn_{19(1)}$ the crystal structure refinement does not show any inconsistence with respect to the amount of Na atoms. Comparing the contact M10–M11 (2.749(1) Å) with the corresponding Ga–Ga distance in the compounds Na_7Ga_{13}-II and $Na_{22}Ga_{39}$ (2.28 Å and 2.43 Å, respectively) it is not the shortest bond of the cluster for the present compound. It lies well in the range of a normal covalent interaction, suggesting electron lone pairs at the participating M atoms as in rhombohedral Na_7Ga_{13}-I. In $Na_{22}Zn_{20}Sn_{19(1)}$ the electron balance is as follows. Based on the stoichiometry and with respect to the mixed site occupancies icosahedron A is formulated as $\{Zn_{7.06}Sn_{4.94}\}$ with a total of 33.88 valence electrons. Subtraction of one electron for each of the nine *exo*-bonds, and two for each of the three non-*exo*-bonded Sn atoms, leaves 18.88 electrons available for skeletal bonding.

To achieve the 26 cluster electrons needed for a *closo*-icosahedron, according to Wade's rules, a charge of –7.12 has to be assigned. The same calculation, considering 12 *exo*-bonds, for cluster B $\{Zn_{8.27}Sn_{3.73}\}$ leads to a final charge of –6.54. The 15-atom cage consists of $\{Sn_{10.13}Zn_{4.87}\}$ with a total of 50.26 VE and considering the 13 *exo*-bonds this results in a charge of –8.74, assuming a stabilization with 46 skeletal electrons (see above). As clusters A, B, and C are present at a ratio of 1 : 1 : 1 a total negative charge (electron demand) of 22.40 results. This is counterbalanced by the crystallographically determined 22 Na atoms, which roughly leads to charge balance qualifying the phase as a closed shell compound. However, due to the normal bond length (M10–M11) no double bond can be considered and the 15-atom unit should have been calculated with 44 rather than 46 skeletal electrons according to Burdett (see above). This would mean that the charge of the spacer is reduced to –6.74 and two Na atoms less are needed, meaning the compound is two electrons rich. Thus, in the present compound an interesting situation is present by having a 15-vertex spacer with normal M10–M11 separation, albeit for the space group *Pnma* the 46 cluster electron spacer with a double-bond is expected.

4.6.4 Crystal Structure Description and Discussion of $Na_{34}Zn_{65}Sn_{40(1)}$

The compound crystallizes in the rhombohedral space group *R*–3*m* with Pearson code *hR*201. The unit cell (Figure 4.33a) contains three formula units of $Na_{34}Zn_{65}Sn_{40(1)}$ and is isostructural to $Na_{102}Cu_{36}Ga_{279}$.[79] The complex network structure is made of three clusters, namely icosahedron A, icosahedron B, and a triply fused icosahedron C at a ratio of 3 : 1 : 2.

The arrangement of the three clusters in the unit cell is shown in Figure 4.33b. As the compound contains bigger and smaller clusters at the ratio of 1 : 2 the 3D-structure can be understood as a hierarchical variant of the cubic *Laves* phase $MgCu_2$ in which each copper atom is replaced by a icosahedron and each Mg atom by cluster C. Unit A forms Kagomé layers (3.6.3.6) in the (001) plane. Due to symmetry, another Kagomé net made of unit A and B in the ratio 2 : 1 is formed. The one made throughout of cluster A is shown in Figure 4.33c. In this case the 3^6 hexagonal close layer is throughoutly formed by icosahedron B. The latter interconnects the Kagomé nets by formation of two vertex-sharing supertetrahedra (outlined in red in Figure 4.33b) along *c*. Each of the latter is made of three units A and one unit B and is centered by Na3.

The arrangement of the supertetrahedra corresponds to that found in cristobalite (which is a diamond structure with vertex sharing SiO_4 tetrahedra). The big voids are filled with unit C, which, if connected to each other form a diamond lattice (Figure 4.33d and 4.33e). The corrugated layers made of hexagons of clusters are connected through Sn4 atoms (Figure 4.35d).

Icosahedron A (gray in all Figures), the more ordered one, is made of Zn14 (×2), M3 (×2), M10 (×4), and four M11 positions. It is located at (9*e*)-position and has (*2*/*m*)-symmetry. The Zn–M intracluster bonds range from 2.699(2) to 2.851(2) Å and are slightly smaller than the M–M intracluster bonds, which lie in the range of 2.765(2) to 3.026(2) Å. The cluster is 12-fold *exo*-bonded to four other icosahedra A (*d*(M11–M11) = 2.834(3) Å), two icosahedra B (*d*(M3–M6) = 2.696(2) Å), and six units C with *d*(M10–M8) = 2.670(2) Å and *d*(Zn14-Sn1) = 2.700(3) Å (Figure 4.34a).

Icosahedron B (Figure 4.34b) lies on the (3*b*)-site and has (*–3m*)-symmetry. It is composed of M5 (×6) and M6 (×6) atoms. The intracluster M–M bonds are in the range of 2.707(3) to 2.845(3) Å. The 12 *exo*-bonds point towards six icosahedra A with *d*(M6–M3) = 2.696(2) Å and six tri-icosahedra C (Figure 4.33d) via M5–M7 with bond length 2.657(2) Å.

***Table 4.19*: Atomic coordinates and equivalent isotropic displacement parameters for $Na_{34}Zn_{65}Sn_{40(1)}$ (2).**

Atom	Wyck.	Occ. ≠ 0	*x*	*y*	*z*	U_{eq} / Å^2
Sn1	18*h*		0.5698(1)	0.4302(1)	0.1337(1)	0.014(1)
M2 = Sn2 / Zn2	6*c*	0.50 / 0.50(2)	⅔	⅓	0.2198(1)	0.015(1)
M3 = Sn3 / Zn3	18*h*	0.80 / 0.20(2)	0.4441(1)	0.5559(1)	0.0517(1)	0.013(1)
Sn4	3*a*		⅔	⅓	⅓	0.017(1)
M5 = Sn5 / Zn5	18*h*	0.54 / 0.46(2)	0.4210(1)	0.5790(1)	0.1809(1)	0.014(1)
M6 = Sn6 / Zn6	18*h*	0.23 / 0.77(2)	0.3866(1)	0.6134(1)	0.1087(1)	0.015(1)
M7 = Sn7 / Zn7	18*h*	0.50 / 0.50(2)	0.5096(1)	0.4904(1)	0.1953(1)	0.015(1)
M8 = Sn8 / Zn8	36*i*	0.70 / 0.30(2)	0.4479(1)	0.3689(1)	0.2552(1)	0.018(1)
M9 = Sn9 / Zn9	18*h*	0.28 / 0.72(2)	0.4868(1)	0.2434(1)	0.2330(1)	0.017(1)
M10 = Zn10 / Sn10	36*i*	0.67 / 0.33(2)	0.6327(1)	0.6412(1)	0.0364(1)	0.019(1)
M11 = Zn11 / Sn11	36*i*	0.56 / 0.44(2)	0.3295(1)	0.4918(1)	–0.0137(1)	0.020(1)
Zn12	18*h*		0.7214(1)	0.4427(2)	0.1628(1)	0.016(1)
Zn13	18*h*		0.6094(1)	0.3906(1)	0.2768(1)	0.030(1)
Zn14	18*h*		0.5397(1)	0.4603(1)	0.0645(1)	0.020(1)
Zn15	36*i*		0.4132(1)	0.2969(1)	0.1794(1)	0.017(1)
Na1	36*i*		0.5843(4)	0.6227(4)	0.1226(2)	0.021(1)
Na2	18*h*		0.2220(3)	0.4441(6)	0.0642(2)	0.021(2)
Na3	6*c*		⅓	⅔	0.0294(4)	0.024(3)
Na4	18*h*		0.4112(8)	0.2056(4)	0.3226(3)	0.045(3)
Na5	18*h*		–0.2036(4)	0.5928(7)	0.0968(3)	0.046(3)
Na6	6*c*		⅔	⅓	0.0749(5)	0.047(5)

***Table 4.20*: Anisotropic displacement parameters (/ Å^2) for $Na_{34}Zn_{65}Sn_{40(1)}$ (2).**

Atom	U_{11}	U_{22}	U_{33}	U_{23}	U_{13}	U_{12}
Sn1	0.015(1)	0.015(1)	0.012(1)	0.002(1)	–0.002(1)	0.008(1)
M2	0.017(1)	0.017(1)	0.012(1)	0	0	0.008(1)
M3	0.015(1)	0.015(1)	0.012(1)	0	0	0.008(1)
Sn4	0.022(1)	0.022(1)	0.009(1)	0	0	0.011(1)
M5	0.014(1)	0.014(1)	0.014(1)	0	0	0.006(1)
M6	0.016(1)	0.016(1)	0.013(1)	0	0	0.008(1)
M7	0.016(1)	0.016(1)	0.012(1)	0	0	0.008(1)
M8	0.020(1)	0.020(1)	0.018(1)	0.002(1)	0.004(1)	0.013(1)
M9	0.018(1)	0.015(1)	0.019(1)	0	–0.003(1)	0.009(1)
M10	0.021(1)	0.019(1)	0.014(1)	–0.003(1)	0	0.008(1)
M11	0.020(1)	0.024(1)	0.016(1)	0	0	0.012(1)
Zn15	0.014(1)	0.020(1)	0.017(1)	0	0	0.009(1)
Zn12	0.014(1)	0.017(1)	0.017(1)	–0.002(1)	0	0.009(1)
Zn13	0.031(1)	0.031(1)	0.031(1)	0.003(1)	–0.003(1)	0.018(1)
Zn14	0.026(1)	0.026(1)	0.011(1)	0	0	0.016(1)
Na1	0.022(3)	0.016(3)	0.024(3)	0	0	0.009(2)
Na2	0.019(3)	0.021(4)	0.025(4)	0.004(4)	0.002(2)	0.010(2)
Na3	0.023(5)	0.023(5)	0.026(8)	0	0	0.011(2)
Na4	0.051(7)	0.054(5)	0.029(5)	–0.002(2)	–0.004(5)	0.025(3)
Na5	0.061(6)	0.028(6)	0.037(6)	0.008(5)	0.004(2)	0.014(3)
Na6	0.050(7)	0.050(7)	0.042(11)	0	0	0.025(4)

As expected, in both icosahedra the average values of the multicenter intracluster bonds are longer than the *exo*-bonds, which therefore can be regarded as 2*c*-2*e* bonds. Around both icosahedra the typical dual coordination polyhedron (a pentagon dodecahedron) of twenty Na atoms is formed.

The third unit is the eye catching triply fused icosahedron (Figure 4.33f) composed of Sn1(×3), Zn12 (×3), Zn13 (×3), Zn15 (×6), M2 (×1), M7 (×3), M8 (×6), and M9 (×3) atoms, which is also a building unit in the *β*-rhombohedral boron structure. In the present compound (**2**) it results from the condensation of three icosahedral units (Figure 4.35a), each of them sharing one triangular face (indicated with black lines) with each of its neighbors and one atom (M2, pink). Another figurative description is that this 28-atom cluster is generated from a single icosahedron by means of a three-fold axis through the shared M2 atom (site 6*c*); the polyhedron has (3*m*)-symmetry. The intracluster separations involve 15× Zn–Zn (2.682(3) to 3.062(3) Å), 12× Zn–Sn (2.694(1) to 3.000(2) Å), 40× Zn–M (2.645(3) to 2.986(2) Å), 3× Sn–M (2.877(2) Å), and 18× M–M (2.685(2) to 3.106(2) Å) contacts. This unit has been reported to be stable with 64 skeletal electrons.[84] With respect to the analysis of all Zn–Sn icosahedra (Chapter 4.9) this nicely illustrates the condensation of individual to fused icosahedra at low valence electron concentrations.

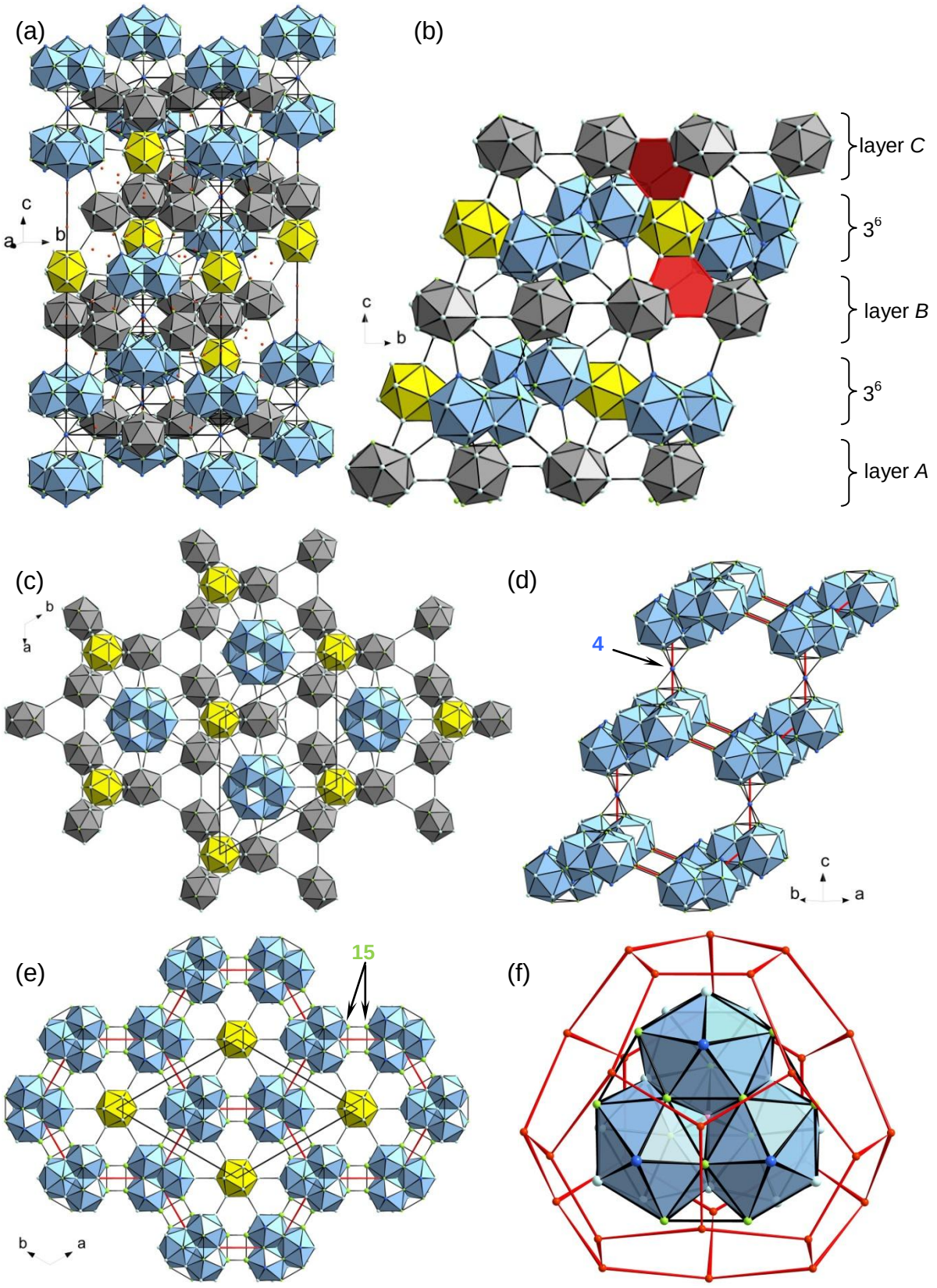

***Figure 4.33*. (a) Projection of the unit cell of $Na_{34}Zn_{65}Sn_{40(1)}$ (2). (b) Cubic stacking of the Kagomé layers (c) Single 3^6 net of icosahedra B (at z = ½) and single Kagomé layer of icosahedra A (at z = ⅓), and cluster C at z = 0.21 and 0.46. (d) and (e) Diamond array of cluster C (outlined with red lines). (f) 28-atom tri-icosahedron (unit C) surrounded by 28 Na ([001] view). In all pictures: Icosahedron A (gray), icosahedron B (yellow), and cluster C (blue).**

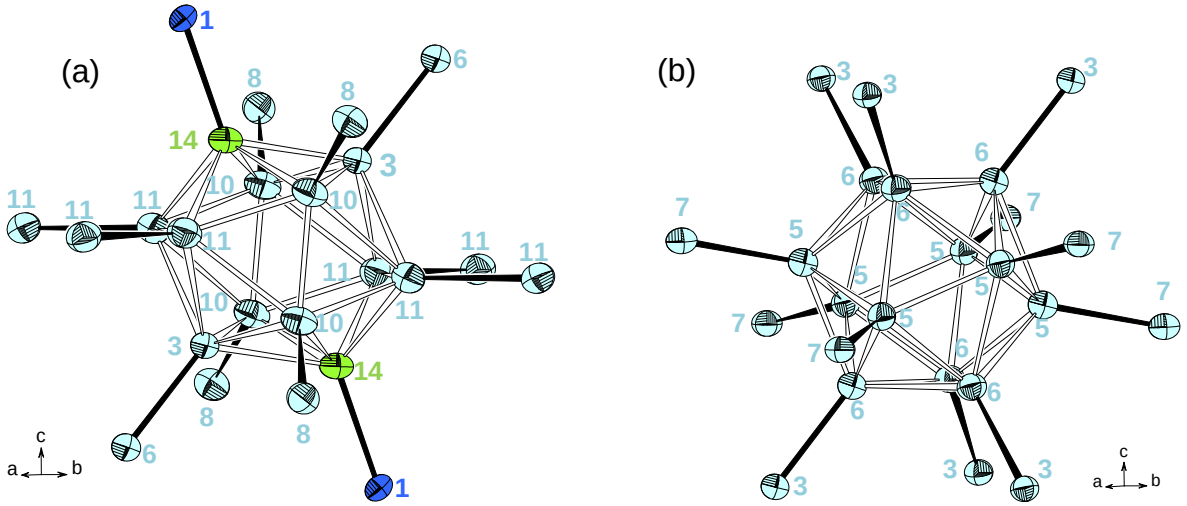

***Figure 4.34*. Anisotropic representations (90%) (a) icosahedron A. (b) Icosahedron B. Zn (green), Sn (blue), M = Zn / Sn (light blue).**

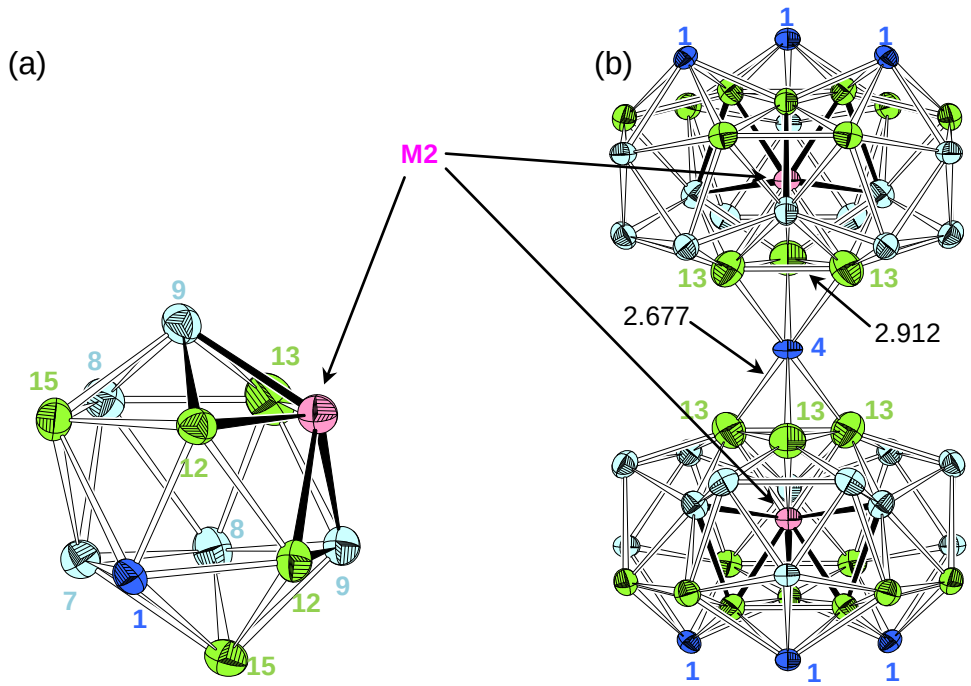

***Figure 4.35*. (a) One of the three icosahedra that build up cluster C with the triply-shared atom M2 (purple). (b) Pair of triply fused icosahedra C. The shared edgese are outlined and the *exo*-bonds are omitted. Zn (green), Sn (blue), M = Zn / Sn (light blue).**

Figure 4.33e shows that six of the 18 *exo*-bonds are distributed to three other units C that are bonded in the (001) plane via Zn15–Zn15 (2.527(3) Å) contacts. In the same plane three icosahedra B are coordinated via three M7–M5 bonds (2.657(2) Å). Nine icosahedra A that are bonded through M8–M10 (2.670(2) Å ×6) and Sn1–Zn14 (2.700(3) Å ×3) complete the coordination sphere. The Zn13 apices (one of each participating icosahedron) form equilateral triangular rings (*d*(Zn13–Zn13) = 2.912(5) Å) which are interlinked by Sn4 at site 3*a*.

Thus, a sandwich complex {($Sn_3Zn_{12}M_{13}$)Sn4($Sn_3Zn_{12}M_{13}$)} with a six-fold-coordinate Sn4 (site symmetry –3*m*) in the center is realized (Figure 4.35b). To sum it all up, the triply fused icoshedron has (18+3) *exo*-bonds (+3 indicates the three Zn *exo*-bonds to the same bridging Sn4 atom). Nevertheless, a six-fold-coordinated Sn atom by Zn in the present geometry has not been discussed in the solid state yet.

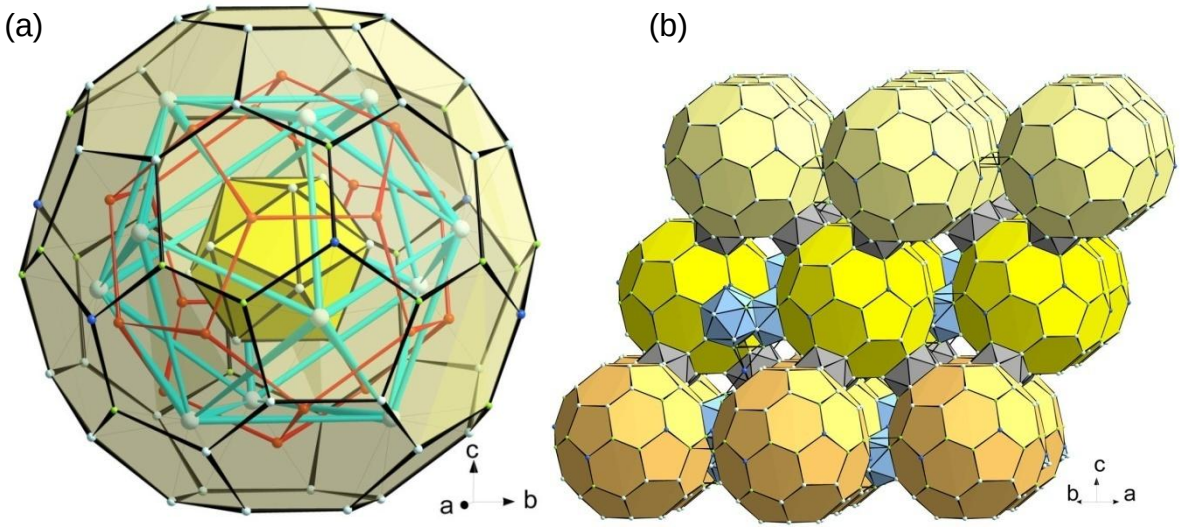

***Figure 4.36*. (a) Extension of the pseudo five-fold symmetry from icosahedron B to Samson's polyhedron. The shown unit can be formulated as M_{12}@Na_{20}@$(M3)_6(M7)_6$@fullerane. (b) Representation of the cubic (*ABCABC*) fullerane packing along *c*.**

In similar phases containing such clusters, a transition metal atom - Cu or Cd - is located on the inversion center. Often the tri-icosahedra in gallides, such as in $Na_{13}K_4Ga_{47.45}$, exhibit atomic defects at sites corresponding to the present Zn13 triangle. According to EHMO calculations (on a defect free $Ga_{28}H_{18}$) this feature was linked to the population of the degenerate LUMO with two electrons by Tillard-Charbonnell and co-workers.[84] Due to an increasing HOMO-LUMO gap more stable configurations for an inverted pair of the tri-icosahedron are obtained when they are formed of doubly *nido*- or triply *nido*-tri-icosahedra. Such complexes with a bridging atom have been found in the phases $Na_{102}Cu_{36}Ga_{279}$,[79] $K_{34}In_{92.30}Li_{12.70}$,[102] or $K_{34}In_{96.19}Au_{8.81}$.[95] Two other kinds of interconnections between pairs of neighboring triply fused icosahedra dependent on the occupancy of the participating triangles are known. A case with interbridging Zn-dimers has been reported for $K_{34}In_{89.95(1)}Zn_{13.05(7)}$ when 'Zn13' is partially (< 50%) occupied. At very low occupancies ($K_4Na_{13}Ga_{49.57}$[75]) no interconnection between adjoining tri-icosahedra was found.[95] The stability of the non-defective tri-icosahedron inverted pair is increased with smaller and electron poorer elements, such as Zn.

The polyhedral geometry is relaxed by the enlarged triangle, which is caused by increased interatomic separations. The long Zn13–Zn13 separation is consistent with these arguments. On average the intracluster bonds are longer than the *exo*-bonds, thus the latter can be treated as 2*c*-2*e* bonds. An alternative, more topological view of the structure is illustrated in Figure 4.36. Icosahedron B fills a large coordination 72 atom complex comprising 18 Zn (6× Zn14, 12× Zn15), six Sn1 and 48 M (6× M3, 6× M7, 12× M8, 12× M10, 12× M11) atoms. Formal removal of 12 M atoms that mark the capping atoms of neighboring icosahedra A (6× M3) and clusters C (6× M7) leaves a 60 atom carbon-free fullerane like cage (the suffix '-ane' indicates the absence of double bonds). A closer look at this fullerane cage (which can be derived from a fully truncated icosahedron) reveals another interesting feature. The 20 Na atoms that radiate from the centers of the 20 triangular faces of icosahedron B form the dual pentagonal dodecahedron. 12 M (6× M3 and 6× M7) atoms surmounting the centers of the pentagonal faces of the dodecahedron are 2*c*-2*e* connected to the central icosahedron and cap the 12 pentagonal faces of the fullerane cage from the inside. The 84 atom unit (a central icosahedron surrounded by 12 pentagonal pyramids) is called Samson complex and the successive onion-like layers of electropositive and electronegative elements resulting in a 104-atom polyhedron can be formulated as $M_{12}@Na_{20}@(M3)_6(M7)_6@$fullerane according to an endohedral formalism. The extended nature of the structure causes the fullerane cages to be interconnected by clusters A and C (Figure 4.36b). Following the packing of icosahedra B the fullerane cages, with clusters B and C interlinking them, form close packed 3^6 layers in the (001) plane and are stacked in the sequence *ABCABC*.

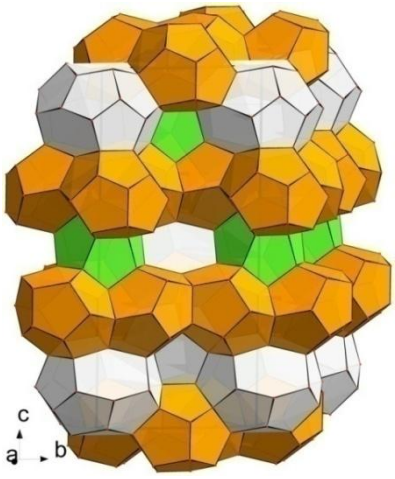

***Figure 4.37*: The clathrate-II like Na array made of two kinds of {Na_{20}} dodecahedra (orange, around cluster A and green, around cluster B) and {Na_{28}} hexacaidecahedra (light gray, around cluster C).**

The cations around unit C generate a {Na_{28}} hexacaidecahedron. The latter occurs at the ratio of 1 : 2 with the {Na_{20}} dodecahedra around icosahedra A and B, resulting in a Na_{136} clathrate-II type cation network (Figure 4.37).[103] This arrangement around different sized anionic clusters has been found in many other compounds, e.g. $K_{17}In_{41}$, $K_{39}In_{80}$, $K_{22}In_{39}$, or $Na_{35}Cd_{24}Ga_{56}$. The presence of this regular cationic array is decisive for struture stabilization: The arrangement not only fills space more efficiently but also keeps the clusters apart.

The average electron count of $Na_{34}Zn_{65}Sn_{40(1)}$ can be derived by applying Wade's rules to the icosahedra and the *mno* rule to the sandwich complex. With respect to the mixed occupied sites and the *exo*-bond requirements (both 12-fold) icosahedron A and B are formulated as $\{Zn_{7.32}Sn_{4.78}\}^{4.64-}$ and $\{Zn_{7.38}Sn_{4.62}\}^{4.76-}$, respectively. The sandwich complex requires $m + n + o = 8 + 57 + 1 = 66$ skeletal electron pairs or 132 electrons for stabilization. Counting four electrons from Sn4 and subtracting 18 × 2 *exo*-bonds leads to the formulation $\{(Sn_{10}Zn_{18})Sn(Sn_{10}Zn_{18})\}^{12-}$. 20 atoms and the interbridging Sn4 atom do not have any *exo*-bonds and in the addtition they are treated with their elemental valence. Hence, per formula unit the number of valence electrons to fill all of the bonding levels adds up to 3 × 4.64 + 1 × 4.76 + 12 = 30.68, which means the experimental number of valence electrons per cell exceeds the electron demand by 3.32. The total amount of valence electrons in the unit cell is ~ 972 electrons and E_F is located above a gap and cuts through finite DOS (not shown) meaning some electrons remain in the valence band of the alkali metals and the material behaves as a poor metallic conductor. This result of electron counting for the present compound is consistent with reported isostructural phases, such as $K_{34}In_{92.3}Li_{12.7}$, $K_{14}Na_{20}In_{91.82}Li_{13.18}$, or $K_{14}Na_{20}In_{96.3}$,[102] which all have ~ 970 electrons per unit cell. In these phases electronic tuning within the complex anionic networks is realized by partial substitution of In by electron poorer elements or by underoccupied atomic sites. Furthermore, based on EH calculations, it has been reported that the non-existence of any corresponding ordered $K_{34}In_{105}$ indicates only electron poorer lattices than the ideal $A_{34}In_{105}$ to be stable, since 1034 (Z = 3) electrons per unit cell would place E_F within strongly antibonding states. A comparable situation has been reported for $Na_{102}Cu_{36}Ga_{279}$[79] and $K_4Na_{13}Ga_{49.57}$[104], where the total available valence electrons also exceed the count required for lattice stabilization. On the other hand the clathrate like Na array seems to be important in order to maximize packing efficiency and other energy terms, such as the Madelung energy.

Considering the standard deviations of the statistically occupied sites in $Na_{34}Zn_{65}Sn_{40(1)}$, that add up to a rather large uncertainty in the structure determination the compound might as well be charge balanced within 3σ-error values. As mentioned in the experimental section the refinement of the Sn sites with equal ADP values led to slightly Zn richer stoichiometries, which would increase the electron demand of the anionic network. Nevertheless, due to the multiple possible permutations the modelling of the statistical occupancies is rather difficult. Experiments on the Zn-richer side might result in further clustering and the formation of the *hitherto* unreported tetra-icosahedron.

4.7 Na_6ZnSn_2 and $Na_{6-x}K_xZnSn_2$ (x = 1.77) - $\{ZnSn_2\}$ Units with 16 Valence Electrons

This chapter includes two compounds that mark the *hitherto* alkaline richest phases in the ternary system Na(K)–Zn–Sn. The known binary Na stannides with ratios Na : Sn > 1 are Na_9Sn_4 and $Na_{15}Sn_4$.[105] Whereas the VEC for Sn (= 6.25) for Na_9Sn_4 still requires Sn–Sn bonding, which is realized in dumbbells, the VEC/Sn (= 7.75) in $Na_{15}Sn_4$ formally leads to 'electron saturated' isolated $\{Sn\}^{4-}$ anions. Monomeric and oligomeric cluster units are generally of interest as building blocks in solution chemistry. Nevertheless, the higher the charge/nuclei ratio, the more the isolation as an intact unit or the mere dissolving process is hampered. The tetrahedral anions in Na_4Sn_4 for instance could not be dissolved yet. Especially isolated cluster anions, which are accessible by the use of larger alkali metal cations, such as Rb and Cs, are of preferred choice due to their good solubility in certain organic solvents. Further reactions, such as oxidative coupling or polymerization, can lead to a tremendous variety of new anionic species. In this field the chemistry of naked tetrelide clusters such as the prominent Wade clusters $\{Tt_9\}^{4-}$ in A_4Tt_9 (A = K, Rb, Cs; Tt = Ge, Sn, Pb) has been well explored.[68, 106, 107]

4.7.1 Synthesis and Characterization

Synthesis The two compounds Na_6ZnSn_2 (**1**) and $Na_{4.23}K_{1.77(1)}ZnSn_2$ (**2**) were prepared by direct fusion of stoichiometric amounts of the pure elements in tantalum crucibles. Na_6ZnSn_2 was first obtained by successively increasing the amount of Na starting from the ratio Na : Zn : Sn = 1 : 1 : 1, via 2 : 1 : 1, to 3 : 1 : 1. Wheras the second mixture led to the discovery of a compound discussed in Chapter 4.8 the latter contained **1** and $NaZn_{13}$. An almost pure phase (see powder diagram below) was synthesized by reacting stoichiometric amounts for 6 h at 500 °C, quenching to room temperature, heating up to 360 °C, annealing there for two weeks, followed by fast cooling (2 $K \cdot min^{-1}$) to room temperature. The sample was prepared from a total sample loading of 1.259 g, with m(Na) = 0.394 g, m(Zn) = 0.187 g, and m(Sn) = 0.678 g. The compound was obtained as large dark plate-shaped crystals with metallic luster.

Attempts to synthesize the K analogue resulted in amorphous gray powders with K_8Sn_{44} as the only crystalline phase. Therefore, a stepwise increase of K led to compound **2**, which was obtained in a phase mixture together with unknown phases (Figure 4.39) by fusing stoichiometric amounts of the elements in the ratio Na : K : Zn : Sn = 3 : 2 : 1 : 2 at 500 °C, followed by slow cooling (0.1 $K \cdot min^{-1}$) to room temperature. The compound was prepared in a sealed Ta ampoule under Ar atmosphere from a total sample loading of 1.184 g, with m(Na) = 0.181 g, m(K) = 0.206 g, m(Zn) = 0.172 g, and m(Sn) = 0.625 g.

EDX Analyses Elemental analyses of both compounds were carried out on several crystallites. Immediate decomposition of the compounds while transferring into the microscope's sample chamber hampered the location of suitable crystal faces for measurements. For **1** three measurements showed the presence of all elements with ratios: Na : Zn : Sn = 61(6) : 10(2) : 29(2), 70(6) : 8(2) : 22(2), and 65(5) : 8(2) : 27(2). These values compare quite well with the calculated ratio 66.6 : 11.1 : 22.2. Quantitative analyses for crystals of compound **2** showed varying crystal compositions ranging from Na : K : Zn : Sn = 58(5) : 11(2) : 12(2) : 19(1); 39 : 30 : 6 : 25, 68 : 14 : 7 : 11, to 72 : 13 : 6 : 9. The large variation and deviations from the theoretical value for $Na_{4.23}K_{1.77(1)}ZnSn_2$ (47 : 19.6 : 11.1 : 22.2) indicate the presence of a phase width which is also proved by the discovery of a K-poorer phase $Na_{5.57}K_{0.43(1)}ZnSn_2$ (not presented here).

Powder X-ray Diffraction The powder diffraction results of the phase mixtures that contained **1** and **2** are shown in Figures 4.38 and 4.39. For both compounds the samples were prepared by diluting with diamond powder and measuring in Debye-Scherrer mode for 18 h. The diagrams show that the target compounds are clearly present as the main phases. For **1** few weak reflections are present, which could not be assigned to known binary phases. In the diagram for **2**, the strongest reflections originating from the compound together with distinct reflections (e.g. 2θ ~ 15°) from KSn, marked with red stars, can be seen.

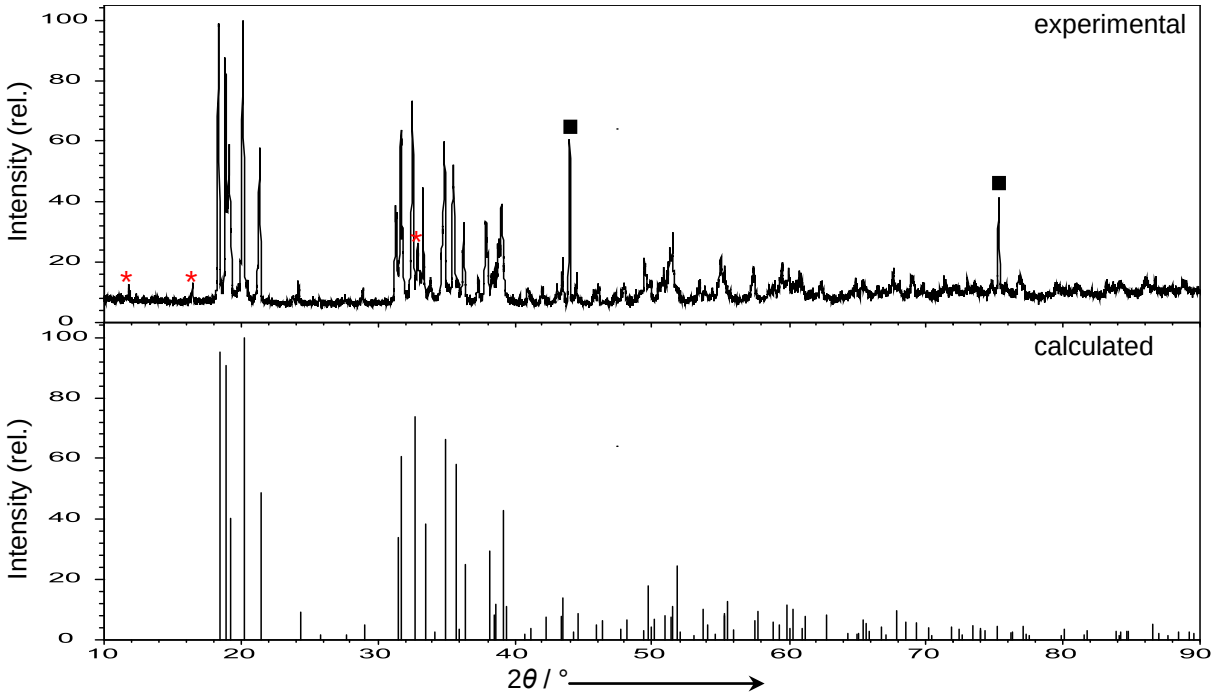

***Figure 4.38*. Experimental and calculated powder diagram for Na_6ZnSn_2 (from loading Na : Zn : Sn = 6 : 2 : 1). Unindexed reflections are marked with a red star and reflections originating from diamond powder with a square.**

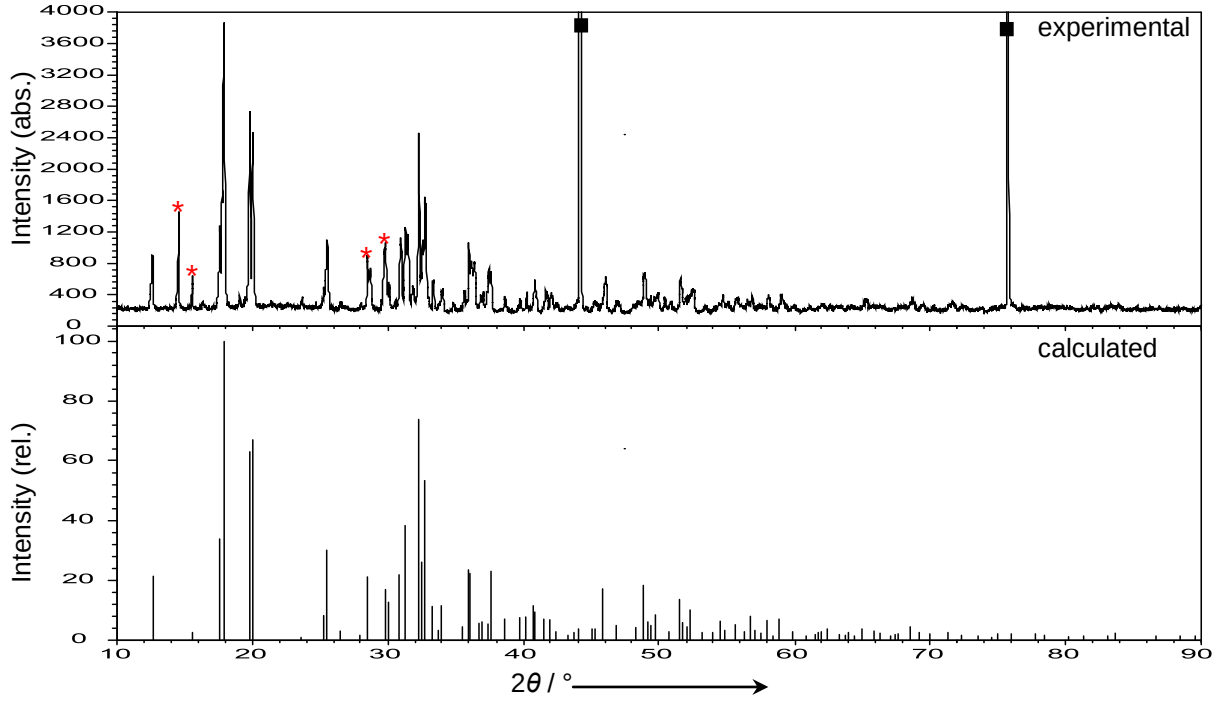

***Figure 4.39*. Experimental (from loading Na : K : Zn : Sn = 3 : 2 : 1 : 2) and calculated powder diagram for $Na_{4.23}K_{1.77(1)}ZnSn_2$. Reflections of KSn are marked with a red star and reflections originating from diamond powder with a square.**

Thermal Analyses For the thermal behavior of Na_6ZnSn_2 the product of the above mentioned prepared sample was heated under continuous Ar flow from room temperature to 600 °C at a rate of 10 $K \cdot min^{-1}$ and cooled down to 100 °C at the same rate. Isothermal dwelling times were 10 min. Two loops were recorded. Additionally to little amounts of elemental Sn (at ~ 230 °C) the heating curves in Figure 4.40 show two endothermal peaks in the range of 366.3 (onset) - 402.9 °C (peak). In the cooling curves the two signals are more confined from 410.2 (411.3 °C) (cooling-end) and 373.6 (369.8) °C. It should be noted that sealing the small Nb ampoule for the DTA measurement was hampered by fast evaporation of the Na-rich compound and possible decomposition, even when using little amounts and stronger cooling. The signal at lower temperatures can be assigned to Na_6ZnSn_2, since the highest yields of this compound were obtained when annealing in this temperature region. The peak at higher temperature corresponds to the melting point of binary $NaZn_{13}$, that might have formed during sealing the ampoule. The diagram of an X-ray powder measurement carried out after the DTA measurement showed characteristic reflections of $NaZn_{13}$. The weak signal in the range of 100 °C in the first heating cycle may be assigned to the melting of elemental Na, which also hints for decomposition during sealing. Due to even higher volatility of K a DTA sample of the quaternary compound **2** could not be prepared.

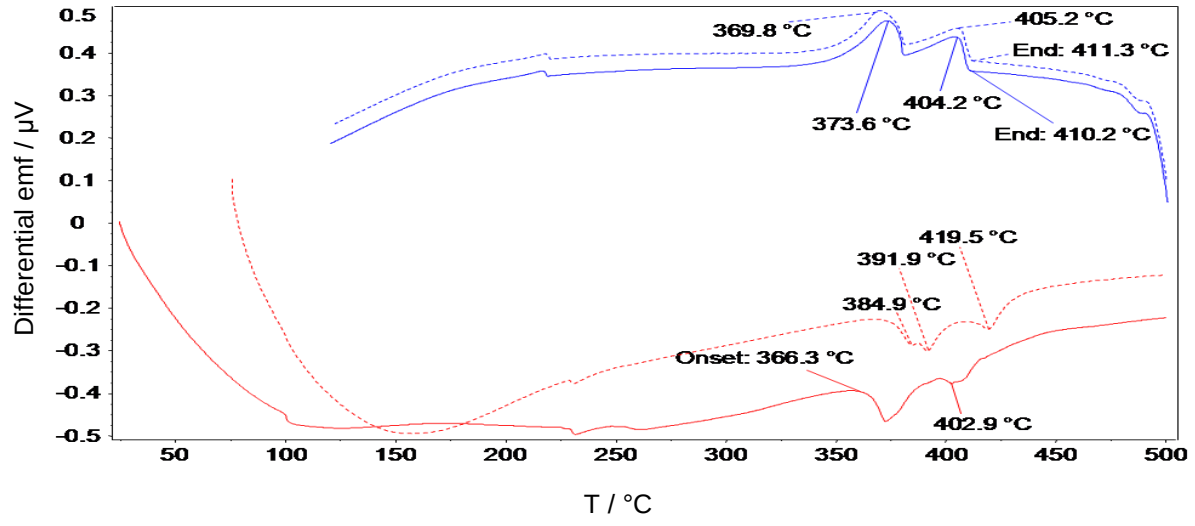

***Figure 4.40*. DTA curves of the product of a reaction with Na : Zn : Sn = 6 : 1 : 2 at 500 °C. Heating (red), cooling (blue). 2nd loop is shown in dashed lines.**

4.7.2 Crystal Structure Determination and Description of Na_6ZnSn_2 and $Na_{4.23}K_{1.77(1)}ZnSn_2$

Structure Determination Single-crystals (dark plates for **1** and dark blocks for **2**) were selected in the glovebox, sealed into glass capillaries and X-ray diffraction data was collected on an Oxford Xcalibur3 diffractometer at 293 K. The measurements each ran four sets of *ω* scans (–28° to 24°) and a *φ* scan with exposure times of 20 s per frame and a scan width of 1°. After application of an empirical absorption correction the structures for **1** and **2** were solved with direct methods and refined anisotropically in the monoclinic space groups *C*2/*m* (**1**) and $P2_1/c$ (**2**), respectively. The space groups were assigned at the basis of systematic absences and the statistical analyses of the intensity distributions. However for **1**, since many compounds reported in *C*2/*m* were afterwards correctly solved in higher symmetry space groups, the solution involved solutions in space groups with enlarged unit cell parameters such as *R*–3*m* and lower symmetry, such as *Cm*, *C*2, and $P2_1/m$. The latter ones were checked due to the presence of bent $\{ZnSn_2\}$ units in **2**, that gave rise to question the linearity, which could be forced by symmetry. The solution in *Cm* resulted in two different Zn–Sn bonds and slightly bent (179.7°) units but was accompanied with significantly higher residuals (R_1 = 0.046, wR_2 = 0.111). Additionally the thermal displacement parameters for Sn and Zn do not show a significant elongation in *C*2/*m*, therefore the latter solution was kept. During refinement of **1** three independent Na sites and one for Sn and Zn, respectively, could be assigned. Besides two Sn, one Zn, one K, and four Na positions, a mixed occupied (A = K1 / Na1) site was introduced for **2**. The structure solution for **2** was carried out in the space group $P2_1/c$. Details of the X-ray data collection and structural refinements for both compounds are listed in Table 4.21. The final positional and equivalent isotropic displacement parameters for both structures are listed in Tables 4.22 and 4.23. Selected distances are shown in Table 8.7 (see Appendix).

***Table 4.21*: Selected crystallographic and refinement data for Na_6ZnSn_2 and $Na_{4.23}K_{1.77(1)}ZnSn_2$.**

Empirical formula	**Na_6ZnSn_2 (1)**	**$Na_{4.23}K_{1.77(1)}ZnSn_2$ (2)**
Formula weight / g·mol^{-1}	440.69	469.12
Temperature / K	293(2)	
Crystal size / mm^3	0.05 × 0.05 × 0.01	0.04 × 0.04 × 0.04
Crystal color; shape	Dark metallic; Plate	Dark metallic; Block
Diffractometer	Oxford Xcalibur3 (CCD)	
Crystal system	Monoclinic	Monoclinic
Space group	*C*2/*m* (No. 12)	$P2_1/c$ (No. 14)
Unit cell parameters / Å	*a* = 10.077(3)	*a* =11.572(1)
	b = 5.473(1)	*b* = 9.862(1)
	c = 9.316(2)	*c* = 11.382(1)
	β = 98.07(2)°	*β* = 119.33(1)°
Unit cell volume / Å^3; *Z*	508.7(1); 2	1132.3(1); 4
ρ_{calc} / g·cm^{-3}	2.88	2.752
μ / mm^{-1} (Mo K_α)	7.38	7.215
Absorption correction	empirical	empirical
F(000)	392	840
Θ range / °	4.08 - 27.90	2.89 - 27.85
Index range	$-13 \le h \le 9$; $-7 \le k \le 6$	$-14 \le h \le 15$; $-12 \le k \le 12$
	$-12 \le l \le 12$	$-14 \le l \le 14$
Data completeness / %	98.4	99.7
Integrated reflections	1985 (R_σ = 0.033)	15918 (R_σ = 0.035)
Independent reflections	668 (R_{int} = 0.021)	2671 (R_{int} = 0.041)
Refinement method	Full-matrix least-squares on F^2 (SHELXTL)	
Parameters	30	84
Goodness of fit on F^2	0.928	0.986
Observed reflections [$I > 2\sigma(I)$]	535	1961
R_1 / wR_2 [$I > 2\sigma(I)$]	0.022 / 0.044	0.029 / 0.062
R_1 / wR_2 (all data)	0.032 / 0.045	0.045 / 0.067
Weighting scheme[a]	a = 0.026; b = 0	a = 0.037; b = 0
Extinction coefficient	0.0004(3)	0.00017(16)
Residual map / e$^-$·Å^{-3}	+1.21 [1.55 Å from Na3]	+0.87 [1.04 Å from Sn1]
	–0.50 [1.85 Å from Na3]	–0.97 [0.82 Å from Sn2]

[a] $w = 1 / [\sigma^2(F_o^2) + (aP)^2 + bP]$, where $P = (F_o^2 + 2F_c^2) / 3$

***Table 4.22*: Atomic coordinates and equivalent isotropic displacement parameters for Na_6ZnSn_2 and $Na_{4.23}K_{1.77(1)}ZnSn_2$.**

Atom	**Wyck.**	**Occ. ≠ 1**	***x***	***y***	***z***	U_{eq} **/ Å^2**
			Na_6ZnSn_2 (1)			
Sn	4*i*		0.1447(1)	0	0.2490(1)	0.031(1)
Zn	2*a*		0	0	0	0.037(1)
Na1	4*i*		0.4703(2)	0	0.2753(3)	0.053(1)
Na2	4*i*		0.2926(3)	0	0.9295(3)	0.055(1)
Na3	4*i*		0.1736(2)	0	0.5908(3)	0.056(1)
			$Na_{4.23}K_{1.77(1)}ZnSn_2$ (2)			
Sn1	4*e*		0.3397(3)	0.7238(3)	0.0788(1)	0.033(1)
Sn2	4*e*		0.1485(1)	0.1922(1)	0.8852(1)	0.036(1)
Zn	4*e*		0.2565(1)	0.9648(1)	0.9885(1)	0.038(2)
A = K1 / Na1	4*e*	0.77 / 0.23(1)	0.3243(1)	0.3913(1)	0.2036(1)	0.047(5)
K2	4*e*		0.6447(1)	0.5333(1)	0.1828(1)	0.052(3)
Na2	4*e*		0.5072(2)	0.8222(2)	0.9263(2)	0.050(5)
Na3	4*e*		0.1683(2)	0.7224(2)	0.2380(2)	0.048(5)
Na4	4*e*		0.0766(2)	0.5241(2)	0.8787(2)	0.053(5)
Na5	4*e*		0.0112(2)	0.3404(3)	0.5769(2)	0.055(6)

***Table 4.23*: Anisotropic thermal displacement parameters (*l* Å^2) for Na_6ZnSn_2 and $Na_{4.23}K_{1.77(1)}ZnSn_2$.**

Atom	U_{11}	U_{22}	U_{33}	U_{23}	U_{13}	U_{12}
			Na_6ZnSn_2 (1)			
Sn	0.034(1)	0.027(1)	0.032(1)	0	0.004(1)	0
Zn	0.033(1)	0.037(1)	0.039(1)	0	–0.003(1)	0
Na1	0.041(1)	0.043(1)	0.077(2)	0	0.015(1)	0
Na2	0.078(1)	0.034(1)	0.059(1)	0	0.034(1)	0
Na3	0.067(1)	0.050(1)	0.050(1)	0	0	0
			$Na_{4.23}K_{1.77(1)}ZnSn_2$ (2)			
Sn1	0.034(1)	0.035(1)	0.032(1)	0.004(1)	0.017(1)	0.003(1)
Sn2	0.033(1)	0.039(1)	0.035(1)	0.006(1)	0.016(1)	0.006(1)
Zn	0.040(1)	0.031(1)	0.039(1)	0	0.017(1)	0
A = K1 / Na1	0.054(1)	0.043(1)	0.048(1)	0.005(1)	0.028(1)	0
K2	0.053(1)	0.049(1)	0.055(1)	0.006(1)	0.028(1)	0.008(1)
Na2	0.044(1)	0.058(1)	0.046(1)	0	0.022(1)	–0.007(1)
Na3	0.040(1)	0.063(1)	0.040(1)	0	0.020(1)	0.004(1)
Na4	0.055(1)	0.049(1)	0.056(1)	0	0.028(1)	0
Na5	0.050(1)	0.072(2)	0.043(1)	0.003(1)	0.023(1)	0.004(1)

Structure Description of Na_6ZnSn_2 The unit cell, as shown in Figure 4.41a, features isolated linear units of {$ZnSn_2$} with *d*(Zn–Sn): 2.561(1) Å. The more electropositive Zn (Pauling scale) is located in the middle as predictable by the three-center model.[39] The Zn–Sn bond length is considerably shorter compared to Zn–Sn separations found in other solid state phases, such as in $BaZn_2Sn_2$[14] (2.794 Å), the shortest Zn–Sn contacts in $Na_{29}Zn_{24}Sn_{32}$ (2.724 Å, Chapter 4.4), BaZnSn[15] (2.713 Å), GdZnSn[108] (2.680 Å), or the sum of Pauling's single bond covalent radii.[36, 37] When calculating bond orders with the Pauling formula,[36] which is 1.76 (with single bond radii 1.309 and 1.399 Å for Zn and Sn, respectively) here, questions about the nature of the Zn–Sn bonding arise. Comparison of the observed distances with single bond lengths observed in molecular compounds, such as in heterodimetallic complexes [MeSi{Si-Me_2N(*p*-Tol)}$_3$Sn]$_2$M (M = Zn, Cd, Hg. The second Sn substituent is not bonded in a Sn–M–Sn arrangement for M = Zn)[109] and Zn[bis[3-(dimethylamino)propyl-C,N]Sn]bis(dibenzoylmethanato)-(Sn–Zn),[110] with *d*(Zn–Sn) = 2.578(1) Å, and 2.634(6) Å, respectively, are possible but may not be very objective since the atoms of isolated molecules in the latter have only few directional interactions, which usually is not the case in neat solids where there are many non-directional and directional interactions due to lattice effects. In the latter two molecular compounds the Zn–Sn bond is strongly ionic, according to ^{119}Sn NMR studies, and therefore described as a classical metal-ligand coordinative bond. The Zn(I)–Zn(I) bond length in decamethyldi-zincocene[111] with *d*(Zn(I)–Zn(I)) = 2.305 Å is significantly shorter.

In Na_6ZnSn_2 the anions are oriented parallel to each other (roughly along [102]) and are well separated (nearest Sn–Sn or Zn–Zn contacts are > 5.4 Å) by Na atoms. Regarding Na–Sn, Na–Zn, and Na–Na contacts up to 3.8 Å (above 3.8 Å the next Na neighbours for Sn, Zn, and Na are at ~ 4.5, 4.4, 4.1 Å, respectively) the anionic units are embedded into asymmetric (4, 6, 6, 4) $\{Na_{20}\}$ cages (Figure 4.41c). Similar cages, i.e. M_{14} or M_{14+3}, were found in K_5CuSb_2[112] and K_5CuAs_2[113], respectively. Additionally, the partial Na structure contains distorted empty $\{(Na3)_6(Na1)_2\}$ cubes that form layers in the (001) plane (Figure 4.41e). Via six edges six adjacent cubes are bonded, and each of the six faces is part of one of six different $\{Na_{20}\}$ cages, thus separating the layers of condensed $\{Na_{20}\}$ polyhedra (Figure 4.41c). The Na–Na distances in these cubes are 3.414 to 3.668 Å and well within the range of interaction distances in elemental Na (3.67 Å, space group *Im*–3*m*). As depicted in Figure 4.41b the structure can also be viewn as close packed layers of Sn atoms that are stacked in the sequence *ABCABC* perpendicular to the (001) plane. Each two $\{ZnSn_2\}^{6-}$ anions represent the basal plane of a distorted Sn octahedron with *Niggli* formula $^{2}_{\infty}[\square Sn_{6/2}]$. Each one shares six edges with adjacent octrahedra in the (100) plane. Each three octahedra confine a tetrahedral hole, which are empty. Four of the eight octahedral faces are centered by Na atoms (Na1 and Na2). At the same time the Na1 atoms form hexagonal layers which interpenetrate the Sn layers in a way that the two together form an almost planar two- colored diamond like layer, such as in ZnS. Na3 is tetrahedrally coordinated with Sn and separates the layers of octahedra along [001].

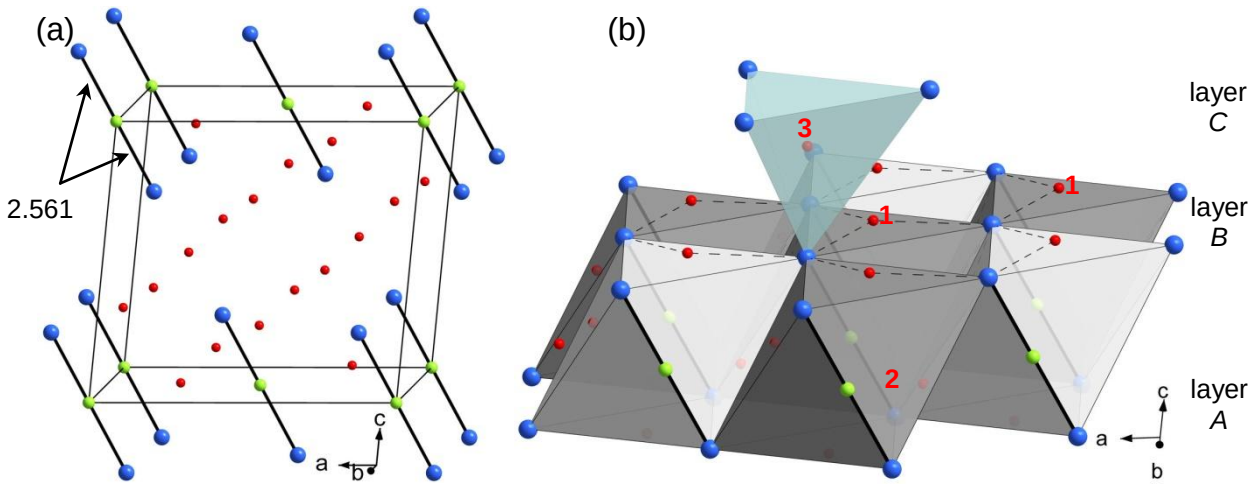

***Figure 4.41*. For figure captions see next page.**

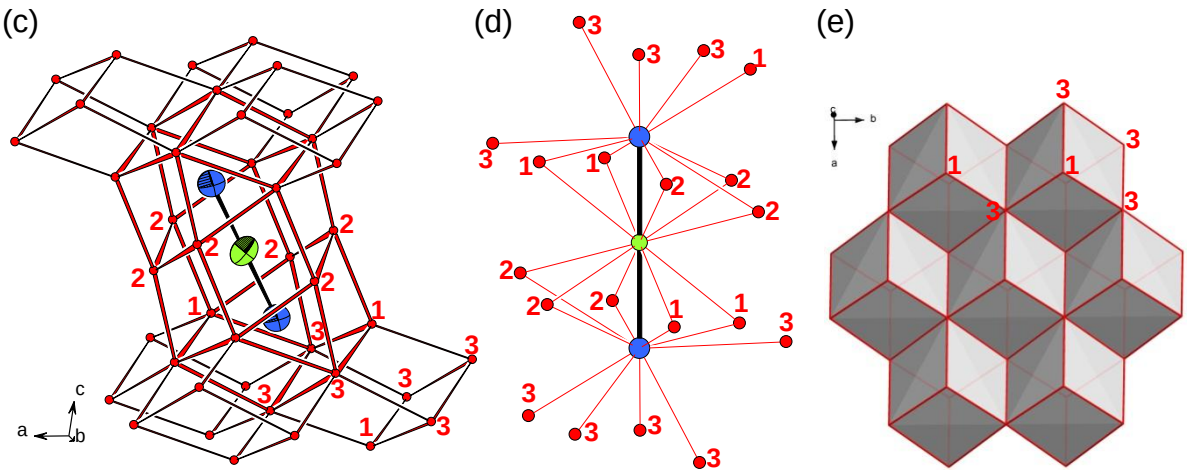

***Figure 4.41 continued*. The structure of Na_6ZnSn_2: (a) Unit cell (90% representation). (b) Projection emphasizing the coordination environments of Na1 to Na3. The wurzite like layer formed by Na1 and Sn atoms is indicated (dashed line). (c) Na polyhedra. (d) First coordination sphere of Na atoms (up to 4 Å) around the $\{ZnSn_2\}$ unit, (e) layer of distorted Na cubes. Na (red), Sn (blue), and Zn (green).**

The Na–Sn and Na–Zn bond lengths within the confining Na cage (Figure 4.41d) are on average $d(\text{Zn–Na})_{\varnothing}$ = 3.49 and $d(\text{Sn–Na})_{\varnothing}$ = 3.36 Å. The slight preference of Na towards Sn can be explained by available space and higher electronegativity (Pauling scale) of Sn.

Structure Description of $Na_{4.23}K_{1.77(1)}ZnSn_2$ Comparable but less symmetric units $\{ZnSn_2\}^{6-}$ are present in compound **2**. The unit is slightly bent with ∠SnZnSn of 172.26(1)° and two different Zn–Sn bond lengths (2.586(1), 2.561(1) Å), that are again very short compared to Zn–Sn contacts in other intermetallic phases. The calculated PBO for the average distance (2.57 Å) is 1.70. The deviation from linearity of such ions have been reported for the $\{BPn_2\}^{3-}$ 'linear' anions (Pn = P, As)[114] and have its origin in matrix effects. The unit cell (Figure 4.42a) shows the anions well isolated with shortes Sn–Sn and Sn–Zn distances between the units longer than 5 Å. Regarding only distances up to 4 Å the anions are encaged by 20 atoms (12× Na, 4× K, 4× A) in an arrangement with no special symmetry (Figure 4.42b). From a topologic point of view the anions are arranged as shown in Figure 4.42d.

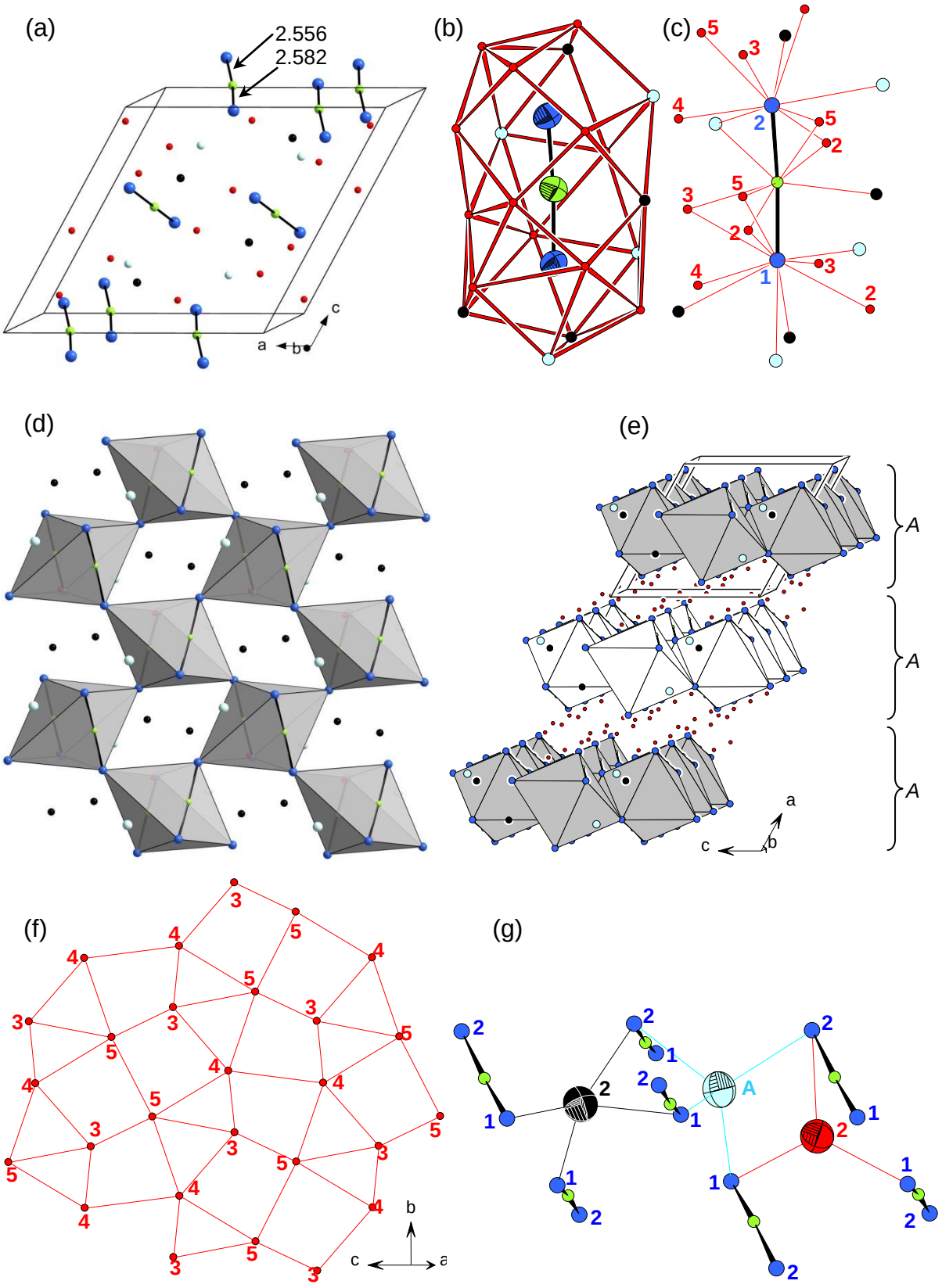

Figure 4.42. **(a) Projection of the unit cell of $Na_{4.23}K_{1.77(1)}ZnSn_2$. (b) Cation coordination around the $\{ZnSn_2\}^{6-}$ unit (atoms at 90% thermal ellipsoids). (c) First coordination sphere (< 4 Å) of the $\{ZnSn_2\}$ unit. (d) Single layer of corner sharing distorted $\{\square Sn_{2/1}Sn_{4/2}\}$ octahedra. (e) primitive stacking of these layers along *a*. (f) Single puckered layer made of Na3 to Na5. (g) Coordination of K2, A = K/Na, and Na2 (90% probability level) in $Na_{4.23}K_{1.77(1)}ZnSn_2$. Na (red), K (black), A = Na/K (light blue), Zn (green), and Sn (blue).**

The terminal Sn atoms (Sn1 and Sn2) of a pair of $\{ZnSn_2\}^{6-}$ units form the basal plane of a $\{Sn_6\}$ octahedron with *Niggli* formula $^{2}_{\infty}[\square Sn_{2/1}Sn_{4/2}]$. The octahedra are distorted and form layers of vertex sharing octahedra in the (100) plane. Along *a* these layers are primitively stacked (Figure 4.42e). Within the octahedron Na2 atoms are located and they are off-trigonal planar coordinated with Sn atoms with distances ranging from 3.317(2) to 3.482(2) Å and thus each Na2 has contacts to three different $\{ZnSn_2\}$ anions (Figure 4.42d and 4.42g). Whereas the M atoms surmount triangular faces of the octahedra, Na2 atoms are located within the $\{Sn_6\}$ octahedra. Atoms Na3 to Na5 are located between the layers of octahedra and form puckered layers of Na atoms that can be expressed as a $(3^2.4^2)(3.4.3.4^2)(3^2.4^3)$ net (for distances < 4 Å, Figure 4.42f). The Na–Na distances in this net range from 3.406(3) to 3.973(4) Å and are therefore in the range of elemental Na (space group *Im*–3*m*). The average Na3–Zn/Sn, Na4–Zn/Sn, and Na5–Sn distances are 3.29, 3.35, and 3.47 Å, respectively. The K for Na substitution results in K occupying the free space between the octahedra but within the octahedral layers. As shown in Figure 4.42g, A = K1/Na1 and K2 are each coordinated with four Sn atoms in a very distorted tetrahedral fashion. The average K2–Sn and M–Sn distances are 3.90 and 3.70 Å, respectively. These values are significantly larger than the Na–Sn and Na–Zn separations.

4.7.3 Electronic Structure of Na_6ZnSn_2

DOS and –COHP calculations were carried out in order to gain deeper insights into the nature of the bonding, especially of the Zn–Sn contact. The *k*-space integration was performed by the tetrahedron method on a set of 2048 irreducible *k* points and a basis set with Na-3*s*/(2*p*), Zn-4*s*/3*p*/3*d*, Sn-5*s*/5*p*/(4*d*)/(4*f*) (down folded orbitals in parentheses). The calculated band structure, density of states (DOS and projected DOS), and crystal orbital Hamilton populations (–COHP) for selected interactions, cumulated over all bonds per unit cell are shown in Figure 4.43. The DOS projections for all three elements are shown in Figure 4.44. As expected from the ionic formula splitting $(Na^+)_6Zn^0(Sn^{3-})_2$ (or $(Na^+)_6Zn^{2-}(Sn^{2-})_2$) the Fermi level coincides with low but non-zero DOS indicating an almost optimized electron count with most bonding states occupied. Although it should be noted that gaps are underestimated by the LDA, the band structure clearly reveals two band crossings of the Fermi level around the Γ point. The intersecting bands have mainly Sn-*s* and *p* character and minor contributions from Na orbitals.

The detached valence band between –3.3 eV and the Fermi level mainly consists of Sn-5*p* bonding states and some significant contributions from Na-3*s* and 3*p* orbitals, which implies an incomplete charge transfer to the anions. However, one must also take into account that three times more Na atoms than Sn atoms are present per formula unit. The missing shoulder of the DOS (at around ~ –0.3 eV) in the –COHP diagram indicates non-bonding Sn and Na states. Consistent with that the band touching the Fermi level in the direction Γ → A has mainly Sn-*p* character. Furthermore, in the valence band low but noticeable amounts of Zn-4*p* states are present that mix with Sn-*p* states. This may indicate a polarization of the Zn–Sn bond towards tin. At –4 eV a separated band emerges with mainly Zn-4*s* character and also significant contributions from Na-3*s*, and low lying Sn-5*s* and 5*p* states. On the one hand this orbital mixing indicates the *sp* hybridization of Sn, and on the other it shows Zn-*s* interaction with Sn orbitals, meaning completely filled 4*s* orbitals of Zn. Due to increased energetic separation of (n–1)*d* and n*s*, n*p* orbitals with growing atomic number the Zn-3*d* states are well localized at –8 eV below the Fermi level and have core electron character. They are confined to a 2 eV range (–7 to –9 eV) and do not decisively interact with the *sp* bonding regions. The –COHP in this regions does not show the sharp Zn-*d* peaks of the DOS and proves the non-bonding character of the *d* orbitals. The band at –7 eV shows mainly Sn-5*s* character with low contributions of Zn-3*d* and Na-3*p* states. The –COHP plots show all Na–Zn, Na–Sn, and Sn–Zn interactions optimized and overall bonding. Na–Sn and Na–Zn interactions were considered up to 4 Å and have averaged –ICOHP values of 0.12 and 0.32 eV per ‘bond’ (Table 4.24). Their sums are high (for all Na–Sn: 3.2; Na–Zn: 1.6 eV) but one has to consider there are eight times more Na–Sn and Na–Zn contacts than Zn–Sn contacts. The average Na–Na ‘bond’ with 0.07 eV is considerably weaker and altogether they are significantly weaker than the Zn–Sn bonding energy of 2.74 eV. Whereas all bonding Zn–Sn and Na–Sn states are filled, further bonding Na–Zn and Na–Na states are present above the Fermi level.

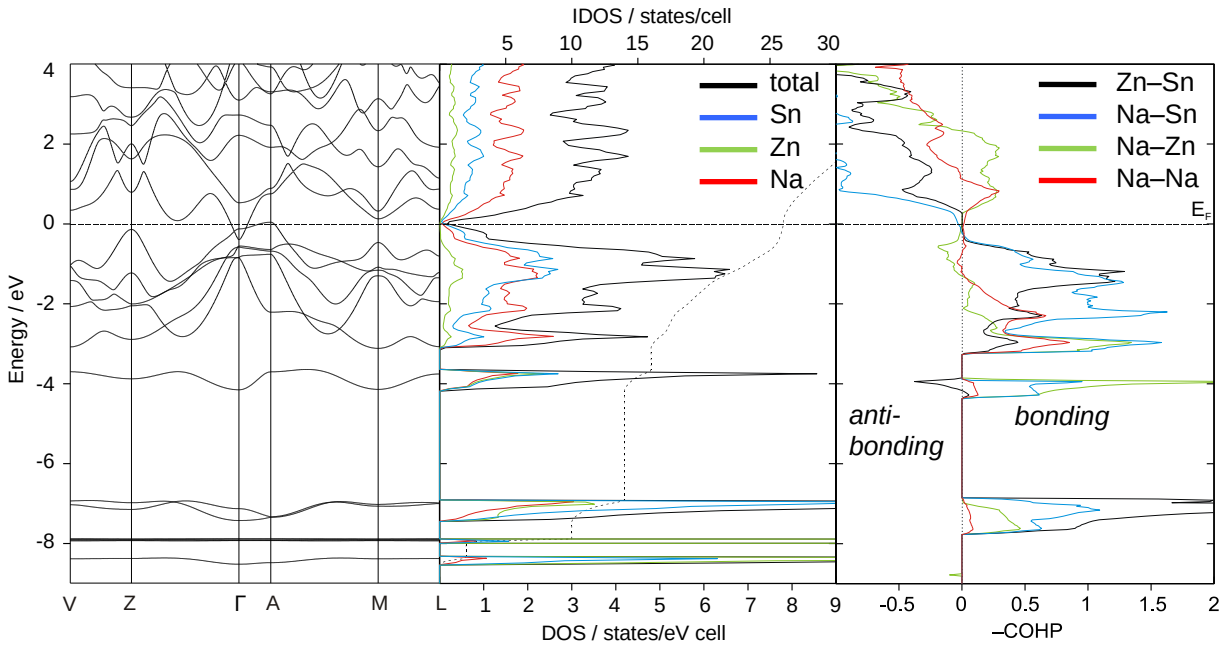

***Figure 4.43*. (left) Band structure of Na_6ZnSn_2. (center) DOS with pDOS of Sn (blue), Zn (green), Na (red). (right) –COHP diagrams over the sum of all Zn–Sn (black), Na–Sn (blue), Na–Zn (green), and Na–Na (red) interactions.**

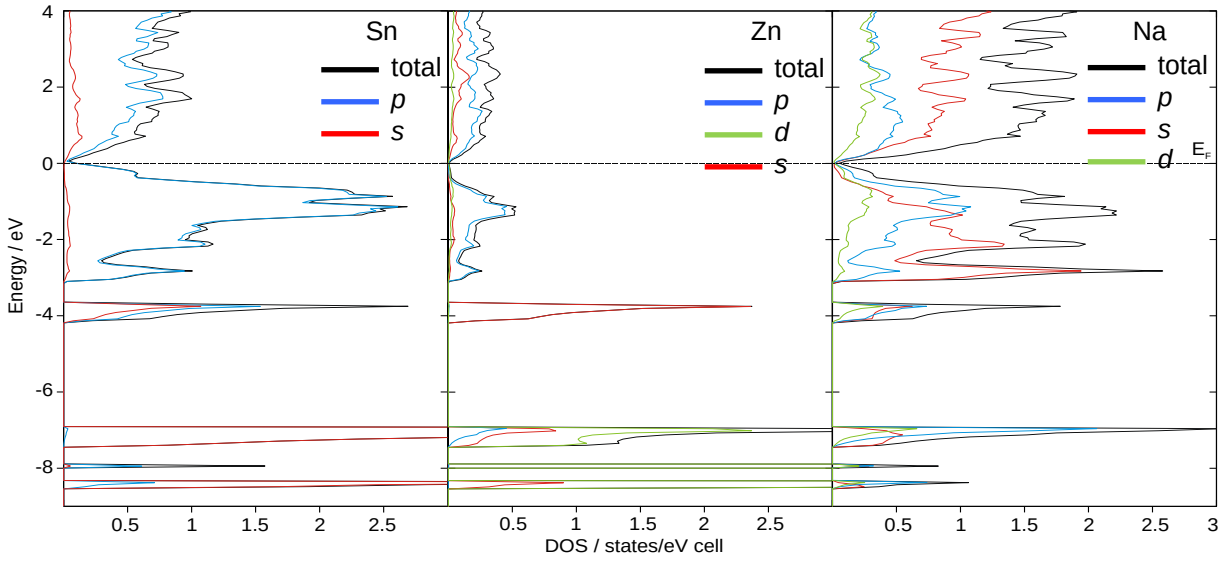

***Figure 4.44*. (from left to right) Projected DOS diagrams for Sn, Zn, and Na in Na_6ZnSn_2. Orbital contributions: total (black), *p* (blue), *s* (red), and *d* (green).**

***Table 4.24*: –ICOHP values for selected interatomic contacts in Na_6ZnSn_2. Energies are given in eV/bond.**

interaction		*d* / Å	–ICOHP (at E_F)	–ICOHP (max.)
Sn	Zn	2.561(1)	2.74	2.74
Na	Sn	3.156(1) - 3.723(1)	0.32	0.32
Na	Zn	3.109(2) - 3.791(1)	0.12	0.16
Na	Na	3.260(1) - 3.668(1)	0.07	0.09

For further investigations of the unusual short and strong Zn–Sn bond NBO, AIM and ELF calculations were performed. The calculations were done for a $\{ZnSn_2\}^{6-}$ (solv.) ion in acetonitrile solution and, for comparison, for a cation encaged anion $\{Na_{20}ZnSn_2\}^{14+}$. These models were taken into account, since a naked anion with such a high charge in the gas phase is very unlikely to be stable. Solution experiments in dimethylformaide (DMF) and ethylenediamine (En) pointed in that direction. The compound Na_6ZnSn_2 readily dissolves yielding a dark brown colour and crystallizes in nicely octahedral shaped crystals. However, the anion $\{ZnSn_2\}^{6-}$ could not be structurally characterized but the formation of a $\{Sn_9\}^{3-}$ cluster was observed. *Hartree-Fock* single point calculations and geometry optimization were performed with the following basis sets: Na: 3–21G, Zn: 3–21G, and Sn: 3–21G. The basis sets were obtained from ref. [115].

4.7.4 Discussion and Results of Molecular Calculations

The unique anionic units of the compounds **1** and **2** were obtained through an approach to generate isolated anionic species by increasing the amount of electrons transferred to the more electronegative atoms. In general this method reduces the nuclearity to charge ratio leading to the formation of small, highly charged polyanions. Various homoatomic units have been reported recently, including ozone-like $\{Bi_3\}^{3-}$ [116] and metallic salts containing $\{Bi_2\}^{2-}$[117] or $\{Pn_4\}^{4-}$ (Pn = As, Sb, Bi).[118] An interesting family are the 16 valence electron 3-atomic linear monomers that are isosteric with $HgCl_2$. Many solid state compounds containing such species have been discussed in terms of structure and results of vibrational measurements. Prominent representatives of these are the alkaline boron and beryllium pnictides, such as K_4BePn_2 (Pn = P, As, Sb),[119] K_3BP_2, K_3BAs_2,[120] Rb_3BP_2, Cs_3BP_2, Rb_3BAs_2, Cs_3BAs_2, Na_3BP_2, K_2NaBP_2 [114], as well as phases with late transition elements, such as Na_4HgP_2, K_4ZnP_2, K_4CdP_2, K_4HgP_2,[121] K_5AuP_2, K_5AuAs_2, K_5CuAs_2, [113] and K_5CuSb_2.[112] The nitridoborate $\{BN_2\}^{3-}$[122, 123] and carbidoborate $\{BC_2\}^{5-}$[124, 125] anions can be counted in as well. In addition, $\{TtPn_2\}^{2-}$ units with tetrel elements as central atom are found as parts of anionic strands in K_2SiP_2[126] or Rb_2SiAs_2.[127] In the phases with isolated anions a notably short M–Pn contact is present which brings up the question of the nature of the chemical bond. In the case of $\{BPn_2\}^{3-}$ (Pn = P, As) a 1,2-propadiene C_3H_4 structure was concluded from X-ray and vibrational spectra.[120]

Looking for such analogies between the structure and properties of molecules and intermetallic moieties is a suggestive approach to probe classical bonding principles. However, theoretical bonding analyses and the electronic structure of 16 VE 3-atomic linear monomers (XAX), which would reveal more detailed insights into the nature of the chemical bonding, especially in the presence of heavier carbon homologues i.e. Ge or Sn, are still missing.

The novel phases Na_6ZnSn_2 and $Na_{4.23}K_{1.77(1)}ZnSn_2$ can be placed in this context. The Zintl concept leads to an ionic formula splitting with VEC ~ 5.33 for the atoms in the triatomic units. Several possibilities for assigning the 16 valence electrons in the linear unit can be formulated. As shown in Scheme 4.1 these resonance formulae involve (I) a purely ionic model with Zn^{2+} and two isolated Sn^{4-}, (II) covalently single bonded Sn^{3-} atoms, with Zn^0 as central atom, and (III) a propadienyl like π-system with 2b-Sn^{2-} and 4b-Zn^{2-}.

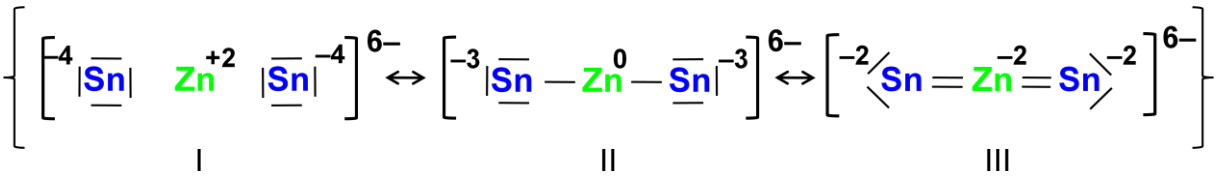

***Scheme 4.1*. Three possible assignations of 16 valence electrons for the linear unit $\{ZnSn_2\}^{6-}$.**

The geometry optimizations with Gaussian03, calculating energy minima on the potential energy surface, converged to a ground state (minimum) with $D_{\infty h}$ symmetry and a transition state (1st order saddle point) with C_S symmetry. The latter suggests two different Zn–Sn bond lengths and a bent unit. The energy difference between the two conformations is ~ 0.9 kcal/mol. The outcome of the ELF calculation of the solvated anion is shown in Figure 4.45, which reveals the localized nature of the chemical bond between the atoms. The all electron 3D ELF (ELF value = 0.78) and the contour diagram in a plane including the C_∞ axis of rotation of the $\{ZnSn_2\}$ rod show domains with high ELF values and the presence of lone pairs (monosynaptic valence basins) centered on each Sn. In addition, two torus-like localization regions are found perpendicular to the Zn–Sn vector. This attractor shape usually reflects a σ-π bonding situation like in ethyne.[128, 129] Due to the asymmetric Na coordination (Figure 4.41c) this torus separates into two attractors in the $\{Na_{20}ZnSn_2\}^{14+}$ model (not shown).

The 3D visualization implies two ‘triple bonds’ in the {$ZnSn_2$} unit (similiar to ethyne, see Figure 4.45e). This, however, cannot be rationalized with established bonding schemes. Therefore further calculations, namely NBO and AIM were performed to assess the electron configurations of all atoms and the numbers of bonding electrons. The obtained values are comprised in Table 4.25 and 4.26. According to the ELF analysis for the solvated $\{ZnSn_2\}^{6-}$ 45.8 and 28.2 core electrons can be assigned to Sn and Zn, respectively. This is in agreement with the corresponding [Kr]4d^{10} and [Ar]3d^{10} shells. The valence population is 6.2 (5.8 for $\{Na_{20}ZnSn_2\}^{14+}$) for Sn and each 2-center bond between Sn and Zn is occupied by 1.9 (2.4 for $\{Na_{20}ZnSn_2\}^{14+}$) electrons, which is close to the value expected for a simple 2*c*-2*e* bond. On the other hand a high variance of σ^2 = 1.22 was calculated, which, representing quantum mechanical uncertainty, is typical for bonds with a high degree of delocalization.

An alternative way to assign atomic charges is to integrate the electron density in the part of space the atom occupies. Whereas the ELF can be defined from either wavefunctions or electron density ρ(r), the AIM[130, 131] method is exclusively based on derivatives of ρ(r) and partitions molecules into nuclei and atomic basins based on a bundle of gradient paths of ρ(r). Interatomic surfaces (IAS) are zero flux surfaces and bind the atomic basins. The result of charge integrations show AIM populations of 53.4 (Sn), 29 (Zn) on the solvated and of 52.6 (Sn) and 29.7 (Zn) of the Na_{20} coordinated $\{ZnSn_2\}^{6-}$. Secondly, NBO analyses for core and valence populations lead to natural charges of –3.6 ($\{Na_{20}ZnSn_2\}^{14+}$) or –3 (solv.) for Sn and +0.77 ($\{Na_{20}ZnSn_2\}^{14+}$) or +1.24 (solv.) for Zn. The results of the AIM and NBO analyses point into the directions of formulation I and II in Scheme 4.1 with a two-fold single bonded Zn^0 or with the classical role of Zn as a cation. Lewis acidic Zn can form linear zinc organyls, such as ZnR_2 (R = Me, Et), which exist as isolated species and have σ-metal-carbon bonds. In such complexes Zn is two-fold single bonded and they represent 16 VE complexes with carbon as σ donors, meaning each of the latter formally provides two electrons and occupies a single coordinate site of Zn. Such complexes have reactivity similar to Grignard compounds (they are nucleophilic) which means the metal-tetrel bond is considerably polarized. Whereas the high and low contributions of Sn and Zn in the valence band of the DOS point in that direction, the ELF results on the other hand suggest a strong covalent bond with high delocalization, implying a partial π-type bonding character.

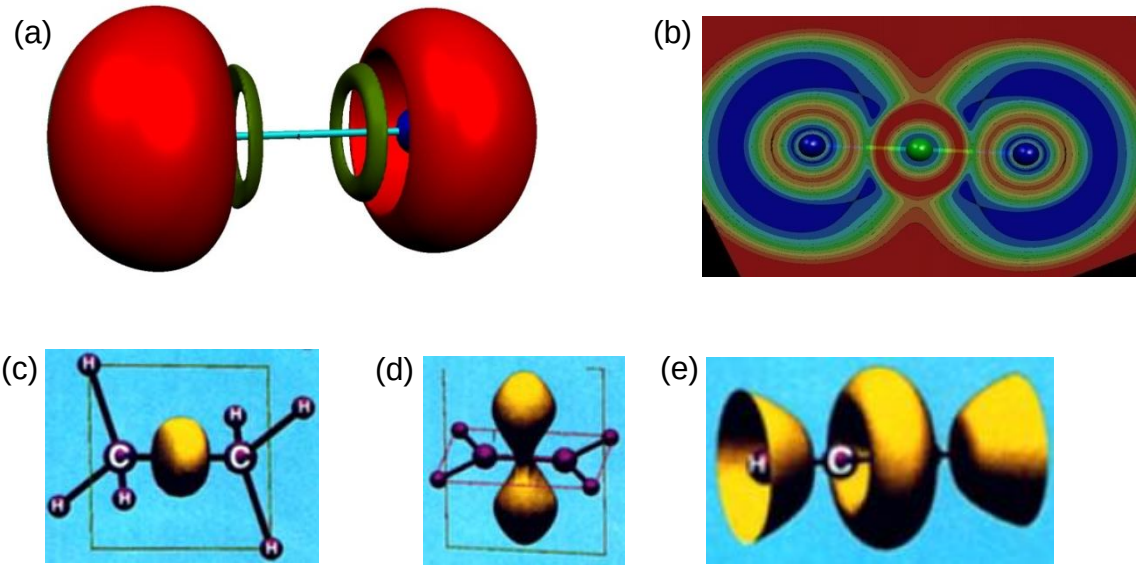

***Figure 4.45*. (a) ELF isosurface with ELF = 0.78, (b) 2D ELF contour diagram of $\{ZnSn_2\}^{6-}$. Zn (green, central position), Sn (blue) terminal positions, (c) to (e) ELF isosurfaces (ELF = 0.8) for ethane, ethene, and ethyne, taken from ref. [129].**

***Table 4.25*: Values obtained by NBO and ELF calculations (using the wavefunction calculated with Gaussian03) for a solvated $\{ZnSn_2\}^{6-}$ anion and calculated HOMO-LUMO gap. The values in parentheses denote results calculated for a $\{Na_{20}ZnSn_2\}^{14+}$ unit.**

	NBO	ELF	
Population for Sn: Core / Valence / **charge**	46 / 7.6 / **–3.6** (46 / 7 / **–3.0**)	45.8 / 6.2 / **–2.0** (45.7 / 5.8 / **–1.5**)	
Population for Zn: Core / Valence / **charge**	18 / 10.6 / **+1.2** (18 / 10.9 / **+0.8**)	28.2 / - / **+1.8** 28.2 / - / **+1.8**	
Bond population (Zn–Sn)		1.9; (2.4)	
$\Delta E_{Homo-Lumo}$			0.3 Hartree (0.2 Hartree)

***Table 4.26*: AIM for a solvated $\{ZnSn_2\}^{6-}$ anion. The values in parentheses denote results calculated for a $\{Na_{20}ZnSn_2\}^{14+}$ unit.**

	AIM
Population for Sn: Core + Valence / **resulting charge**	53.4 / **–3.4** (52.6 / **–2.6**)
Population for Zn: Core + Valence / **resulting charge**	29.0 / **+1.0** (29.7 / **+0.3**)

Another output of the Gaussian calculation can be utilized in terms of molecular orbital diagrams that are based on Mulliken populations. As shown in Figure 4.46 the shape of the molecular orbitals (MOs) and their degeneration compare well with the prominent diagram known for the double-bonded system of CO_2. The eight frontier orbitals are completely filled with the 16 valence electrons and the shapes of the bonding orbitals can be well derived by linear combinations of the atomic orbitals.

The molecular orbital of interest here is the two-fold degenerated *π*-bond at –0.148 Hartree. In the present anion the contributions from Zn-*p* orbitals to this MO are very low. Unfortunately the origin, i.e. the amount of Zn-*p* character involved, of this molecular orbital was impossible to trace back, due to the nature of the basis functions, which involve functions with higher principal quantum numbers.

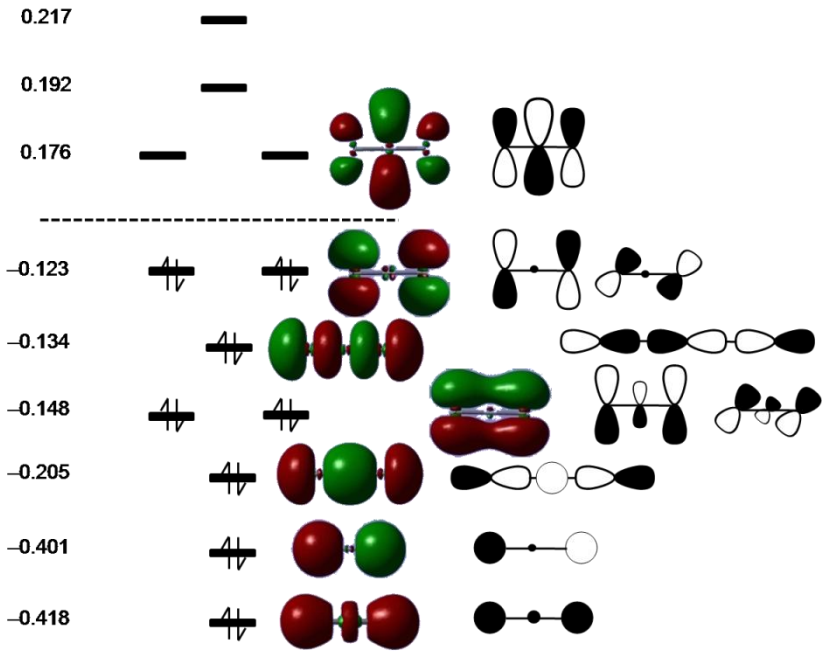

***Figure 4.46*. Molecular orbital diagram for the solvated anion $\{ZnSn_2\}^{6-}$. Orbital energies are given in Hartree.**

Conclusively, the results of three methods do not allow a definite classification of the bonding situation in the linear unit $\{ZnSn_2\}^{6-}$. Charge assignements from NBO and AIM calculations hint for covalent interactions between the atoms and ELF suggests a delocalized nature of the Zn–Sn bond. Combined with the high bonding energy according to the –ICOHP values the assignment of electron pairs may indicate the presence of higher bond orders. Nonetheless, the calculated metallic property and the underestimated role of Na in terms of bonding Na–Sn interactions additionally impedes a clear statement. Vibrational measurements, such as Raman spectroscopy (from a $D_{\infty h}$ symmetrical body one *Raman* mode is expected), would help to clarify results from any calculations. They are ongoing but hampered due to the metallic character of the sample and the resulting high absorption.

4.8 Synthesis and Crystal Structure of $Na_{20}Zn_8Sn_{11}$ - An Intergrowth Structure Made of Electron Deficient and Electron Precise Layers

4.8.1 Synthesis and Characterization

Synthesis Chronologically this compound was synthesized after the phase Na_6ZnSn_2 (see Chapter 4.7) had been discovered. Since Na_6ZnSn_2 was the first compound with an 'almost' balanced Zn : Sn ratio showing no formation of icosahedra and containing only highly charged triatomic $\{ZnSn_2\}^{6-}$ units, the question arose from which Na concentration on the icosahedral theme will start to form. Consecutively, from the previously used reaction composition Na : Zn : Sn = 6 : 1 : 2 the Na loading was stepwise lowered to 2 : 1 : 2, which led to the discovery of the title compound. Later $Na_{20}Zn_8Sn_{11}$ was obtained in higher yields by reacting stoichiometric amounts of the elements at 500 °C and slow cooling (0.1 $K \cdot min^{-1}$) to room temperature. The compound was prepared in sealed Ta ampoules under Ar atmosphere from a total loading mass of 1.271 g, with m(Na) = 0.255 g, m(Zn) = 0.291 g, and m(Sn) = 0.725 g. The resulting crystals exhibit metallic luster and are air sensitive at ambient temperature.

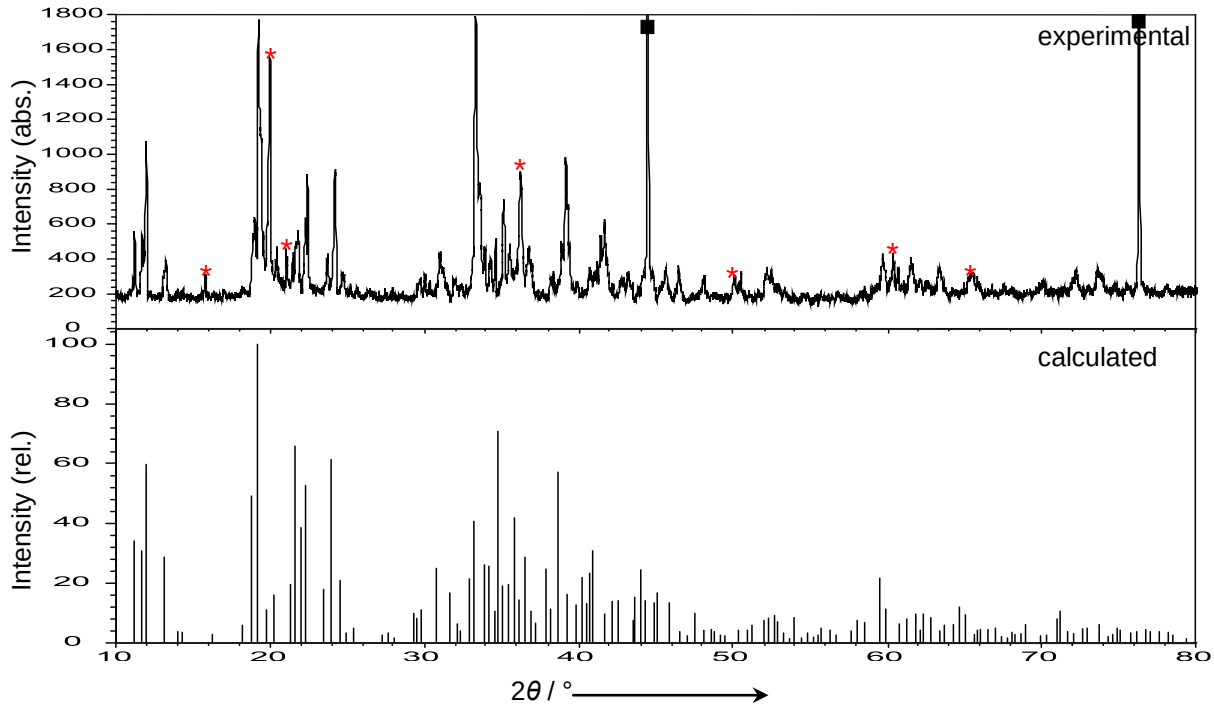

***Figure 4.47*. Experimental (top) powder diagram of a reaction with loading Na : Zn : Sn = 20 : 8 : 11 and calculated diagram for $Na_{20}Zn_8Sn_{11}$. Reflections from diamond powder are marked with a square. Unindexed reflections are labeled with a red star.**

Powder X-ray Diffraction The experiments on a powdered sample were carried out in Debye-Scherrer mode. The reaction product obtained from a stoichiometric loading with ratio Zn : Sn = 20 : 8 : 11 was finely ground, mixed with diamond powder, and loaded in a capillary (0.3 mm diameter) in the glovebox. The X-ray data was collected up to 2θ = 80° on a linear PSD with step width 1.5° and lasted for 16 h. The outcome of this experiment (Figure 4.47) reveals the formation of the target compound and additional unknown phases (marked with red stars).

4.8.2 Crystal Structure Determination and Description

Structure Determination A dark block shaped crystal was selected in the glovebox and sealed into a glass capillary. The data collection was performed with a detector distance of 80 mm to take care of broad spike shaped reflections occurring along the *c**-axis, which already gave a hint for the presence of a disordered structure. 600 frames were collected in four ω scans (each –70° to +80°) with scan width 1°/frame and exposure time 20 s/frame. Based on lattice and systematic absence exceptions the structure was solved in the monoclinic space group *C*2/*c* (No. 15), Pearson code *mC*156. Upon anisotropic refinement six Sn, four Zn, and 10 Na positions could be assigned. Sn5 showed slightly larger displacement values and was refined mixed occupied with Zn, resulting in 49.3% Zn for this position. This value was fixed to 50.0% during the final refinement cycles. The Zn4 atom is located on the only special position with (–1)-symmetry and showed a significant large U_{11} value, which indicated a possible symmetry problem. Since it showed distances to neighboring Sn atoms comparable to that found in Na_6ZnSn_2 (Chapter 4.7) it was retained as Zn in the final refinement. The adjacent Na10 atom is considerably disordered with anisotropic displacement values ranging from 0.002 to 0.176 (Table 4.29). Replacing the Na by Sn or Zn, which would result in more common interatomic distances, showed even larger displacement parameters. Also splitting the site, as proposed by the software, of either Na, Sn, or Zn for this position, did not lead to a significant improvement for the final residual values. Lowering the symmetry to subgroups such as *Cc* (No. 9) or *C*2 (No. 5) resulted in comparable structure models. Several crystals from different samples were measured, all showing broad and slurred reflections, resulting in the same characteristics for Na10 and Zn4 positions. Relevant crystallographic data is comprised in Tables 4.27 to 4.29. Selected interatomic distances are listed in Table 8.8 (see Appendix).

***Table 4.27*: Selected crystallographic and refinement data for of $Na_{20}Zn_8Sn_{11}$.**

Empirical formula	**$Na_{20}Zn_8Sn_{11}$**
Formula weight / g·mol^{-1}	2288.35
Temperature / K	293(2)
Crystal size / mm^3	0.05 × 0.05 × 0.05
Crystal color; shape	Silvery; Block
Diffractometer	Oxford Xcalibur3 (CCD)
Crystal system	Monoclinic
Space group	*C*2/*c* (No. 15)
Unit cell parameters / Å	*a* = 16.151(1); *b* = 9.276(1); *c* = 27.594(2) *β* = 102.97(1)°
Unit cell volume / Å^3; *Z*	4028.6(5); 4
ρ_{calc} / g·cm^{-3}	3.77
μ / mm^{-1} (Mo K_α)	11.56
Absorption correction	Empirical
F(000)	4040
Θ range / °	4.32 - 26.93
Index range	–20 ≤ *h* ≤ 17; –11 ≤ *k* ≤ 11; –33 ≤ *l* ≤ 34
Data completeness / %	91.1
Integrated reflections	13789 (R_{int} = 0.021)
Independent reflections	3985 (R_σ = 0.019)
Refinement method	Full-matrix least-squares on F^2 (SHELXTL)
Parameters	179
Goodness of fit on F^2	1.222
Observed reflections [$I > 2\sigma(I)$]	3626
R_1 / wR_2 [$I > 2\sigma(I)$]	0.035 / 0.078
R_1 / wR_2 (all data)	0.041 / 0.087
Weighting scheme[a]	a = 0.022; b = 157.656
Extinction coefficient	0.00052(2)
Residual map / e$^-$·Å^{-3}	+2.64 [0.62 Å from Na10] / –2.49 [0.45 Å from Zn4]

[a] $w = 1 / [\sigma^2(F_o^2) + (aP)^2 + bP]$, where $P = (F_o^2 + 2F_c^2) / 3$

***Table 4.28*: Atomic coordinates and equivalent isotropic displacement parameters for $Na_{20}Zn_8Sn_{11}$.**

Atom	**Wyck.**	**Occ. ≠ 1**	***x***	***y***	***z***	U_{eq} / Å^2
Sn1	8*f*		0.1844(1)	0.2199(1)	0.2932(1)	0.017(1)
Sn2	8*f*		0.1351(1)	–0.2843(1)	0.3308(1)	0.018(1)
Sn3	8*f*		–0.0238(1)	–0.4429(1)	0.3311(1)	0.016(1)
Sn4	8*f*		–0.0477(1)	0.0351(1)	0.4065(1)	0.024(1)
Sn5	8*f*		0.3241(1)	0.0137(1)	0.4892(1)	0.027(1)
M = Sn / Zn	8*f*	0.50 / 0.50	0.0873(1)	–0.0402(1)	0.2655(1)	0.020(1)
Zn1	8*f*		–0.0237(1)	–0.1322(1)	0.3314(1)	0.021(1)
Zn2	8*f*		0.0870(1)	0.4697(1)	0.2680(1)	0.018(1)
Zn3	8*f*		0.3441(1)	0.2133(1)	0.2694(1)	0.019(1)
Zn4	4*d*		¼	¼	½	0.077(1)
Na1	8*f*		0.0145(3)	0.2141(4)	0.1873(2)	0.028(1)
Na2	8*f*		0.2067(2)	0.0228(4)	0.1880(2)	0.027(1)
Na3	8*f*		0.1570(3)	0.0256(5)	0.3936(2)	0.032(1)
Na4	8*f*		0.2058(3)	0.4039(5)	0.1881(2)	0.037(1)
Na5	8*f*		0.1564(3)	0.4021(5)	0.3935(2)	0.038(1)
Na6	8*f*		0.3470(3)	0.2156(5)	0.3937(2)	0.032(1)
Na7	8*f*		0.0657(3)	–0.2681(5)	0.4399(2)	0.040(1)
Na8	8*f*		–0.0240(3)	–0.6179(5)	0.4392(2)	0.041(1)
Na9	8*f*		0.2863(3)	–0.3098(5)	0.4397(2)	0.041(1)
Na10	8*f*		0.0823(5)	0.0852(7)	0.4998(2)	0.087(3)

***Table 4.29*: Anisotropic thermal displacement parameters (*I* Å^2) for $Na_{20}Zn_8Sn_{11}$.**

Atom	U_{11}	U_{22}	U_{33}	U_{23}	U_{13}	U_{12}
Sn1	0.014(1)	0.013(1)	0.024(1)	0	0.005(1)	0
Sn2	0.015(1)	0.016(1)	0.024(1)	–0.003(1)	0.005(1)	–0.002(1)
Sn3	0.015(1)	0.013(1)	0.020(1)	0	0.004(1)	0
Sn4	0.026(1)	0.021(1)	0.025(1)	–0.003(1)	0.008(1)	0
Sn5	0.033(1)	0.023(1)	0.024(1)	0	0.005(1)	0.008(1)
M = Sn / Zn	0.021(1)	0.013(1)	0.026(1)	0	0.006(1)	0
Zn1	0.022(1)	0.016(1)	0.024(1)	–0.002(1)	0.006(1)	0
Zn2	0.018(1)	0.015(1)	0.021(1)	0	0.004(1)	0
Zn3	0.017(1)	0.017(1)	0.023(1)	0.002(1)	0.005(1)	0.002(1)
Zn4	0.131(3)	0.059(2)	0.039(1)	0.002(1)	0.013(1)	0.062(1)
Na1	0.032(2)	0.019(2)	0.033(2)	–0.004(2)	0.009(2)	0
Na2	0.021(2)	0.027(2)	0.034(2)	0	0.006(2)	–0.004(2)
Na3	0.032(2)	0.030(2)	0.034(2)	0	0.006(2)	–0.004(2)
Na4	0.023(2)	0.033(2)	0.057(3)	0.004(2)	0.012(2)	0.007(2)
Na5	0.045(2)	0.040(3)	0.029(2)	–0.003(2)	0.005(2)	0.012(2)
Na6	0.030(2)	0.033(2)	0.033(2)	0.003(2)	0.011(2)	0
Na7	0.046(3)	0.039(3)	0.033(2)	0.006(2)	0.004(2)	0.012(2)
Na8	0.046(3)	0.032(2)	0.048(3)	0	0.020(2)	0
Na9	0.032(2)	0.043(3)	0.046(3)	–0.009(2)	0.006(2)	0
Na10	0.176(7)	0.075(4)	0.002(2)	0	0.004(3)	0.085(5)

Structure Description The compound $Na_{20}Zn_8Sn_{11}$ represents a new structure type in intermetallic crystal structures. The rather simple structure, shown in Figure 4.48a, can be described as an alternate stacking of two types of layers, namely an 'electron-deficient' cluster layer and an electron precise Zintl layer. The latter consists of linear $\{ZnSn_2\}$ units, the former of Zn and Sn atoms composed in icosahedral units that are interlinked by Sn atoms.

The icosahedral unit $\{Zn_7Sn_5\}$ is located at the (4*e*)-site and has (2)-symmetry (Figure 4.49b). It consists of Zn1 to Zn3, Sn2 to Sn3 atoms, and the mixed occupied position M = Sn / Zn (50% / 50%). The intracluster Zn–Zn bonds range from 2.763(1) to 2.815(1) Å, the Zn–Sn bonds from 2.813(1) to 2.929(1) Å, and the longest one is the Sn2–Sn3 bond with 2.959(1) Å. The M–Zn and M–Sn bonds are intermediate to those and range from 2.774(1) to 2.890(1) Å. Interestingly, the M–M contact is slightly shorter (2.756 Å) than the shortest Zn–Zn separation. However, all these values are in the range of the sum of Pauling's covalent radii for Zn and Sn and comparable to distances found in other cluster compounds reported in this thesis. The *exo*-bonds between Zn1–Sn4, Zn3–Sn1, Zn2–Sn1, and M–Sn1 (×2) with values of 2.687(1), 2.802(1), 2.799(1), and 2.886(1) Å, respectively, are slightly shorter than the corresponding intracluster bonds. This indicates that *exo*-bonds can be viewed as localized 2*c*-2*e* bonds, whereas the contacts between the cluster atoms are multicenter bonds, typical for deltahedral clusters. The eight-fold *exo*-bonded icosahedra are each linked by six bridging 3b-Sn1 atoms forming a two-dimensional

slightly corrugated layer in the (010) plane as shown in Figure 4.49a. The bridging Sn1 atom, together with Zn3, Zn2, and M (each from different adjacent icosahedra), form a flat trigonal pyramid with bond angles of 117.1°, 112.6°, and 113.2°, rspectively at the central Sn1 atom (Figure 4.50). This causes a slight corrugation of the layer. In metallorganic chemistry Sn in such a coordination environment has been reported in triphenyltin substituted derivatives.[132] The remaining two *exo*-positions of the icosahedron are occupied by 1b-Sn4 atoms at a distance of 2.687(1) Å to Zn1.

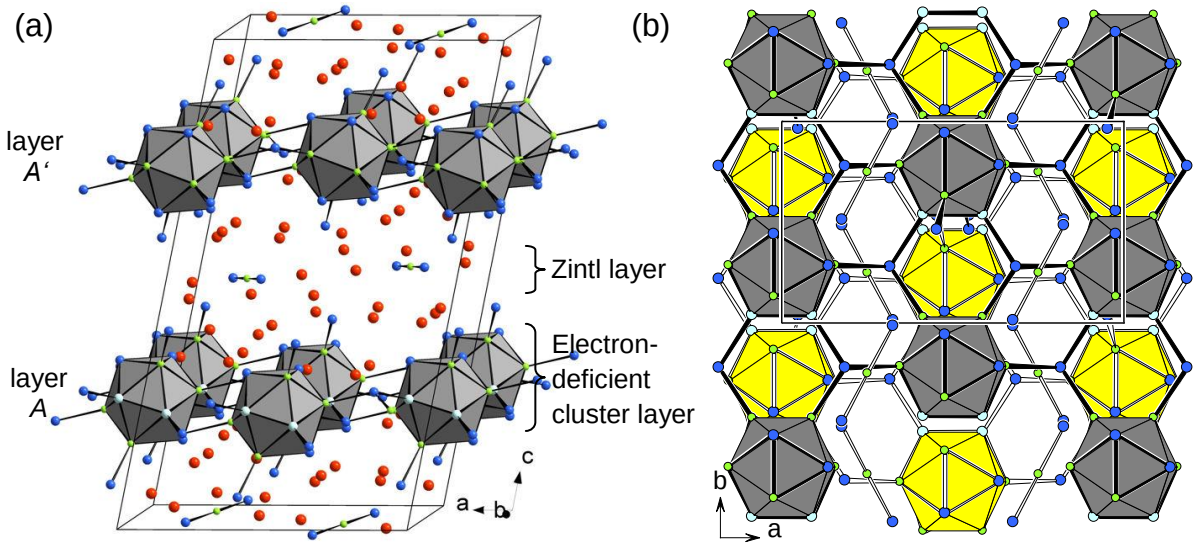

***Figure 4.48*. Off-[010] projection of the unit cell of $Na_{20}Zn_8Sn_{11}$. Na (red), Zn (green), Sn (blue). (b) [001] View of the unit cell with yellow icosahedra at *z* = 0.25 (layer *A*) and dark gray icosahedra at *z* = 0.75 (layer *A'*).**

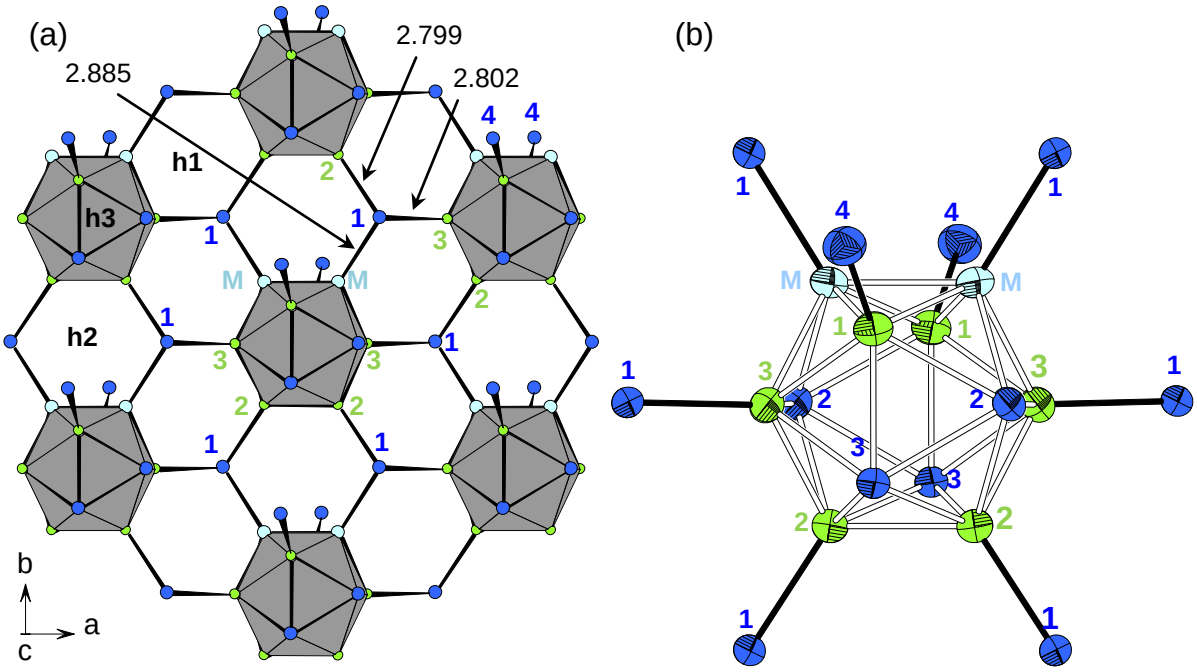

***Figure 4.49*. (a) A corrugated layer made of Sn1 and interconnected icosahedra. The layer can be regarded made of three different hexagons h1 to h3. (b) Anisotropic representation (90% probability) of the eight-fold *exo*-bonded $\{Zn_7Sn_5\}$ icosahedron.**

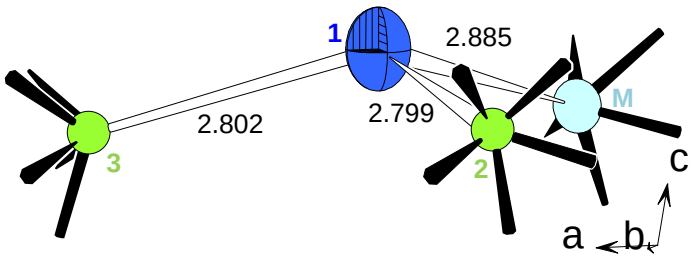

***Figure 4.50*: Trigonal pyramidal coordination of Sn1 (90% probability level). For angle values see text. Sn (blue), Zn (green), M (light blue).**

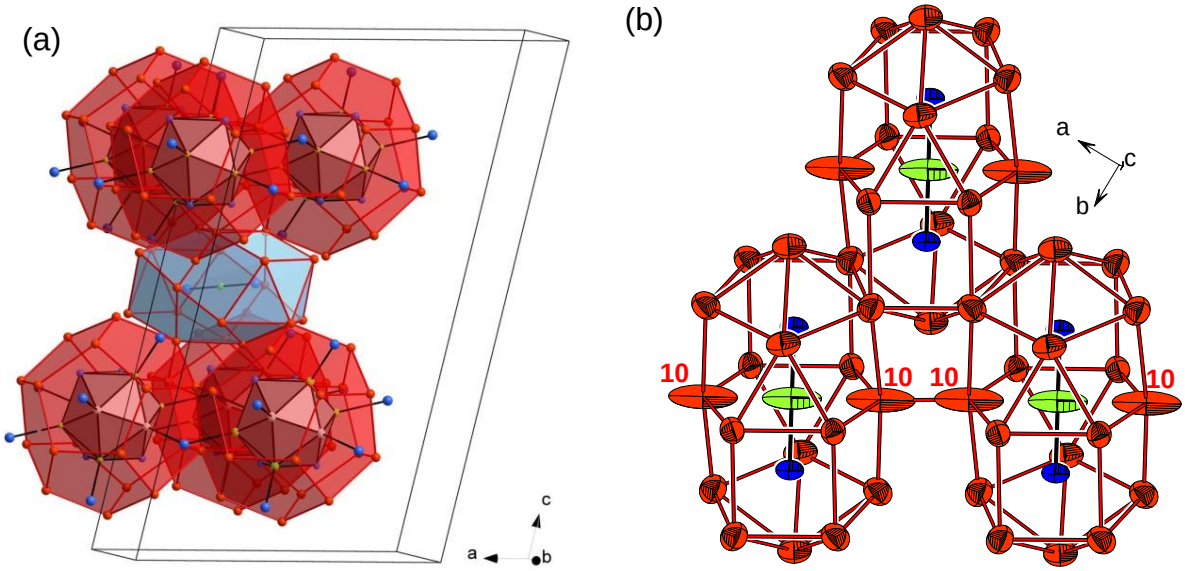

***Figure 4.51*. (a) The icosahedra are encaged in $\{Na_{20}\}$ pentagondodecahedra and each $\{Na_{18}\}$ cage (around a $\{ZnSn_2\}$ unit) interconnects six such $\{Na_{20}\}$ dodecahedra. (b) Encaged $\{ZnSn_2\}$ units.**

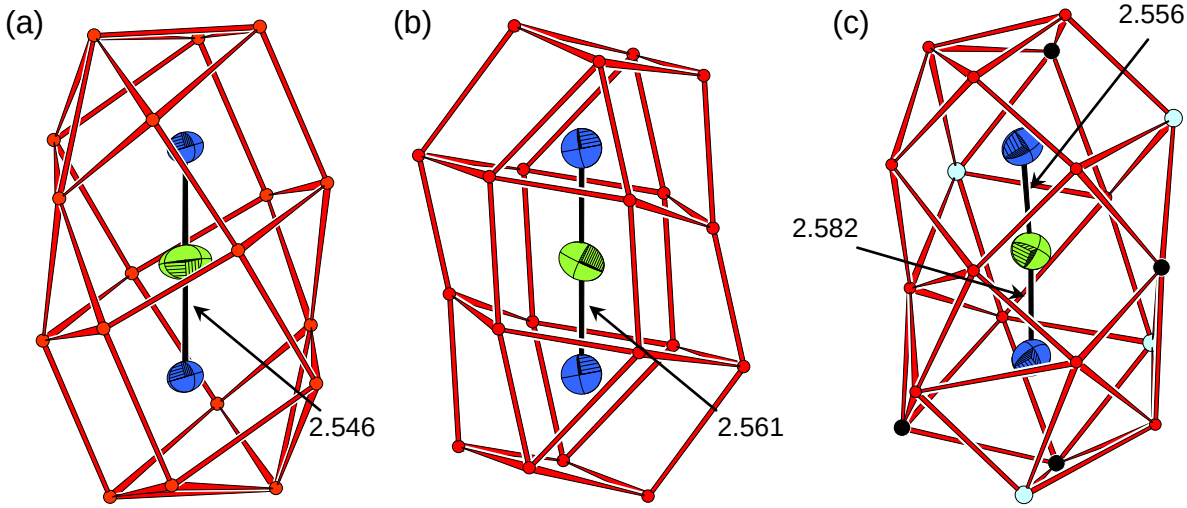

***Figure 4.52*. The different $\{ZnSn_2\}$ units together with the A cages found in (a) $Na_{20}Zn_8Sn_{11}$, (b) Na_6ZnSn_2, and (c) $Na_{4.23}K_{1.77(1)}ZnSn_2$.**

The layer can be described as a corrugated $(6^3)(6^3)(6^3)(6^3)$ net (Figure 4.49a) made of almost planar honeycomb like MZn_3Sn_2 (h1), $M_2Zn_2Sn_2$ (h2) hexagons and a M_2Zn_4 (h3) hexagon in chair conformation. The net nodes are Sn1, M, Zn2, and Zn3. By the presence of Sn1 (the only atom not part of an icosahedron) the icosahedral clusters become separated from each other. As shown in Figure 4.48b the layers of icosahedra are stacked in a *AA'AA'* sequence (A at z = 0.25 and A' at z = 0.75) in such a way that in every 2nd layer the icosahedra are inverted and shifted along *b* by y ~ 0.43. Noteworthily, due to the high amount of Na atoms, the present icosahedra only exhibit eight *exo*-bonds. That number is lower compared to the less reduced $Na_xZn_ySn_z$ ternaries, where the icosahedra are interconnected forming 3D networks. Furthermore, the *exo*-bonds are not established via Sn atoms, but only via Zn or M sites.

The layers containing icosahedra are separated by layers of isolated $\{ZnSn_2\}$ triatomic units (Figure 4.48a and 4.51a). The latter triatomic anionic units are linear and composed of a central Zn4 and two terminal Sn5 atoms with a short interatomic distance of 2.546(1) Å. This unit is similar to the one found in the compounds Na_6ZnSn_2 and $Na_{4.23}K_{1.77(1)}ZnSn_2$ (Figure 4.52). In Na_6ZnSn_2 the Zn–Sn distance in the linear anion is 2.561(1) Å and the unit is surrounded by a $\{Na_{20}\}$ polyhedron. In the present compound the triatomic anion is surrounded by 18 Na atoms, from which two (Na10) show significant elongation in the direction of the central Zn atoms (Figure 4.51b). Regarding the Na substructure (Figure 4.51a), $\{Na_{20}\}$ dodecahedra surround the icosahedra, which follow the array of the icosahedra resulting in layers of edge sharing dodecahedra in the (001) plane. Along [001] the layers are separated by the $\{Na_{18}\}$ cages which surround the $\{ZnSn_2\}$ units. Thus, the structure is decisively separated into electron deficient and electron precise layers.

4.8.3 Discussion

The present compound can be allocated within the field of intergrowth structures, which are suitable for the synthesis of complex metal oxides and can also lead to the discovery of novel polar intermetallic phases. Multilayer intergrowth routines have been particularly successful in the exploration of new layered complex oxides, such as the cuprate superconductors and layered perovskites.

Complex functional layered materials based on intergrowth structures of layered transition metal oxides and intermetallics have been reported to exhibit novel physical properties such as superconductivity, giant magnetoresistance (GMR), and other electronic and magnetic phenomena.[133-135] Similar intergrowth approaches for Zintl phases have also been shown, e.g. Corbett et al. reported several related Zintl phases in the Mg–La–Sb system based on the intergrowth of intermetallic LaSb and Mg_3Sb_2 Zintl layers.[136] Intergrowth by means of chemical twinning led to the preparation of complex but electron precise silicides, such as $BaMg_4Si_3$ and $BaMg_4Ge_3$.[137] In this context also $NaSn_5$[7] should be highlighted, as it features both the covalent *α*-Sn and metallic *β*-Sn layers. As reported recently, the compound $Ca_{18}Li_5In_{25.07}$[138] represents a new three dimensional network in which layers of electron deficient indium clusters exhibiting delocalized cluster bonding are intergrown with Zintl layers of electron precise covalently bonded In atoms. Nevertheless, band structure calculations revealed the metallic character of that electron deficient metallic Zintl phase.

Application of Zintl's electron counting scheme to $Na_{20}Zn_8Sn_{11}$ results in $(Zn_8Sn_{11})^{20-}$ for the anionic part that are counterbalanced by 20 Na^+. According to Wade's rules the $\{Zn_7Sn_5\}$ icosahedron should be electron precise with 26 skeletal electrons, as in $\{B_{12}H_{12}\}^{2-}$. Taking into account the eight *exo*-bonds and four electron lone pairs the available electrons for cluster bonding are reduced from 34 to 18 (34 – (8 × 1) – (4 × 2)) and therefore a negative charge of 8– has to be assigned to each icosahedron. On assumption of the same highly charged unit $\{ZnSn_2\}^{6-}$ (as found in Na_6ZnSn_2), the remaining Sn atoms and the ratio of all anions per formula unit (one $\{Zn_7Sn_5\}^{8-}$, one $\{ZnSn_2\}^{6-}$, two 3b-$Sn1^-$, and two 1b-$Sn4^{3-}$) the compound is two electrons short. Interestingly, the compound would be electron precise neglecting the mixed occupied position and assuming full occupancy by Sn, which would lower the electron demand by two. However, the significant site occupancy factors on refinement cannot be neglected. Defects in atomic positions, preferentially located at *exo*-bonded icosahedral vertices, in homoatomic $\{Tr_{12}\}$ icosahedra (Tr = Ga, In) have been reported to be fairly common. In that case, these vacancies have an electronic origin associated with an electron counting scheme that optimizes the occupancy of cluster bonding levels.[82, 90] Without electronic structure calculations a final statement on the nature of this compound, be it an electron deficient metallic or an electron precise Zintl phase is difficult.

Quantum chemical calculations should involve the two component layers with ideal 100% occupancies. As a speculation, magnetic susceptibilty measurements might show weak temperature independent paramagnetism that originates from incomplete valence bands or overlapping of filled valence bands with empty conduction bands to show the poor metallic character of this compound. Additionally, low temperature X-ray diffraction experiments might provide further information on the atomic disorder.

4.9 General Discussion

The new ternary compounds synthesized in the system Na–Zn–Sn reflect the smooth transition of chemical bonding when tuning the valence electron concentration. Based on the crystallographically determined average compositions the phases can be marked in the phase triangle (Figure 4.53). Compounds doped with slight amounts of Zn on the Na poor and tin rich side should or were expected to contain anionic substructures consistently built up of four bonded atoms, reminiscent of those found in clathrates or diamond. Reminiscent to the Grimm-Sommerfeld rule at more balanced Zn : Sn ratios the covalent motifs compete with motifs that can be found in trielide structures. The electron deficiency in such intermetallic compounds is reflected by the formation of multicenter 2-electron bonds that leads to the formation of linked cluster units in complex 3D networks. This happens in order to compensate the lack of electrons (Na counterions) in less reduced environments. On the Na rich side the icosahedral clusters competed with smaller highly charged anions.

The reported less reduced ternary phases of the system Na–Zn–Sn (Chapter 4), containing icosahedral clusters share the same structural feature: Kagomé layers made of icosahedra with different embedded structure motifs. Another point is the significant and ubiquitous occupational disorder, which reflects their relationship to the intermetallic gallide and indide phases, which are often non-stoichiometric in composition and contain defective deltahedra. With respect to the different individual icosahedra found in the ternary compounds the question arises of how such a network of interconnect icosahedra is *colored*, i.e., how do the two types of atoms (Zn and Sn) arrange themselves over the twelve icosahedral sites and why are some icosahedra ordered whereas others are not? In Table 4.30 the average compositions together with the average VEC per cluster atom of individual icosahedra presented within Chapter 4 are summarized. On average, the surface of each icosahedron is randomly decorated with ($7.64 \pm \sigma$) Zn and ($4.36 \mp \sigma$) Sn atoms. The observed amounts of the two elements are forced to this ratio in order to fulfill valence electronic requirements for cluster stabilization, which were formulated in a rule found by Burdett et al.[82, 91] (the preference for three-member is replaced by six-member rings at an average VEC/cluster atom of ~ 3.5) and is based on the method of moments.[100] The valence electron concentration per cluster atom of the different icosahedra varies from 3.17 to 3.50 which is still in perfect agreement with that.

The different icosahedra were analyzed closer by counting the different types of intra- and intercluster contacts, shown as histograms in Figure 4.54.

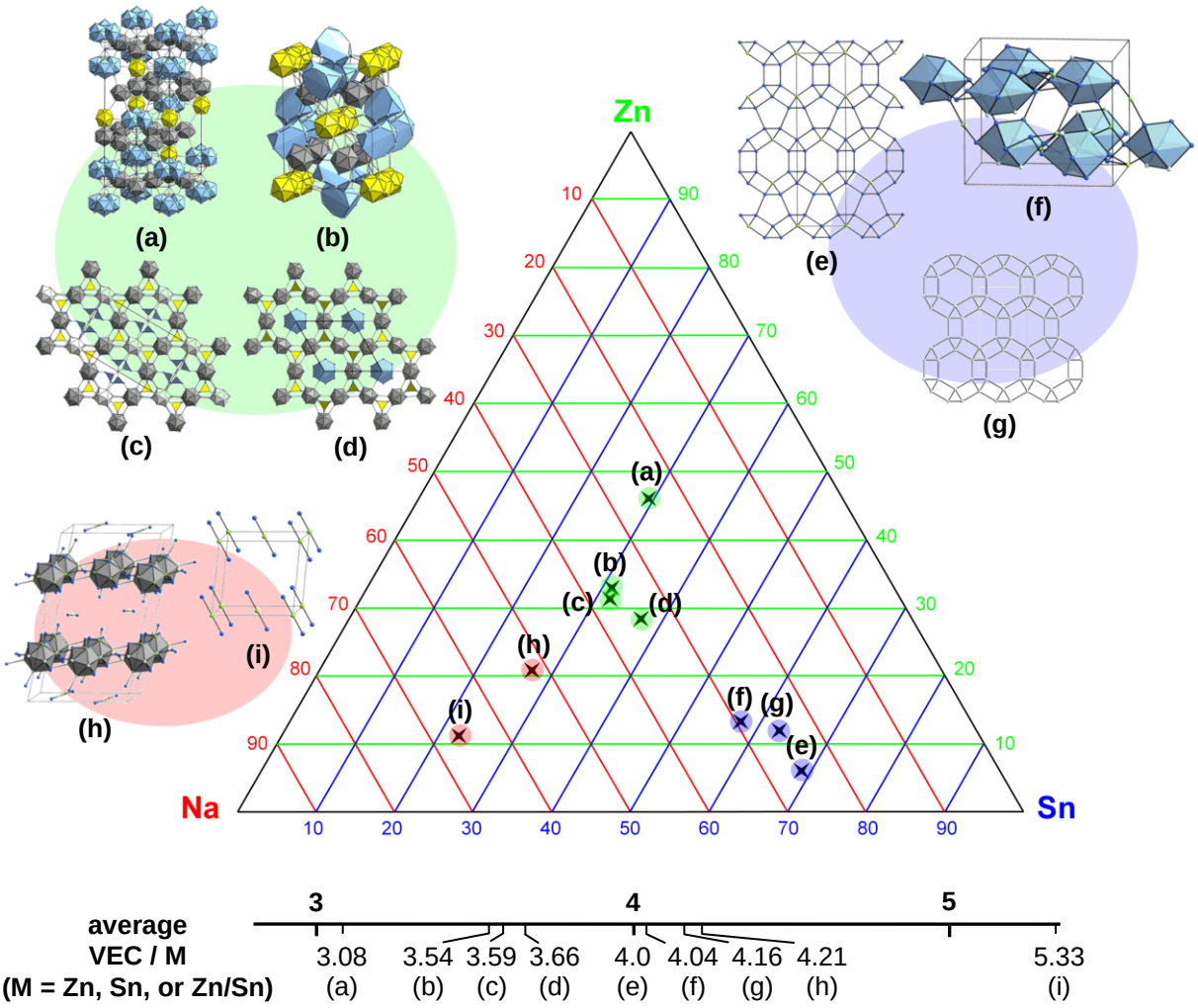

***Figure 4.53*. Structure motifs of the new ternary compounds found in the system Na–Zn–Sn (Na atoms are omitted). The average compositions of the discovered phases - stable at room temperature - are marked with a star (possible phase widths are not marked). The corresponding average values of VEC / M are shown. Compounds: (a) $Na_{34}Zn_{65}Sn_{40(1)}$; (b) $Na_{22}Zn_{20}Sn_{19(1)}$; (c) $Na_{16}Zn_{13.54}Sn_{13.47(5)}$; (d) $Na_{29}Zn_{24}Sn_{32}$; (e) Na_2ZnSn_5; (f) $Na_5Zn_{2.28}Sn_{9.72(2)}$; (g) $NaZn_{0.3}Sn_{2.7(1)}$; (h) $Na_{20}Zn_8Sn_{11}$; (i) Na_6ZnSn_2.**

***Table 4.30*: Average compositions and VEC per cluster atom of the different icosahedra found in selected ternary compounds of this thesis.**

compound	icosahedron*	VEC / cluster atom
$Na_{29}Zn_{24}Sn_{32}$	$\{Zn_8Sn_4\}^{8-}$	3.33
	($\{Zn_8Sn_4\}^{6-}$) (see Chapter 4.4)	(3.17)
$Na_{16}Zn_{13.54}Sn_{13.47(5)}$	$\{Zn_8Sn_4\}^{8-}$	3.33
	$\{Zn_{8.09}Sn_{3.91}\}^{6.18-}$	3.17
$Na_{34}Zn_{65}Sn_{40(1)}$	$\{Zn_{7.32}Sn_{4.78}\}^{4.64-}$	3.20
	$\{Zn_{7.38}Sn_{4.62}\}^{4.76-}$	3.17
$Na_{22}Zn_{20}Sn_{19(1)}$	$\{Zn_{7.06}Sn_{4.94}\}^{7.12-}$	3.42
	$\{Zn_{8.27}Sn_{3.73}\}^{6.54-}$	3.17
$Na_{11}Zn_8Sn_{20}$	$\{Zn_7Sn_5\}^{8-}$	3.50

*) charges according to an electron precise *closo*-cluster

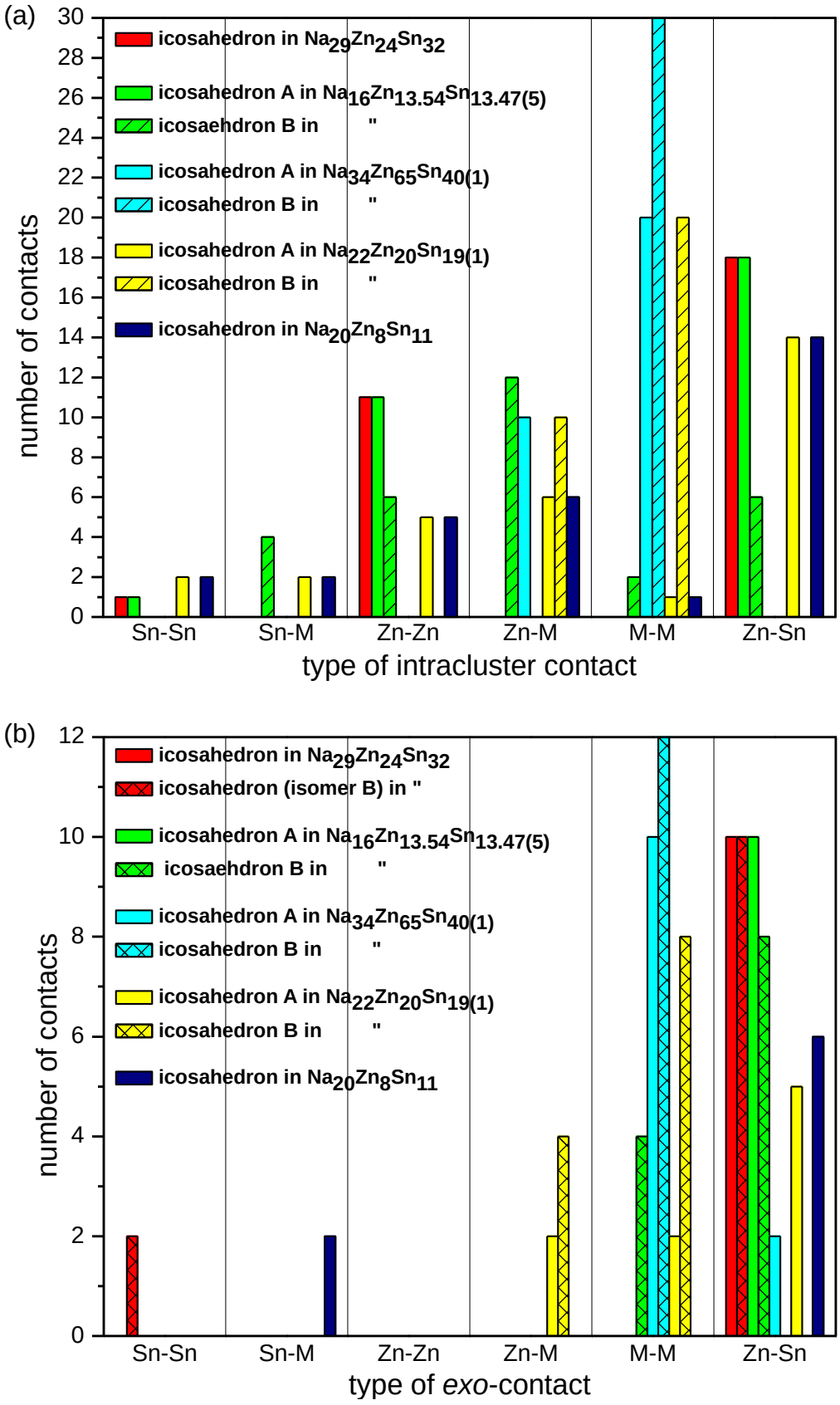

***Figure 4.54*. (a) Histogram of intracluster bonds. (b) Histogram of *exo*-contacts of nine individual Zn–Sn icosahedra found within this thesis. ('isomer B' denotes the connectivity of the icosahedron if isomer B of the {Sn_{14}} enneahedron is present, see Chapter 4.4).**

The distribution of the intracluster bonds reveals that heteroatomic Zn–Sn and M–M contacts (M = statistical Zn / Sn occupancy) are most frequent followed by Zn–M and Zn–Zn bonds. Sn–M and homoatomic Sn–Sn contacts are rather rare. This means that the number of heteroatomic contacts is maximized, whereas it is minimized for homoatomic contacts. This is even more significant regarding the *exo*-contacts, where Sn–Sn bonding is only present for very specific reasons (see Chapter 4.4). General enumeration of number and composition of polytypes, which is related to combinatorial problems in mathematics, of two colored icosahedra, based on Polya's theorem,[139] have been reported by Teo et al.[140] For example, for the non-centrosymmetric $\{Zn_8Sn_4\}$ a total of 12! / (8! × 4!) = 495 arrangements in space are distinguishable, only 12 of which are stereoisomers with different valence electron energies. The presence of statistically occupied positions M adds a further variable and the different numbers of icosahedra per unit cell increases the amount of possible colorings of the three dimensional networks. Synthetic investigations (annealing experiments) indicate that no ordering of Zn and Sn on the icosahedra occurs, also at lower temperatures. As in most cases linking between the icosahedra is present *there is little energetic driven force for the ordering of Zn and Sn with entropic effects at elevated temperatures certainly favoring the disordered arrangement of atoms. Nevertheless, there may be enthalpic influences that limit the local structure of each icosahedron yet do not affect the crystallographic results*.[141]

In the present icosahedra the preference for heteroatomic contacts can be explained by attaining lower energy configurations according to the following rules:

a) Maximizing separations between two Sn atoms,
   and at the same time
b) Maximizing the number of heteroatomic contacts.

Although no evaluation of relative energy configurations are provided, this observations are in agreement with results from Miller et al.[141] who evaluated different colorings of $\{Au_4Al_8\}$ and $\{Cu_4Al_8\}$ icosahedra with EH calculations and found a linear dependency of energy and number of homoatomic contacts. Usually, the energy differences between colorings are small enough to assume that a mixture of several or all of these colorings contributes to the disorder observed in the X-ray diffraction experiment. In addition to this, the compound's effort to attain overall closed shell configuration has to be taken into account.

4.10 References

[1] W. Müller, K. Volk, *Z. Naturforsch.* **1977**, *32 B*, 709.
[2] K. Wade, *J. Chem. Soc. D* **1971**, 792.
[3] K. Wade, *Adv. Inorg. Chem. Radiochem.* **1976**, *18*, 1.
[4] S. Hoffmann, T. F. Fässler, *Inorg. Chem.* **2003**, *42*, 8748.
[5] F. Dubois, M. Schreyer, T. F. Fässler, *Inorg. Chem.* **2005**, *44*, 477.
[6] J. T. Vaughey, J. D. Corbett, *Inorg. Chem.* **1997**, *36*, 4316.
[7] C. Kronseder, T. F. Fässler, *Angew. Chem.* **1998**, *110*, 1641.
[8] E. B. Evans, I. Thompson, U. Erb, *J. Mater. Sci. Lett.* **1987**, *6*, 806.
[9] J. E. Lee, *Mater. Trans* **2005**, *46*, 2413.
[10] D. G. Pettifor, *Solid State Commun.* **1984**, *51*, 31.
[11] D. G. Pettifor, *Solid State Phys.* **1986**, *19*, 285.
[12] A. Guloy, R. Ramlau, Z. Tang, W. Schnelle, M. Baitinger, Y. Grin, *Nature* **2006**, *443*, 320.
[13] H. U. Schuster, *Naturwiss.* **1966**, *53*, 361.
[14] B. Eisenmann, N. May, W. Müller, H. Schäfer, *Z. Naturforsch.* **1972**, *27*, 1155.
[15] F. Merlo, M. L. Fornasini, M. Pani, *J. Less-Comm. Met.* **1991**, *171*, 329.
[16] V. Kuntze, K. Gebhardt, H. Hillebrecht, *Z. Kristallogr.* **1997**, *212*, 840.
[17] M. Jansen, C. Schön, *Angew. Chem.* **2006**, *118*, 3484.
[18] H. Schoenemann, H. U. Schuster, *Z. Anorg. Allg. Chem.* **1977**, *432*, 87.
[19] K. Kuriyama, M. Yahagi, K. Iwamura, *Z. Naturforsch.* **1978**, *33 B*, 115.
[20] H. O. Cullmann, H. W. Hinterkeuser, H. U. Schuster, *Z. Naturforsch.* **1981**, *36 B*, 917.
[21] R. Matthes, H. U. Schuster, *Z. Naturforsch.* **1980**, *35 B*, 778.
[22] E. Todorov, S. C. Sevov, *Angew. Chem. Int. Ed.* **1999**, *38*, 1775.
[23] H. U. Schuster, *Z. Anorg. Allg. Chem.* **1969**, *370*, 149.
[24] E. Todorov, S. C. Sevov, *J. Am. Chem. Soc.* **1997**, *119*, 2869.
[25] R. Matthes, H. U. Schuster, *Z. Naturforsch.* **1979**, *34 B*, 541.
[26] F. Chevire, F. J. DiSalvo, *Acta Crystallogr.* **2007**, *63 E*, 62.
[27] V. Queneau, S. C. Sevov, *J. Am. Chem. Soc.* **1997**, *119*, 8109.
[28] E. Todorov, S. C. Sevov, *Inorg. Chem.* **1997**, *36*, 4298.
[29] W. Blase, G. Cordier, *Z. Naturforsch.* **1988**, *43 B*, 1017.
[30] W. Blase, G. Cordier, R. Kniep, R. Schmidt, *Z. Naturforsch.* **1989**, *44 B*, 505.
[31] J. T. Vaughey, J. D. Corbett, *J. Am. Chem. Soc.* **1996**, *118*, 12098.
[32] Zeolite Database, *http://www.iza-structure.org/databases*.
[33] W. B. Pearson, *The Crystal Chemistry and Physics of Metals and Alloys; Wiley-Interscience, New York* **1972**.
[34] H. G. Von Schnering, **1994**, private communication.
[35] R. Kröner, *Dissertation, Universität Stuttgart* **1989**.
[36] L. Pauling, *J. Am. Chem. Soc.* **1947**, *69*, 542.
[37] L. Pauling, *Die Natur der chemischen Bindung, Verlag Chemie, Weinheim* **1968**.
[38] G. J. Miller, *Eur. J. Inorg. Chem.* **1998**, 523.
[39] J. Burdett, N. J. Lawrence, J. J. Turner, *Inorg. Chem.* **1984**, *23*, 2419.
[40] E. Todorov, S. C. Sevov, *Inorg. Chem.* **1998**, *37*, 6341.
[41] B. Li, J. D. Corbett, *Inorg. Chem.* **2007**, *46*, 6022.
[42] X. J. Wu, Y. Fujika, M. Ishigame, S. Horiuchi, *Acta Crystallogr.* **1991**, *47 A*, 405.
[43] M. F. Lulei, J. D. Corbett, *Eur. J. Solid State Inorg. Chem.* **1996**, *33*, 241.
[44] A. K. Cheetham, G. Ferey, T. Loiseau, *Angew. Chem. Int. Ed.* **1999**, *28*, 3268.
[45] J. Gallmeier, H. Schäfer, A. Weiss, *Z. Naturforsch.* **1969**, *24 B*, 665.
[46] C. Cros, M. Pouchard, P. Hagenmuller, *J. Solid State Chem.* **1970**, *2*, 570.
[47] S. Bobev, S. C. Sevov, *Inorg. Chem.* **2000**, *39*, 5930.
[48] S. Ponou, S.-J. Kim, T. F. Fässler, **2007**, in preparation.
[49] B. Li, J. D. Corbett, *Inorg. Chem.* **2006**, *45*, 2960.
[50] A. V. Mudring, J. D. Corbett, *J. Am. Chem. Soc.* **2004**, *126*, 5277.

[51] S. Ponou, T. F. Fässler, *Inorg. Chem.* **2004**, *43*, 6124.
[52] H. Nowotny, W. Sibert, *Z. Metallkunde* **1941**, *33*, 391.
[53] *Thermoelectric Materials 2000, edited by T. M. Tritt, G. S. Nolas, G. Mahan, M. G. Kanatzidis, and D. Mandrus, MRS Symposium Proceedings No. 626, Materials Research Society, Pittsburgh, 2000.*
[54] P. Larson, S. D. Mahanti, J. Salvador, M. G. Kanatzidis, *Phys. Rev.* **2000**, *74B*, 35111.
[55] K. Volk, W. Müller, *Z. Naturforsch.* **1978**, *33B*, 598.
[56] T. F. Fässler, *Z. Anorg. Allg. Chem.* **1998**, *624*, 569.
[57] A. L. Spek, *PLATON, A Multipurpose Crystallographic Tool, Universität Utrecht* **2006**.
[58] S. Alvarez, *Dalton Trans.* **2005**, 2209.
[59] R. M. Imamov, Z. G. Pinsker, *Kristallografiya* **1966**, *11*, 182.
[60] M. Stackelberg, H. R. Müller, *J. Chem. Phys.* **1951**, *19*, 1913.
[61] *Metal Clusters in Chemistry (Eds.: P. Braunstein, L. A. Oro, P. R. Raithby), Wiley–VCH, Weinheim, 1999*.
[62] *Clusters and Colloids: From Theory to Applications (Ed.: G. Schmid), VCH, Weinheim, 1994.*
[63] *Molecular Clusters of the Main Group Elements (Eds.: M. Driess, H. NNth), Wiley–VCH, Weinheim, 2004.*
[64] M. Brynda, R. Herber, P. B. Hitchcock, M. F. Lappert, I. Nowik, P. P. Power, A. V. Protchenko, A. Ruzicka, J. Steiner, *Angew. Chem.* **2006**, *118*, 4325.
[65] A. Schnepf, H. Schnöckel, *Angew. Chem.* **2002**, *114*, 3682.
[66] J. D. Corbett, *Angew. Chem.* **2000**, *112*, 682.
[67] M. Tillard-Charbonnel, C. Belin, *Prog. Solid State Chem.* **1993**, *22*, 59.
[68] T. F. Fässler, S. D. Hoffmann, *Angew. Chem.* **2004**, *116*, 6400.
[69] A. Ecker, E. Weckert, H. Schnöckel, *Nature* **1997**, *387*, 379.
[70] C. Klemp, R. Köppe, E. Weckert, H. Schnöckel, *Angew. Chem.* **1999**, *111*, 1851.
[71] J. Steiner, G. Stösser, H. Schnöckel, *Z. Anorg. Allg. Chem.* **2004**, *630*, 1879.
[72] E. Busmann, *Z. Anorg. Allg. Chem.* **1961**, *313*, 90.
[73] W. Klemm, *Proc. Chem. Soc. London* **1958**, 329.
[74] E. Zintl, *Angew. Chem.* **1939**, *52*, 1.
[75] C. Belin, M. Tillard-Charbonnel, *J. Solid State Chem.* **1986**, *64*, 57.
[76] M. Charbonnel, C. Belin, *Nouv. J. Chim.* **1984**, *10*, 595.
[77] M. Charbonnel, C. Belin, *J. Solid State Chem.* **1987**, *67*, 210.
[78] G. Cordier, V. Müller, *Z. Naturforsch.* **1995**, *50 B*, 23.
[79] M. Tillard-Charbonnel, N. Chouaibi, C. Belin, J. Lapasset, *J. Solid State Chem.* **1992**, *100*, 220.
[80] D. M. Flot, M. Tillard-Charbonnel, C. Belin, *J. Am. Chem. Soc.* **1996**, *118*, 5229.
[81] R. Nesper, *Angew. Chem. Int. Ed.* **1989**, *28*, 58.
[82] J. Burdett, E. Canadell, *Inorg. Chem.* **1991**, *30*, 1991.
[83] S. P. Mallela, Y. Saar, S. Hill, R. A. Geanangel, *Inorg. Chem.* **1999**, *38*, 2957.
[84] M. Tillard-Charbonnel, A. Manteghetti, C. Belin, *Inorg. Chem.* **2000**, *39*, 1684.
[85] Z. C. Dong, J. D. Corbett, *J. Am. Chem. Soc.* **1990**, *117*, 6447.
[86] C. Belin, *Acta Crystallogr.* **1981**, *B37*, 2060.
[87] D. P. Shoemaker, R. E. Marsh, F. J. Ewing, L. Pauling, *Acta Crystallogr.* **1952**, *5*, 637.
[88] J. Adam, J. B. Rich, *Acta Crystallogr.* **1954**, *7*, 813.
[89] M. Tillard-Charbonnel, C. Belin, A. Manteghetti, D. M. Flot, *Inorg. Chem.* **1996**, *35*, 2583.
[90] C. Belin, M. Tillard-Charbonnel, *Coord. Chem. Rev.* **1998**, *178-180*, 529.
[91] J. Burdett, E. Canadell, *J. Am. Chem. Soc.* **1990**, *112*, 7207.
[92] D. St. Clair, A. Zalkin, D. H. Templeton, *J. Am. Chem. Soc.* **1970**, *92*, 1173.
[93] C. Belin, R. G. Ling, *C. R. Acad. Sci. Ser. B* **1982**, *294*, 1083.
[94] R. Naslain, A. Guette, M. Barret, *J. Solid State Chem.* **1973**, *8*, 68.
[95] B. Li, J. D. Corbett, *Inorg. Chem.* **2006**, *45*, 8958.
[96] R. G. Ling, C. Belin, *Acta Crystallogr.* **1982**, *38 B*, 1101.
[97] U. Frank-Cordier, G. Cordier, H. Schäfer, *Z. Naturforsch.* **1982**, *37B*, 119.

[98] U. Frank-Cordier, G. Cordier, H. Schäfer, *Z. Naturforsch.* **1982**, *37B*, 127.
[99] G. Cordier, V. Müller, *Z. Kristallogr.* **1992**, *198*, 302.
[100] J. Burdett, S. Lee, *J. Am. Chem. Soc.* **1985**, *107*, 3050.
[101] R. B. King, *Inorg. Chem.* **1989**, *28*, 2796.
[102] B. Li, J. D. Corbett, *J. Am. Chem. Soc.* **2005**, *127*, 926.
[103] W. F. Claussen, *J. Chem. Phys.* **1951**, *19*, 1425.
[104] C. Belin, M. Charbonnel, *J. Solid State Chem.* **1986**, *64*, 57.
[105] W. Müller, K. Volk, *Z. Naturforsch.* **1978**, *33B*, 275.
[106] J. D. Corbett, *Chem. Rev.* **1985**, *85*, 383.
[107] J. M. Goicoechea, S. C. Sevov, *Organometallics* **2006**, *25*, 5678.
[108] P. Manfrinetti, M. Pani, *J. Alloys Compd.* **2005**, *393*, 180.
[109] M. Lutz, B. Findeis, M. Haukka, R. Graff, P. A., L. H. Gade, *Chem. Eur. J.* **2002**, *8*, 3269.
[110] J. T. B. H. Jastrzebski, H. A. J. Sypkens, F. J. A. des Tombe, J. Boersma, G. von Koten, A. L. Spek, A. J. M. Duisenberg, *J. Organomet. Chem.* **1990**, *396*, 25.
[111] I. Resa, E. Carmona, E. Gutierrez-Puebla, A. Monge, *Science* **2004**, *305*, 1136.
[112] G. Savelsberg, H. Schäfer, *Z. Naturforsch.* **1979**, *34 B*, 771.
[113] B. Eisenmann, J. Klein, M. Somer, *J. Alloys Compd.* **1992**, *178*, 431.
[114] M. Somer, W. Carillo-Cabrera, K. Peters, H. G. Von Schnering, *Z. Anorg. Allg. Chem.* **2000**, *626*, 897.
[115] Basis Set Exchange: A Community Database for Computational Sciences Schuchardt, K.L., Didier, B.T., Elsethagen, T., Sun, L., Gurumoorthi, V., Chase, J., Li, J., and Windus, T.L. J. Chem. Inf. Model., **2007**, 10.1021/ci600510j
[116] L. Xu, A. Ugrinov, S. C. Sevov, *J. Am. Chem. Soc.* **2001**, *123*, 4091.
[117] F. Gascoin, S. C. Sevov, *J. Am. Chem. Soc.* **2000**, *122*, 10251.
[118] F. Gascoin, S. C. Sevov, *Inorg. Chem.* **2001**, *40*, 5177.
[119] M. Somer, M. Hartweg, K. Peters, T. Popp, H. G. von Schnering, *Z. Anorg. Allg. Chem.* **1991**, *595*, 217.
[120] H. G. von Schnering, M. Somer, M. Hartweg, K. Peters, *Angew. Chem.* **1990**, *102*, 63.
[121] B. Eisenmann, M. Somer, *Z. Naturforsch.* **1989**, *44 B*, 1228.
[122] J. Goubeau, W. Anselment, *Z. Anorg. Allg. Chem.* **1961**, *310*, 248.
[123] M. Häberlen, J. Glaser, H. J. Meyer, *J. Solid State Chem.* **2005**, *178*, 1478.
[124] O. Reckeweg, F. J. DiSalvo, H. J. Meyer, *Z. Anorg. Allg. Chem.* **1999**, *625*, 1408.
[125] O. Reckeweg, H. J. Meyer, *Angew. Chem.* **1998**, *110*, 3619.
[126] B. Eisenmann, M. Somer, *Z. Naturforsch.* **1984**, *41 B*, 736.
[127] J. Wolf, D. Weber, H. G. Von Schnering, *Z. Naturforsch.* **1986**, *41 B*, 731.
[128] T. F. Fässler, A. Savin, *Chemie in unserer Zeit* **1997**, *3*, 110.
[129] A. Savin, R. Nesper, S. Wengert, T. F. Fässler, *Angew. Chem.* **1997**, *109*, 1892.
[130] R. F. W. Bader, *An Introduction to the Electronic Structure of Atoms and Molecules, Clarke, Toronto* **1970**.
[131] R. F. W. Bader, *Atoms in Molecules (Oxford, New York)* **1994**.
[132] U. Englich, K. Ruhland-Senge, F. Uhlig, *J. Organomet. Chem.* **2000**, *613*, 139.
[133] S. L. Brock, S. M. Kauzlarich, *CHEMTECH* **1995**, *25*, 18.
[134] R. J. Cava, H. W. Zandbergen, J. J. Krajewski, T. Siegrist, H. Y. Hwang, B. Batlogg, *J. Solid State Chem.* **1997**, *129*, 250.
[135] A. Guloy, J. Goodey, *Condens. Matter News* **1998**, *7*, 24.
[136] A. K. Ganguli, Y.-U. Kwon, J. D. Corbett, *Inorg. Chem.* **1993**, *32*, 4354.
[137] F. Zürcher, S. Wengert, R. Nesper, *Inorg. Chem.* **1999**, *38*, 4567.
[138] J. G. Mao, J. Goodey, A. M. Guloy, *Inorg. Chem.* **2004**, *43*, 282.
[139] G. Polya, *Acta Math.* **1937**, *68*, 145.
[140] B. K. Teo, H. Zhang, Y. Kean, H. Dang, X. Shi, *J. Phys. Chem.* **1993**, *99*, 2929.
[141] K. Nordell, G. J. Miller, *Inorg. Chem.* **1999**, *38*, 579.

5 Substitution Effects in Sr_2Bi_3 and Sr_3Sn_5

5.1 The System $Sr_{2-x}Ba_xBi_3$ ($0 \leq x \leq 1.3$) - Structural Distortions Induced by Chemical Pressure

5.1.1 Introduction

Intermetallic systems namely between *s*-block metals and metallic *p*-block elements often require an extension of the Zintl concept due to the far more diverse and complex structures and bonding situations. Therefore, bonding in such intermetallic compounds is intermediate between semiconducting Zintl phases and *s*-*p* bonded metallic systems with completely delocalized bonding electrons. Additionally, other factors such as optimization of Madelung energy, space filling, and the often underestimated stabilizing effect from the electropositive element, i.e. covalent cation–anion interactions that often help to maximize bonding energies.[1-5]

The alkaline earth bismuthides are good candidates to show the interesting interplay between various bond types. On the one hand the pnictide richest compounds such as cubic $SrBi_3$[6] ($AuCu_3$-type) and tetragonal $BaBi_3$[6] (distorted $AuCu_3$-type) represent pure intermetallic compounds, on the other hand there are electron precise Zintl phases such as tetragonal $Ae_{11}Bi_{10}$ with square $\{Bi_4\}^{4-}$ units (*d*(Bi-Bi) 3.275(5) to 3.286(4) Å) and $\{Bi_2\}^{4-}$ dumbbells (*d*(Bi-Bi) = 3.187(3) and 3.152(3) Å) exist for Ae = Ca, Sr, Ba ($Ho_{11}Ge_{10}$ structure type).[7, 8] However, many bismuthides show deviations when applying simple electron counting rules and have to be discussed in a more diverse way. The structures on the Ae-richer side can be traced back to Zintl type compounds, but with extra (metallic) electrons, such as tetragonal Ae_2Bi[9] (Ae = Ca, Sr, Ba; La_2Sb structure type) with isolated $\{Bi\}^{3-}$ and one extra electron or hexagonal Ae_5Bi_3[10] (Ae = Sr, Ba; Mn_5Si_3 structure type) as well as orthorhombic Ca_5Bi_3[11] (Yb_5Sb_3 structure type), both again with isolated $\{Bi\}^{3-}$ and one extra electron. Electron deficient phases are observed for cubic Ae_4Bi_3[12] (Ae = Sr, Ba; anti Th_3P_4 structure type) with formally isolated $\{Bi\}^{2.67-}$ and metallic property. Additionally, extended Bi structures such as one-dimensional $^1_\infty[Bi^-]$ zigzag chains and $^2_\infty[Bi^-]$ square sheets are present in orthorhombic $CaBi_2$[13] ($ZrSi_2$-type) and tetragonal $BaBi_2$[14] ($HfGa_2$-type), respectively. As reported the orthorhombic phase Sr_2Bi_3[13] contains infinitely extended slabs of three (3b)- and two bonded (2b)-Bi atoms. Based on the assumption of a full charge transfer from Sr to the anionic network the ionic formula splitting $[(3b\text{-}Bi^0)_2(2b\text{-}Bi^-)]$ exceeds the required number of

electrons by three. A similar situation can be found in Ba_2Bi_3 (space group *Immm*)[15] that crystallizes in the W_2CoB_2 structure type (Figure 5.1). The anionic substructure shows a layered structure with planar two-dimensional $(4.6.4.6)(4.6^2)_2$ nets with (4b)- and (3b)-Bi atoms. A local description of the chemical bond is possible using a non-classical bond description and involves one extra (metallic) electron. So, in contrast to the majority of other Ae pnictides that involve polyanionic networks, bonding and structure change dramatically by altering the Ae metal in the Ae_2Bi_3 structure. In contrast to the features in Ba_2Bi_3, Sr_2Bi_3 contains a one-dimensional Bi polymer and represents an interesting case study of how the interplay between electronic factors, such as cation-anion interactions and cation size, determine the structure and bonding of such borderline polar intermetallic compounds.

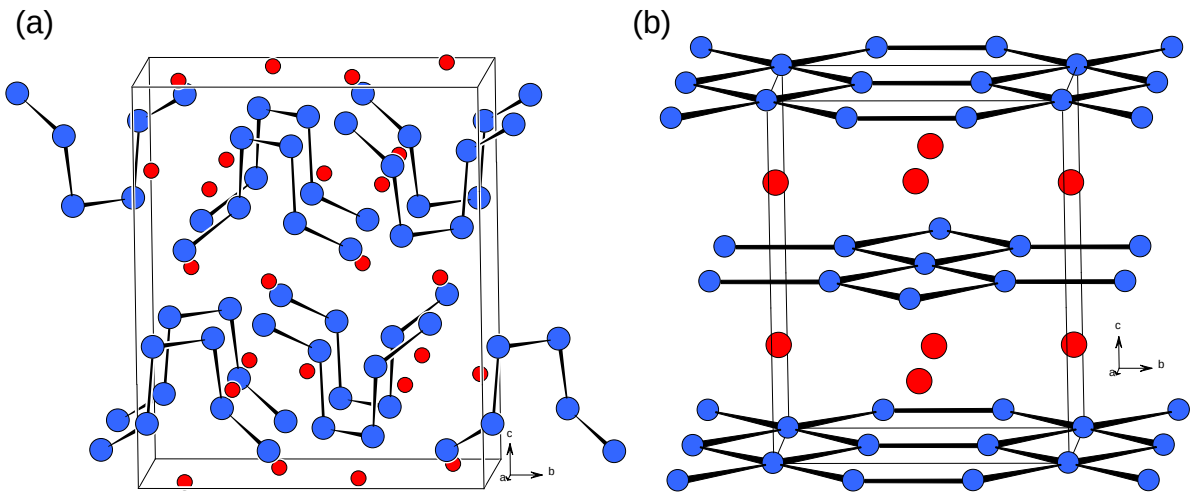

***Figure 5.1*. The unit cell of (a) Sr_2Sb_3 and (b) Ba_2Bi_3. Pnictide atoms (blue), Ae cations (red).**

5.1.2 Synthesis and Characterization

Synthesis Single-crystals of the substitution series $Sr_{2-x}Ba_xBi_3$ for x = 0, 0.45, 0.86, 1.08, and 1.28 were obtained from stoichiometric sample loadings Sr : Ba : Bi = (2–y) : y : 3 with y = 0, 0.4, 0.8, 1.0, and 1.2, respectively. The compounds were prepared from total loadings of 1.500 g. The pure elements were handled and crucibles were loaded in an Ar-filled glovebox. Sr, Ba and Bi were weighted into Nb ampoules and sealed under reduced Ar atmosphere. The crucibles were subsequently enclosed in evacuated silica tubes, heated to 850 °C at a rate of 2 $K \cdot min^{-1}$, slowly cooled (0.1 $K \cdot min^{-1}$) to 550 °C, and annealed at this temperature for five days. The crystalline products exhibit metallic lustre and are air sensitive.

EDX Measurements Qualitative and quantitative analysis were carried out on different crystallites from each sample by use of a JEOL 5900LV scanning electron microscope. All measurements proved the presence of the expected elements with atomic concentrations that were in the range of the calculated values. Due to the rather big standard deviations of the measurements only rough distinctions between the crystal compositions could be made.

Powder X-ray Diffraction Powder diffraction data of the products of samples loaded as Sr : Ba : Bi = (2–y) : y : 3 (y = 0, 0.2, 0.4, 0.6, 0.8, 1.0, 1.2) were carried out in Debye-Scherrer mode on a STOE STADI P powder diffractometer equipped with a position sensitive detector (PSD) using Cu $K_{\alpha 1}$ radiation (λ = 1.540598 Å). The patterns where indexed and refined using the software package WinXPOW (STOE). The powder diagrams for products with loadings Sr : Ba : Bi = (2–y) : y : 3 (y = 0, 0.2, 0.4, 0.6, 0.8, 1.0, 1.2) are shown in Figure 5.2. Due to decreasing crystallinity and higher absorption of the samples with higher Ba loadings the samples were diluted with glass. This caused the broad amorphous background shoulder in the area of 2θ = 20° to 30°. However, this treatment was necessary to obtain acceptable intensities. Measuring times were 16 h with a step width of 1.5°. As shown, with increasing Ba content the Bragg positions are shifted to lower diffraction angles and at the same time some reflections (e.g. ~ 30° area) change their intensities.

Magnetic Properties The magnetic property measurements were carried out on a MPMS XL SQUID-Magnetometer (Quantum Design). 51.9 mg of a sample with loading y = 1.0 and 50.0 mg of a sample with y = 0.4 were cooled in the absence of a magnetic field checked by an external Hall probe. Subsequent to the introduction of a 100 Oe field data was collected while the samples were warmed (“shielding”) and then cooled (“Meissner”). The magnitudes of the shielding fraction indicate that the samples are in a superconducting state below T_C. Suprasil silica capillaries (5 mm diameter) served as sample holders. For further details see Chapter 5.1.5.

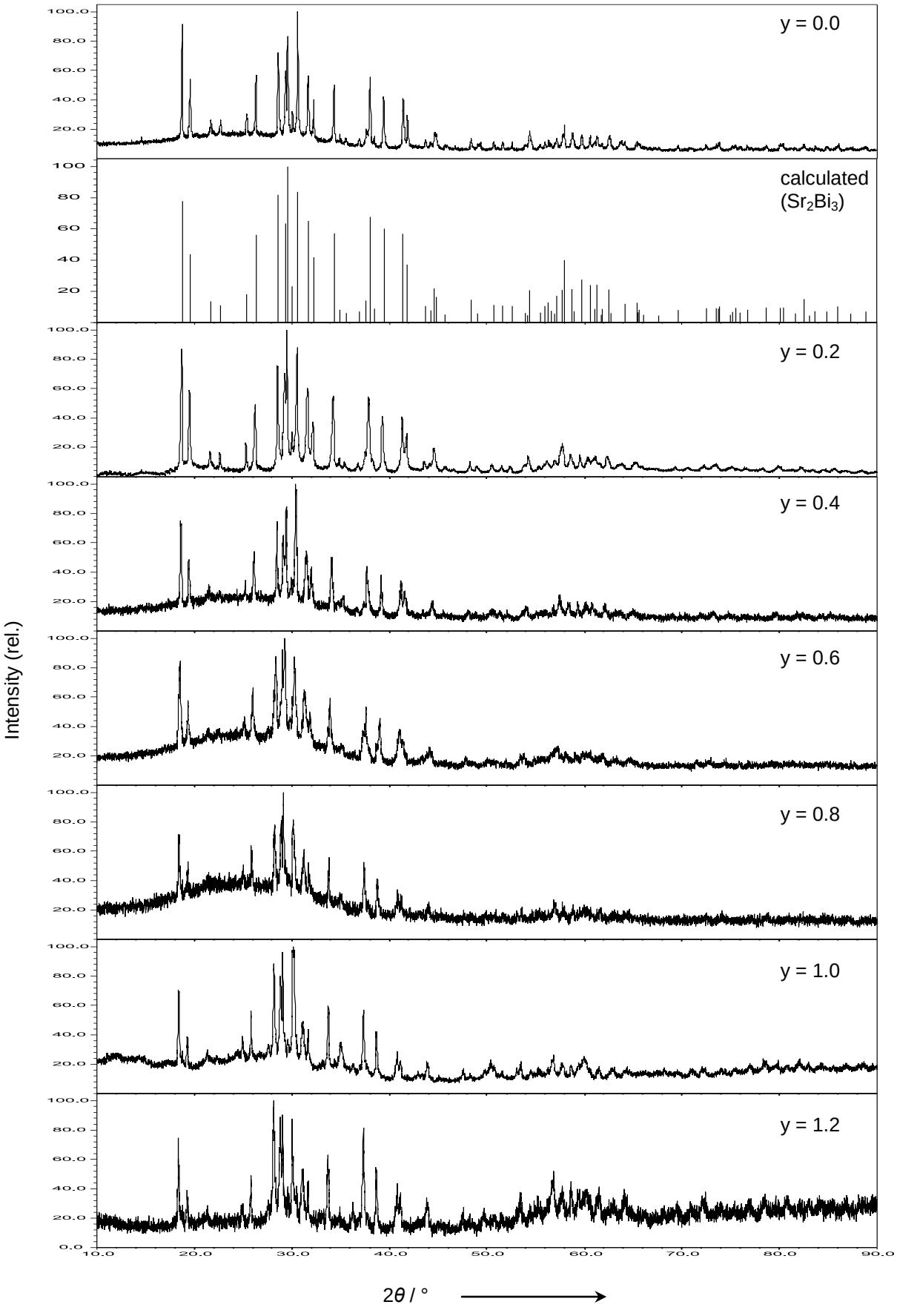

***Figure 5.2*. Experimental powder diagrams from sample loadings $Sr_{2-y}Ba_yBi_3$ (y = 0 to 1.2). The basic pattern is preserved with gradual changes in the intensity distribution and Bragg positions of the reflections.**

5.1.3 Crystal Structure Determination and Description of Sr_2Bi_3 and $Sr_{2-x}Ba_xBi_3$

Structure Determination Single-crystals were picked from each sample that was loaded with $Sr_{2-y}Ba_yBi_3$ (y = 0, 0.4, 0.8, 1.0, 1.2). Each crystal was checked for singularity, placed on a glass tip and sealed into a capillary. Reflection data sets were collected at room temperature using a Nonius κ-CCD (x = 0, 0.86), an Oxford Xcalibur3 (CCD detector) (x = 0.45), and a Nonius DIP2020 (Image plate) (x = 1.08, 1.28) single-crystal diffractometer. All operated with Mo Kα radiation (λ = 0.71073 Å). Absorption effects were corrected by numerical absorption correction using the STOE programs X-Red and X-Shape. The crystal structures were then solved by direct methods and refined by full matrix least-square on F^2 with the aid of the SHELXTL program package. All four independent atomic positions (Bi1, Bi2, Ae1, Ae2) were refined with anisotropic atomic displacement parameters. For the ternary phases the model significantly converged when introducing mixed occupancies (Sr/Ba) in the two Ae sites. Some data collection and refinement parameters of the five measured crystals are listed in Table 5.1. Tables 5.2 and 5.3 summarize the corresponding atomic coordinates and the anisotropic displacement parameters. Important interatomic distances are shown in Table 8.9 (see Appendix).

Description of the Crystal Structure of Sr_2Bi_3 The compound Sr_2Bi_3 crystallizes in the orthorhombic space group *Pnna* (No.52) with Pearson code *oP*20. The structure determination validates the results of Merlo and Fornasini.[13] Lattice parameters and structure refinement details are identical within standard deviations and are presented here again for reason of comparison with the substitution variants. As described in the original publication the Bi atoms form a two-dimensional slab in *b* and *c* directions with 3b- and 2b-Bi atoms (Figure 5.3a and 5.3b) and three different homoatomic distances b_1 := *d*(Bi1–Bi1) = 3.132(1) Å, b_2 := *d*(Bi1–Bi2) = 3.310(1) Å, and b_3 := *d*(Bi1–Bi1) = 3.392(1) Å . Regarding the Bi substructure and taking into account only the shortest Bi–Bi contacts b_1, Bi_2 dumbbells of Bi1 atoms and isolated atoms of Bi2 result. The dumbbells are aligned along [100] and tilted in the (001) plane by 16.2°. They are connected to four other dumbbells via direct contacts (b_3) or bridging Bi2 atoms, which form b_2-type contacts (Figure 5.3d). Each Bi1 atom of the dumbbells forms one b_3 contact to a neighboring dumbbell and one b_2 contact to Bi2 atoms (b_2 and b_3 are mean oriented along [011] and [01–1]).

***Table 5.1*: Selected crystallographic and refinement data for the compounds $Sr_{2-x}Ba_xBi_3$ (x = 0, 0.45, 0.86, 1.08, 1.28).** [a] $w = 1 / [\sigma^2(F_o^2) + (aP)^2 + bP]$, where $P = (F_o^2 + 2F_c^2) / 3$

Empirical formula	**Sr_2Bi_3 (1)**	**$Sr_{1.55}Ba_{0.45(2)}Bi_3$ (2)**	**$Sr_{1.14}Ba_{0.86(2)}Bi_3$ (3)**	**$Sr_{0.92}Ba_{1.08(4)}Bi_3$ (4)**	**$Sr_{0.72}Ba_{1.28(4)}Bi_3$ (5)**
Formula weight / g·mol^{-1}	802.18	824.68	844.69	856.00	865.57
Temperature / K	293(2)	293(2)	293(2)	293(2)	293(2)
Crystal size / cm^3	0.01 × 0.01 × 0.01	0.02 × 0.01 × 0.02	0.01 × 0.01 × 0.01	0.01 × 0.01 × 0.01	0.01 × 0.01 × 0.01
Crystal color; shape	Metallic; Block				
Diffractometer	Nonius κ-CCD	Oxford Xcalibur3 (CCD)	Nonius κ-CCD	Nonius DIP2020 (Image Plate)	
Crystal system	Orthorhombic				
Space group	*Pnna* (No. 52)				
Unit cell parameters / Å	*a* = 15.645(3)	*a* = 15.745(3)	*a* = 15.881(3)	*a* = 15.887(3)	*a* = 15.908(3)
	b = 6.797(1)	*b* = 6.829(1)	*b* = 6.888(1)	*b* = 6.893(1)	*b* = 6.908(1)
	c = 6.601(1)	*c* = 6.647(1)	*c* = 6.704(1)	*c* = 6.717(1)	*c* = 6.731(1)
Unit cell volume / Å^3; *Z*	701.9(2); 4	714.8(2); 4	733.4(3); 4	735.6(3); 4	739.7(3); 4
ρ_{calc} / g·cm^{-3}	7.59	7.66	7.65	7.73	7.77
μ / mm^{-1} (Mo K$_\alpha$)	89.92	87.41	84.41	83.72	82.89
Absorption correction	empirical	numerical	numerical	empirical	empirical
F(000)	1300	1333	1336	1378	1392
Θ range / °	2.60 - 25.34	3.95 - 27.80	2.57 - 30.10	2.56 - 25.35	2.56 - 25.33
Index range	$-11 \le h \le 10$; $-11 \le k \le 10$; $-14 \le l \le 16$	$-20 \le h \le 20$; $-8 \le k \le 8$; $-5 \le l \le 8$	$-21 \le h \le 0$; $0 \le k \le 9$; $-9 \le l \le 0$	$0 \le h \le 19$; $-8 \le k \le 0$; $0 \le l \le 8$	$-19 \le h \le 19$; $-8 \le k \le 8$; $0 \le l \le 8$
Data completeness / %	99.7	99.8	94.7	99.9	100
Integrated reflections	2162 (R_σ = 0.056)	5030 (R_σ = 0.035)	1032 (R_σ = 0.040)	681 (R_σ = 0.027)	2283 (R_σ = 0.081)
Independent reflections	645 (R_{int} = 0.041)	853 (R_{int} = 0.064)	1032 (R_{int} = 0.095)	681 (R_{int} = 0.065)	688 (R_{int} = 0.111)
Refinement method	Full-matrix least-squares on F^2 (SHELXTL)				
Parameters	26	28	28	28	28
Goodness of fit on F^2	1.251	1.224	0.931	1.311	1.286
Observed reflections [$I > 2\sigma(I)$]	609	787	777	638	661
R_1 / wR_2 [$I > 2\sigma(I)$]	0.048 / 0.126	0.034 / 0.076	0.032 / 0.079	0.060 / 0.160	0.064 / 0.160
R_1 / wR_2 (all data)	0.051 / 0.128	0.039 / 0.078	0.041 / 0.082	0.063 / 0.163	0.066 / 0.162
Weighting scheme[a]	a = 0.066	a = 0.023	a = 0.052	a = 0.066	a = 0.051
	b = 30.675	b = 21.238	b = 0	b = 149.289	b = 80.081
Extinction coefficient	0.0023(4)	0.0027(2)	0.0014(1)	0.0009(2)	0.0008(3)
Residual map / e$^-$·Å^{-3}	+2.82 [1.48 Å from Bi1] / −4.10 [0.85 Å from Bi2]	+1.97 [0.89 Å from Bi1] / −2.18 [0.96 Å from Bi1]	+4.41 [0.73 Å from Bi2] / −2.55 [0.88 Å from Bi1]	+4.55 [0.84 Å from Bi2] / −3.75 [0.87 Å from Bi2]	+3.94 [2.47 Å from Bi1] / −3.62 [0.94 Å from Bi1]

***Table 5.2*: Atomic coordinates and equivalent isotropic displacement parameters for $Sr_{2-x}Ba_xBi_3$ (x = 0, 0.45, 0.86, 1.08, 1.28). U_{eq} is defined as one third of the trace of the orthogonalized U_{ij} tensor ($U_{eq} = \frac{1}{3}(U_{11} + U_{22} + U_{33})$).**

Atom	Wyck.	Occ. ≠ 1	*x*	*y*	*z*	U_{eq} / Å^2
			Sr_2Bi_3 (1)			
Bi1	8*e*		0.3461(1)	0.5641(1)	0.0787(1)	0.021(1)
Bi2	4*d*		0.4293(1)	¼	¾	0.019(1)
Sr1	4*c*		¼	0	0.9434(4)	0.018(1)
Sr2	4*d*		½	¼	¼	0.020(1)
			$Sr_{1.55}Ba_{0.45(2)}Bi_3$ (2)			
Bi1	8*e*		0.3462(1)	0.5613(1)	0.0770(1)	0.025(1)
Bi2	4*d*		0.4307(1)	¼	¾	0.022(1)
Sr1 / Ba1	4*c*	0.66 / 0.34(1)	¼	0	0.9448(2)	0.020(1)
Sr2 / Ba2	4*d*	0.90 / 0.10(1)	½	¼	¼	0.019(1)
			$Sr_{1.14}Ba_{0.86(2)}Bi_3$ (3)			
Bi1	8*e*		0.3459(1)	0.5591(1)	0.0752(1)	0.021(1)
Bi2	4*d*		0.4313(1)	¼	¾	0.020(1)
Sr1 / Ba1	4*c*	0.44 / 0.56(1)	¼	0	0.9463(2)	0.013(1)
Sr2 / Ba2	4*d*	0.70 / 0.30(1)	½	¼	¼	0.015(1)
			$Sr_{0.92}Ba_{1.08(4)}Bi_3$ (4)			
Bi1	8*e*		0.3457(1)	0.5585(1)	0.0747(1)	0.023(1)
Bi2	4*d*		0.4313(1)	¼	¾	0.018(1)
Sr1 / Ba1	4*c*	0.30 / 0.70(2)	¼	0	0.9478(3)	0.017(1)
Sr2 / Ba2	4*d*	0.60 / 0.40(2)	½	¼	¼	0.017(1)
			$Sr_{0.72}Ba_{1.28(4)}Bi_3$ (5)			
Bi1	8*e*		0.3455(1)	0.5578(1)	0.0741(2)	0.029(1)
Bi2	4*d*		0.4313(1)	¼	¾	0.025(1)
Sr1 / Ba1	4*c*	0.25 / 0.75(2)	¼	0	0.9479(4)	0.021(1)
Sr2 / Ba2	4*d*	0.47 / 0.53(2)	½	¼	¼	0.024(1)

***Table 5.3*: Anisotropic thermal displacement parameters (/ Å^2) for $Sr_{2-x}Ba_xBi_3$ (x = 0, 0.45, 0.86, 1.08, 1.28).**

Atom	U_{11}	U_{22}	U_{33}	U_{23}	U_{13}	U_{12}
			Sr_2Bi_3 (1)			
Bi1	0.012(1)	0.021(1)	0.017(1)	0.005(1)	0.005	0.006
Bi2	0.014(1)	0.017(1)	0.014(1)	0	0	0
Sr3	0.009(1)	0.017(1)	0.014(1)	0	0	0
Sr4	0.007(1)	0.021(1)	0.017(1)	0.004(1)	0	0
			$Sr_{1.55}Ba_{0.45(2)}Bi_3$ (2)			
Bi1	0.026(1)	0.024(1)	0.023(1)	–0.007(1)	–0.006(1)	0.006(1)
Bi2	0.030(1)	0.019(1)	0.019(1)	0	0	0
Ae1	0.021(1)	0.018(1)	0.019(1)	0	0	0.002(1)
Ae2	0.016(1)	0.021(1)	0.021(1)	–0.004(1)	0	0
			$Sr_{1.14}Ba_{0.86(2)}Bi_3$ (3)			
Bi1	0.025(1)	0.022(1)	0.017(1)	0.009(1)	0.006(1)	0.008(1)
Bi2	0.030(1)	0.014(1)	0.012(1)	0.002(1)	0	0
Ae1	0.018(1)	0.011(1)	0.010(1)	0	0	0.002(1)
Ae2	0.016(1)	0.014(1)	0.014(1)	0.005(1)	0	0
			$Sr_{0.92}Ba_{1.08(4)}Bi_3$ (4)			
Bi1	0.018(1)	0.020(1)	0.025(1)	–0.009(1)	–0.006(1)	0
Bi2	0.023(1)	0.012(1)	0.019(1)	–0.002(1)	0	0
Ae1	0.014(2)	0.009(2)	0.021(2)	0	0	0
Ae2	0.011(2)	0.015(2)	0.020(2)	–0.003(1)	0	0
			$Sr_{0.72}Ba_{1.28(4)}Bi_3$ (5)			
Bi1	0.030(1)	0.021(1)	0.029(1)	–0.009(1)	–0.006(1)	0.008(1)
Bi2	0.034(1)	0.011(1)	0.024(1)	0	0	0
Ae1	0.025(2)	0.011(2)	0.023(2)	0	0	0
Ae2	0.024(2)	0.016(2)	0.028(2)	–0.004(1)	0	0

Another view of the Bi substructure arises by considering the shorter b_1 and b_2 contacts. A one-dimensional helical Bi substructure results. The spirals have six atoms per turn (4× Bi1, 2× Bi2) and proceed along [010] (Figure 5.3d). Those chains are interlinked in *c* direction by longer b_3 contacts between Bi1 atoms of different helices, resulting in two-dimensional Bi slabs in the (100) plane (Figure 5.3a). The Bi–Bi separation between the slabs is 3.902(1) Å. The interatomic distance b_1 is longer than the one observed in elemental Bi (3.072 Å, intralayer distance) but is in the range of 2*c*-2*e* covalent bonds as found e.g. for $\{Bi_2\}^{4-}$ dumbbells in $Sr_{11}Bi_{10}$ (3.187(3) and 3.152(3) Å). The longer distances b_2 and b_3 are longer than normal covalent bonds and are typical for multicenter bonding as it is observed in the two-dimensional Bi net in Ba_2Bi_3, where Bi–Bi distances range from 3.247 to 3.380 Å or the six-atom-wide Bi ribbon found in $HfBi_2$, with Bi–Bi separations of 3.289 Å. However, considering the coordination number of Bi1, we still assume some degree of directive chemical bonding to Bi2. Sr1 atoms with Wyckoff position 4*c* are distributed in layers in the (100) plane with x coordinates centring b_1 of the Bi1 dumbbells along [100]. Sr2 atoms with Wyckoff position 4*d* are also distributed in layers in the (100) plane and separate the 2D-Bi slabs along [100] (Figures 5.3a and 5.3b). Sr1 resides approximately in the center of four Bi1 dumbbells (Figure 5.3e) with Sr1–Bi1 distances of 3.440(1), 3.521(1), 3.787(3), and 4.214(1) Å. The coordination sphere is completed by two Bi2 atoms connecting three of the four $\{Bi_2\}$ dimers with Sr1–Bi2 distance of 3.519(1) Å. Considering only distances up to 4 Å, an average Sr–Bi distance of 3.582 Å results. The high coordination number of the Sr1 site by Bi1 is significant for the bonding considerations, as will be described later. As shown in Figure 5.4a the Sr2 coordination consists of a polyhedron with eight Bi atoms: four Bi1 atoms (*d*(Bi–Bi) = 3.409(2) and 3.479(2) Å) of the dumbbells and four bridging Bi2 atoms (*d*(Bi–Bi) = 3.481(1) and 3.575(1) Å) generate a rectangular antiprism with average Sr–Bi distance of 3.486 Å. One rectangular face is defined by b_2 contacts of two different helical chains and longer b_4 contacts of 3.902(1) Å between Bi1 and Bi2 atoms that are part of two different 2D-slabs. The resulting polyhedra are base-fused and piled to columns in [011] direction (Figure 5.4b).

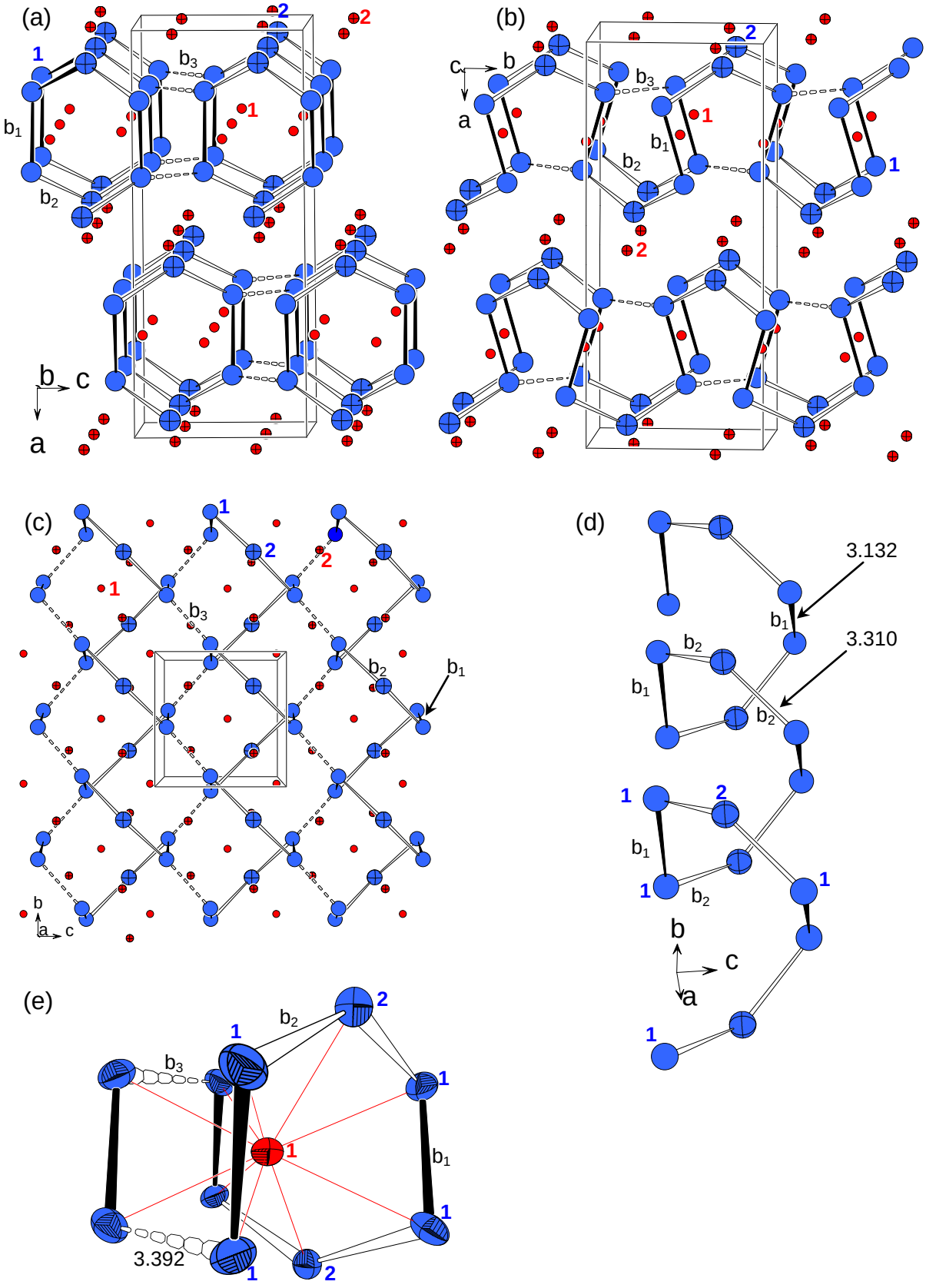

***Figure 5.3*. (a) Off-[010] projection of the unit cell of Sr_2Bi_3. (b) Off-[001] projection. The anionic Bi substructure shows three different Bi–Bi bonds, b_1, b_2, and b_3. Sr1 positions are located in the helical Bi chains, Sr2 separates layers of interconnected spirals. (c) [100] view of the structure of Sr_2Bi_3. (d) The helical Bi substructure. (e) Coordination sphere of Sr1 (all atoms are drawn at 90% probability level). Bi1 (open, blue), Bi2 (cross hatched, blue), Sr1 (open, red), Sr2 (cross hatched, red). Long contacts are drawn with dashed lines.**

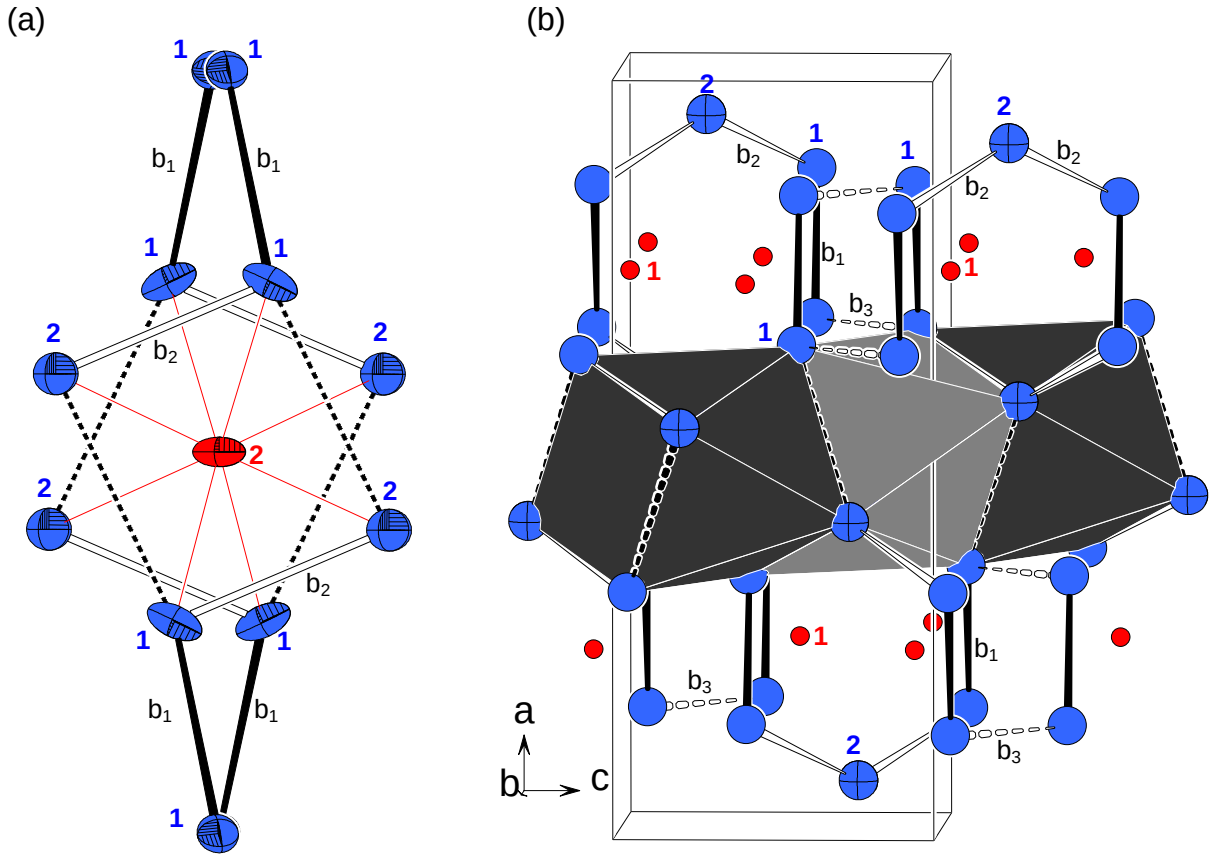

Figure 5.4. **(a) Rectangular antiprismatic coordination of Sr2 (all atoms are drawn at 90% probability level). (b) The rectangular antiprisms are base-fused and piled along [011]. Bi1 (open, blue), Bi2 (cross hatched, blue), Sr1 (open, red), Sr2 (cross hatched, red). Long contacts are dashed.**

Crystal Structure of $Sr_{2-x}Ba_xBi_3$ (x = 0.45, 0.86, 1.08, 1.28) Incremental increase of the Ba content in steps of 0.2 in the substitution series $Sr_{2-x}Ba_xBi_3$ leads to an increase in the lattice parameters (Figure 5.5). Due to the bigger size of Ba compared to the size of Sr such enlargement of the unit cell dimensions is expected upon substitution. Following Vegard's rule the increase is approximately linear form x = 0 to 0.8 and a decreasing gradient from 0.8 to 1.2 is observed. Lattice parameters calculated from powder diffractograms show that the *a, b* and *c* axes increase by 1.93%, 1.60%, and 1.91%, respectively, i.e. the expansion occurs almost uniform in all three dimensions by approximately 2% but is slightly less pronounced along the *b* direction. The cell volume is increased by 5.56 %. The lattice expansion correlates directly with anisotropic changes in interatomic distances as discussed in the following. Single-crystals were obtained from the reactions with starting stoichiometries Sr : Ba : Bi = (2 – y) : y : 3 and y = 0, 0.4, 0.8, 1.0, and 1.2. The structure refinements were carried out using the space group and atomic positions of Sr_2Bi_3. No reflections indicating a superstructure were observed. Samples with Ba

loading higher then y = 1.0 show lower crystallinity and are less homogeneous. In the corresponding powder diagrams the presence of additional reflections indicates the formation of an unknown phase. Therefore, we did not investigate the systematic substitution properties of $Sr_{2-y}Ba_yBi_3$ beyond y = 1.2. Lattice parameter determination and refinement with partial Ba occupation on the Sr positions reveal that the compositions of the single-crystals confirm the results of the powder X-ray studies within standard deviations (3σ rule). Lattice parameters determined from single-crystals and from powder data nearly coincidence with exceptions for samples loaded as y = 1.0 and 1.2 (Figure 5.5a). In these cases the *a* lattice parameter determined from the powdered samples is slightly longer than the one identified from the single-crystals with x = 1.08(4) and 1.28(4), respectively. As illustrated in Figure 5.6a the selected crystals are slightly Bi richer with respect to the reaction mixtures.

The degree of Sr substitution with Ba is not equally distributed over the two sites Sr1 and Sr2. In all cases we find a higher Ba content on the Sr1 than on the Sr2 position. Figure 5.6b and Table 5.4 clearly show that Ba is preferably substituted in the 4*c* (Sr1) position at lower Ba contents. Based on the crystallographically determined compositions for x = 0.45(2) we find approximately 35% Ba on Sr1 compared to 10% on the Sr2 position and for x = 1.28(4) approximately 75% and 53%, respectively. This trend reflects the situation of a larger coordination sphere of Sr1 with coordination number 10 and longer mean Sr-Bi distances compared to those of Sr2.

Increasing the Ba content leads to a change of the tilt angle of $\{Bi_2\}$ dumbbells with respect to the *a* axis with values of 15.5°, 15.0°, 14.9°, and 14.7° for x = 0.45, 0.86, 1.08, and 1.28, respectively. The enlargement of the lattice parameters from Sr_2Bi_3 to $Sr_{0.71}Ba_{1.28(4)}Bi_3$ is accompanied with a change of interatomic separations in the crystal structure (Table 8.9, see Appendix). Even more significant is the fact that interatomic distances change anisotropically. Certain distances remain almost unaffected, whereas others change to a greater extent. While the shorter distances b_1 and b_2 remain almost unaltered with 3.132(1) to 3.142(2) Å for b_1 and 3.310(1) to 3.339(1) Å for b_2, the longer b_3 contact increases to a much larger extent from 3.392(1) to 3.557(2) Å for x = 0 to 1.28(4), respectively. The larger expansion of the inter-spiral bond b_3 by approximately 5% compared to the other Bi–Bi contacts which are enlarged by less than 1% originates from the site preference of Ba on the Sr1 position. This pushes two adjacent $(Bi1)_2$ dumbbells that are coordinated by the same

Ae1 atom further apart from each other (Figure 5.3e). The final b_3 distance of 3.557(2) Å lies in the region of Bi–Bi contacts of interlayer Bi–Bi distances in elemental bismuth (3.529 Å) and contacts in $BaBi_3$ (3.66 Å). This indicates a loss of the directional interaction and a shift to a more electronically delocalized system.

The cation–anion separations disclose another feature of the structure. Whereas for x = 0 the distances Ae1–Bi1, Ae2–Bi2 and Ae2–Bi1 are longer (3.409(2) to 3.481(1) Å) than b_3 (3.392(1) Å), the situation is inversed for x = 1.28 Å, where the heteratomic distances of 3.462(2) to 3.540(1) Å are shorter than b_3 with a value of 3.557(2) Å. This clearly indicates a weakening (elongation) of the homoatomic contact b_3 if compared to the contacts between positively and negatively charged atoms. This result can be interpreted geometrically as a simultaneous separation and stretching of the Bi helices along [010].

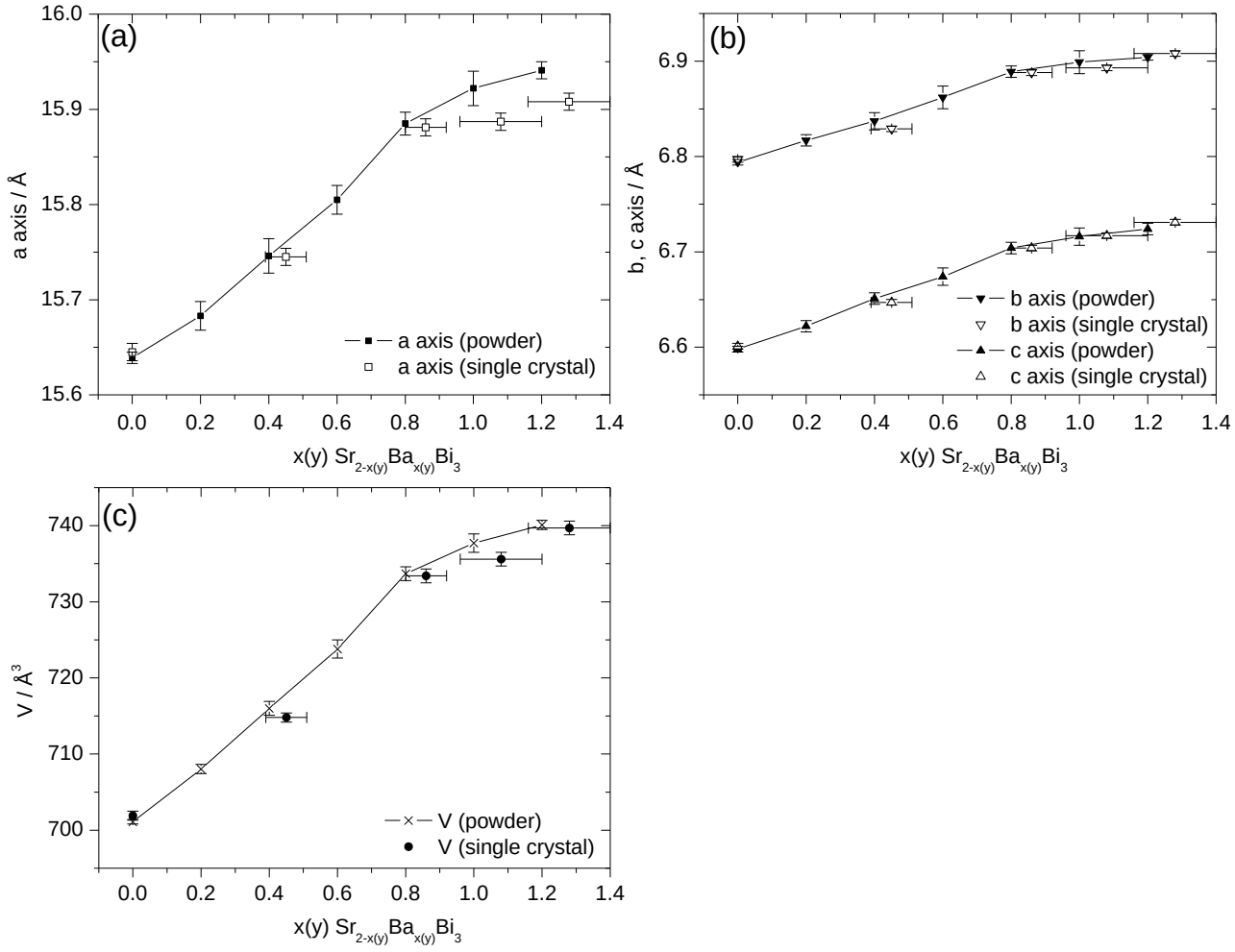

***Figure 5.5*. Development of the unit cell parameters of single-crystals $Sr_{2-x}Ba_xBi_3$ and data from room temperature powder measurements of samples loaded as $Sr_{2-y}Ba_yBi_3$. (a) *a*-axis, (b) *b*- and *c*-axis. (c) Unit cell volume. Error bars are ±3σ of the values.**

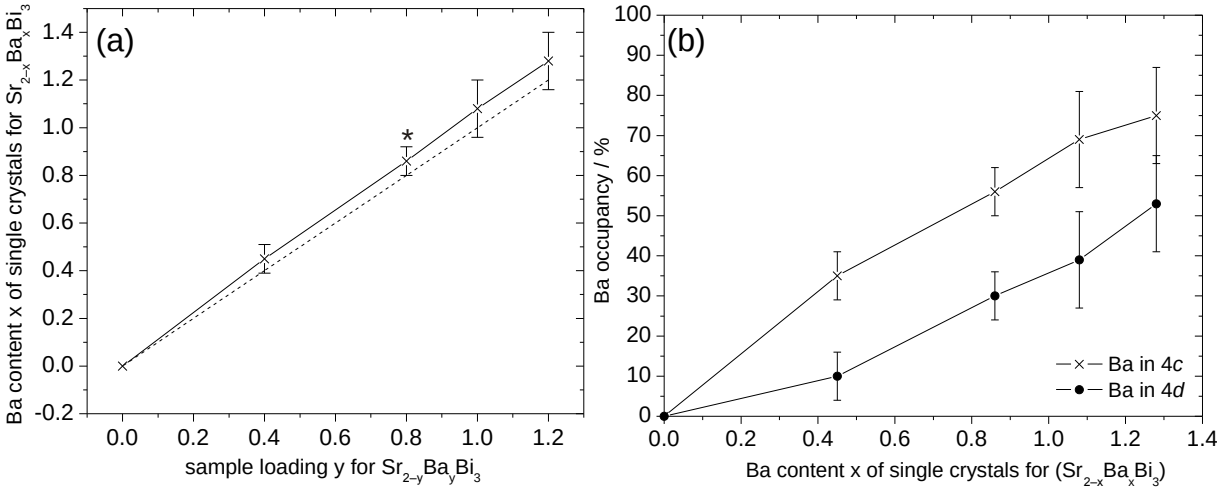

Figure 5.6. **(a) Crystallographically determined composition x of $Sr_{2-x}Ba_xBi_3$ versus stoichiometric parameter y used for sample loading $Sr_{2-y}Ba_yBi_3$; dashed line x = y. *) crystal obtained from loading ratio = 1 : 1 : 3.3. (b) Occupancy of Ba in 4*c* and 4*d* position in substituted $Sr_{2-x}Ba_xBi_3$ plotted against Ba content. Error bars are ±3σ of the values.**

Table 5.4: **Occupancy of Ba in 4*c* and 4*d* position in substituted $Sr_{2-x}Ba_xBi_3$ together with shortest Bi–Bi distances $b_3$between two neighbouring Bi spirals.**

x	Occ. (*l* %) Ba in 4*c*	Occ. (*l* %) Ba in 4*d*	b_3 / Å
0	0	0	3.392(2)
0.45	34	10	3.454(1)
0.86	56	30	3.523(1)
1.08	69	39	3.537(2)
1.28	75	53	3.558(2)

5.1.4 Electronic Structure

To gain deeper insights into the complex electronic situation of Sr_2Bi_3 and the effects of Ba substitution i.e. the cation-anion interactions, computational calculations were carried out. The band structure of Sr_2Bi_3 along specific symmetry paths of the primitive orthorhombic Brillouin zone and the total density of states together with the projections (pDOS) for Sr and Bi are depicted in Figure 5.7. Various bands that cross the Fermi level show an isotropic conducting property for Sr_2Bi_3. As revealed by fat band representations (Figure 5.11) the bands that cross E_F with large dispersions have mainly Bi-*p* character and a local maximum just below E_F is caused by flat bands at Γ, T and R symmetry points. The projected DOS show that in an energy window of ±4 eV around E_F significant numbers of Bi-*p* states with larger contributions from Bi1 according to the ratio Bi1 : Bi2 = 2 : 1 are present. The Bi-*s* states are clearly separated in a band ranging from –9 to –12 eV. This is caused by relativistic effects; as one moves down group 15, *p*-orbitals become more diffuse and their interactions are weaker. In contrast, the *s*-orbitals become compact and their energies decrease, due to the relativistic effect.

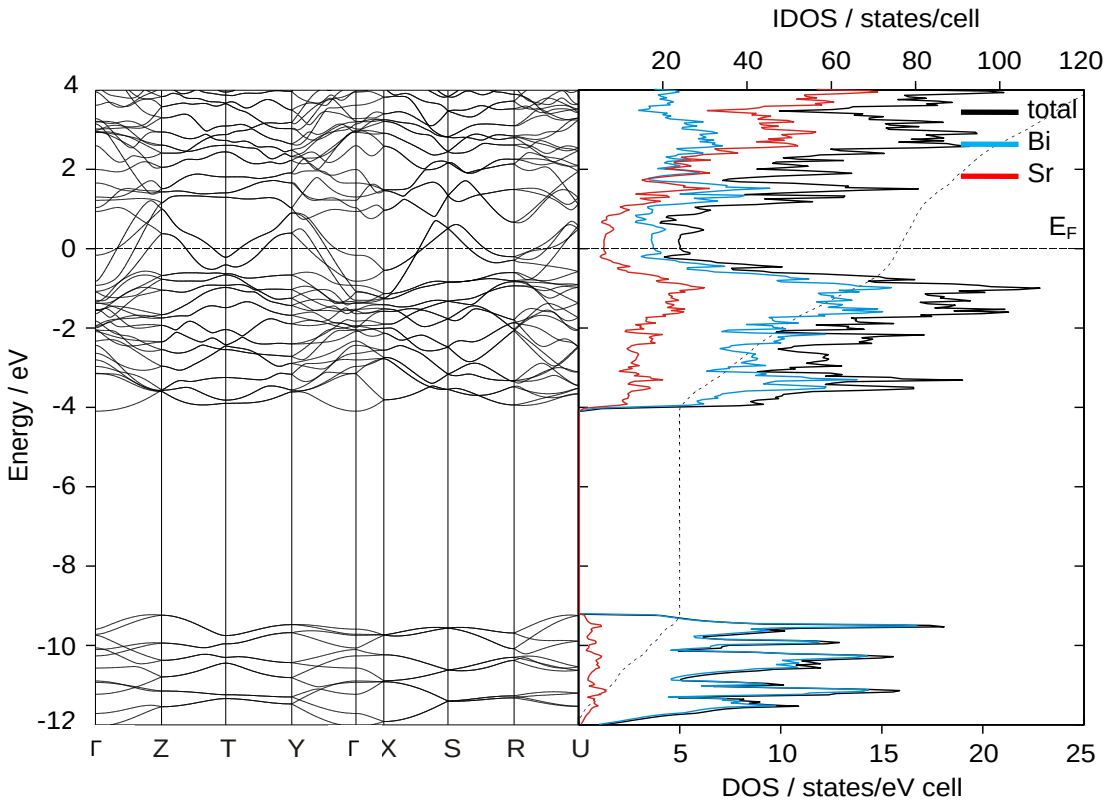

***Figure 5.7*. Band structure and DOS projections of Sr_2Bi_3. The Bi-s states are well separated (caused by relativistic effects) from the *p* states. Sr contributions (red), Bi contributions (blue). The Fermi level is taken as the point of zero energy.**

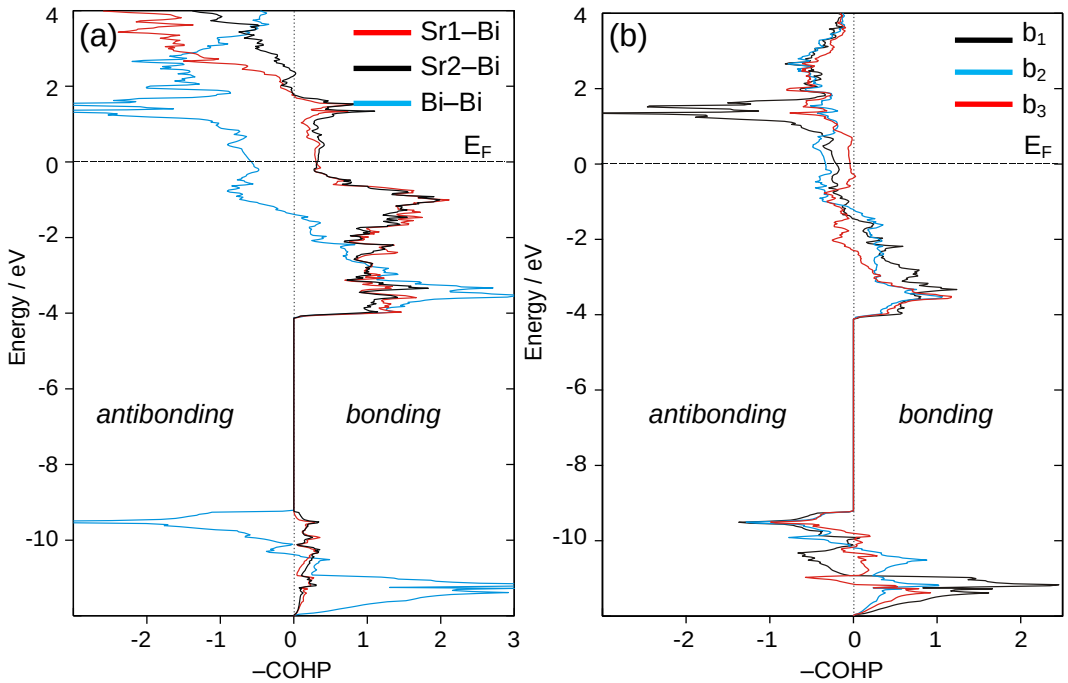

***Figure 5.8*. (a) Crystal orbital Hamilton population (–COHP) plot for sum of all Bi–Bi (blue), Sr1–Bi (red), Sr2–Bi (black) interactions as a function of energy in Sr_2Bi_3. (b) –COHP plot for the three different Bi–Bi pairs in Sr_2Bi_3. b_1 = intraspiral Bi1–Bi1 (black), b_2 = Bi1–Bi2 (blue), b_3 = interspiral Bi1–Bi1 (red).**

As a result, *s*-*p* mixing decreases drastically on going down a group in the periodic table. Sr-*d* orbitals are clearly present in the valence band and mix with Bi-*p* states. These two sets of orbitals are responsible for the metallic character of Sr_2Bi_3 which is additionally revealed by a fat band analysis of the band structure showing the orbital contributions of different atoms to these bands and states (Figures 5.11 and 5.12).

Figure 5.8 shows the –COHP diagrams of the three different Bi–Bi bonds (eV / bond) and the sums of all Bi–Bi, Sr1–Bi, and Sr2–Bi bonds. All bonding states of the different Bi–Bi interactions are completely filled and are located below the Fermi level. Some antibonding states are filled as well meaning the compound is electron rich. E_F lies in antibonding regions for all Bi–Bi contacts and although they are overall bonding the Bi–Bi contacts alone appear to be too weak to control the overall structure stability. As revealed by separate calculation of b_1, b_2, and b_3, the antibonding Bi–Bi states start to get filled at ~ 2 eV below E_F. This means that in all cases the maximum value for –ICOHP lies well below E_F and the bonds are weakened. The shortest Bi1–Bi1 bond (3.13 Å) is more than twice as strong as the longest bond (3.39 Å), which is reflected in the respective –ICOHP values of 1.38 and 0.49 eV/bond (Table 5.5). At E_F the b_3 contact is almost non-bonding, which suggests weakly interacting lone pairs at Bi1. The Ae–Bi interactions are clearly present at E_F and the corresponding –COHP plots show a strong bonding nature with approximately equal values for Sr1–Bi and Sr2–Bi. The loss of bonding in the Bi–Bi bonds is compensated by additional bonding interactions of the excess of electrons with the cations.

For comparison the electronic structure of hypothetical 'Ba_2Bi_3' was calculated. Both Ae sites were occupied with Ba and unit cell parameters of the Ba-richest crystal $Sr_{0.72}Ba_{1.28(4)}Bi_3$ (5) (Table 5.1) were used. The band structure together with the DOS plots is shown in Figure 5.9. Compared to the pure Sr compound the valence band in 'Ba_2Bi_3' has a slightly weaker dispersion and a width indicating less interactions between the bands due to longer interatomic distances and somewhat more localized electrons. A closer look at the area around –0.5 eV reveals the opening of a pseudo gap when putting Ba in the two Sr positions and increasing the lattice parameters. The corresponding energy matches a valence electron count of 72 per unit cell. This can be correlated with stronger covalent interactions between Ba and Bi hence leading to a more localized electronic model.

However, the Ba-*d* / Bi-*p* mixing does not seem to be strong enough to completely open up the gap and thus, the compound conserves its metallic character.

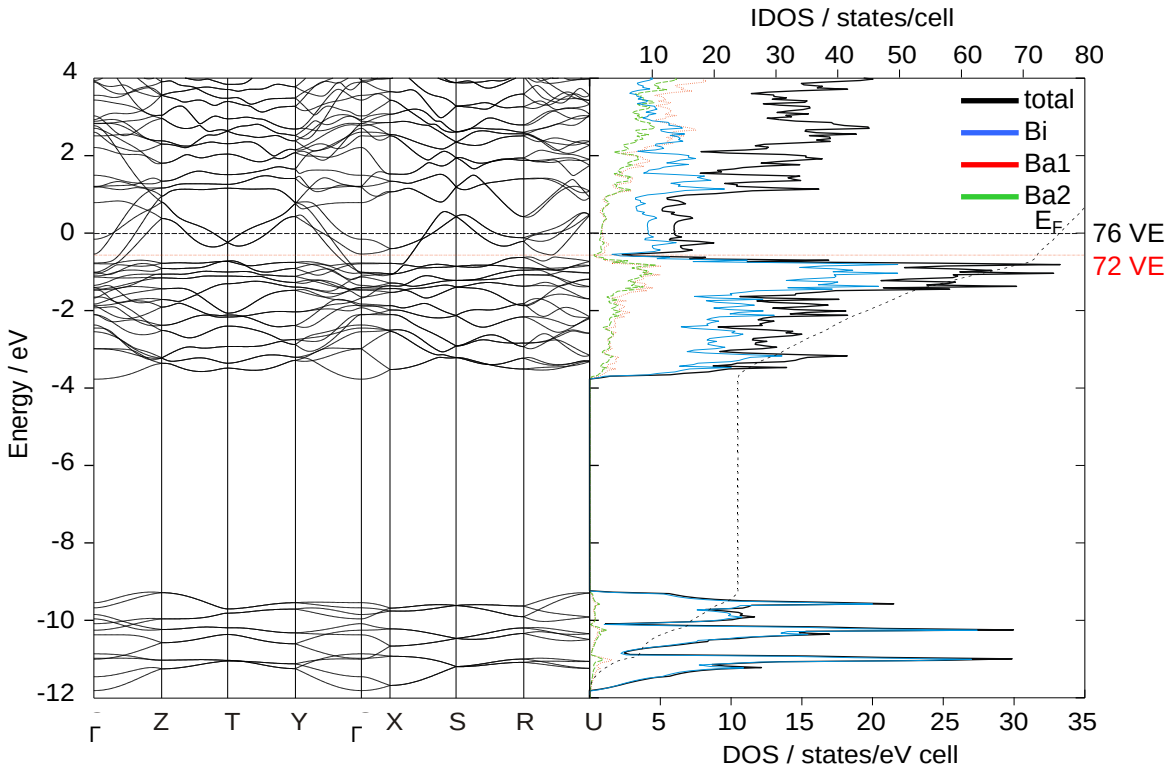

***Figure 5.9*. Band structure and DOS diagram of hypothetical fully ordered 'Ba_2Bi_3'. Bi (blue), Ba1 (red), Ba2 (green). The Fermi level is taken as the point of zero energy.**

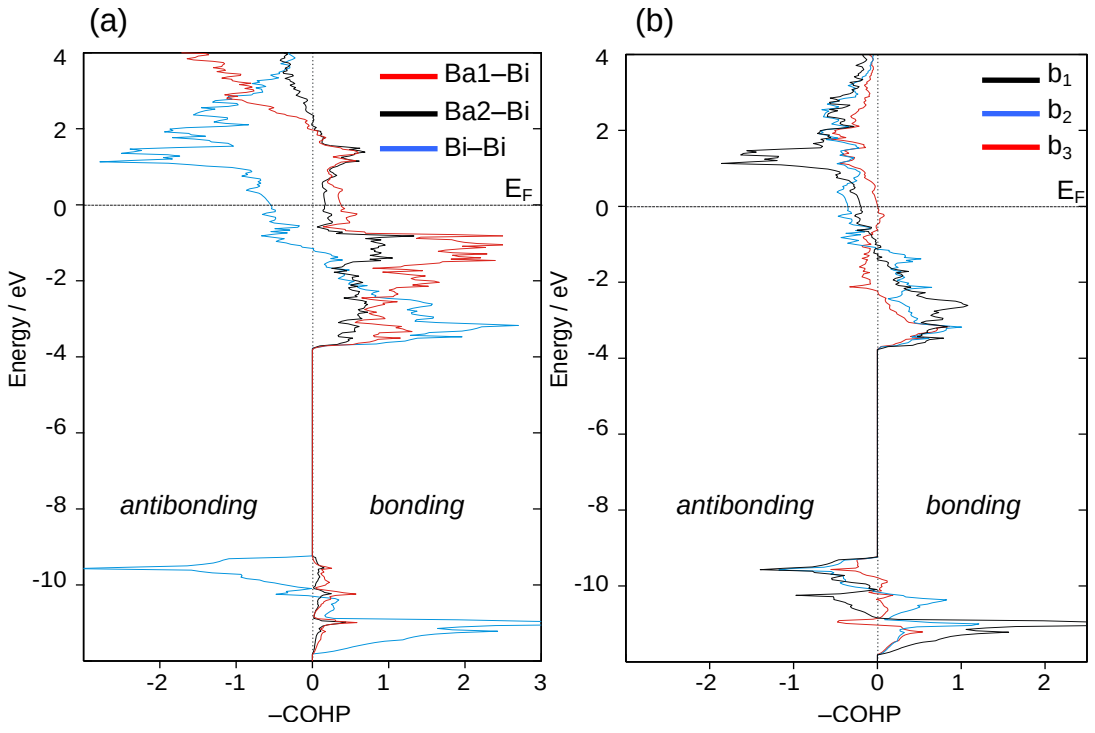

***Figure 5.10*. (a) –COHP plots for the sum of all Bi–Bi (blue), Ba1–Bi (red), Ba2–Bi (black) interactions. (b) –COHP plot for the three different Bi–Bi pairs in hypothetical 'Ba_2Bi_3'. b_1 = Bi1–Bi1 (black), b_2 = Bi1–Bi2 (blue), b_3 = Bi1–Bi1(red).**

Comparing the Ba–Bi –ICOHP values in 'Ba_2Bi_3' with the Bi1–Bi1 values reveals a significant change in bonding energies (Table 5.5). The value of the weakest interaction b_3 (0.49 eV) in Sr_2Bi_3, which was in the range of the average Sr1-Bi (0.54 eV) significantly drops in 'Ba_2Bi_3', (b_3: 0.33 eV). The corresponding average Ba1–Bi remains almost unchanged (0.55 eV). Therefore, it can be concluded that the differential site preference of the cation might also be triggered by gaining additional bonding energies through the comparable values for the cation-anion interactions.

***Table 5.5*: –ICOHP values for selected interatomic contacts in Sr_2Bi_3 and hypothetical 'Ba_2Bi_3'. Energies are given in eV/bond.**

Interaction	*d* / Å	–ICOHP (at E_F)	*d* / Å	–ICOHP (at E_F)
	Sr_2Bi_3		**'Ba_2Bi_3'**	
Bi1–Bi1	3.129(1)	1.38	3.142(2)	1.37
Bi1–Bi2	3.311(1)	0.80	3.339(1)	0.84
Bi1–Bi1	3.392(1)	0.49	3.557(2)	0.33
Sr1–Bi1	3.440(1) - 3.787(3)	0.48	-	-
Ba1–Bi1		-	3.515(1) - 3.853(3)	0.52
Sr1–Bi2	3.519(1)	0.72	-	-
Ba1–Bi2		-	3.617(2)	0.64
Ae1–Bi (sum)		4.34		4.39
Sr2–Bi1	3.409(2) - 3.479(2)	0.62	-	-
Ba2–Bi1		-	3.462(2) -3.541(2)	0.52
Sr2–Bi2	3.481(1) -3.575(1)	0.56	-	-
Ba2–Bi2	-	-	3.540(1) - 3.621(1)	0.49
Ae2–Bi (sum)		4.71		4.00

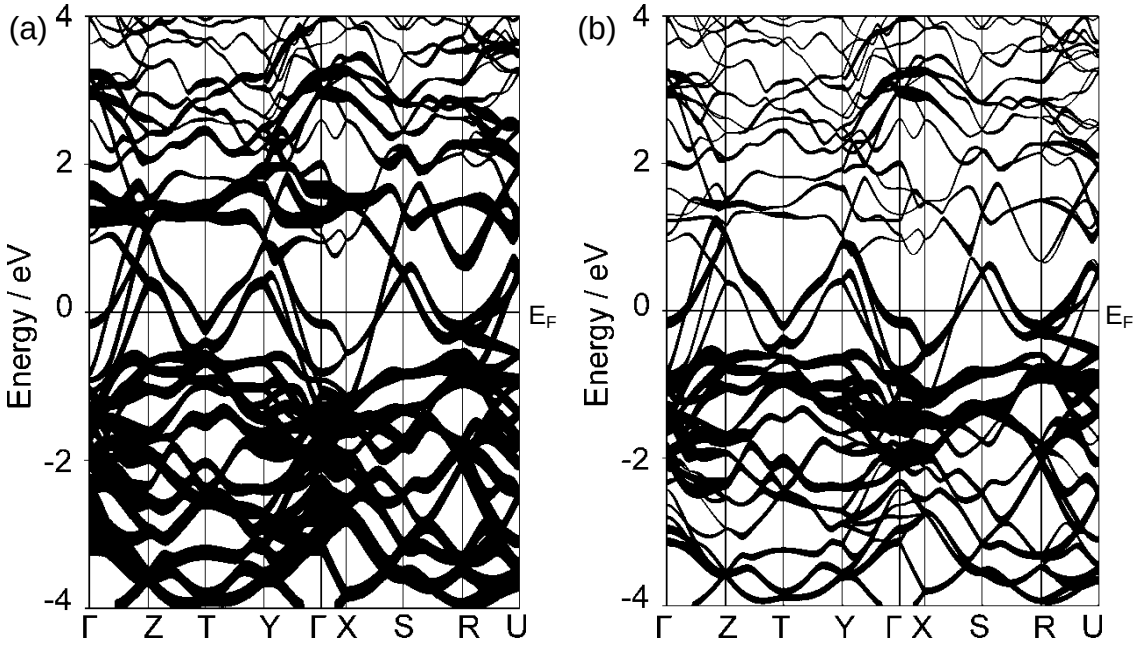

***Figure 5.11*. Fat band representations of selected bands in Sr_2Bi_3: (a) Bi1-*p* and (b) Bi2-*p*.**

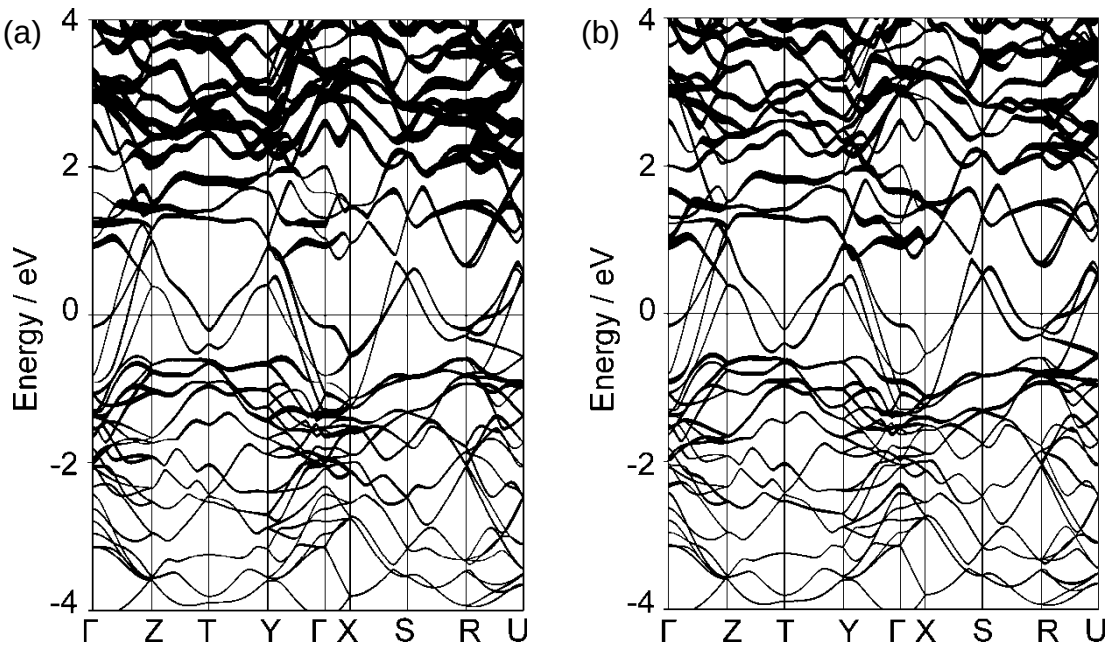

***Figure 5.12*. Fat band representations of selected bands inSr_2Bi_3: (a) Sr1-*d* and (b) Sr2-*d*.**

5.1.5 Magnetic Properties

The temperature-dependent magnetic behavior of samples with loadings Sr_2Bi_3, $Sr_{1.6}Ba_{0.4}Bi_3$, and $Sr_1Ba_1Bi_3$ was investigated on a SQUID magnetometer. Figure 5.13 shows the experimental diagrams of the samples for y = 0, 0.4, and 1.0. The sample was cooled without external field to 2 K. After applying a field of 100 Oe the sample was heated to 10 K. At low temperatures the samples are diamagnetic. This property disappears at higher temperatures and occurs again when cooling in the external field at a transition temperature of approximately 4.4 K. Presence of elemental Ta was excluded since the curves nearly coincide with the ones from a measurement of binary Sr_2Bi_3 prepared in a Nb ampoule. The magnitudes at 100 Oe are in the range of the values reported for other intermetallic superconductors such as $BaSn_3$[16] and $BaSn_5$[17] and are therefore indicative for the bulk property of the sample. The plots have the characteristics of a type-II superconductor showing diamagnetic shielding (zero-field-cooled) and Meissner effect (field-cooled).

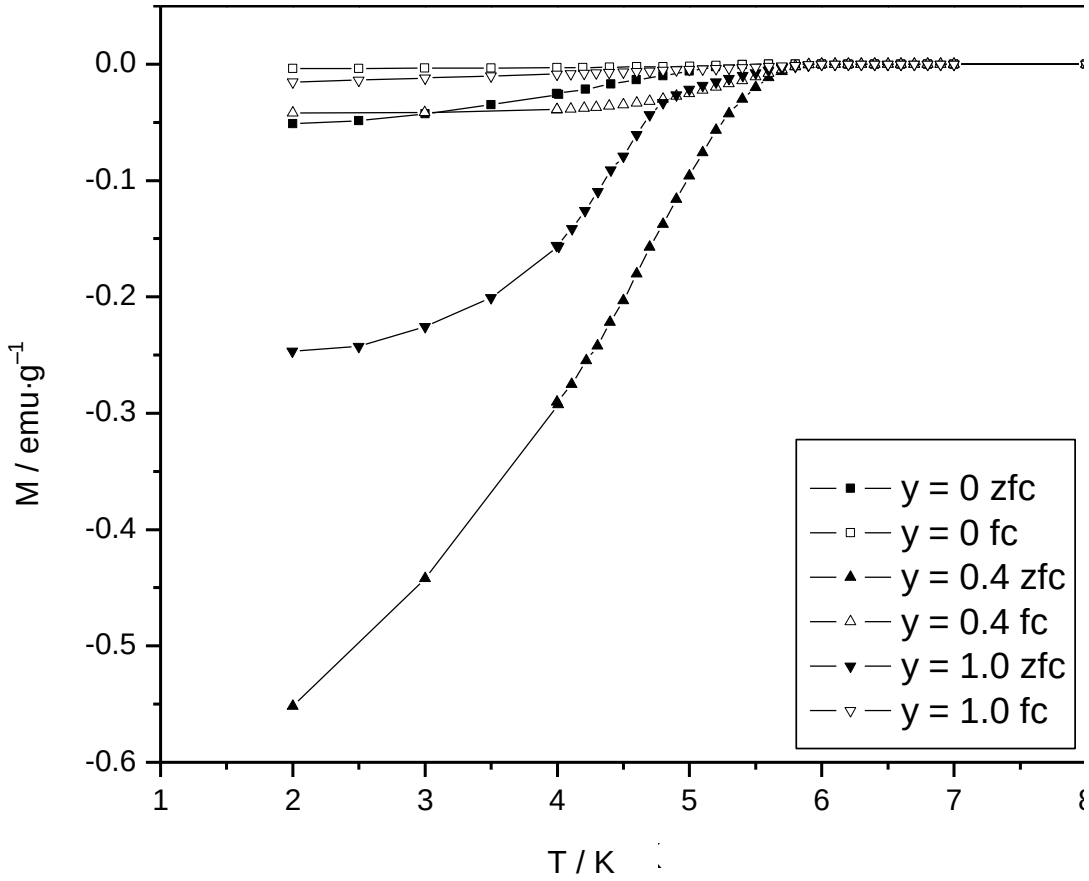

***Figure 5.13*. Diamagnetic shielding (filled symbols) and Meissner effect (open symbols) as a function of temperature for samples $Sr_{2-y}Ba_yBi_3$ with y = 0, 0.4, and 1.0 (100 Oe; zfc: zero-field-cooled; fc: field-cooled).**

5.1.6 Discussion

Trying to apply the Zintl-Klemm concept for Sr_2Bi_3 leads to the following descriptions: a) Bi1 dumbbells $\{Bi_2\}^{4-}$ and isolated $\{Bi\}^{3-}$ lead to $[(1b\text{-}Bi^{2-})_2(Bi^{3-})]$ when ignoring b_2 and b_3, and thus to an electron deficiency of three electrons; b) the assumption of isolated spirals with two-bonded atoms only and neglecting just the longer b_3 contact results in the charge assignment $[(2b\text{-}Bi^{1-})_3]$ with one extra electron, and finally c) according to Merlo and Fornasini, considering a three-bonded Bi1 atom leads to the charge assignments: $[(2b\text{-}Bi^{1-})(3b\text{-}Bi^{0})_2]$ and three additional electrons. None of the descriptions represents a classical closed-shell bonding situation. Sr_2Bi_3 can therefore not be considered as a Zintl phase and multicenter interactions as well as cation effects might play a crucial role to stabilize the Bi substructure. In contrast to the structure of Sr_2Sb_3,[18] which contains discrete six member $[Sb_6]^{8-}$ zigzag chain segments and which represents an electron-precise Zintl compound, the electronic situation in Sr_2Bi_3 is puzzling and does not follow the (8–N) rule.

As indicated in the original literature, Sr_2Bi_3 adopts a more symmetrical variant of the monoclinic Sr_2Sb_3 structure as well as the related Eu_2Sb_3[19, 20] and Ca_2As_3[21] structure. Figure 5.14 depicts the topological transformation of Sr_2Sb_3 to Sr_2Bi_3 by bond breaking and formation. The six-member chain unit in the Zintl phase Sr_2Sb_3 $[Sb1–Sb2–Sb3–Sb4–Sb5–Sb6]^{8–}$ is split into two parts of equal length by releasing the originally longest Sb3-Sb4 bond of 3.006 Å and transforming it to a b_3-type contact. The two shortest Sb2–Sb3 and Sb4–Sb5 bonds are preserved as b_1 contacts. Weaker b_2-type contacts are established between originally not bonded Sb3 and Sb6 (and Sb1 and Sb4) atoms of adjacent six-atom units forming the one-dimensional spirals as described for Sr_2Bi_3. The transformation follows the path of a group-subgroup relationship as discussed for Eu_2Sb_3.[19] Chemically the transition of $\{E_6\}^{8–}$ oligomers to a one-dimensional $^1_\infty[Bi_6]^{6–}$ polymer represents an oxidative coupling reaction accompanied by the loss of two electrons per oligomer. As outlined by the calculations, the ordered phase 'Ba_2Bi_3' shows a pseudo gap corresponding to an IDOS of 72 VE per unit cell due to larger polymer separation. In the bismuthide, electrons are weakly bound in Ae–Bi interactions and therefore not available for complete charge transfer as in Sr_2Sb_3. Thus Sr_2Bi_3 overall reaches a better electronic situation by formation of a polymer with weakly connected dumbbells and by using the excess electrons for Ae–Bi bonding. This situation suggests that multi-center Bi–Bi contacts (b_3) are less important and that the contacts b_1 and b_2 single out a one-dimensional polymer chain. Applying the (8–N) rule to a one-dimensional Bi chain formally leads to one negative charge per atom, $^1_\infty[Bi^-]$, with one transferred electron located at the Bi atom and therefore three Bi atoms per formula unit result in $Bi_3^{3–}$. According to the band structure analyses the fourth electron transferred from the two Ba atoms is involved in more delocalized Ae1-Bi bonds. Longer Bi–Bi contacts (3.38 Å) are also found in the interconnected three-atom-wide ribbons in Ba_2Bi_3 and were discussed in terms of multi-center bonds between Bi atoms with planar coordination. This is not the case for the present Bi partial structure where Bi atoms have a rather staggered than planar environment with respect to the shorter Bi1–Bi1 contacts (Figure 5.15). The flat band region which is most distinct between R and U at E_F originates mainly from Bi-*p* states.

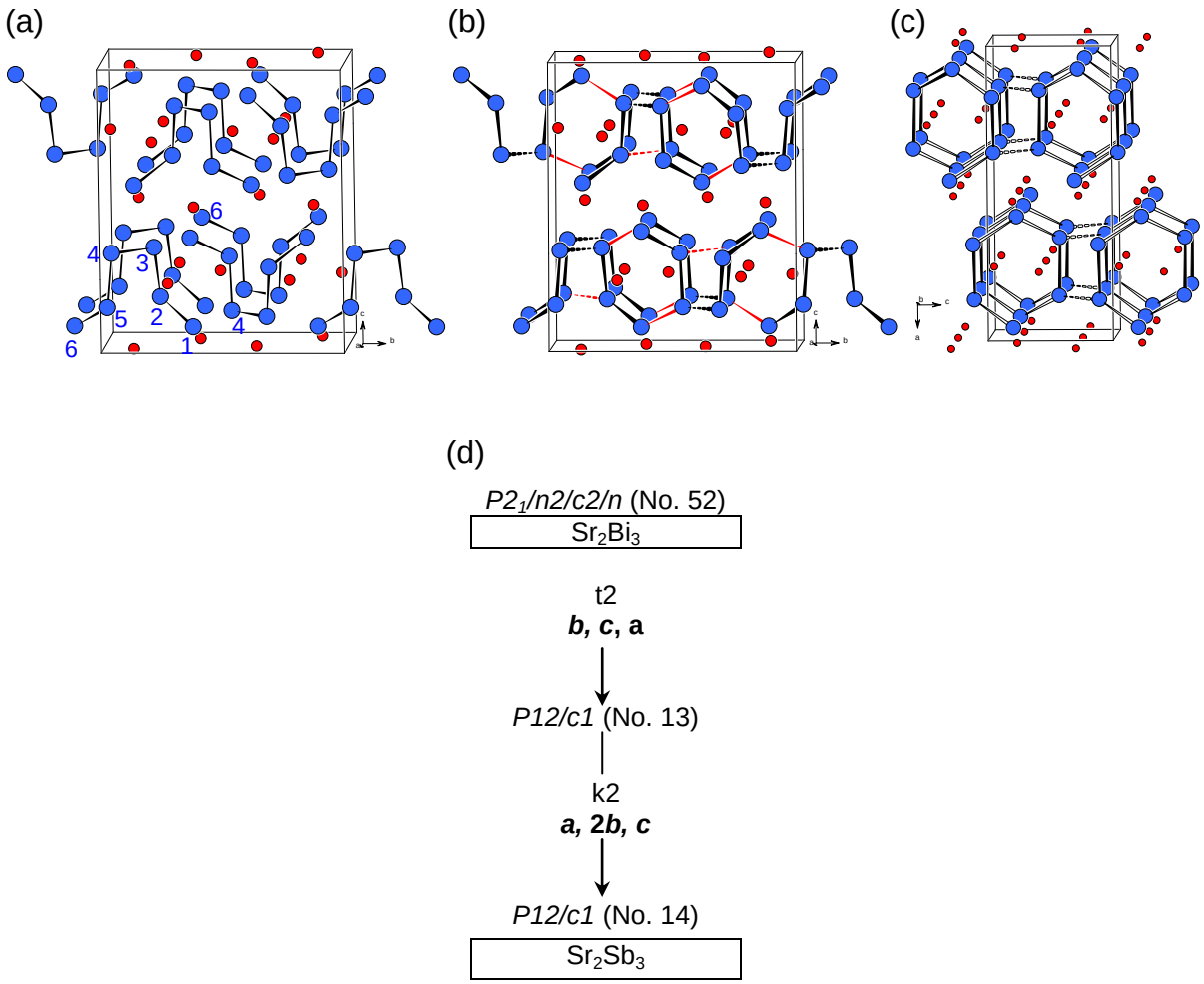

***Figure 5.14*. (a) to (c) Through condensation of the isolated {Sb_6} segments (*d*(Sb–Sb) = 2.887(4) to 3.006(4) Å) in Sr_2Sb_3 the Bi sublattice of Sr_2Bi_3 is formed. Red bonds are newly formed, dashed bonds mark long interactions, which are weakened or additionally established (dashed, red), (d) group-subgroup diagram showing the relation between Sr_2Bi_3 and Sr_2Sb_3 according to ref [19].**

The importance of such saddle points and the associated van Hove singularities in the DOS was discussed for the cuprate superconductors[22] and have also been discussed for the superconducting intermetallic compounds $BaSn_3$,[16] $SrSn_3$,[23] $SrSn_4$,[24] and $BaSn_5$.[17] This characteristic can be interpreted in a chemical sense - as an interplay between localized and delocalized bonds.[25-27]. Such a steep-band-flat-band scenario can be seen as a “fingerprint” in the band structure which hints for the measured superconductivity.

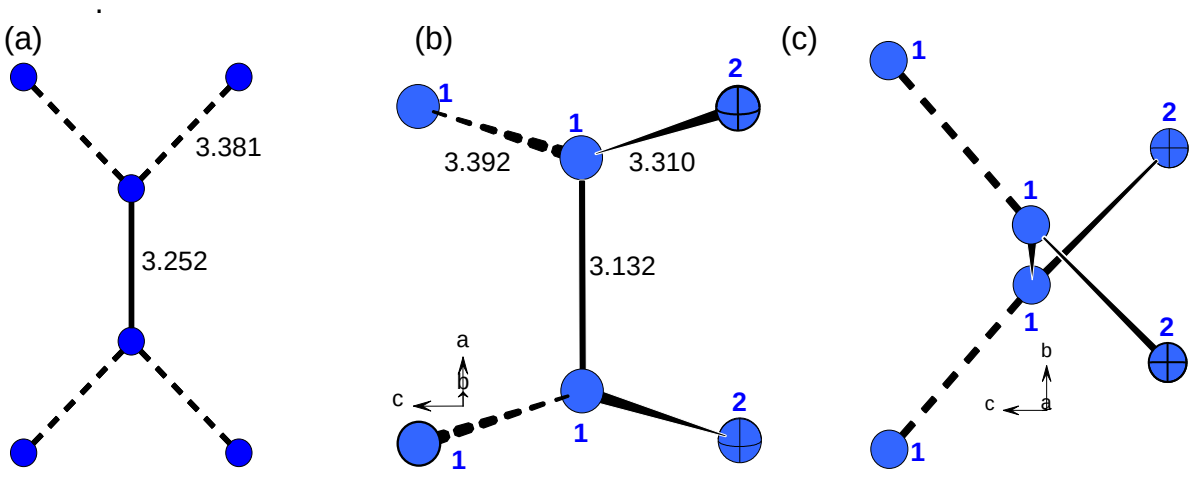

***Figure 5.15*. (a) Planar sawhorse arrangement of Bi atoms (dark blue) in Ba_2Bi_3, (b) and (c) two projections of the staggered Bi sawhorse in Sr_2Bi_3 (Bi atoms blue, Bi2 is cross hatched). Dashed lines denote long contacts.**

5.2 Substitution Effects in Sr_3Sn_5: Synthesis, Structure, and Electronic Effects in $Sr_3Sn_{3.36}Bi_{1.64(3)}$

5.2.1 Introduction

The influence of atomic properties on the structure and bonding of Zintl phases has been reported by examination of the valence electron concentration (VEC) when substituting Bi for Sb in the Zintl phase Ba_2Sb_3.[18, 28] It triggered a radical change of the structure and bonding principles, from a semiconducting phase with localized bonds to a metallic phase $Ba_2Bi_{1+x}Sb_{2-x}$ ($0 \leq x \leq 2$) with planar geometry and delocalized non-classical (hypervalent) bonds.[14, 15] Investigation of the effects when changing the VEC in Zintl phases at the border to intermetallics led to the results presented in this chapter. The partial substitution in Ae_3Sn_5 (Ae = Sr, Ba) of Sn by electron richer Bi was investigated in order to show how dominant the electron count factor is for the stability of the parent structure. The corresponding substitution on the Ba_3Sn_5 are reported in ref.[14] and led to the discovery of the Ba analogue of the title phase. Herein, the synthesis and characterization of the novel phase $Sr_3Sn_{3.36}Bi_{1.64(3)}$, which is isopointal to the In_5Bi_3 structure, is reported. A short overview of the *hitherto* known tin-rich Ae stannides is provided in the following.

The AeSn phases (Ae = Ca, Sr, Ba) crystallize in the CrB structure type.[29] The structure contains planar zigzag chains $^1_\infty[Sn^{2-}]$. Exclusively two-fold bonded Sn atoms are expected from the (8–N) rule and thus, the compounds fulfil the valence rules with the difference that corresponding structures of group 16 elements posses non-planar structures. At higher tin content the phases Ae_3Sn_5 (Ae = Sr, Ba) form.[30, 31] The tin atoms form five-atom clusters with weak interactions between them (shortest intercluster tin–tin distances are 3.397 and 3.694 Å, respectively). In this case the Zintl concept can be extended by the introduction of the electron-counting scheme according to Wade's rules.[32] Electron transfer from the Ae atoms to tin leads to the polyanion $\{Sn_5\}^{6-}$, which indeed has an *arachno*-type structure and is derived from a pentagonal bipyramid by removing two adjacent cluster vertices. However, band structure calculations show that these compounds are metallic. At higher tin contents (for Ae = Sr, Ba) the binary phases $BaSn_3$,[16] $SrSn_3$,[23] $SrSn_4$,[24] and $BaSn_5$[17] were structurally and electronically characterized. They are metallic and even superconducting at temperatures below 2.4 K ($BaSn_3$), 5.4 K ($SrSn_3$), 4.8 K ($SrSn_4$) and 4.4 K ($BaSn_5$).

5.2.2 Synthesis and Characterization

Synthesis All manipulations were performed in an argon-filled glovebox (with oxygen and moisture levels below 0.1 ppm). $Sr_3Sn_{3.36}Bi_{1.64(3)}$ was synthesized using a tin flux and centrifugation technique. Under this condition the ternary solid is in equilibrium with a tin-richer melt (self-flux condition). A mixture of Sr, Bi and Sn with atomic ratio of 3 : 1 : 14 was loaded into an especially prepared stainless steel ampoule as described by Boström[33] (Chapter 3.1). This ampoule contained the reaction mixture at the bottom and a layer of coarsely crushed silica glass fixed by a plug of silica wool at the top. The sealed ampoule was put into a silica wool insulated centrifugation container made of stainless steel, which was subsequently placed into a furnace. The reaction mixture was first heated to 800 °C for 12 h to ensure the complete melting and mixing of the metals. After that, the temperature was lowered to a reaction temperature between 400 and 500 °C for 48 h and the centrifugation container was turned upside down into a centrifuge (Heraeus Megafuge 1.0) which was operated at 3000 rpm for 5 min. The ampoule was opened, and the crystalline product was collected on the silica wool plug. The compound was prepared from a total loading of 2.134 g, with m(Sr) = 0.263 g, m(Sn) = 1.662 g, and m(Bi) = 0.209 g. All attempts to produce the compound as a single phase from stoichiometric mixtures have been unsuccessful so far.

EDX Analysis and Powder X-ray Diffraction Semi-quantitative EDX analyses for different crystallites were carried out and showed the presence of all three elements. The sample powders were finely ground in an agate mortar to a homogeneous powder and filled into a glass capillary which was in turn sealed using a red-hot platinum wire. The theoretical diagram of the phase was calculated from the structure obtained from the single-crystal refinement. According to the X-ray powder diffraction pattern (Figure 5.16) $Sr_3Sn_{3.36}Bi_{1.64(3)}$ was obtained almost as a pure phase with very small amounts of an unknown phase (marked with question marks). Nevertheless, the side product(s) is essentially in form of microcrystalline powder, while the compound of interest forms quite large single-crystals that are suitable for diffraction experiments.

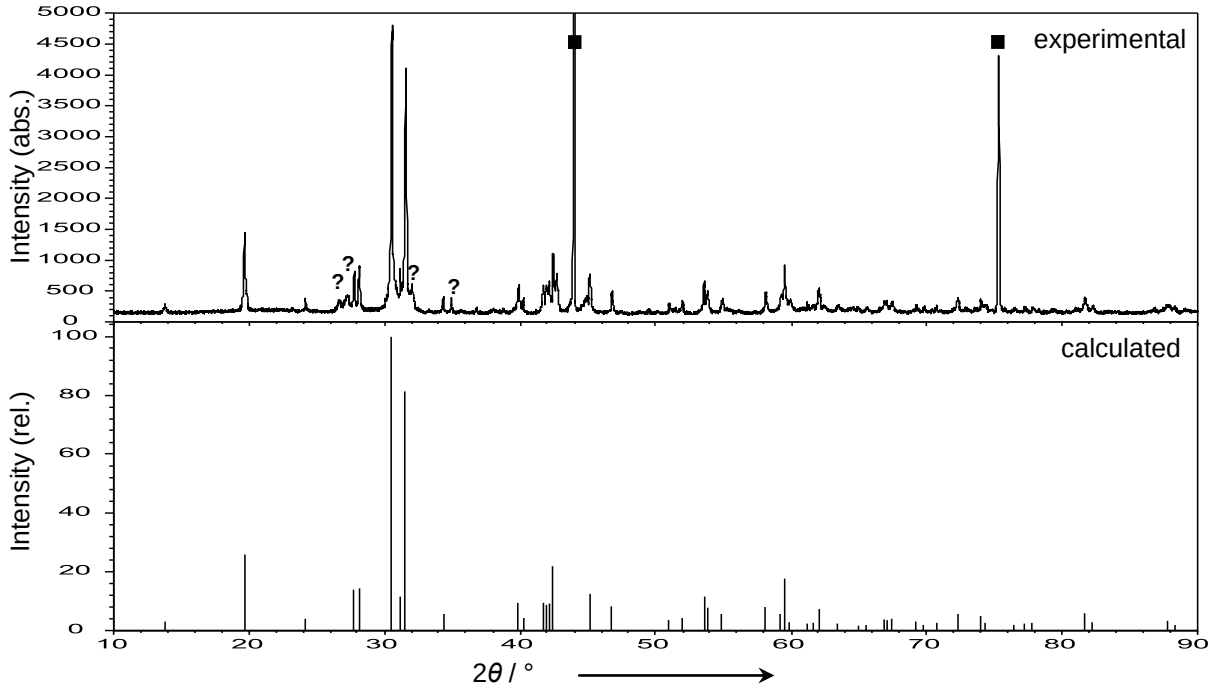

***Figure 5.16*. Experimental (top) from sample loading $Sr_3Sn_{3.36}Bi_{1.64(3)}$ and calculated (bottom) powder diagram of $Sr_3Sn_{3.36}Bi_{1.64(3)}$. Reflections from diamond powder (internal standard) are marked with a square. Unindexed reflections are marked with a question mark.**

5.2.3 Crystal Structure Determination and Description

Structure Determination Air and moisture sensitive gray crystals with metallic luster and highly regular shape were selected and sealed in a capillary inside the glovebox. The diffraction data was collected at room temperature on an Oxford Xcalibur3 using Mo-K_α radiation (λ = 0.71073 Å, graphite monochromator) at ~ 293 K. The absorption correction (empirical) of the data set was done using the program CrysAlis RED (Oxford Diffraction Ltd). The structure was solved by direct methods and refined by least-squares cycles based on F^2 with the SHELXTL software package. The XPREP subprogram of the SHELXTL software package was used to determine the space group. Relevant crystallographic and refinement details are listed in Table 5.6. Tables 5.7 and 5.8 contain the atomic positions and anisotropic displacement parameters. Reflection data sets of several crystals were collected and resulted in comparable compositions with respect to standard deviations (3σ rule). Table 8.10 (Appendix) contains important interatomic distances.

***Table 5.6*: Selected crystallographic and refinement data for $Sr_3Sn_{3.35}Bi_{1.64(3)}$.**

Empirical formula	**$Sr_3Sn_{3.35}Bi_{1.64(3)}$**
Formula weight / g·mol^{-1}	1004.39
Temperature / K	293(2) K
Crystal size / mm^3	0.05 × 0.1 × 0.1
Crystal color; shape	Silvery metallic; Block
Diffractometer	Oxford Xcalibur3 (CCD)
Crystal system	Tetragonal
Space group	*I*4/*mcm* (No. 140)
Unit cell parameters / Å	*a* = 8.968(2) *c* = 12.859(1)
Unit cell volume / Å^3; *Z*	1034.3(3); 4
ρ_{calc} /g·cm^{-3}	6.45
μ / mm^{-1} (Mo K_α)	51.04
Absorption correction	empirical
F(000)	1672
Θ range / °	3.21 - 27.81
Index range	–11 ≤ *h* ≤ 10; –11 ≤ *k* ≤ 10; –14 ≤ *l* ≤ 16
Data completeness / %	99.7
Integrated reflections	3856 (R_σ = 0.023)
Independent reflections	356 (R_{int} = 0.057)
Refinement method	Full-matrix least-squares on F^2 (SHELXTL)
Parameters	16
Goodness of fit on F^2	1.106
Observed reflections [$I > 2\sigma(I)$]	336
R_1 / wR_2 [$I > 2\sigma(I)$]	0.024 / 0.051
R_1 / wR_2 (all data)	0.027 / 0.052
Weighting scheme[a]	a = 0.019; b = 25.438
Extinction coefficient	0.0017(1)
Residual map / e$^-$·Å^{-3}	+1.36 [1.33 Å from Bi1] / –1.30 [0.69 Å from Bi1]

[a] $w = 1 / [\sigma^2(F_o^2) + (aP)^2 + bP]$, where $P = (F_o^2 + 2F_c^2) / 3$

***Table 5.7*: Atomic coordinates and equivalent isotropic displacement parameters for $Sr_3Sn_{3.36}Bi_{1.64(3)}$.**

Atom	**Wyck.**	**Occ. ≠ 1**	***x***	***y***	***z***	U_{eq} / Å^2
M = Sn1 / Bi1	16*l*	0.84 / 0.16(1)	0.1416(1)	0.3584(1)	0.3119(1)	0.020(1)
Sr1	8*h*		0.3370(1)	0.1630(1)	½	0.022(1)
Sr2	4*a*		0	0	¼	0.020(1)
Bi2	4*c*		0	0	0	0.021(1)

***Table 5.8*: Anisotropic thermal displacement parameters (*l* Å^2) for $Sr_3Sn_{3.36}Bi_{1.64(3)}$.**

Atom	U_{11}	U_{22}	U_{33}	U_{23}	U_{13}	U_{12}
Sr1	0.022(1)	0.022(1)	0.021(1)	0	0	0
Sr2	0.022(1)	0.022(1)	0.019(1)	0	0	0
M	0.020(1)	0.020(1)	0.020(1)	0.003(1)	0	0
Bi2	0.023(1)	0.023(1)	0.017(1)	0	0	0

Structure Description The space group and atomic positions for $Sr_3Sn_{3.35}Bi_{1.64(3)}$ reveal the isostructural relationship with the compound La_3In_4Ge (*c*/*a* 1.45)[34] and a rather similar *c*/*a* ratio of 1.43. The structure is isopointal with the inverse Cr_5B_3 family.[35] It belongs to the In_5Bi_3-type subfamily which is characterized by a smaller ratio (*c*/*a* = 1.45) while larger values are found for the Cr_5B_3 aristotyp (*c*/*a* = 1.85).[36] The structure of $Sr_3Sn_{3.35}Bi_{1.64(3)}$ contains four crystallographic sites (Table 5.7) from which two are occupied by the alkaline-earth metal, Sr1 (8*h*) and Sr2 (4*a*). The *p*-block atoms are Bi2 (4*c*) and Sn1 at the site 16*l*. The latter is mixed occupied with Bi1 (16%). A projection of the crystal structure is represented in Figure 5.17a. It can be described as a *ABA'B'* stacking of planar and corrugated nets which alternate along [001]: planar (3^2.4.3.4) nets of Sr1, centered by larger planar 4^4 nets of Bi2 are found at z = 0 and corrugated 48^2 nets (by projection of all Sn1/Bi atoms in their mean plane) of Sn1/Bi, centered by larger planar 4^4 nets of Sr2 at z = 0.25. Bi2 and Sr2 form linear chains along the *c*-axis. The coordination of Bi2 atoms with Sr1 and Sr2 results in the shape of a distorted octahedron with four Bi2–Sr1 interactions (*d*(Bi2–Sr1) = 3.357(1)) in the waist and, two shorter Bi2–Sr2 distances (*d*(Bi2–Sr2) = 3.215(1) Å) in the axial direction (Figure 5.18a). In fact, those compressed octahedra share corners to form a $^3_\infty[Sr_{6/2}Bi]$ framework of twisted octahedra and can be derived from an inverse ReO_3-like distorted structure (Figure 5.18b). The shortest distances (Table 8.10, see Appendix) between M = Sn1 / Bi1 atoms of the corrugated layers running in the (001) plane and Sr atoms are quite long: *d*(Sr1–M) = 3.463(1) Å and *d*(Sr2–M) = 3.546(1) Å. This means that the Sn1/Bi1 network is quite apart from the $[Sr_{6/2}Bi2]$ framework. The Sn1/Bi1 substructure $^2_\infty[Sn_{4-x}Bi_x]$ corresponds to one of the three types of corrugated layers of homogeneous spheres packing with tetragonal symmetry that are illustrated in Figure 5.19. The M = Sn1 / Bi1 atoms have two shorter contacts of 2.998(1) Å resulting in 4-member units with a bodyless *butterfly*-like shape (Figure 5.17c), which are in turn interconnected by longer distances (3.177(1) Å) forming corrugated nets with wrenched quadrangles (Figure 5.17b). They are better described using the symbol of the Shubnikov nets as $4_c(8+2)^2$.[37, 38] Similar butterfly-like units have been discovered in Ba_3Ge_4[39] and $M_2Ba_2Sn_6$ (M = Yb, Ca).[40]

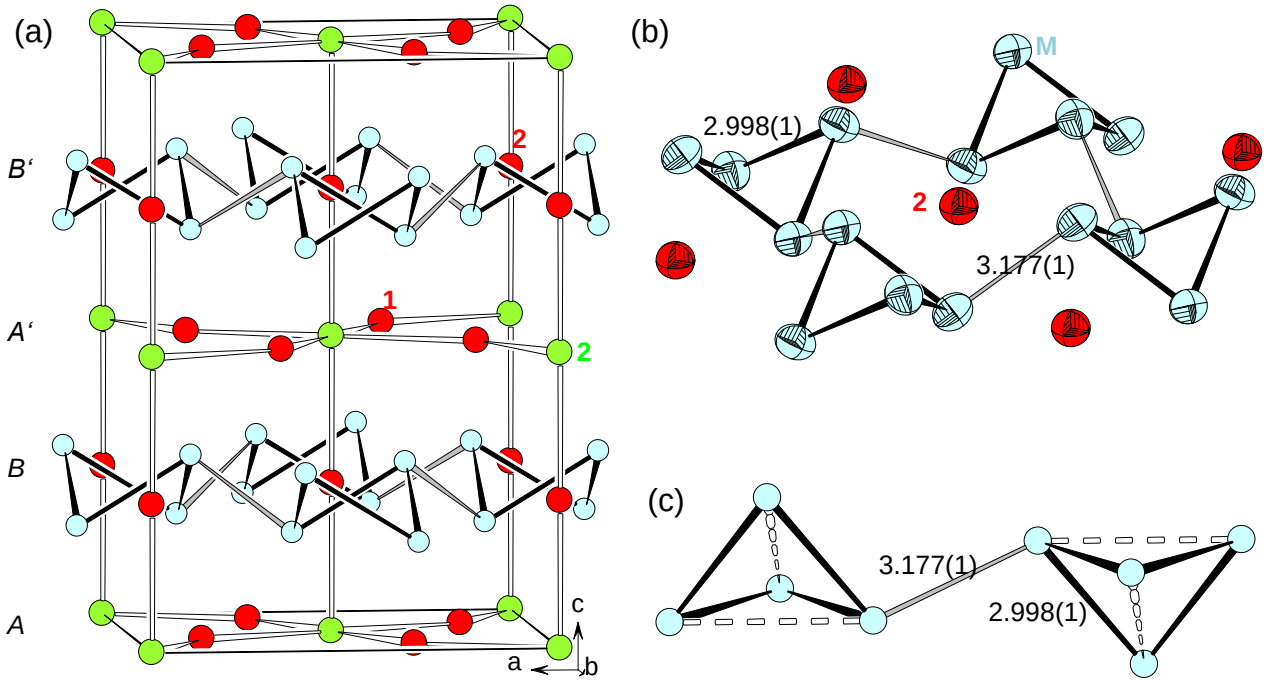

***Figure 5.17*. (a) Off-[010] projection of the unit cell of $Sr_3Sn_{3.35}Bi_{1.65(3)}$. (b) A corrugated layer of bodyless M butterflies centered by Sr2 (90% probability level). (c) Two bodyless butterflies, dashed lines indicate missing bonds from tetrahedral shapes. M = Sn1 / Bi1 (blue), Bi2 (green), Sr (red).**

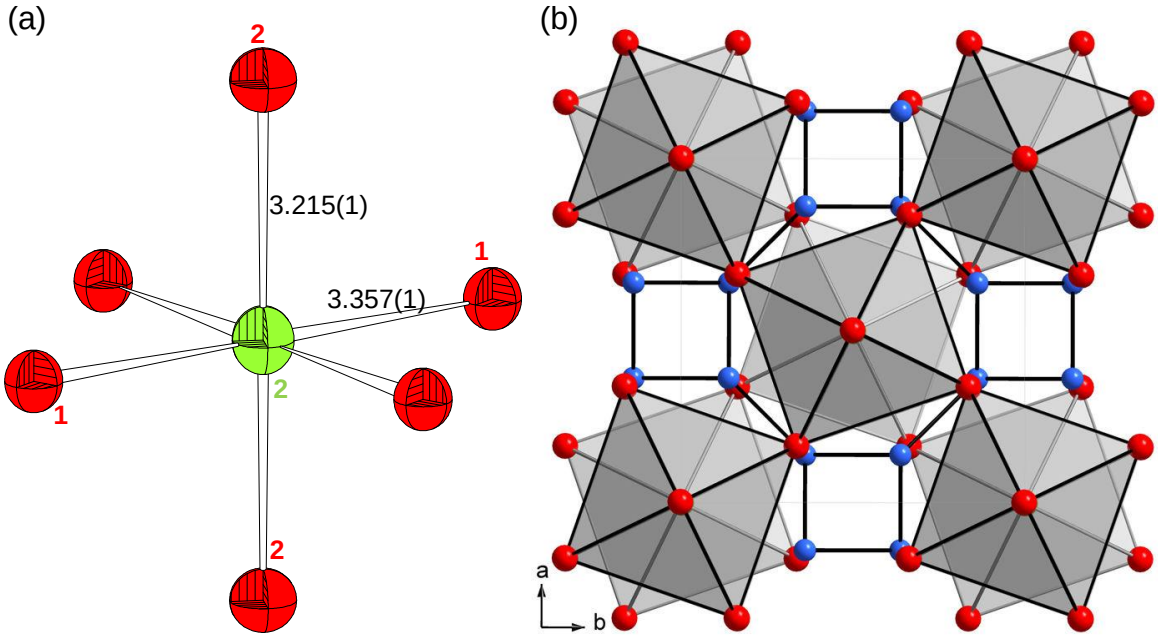

***Figure 5.18*. (a) view of the Bi2 coordination in a $\{BiSr_6\}$ octahedron with the interaction distances (see text). (b) Projection of the structure of $Sr_3Sn_{4-x}Bi_{1+x}$ (x = 0.65(3)) along [001]. The $^{3}_{\infty}[Sr_{6/2}Bi]$ octahedral framework (with polyhedral representation) corresponds to an anti-perovskite framework where the octahedra are turned alternatively clockwise and anti-clockwise along the *c*-axis. Sn1/Bi1 (blue), Bi2 (green), and Sr (red).**

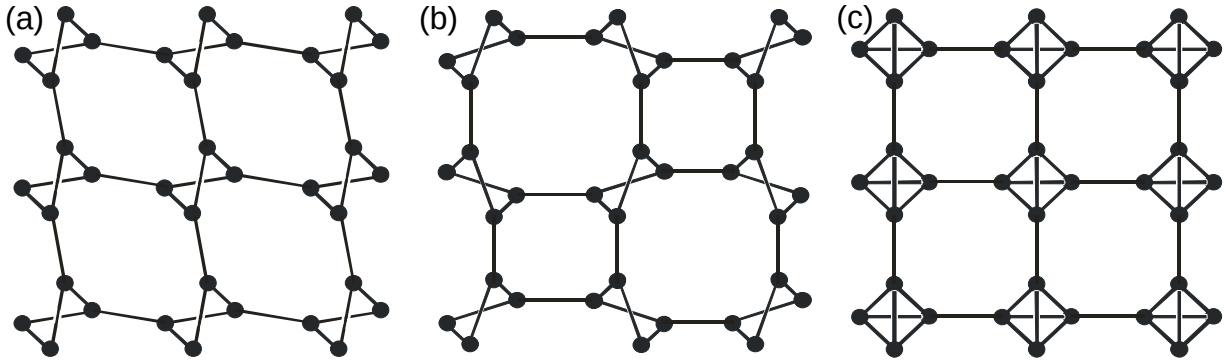

***Figure 5.19*. The three tetragonal types of sphere packing with layer like subunits corresponding to non-planar nets after ref. [37, 38]. The symbols of the respective Shubnikov nets are: (a) $4_c(8+2)^2$ layer, (b) $4_c8(8+4)$ layer, (c) 4_t8^2 layer.**

The short M–M distance (2.998(1) Å) within the 4-member units is in the range of interatomic separations in elemental *α*-Sn (2.81 Å) and *β*-Sn (3.02 and 3.18 Å) and can be considered as a localized bond (2*c*-2*e*), while the distance between the 4-member units are much longer than expected for covalent Sn–Sn bonds. A similar bond length distribution is found in $SrSn_4$[24] with localized bonds of 2.900(1) Å and 3.044(1) Å, as well as longer distances of 3.287(1) Å and 3.302(1) Å.

5.2.4 Electronic Structure

The electronic structure was calculated with the local density-functional approach and the linear muffin-tin orbital (LMTO) method in the atomic sphere approximation (ASA) using the tight-binding (TB) program LMTO-ASA. For the calculation *s*, *p*, and '*down folded*' *d*-partial waves for Sn, and *s*, *d*, and '*down folded*' *p*-partial waves for Sr were used. The *k*-space integration was performed by the tetrahedron method on a set of 16 × 16 × 16 irreducible *k* points. COHP calculations were carried out to investigate bond strenghts. The Fermi level in all figures is set to zero, and the COHP diagrams are drawn by reversing their values with respect to the energy scale (–COHP vs. *E*). This is done so that the calculated peak values are negative for antibonding and positive for bonding interactions. The band structure along the main directions of the reciprocal lattice for the hypothetical fully ordered variant 'Sr_3BiSn_4' (no mixed occupancy and formally one electron deficient) and DOS projections of the elements are represented in Figure 5.20. –COHP diagrams are shown in Figure 5.21 and enlarged sections of the band structure represented as fat bands are provided in Figure 5.22. Due to relativistic effects included in the DFT levels, the energy separation between the band with mainly Bi-6*s* character

(at the bottom of the energy scale) and those associated with Bi-6*p* is very high. The energy of the bands with Sn-5*s* character are intermediate between the two former and those associated with Sn-5*p* overlap with the Bi-6*p* bands. It is clear from the DOS diagram and band structure that the hypothetical phase 'Sr_3BiSn_4' would be metallic.

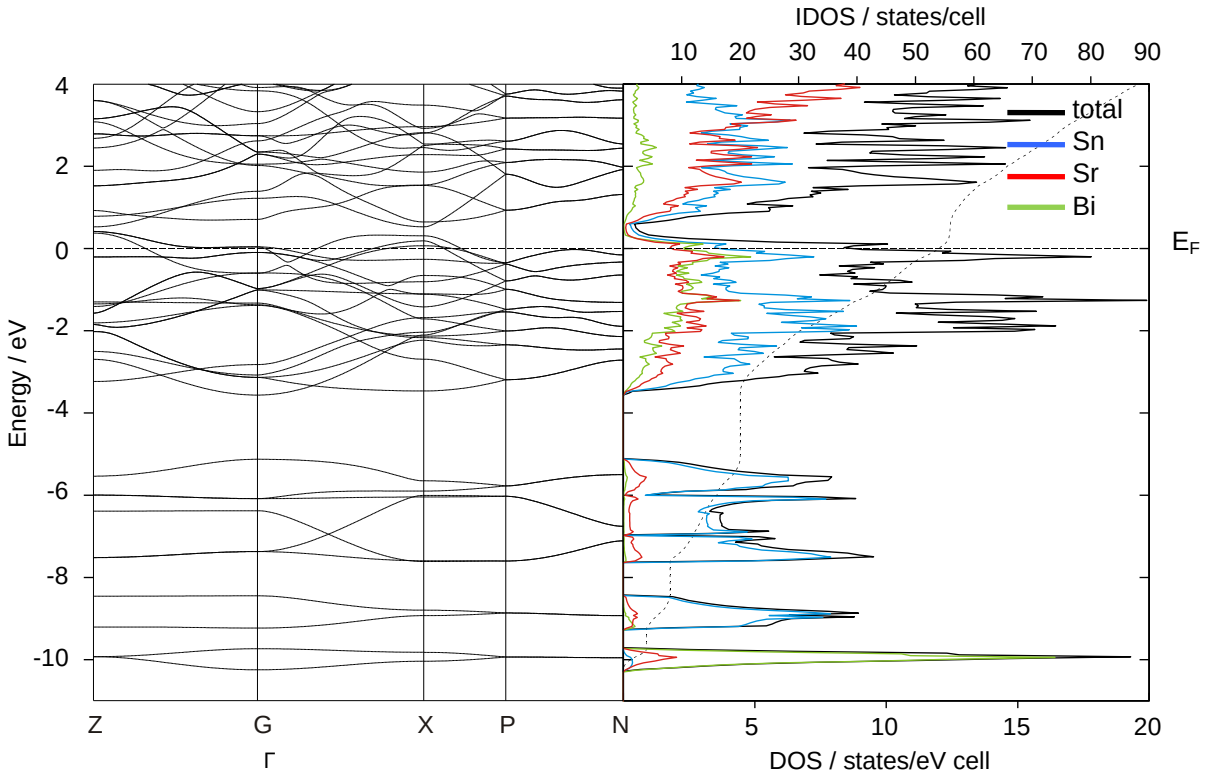

***Figure 5.20*. Band structure diagram of the hypothetical phase $Sr_3Sn_{4-x}Bi_{1+x}$ (x = 0) along the high symmetry directions of the tetragonal body centered Brillouin zone. DOS plot and integrated DOS (dashed line). The Fermi Energy E_F corresponds to an electron count of 54 valence e^-/cell (x = 0) and the pseudo-gap (at +0.36 eV) to 56 valence e^-/cell (x = 1).**

The Fermi level (E_F) is very near to a deep minimum (pseudo-gap) in the DOS. This very narrow band gap is opened at about +0.4 eV above E_F (Figure 5.22) and corresponds to an integrated density of states (IDOS) of 56 e^-/cell. This reflects the situation of $Sr_3Sn_3Bi_2$ (i.e. x = 1) and predicts a zero-gap semiconductor for that composition. The fat band analyses show that the bands just below the narrow gap, which cross the Fermi level at the symmetry line Γ→ X, have mainly Bi-6*p* and Sn-5*p* character. This invokes that in the present compound, $Sr_3Sn_{4-x}Bi_{1+x}$ with x < 1, the electron deficiency is not only associated with the two-dimensional slab of $\{Sn_4\}$ entities, but mainly with the $[Sr_{6/2}Bi]$ substructure. The partial DOS of Sr shows that Sr contributes to the DOS also below E_F.

The fine structure of the pDOS contains the features of the pDOS of Bi and indicates covalent Sr–Bi interactions between –3 eV and the narrow gap. The unusually high contribution of the electropositive *s*-block metal to the covalent bonding of this phase is also visible in the integrated –COHP values (Table 5.9). The strength of the Sr–Bi interactions (–ICOHP = 0.85 eV/bond) is significant and compares well even to those of the longer Sn–Sn interaction of 3.177(1) Å (1.30 eV/bond). Those and the presence of additional weaker Sr–Sn bonding states (bonding levels are not optimized for x = 0) can accept additional electrons.

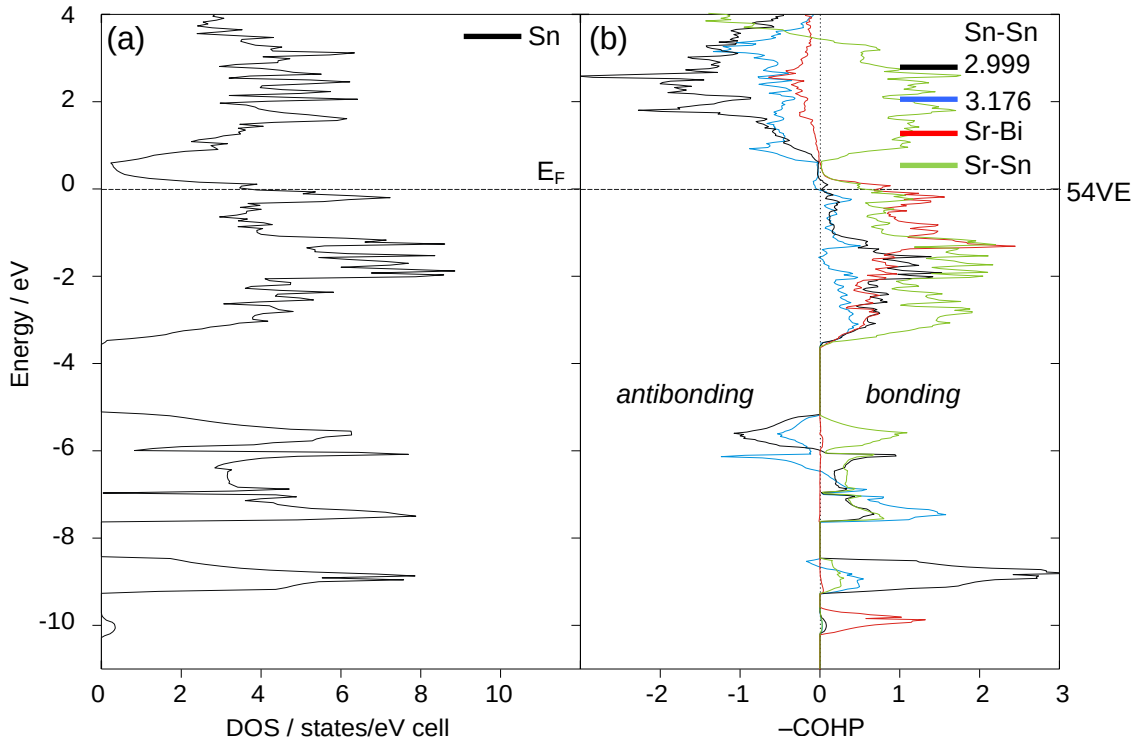

***Figure 5.21*. (a) Projected DOS of Sn emphasizing Sn states at E_F. (b) –COHP plots of selected interactions in the hypothetical fully ordered phase Sr_3BiSn_4, Sn–Sn(3.176 Å) (blue), Sn–Sn(2.999 Å) (black), Sr–Bi (red), and Sr–Sn (green). In all cases the Fermi level is taken as point of zero energy.**

***Table 5.9*: –ICOHP values for selected interatomic contacts in $Sr_3Sn_{3.36}Bi_{1.64(3)}$. Energies are given in eV/bond.**

interaction		*d* / Å	–ICOHP (at E_F)	–ICOHP (max.)
Sn	Sn	2.998	1.680	1.686
Sn	Sn	3.177	1.300	1.300
Sr	Bi	3.215 - 3.357	0.845	0.885
Sr	Sn	3.463 - 3.654	0.425	0.587

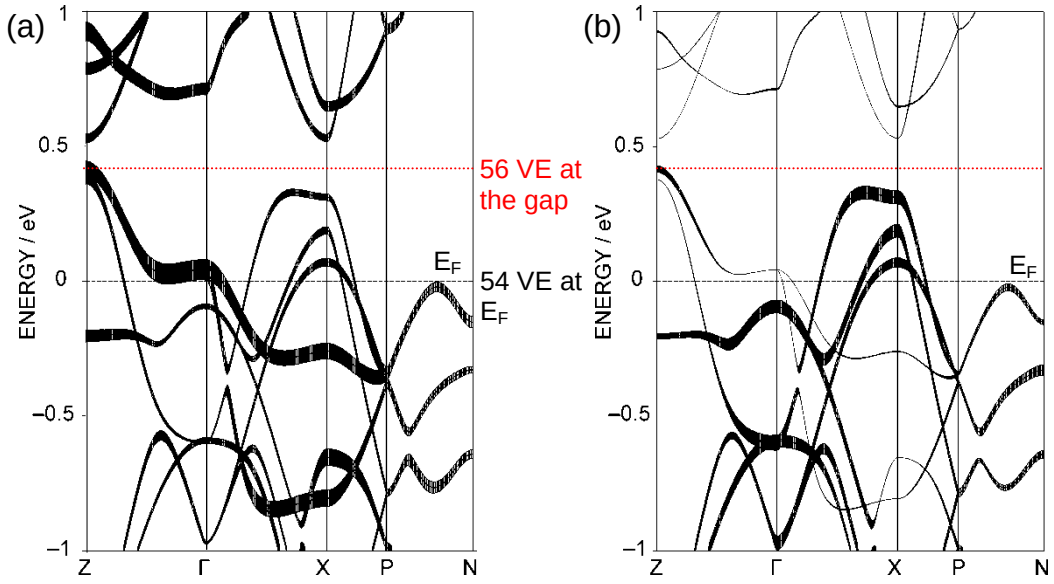

***Figure 5.22*. (a) Fat band plot with bands drawn with a thickness representative of their corresponding orbital contribution for Sn-*p* orbitals in the hypothetical phase $Sr_3Sn_{4-x}Bi_{1+x}$ (x = 0): the gap at +0.40 eV above E_F corresponds to an IDOS of 56 e^-/cell, meaning x = 1. (b) Bi-*p* contributions.**

Looking at the –COHP curves of the two different Sn–Sn bonds (black and blue lines in Figure 5.21b) and the corresponding –ICOHP values the analysis of the bonding interactions shows that all bonding levels are filled up to E_F for the electron count of 54 e^-/cell. As for the Sn–Sn interactions at or above E_F non-bonding Sn levels can be anticipated since Sn contributions show up in the partial DOS (Figure 5.21a) but not in the –COHP plot. This means that the flat bands at E_F are associated with states having non-bonding character. This band characteristic can be interpreted as lone pairs at E_F, which has been observed in polar intermetallic alloys like $BaSn_3$, $SrSn_3$, $SrSn_4$ and $BaSn_5$ and was linked to their superconducting properties. At an electron count of 56 electrons per cell all these non-bonding levels are filled. The integrated COHP values of Sn–Sn interactions (Table 5.9) in the hypothetical phase reach their maximum at the gap. The values of about 1.69 eV/bond for the distance of 2.998 Å (1.68 eV/bond at E_F) and 1.30 eV/bond for the distance of 3.18 Å (1.30 eV/bond at E_F) indicate that the butterfly-like units are interconnected by significantly weaker intercluster bonds if compared to the intracluster bonds. Thus, the phase $Sr_3Sn_{4-x}Bi_{1+x}$ ought to correspond to the charge balanced phase for x = 1 and would be isoelectronic with the phases Ba_3Ge_4X (X = O or C_2).[41, 42] The latter contain $\{Ge_4\}^{4-}$ tetrahedral units, forming the Shubnikov net 4_t8^2[37] in which the distorted quadrangles are replaced by isolated tetrahedra.

However**,** the rigid host structure $[Sr_{6/2}Bi]$ could also prevent the separation of those units. More information on sphere packing can be obtained from ref.[38].

5.2.5 Discussion

Within the Zintl-Klemm concept, a charge transfer from electropositive Sr atoms to the anionic part may be assumed in the formulation $(Sr^{2+})_3[Bi^{3-}(Sn_{4-x}Bi_x)^{3-}]$ where the isolated Bi2 atoms would carry a formal charge of –3. Taking into account the two layer-like substructures, we can write $[Sr_{6/2}Bi]^{3+}[Sn_{4-x}Bi_x]^{3-}$. X = 1 leads to the ion $(Sn_3Bi_1)^{3-}$, which is isoelectronic with $\{Sn_4\}^{4-}$. From this the four-atom unit should form isolated tetrahedra or alternatively a two-dimensional (arsenic like) net of three-bonded atoms, with similar distances between the atoms. Experimental attempts to increase the Bi content to access the semiconducting end-member (x = 1) of this transition resulted in the formation of additional binary phases, such as $Sr_{11}Bi_{10}$.[43] This manifests a general problem in the investigation of quasi-binary systems where the number of possible phase relations in the ternary system is greatly enhanced, and products with a desired quasi-binary stoichiometry may not form for certain compositional ranges. The Bi occupancy (x < 1) in the Sn1/Bi1 layer**,** as obtained from refinement**,** is lower than expected and this implies that the phase is slightly electron deficient on the assumption of three-bonded Sn1/Bi1 atoms. Consequently, the $[Sn_{4-x}Bi_x]$ sublattice is an intermediate between isolated tetrahedra, one of the tetragonal sphere packings, or a regular 2D net of three bonded atoms with similar separation distance. The wide separation between Sn1/Bi1 atoms of different four-member ring units presumably originates from the electron deficiency. Therefore, the optimum Bi content (x = 1) in the $[Sn_{4-x}Bi_x]$ layer should lead either to the shortening of the intracluster distance, along with the increase of the intercluster distance or to more balanced distances as expected for a two-dimensional three-bonded atom arrangement. However, the refinements of Bi occupancy in the M_4 layer with increasing Bi content show only a modest trend in the expected direction.

In conclusion the structure of the $^{2}_{\infty}[Sn_{4-x}Bi_x]$ corrugated net in the solid solutions $Sr_3Sn_{4-x}Bi_{1+x}$ (x < 1) is intermediate between that in the classical Zintl phase Ba_3Ge_4X with $\{Ge_4\}$ tetrahedra and that of the hypothetical $Sr_3Sn_3Bi_2$ (x = 1), where the $[Sn_{4-x}Bi_x]$ substructure may also form layers of 3-bonded atoms with similar bond distances.

The slight electron deficiency in $Sr_3Sn_{4-x}Bi_{1+x}$ ($x < 1$) is accommodated in the $^{2}_{\infty}[Sn_{4-x}Bi_x]$ sublattice by bond isomerism leading to stronger bonds within the four-member ring units, which are in turn interlinked by weaker interactions, resulting in the Shubnikov net $4_c(8+2)^2$. The classical Zintl phase limit for this structure, $Sr_3Sn_3Bi_2$, may also be isostructural with Ba_3Ge_4X containing the $[Sn_3Bi]^{3-}$ anions as tetrahedra. However, the fact that the effective charge transfer from the alkaline-earth metal Sr to Bi is not optimal - and other factors in structure selection like packing efficiency and Madelung's energy may contribute[44] - prevents the formation of the ideal Zintl phase, which is observed in the more ionic phases Ba_3Ge_4X. According to the COHP calculations it is most likely that the Zintl stoichiometry cannot be reached due to strong cation effects and the resulting delocalization of additional electrons into cation–anion bonding states rather than localization in non bonding M states.

It is worth mentioning that two further ternary Sr–Sn–Bi compounds with nominal compositions $Sr_{11}Sn_{12}Bi_4$ (*Ccca*, a = 8.903(1), b = 44.155(5), c = 8.912(1), Z = 4) and $Sr_{15}Sn_{18}Bi_4$ (*I*4*mcm*, a = 8.910(1), c = 55.359(7), Z = 4) have been discovered as crystalline byproducts. Their structures contain the same corrugated layers of bodyless Sn butterflies but with no statistical Sn/Bi occupancy. They represent stacking variants with one enlarged unit cell parameter. The samples could not be reliably reproduced; therefore no further details are reported herein.

5.3 Substitution Effects in Sr_3Sn_5: Synthesis and Structure of $Sr_3Sn_{5-x}Tl_x$ ($x = 1.78, 2.14$) and $Sr_3Sn_{5-x}In_x$ ($x = 1.18$)

5.3.1 Introduction

Substitution effects in the intermetallic phase Sr_3Sn_5 with electron richer Bi have been presented in Chapter 5.2. Phase stabilization, originating from cation effects or VEC, has always been a matter of discussion. Substitution effects in electron rich alkaline earth–tin systems with triel atoms can therefore act as a test case. As a short introduction an overview of selected binary Ae trielides is provided.

The structures of the In-rich Ae binaries, such as $AeIn_2$ (Ae = Ca, Sr, Ba) or $AeIn_4$[44-46] can be explained and understood with the help of the Zintl concept or Wade's rules. These concepts fail for the triel-poorer compounds, such as AeIn (Ae = Ca, Sr, Ba), Ae_5In_3, Ae_2In, or $Ae_{28}In_{11}$.[47] Between these two groups, the compounds with composition Ae_3Tr_5 exist. As a first example the structure of Ba_3Al_5[48] shows three $\{(4b)\text{-}Al\}^-$ and two $\{(3b)\text{-}Al\}^{2-}$ atoms, which need one more electron than is available from electron transfer of the Ba atoms. Additionally, beyond the Zintl boundary, the phases Ca_3Ga_5[49] and Sr_3In_5[50] (VEC/Tr = 2.625, $Hf_3Ni_2Si_3$-type[51]) crystallize in a 3D network with four 4b- and one 2b-triel atom, and therefore have electron deficiency of one electron. The corresponding density of states for the binary alkaline earth triels shows a pseudo gap at E_F with incompletely filled valence bands. In contrast, the rare earth compounds La_3In_5 and β-Y_3In_5[52] (with VEC/Tr = 4.8) crystallize in the Pu_3Pd_5 structure type and are formally Zintl phases with $\{In_5\}^{9-}$ clusters. The gallides with smaller RE = Sc, Y, Tb - Tm, Lu have been described in terms of the Tm_3Ga_5 structure type.[53] As reported by Corbett et al. in the compound α-Y_3In_5 (VEC 4.8) the Tm_3Ga_5-type evolves from the Pu_3Pd_5-type of β-Y_3In_5 by a first-order phase transition at lower temperature. The above listed examples illustrate the fine dependencies of a structure type from VEC and cation size. On the other side the electron richer Ae_3Tt_5, such as Ae_3Sn_5 (Ae = Sr, Ba)[31, 54] phases throughout crystallize in the Pu_3Pd_5-type. They contain *arachno*-$\{Sn_5\}^{6-}$ clusters with two metallic electrons.

Substitution experiments in the Ae_3M_5 system have recently been reported by Röhr et al.[55] who investigated phase stability in the $Ae_3(Tr/Tt)_5$ systems (Tr = In, Al; Tt = Pb) by adjusting the VEC/M and by the effect of the relative size ($r_{Ae} : r_{Tr/Tt}$) of the atoms.

As reported, the compounds $Ae_3Pb_{5-x}In_x$ (x = 0.7 for Sr, x = 0.6 for Ba) crystallize in the Pu_3Pd_5-type, while the Zintl phase Sr_3In_4Pb (VEC/M = 4.4) favors the $Hf_3Ni_2Si_3$-type. According to Röhr et al. the electronically stabilized area for the Pu_3Pd_5-type ranges from Ba_3Pb_5 (VEC / Pb = 5.2, with *arachno*-clusters) to La_3In_5 (VEC/In = 4.8, with *nido*-clusters). Tetrel for tetrel substitution in the compound $Ba_3Ge_{2.82}Sn_{2.18}$ preserving the Pu_3Pd_5-type was reported by Fässler et al.[31] Recent reports also include the investigation of the role of the cations in the formation of different Zintl polyanions, i.e. size (matrix effects) and polarizing power.[44] Small Mg^{2+} ions, for example, lead to highly charged anionic sublattices, whereas larger cations with lower charge densities lead to coordination among anions. In this sense, the Sr_3Sn_5 system has been substituted with Ca, leading to an interesting bond stretching isomerism[56] which is similar to the situation in Ba_3Ge_4.[39] Regarding the structures of Ae_3Tl_5 (Ae = Ca, Sr), as presented in Chapter 6.3, which crystallize in the Pu_3Pd_5-type, the substituted Sr stannide compounds, presented in this chapter, show an interesting packing effect that leads to crystallization in the Tm_3Ga_5 structure type.

5.3.2 Synthesis and Characterization

Synthesis Single-crystals of $Sr_3Sn_{3.22}Tl_{1.78(5)}$ (**1**) and $Sr_3Sn_{3.8}In_{1.2(3)}$ (**3**) were obtained by direct fusion of the pure elements using stoichiometric ratios according to Sr : Sn : (Tl/In) = 3 : (5 – y) : y. The loading of the Nb crucibles (total loading for all compounds ~ 1.300 g) took place in an Ar-filled glovebox. After sealing the crucible under reduced Ar pressure they were heated to 800 °C in evacuated silica tubes at a rate of 2 $K \cdot min^{-1}$. After annealing at this temperature for 6 h the samples were cooled down to 500 °C with a rate of 2 $K \cdot min^{-1}$ and annealed for three days. The crystalline products exhibit metallic luster and are air sensitive. **1** was obtained from a balanced stoichiometric loading with y = 1.5. The Tl-richer compound $Sr_3Sn_{2.86}Tl_{2.14(5)}$ (**2**) was picked from the reaction mixture of a Tl-rich sample loaded with the ratio Sr : Sn : Tl = 3 : 1.5 : 7.5. Compounds with crystallographic compositions x ~ 1.9 (not presented here) were obtained from a sample loaded with y = 2. Compound **3** was found in a sample loaded as Sr : Sn : In = 3 : (5 – y) : y (y = 2) which was synthesized in order to investigate a possible dependency of phase formation on atomic size or electronic effects.

However, Tl-poorer loadings, with y < 1.5 led to the formation of crystals with compositions such as $SrSn_{1.25}Tl_{1.75(3)}$, which, like $BaSn_3$,[16] crystallize in the Ni_3Sn structure type (the hexagonal variant of the $AuCu_3$-type).

Although not investigated further in this context it should be noted that the pure binary $SrSn_3$[23] evolves in a trigonal rhombohedral unit cell with an entirely different structure. This series of experiments reveals the formation of the target structures if the sample loadings involve y ≥ 1.5. The maximum Tl for Sn substitution in the solid solutions is obtained by the loading used for **2**. Similar attempts to synthesize the Ba analogue by reacting loadings of various reaction mixtures such as Ba : Tl : Sn = 3 : 4 : 1; 3 : 3.5 : 1.5; or 3 : 3 : 2 only resulted in mixtures of Ba_3Sn_5 and $BaSn_{3-x}Tl_x$ (Ni_3Sn-type).

EDX Analyses Quantitative and qualitative elemental analyses on several single-crystals of the product of a reaction loaded as Sr : Sn : Tl = 3 : 3.5 : 1.5 confirmed the presence of all three elements with ratios of Sr : Tl : Sn = 32(3) : 47(5) : 21(2) at% (calculated values, based on the single-crystal composition (compound **1**) taken from this sample: Sr: 38, Sn: 40, Tl: 22 at%). EDX analyses carried out on a single-crystal with composition $Sr_3Sn_{3.8}In_{1.2(3)}$ (**3**) (obtained from a stoichiometric loading with Sr : Sn : In = 3 : 3 : 2) confirmed the presence of all three elements with a ratio of Sr : In : Sn = 53(6) : 32(4) : 15(3) (calculated values: Sr: 37.5, Sn: 47.5, In: 15.0 at%).

5.3.3 Crystal Structure Determination and Description

Structure Determination Single-crystals of $Sr_3Sn_{5-x}Tr_x$ (Tr = In, Tl; x ~ 2) were selected and checked for singularity in the glovebox and fixed on a glass capillary, which afterwards was introduced into a capillary (0.3 mm diameter) and closed by fusing the open end. All crystals were measured on an Oxford Xcalibur3 diffractometer equipped with a CCD detector. Each data collection (776 frames) involved 4 sets of ω scans (–41° to +63° for different φ positions: 0°, +90°, +180°, +270°) and a φ scan (0° - 360° with θ = 30°) with scan width 1°/frame and exposure time 20s/frame. The integrated data of all three crystals was corrected for absorption by use of an empirical method implemented in the CrysAlis software (ABSPACK, Oxford Diffraction 2006). The structures were solved by direct methods with the software package SHELXTL from Bruker. The solutions in the space group *Pnma* showed four independent Sn and two Sr positions. Smaller displacement parameters on all Sn atoms in the substituted crystals lead to the introduction of additional free variables and mixed occupancy of these sites with Tl (M = Sn / Tl).

In the indium substituted compound only two of the four Sn sites showed significant mixed occupancy. Although the crystallographic composition is in acceptable agreement with EDX results, and since In and Sn are hard to distinguish by X-ray experiments, the absolute values of the refinement should be treated with caution, as reflected in the large standard deviations. Nevertheless, the refinement converged significantly by introducing the mixed sites. For Tl substitutions various crystals were refined and resulted in crystallographic compositions with x = 1.73, 1.78, 1.82, 1.95, 2.07, and 2.14. However, the lattice parameters in this series do not uniformly scale with composition, i.e. there was no dependency in the sense of Vegard's law. For discussions the values of $Sr_3Sn_{3.22}Tl_{1.78(5)}$ and $Sr_3Sn_{2.86}Tl_{2.14(5)}$, serving as representatives for the series, are presented. Table 5.11 contains relevant crystallographic and refinement data. Atomic positions and displacement parameters of the three compounds are comprised in Tables 5.10 and 5.12. Important interatomic distances are provided in Table 8.11 (see Appendix).

***Table 5.10*: Atomic coordinates and equivalent isotropic displacement parameters for $Sr_3Sn_{3.22}Tl_{1.78(5)}$, $Sr_3Sn_{2.86}Tl_{2.14(5)}$, and $Sr_3Sn_{3.8}In_{1.2(3)}$.**

Atom	Wyck.	Occ. ≠ 1	*x*	*y*	*z*	U_{eq} / Å^2
			$Sr_3Sn_{3.22}Tl_{1.78(5)}$ (1)			
M1 = Sn1 / Tl1	8*d*	0.60 / 0.40(1)	0.5967(1)	0.4456(1)	0.3620(1)	0.019(1)
M2 = Sn2 / Tl2	4*c*	0.70 / 0.30(1)	0.7072(1)	¼	0.5964(1)	0.021(1)
M3 = Sn3 / Tl3	4*c*	0.78 / 0.22(1)	0.5068(1)	¼	0.1052(1)	0.021(1)
M4 = Sn4 / Tl4	4*c*	0.54 / 0.46(1)	0.7361(1)	¼	0.1484(1)	0.020(1)
Sr1	4*c*		0.9311(1)	¼	–0.1347(2)	0.017(1)
Sr2	8*d*		0.6470(1)	0.5004(1)	–0.1289(1)	0.018(1)
			$Sr_3Sn_{2.86}Tl_{2.14(5)}$ (2)			
M1 = Sn1 / Tl1	8*d*	0.56 / 0.44(1)	0.0976(1)	0.4456(1)	0.3620(1)	0.022(1)
M2 = Sn2 / Tl2	4*c*	0.56 / 0.44(1)	0.2092(1)	¼	0.5985(1)	0.025(1)
M3 = Sn3 / Tl3	4*c*	0.76 / 0.24(1)	0.0074(1)	¼	0.1065(2)	0.025(1)
M4 = Sn4 / Tl4	4*c*	0.42 / 0.58(1)	0.2352(1)	¼	0.1409(1)	0.024(1)
Sr1	4*c*		0.4329(1)	¼	–0.1341(2)	0.019(1)
Sr2	8*d*		0.1465(1)	0.5026(1)	–0.1303(2)	0.021(1)
			$Sr_3Sn_{3.8}In_{1.2(3)}$ (3)			
M1= Sn1 / In1	8*d*	0.46 / 0.54(10)	–0.0919(1)	0.4428(1)	0.3666(1)	0.012(1)
Sn2	4*c*		–0.0078(1)	¼	0.1056(1)	0.013(1)
Sn3	4*c*		–0.2026(1)	¼	0.5925(1)	0.012(1)
M4 = Sn4 / In4	4*c*	0.92 / 0.08(7)	–0.2319(1)	¼	0.1592(1)	0.011(1)
Sr1	4*c*		–0.4256(1)	¼	–0.1374(1)	0.010(1)
Sr2	8*d*		0.1488(1)	0.5003(1)	0.1244(1)	0.011(1)

***Table 5.11*: Selected crystallographic and refinement data for $Sr_3Sn_{3.22}Tl_{1.78(5)}$, $Sr_3Sn_{2.86}Tl_{2.14(5)}$, and $Sr_3Sn_{3.8}In_{1.2(3)}$.** [a] $w = 1 / [\sigma^2(F_o^2) + (aP)^2 + bP]$, where $P = (F_o^2 + 2F_c^2) / 3$

Empirical formula	**$Sr_3Sn_{3.22}Tl_{1.78(5)}$ (1)**	**$Sr_3Sn_{2.86}Tl_{2.14(5)}$ (2)**	**$Sr_3Sn_{3.8}In_{1.2(3)}$ (3)**
Formula weight / g·mol^{-1}	1008.69	1040.74	851.84
Temperature / K	293(2)	293(2)	293(2)
Crystal size / cm^3	0.05 × 0.05 × 0.05	0.05 × 0.05 × 0.05	0.04 × 0.04 × 0.05
Crystal color; shape	Silvery metallic; Block shaped		
Diffractometer	Oxford Xcalibur3 (CCD)		
Crystal system	Orthorhombic		
Space group	*Pnma* (No. 62)		
Unit cell parameters / Å	a = 13.422(1); b = 10.897(1) c = 6.897(1)	a = 13.482(2); b = 10.938(2) c = 6.850(1)	a = 13.349(3); b = 10.857(3) c = 6.883(2)
Unit cell volume / Å^3; Z	1008.65(11); 4	1010.1(2) ; 4	997.6(5); 4
ρ_{calc} / g·cm^{-3}	6.64	6.84	5.67
μ / mm^{-1} (Mo K$_\alpha$)	51.75	56.75	27.91
Absorption correction	empirical	empirical	empirical
F(000)	1677	1723	1451
Θ range / °	3.32 - 27.82	3.34 - 27.84	3.05 - 27.81
Index range	–17 ≤ h ≤ 16; –10 ≤ k ≤ 14 –9 ≤ l ≤ 9	–17 ≤ h ≤ 14; –13 ≤ k ≤ 14 –8 ≤ l ≤ 8	–17 ≤ h ≤ 17; –14 ≤ k ≤ 14 –7 ≤ l ≤ 9
Data completeness / %	99.8		
Integrated reflections	5052 (R_σ = 0.035)	4992 (R_σ = 0.058)	13560 (R_σ = 0.025)
Independent reflections	1254 (R_{int} = 0.055)	1254 (R_{int} = 0.083)	1241 (R_{int} = 0.049)
Refinement method	Full-matrix least-squares on F^2 (SHELXTL)		
Parameters	48	48	46
Goodness of fit on F^2	1.199	1.102	1.114
Observed reflections [$I > 2\sigma(I)$]	1124	992	1007
R_1 / wR_2 [$I > 2\sigma(I)$]	0.031 / 0.058	0.038 / 0.063	0.021 / 0.046
R_1 / wR_2 (all data)	0.040 / 0.061	0.062 / 0.070	0.030 / 0.047
Weighting scheme[a]	a = 0.022; b = 0	a = 0.020; b = 0	a = 0.022; b = 2.207
Extinction coefficient	0.0010(1)	0.0016(1)	0.0036(1)
Residual map / e$^-$·Å^{-3}	+1.48 [1.68 Å from Tl4] –1.45 [0.97 Å from Tl3]	+2.03 [1.27 Å from Tl1] –1.62 [0.83 Å from Tl3]	+1.27 [0.94 Å from Sn2] –0.92 [1.69 Å from Sr1]

***Table 5.12*: Anisotropic thermal displacement parameters (*I* Å^2) for $Sr_3Sn_{3.22}Tl_{1.78(5)}$, $Sr_3Sn_{2.86}Tl_{2.14(5)}$, and $Sr_3Sn_{3.8}In_{1.2(3)}$.**

Atom	U_{11}	U_{22}	U_{33}	U_{23}	U_{13}	U_{12}
			$Sr_3Sn_{3.22}Tl_{1.78(5)}$ (1)			
M1	0.017(1)	0.018(1)	0.021(1)	0	0	0
M2	0.025(1)	0.018(1)	0.021(1)	0	0	0
M3	0.020(1)	0.018(1)	0.026(1)	0	–0.004(1)	0
M4	0.017(1)	0.019(1)	0.024(1)	0	0.003(1)	0
Sr1	0.015(1)	0.016(1)	0.019(1)	0	0	0
Sr2	0.015(1)	0.020(1)	0.019(1)	0	0	0
			$Sr_3Sn_{2.86}Tl_{2.14(5)}$ (2)			
M1	0.024(1)	0.022(1)	0.021(1)	0	0	0
M2	0.030(1)	0.020(1)	0.024(1)	0	0	0
M3	0.027(1)	0.012(1)	0.028(1)	0	–0.005(1)	0
M4	0.023(1)	0.022(1)	0.028(1)	0	0.004(1)	0
Sr1	0.021(1)	0.018(1)	0.019(1)	0	0.002(1)	0
Sr2	0.020(1)	0.024(1)	0.020(1)	0	0	0
			$Sr_3Sn_{3.8}In_{1.2(3)}$ (3)			
M1	0.015(1)	0.008(1)	0.013(1)	0	0	0
Sn2	0.015(1)	0.008(1)	0.015(1)	0	0.004(1)	0
Sn3	0.017(1)	0.008(1)	0.011(1)	0	0.002(1)	0
M4	0.013(1)	0.010(1)	0.012(1)	0	–0.003(1)	0
Sr1	0.012(1)	0.006(1)	0.011(1)	0	0	0
Sr2	0.013(1)	0.010(1)	0.011(1)	0	0	0

Structure Description All three compounds (**1**, **2**, and **3**) crystallize in the Tm_3Ga_5 structure type in the orthorhombic space group *Pnma* and Pearson code *oP*52. A projection of the unit cell of $Sr_3Sn_{2.86}Tl_{2.14(5)}$, as a representative for all three compounds, is shown in Figure 5.23a. The M = Sn / Tl sites form similarly distorted square pyramidal clusters that are interconnected by longer intercluster bonds like in Ae_3Sn_5[31] (Ae = Sr, Ba, Pu_3Pd_5-type). Compared to the Pu_3Pd_5-type compounds, the present alignment only differs in terms of the relative arrangement of the cluster chains. The reorientation takes place in a lower symmetry rearrangement, with no direct group-subgroup symmetry relation and a tilt with respect to the *a*-axis of ±36.26°, ±35.72°, and ±36.83° for **1**, **2**, and **3**, respectively. The square pyramids now lie on mirror planes at y = ¼, ¾ with M4 as apices. A comparison to the cluster orientation in non-substituted Sr_3Sn_5 is shown in Figure 5.23. In contrast to Sr_3Sn_5, where the cluster chains are oriented parallel to each other, in the compounds **3**, **2**, and **1** they are tilted and comprise angles of 73.65°, 72.52°, and 71.43°, respectively. In compounds **1** and **2** all atomic sites of the cluster atoms are statistically occupied by Sn and Tl atoms. The highest site occupancies of Sn are on the M2 site: 70% in **1**, 56% in **2** and on the M3 site: 78% in **1**, 76% in **2**. The corresponding sites are not mixed occupied in compound **3**.

This distribution of Sn occupancy is consistent with the fact that the more electronegative Sn ($X_{Pauling}$(Tl) = 1.62, $X_{Pauling}$(Sn) = 1.96) is preferentially located at sites with lower coordination numbers (here the M2 and M3 sites), thus being positioned at sites with higher electron density. This method of 'topological charge stabilization' has been shown for many other 'coloring problems' and was reviewed in detail by Burdett and Miller.[57-59]

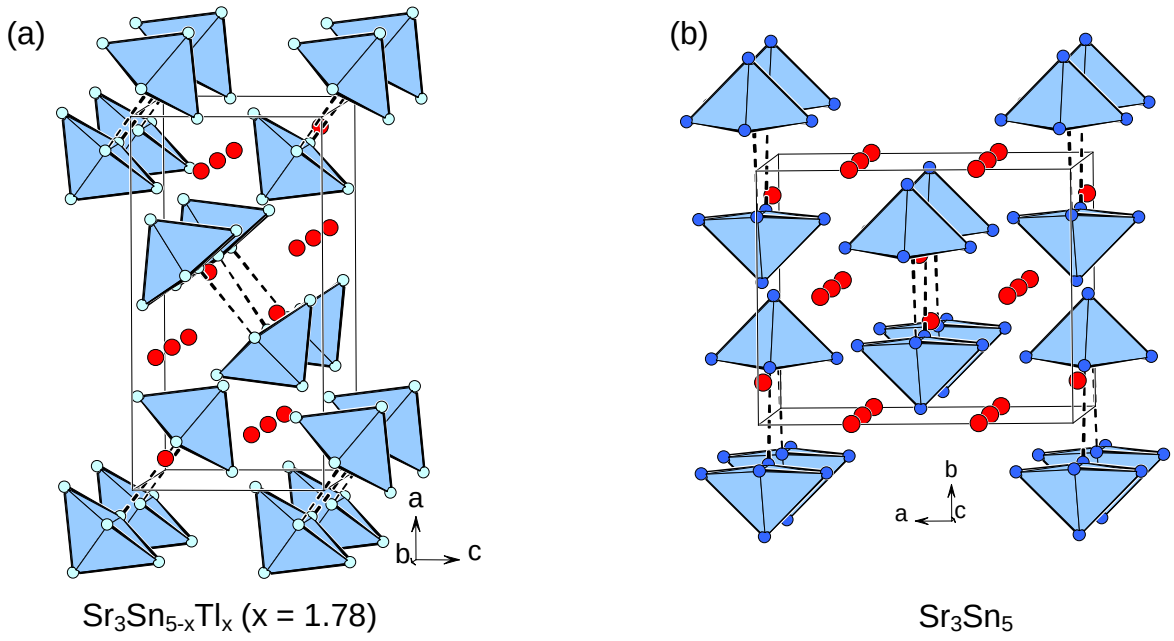

***Figure 5.23*. (a) Projection of the unit cell of $Sr_3Sn_{5-x}Tl_x$ (x = 1.78). M = Sn / Tl (light blue), Na (red), (b) unit cell projection of Sr_3Sn_5. Sn (blue), Na (red). Longer intercluster bonds are shown as dashed lines.**

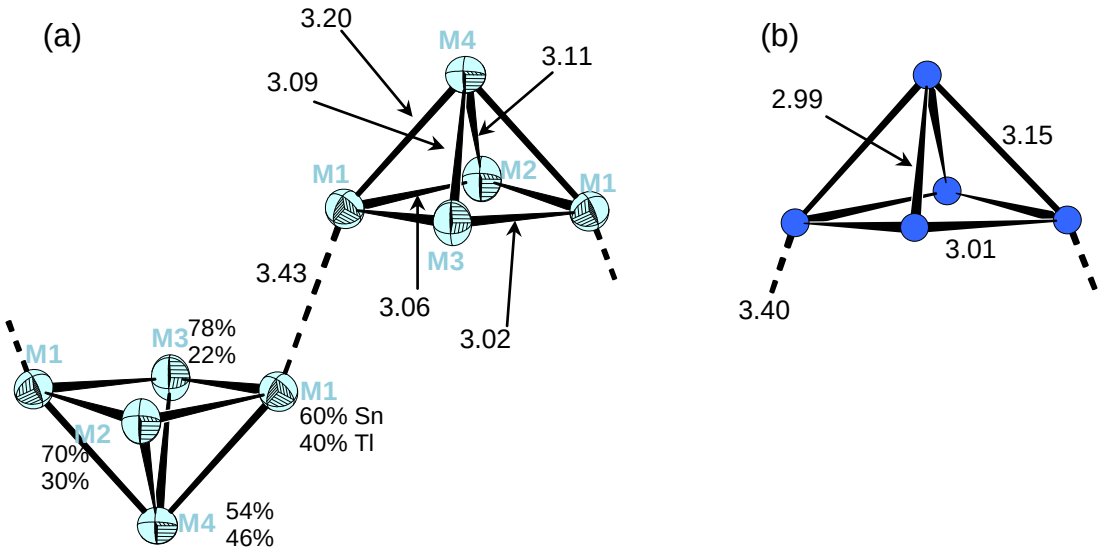

***Figure 5.24*. (a) Connectivity of the M atoms (90% level) in $Sr_3Sn_{5-x}Tl_x$ (x = 1.78). The occupancy factors are shown. M = Sn / Tl (light blue). (b) {Sn_5} cluster in Sr_3Sn_5. Sn (blue). Longer intercluster bonds are drawn as dashed lines.**

This is also consistent with the Zintl-Klemm concept, stating that the sites with lower bonding number are more negatively charged than the positions with a higher one. The shortest intracluster contacts occur between atoms of the pyramidal bases, which are formally three-bonded. The contacts are in the range of 3.023(1) to 3.196(1) Å in **1** and intermediate to the corresponding distances in Sr_3Sn_5 (2.99 to 3.15 Å) and Sr_3Tl_5 (3.11 to 3.45 Å) (see Chapter 6.3). The intracluster distances in **3** (2.978(1) to 3.306(1) Å) are in the range of In–In contacts, for example reported in *β*-Y_3In_5 (2.99 to 3.19 Å). The basal planes of the pyramidal clusters are slightly concave with dihedral angles of 8.31°, 8.17°, and 11.73° for **1**, **2**, and **3**, respectively. For **1** and **2** these values are significantly smaller compared to the angles found in Sr_3Tl_5 (13.68°) or Sr_3Sn_5 (10.34°), meaning the pyramidal base is more regular in the ternary phases. Nevertheless, the comparison of relative bond distances of the compounds Sr_3Sn_5, $Sr_3Sn_{5-x}Tl_x$ (x = 1.78, 2.14), and Sr_3Tl_5 (Table 5.13) does not reveal any significant parameter for preference of either the Pu_3Pd_5-type or the Tm_3Ga_5-type, meaning that rather intercluster and/or cation–anion interactions might play the decisive role. Intercluster distances *d*(M1–M1) are 3.429(1), 3.451(1), and 3.306(1) Å for **1**, **2**, and **3**, respectively. The values for **1** and **2** are again intermediate to the corresponding distances found in Sr_3Tl_5 (3.56 Å) and Sr_3Sn_5 (3.40 Å). The intercluster distance in **3** (3.306(1) Å) is comparable to the values found in La_3In_5 (3.43 Å) or *β*-Y_3In_5 (3.22 Å). Cation coordination (Figure 5.25) is virtually the same as in the compounds with Pu_3Pd_5-type structures.

The Sr1 atoms lie on the same mirror planes as the square pyramids and are nine-fold coordinated with contacts to clusters of four different chains (*d*(Sr1–M/Sn) = 3.266(1) to 3.608(1) Å for **1**, 3.264(2) to 3.603(2) Å for **2**, and 3.295(1) to 3.575(1) Å for **3**). Sr2 is nested in the spaces between the zigzag cluster chains with contacts to 10 M/Sn atoms of three different chains (*d*(Sr2–M/Sn) = 3.418(1) to 3.540(1) Å for **1**, 3.413(1) to 3.538(1) Å for **2**, and 3.416(1) to 3.638(1) Å for **3**.

***Table 5.13*: Comparison of Sn–Sn, M–M, and Tl–Tl bond lengths normalized to the shortest bond in Sr_3Sn_5, $Sr_3Sn_{5-x}Tl_x$ (x = 1.78, 2.14), and Sr_3Tl_5.**

	Pu_3Pd_5-type		Tm_3Ga_5-type	
Bond type	**Sr_3Sn_5**	**Sr_3Tl_5**	**$Sr_3Sn_{3.22}Tl_{1.78}$ (1)**	**$Sr_3Sn_{2.86}Tl_{2.14}$ (2)**
	1.00 (2.99)	1.00 (3.11)	1.00 (3.02)	1.00 (3.02)
	1.05 (3.15)	1.04 (3.23)	1.01 (3.06)	1.02 (3.08)
intracluster	1.01 (3.01)	1.11 (3.45)	1.02 (3.09)	1.02 (3.08)
			1.03 (3.11)	1.04 (3.16)
			1.06 (3.20)	1.06 (3.21)
intercluster	1.14 (3.40)	1.15 (3.56)	1.13 (3.43)	1.14 (3.45)

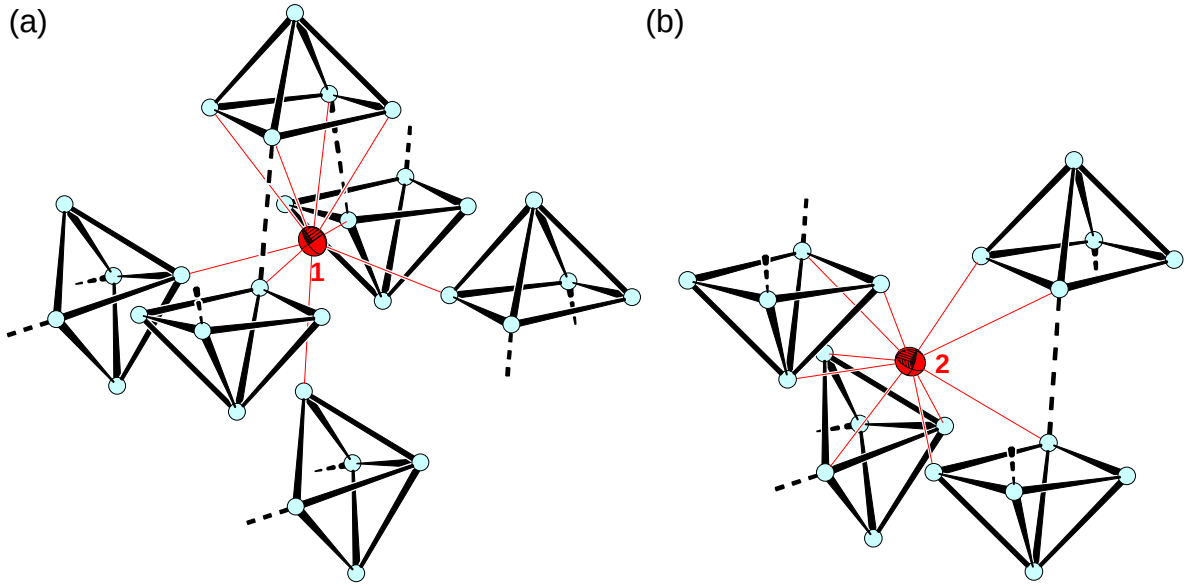

***Figure 5.25*. (a) Coordination sphere around Sr1, (b) coordination sphere around Sr2 in $Sr_3Sn_{5-x}Tl_x$ (x = 1.78). Sr atoms are drawn with 90 % probability level. Intercluster bonds are drawn with dashed lines.**

5.3.4 Discussion

Applying the Zintl concept leads to the assignments: $(Sr^{2+})_3(Sn_{3.22}Tl_{1.78(5)})^{6-}$ and $(Sr^{2+})_3(Sn_{2.86}Tl_{2.14(5)})^{6-}$ for **1** and **2**, respectively. The average VEC/M is 4.84 and 4.77 for **1** and **2**, respectively. The corresponding values for the binary stannides (Sr_3Sn_5: VEC/Sn = 5.2) and indides (La_3In_5: VEC/In = 4.8), both crystallizing in the Pu_3Pd_5 structure type, suggest a great structural flexibility of the latter and different roles of the cations in the two A_3B_5 structure types. With respect to the results of Chapter 6.3 (the binary Ae_3Tl_5 (VEC/Tl = 4.2) also crystallizes with Pu_3Pd_5 structure), the present reorientation in the lower symmetry space group (*Cmcm* to *Pnma*) cannot be simply understood in terms of the VEC (electronic effects). Comparing the cluster anions in Sr_3Sn_5 and in the present case (Figure 5.23), except for cluster reorientation the partial substitution of Sn by a triel metal (Tl, In) does not lead to a significant change regarding the cluster structure. However, a closer look onto the structures reveals shorter average Ae–M distances. Ae–Sn distances in Sr_3Sn_5 are in the range of 3.32 to 3.71 Å ($d(Sr–Sn)_{ø}$ = 3.48 Å) for Sr1 and 3.42 to 3.69 Å ($d(Sr–Sn)_{ø}$ = 3.53 Å) for Sr2. The corresponding values in Sr_3Tl_5 are 3.32 to 3.67 Å ($d(Sr–Tl)_{ø}$ = 3.45 Å) and 3.48 to 3.63 Å($d(Sr–Sn)_{ø}$ = 3.53 Å) for Sr1 and Sr2 positions, respectively. In the present ternary $Sr_3Sn_{5-x}Tl_x$, on average the Sr atoms ($d(Sr1–M)_{ø}$ = 3.42 Å and $d(Sr2–M)_{ø}$ = 3.49 Å for **1**) are situated slightly closer to the cluster atoms.

Especially Sr1 is located considerably closer to the apical M4 atoms. Whereas in Sr_3Sn_5 this contact is average with respect to the distribution of all Sr–Sn separations, in the present cases it is the shortest. Average Sr–In distances in **3** are also significantly smaller compared to values in Sr_3In_5. On the other hand intercluster separations are scaled according to the size of the *p*-element. On the bottom line the reduced cation–anion distances must be accompanied with higher Madelung terms and/or enhanced packing efficiency. Taking into account the possible strong stabilizing cation–anion interactions, calculated for many alkaline earth polar intermetallics,[2-4] it can be speculated that the present situation represents an energetically favored situation between the two extremes, Sr_3Sn_5 and Sr_3Tl_5. In the latter other terms, such as valence electron concentration and intercluster interactions gain more importance (see Chapter 6.3). However, the structure of $Sr_3Sn_{5-x}Tr_x$ (Tr = In, Tl; x ~ 2) is a new polymorph for any Pu_3Pd_5-type phase. Additionally it should be noted that the above mentioned “slow first-order phase transition” from metastable *β*-Y_3In_5 (Pu_3Pd_5-type) to low temperature *α*-Y_3In_5 (Tm_3Ga_5-type) has been reported to take place when *β* (high-temperature)-Y_3In_5 is annealed at 700 °C, while the higher symmetric *β*-polymorph was synthesized at T > 1000 °C.[52] In the present case, the phases were prepared at relatively low temperatures (500 °C) so that annealing at higher temperatures might have a similar impact.

5.4 Substitution Effects in Sr_3Sn_5: Na_2SrSn_4 - A Polar Intermetallic Compound with a Novel Sn Substructure

5.4.1 Introduction

The present compound Na_2SrSn_4 features a new anionic sublattice of tin which again emphasizes the great diversity and flexibility of Sn in the formation of nominal Zintl or polar intermetallic phases with new bonding and structure motifs. Whereas in the previous Chapters 5.2 and 5.3 substitution was carried out with respect to the electronegative atoms, the important roles of the cations is reflected in this compound. As mentioned earlier tin is very diverse in the formation of nominal Zintl phases with either homo- or heteroatomic polyanions in binary or higher order systems.

Many compounds were obtained in the A–Sn systems. Prominent examples are the tetrahedral anion $\{Sn_4\}^{4-}$ in ASn (A = Na, K, Rb, Cs),[60, 61] in combination with $\{Sn_9\}^{4-}$ clusters in $A_{52}Sn_{82}$,[62] or condensed pentagonal dodecahedra in K_8Sn_{25}.[63, 64] Higher degrees of connectivity are also present in $NaSn_2$,[65] Na_7Sn_{12},[66] Na_5Sn_{13},[67] and $NaSn_5$.[68] Compared to that, the phases and structures in the Ae–Sn systems are far less plentiful. In recent years only few new compounds in these binary systems have been published e.g.: metallic Ae_3Sn_5[30, 31] (Ae = Sr, Ba, Yb) contains interconnected *arachno*-$\{Sn_5\}$ clusters; $Ca_{31}Sn_{20}$[69] with tin dumbbells, linear pentamers and isolated Sn atoms; $Yb_{36}Sn_{23}$[70] shows dimers, linear hexamers, and isolated Sn atoms; the phases $AeSn_3$ (Ae = Ba, Sr)[16, 23] feature $\{Sn_3\}$ ring motifs; more extended Sn networks are found in $SrSn_4$,[24] and $BaSn_5$.[17] However, the combinations resulting in binary phases are rather limited and already well explored. But the diversity can be greatly enhanced by mixing alkali metals, alkali with Ae/RE, or Ae with RE metals because of the increased opportunities to achieve well packed lattices. $MNa_{10}Sn_{12}$ (M = Ca, Sr)[71] contains isolated truncated tetrahedral clusters $\{Sn_{12}\}^{12-}$, and Na_8MSn_6 (M = Ba, Eu)[72] features cyclopentadienyl like anions $\{Sn_5\}^{6-}$. $M_2Ba_2Sn_6$ (M = Yb, Ca)[40] contains corrugated layers of linked butterfly like $\{Sn_4\}$ anions. Many of these phases are electron precise and can be rationalized as Zintl phases. However, many compounds, originally reported as semiconducting closed shell compounds, show metallic conductivity caused by dominant *d-p* orbital bonding between cations and anions.[2]

5.4.2 Synthesis and Characterization

Synthesis The compound Na_2SrSn_4 was first found when investigating the Sr substitution by Na in Sr_3Sn_5 in a sample loaded with Na : Sr : Sn = 1 : 2 : 5. After heating this mixture to 800 °C and cooling down to room temperature (2 $K \cdot min^{-1}$) the powder diagram of the crystalline product revealed *β*-NaSn, plate shaped Na_2SrSn_4, and small amounts of Sr_3Sn_5. A stoichiometrically loaded Nb crucible, with element ratio Na : Sr : Sn = 2 : 1 : 4, was heated to 800 °C (2 $K \cdot min^{-1}$) and quenched to room temperature. After annealing at 600 °C for seven days the target compound was obtained in higher yields with reliable reproducibility. The product contained two kinds of crystalline compounds, block shaped *β*-NaSn, and the plate shaped target compound. Crystals of the latter are systematically intergrown. The compound was obtained from a total loading mass of 1.014 g, with m(Na) = 0.077 g, m(Sr) = 0.146 g, and m(Sn) = 0.791 g.

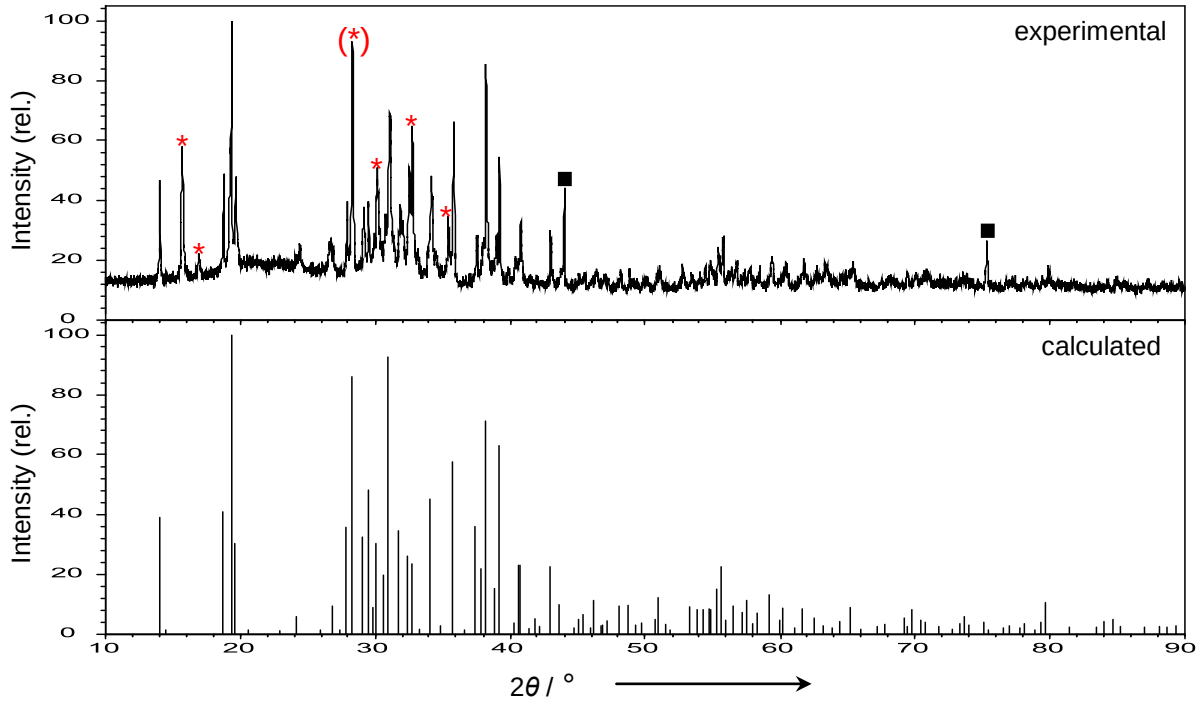

Figure 5.26. **Experimental (top) from sample loading Na : Sr : Sn = 2 : 1 : 4 and calculated (bottom) powder diagram of Na_2SrSn_4. Reflections from the byproduct *β*-NaSn are labeled with a red star. Reflections from diamond powder (internal standard) are marked with a square.**

EDX Analysis Elemental analyses on several single-crystals confirmed the presence of all three elements with an average ratio of Na : Sr : Sn = 34(7) : 11(2) : 55(4) (calculated values: Na 29, Sr 14, Sn 57 at%).

Powder X-ray Measurements Diffraction data was collected on capillary samples which were diluted with diamond powder. The measurement was carried out in Debye-Scherrer mode and lasted for 16 h. The resulting diagram (Figure 5.26) matches well with the calculated powder pattern from the single-crystal solution. However, the phase is not pure and shows reflections originating from *β*-NaSn.

DTA Measurement 200 mg of a product obtained from a reaction loaded as Na : Sr : Sn = 2 : 1 : 4 (and reacted at 800 °C) were filled in a Nb crucible and sealed by arc welding. The sample was heated under continuous Ar flow (50 ml/min) from room temperature to 1000 °C at a rate of 10 $K \cdot min^{-1}$ and cooled down to 100 °C at the same rate. The DTA curves for the two cycles are shown in Figure 5.27. The heating curves (red) reveal one endothermal peak at 494.7 °C (2^{nd} cycle 484.3 °C) (onsets) and a very broad signal in the range of ~ 600 - 800 °C. Upon cooling down the diagram shows a sharp exothermal peak at 650.4 °C (2^{nd} cycle 635.1 °C) and a second one at lower temperatures which corresponds to the signal detected on heating. While the lower temperature signal is in good agreement with the melting point of *β*-NaSn (which was detected in the powder X-ray experiment) the broad peak in the heating curve is less distinctive and may be caused by a slow process e.g. the gradual dissolving of Na_2SrSn_4 in a melt of *β*-NaSn. On the other hand the sharp signal in the cooling curve describes fast crystallization, which may be ascribed to the high cooling rate. Nevertheless the peak at ~ 650 °C can be assigned to the melting of Na_2SrSn_4 as annealing at that temperature resulted in higher yields.

5.4.3 Crystal Structure Determination and Description

Structure Determination A single-crystal of Na_2SrSn_4 was selected and checked for singularity in the glovebox and fixed on a glass capillary, which afterwards was introduced into a capillary (0.3 mm diameter) and closed by melting the open end. The crystals of Na_2SrSn_4 are systematically twinned and clearly distinguishable by their plate like habitus. The data collection was carried out on an Oxford Xcalibur3 diffractometer equipped with a CCD detector at room temperature.

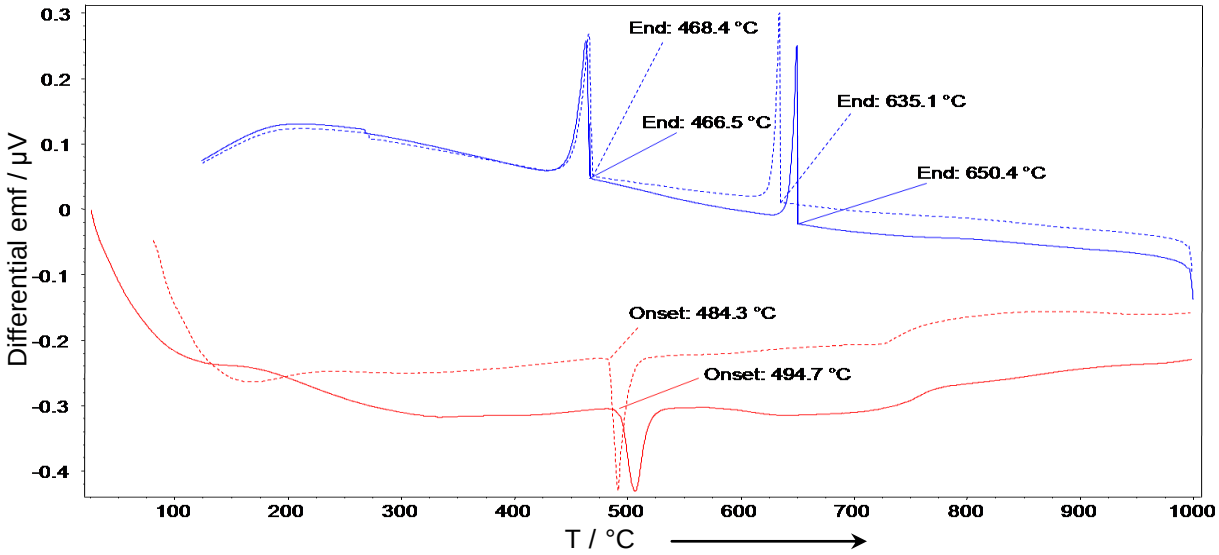

***Figure 5.27*. DTA curves of the product of a reaction with Na : Sr : Sn = 2 : 1 : 4 at 800 °C. Dashed lines represent the 2nd cycle. Heating (red), cooling (blue).**

The data collection (208 frames) involved 4 sets of ω scans (–41° to +63° for different φ positions: 0°, +90°, +180°, +270°) with a scan width of 2°/frame and an exposure time of 30 s/frame. After integration and application of an empirical absorption correction (ABSPACK, CrysAlis RED1.171.29.9, Oxford Diffraction 2006) the structure was solved with direct methods and refined anisotropically in the monoclinic space group *C*2/*c* on F^2 using the SHELXTL package. The space group was assigned on the basis of systematic absences and the statistical analyses of the intensity distributions. Details of the X-ray data collection and structural refinements for Na_2SrSn_4 are listed in Table 5.14. The final positional and anisotropic displacement parameters for the structure is listed in Tables 5.15 and 5.16. Selected distances are shown in Table 8.12 (see Appendix).

Structure Description The compound Na_2SrSn_4 crystallizes in the space group *C*2/*c* (No. 15) with Pearson code *mC*28. As depicted in Figure 5.28 the structure contains Sn polyanions which consist of infinite tubes that propagate along [001]. They are well separated from each other and are made up of condensated Sn_6 rings, which are built of 3b-Sn1 and 2b-Sn2 atoms. Each ring is slightly corrugated (Figure 5.29) and shows two Sn1–Sn1 bonds of 2.909(4) Å and four Sn1–Sn2 contacts of 2.918(3) Å. These values are consistent with covalent bonds found in other intermetallic tin compounds.

***Table 5.14*: Selected crystallographic and refinement data for Na_2SrSn_4.**

Empirical formula	**Na_2SrSn_4**
Formula weight / g·mol^{-1}	608.36
Temperature / K	293(2)
Crystal size / mm^3	0.1 × 0.2 × 0.01
Crystal color; shape	Silvery metallic; Plate
Diffractometer	Oxford Xcalibur3 (CCD)
Crystal system	Monoclinic
Space group	*C*2/*c* (No.15)
Unit cell parameters / Å	*a* = 18.829(8); *b* = 6.644(3); *c* = 6.602(3) *β* = 93.86(4)
Unit cell volume / Å^3; *Z*	824.0(6); 8
ρ_{calc} / g·cm^{-3}	4.90
μ / mm^{-1} (Mo K_α)	18.39
Absorption correction	empirical
F(000)	1040
Θ range / °	3.09 - 27.91
Index range	–24 ≤ *h* ≤ 21 , –7 ≤ *k* ≤ 8 , –8 ≤ *l* ≤ 8
Data completeness / %	98.9
Integrated reflections	3130 (R_σ = 0.054)
Independent reflections	986 (R_{int} = 0.068)
Refinement method	Full-matrix least-squares on F^2 (SHELXTL)
Parameters	34
Goodness of fit on F^2	1.230
Observed reflections [$I > 2\sigma(I)$]	657
R_1 / wR_2 [$I > 2\sigma(I)$]	0.065 / 0.206
R_1 / wR_2 (all data)	0.090 / 0.211
Weighting scheme[a]	a = 0.099, b = 28.593
Extinction coefficient	0.0003(4)
Residual map / e$^-$·Å^{-3}	+4.68 [1.12 Å from Sn1] / –1.64 [1.65 Å from Sn1]

[a] $w = 1 / [\sigma^2(F_o^2) + (aP)^2 + bP]$, where $P = (F_o^2 + 2F_c^2) / 3$

***Table 5.15*: Atomic coordinates and equivalent isotropic displacement parameters for Na_2SrSn_4.**

Atom	**Wyck.**	***x***	***y***	***z***	U_{eq} / Å^2
Sr	4*e*	½	0.2787(4)	0.25	0.024(1)
Sn1	8*f*	0.5774(1)	0.2069(2)	–0.2288(2)	0.034(1)
Sn2	8*f*	0.6520(1)	0.5186(2)	0.0134(3)	0.034(1)
Na	8*f*	0.7021(5)	0.0975(15)	0.2025(16)	0.045(2)

***Table 5.16*: Anisotropic thermal displacement parameters (*I* Å^2) for Na_2SrSn_4.**

Atom	U_{11}	U_{22}	U_{33}	U_{23}	U_{13}	U_{12}
Sr	0.027(1)	0.021(1)	0.025(1)	0	0	0.002(1)
Sn1	0.048(1)	0.025(1)	0.030(1)	–0.002(1)	0.011(1)	–0.004(1)
Sn2	0.025(1)	0.034(1)	0.043(1)	0.009(1)	0	–0.003(1)
Na	0.040(1)	0.046(6)	0.050(6)	0.011(5)	0.010(4)	0.007(4)

The six-member rings are connected through a common Sn1–Sn1 contact and progress in an infinite zigzag arrangement along [001]. The as formed Sn tubes are aligned parallel in the (100) plane, distorted hexagonally packed along *a* direction, and well separated with a shortest interspiral Sn–Sn distance of 4.296(1) Å. The as formed infinite arrangement of fused Sn hexagons can be described in terms of the repeat units $\{–Sn2–Sn1–Sn1–Sn2–\}_n$, which would have a closed shell charge of –6 according to classical octet binding concepts. However, a significantly longer and weak contact between Sn2 atoms of two adjacent Sn_6 rings is present. The bond length of 3.311(3) Å exceeds the value of Sn–Sn separations in metallic *β*-Sn, but it cannot be neglected as they are shorter than the sum of the van der Waals radii of Sn. Additionally, the small ∠ Sn2Sn1Sn2 of 69.1° elucidates the presence of a bonding Sn–Sn interaction. Along [001], Sn2 atoms are slightly displaced from a linear chain conformation (Figure 5.30a) with a bond angle ∠ Sn2Sn2Sn2 of 171.3°. This segment is reminiscent of the linear anion chains in K_2SnBi[73] and K_6Pb_5.[74] The Sr atoms are nested inside the Sn tubes. They are not exactly located in the tube center but shifted into the direction of the Sn1–Sn1 bond of an adjacent polyanion in the (100) plane (Figure 5.31a). Considering only cation–anion contacts up to 4 Å Sr is 12-fold connected to Sn atoms with the shortest distance (3.515(2) Å) to Sn2. As recognizable from the sheer number of cation–anion interactions the Sr–Sn functions should play a crucial role in the bonding considerations, as will be shown later. The Sr atoms are arranged in planar (4^4) nets in the (100) plane.

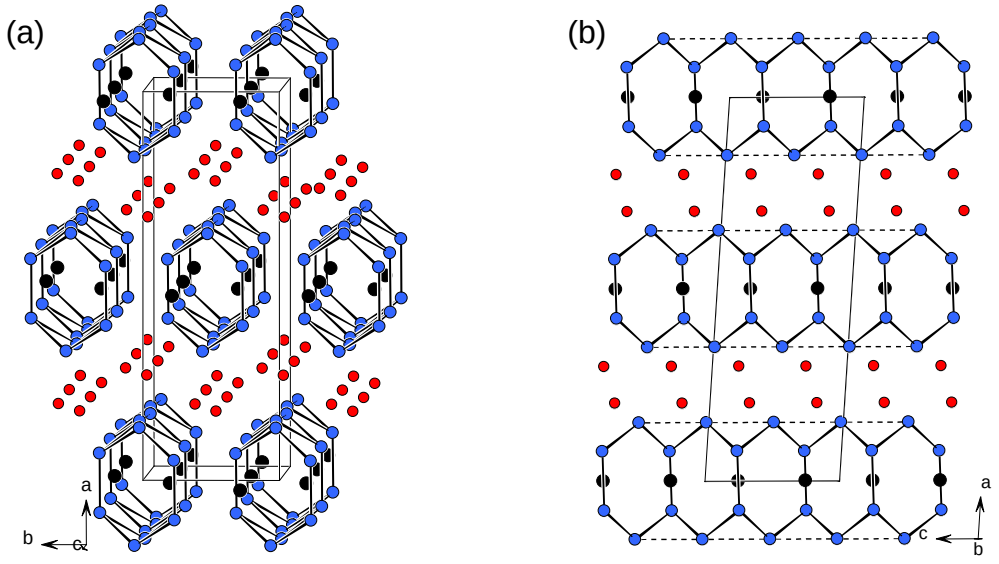

***Figure 5.28*. (a) Off-[001] projection of the unit cell of Na_2SrSn_4. (b) [010] projection of the unit cell of Na_2SrSn_4. Na (red), Sr (black), Sn (blue).**

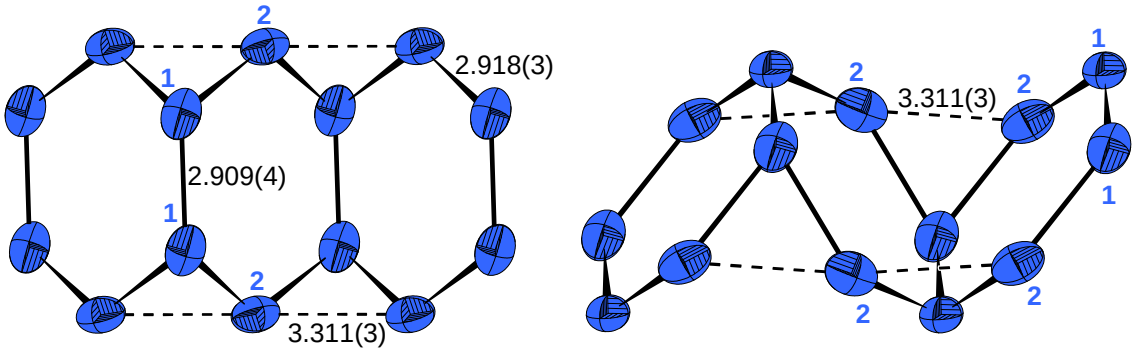

***Figure 5.29*. Two projections of the polymeric Sn anion in Na_2SrSn_4. The anisotropic representations are drawn at 90% probability level.**

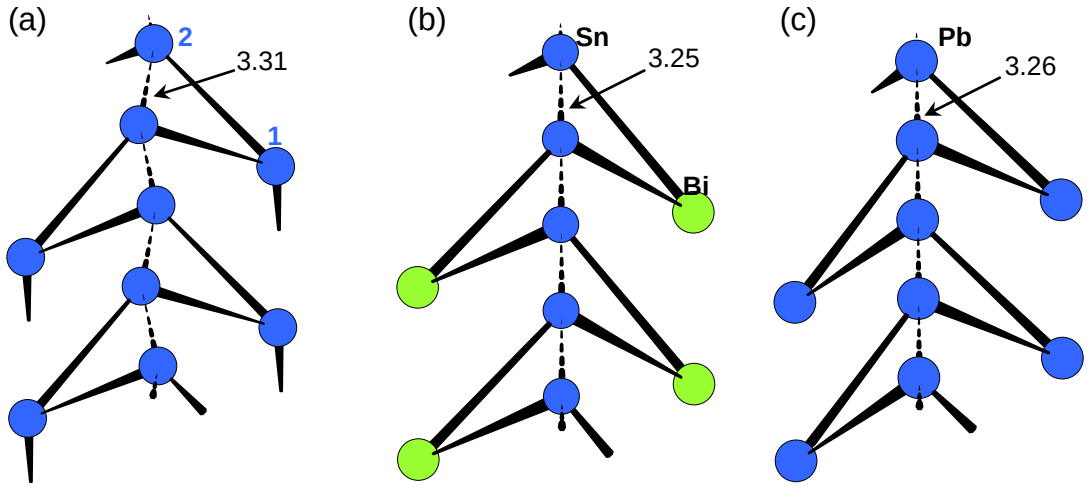

***Figure 5.30*. (a) to (c) Structure segments of Na_2SrSn_4, K_2SnBi, and K_6Pb_5. Longer Sn–Sn and Pb–Pb interactions are drawn with dashed lines.**

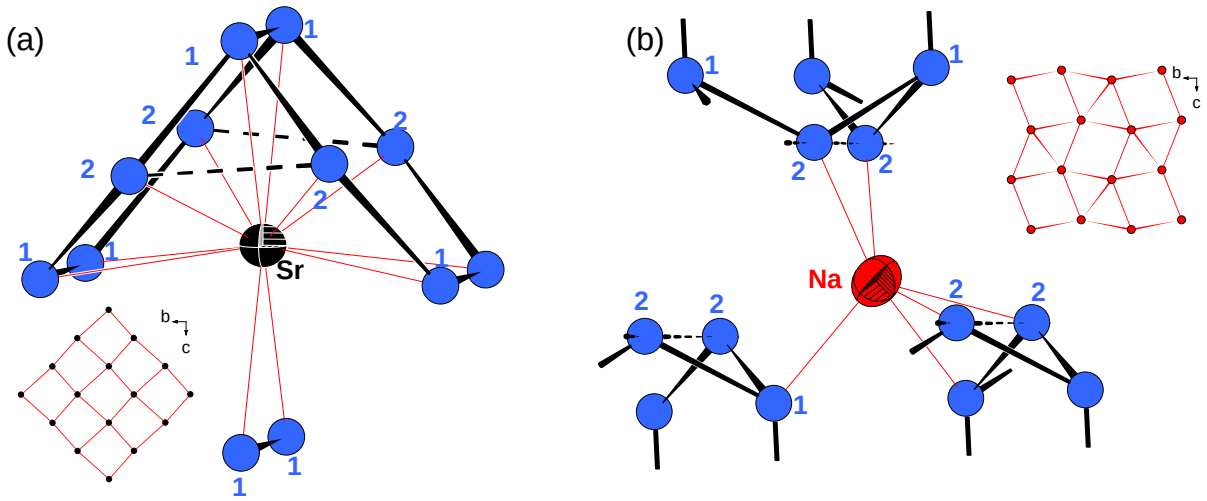

***Figure 5.31*. Cation coordination spheres. (a) Sr embedded in a Sn tube. (b) Na occupies a bridging position between three Sn tubes. Sr and Na atoms are drawn at 90% probability level. The insets show layers of Sr and Na atoms in [100] projection. Sr (black), Na (red), Sn (blue).**

The Na atoms are arranged in corrugated (3^2434) layers (which is a common feature in intermetallic structure chemistry) and can be seen to separate slabs of Sn tubes in [100] direction. As shown in Figure 5.31b each Na is six bonded to Sn in three tubes with distances ranging from 3.15(1) to 3.64(1) Å.

5.4.4 Electronic Structure

To gain deeper insights into the nature of the chemical bonds in Na_2SrSn_4 band structure, DOS, and COHP diagrams were calculated. The *k*-space integration was performed by the tetrahedron method on a set of 16 × 16 × 16 irreducible *k* points and a basis set with Na-3*s*/(3*p*), Sr-5*s*/(5*p*)/5*d*/(5*f*), Sn-5*s*/5*p*/(4*d*)/(4*f*) (down folded orbitals in parentheses). The total density of states (DOS) and projections of the Sn, Na, and Sr states are illustrated in Figure 5.32.

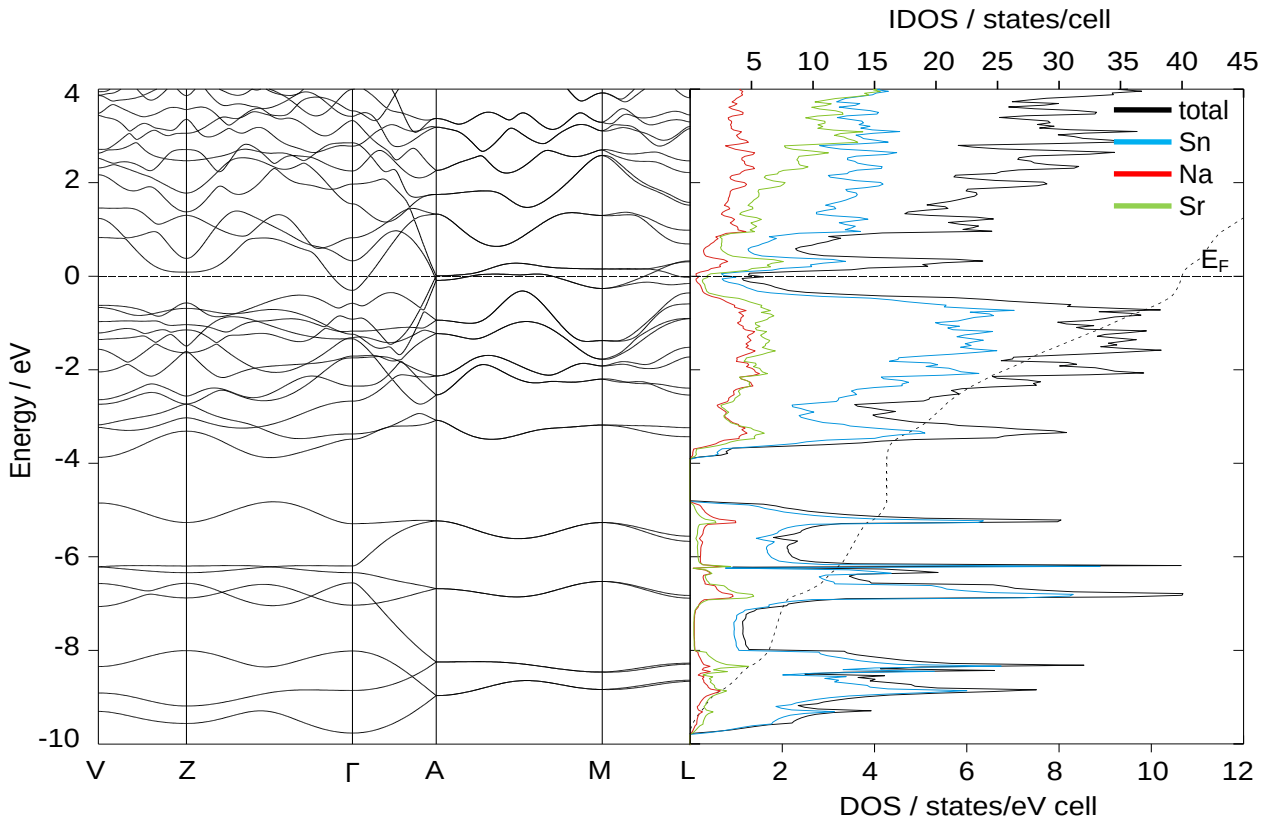

***Figure 5.32*. Band structure along symmetry points in the 1st Brillouin zone and DOS projections of Na_2SrSn_4. The Fermi level is taken as the point of zero energy. Sn (blue), Sr (green), Na (red).**

The DOS shows two separated band regions. The lower band, dispersed from –10 to –5 eV, mainly consists of Sn-*s* states and has only small amounts of Na-*s* and Sr-*s* contributions.

In the valence band Sn-*p* states and significant amounts of Na-*p* and Sr-*d* states are present. The Fermi level for Na_2SrSn_4 lies in a pseudo gap at the flank of a local maximum in the DOS curve. However, this region is non-zero and shows contributions from all three elements.

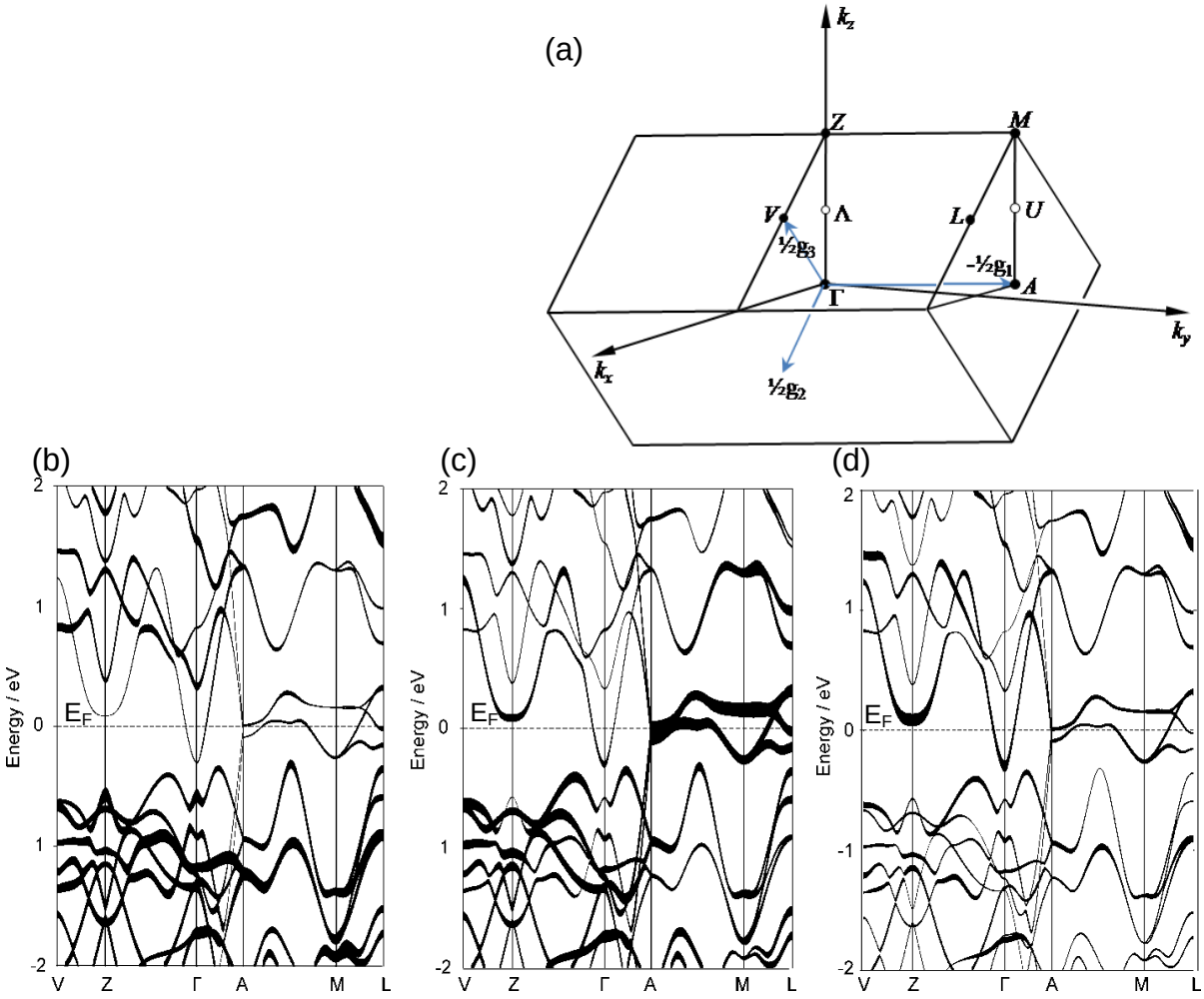

***Figure 5.33*. (a) The first Brillouin zone for a monoclinic base centered lattice with Γ = (0,0,0); *A* = (– ½,0,0); *Z* = (0, –½,½); *M* = (–½,–½½); *L* = (–½,0,½); *V* = (0,0,½). Fat band representations for (b) Sn1-*p*, (c) Sn2-*p*, and (d) Sr-*d*. Bands are drawn with thickness representative of their orbital contributions.**

The local maximum, located +0.5 eV above the Fermi level, corresponds to two flat bands running from A → M → L in the first Brillouin zone which corresponds to the [001] direction. Fatband plots (Figure. 5.33) reveal their characters being mainly Sn2-*p* indicating an anisotropic metallic conductivity along the zigzag chain of Sn2 atoms. Together with the steep band in the proximity of Γ, which has mainly Sr-*d* character, this might also suggest a scenario found in other intermetallics, such as $BaSn_5$, and superconductive behavior.

However, the corresponding bands, revealed by –COHP plots, cannot be clearly classified as lone pairs, since they exhibit Sn–Sn antibonding character.

These results are in good agreement with a calculation carried out on K_2SnBi[73] (not shown). The –COHP curves (Figure 5.34) for the sum over all interactions show that the Na–Sn bonding is roughly optimized with few bonding states left. In contrast to this, significant amounts of bonding states are unfilled for the Sr–Sn interactions, whereas for Sn–Sn bonding E_F lies in an antibonding region. For quantification of the strength of interactions (up to 4 Å) between atoms –ICOHP values were evaluated.

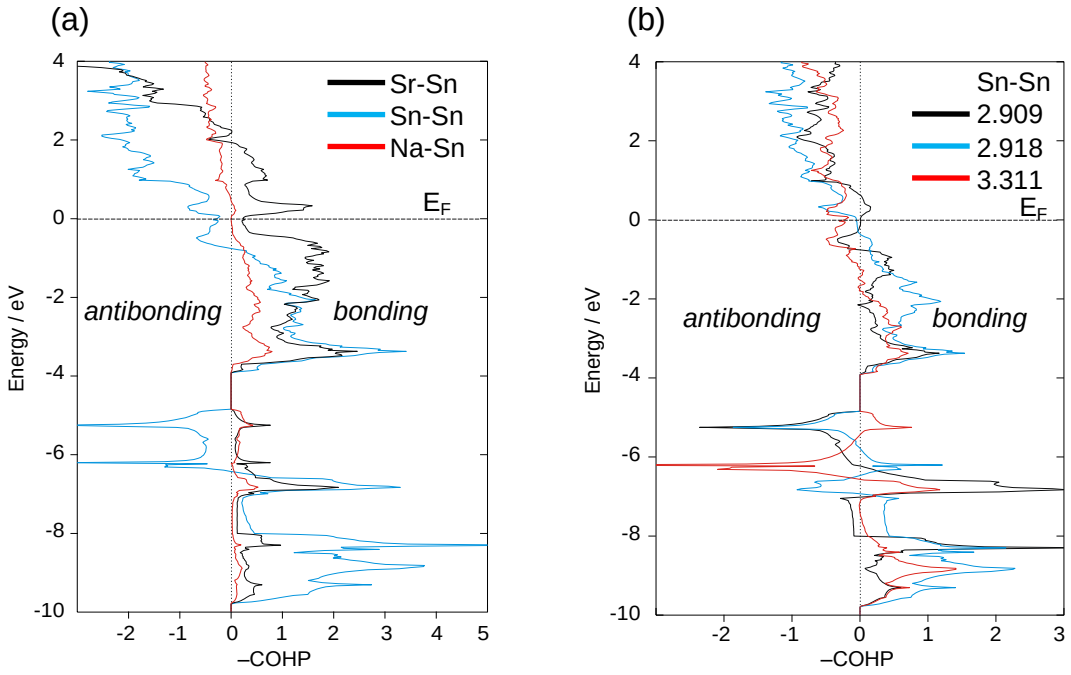

***Figure 5.34*. (a) –ICOHP plots for the sum of all Sn–Sn (blue), Na–Sn (red), and Sr–Sn (black) interactions. (b) –ICOHP plots for individual Sn–Sn pairs. 2.909(4) Å (black), 2.918(3) Å (blue), 3.311(3) Å (red).**

***Table 5.17*: –ICOHP values for selected interatomic contacts in Na_2SrSn_4. Energies are given in eV/bond.**

interaction		*d* / Å	–ICOHP (at E_F)	–ICOHP (max.)
Sn1	Sn1	2.909(4)	1.87	1.95
Sn1	Sn2	2.918(3)	1.89	1.91
Sn2	Sn2	3.311(3)	0.24	0.75
Sr	Sn	3.515(2) - 3.714(3)	0.53	0.62
Na	Sn	3.154(11) - 3.639(11)	0.32	0.32

All contacts are overall bonding and the Na–Sn interactions are optimized at E_F with 0.32 eV/bond (six bonds in total). Whereas the sum over all Sn–Sn interactions is bonding the energies scale with bonding distances.

The shorter Sn–Sn contacts (–ICOHP$_{Sn1–Sn1}$: 1.87 eV and –ICOHP$_{Sn1–Sn2}$: 1.89 eV) are nearly optimized with values typical for covalent bonding. However, when calculating the –ICOHP values (1.36 eV/bond at E_F and –ICOHP$_{max}$: 1.43 eV/bond) for all Sn-Sn interactions (up to 4 Å) the overall Sn–Sn bonding is not optimized, which is mainly caused by the longest Sn2–Sn2 bond (0.24 eV/bond at E_F, optimized for 0.75 eV/bond) for which antibonding states start to get filled from around –1.5 eV. Thus, the Sn–Sn bonding alone is insufficient to govern structure stabilization. The Sr–Sn bonds are of 0.53 eV/bond (average value over 12 bonds) which is approximately twice the value calculated for Sn2–Sn2. Further bonding states are located above E_F. They would be optimized at a –ICOHP$_{max}$ value of 0.62 eV/bond.

5.4.5 Discussion

The present compound is yet another example of how novel Sn substructures can be obtained only by changing the number and characters of the active metals. Considering only the short Sn–Sn contact and applying the Zintl concept to the compound the ionic formulation $(Na^+)_2(Sr^{2+})(3b\text{-}Sn1^{1–})_2(2b\text{-}Sn2^{2–})_2$ results. The formal electron transfer from two Na^+ and one Sr^{2+} results in an electron deficiency of 2. Therefore, the long contacts *d*(Sn2–Sn2) have to be more carefully investigated. They cannot be classical 2*c*-2*e* bonds (which would result in $(4b\text{-}Sn2^0)_2$ and two excess electrons), as they are too long and the valence angles are too far away from the ideal tetrahedral value. As mentioned earlier, one part of the spiral can be compared to the anionic chains in K_6Pb_5[74] (Figure 5.30c). There, the two kinds of Pb atoms are formally two bonded and one Pb atom is aligned in a linear chain with longer distances (3.26 Å), which are smaller than the metallic contacts in elemental Pb (3.5 Å). However, in that case one of the two Pb positions is underoccupied. Another similar motif is the 11 valence electron unit $^1_\infty[(SnBi)^{2–}]$ in K_2SnBi[73] (Figure 5.30b) with homoatomic Sn–Sn distances of 3.25 Å, which were interpreted as partial bonds.[75] In addition to the Sn–Bi zigzag-chain, '2*c*-1*e*' bonds between adjacent Sn atoms (*d*(Sn–Sn) = 3.25 Å) are discussed in that compound with no presence of a Peierls-type distortion.[76] In Na_2SrSn_4 a rather similar situation is present.

Applying the same formalism and distributing one of the two remaining electrons at each Sn2 atom between pairs of Sn2 atoms, each atom satisfies the octet rule if the Sn2–Sn2 bonds are considered to be fractional '2*c*-1*e*' bonds (half bonds with bond order 0.5).[77, 78] Half-bonds originate from electron deficiency and for a system A–B–A it can also be regarded as composed of two electrons with paired spins and three atomic orbitals and may be thought of as resonating between the principal contributing structures [A–B A] and [A B–A]. Hence, half-bonds occur in pairs. This results in a formal charge of –1 for the 4-fold coordinated Sn2 with two 2*c*-2*e*, two 2*c*-1*e* bonds, and would qualify the compound as a charge balanced phase: $(Na^{+})_2Sr^{2+}(3b\text{-}Sn1^{-})_2((2 + 2\cdot½)b\text{-}Sn2^{-})_2$. The saturation of the valence of the Sn atoms can be explained by these additional bonding interactions. However, considering the band structure calculations, which revealed the metallic nature of the compound, and the results from COHP calculations, Na_2SrSn_4 cannot be regarded as a Zintl phase. The presence of strongly bonding cation–anion and antibonding Sn2–Sn2 interactions at the Fermi level rather suggest delocalized electrons meaning that the bond order of the fractional bond does not necessarily have to be ½, since incomplete transfer from Sr (and Na) is clearly present. Additionally, the many interactions between Sr-*d* and Sn-*p* orbitals (12 Sr1–Sn interactions) and especially the short distance to the Sn2 atoms points towards stabilizing cation–anion interactions and delocalized bonding. According to the –COHP diagrams additional electrons would occupy antibonding Sn–Sn states and therefore would rather be delocalized in bonding cation–anion states. Thus, Na_2SrSn_4 is better described as a borderline polar intermetallic.

5.5 References

[1] L. Gagliardi, P. Pyykkö, *Theor. Chem. Acc.* **2003**, *110*, 205.
[2] A. V. Mudring, J. D. Corbett, *J. Am. Chem. Soc.* **2004**, *126*, 5277.
[3] S. Ponou, T. F. Fässler, G. Tobias, E. Canadell, A. Cho, S. C. Sevov, *Chem. Eur. J.* **2004**, *10*, 3615.
[4] S. Ponou, S.-J. Kim, T. F. Fässler, *Z. Anorg. Allg. Chem.* **2007**, *633*, 1568.
[5] P. Alemany, M. Llunell, E. Canadell, *Inorg. Chem.* **2006**, *45*, 7235.
[6] N. N. Zhuravlev, V. P. Melik-Adamyan, *Sov. Phys. Crystallogr.* **1961**, *6*, 99.
[7] K. Deller, B. Eisenmann, *Z. Naturforsch.* **1976**, *31 B*, 29.
[8] G. Derrien, M. Tillard-Charbonnel, A. Manteghetti, *J. Solid State Chem.* **2002**, *164*, 169.
[9] M. Martinez-Ripoll, A. Haase, G. Brauer, *Acta Crystallogr.* **1974**, *30 B*, 2003.
[10] B. Eisenmann, K. Deller, *Z. Naturforsch.* **1975**, *30 B*, 66.
[11] M. Martinez, A. Haase, G. Brauer, *Acta Crystallogr.* **1974**, *30B*, 2004.
[12] B. Li, A. V. Mudring, J. D. Corbett, *Inorg. Chem.* **2003**, *42*, 6940.
[13] F. Merlo, M. L. Fornasini, *Mater. Res. Bull* **1994**, *29*, 149.
[14] S. Ponou, *Dissertation, Technische Universität München* **2006**.
[15] S. Ponou, T. F. Fässler, *Inorg. Chem.* **2004**, *43*, 6124.
[16] C. Kronseder, T. F. Fässler, *Angew. Chem.* **1997**, *109*, 2800.
[17] T. F. Fässler, S. Hoffmann, C. Kronseder, *Z. Anorg. Allg. Chem.* **2001**, *627*, 2486.
[18] B. Eisenmann, *Z. Naturforsch.* **1979**, *34 B*, 1162.
[19] G. Chapuis, F. Hulliger, R. Schmelczer, *J. Solid State Chem.* **1980**, *31*, 59.
[20] J. B. Taylor, L. D. Calvert, T. Utsunomiya, Y. Wang, J. G. Despault, *J. Less-Comm. Met.* **1978**, *57*, 39.
[21] K. Deller, B. Eisenmann, *Z. Naturforsch.* **1976**, *31 B*, 1023.
[22] D. M. Newns, H. R. Krishnamurthy, P. C. Pattnaik, C. C. Tsuei, C. C. Chi, C. L. Kane, *Physica B* **1993**, *801*, 186.
[23] S. Hoffmann, T. F. Fässler, *Z. Anorg. Allg. Chem.* **2000**, *626*, 106.
[24] S. Hoffmann, T. F. Fässler, *Inorg. Chem.* **2003**, *42*, 8748.
[25] M. Bäcker, A. Simon, R. K. Kremer, H. J. Mattausch, R. Dronskowski, J. Rouxel, *Angew. Chem.* **1996**, *108*, 837.
[26] A. Simon, *Angew. Chem.* **1987**, *99*, 602.
[27] A. Simon, *Angew. Chem.* **1997**, *109*, 1873.
[28] B. Eisenmann, H. Jordan, H. Schäfer, *Z. Naturforsch.* **1985**, *40 B*, 1603.
[29] P. Eckerlin, H. J. Meyer, E. Wölfel, *Z. Anorg. Allg. Chem.* **1955**, *307*, 145.
[30] M. T. Klem, J. T. Vaughey, J. G. Harp, J. D. Corbett, *Inorg. Chem.* **2001**, *40*, 7020.
[31] F. Zürcher, R. Nesper, S. Hoffmann, T. F. Fässler, *Z. Anorg. Allg. Chem.* **2001**, *627*, 2211.
[32] K. Wade, *Adv. Inorg. Chem. Radiochem.* **1976**, *18*, 1.
[33] M. Boström, S. Hovmöller, *J. Solid State Chem.* **2000**, *153*, 398.
[34] A. M. Guloy, J. D. Corbett, *Inorg. Chem.* **1996**, *35*, 2616.
[35] W. B. Pearson, *The Crystal Chemistry and Physics of Metals and Alloys; Wiley-Interscience, New York* **1972**.
[36] I. Schewe, P. Böttcher, H. G. Von Schnering, *Z. Kristallogr.* **1989**, *188*, 287.
[37] A. V. Shubnikov, *Izv. Akad. Nauk SSSR Ser. 6* **1916**, *10*, 755.
[38] H. Sowa, E. Koch, *Acta Crystallogr.* **2005**, *61 A*, 331.
[39] F. Zürcher, R. Nesper, *Angew. Chem.* **1998**, *110*, 3451.
[40] M. H. Ge, J. D. Corbett, *Inorg. Chem.* **2007**, *46*, 4138.
[41] J. Curda, W. Carrillo-Cabrera, A. Schmeding, K. Peters, M. Somer, H. G. Von Schnering, *Z. Anorg. Allg. Chem.* **1997**, *623*, 929.
[42] J. Llanos, *Dissertation, Universität Stuttgart* **1984**.

[43] G. Derrien, M. Tillard-Charbonnel, A. Manteghetti, L. Monconduit, C. Belin, *J. Solid State Chem.* **2002**, *164*, 169.
[44] U. Häussermann, S. Amerioun, L. Eriksson, C. S. Lee, G. J. Miller, *J. Am. Chem. Soc.* **2002**, *124*, 4371.
[45] A. Iandelli, *Z. Anorg. Allg. Chem.* **1964**, *330*, 221.
[46] C. Zheng, R. Hoffmann, *Z. Naturforsch.* **1986**, *41B*, 292.
[47] M. Wendorff, C. Röhr, *Z. Naturforsch.* **2004**, *59B*, 619.
[48] M. L. Fornasini, *Acta Crystallogr.* **1975**, *C44*, 1355.
[49] G. Cordier, H. Schäfer, M. Stelter, *Z. Anorg. Allg. Chem.* **1986**, *539*, 33.
[50] D. K. Seo, J. D. Corbett, *J. Am. Chem. Soc.* **2001**, *123*, 4512.
[51] P. Yarmolyuk, *Kristallografiya* **1977**, *22*, 726.
[52] J. T. Zhao, J. D. Corbett, *Inorg. Chem.* **1995**, *34*, 378.
[53] S. P. Yatsenko, K. A. Tschuntonow, P. Yarmolyuk, Y. Grin, *J. Less -Comm. Met.* **1983**, *91*, 21.
[54] M. T. Klem, J. D. Corbett, *Inorg. Chem.* **2005**, *44*, 5990.
[55] M. Rhode, M. Wendorff, C. Röhr, *Z. Anorg. Allg. Chem.* **2006**, *632*, 1195.
[56] S. Gupta, A. K. Ganguli, *Inorg. Chem.* **2005**, *44*, 7443.
[57] J. Burdett, E. Canadell, T. Hughbanks, *J. Am. Chem. Soc.* **1986**, *108*, 3971.
[58] J. Burdett, N. J. Lawrence, J. J. Turner, *Inorg. Chem.* **1984**, *23*, 2419.
[59] G. J. Miller, *Eur. J. Inorg. Chem.* **1998**, 523.
[60] I. F. Hewaidy, E. Busmann, W. Klemm, *Z. Anorg. Allg. Chem.* **1964**, *328*, 283.
[61] W. Müller, K. Volk, *Z. Naturforsch.* **1977**, *32 B*, 709.
[62] C. Hoch, M. Wendorff, C. Röhr, *Z. Anorg. Allg. Chem.* **2003**, *629*, 2391.
[63] F. Dubois, T. F. Fässler, *J. Am. Chem. Soc.* **2005**, *127*, 3264.
[64] J. T. Zhao, J. D. Corbett, *Inorg. Chem.* **1994**, *33*, 5721.
[65] F. Dubois, M. Schreyer, T. F. Fässler, *Inorg. Chem.* **2005**, *44*, 477.
[66] T. F. Fässler, S. Hoffmann, *Inorg. Chem.* **2003**, *42*, 5474.
[67] J. T. Vaughey, J. D. Corbett, *Inorg. Chem.* **1997**, *36*, 4316.
[68] C. Kronseder, T. F. Fässler, *Angew. Chem.* **1998**, *110*, 1641.
[69] A. K. Ganguli, A. M. Guloy, E. A. Leon-Escamilla, J. D. Corbett, *Inorg. Chem.* **1993**, *32*, 4349.
[70] E. A. Leon-Escamilla, J. D. Corbett, *Inorg. Chem.* **1999**, *38*, 738.
[71] S. Bobev, S. C. Sevov, *Inorg. Chem.* **2001**, *40*, 5361.
[72] I. Todorov, S. C. Sevov, *Inorg. Chem.* **2004**, *43*, 6490.
[73] M. Asbrand, B. Eisenmann, *Z. Naturforsch.* **1996**, *51B*, 1301.
[74] C. Kronseder, T. F. Fässler, *Z. Kristallogr. NCS* **1999**, *214*, 437.
[75] S. M. Kauzlarich, *Ed., Chemistry, Structure and Bonding of Zintl Phases and Ions, VCH* **1996**, 62.
[76] R. E. Peierls, *Quantum Theory of Solids, Oxford University Press, Oxford* **1964**.
[77] R. E. Rundle, *J. Am. Chem. Soc.* **1947**, *69*, 1327.
[78] R. E. Rundle, *J. Chem. Phys.* **1949**, *17*, 671.

6 Synthesis and Characterization of the Binary Phases $K_{70}Sn_{103}$, $BaSn_2$, and Ae_3Tl_5 (Ae = Ca, Sr)

6.1 $K_{70}Sn_{103}$ - A Zintl Phase Containing Isolated $\{Sn_9\}^{4-}$, $\{Sn_5\}^{2-}$, and $\{Sn_4\}^{4-}$ Wade Clusters

6.1.1 Introduction

Many intermetallic phases in the binary systems A_xE_y (A = alkali metal, E = Si, Ge, Sn, Pb) can be rationalized by applying the electron counting rules of Zintl-Klemm or Wade. The anions formed show a large structural diversity depending on the amount of charge transfer from the electropositive alkali metal to the tetrel atoms. In addition to extended tin frameworks e.g. in K_8Sn_{46}[1] or K_6Sn_{25},[2] isolated four- and nine-atom deltahedral Sn clusters can be found in the binary compounds K_4Sn_4,[3] K_4Sn_9,[4] or in combinations such as $K_{12}Sn_{17} = K_{12}\{Sn_9\}\{Sn_4\}_2$,[5] and $K_{52}Sn_{82} = K_{52}\{Sn_9\}_6\{Sn_4\}_7$.[6] Among the white phosphorous analogue $\{E_4\}^{4-}$ (E = Si, Ge, Sn, Pb)[7, 8], which can be described both with (8–N) or Wade's rules[9, 10], the prominent *nido*-$\{E_9\}^{4-}$ Wade cluster is known for all tetrel elements except for carbon.[4, 5, 11, 12] In contrast to their pendants in the solid state, the homoatomic tetrelide clusters isolated and characterized from solution show a much higher diversity in terms of shape, nuclearity and bonding. In addition to the above mentioned $\{E_4\}$ and $\{E_9\}$ species, various oligomers and polymers from oxidative coupling experiments, such as $\{Ge_9\}_4^{8-}$ or $\{HgGe_9\}_\infty^{2-}$,[13, 14] could be isolated. Furthermore, recently unprecedented *closo*-$\{Pb_{10}\}^{2-}$,[15] and $\{Si_9\}^{2-}$[16] have been reported. *Closo*-$\{Tt_5\}^{2-}$ (Tt = Sn, Pb) was found to crystallize as $[2.2.2crypt\text{-}K^+]_2Sn_5$[17] and $[2.2.2crypt\text{-}Na^+]_2Tt_5$[18] (Tt = Sn, Pb) from alloys with compositions $K_{1.33}Sn$ and $Na_{1.7}Sn$. It is worth mentioning that many of such compounds, obtained with large cations, e.g. crypted alkali metal or with crown ether from organic solvents (usually ethylenediamine or liquid ammonia), are the outcome of the dissolution of such binary A_xE_y compounds, usually referred to as a 'melt' or an 'alloy'. Since not much is known about the species in solution which finally crystallizes, the importance of well characterized precursor alloys speaks for itself. Whereas $\{Tl_5\}^{7-}$, a trigonal bipyramidal *closo*-cluster, exists in the solid state, the *hitherto* absence of $\{Sn_5\}^{2-}$ reflects the difficulty of characterization of compounds with isolated tetrel clusters, which is caused by crystal quality, twinning, atomic disorder, or large unit cells.[19, 20]

The synthesis and structural description of the new binary Zintl phase $K_{70}Sn_{103}$ - the first solid state compound that contains isolated *nido*-{Sn_5} clusters - is presented herein.

6.1.2 Synthesis and Characterization

Synthesis The compound was obtained by reaction of the pure elements in a Tl flux. In an Ar-filled glovebox stoichiometric amounts of K, Sn, and Tl were placed into a Nb crucible with ratios 4 : 7 : 2. The total loading equaled to 1.396 g, with m(K) = 0.156 g, m(Sn) = 0.831 g, and m(Tl) = 0.409 g. The crucible was sealed afterwards and placed into a silica tube. The temperature treatment involved heating to 1000 °C with a rate of 2 $K \cdot min^{-1}$, holding at that temperature for 5 h, and slow cooling (0.1 $K \cdot min^{-1}$) to room temperature. A dark crystalline and highly air sensitive product was obtained. The same result was observed when increasing the ratio of the reaction mixture to K : Sn : Tl = 4 : 6 : 3. Although experiments with considerable excess of Tl were not carried out, the repeated syntheses using stoichiometries without Tl did not lead to the formation of the target compound. Lowering the Tl content as in the ratio 4 : 8 : 1 led to the formation of K_6Sn_{25} as the only distinguishable crystalline component. This means that crystal growth out of the Tl-flux seems to be essential.

EDX Analysis Qualitative and quantitative analysis of several single-crystals confirmed the presence of the two elements and very small amounts of Tl with average ratio K : Sn : Tl = 40(8) : 57(2) : 2(2) (calculated values: K: 40.5, Sn: 59.5 at%). In the sample only crystals of $K_{70}Sn_{103}$ could be found. Therefore the presence of elemental Tl, which was confirmed in powder X-ray diffraction experiments (see below), can likely be explained by the formation of thin layers of microcrystalline Tl on the surface of single-crystals of $K_{70}Sn_{103}$.

Powder X-ray Diffraction Measurements on a STOE STADI P at room temperature revealed the characteristic reflection pattern of a cluster compound with a large unit cell. A group of sharp reflections in the low angle area of 2θ = 10° and a group of weaker signals in the range of 2θ = 25° to 35° (Figure 6.1). Although the measurement lasted for 16 h the reflection data has low overall intensity. Additional reflections of elemental Tl are present (red stars). The lines of the calculated diagram from the single-crystal refinement of $K_{70}Sn_{103}$ do not throughout match with the experimental data set.

Reflections from similar cluster compounds, such as $K_{52}Sn_{82}$, K_4Sn_9, or $K_{12}Sn_{17}$ are also not in significant agreement (Figure 6.1c, d). The Sn-rich phase K_6Sn_{25} was not present either. Two sharp reflections (question marks) in the low angle region could not be assigned. This means that the title compound had formed within a phase mixture. However, it was the only species in the reaction mixture that forms collectable single-crystals, meaning the byproducts are essentially in the form of microcrystalline powder.

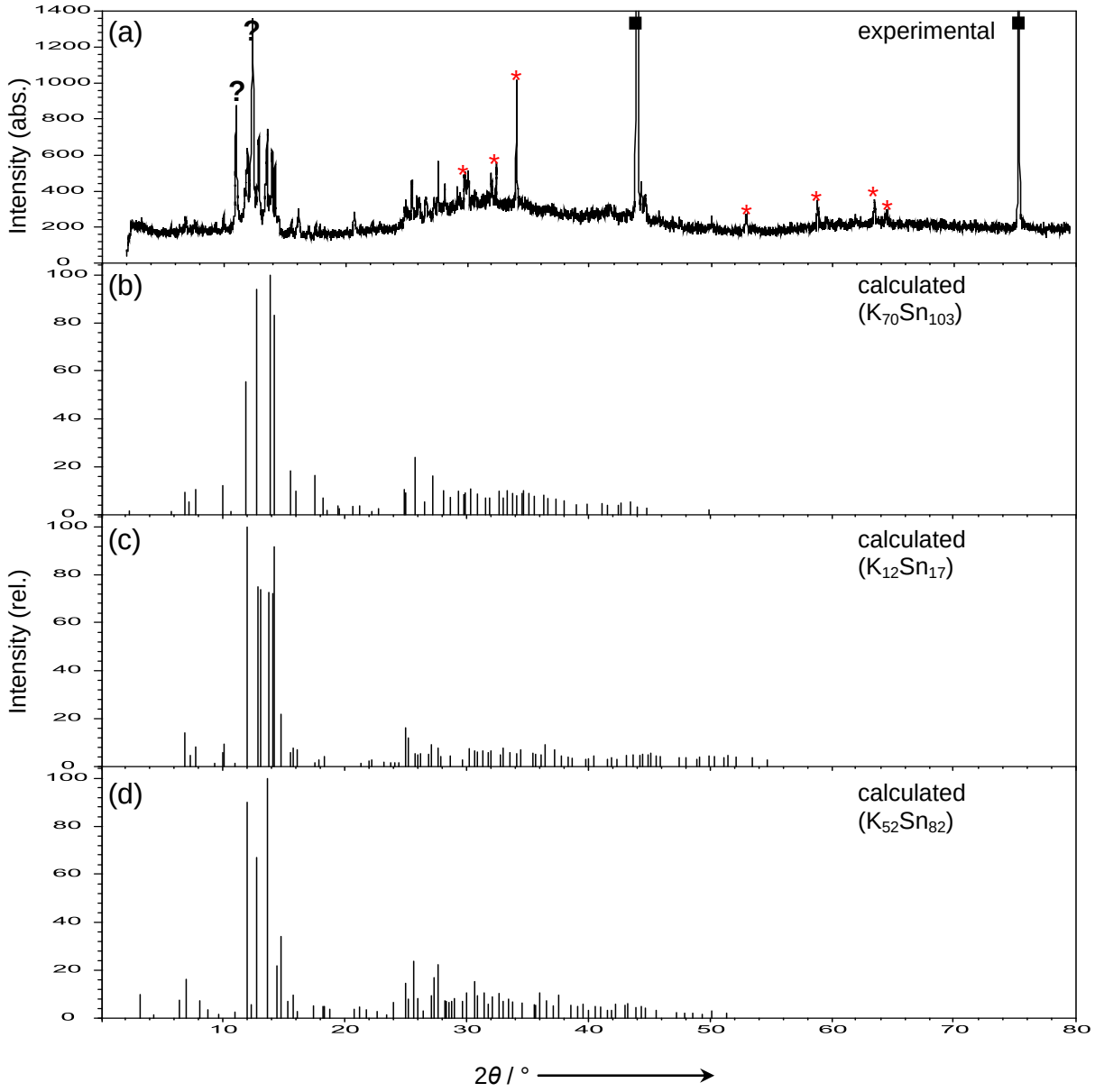

***Figure 6.1*. (a) Experimental powder diagram of the reaction of a sample loaded with K : Sn : Tl = 4 : 7 : 2. Reflections from diamond (square), from Tl (red stars), and unindexed reflections (question marks), (b) to (d) calculated powder diagrams of $K_{70}Sn_{103}$, $K_{12}Sn_{17}$, and $K_{52}Sn_{82}$.**

6.1.3 Crystal Structure Determination and Description

Structure Determination A dark single-crystal was selected from a sample loaded as K : Sn : Tl = 4 : 7 : 2. It was fixed on a glass tip and sealed into a capillary in the glove box. X-ray diffraction data were then collected on a STOE IPDS II (Detector distance: 200 mm, exposure times: 15 min per frame, ω scans 0° - +90° (for φ = 0°) and +90° - +180° (for φ = +90°), and with a scan width of 1°/frame. Diffraction experiment parameters had to be adjusted carefully with respect to the big unit cell dimensions and crystal scattering profiles. Fixing the crystal with nail polish in the capillary resulted into decomposition of the crystals due to dissolution. Therefore the crystal had to be fixed with silicon grease.

Based on systematic absences and the statistical analyses of the intensity distributions the structure could be solved in the primitive orthorhombic space group *Pbca* (No. 61), Pearson code *oP*1384. For solution SHELXS and for refinement the procedure for large structures SHELXH was used. 103 independent Sn and 70 independent K positions were found and refined anisotropically. In Table 6.1 some important crystallographic and refinement data are comprised. Atomic positions, displacement parameters and interatomic distances are found in Tables 8.13 to 8.15 (see Appendix). The relatively high final residuals of R_1 / wR_2 (all data) = 0.106 / 0.261 and residual electron peaks (+9.84 / –3.92) are similar to the ones reported for e.g. $A_{52}Sn_{82}$ (A = K, Rb)[6] and are normal for such kinds of compounds with large unit cells. Similar residuals were refined from a dataset measured on an Oxford Xcalibur3 diffractometer (CCD). The procedure ADSYM in the PLATON[21] software package was used to check for additional symmetry elements. No mirror planes could be found with none of the atoms lying on special positions.

Structure Description The binary compound crystallizes in the *c*-centered orthorhombic space group *Pbca* and a rather large unit cell with a volume of 56.063(19) $Å^3$. The 103 independent crystallographic sites for the Sn atoms generate six different $\{Sn_9\}$, 11 different $\{Sn_4\}$, and one $\{Sn_5\}$ cluster. Therefore $K_{70}Sn_{103}$ can be written as $K_{70}\{M_9\}_6\{M_5\}\{M_4\}_{11}$. Their arrangement in the unit cell is shown in Figure 6.2. The Sn atoms labeled as Sn(xA) to Sn(xF) (with x = 1 to 9) are connected to the six independent (clusters A to F) anions $\{Sn_9\}^{4-}$, drawn in light blue.

***Table 6.1*: Selected crystallographic and refinement data for $K_{70}Sn_{103}$.**

Empirical formula	**$K_{70}Sn_{103}$**
Formula weight / g·mol^{-1}	14962.07
Temperature / K	293(2)
Crystal size / mm^3	0.01 × 0.01 × 0.02
Crystal color; shape	Dark; Block
Diffractometer	STOE IPDS II (Image Plate)
Crystal system	Orthorhombic
Space group	*Pbca* (No. 61)
Unit cell parameters / Å	a = 24.471(5); b = 29.652(6); c = 77.261(16)
Unit cell volume / Å^3; Z	56063(19); 8
ρ_{calc} / g·cm^{-3}	3.55
μ / mm^{-1} (Mo K_α)	10.03
Absorption correction	-
F(000)	51840
Θ range / °	3.71 - 19.53
Index range	$0 \le h \le 22$, $0 \le k \le 27$, $0 \le l \le 72$
Data completeness / %	98.5
Integrated reflections	24051 (R_σ = 0.045)
Independent reflections	24051 (R_{int} = 0.084)
Refinement method	Full-matrix least-squares on F^2 (SHELXTL)
Parameters	1558
Goodness of fit on F^2	1.083
Observed reflections [$I > 2\sigma(I)$]	17729
R_1 / wR_2 [$I > 2\sigma(I)$]	0.087/ 0.249
R_1 / wR_2 (all data)	0.106 / 0.261
Weighting scheme[a]	a = 0.162; b = 2088.774
Extinction coefficient	-
Residual map / e$^-$·Å^{-3}	+9.84 [2.45 Å from Sn2H] / –3.92 [0.51 Å from Sn1F]

[a] $w = 1 / [\sigma^2(F_o^2) + (aP)^2 + bP]$, where $P = (F_o^2 + 2F_c^2) / 3$

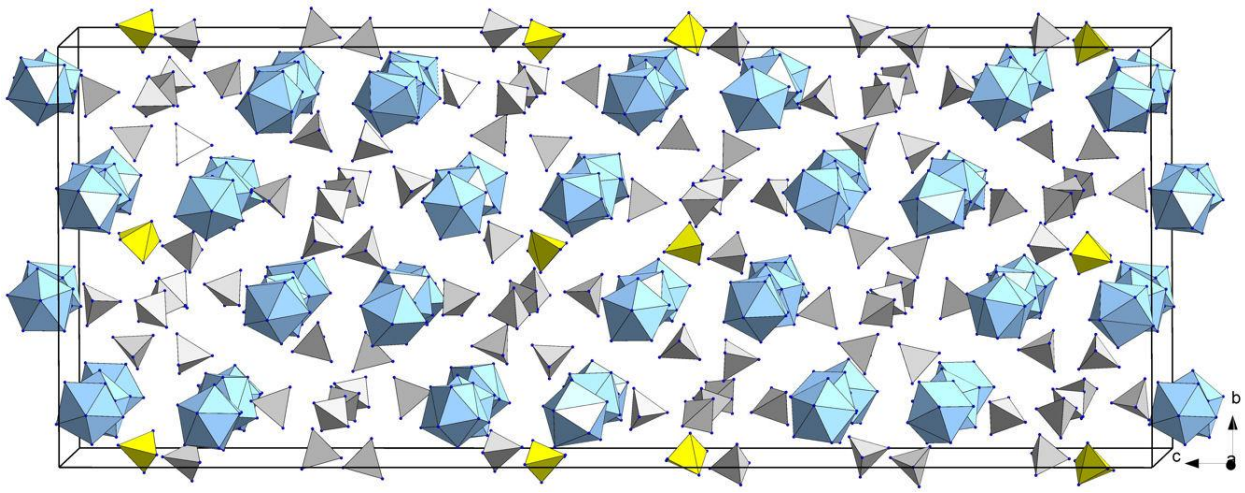

***Figure 6.2*. Arrangement of the clusters in $K_{70}Sn_{103}$ (off-[100] projection), the cations are omitted for clarity. Clusters: $\{Sn_9\}^{4-}$ (blue); $\{Sn_5\}^{2-}$ (yellow); $\{Sn_4\}^{4-}$ (gray).**

According to Wade's rules the nine atom cluster can be a C_{4v} symmetrical *nido*-$\{Sn_9\}^{4-}$ with 40 VE and the shape of a monocapped square antiprism, or a *closo*-$\{Sn_9\}^{2-}$ with 38 VE, D_{3h} symmetry, and the shape of a tri-capped trigonal prism. In both cases 18 electrons are needed for the nine *exo*-electron lone pairs.[22] Both clusters can be described as rotational ellipsoids.[23] When drawing idealized polyhedra both types of clusters should cover geometric restrictions for certain intracluster bonds. An ideal *closo*-cluster shows three longer bonds and 18 shorter, whereas in an ideal *nido*-case four longer (between 5b-atoms) and 16 shorter bonds (between 4b-and 5b atoms and between two 4b-atoms) are present.[24] The D_{3h} symmetrical nine atom cluster with 20 skeletal electrons possesses a LUMO which is bonding along the edges *e* (Figure 6.4), but antibonding along the heights *h* of the trigonal prism. Occupation of the LUMO with one or two further electrons (leading to $\{Sn_9\}^{3-}$ or $\{Sn_9\}^{4-}$) leads to a distortion towards larger *h* / *e* ratios in comparison to an ideal polyhedron with equal edge lengths (*h* / *e* = 1).[25] However, reported results of different compounds including such clusters show that $\{Sn_9\}^{4-}$ clusters are very sensitive to deformation and can exhibit conformations that are intermediate to the two ideal shapes.

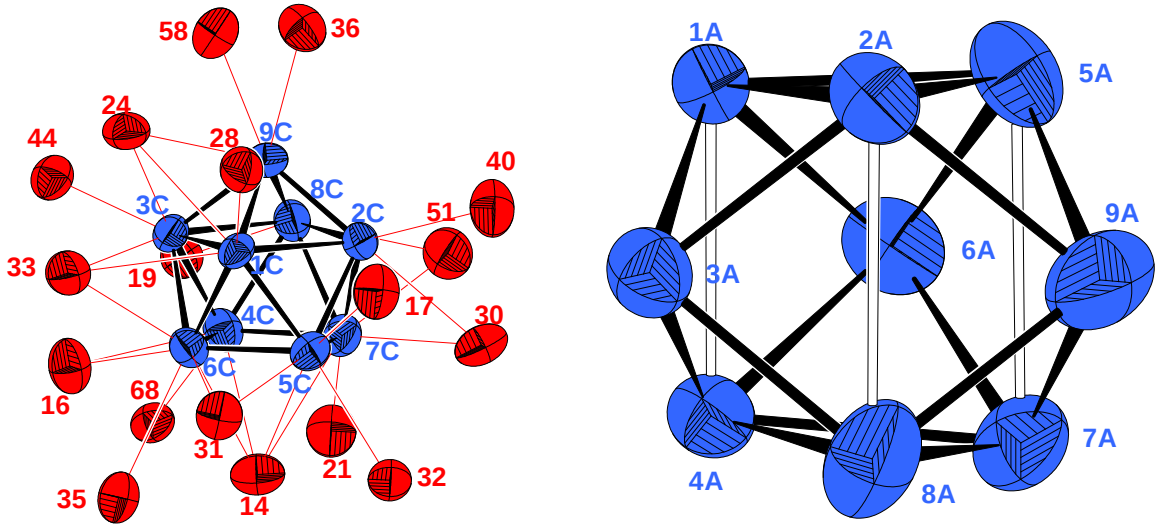

Figure 6.3. **(a) Anisotropic representation of $\{Sn_9\}^{4-}$ (cluster C) and neighboring K^+ cations (up to 4 Å), with several of them capping the deltahedral faces (all atoms are drawn at 70% probability level). (b) More symmetrical cluster A, white lines indicate long heights of a hypothetical tricapped trigonal prism.**

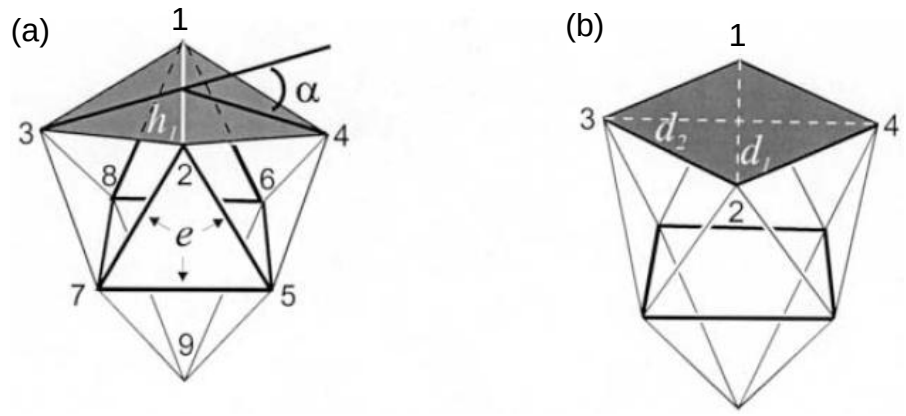

***Figure 6.4*. Parameters for the description of the ideal structures and distortions from (a) D_{3h} and (b) C_{4v} symmetry taken from ref. [23].**

In the present $\{Sn_9\}$ clusters this is the case for all clusters A to F. In order to provide a rough idea to which type the present nine atom clusters belong, several geometrical parameters have been calculated and are listed in Table 6.2. The average *h* / *e* ratio of all clusters A to F is significantly larger than 1 and are in the range of typical $\{Sn_9\}^{4-}$ clusters crystallized from solution. Albeit not all values are indicating exact C_{4v} symmetrical clusters, the throughout presence of one significantly smaller d_1 / d_2 value and therefore one significantly smaller dihedral angle, together with the considerable deviations of the heights of the trigonal prism, point into the direction of $\{Sn_9\}^{4-}$ clusters.

***Table 6.2*: Values of geometrical parameters for all $\{Sn_9\}$ clusters (A to F) in $K_{70}Sn_{103}$.**

cluster	3× (d_1 / d_2)	α_1 / °	α_2 / °	α_3 / °	h_1 / Å	h_2 / Å	h_3 / Å	$h_ø$ / $e_ø$
A	1.20 / 1.41 / 1.24	13	18	33	3.40	3.69	3.78	1.18
B	1.03 / 1.33 / 1.53	3	27	34	3.19	3.52	4.12	1.16
C	1.02 / 1.41 / 1.46	1	31	35	3.28	3.36	4.12	1.45
D	1.10 / 1.33 / 1.47	7	23	31	3.28	3.56	3.96	1.17
E	1.06 / 1.37 / 1.44	9	37	39	3.29	3.38	4.16	1.17
F	1.09 / 1.27 / 1.39	8	27	35	3.40	3.54	3.93	1.17

The single five atom cluster $\{Sn_5\}^{2-}$ is made up of Sn1G to Sn5G. All intracluster bonds are in the range of Sn–Sn bonds reported for deltahedral Sn clusters. However, as shown in Figure 6.5b, the cluster shows significant deviations from the ideal D_{3h} symmetry. The valence angles in the trigonal base (Sn2GSn3GSn5G) are 59.7°, 58.7°, 61.6° and the apical atoms Sn1G and Sn4G have two different distances to the basal plane (h_{Sn1G}: 2.53 Å; h_{Sn4G}: 2.33 Å).

Also the maximum difference between axial and equatorial distances with ~ 0.18 Å is clearly larger than those found for $\{Sn_5\}^{2-}$ clusters in compounds crystallized from solution, $[2.2.2\text{-cryptK}^+]_2Sn_5$[17] and $[2.2.2\text{-cryptNa}^+]_2Sn_5$.[18] Compared to those the present five atom cluster apparently suffers from significant matrix effects. A comparison of intracluster bonds and angles to $\{Sn_5\}^{2-}$ clusters reported in the literature is given in Table 6.3 and emphasizes the significant distortions from D_{3h} symmetry.

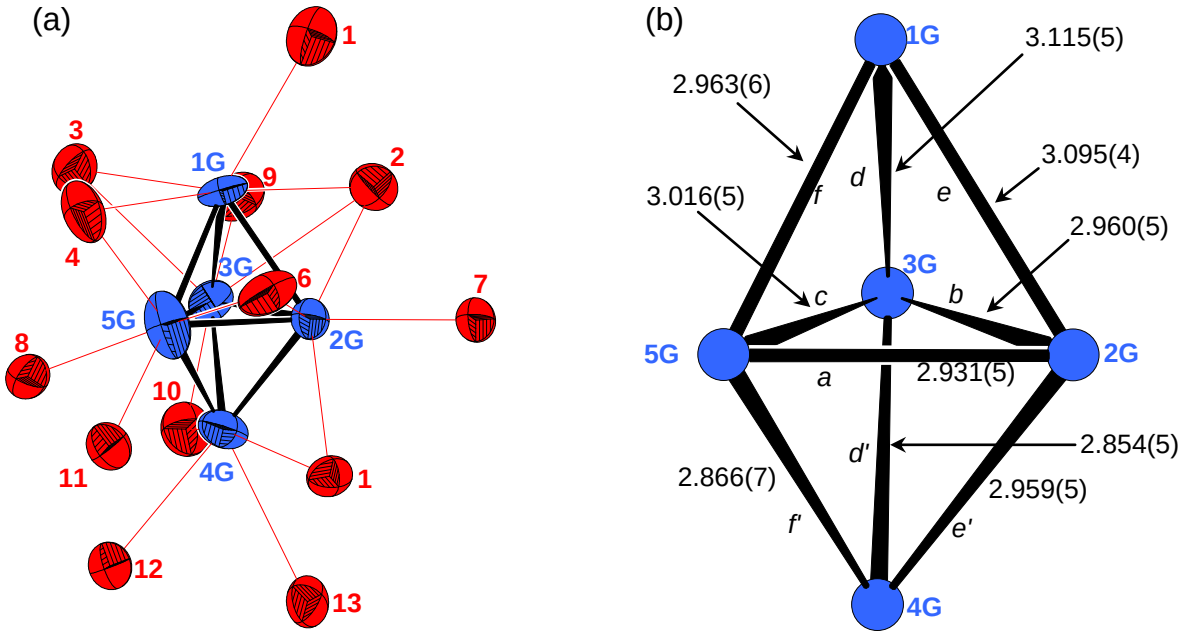

***Figure 6.5*. The five atom cluster $\{Sn_5\}^{2-}$ in $K_{70}Sn_{103}$. (a) Anisotropic representation with coordination with K^+ cations (< 4 Å) at 70% probability level, (b) ball and stick model with interatomic distances.**

***Table 6.3*: Comparison of intracluster bond lengths of $\{Sn_5\}^{2-}$ in $K_{70}Sn_{103}$, $[2.2.2\text{-cryptNa}^+]_2Sn_5$, and $[K\text{-}(2,2,2\text{-crypt})]_2Sn_5$.**

distances and angles	$K_{70}Sn_{103}$		$[2.2.2\text{-cryptNa}^+]_2Sn_5$	$[(2,2,2\text{-cryptK}^+)]_2Sn_5$
a	2.931(5)	Ø2.969	3.095(10) / 3.24(4)	3.072(2)
b	2.960(5)			
c	3.016(5)			
d	3.115(5)	Ø2.975	2.877(7) / 2.854(6)	2.866(1)
e	3.095(4)			
f	2.963(6)			
d'	2.854(5)			
e'	2.959(5)			
f'	2.866(7)			
eq.-ax.-eq. /°	Ø59.9		65.1(2) / 65.7(2)	
ax-eq.-ax. /°	Ø109.4		102.8(2)	
eq.-eq.-ax. /°	Ø60.1		57.5(2) / 57.2(2)	

The eleven crystallographically independent $\{Sn_4\}^{4-}$ anions (clusters H to R) are made up of atoms Sn(zH) to Sn(zR) (with z = 1 to 4) and exhibit nearly ideal tetrahedral shape. Deviations from the ideal 60° deltahedral angles are ≤ ±2°. The intracluster distances are in the range of 2.818(1) (cluster I) to 3.019(1) Å (cluster I) and in good agreement with corresponding distances in KSn (2.96 to 2.98 Å), or high pressure CsSn (2.90 to 2.95 Å), and are slightly larger than twice the Pauling covalent radii or distances found in *α*-Sn. As a representative, cluster L is shown together with a typical coordination by K^+ cations in Figure 6.6.

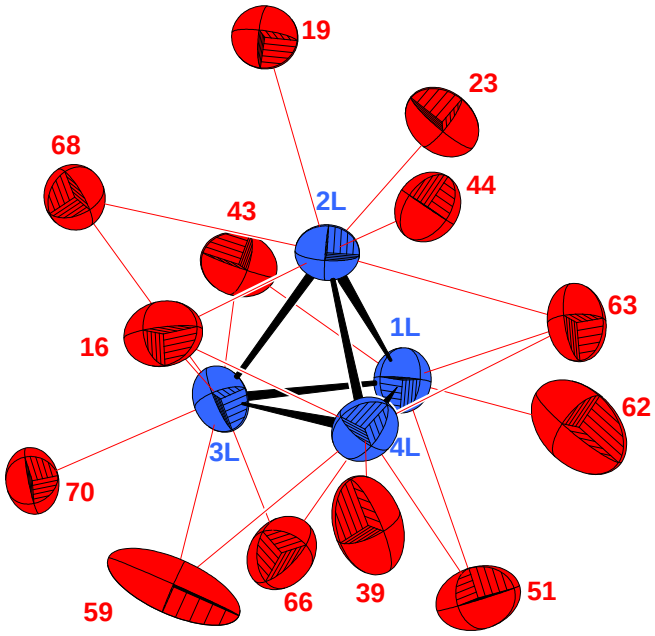

Figure 6.6. **Anisotropic representation of $\{Sn_4\}^{4-}$ (cluster L) with neighboring K^+ cations (up to 4 Å), with several of them capping the deltahedral faces (all atoms are drawn with 70% probability level).**

As the compound contains bigger cluster anions $\{Sn_9\}$ and smaller cluster anions, $\{Sn_5\}$ and $\{Sn_4\}$, in the ratio of 1 : 2, the topological arrangement of the clusters (Figure 6.7a) can be discussed in terms of the distribution of Mg and Zn in the hexagonal Laves phase $MgZn_2$ (a similar situation is present in $A_{12}M_{17}$ = $A_{12}\{M_9\}\{M_4\}_2$). The $\{Sn_9\}$ clusters are organized in a hexagonal diamond array. In the resulting hexagonal channels the $\{Sn_5\}$ and $\{Sn_4\}$ clusters are embedded. As depicted in Figure 6.7b the $\{Sn_9\}$ clusters form hexagons and are arranged in corrugated layers in the (100) plane. The layers are packed antiparallel in a sequence *ABAB* along [100].

They are separated by 3.6.3.6 Kagomé nets that are formed by the smaller $\{Sn_4\}$ and $\{Sn_5\}$ clusters (Figure 6.7c, d, layer *A* at $x = 0.25$ and layer *B* at $x = 0.75$). They are slightly corrugated and also stacked in a *ABAB* sequence (Figure 6.7d). The Kagomé nets are interconnected by $\{Sn_4\}^{4-}$ clusters at $x = 0, 0.5$. Therefore each of the latter is coordinated with six other four-(or five-) atom clusters. The latter form vertex-sharing supertetrahedra (Figure 6.8b) and the tetrahedra at $x = 0$ and 0.5 form 3^6 nets.

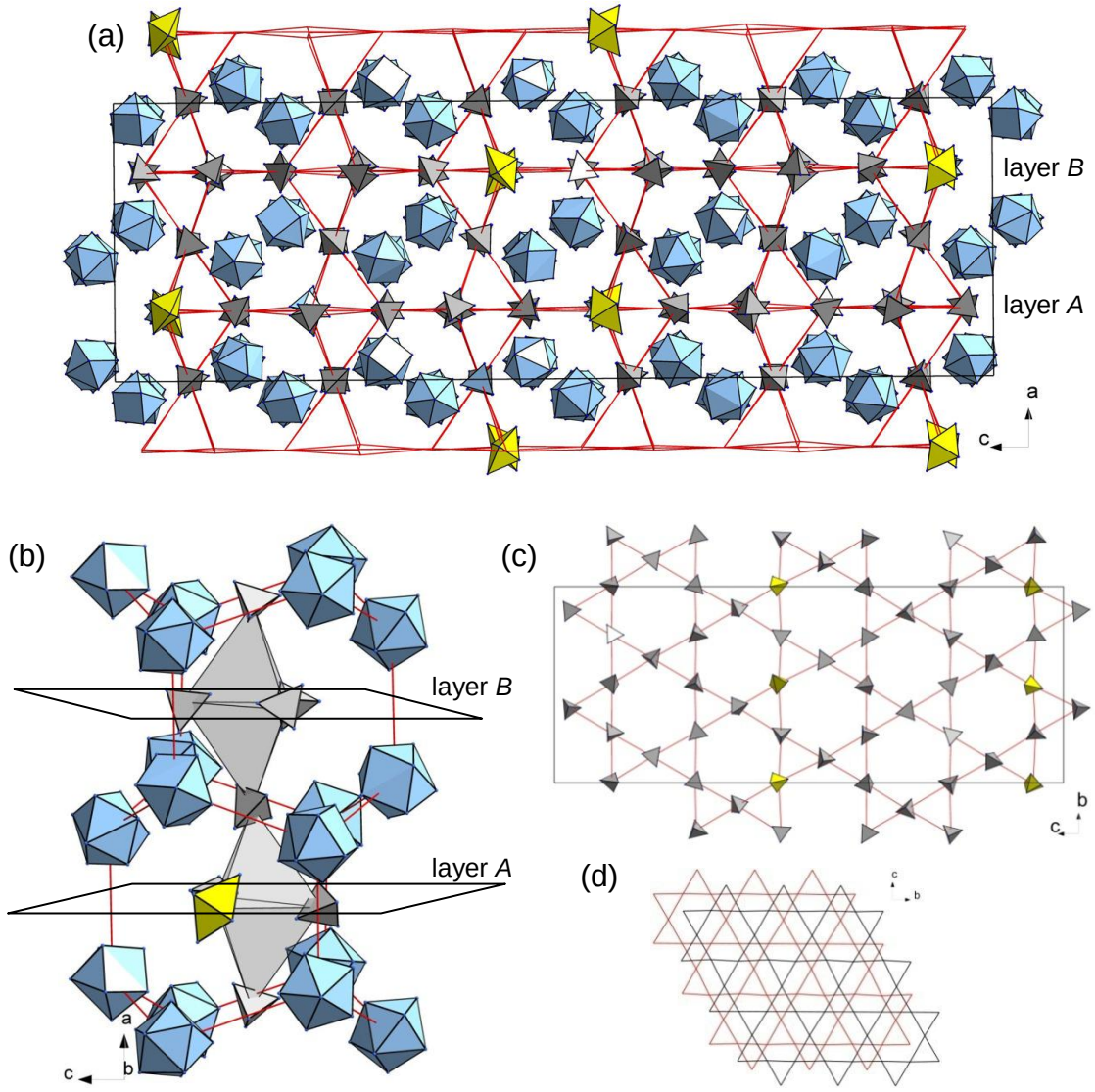

***Figure 6.7*. (a) Unit cell projection emphasizing the relation to $MgZn_2$. (b) Hexagonal diamond like stacking of $\{Sn_9\}$ clusters with embedded $\{Sn_5\}$ and $\{Sn_4\}$ clusters. The latter are arranged as face and vertex sharing tetrahedra. (c) Kagomé nets running parallel to the (100) plane. (d) *ABAB* stacking of the Kagomé nets. Clusters: $\{Sn_9\}^{4-}$ (light blue), $\{Sn_5\}^{2-}$ (yellow), $\{Sn_4\}^{4-}$ (gray). Connections between the clusters' centers of gravity are shown with red and gray lines.**

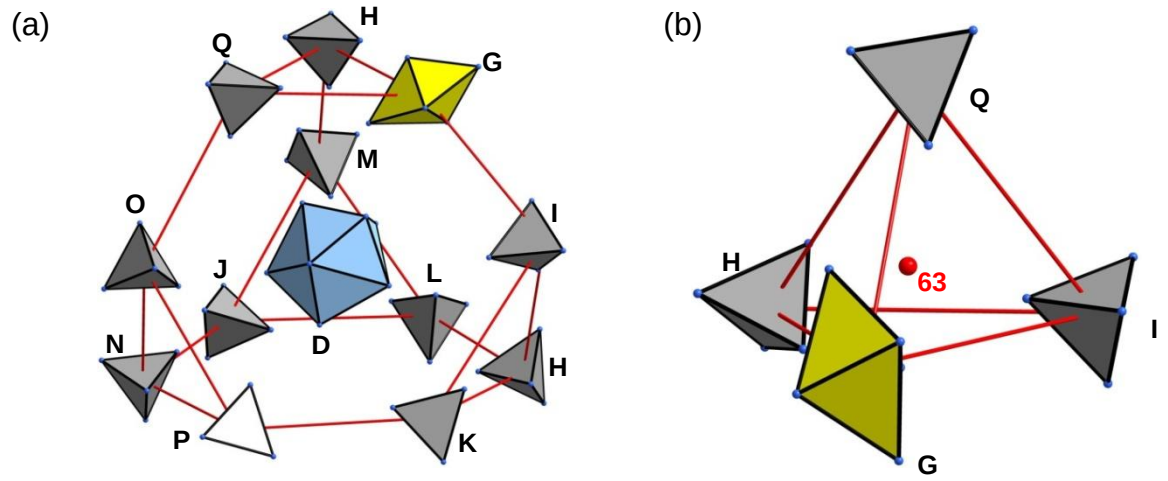

***Figure 6.8*. (a) Truncated supertetrahedron of $\{Sn_4\}$ tetrahedra and one $\{Sn_5\}$ trigonal bipyramid centered by cluster $\{Sn_9\}$-D. (b) One supertetrahedron made of three $\{Sn_4\}$ tetrahedra and one $\{Sn_5\}$ trigonal bipyramid centered by K63. Clusters: $\{Sn_9\}^{4-}$ (light blue), $\{Sn_5\}^{2-}$ (yellow), $\{Sn_4\}^{4-}$ (gray). Connections between the clusters' centers of gravity are shown with red lines.**

Similar to the structure of $Ae_{12}Tt_{17}$, the deformation of the formally hexagonal cell of $MgZn_2$ to an orthorhombic one is a result of site preference due to different orientations of the ellipsoid like nine atom clusters for better packing in the crystal. Further topological structure features are present. A supertetrahedron made of $\{Sn_4\}$ and $\{Sn_5\}$ clusters, centered by a K^+ cation is shown in Figure 6.8b. Truncated supertetrahedra made of $\{Sn_4\}$ and $\{Sn_5\}$ clusters are centered by $\{Sn_9\}^{4-}$ anions as depicted in Figure 6.8a. In this way each $\{Sn_9\}$ cluster is coordinated with 12 $\{Sn_4\}$ units and additional four $\{Sn_9\}$ clusters cap the hexagonal faces resulting in a CN-16 Frank-Kasper polyhedron.

The compound $K_{12}Sn_{17}$ (space group $P2_1/c$ No. 14) can be formulated as 6 × $K_{12}\{Sn_9\}\{Sn_4\}_2 = K_{72}\{Sn_9\}_6\{Sn_4\}_{12}$, which compared to the present phase, only differs by two additional K atoms, counterbalancing the higher charge of the *nido*-$\{Sn_4\}^{4-}$, and one less Sn atom. Comparing the unit cell volumes for the two compounds (V ~ 6860 Å^3 for 6× $V(K_{12}Sn_{17})$ and V ~ 7008 Å^3 for 1× $V(K_{70}Sn_{103})$) suggests a slightly denser packing of the atoms in $K_{12}Sn_{17}$. Comparing the volumes with that of K_4Sn_4 (V = 2427.45, Z = 8) and K_4Sn_9 (V = 1953.10(76), Z = 4) shows the same trend with the volume for $K_{70}Sn_{103}$ being approximately 6.7% larger.

The herein presented compound suggests an uninvestigated structural and compositional diversity in the binary phase system K–Sn, which is located between the stoichiometries K_4Sn_4 and K_4Sn_9. In addition to stacking variants reminiscent of *Laves* structures, other phases may adopt structures of further hierarchy initiators such as AB_3- or AB_5-types.

6.2 $BaSn_2$ - A Zintl Phase with *α*-Arsenic like Sn Layers

6.2.1 Introduction

Bonding situations in Zintl phases are characterized by covalent interactions in the anionic (post transition element) part of the structures, and ionic bonding governing the cation–anion interactions. In the classical understanding this should lead to semiconducting or even insulating electronic properties for Zintl phases. However, the structure alone is insufficient to describe a compound's characteristic. Investigations of physical properties of reported Zintl phases have lagged behind their synthesis and structural studies. In recent years many of these phases (e.g. $Ba_7Ga_4Sb_9$,[26] K_5Bi_4,[27] or $Ba_3As_4Sn_6$[28]) have been found to be metallic conductors. Thus, the term metal-like salts seems to be more appropriate. Additionally, the apparent disagreement between metallic character and closed shell chemical bonding has been utilized within the Zintl concept to identify adventitious impurities. In this sense, semiconducting 'Ca_3Pb' was shown to contain oxygen and had to be reformulated as an inverse perovskite Ca_3PbO. To understand the experimental properties of such compounds it is important to gain deeper insights into their electronic structures to learn why the simple bonding principles fail. As an interesting case study unusual electronic and bonding properties of the Zintl phase Ca_5Ge_3 have been reported by Corbett.[29] A publication closely related to $BaSn_2$ presented in this chapter was given on reexamination of $EuGe_2$ by Bobev et al.[30] The simple title compound is a new binary phase in the Ba–Sn system. The *hitherto* known tin-rich Ba stannides are fairly limited and include the phases Ba_3Sn_5[31] (Pu_3Pd_5-type with pyramidal *arachno*-{Sn_5} clusters), $BaSn_3$[32] (Ni_3Sn-type with cyclopropenyl like $\{Sn_3\}^{2-}$), and $BaSn_5$[33] (a variant of the AlB_2-type with 3^6 and 6^3 nets of Sn).

6.2.2 Synthesis and Characterization

Synthesis $BaSn_2$ was first found in a sample that had been loaded with Na : Ba : Sn = 2 : 1 : 4, which aimed to synthesize the Ba analogon to the compound Na_2SrSn_4 (see Chapter 5.4). According to powder X-ray measurements the outcome of that reaction was a mixture of $BaSn_2$, *β*-NaSn, and Ba_3Sn_5. Later, $BaSn_2$ was obtained again from a stoichiometric sample loading (Ba : Sn = 1 : 2). The temperature treatment involved heating to 850 °C (2 $K \cdot min^{-1}$), holding there for 12 h, cooling down to 700 °C (with 2 $K \cdot min^{-1}$), annealing for 72 h, and quenching to room

temperature. The crystalline product exhibits metallic luster In the latter experiment the compound was prepared in sealed Nb ampoules under Ar atmosphere from a total loading mass of 1.249 g, with m(Ba) = 0.458 g and m(Sn) = 0.791 g.

Powder X-ray Diffraction A powder sample was prepared in the glove box by diluting the substance with diamond powder and filling it into a glass capillary (0.3 mm diameter). The diffraction diagram was measured at room temperature for 20 h on a linear PSD. The resulting powder pattern (Figure 6.9) reveals the formation of a mixture of $BaSn_2$ and $BaSn_3$. The calculated reflections originating from $BaSn_3$, the main phase, are labeled with a red star, diamond reflections are marked with a square.

EDX Measurements Qualitative and quantitative analysis were applied to various crystallites of a sample obtained from loading with Ba : Sn = 1 : 2. The presence of the two elements by measurements of several crystallites which unit cells were previously determined on a Oxford Xcalibur3 diffractometer was confirmed with an average ratio of Ba : Sn = 31(3) : 69(4) at%. (calculated: 33% Ba, 66% Sn).

Thermal Analysis To investigate the thermal behavior of $BaSn_2$ a DTA measurement was performed from the reaction of a mixture at 850 °C which had been loaded with Ba : Sn = 1 : 2. The temperature program contained two equivalent cycles with heating gradients of 10 $K \cdot min^{-1}$ to 800 °C, cooling to 100 °C, and 10 min isothermal dwelling times. As shown in Figure 6.10 the heating and cooling curves reveal the presence of two peaks in a narrow temperature range. As the binary phase diagram is incomplete for the relevant compositions, $BaSn_3$ and $BaSn_2$ (which were detected by powder X-ray measurements), no final conclusion can be drawn from this measurement. Varying annealing temperatures in this narrow temperature sector always yielded a mixture of the two phases with only modest trends towards $BaSn_2$ at the higher temperature.

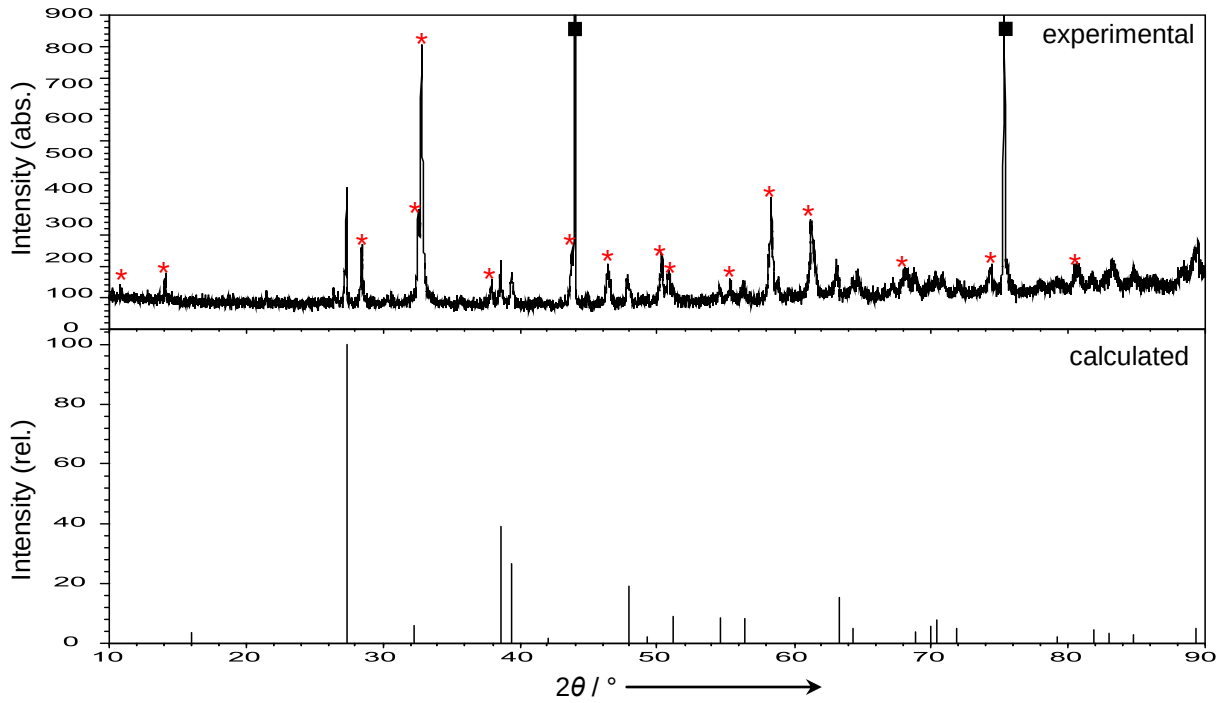

Figure 6.9. **Experimental (top) from a reaction loaded with Ba : Sn = 1 : 2, and simulated (bottom) powder diagrams of $BaSn_2$. Reflections from $BaSn_3$ are marked with red stars, reflections from diamond powder (internal standard) are marked with squares.**

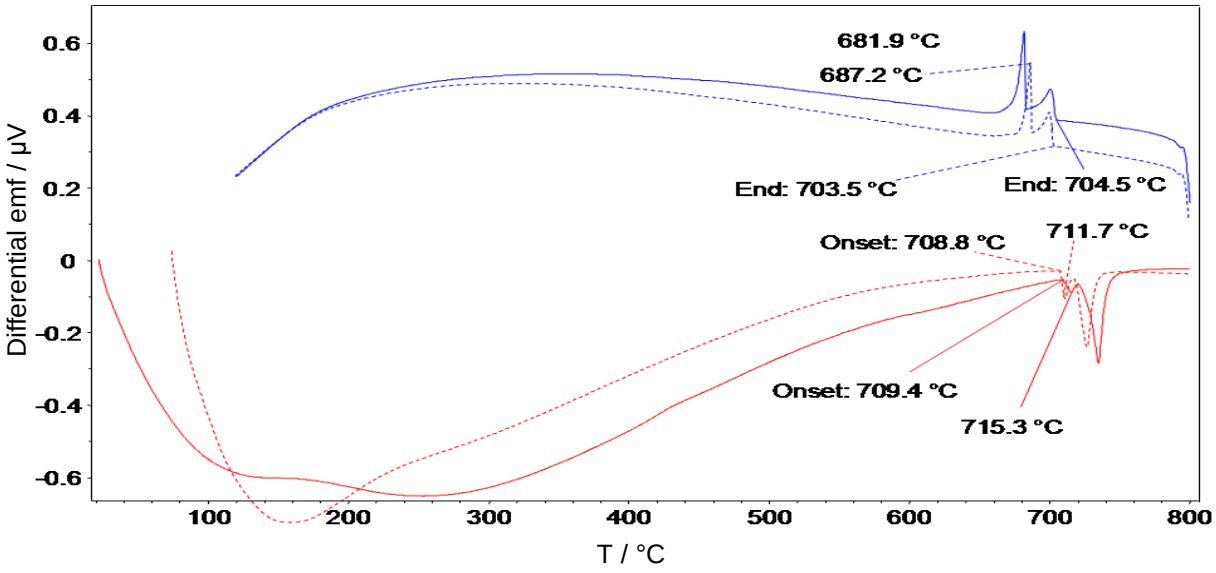

Figure 6.10. **DTA curves of the product of a reaction with Ba : Sn = 1 : 2 at 850 °C. Dashed lines represent the 2nd cycle. Heating (red), cooling (blue).**

6.2.3 Crystal Structure Determination and Description

Structure Determination A silvery single-crystal of $BaSn_2$, checked for singularity in the glovebox and fixed on a glass capillary, which afterwards was introduced into a capillary (0.3 mm diameter) and sealed by fusing the open end. The crystal was measured on an Oxford Xcalibur3 diffractometer equipped with a CCD detector. The data collection (388 frames) involved four sets of ω scans (–41° to +63° for different φ positions: +0°, +90°, +180°, +270°) and a φ scan (0° - 360° with θ = +30°) with a scan width of 2°/frame and exposure time of 10s/frame. The detector distance was 50 mm. The structure was solved by the Patterson method for heavy atoms. Anisotropic refinements of the two atomic positions (Ba and Sn) lead to a converging model in the trigonal space group *P*–3*m*1, Pearson code *hP*3. Some data collection and refinement parameters are summarized in Table 6.4. The atomic coordinates together with anisotropic displacement parameters are comprised in Tables 6.5 and 6.6 and interatomic distances are listed in Table 8.16 (see Appendix).

***Table 6.4*: Selected crystallographic and refinement data for $BaSn_2$.**
[a] $w = 1 / [\sigma^2(F_o^2) + (aP)^2 + bP]$, where $P = (F_o^2 + 2F_c^2) / 3$

Empirical formula	**$BaSn_2$**
Formula weight / g·mol^{-1}	374.72
Temperature / K	293(2)
Crystal size / mm^3	0.01 × 0.01 × 0.01
Crystal color; shape	Silvery metallic; Block
Diffractometer	Oxford Xcalibur3 (CCD)
Crystal system	Trigonal
Space group	*P*–3*m*1 (No.164)
Unit cell parameters / Å	*a*, *b* = 4.652(2); *c* = 5.546(4)
Unit cell volume / Å^3; *Z*	103.95(11); 1
ρ_{calc} / g·cm^{-3}	5.986
μ / mm^{-1} (Mo K_α)	21.04
Absorption correction	empirical
F(000)	156
Θ range / °	3.67 - 27.82
Index range	$-6 \le h \le 6$; $-4 \le k \le 6$; $-7 \le l \le 7$
Data completeness	100%
Integrated reflections	1519 (R_σ = 0.0155)
Independent reflections	118 (R_{int} = 0.0440)
Refinement method	Full-matrix least-squares on F^2 (SHELXTL)
Parameters	7
Goodness of fit on F^2	1.138
Observed reflections [$I > 2\sigma(I)$]	102
R_1 / wR_2 [$I > 2\sigma(I)$]	0.021 / 0.038
R_1 / wR_2 (all data)	0.024 / 0.039
Weighting scheme[a]	a = 0.003; b = 1.381
Extinction coefficient	0.061(4)
Residual map / e$^-$·Å^{-3}	+3.33 [1.02 Å from Sn] / –1.09 [1.56 Å from Sn]

***Table 6.5*: Atomic coordinates and equivalent isotropic displacement parameters for $BaSn_2$.**

Atom	Wyck.	Occ. ≠ 1	*x*	*y*	*z*	U_{eq} / Å^2
Ba	1*b*		0	0	½	0.018(1)
Sn	2*d*		⅔	⅓	0.8970(1)	0.015(1)

***Table 6.6*: Anisotropic thermal displacement parameters (*I* Å^2) for $BaSn_2$.**

Atom	U_{11}	U_{22}	U_{33}	U_{23}	U_{13}	U_{12}
Ba	0.018(1)	0.018(1)	0.019(1)	0	0	0.009(1)
Sn	0.015 (1)	0.015(1)	0.016(1)	0	0	0.008(1)

Structure Description $BaSn_2$ crystallizes in the $EuGe_2$ structure type (*c*/*a* = 1.22) with a *c*/*a* ratio of 1.19. Analogous to $CaSi_2$, the structure (Figure 6.11) is composed of corrugated 2D 6^3 nets of three bonded Sn ($^2_\infty[Sn_2]^{2-}$) and planar 3^6 nets of Ba at *z* = 0.5. Such anion layers are reminiscent of the element structure of (gray, metallic, rhombohedral) *α*-arsenic. The tin layers are made of condensed $\{Sn_6\}$ rings in chair conformation, which are arranged like in trans-decalin, and are primitively (*AAAA*) stacked along [001] (Figure 6.11a). This is in contrast to the arsenic structure where the layers are displaced. Another difference is the clear separation of the layers (~ 4.4 Å, calculated from the two opposing faces along *c* direction of the distorted $SrSn_6$ polyhedron), which, obviously, is caused by the embedded Ba atoms. Another way of describing the Sn substructure is deriving from the AlB_2 structure type by strong corrugation of the planar layers which are built of hexagons. The only Sn–Sn bond present of 2.919(1) Å is slightly longer than covalent bonds found in *α*-Sn (2.803 Å), which is not unusual given the fact that the atoms are not in tetrahedral coordination and carry a formal charge of –1. However, the bond length is comparable to separations found in other intermetallic Sn compounds, such as Na_7Sn_{12} (2.83 – 3.09 Å). The valence angle of 105.7° in the layers is close to the ideal tetrahedral angle of 109.5°. The Ba atoms are positioned as spacers between the corrugated layers. The coordination by the six nearest Sn atoms (up to 4 Å) is represented in Figure 6.11b and shows Ba residing in the center of a distorted $\{BaSn_6\}$ octahedron. The polyhedron is tilted with respect to the unit cell axes and the Ba–Sn distance is 3.473(2) Å. The latter description is consistent with Ba atoms populating the octahedral holes between two close-packed Sn layers. Each octahedron shares six edges with its neighbors, resulting in edge sharing layers of octahedra in the (001) plane. The tetrahedral holes are empty.

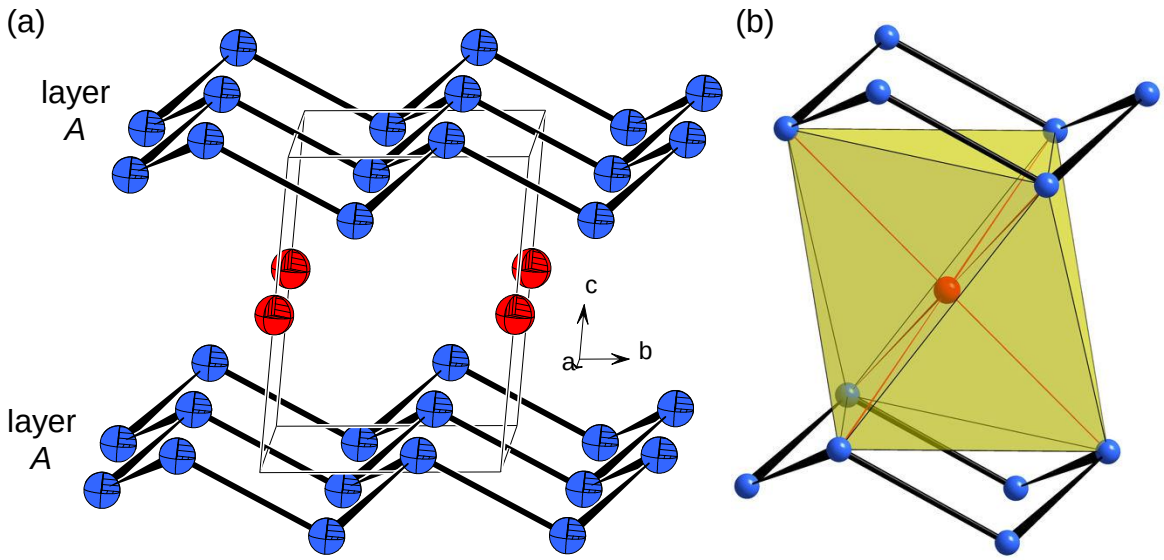

***Figure 6.11*. (a) [100] projection of the unit cell of $BaSn_2$ (atoms are drawn at 90% probability level), (b) coordination sphere around Ba. Sn (blue), Ba (red).**

6.2.4 Electronic Structure

Band structure and COHP calculations were carried out using the TB-LMTO-ASA code (tight binding linear muffin tin orbitals atomic spheres approximation), in which the density functional theory is used with the local density approximation (LDA). The *k*-space integration was performed by the tetrahedron method on a set of 24 × 24 × 26 irreducible *k* points and a basis set with Ba-6*s*/(6*p*)/5*d*/(5*f*) and Sn-5*s*/5*p*/(4*d*)/(4*f*) (down-folded orbitals in parentheses). The calculated band structure and total density of states (DOS) together with projected contributions from Ba and Sn, and –ICOHP plots for Sn–Sn and Ba–Sn interactions are depicted in Figure 6.12. The Fermi level cuts the DOS in a pseudo gap region close to zero. The band structure reveals two band crossings of E_F along H → Γ, which suggests poor metallic character of the compound. Fat band representations classify the characters of these bands being mainly Sn-*p* (with slightly more pronounced p_z-character) and Ba-*d* (Figure 6.13). A look at the valence band between 0 and –4 eV affirms the high contributions from filled Sn-*p* and Ba-*d* orbitals. The Sn-*s* bands are clearly detached at energies of –4 to –10 eV. The –COHP curves show that both Sn–Sn and Ba–Sn interactions are almost fully optimized up to the Fermi level (Sn–Sn: 2.23 eV/bond (–$ICOHP_{max}$ at 2.27 eV) and Ba–Sn 0.73 eV/bond (–$ICOHP_{max}$ at 0.95 eV).

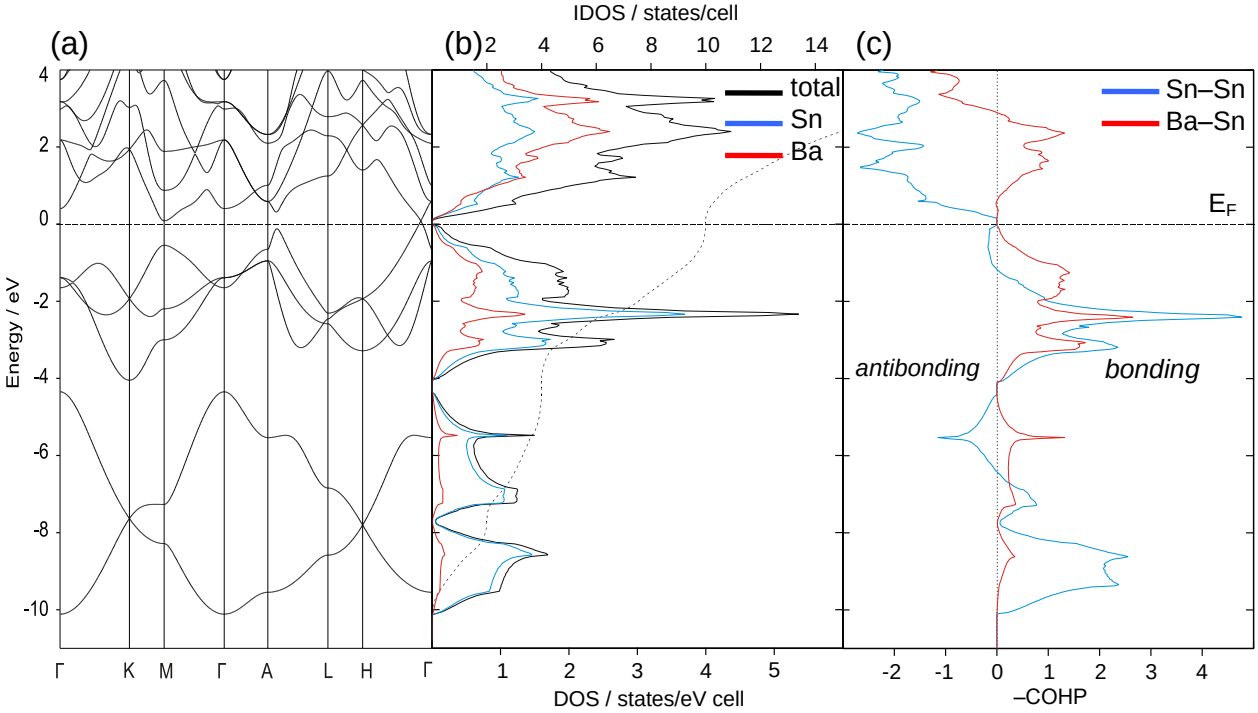

***Figure 6.12*. (a) Band structure along symmetry points of $BaSn_2$. (b) Total DOS and DOS projections Sn (blue), Ba (red). (c) –COHP plots of Sn–Sn (blue) Ba–Sn (red). The Fermi level is taken as the point of zero energy.**

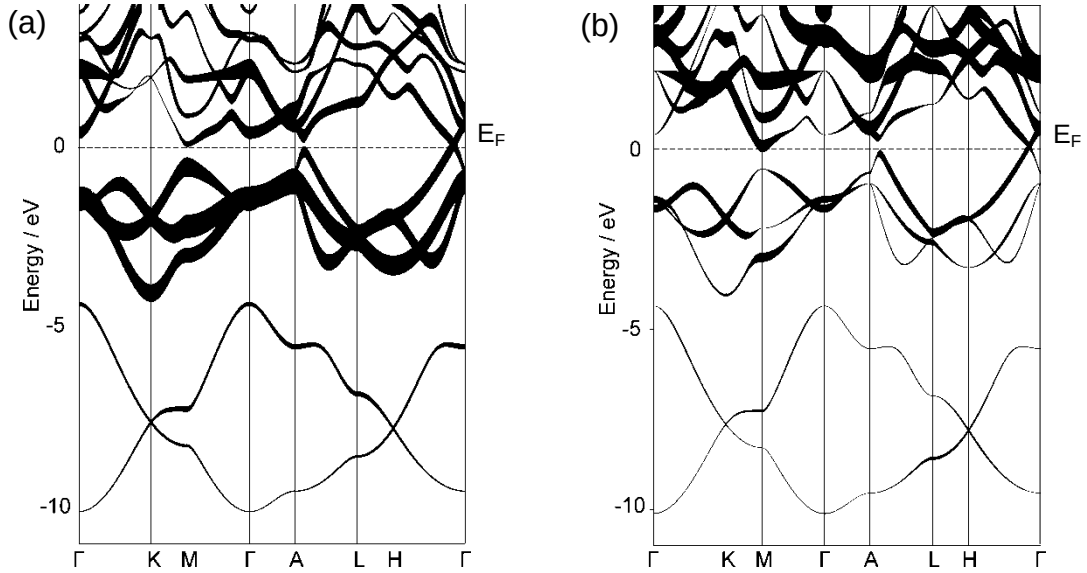

***Figure 6.13*. Fat band plots for (a) Sn-*p*; (b) Ba-*d* bands in $BaSn_2$. The bands are drawn with a thickness representative of their corresponding orbital contribution.**

According to the LMTO results Sn–Sn bonding at E_F with 10 electrons passes through an antibonding region and would be optimized with nine electrons per formula unit. This feature is commonly explained by the antibonding character of the orbital interactions between adjacent corrugated Sn layers. The Fermi level lies in a non-bonding region, and hence the compound is formally electron rich. A look at the Ba–Sn interactions reveals that the overall structure stabilization is caused by filling Ba–Sn bonding states. There is a slight electron deficiency on the Ba–Sn side.

6.2.5 Discussion

$AeTt_2$ (Ae = Ca, Sr, Ba; Tt = Si, Ge, Sn) compounds adopt a number of different crystal structure types, largely dependent on the nature of the alkaline earth element and the reaction conditions (pressure). Table 6.7 lists all known $AeTt_2$ phases together with the anionic structure themes. A comprehensive view on AlB_2 structure types in terms of group-subgroup relations is reported elsewhere.[34]

***Table 6.7*: Known $AeTt_2$ (Ae = Ca, Sr, Ba; Tt = Si, Ge) and their anionic substructures at ambient pressure.**

Compound	Anionic substructure	Structure type
$CaSi_2$	corrugated layers of 6-member rings	WN_2
$BaSi_2$	tetrahedral clusters	$BaSi_2$
$CaGe_2$	corrugated layers of 6-member rings	$CaSi_2$
$BaGe_2$	tetrahedral clusters	$BaSi_2$
$SrSi_2$	3D network of 3 bonded atoms with planar coordination	$SrSi_2$
$SrGe_2$	tetrahedral clusters	$BaSi_2$

As it can be seen the $AeSn_2$ phases have not been reported before and for standard conditions the containing tetrel theme can be reduced to either $\{Tt_4\}^{4-}$ clusters, layer, or networks motifs. As the number of phases is fairly limited it is difficult to find dependencies on atomic radii and/or electronegativities. For Si it may be concluded that differences in $X_{Pauling}$ and radii values are biggest for $BaSi_2$, therefore isolated clusters are stabilized. However, in order to quantify the favor for the arsenic like Sn sublattice in the present compound, similar to the quantification of $BaGe_2$ reported by Vaughey et al.[35] extended Hückel calculations in a variety of structures involving three-connected Sn, such as in AlB_2, α-$ThSi_2$, $SrSi_2$, and $BaSi_2$ will have to be carried out. Nevertheless, the simple binary is another example of how important cation interactions are, as they stabilize the structure by cation-anion interactions that are stronger than normal ionic interactions.

6.3 Ae_3Tl_5 (Ae = Ca, Sr) - Two Intermetallic Phases with Pu_3Pd_5 Structure

6.3.1 Introduction

In Chapter 5.3 the substitution effects on Sr_3Sn_5 with thallium $Sr_3Sn_{5-x}Tl_x$ were presented. The two compounds of this chapter have been discovered by increasing x to the maximum value of 5. The simplest way to achieve a metallic character is for anionic sublattices to have weak non-classical bonds, which can be expanded to some polar intermetallics with extended networks comparable to graphite or polyacetylene. In those cases bonding levels are all occupied in the (multicenter) *π*-bands that are continuous from bonding to antibonding states. Clusters and networks of group 13 elements are often formed via weak multicenter electron-deficient bonds. The following comprises a short overview of the reported binary A/Ae_xTl_y compounds and the polyanions contained in the structures.

Homoatomic thallium contacts have been found in the form of $\{Tl_2\}$ dumbbells in Li_5Tl_2[36] and Sr_5Tl_3 (Cr_5B_3-type).[37] Additionally, $\{Tl_4\}^{8-}$ tetrahedra are present in Na_2Tl,[38] which have 12 skeletal electrons and is isosteric to $\{Pb_4\}^{4-}$ and P_4. Pentacapped trigonal prismatic $\{Tl_{11}\}^{7-}$ ions have been found in A_8Tl_{11} (A = K, Rb, Cs).[39, 40] Tetragonally-compressed 'octahedra' $\{Tl_6\}^{6-}$ in KTl[41], and centered $\{Tl_{13}\}^{11-}$ icosahedra in $Na_3K_8Tl_{13}$[42], or $\{Tl_7\}^{7-}$ in $K_{10}Tl_7$[43] (three extra electrons) show the rich structural chemistry of thallium. Some extended three dimensional network structures also exist. The most prominent is the stuffed diamond array found in NaTl[44] (*d*(Tl–Tl) = 3.24 Å) where the Tl sublattice can be described as a diamond-type $^3_\infty[Tl^-]$ lattice. Extended structures with Tl clusters, such as linked icosahedra, pentagonal antiprisms, and hexagonal antiprisms[45, 46] have also been reported. Five- and nine-atom Tl clusters (distorted trigonal bipyramidal $\{Tl_5\}^{7-}$ and distorted tricapped trigonal prisms $\{Tl_9\}^{9-}$) are reported in the compound $Na_2K_{21}Tl_{19}$.[47] However, up to now the binary Tl compounds with Ae metals are fairly limited in terms of structural diversity and stoichiometry to compounds with isolated Tl atoms: AeTl (Ae = Mg, Ca, Sr),[48] Mg_2Tl, Mg_5Tl_2,[49] Ca_3Tl,[50] $CaTl_3$[51] and three bonded networks of thallium that are reminiscent of the diamond structure are found in $AeTl_2$[52] (for Ae = Ba with intra- and interlayer distances of 3.13 and 3.38 Å, respectively; for Ae = Sr with intra- and interlayer separations of 3.03 and 3.32 Å, respectively).

$BaTl_3$[53] consists of thallium layers formed from two center bond formation between parallel chains of face-sharing octahedral clusters.

The compounds Ae_3Tl_5 (Ae = Ca, Sr) reported in this chapter crystallize in the Pu_3Pd_5 structure type and feature square pyramidal {Tl_5} clusters. Similar triel clusters have been reported for RE_3In_5 (RE = La, Y)[54] and RE_3Ga_5 (RE = Sc, Y, Tb-Tm, Lu).[55] The latter Ga compounds crystallize in the Tm_3Ga_5 structure type and show reorientation of the five atom units. It is worth noting that Sr_3In_5[56, 57] crystallizes in the completely different Ca_3Ga_5[57] structure type with a network of four- and two-bonded In atoms.

6.3.2 Synthesis and Characterization

Synthesis The compounds Ae_3Tl_5 (Ae = Ca (**1**), Sr (**2**)) were prepared by direct fusion of the pure elements. The loading of the niobium crucibles took place in an Ar-filled glovebox. After sealing the ampoules under lowered Ar pressure by arc welding the temperature treatment involved heating to 940 °C at a rate of 2 K·min^{-1}, holding at that temperature for 6 h followed by cooling to 630 °C with the same rate. After annealing at 600 °C for seven days a crystalline product with metallic luster could be obtained in both cases. The Ba analogue could not be synthesized. **1** was prepared from a total loading mass of 1.269 g, with m(Ca) = 0.134 g and m(Tl) = 1.135 g. **2** could be obtained from a total loading of 1.835 g, with m(Sr) = 0.376 g and m(Tl) = 1.460 g.

EDX Analysis on several single-crystals of Sr_3Tl_5 confirmed the presence of the two elements with an average ratio Sr : Tl = 37(4) : 63(5) at% (calculated values: Ae : Tl = 37.5 : 62.5 at%). For Ca_3Tl_5 the experimental values are Ca : Tl = 34(3) : 66(6) at%.

Powder X-ray Diffraction The diffraction data for Ca_3Tl_5 (**1**) (Figure 6.14) at room temperature shows the formation of the phase as a byproduct. The strong reflections of the main phase $CaTl_3$ are marked with a red star. Strong signals that are cut off originate from diamond powder, which was used as internal standard. The measurements lasted for 14 h. The diffraction pattern for Sr_3Tl_5 (**2**) (Figure 6.15) at room temperature compares well with the theoretical pattern calculated from the single-crystal solution. However, $SrTl_2$ is present as the main phase.

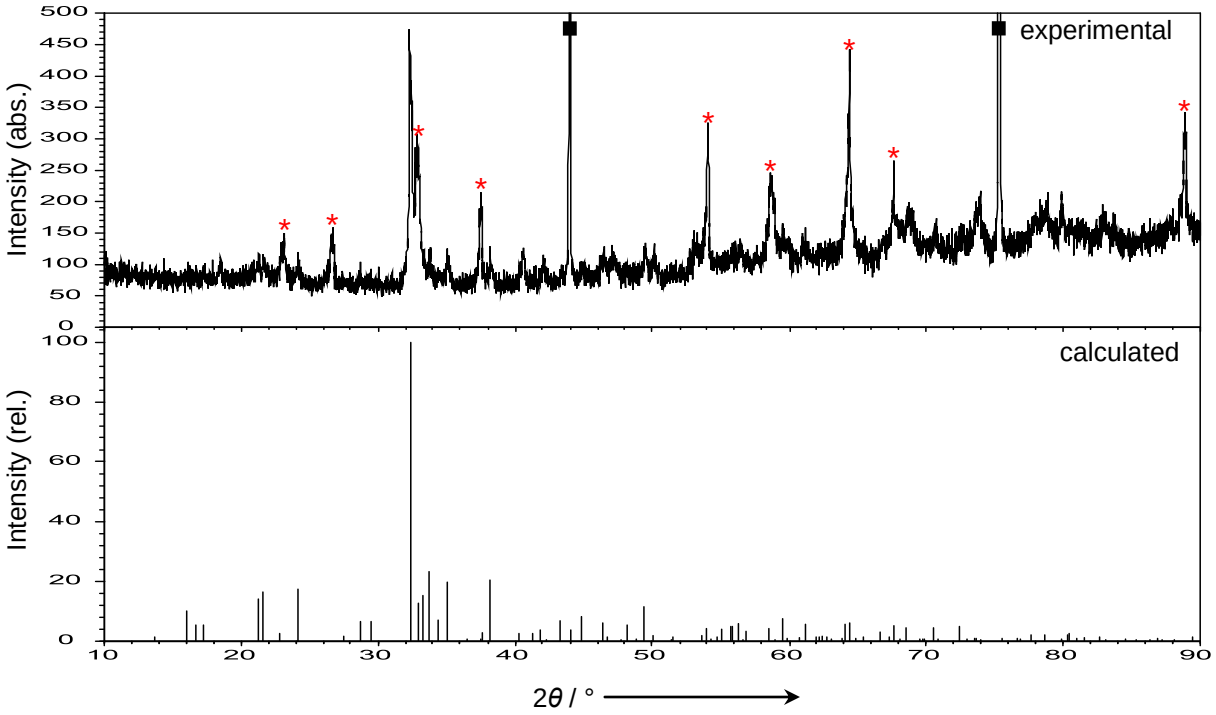

***Figure 6.14*. Experimental powder diagram (top) from sample loading Ca : Tl = 3 : 5 and calculated powder diagram (bottom) of Ca_3Tl_5. Reflections from diamond powder (internal standard) are marked with a square. Reflections from $CaTl_3$ are labeled with a red star.**

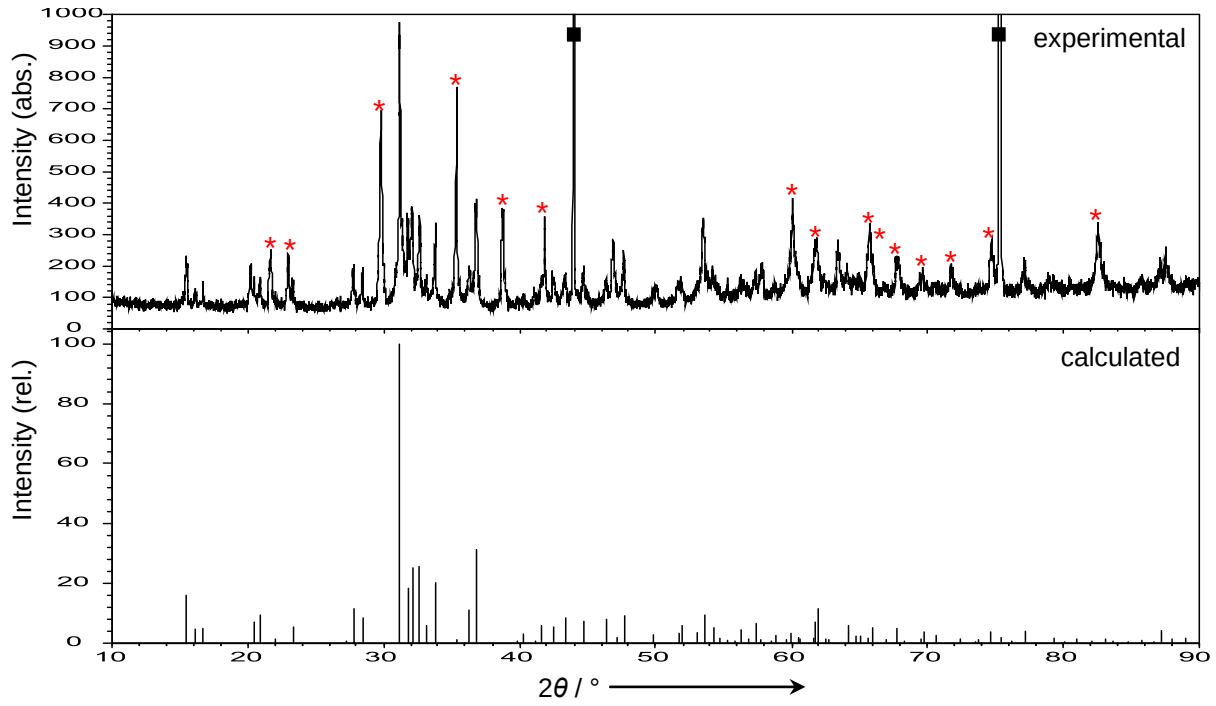

***Figure 6.15*. Experimental powder diagram (top) from sample loading Sr : Tl = 3 : 5 and calculated powder diagram (bottom) of Sr_3Tl_5. Reflections from $SrTl_2$, the main phase, are labeled with a red star. Reflections from diamond powder (internal standard) are marked with a square.**

Thermal Analysis of Sr_3Tl_5 Differential Thermal Analysis (DTA) was used to investigate the thermal behavior of the product of a sample loaded as Sr : Tl = 3 : 5 reacted at 940 °C. 150 mg of the sample were loaded into Nb crucibles that were then sealed by arc welding. The sample was heated under continuous Ar flow (50 ml/min) from room temperature to 1000 °C at a rate of 10 $K \cdot min^{-1}$ and cooled down to room temperature at the same rate. The DTA curves for the two cycles are shown in Figure 6.16. On heating (red curve) two peaks are revealed. The first endothermic signal at ~ 540 °C (onset) can be assigned to $SrTl_2$ which was also clearly present in the powder experiment. The signals in the range of 660.5 to 664.9 °C (onsets) can be assigned to the melting point of Sr_3Tl_5 since annealing at that temperature (see above) resulted in higher crystalline samples with higher yields.

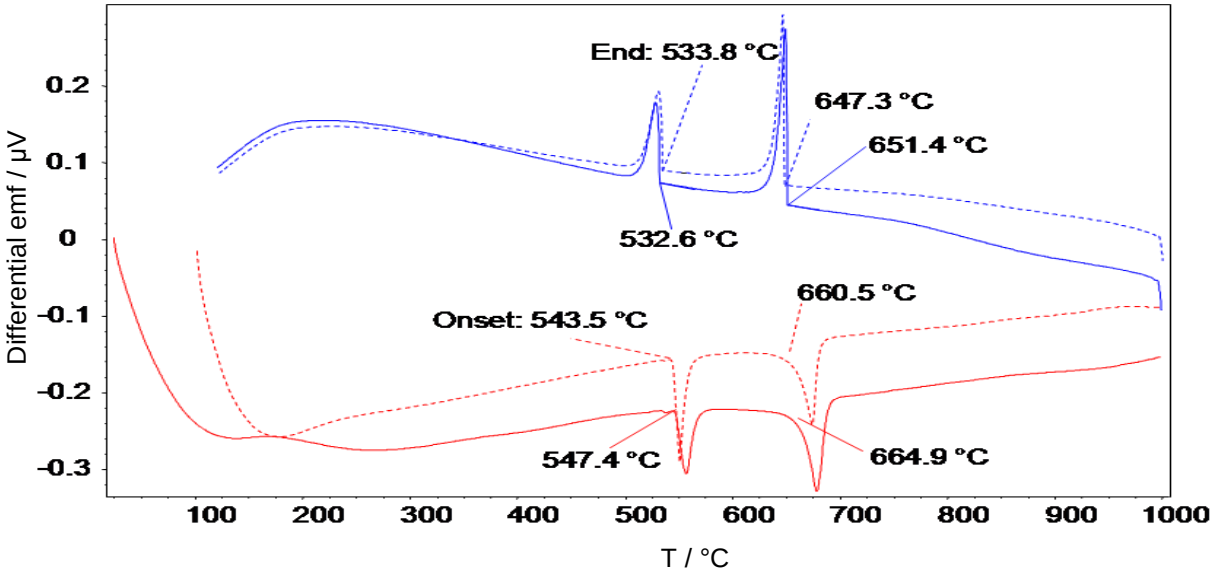

Figure 6.16. **DTA curves of the product of a reaction with Sr : Tl = 3 : 5 at 940 °C. Dashed lines represent the 2nd cycle. Heating (red), cooling (blue).**

6.3.3 Crystal Structure Determination and Description of Ae_3Tl_5 (Ae = Ca, Sr)

Structure Determination Single-crystals of Ae_3Tl_5 (Ae = Ca, Sr) were selected, checked for singularity in the glovebox and fixed on a glass capillary, which afterwards was inserted into a capillary (0.3 mm diameter) and closed by fusing the open end. Sr_3Tl_5 was measured on an Oxford Xcalibur3 diffractometer equipped with a CCD detector. The data collection (388 frames) involved four sets of ω scans (–41° - +63° for different φ positions: 0, 90, 180, 270°) and one φ scan (0° - +360° with θ = +30°) with a scan width of 2°/frame and an exposure time of 20s/frame.

The detector distance was 50 mm. A single-crystal of Ca_3Tl_5 was measured on a STOE IPDS II diffractometer equipped with an image plate detector. The data collection (180 frames) consisted of two ω scans (0° - +180° for φ = 0°, +90°) with a scan width of 2°/frame and an exposure time of 3 min/frame. The detector distance was 100 mm. After application of a numerical absorption correction for **1** and an empirical absorption correction for **2**, both structures were solved by direct methods in the orthorhombic space group *Cmcm* (No. 63) by use of the SHELXTL package from Bruker. The five independent atomic positions were refined anisotropically for each compound. Table 6.8 contains relevant crystallographic and refinement data. Atomic positions and displacement parameters are listed in Tables 6.9 and 6.10. Important interatomic distances of the two thallides are comprised in Tables 8.17 (see Appendix).

***Table 6.8*: Selected crystallographic and refinement data for Ca_3Tl_5 and Sr_3Tl_5.**

Empirical formula	**Ca_3Tl_5 (1)**	**Sr_3Tl_5 (2)**
Formula weight / g·mol^{-1}	1142.09	1284.71
Temperature / K	293(2) K	
Crystal size / mm^3	0.02 × 0.02 × 0.04	0.06 × 0.05 × 0.04
Crystal color; shape	Silvery metallic; Block	
Diffractometer	STOE IPDS II (Image Plate)	Oxford Xcalibur3 (CCD)
Crystal system	Orthorhombic	
Space group	*Cmcm* (No. 63)	
Unit cell parameters / Å	a = 10.231(2); b = 8.362(2)	a = 10.592(5); b = 8.667(5)
	c = 10.623(2)	c = 10.973(6)
Unit cell volume / Å^3; Z	908.8(3); 4	1007.3(9); 4
ρ_{calc} / g·cm^{-3}	4.17	4.24
μ / mm^{-1} (Mo K_α)	44.98	47.67
Absorption correction	numerical	empirical
F(000)	930	1038
Θ range / °	4.88 - 29.26	3.04 - 25.47
Index range	–13 ≤ h ≤ 14; –11 ≤ k ≤ 11	–11 ≤ h ≤ 12; –10 ≤ k ≤ 10
	–14 ≤ l ≤ 14	–13 ≤ l ≤ 13
Data completeness / %	94.9	100
Integrated reflections	7999 (R_σ = 0.069)	5920 (R_σ = 0.058)
Independent reflections	653 (R_{int} = 0.208)	527 (R_{int} = 0.104)
Refinement method	Full-matrix least-squares on F^2 (SHELXTL)	
Parameters	27	27
Goodness of fit on F^2	1.296	1.115
Observed reflections [I > 2σ(I)]	597	366
R_1 / wR_2 [I > 2σ(I)]	0.057 / 0.141	0.037 / 0.117
R_1 / wR_2 (all data)	0.063 / 0.156	0.057 / 0.121
Weighting scheme[a]	a = 0.069;	a = 0.064;
	b = 30.1091	b = 0
Extinction coefficient	0.0014(2)	0.0001(1)
Residual map / e$^-$·Å^{-3}	+4.15 [0.86 Å from Tl2]	+3.25 [1.23 Å from Tl1]
	–3.85 [0.78 Å from Tl3]	–2.24 [0.64 Å from Tl3]

[a] $w = 1 / [\sigma^2(F_o^2) + (aP)^2 + bP]$, where $P = (F_o^2 + 2F_c^2) / 3$

***Table 6.9*: Atomic coordinates and equivalent isotropic displacement parameters for Ae_3Tl_5 (Ae = Ca, Sr).**

Atom	Wyck.	*x*	*y*	*z*	U_{eq} / Å^2
			Ca_3Tl_5 (1)		
Tl1	8*f*	0	0.2037(1)	0.5373(1)	0.035(1)
Tl2	8*g*	0.2140(1)	0.2354(2)	¾	0.036(1)
Tl3	4*c*	0	0.5221(2)	¾	0.038(1)
Ca1	4*c*	0	0.0876(9)	¼	0.034(1)
Ca2	8*e*	0.2861(5)	0	½	0.034(1)
			Sr_3Tl_5 (2)		
Tl1	8*f*	½	0.1958(2)	0.4510(1)	0.021(1)
Tl2	8*g*	0.2949(2)	0.2263(2)	¼	0.023(1)
Tl3	4*c*	½	0.5015(3)	¼	0.026(1)
Sr1	4*c*	½	0.1150(6)	¾	0.020(1)
Sr2	8*e*	0.2083(3)	0	½	0.018(1)

***Table 6.10*: Anisotropic thermal displacement parameters (U / Å^2) for Ae_3Tl_5 (Ae = Ca, Sr).**

Atom	U_{11}	U_{22}	U_{33}	U_{23}	U_{13}	U_{12}
			Ca_3Tl_5 (1)			
Tl1	0.034(1)	0.034(1)	0.038(1)	0	0	0
Tl2	0.035(1)	0.038(1)	0.035(1)	0	0	0
Tl3	0.037(1)	0.035(1)	0.043(1)	0	0	0
Ca1	0.036(3)	0.036(4)	0.036(4)	0	0	0
Ca2	0.036(2)	0.036(2)	0.033(2)	0	0	0
			Sr_3Tl_5 (2)			
Tl1	0.022(1)	0.022(1)	0.020(1)	0	0	0
Tl2	0.027(1)	0.028(1)	0.014(1)	0	0	0
Tl3	0.032(1)	0.023(1)	0.022(1)	0	0	0
Sr1	0.022(3)	0.020(3)	0.017(3)	0	0	0
Sr2	0.017(2)	0.017(2)	0.019(2)	0	0	0

Structure Description Both compounds, **1** and **2**, crystallize in the prominent Pu_3Pd_5 structure type. The projection of the unit cell of **1** (Figure 6.17), with cluster representation of the thallium atoms, shows the clusters aligned in parallel zigzag chains. Well defined C_{2v} square pyramids with intracluster Tl–Tl distances of 3.157(1), 3.246(2), 3.492(2) for **1**, and 3.107(2), 3.227(3), 3.447(3) Å for **2** are recognizable (Figure 6.18). The units are best described as distorted pyramids or as *arachno*-type clusters derived from a pentagonal bipyramid with two adjacent atoms of the basal plane missing. Comparing the intracluster bonds, in both cases, the Tl–Tl distances are shortest within the pyramidal base (3.157(1) in **1**, 3.107(2) Å in **2**) where the atoms are formally three bonded. These values are considerably bigger than twice the Pauling's single bond metallic radii for Tl, which is 2.92 Å for three valences.[58] However, they lie in the range of single bonds between clusters in many thallium network structures.[46]

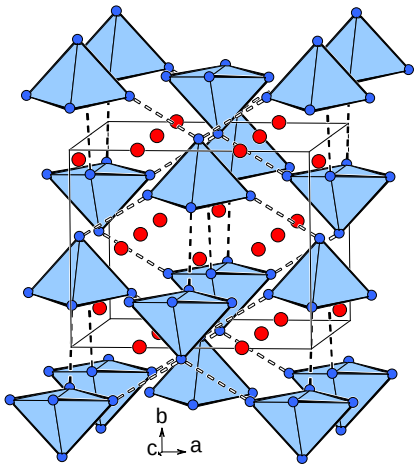

***Figure 6.17*. Projection of the unit cell of Ae_3Tl_5 (Ae = Ca, Sr). Longer intercluster contacts are drawn with dashed lines. White dashed lines indicate additional intercluster bonds in Ca_3Tl_5 (not present in Sr_3Tl_5). Ae (red), Tl (blue).**

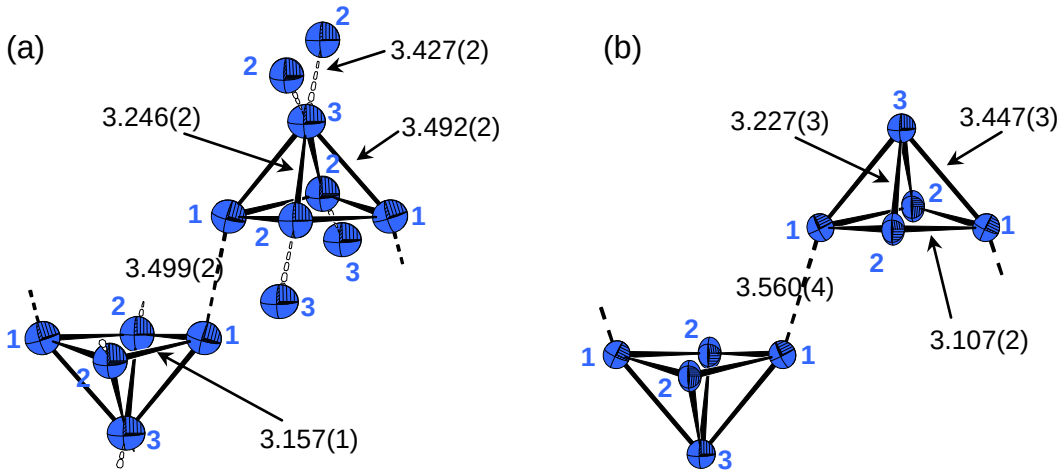

***Figure 6.18*. Connectivity of the Tl atoms in (a) Ca_3Tl_5 (1) and (b) Sr_3Tl_5 (2) (atoms are drawn with 90% probability). Intercluster bonds are drawn with dashed lines. Tl (blue)**

In each case the apical Tl atom (Tl3) has significant longer distances to the basal Tl atoms and as the bases are distorted the clusters cannot be categorized as square pyramids anymore. The values range from 3.246(2) to 3.492(2) Å in **1** and 3.227(3) to 3.447(3) Å in **2**, respectively. The pyramidal base (Tl1–Tl2–Tl1–Tl2) is slightly distorted for **1** and **2** with dihedral angles of 13.36° and 13.68°, respectively. The differences of intercluster bonds in **1** and **2** can be explained in terms of simple matrix effects, meaning that separations are largely dictated by relative cation sizes.

As an isolated *nido*-$\{Tl_5\}^{9-}$ cluster fulfills Wade's rules and would not need any intercluster interactions the latter must play a crucial role as a structural stabilizing factor. The clusters are interconnected along [001] by longer bonds (light segmented lines) (3.499(2) ×2 and 3.560(4) Å ×2 for **1** and for **2**, respectively) to form an extended network structure. In **2** the interconnection is established via Tl1 atoms and is one dimensional along [001]. In addition to this, in **1** further intercluster bonds (via Tl2–Tl3 (via the apex atom)) run along [100], and the intercluster distances (3.427(2) ×4, 3.499(2) ×2 Å) are in the same range as the longest intracluster bond (3.492(2) Å). This means in Ca_3Tl_5 the clusters are polymerized through all Tl atoms and form a three dimensional cluster network rather than isolated cluster zigzag chains as in **2**. The clusters are coordinated with 14 Ae atoms which can be interpreted as a hexacapped quadrangular prism (Figure 6.20).

The coordination spheres around the two types of Ae atoms are shown in Figure 6.19. In both compounds Ae1 is surrounded by six $\{Tl_5\}$ clusters via nine Ae–Tl contacts, with bond lengths of $d(Ae1–Tl)_{Ø}$ = 3.31 and 3.46 Å for **1** and **2**, respectively. Ae2 has contacts to Tl atoms of four pyramids via ten Ae–Tl contacts, with $d(Ae2–Tl)_{Ø}$ = 3.41 and 3.54 Å for **1** and **2**, respectively.

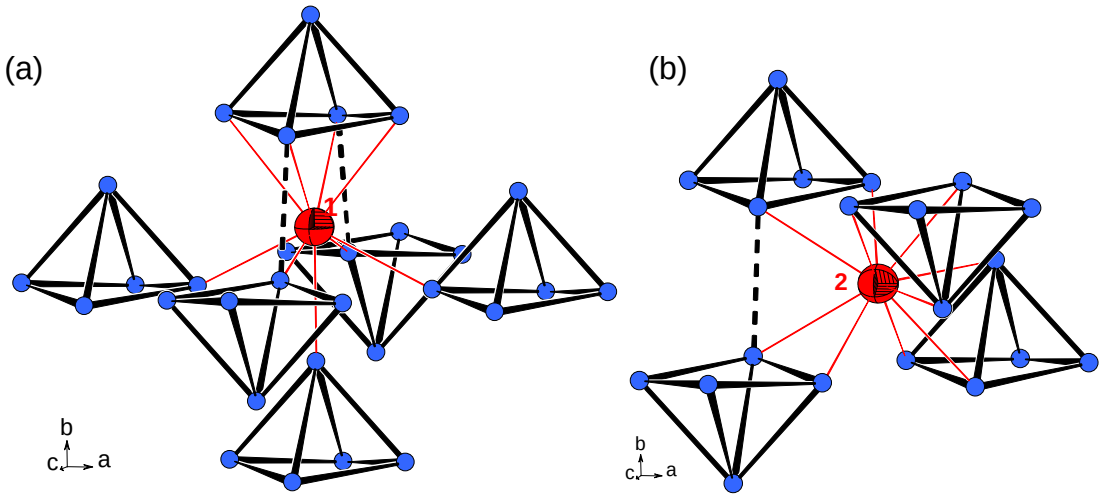

***Figure 6.19*. Coordination spheres in Ae_3Tl_5 (Ae = Ca, Sr) around (a) Ae1 and (b) Ae2. Ae atoms are drawn at 90% probability level. From the longer intercluster contacts only the Tl1–Tl1 bonds are shown with dashed lines. Tl (blue), Ae (red).**

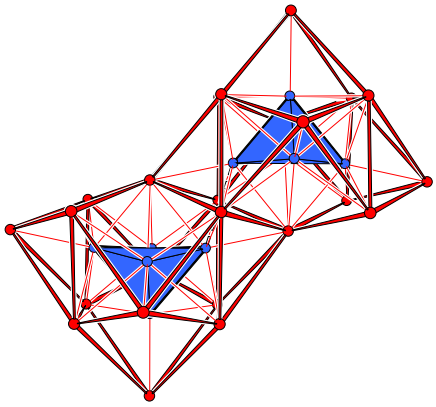

***Figure 6.20*. Each cluster in Ae_3Tl_5 (Ae = Ca, Sr) is coordinated with 14 cations. The cage can be regarded as a hexacapped quadrangular prism. Tl (blue), Ae (red).**

6.3.4 Electronic Structure

Interactions between the pyramidal anions may play a crucial role in the electronic properties of both compounds. Therefore DFT calculations were performed with the LMTO method. The *k* space integration was performed by the tetrahedron method on a set of 16 × 16 × 8 irreducible *k* points and a basis set with Tl-6*s*/(6*p*)/(5*d*)/(5*f*), Ca-4*s*/(4*p*)/3*d*/(4*f*), Sr-5*s*/(5*p*)/4*d*/(4*f*) (down-folded orbitals in parentheses). The band structure together with the total density of states (DOS) and projected DOS contributions from the different elements are plotted in Figure 6.21. Obviously Ca_3Tl_5 and Sr_3Tl_5 are metallic conductors. Various bands cross the respective Fermi level and the transport property is three dimensional. Between the two compounds there are slight differences: It can be observed that the bands of Ca_3Tl_5 have a higher dispersion than for Sr_3Tl_5 which is clearly visible in the energy range from –10 to –4 eV. This can be explained by the denser cation matrix of the Ca compound with the related shorter intercluster distances and the resulting increased interactions between the Tl and the Ae bands. The Tl-*s* states are well separated from the conduction band in an area of –4 to –10 eV below E_F. Around the Fermi level strong contributions from Tl-*p* orbitals and also from the cation (Ca, Sr) are present. The latter mainly consist of Ae-*d* states that considerably mix with the Tl-*p* bands.

To check the interactions between atoms, a variety of crystal orbital Hamilton population functions (–COHP) were evaluated. The total Tl–Tl, Ae1–Tl, and Ae2–Tl –COHP curves for **1** and **2**, in Figures 6.22a and 6.23a, respectively, give more insights and details regarding the bonding in the whole structure.

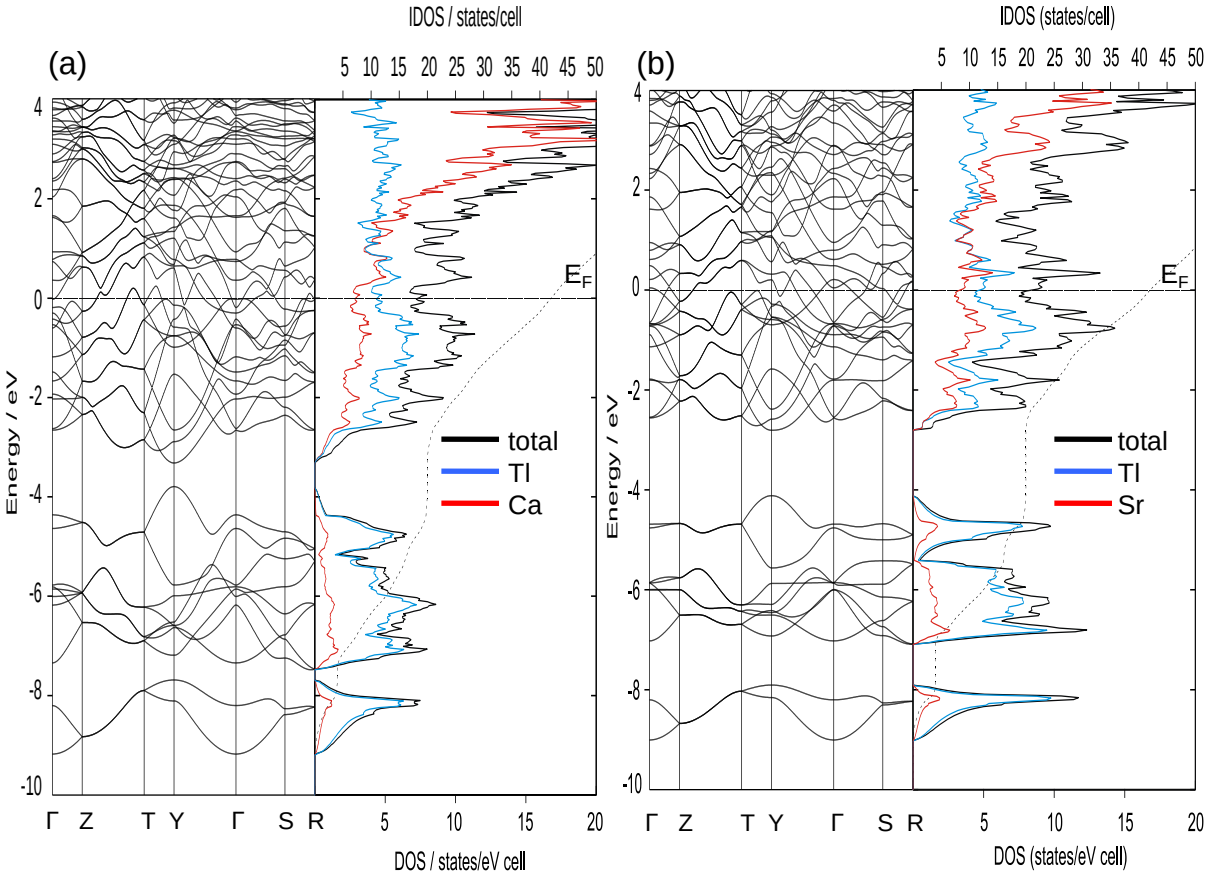

***Figure 6.21*. Band structure and DOS diagrams for (a) Ca_3Tl_5, (b) Sr_3Tl_5. Total DOS (black), Tl contributions (blue), Ae contributions (red). The Fermi level is taken as the point of zero energy.**

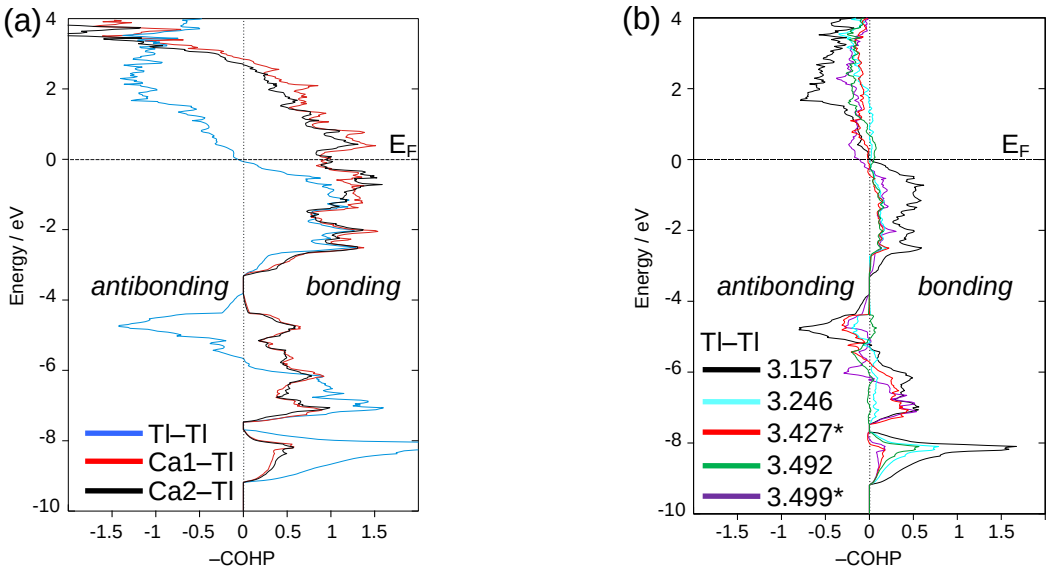

***Figure 6.22*. –COHP plots (a) for the sum of all Ca1–Tl (red); Ca2–Tl (black); Tl–Tl (blue) interactions, (b) for the different Tl–Tl bonds in Ca_3Tl_5. Tl–Tl 3.157 Å (black), 3.246 Å (teal), 3.427 Å (red), 3.492 (green), 3.499 Å (purple). *) intercluster bond.**

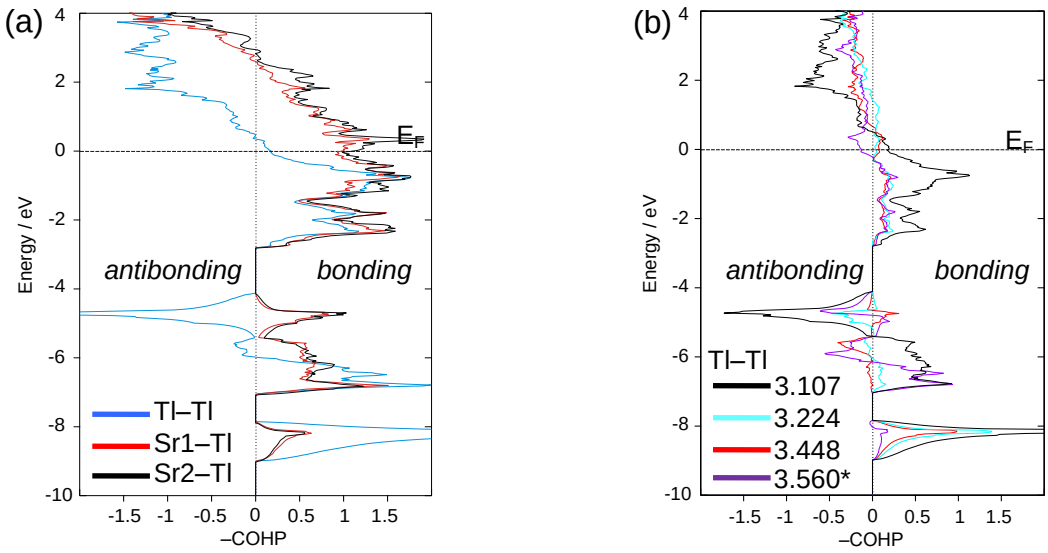

***Figure 6.23*. –COHP plots (a) for the sum of all Sr1–Tl (red), Sr2–Tl (black), Tl–Tl (blue) interactions, (b) for the different Tl–Tl bonds in Sr_3Tl_5. Shortest Tl–Tl 3.107 Å (black), Tl–Tl 3.224 Å (teal), Tl–Tl 3.448 Å (red), Tl–Tl 3.560 Å (purple). *) intercluster bond.**

The Tl–Tl bonds are roughly optimized at E_F with Tl1–Tl2 interactions being clearly the strongest. Additionally substantially more unfilled cation–anion bonding states above the Fermi level (up to +3 eV) are present. Interestingly, the sum over all Tl–Tl bonds is optimized below E_F for **1**, whereas for **2** empty bonding levels exist, and hence **1** is slightly electron rich, whereas **2** is electron poor and it is expected to possibly form electron richer isotypes. The existence of Sr_3Sn_5 points into that direction. Figures 6.22b and 6.23b show that the antibonding contributions of the Tl–Tl interactions at E_F are associated with the long intercluster Tl1–Tl1 bonds, whereas bonding in the other Tl–Tl bonds is almost fully optimized.

***Table 6.11*: –ICOHP values for selected interatomic contacts in Ae_3Tl_5 (Ae = Ca, Sr). Energies are given in eV/bond.**

interaction		*d* / Å	–ICOHP (at E_F)	–ICOHP (max.)
		Ca_3Tl_5 (1)		
Tl1	Tl2	3.157(1)	1.08	1.08
Tl2	Tl3	3.246(2)	0.71	0.74
Tl2	Tl3	3.427(2)*	0.56	0.56
Tl1	Tl3	3.492(2)	0.46	0.50
Tl1	Tl1	3.499(2)*	0.60	0.61
Ca1	Tl	3.203(3) - 3.477(6)	0.57	0.82
Ca2	Tl	3.330(4) - 3.457(1)	0.51	0.68
		Sr_3Tl_5 (2)		
Tl1	Tl2	3.107(2)	1.18	1.21
Tl2	Tl3	3.227(3)	0.77	0.84
Tl1	Tl3	3.447(3)	0.50	0.55
Tl1	Tl1	3.560(4)*	0.52	0.54
Sr1	Tl	3.324(6) - 3.670(5)	0.48	0.65
Sr2	Tl	3.480(3) - 3.627(2)	0.54	0.77

*) intercluster

To quantify these interactions the integrated –ICOHP values were determined are listed for different interactions in Table 6.11 The values are on average 0.5 to 0.6 eV/bond for the different Ca–Tl and Sr–Tl contacts, which are of same magnitude as the longer Tl–Tl bonds > 3.4 Å. Overall, the anionic sublattice in Ca_3Tl_5 gains more bonding energy due to the additional intercluster bonds that are present because of the smaller cation and the resulting increased lattice covalency.

6.3.5 Discussion

According to the Zintl-Klemm concept, assuming complete charge transfer from the cations, the compounds have to be formulated as $(Ae^{2+})_3(Tl_5^{6-})$. Wade's rules leave 11 electrons for cluster bonding, which would be an *arachno*-cluster that is five electrons deficient. This result is somewhat puzzling since the only *isomorphous* binary triel compounds reported that crystallize with Pu_3Pd_5-type are La_3In_5 and *β*-Y_3In_5, which contain formally $\{In_5\}^{9-}$ clusters. Thus, according to Wade's rules they can be classified as *nido*-clusters with 14 skeletal electrons, therefore rendering them Zintl phases. However, they have been reported to be metallic. The corresponding Ae_3Tt_5[31, 59] phases, such as Sr_3Sn_5 contain clusters with a rather similar structure and have been discussed in terms of *arachno*-$\{Tt_5\}^{6-}$ cluster. In these compounds, calculations on 'naked' clusters revealed an energy gap, and the formation of semiconducting Zintl phases for two electrons less (e. g. in $\{In_5\}^{9-}$ or $\{Sn_5\}^{4-}$), resulting in a regular $\{Sn_5\}^{4-}$ pyramid. However, Sr_3Sn_5 is metallic with band crossings caused by tip-to-base bonds, which can contain up to six electrons. This means the two extra electrons fill antibonding states and thus the $\{Sn_5\}^{6-}$ clusters are distorted. Sr_3Sn_5 can be regarded as a Zintl phase with clusters regarded as *'structures found in the oceans, buried by the sea of conduction electrons'*.[60]

M_3Tr_5 phases with divalent active metals, such as Ba_3Al_5, or Sr_3In_5 have been reported to be electron deficient, meaning that the electrons provided are not enough to fill all bonding states and E_F lying below the minimum of the DOS. However, this is not the case in the present compounds **1** and **2**. The DOS clearly underline their metallic character without a noticeable gap, which would mean the absence of a stabilizing electron sink paired with strong interactions between the atomic orbitals.

Comparing the –ICOHP values of intra- and intercluster Tl bonds one can easily recognize that the intercluster interactions are of comparable magnitudes as the longer intracluster bonds. This suggests strong interactions between clusters, and also with the surrounding Ae ions, as noticeable from the bonding Ae–Tl states in the –COHP plots. Although atom size and electronic effects play important roles in structure selection in general, Ca_3Tl_5 and Sr_3Tl_5 indicate the remarkable flexibility of the Pu_3Pd_5 structure type. The lack of electrons for the formation of *arachno*-clusters, like in the present cases, or occupation of antibonding states, such as in the Ae_3Tt_5 phases, is accommodated simply by changing overall anion–anion bonding distances in the pyramidal clusters. For the 26 VE units $\{Tt_5\}^{6-}$ the intercluster bonds are longer compared to the intracluster interactions, whereas in the electron poorer 21 VE $\{Tr_5\}^{6-}$ clusters they are more relaxed. This means the clusters try to compensate the lack of electrons by starting polymerization. The electron deficiency mostly affects the Tl1 positions and causes interconnection of the cluster zigzag chains, as clearly shown for Ca_3Tl_5. The contacts between the clusters cause metallic conduction due to the band broadening and overlapping. Furthermore, the covalent bonds between the Tl atoms (with core-like 6*s* orbitals) alone seem to be too weak to control overall structure stability. Additional alternative energy terms, such as Ae–Tl covalencies, which are in the same range as the Tl–Tl interactions, help to stabilize the structure. A similar situation is present when comparing the systems $BaSn_3$[32] and $BaTl_3$[53]. In the first case isolated columns of Sn octahedra are present, in the second the corresponding building blocks are interconnected.

The apparent electron deficiency in the clusters however may be caused by oxidation of the clusters due to hydrogen impurities. Such cases have been reported for Ae-richer phases like a series of Ae_5Tt_3 phases that were proved to form $Ae_5Tt_3H_x$ ($x \leq 1$) with ‘stuffed’ Cr_5B_3 structures and hydrogen occupying interstitial tetrahedral cavities.[61-63] Experiments using AeF_2, with fluoride as a good stand-in for hydride aiming in this direction are still pending.

6.4 References

[1] J. Gallmeier, H. Schäfer, A. Weiss, *Z. Naturforsch.* **1969**, *24 B*, 665.
[2] T. F. Fässler, C. Kronseder, *Z. Anorg. Allg. Chem.* **1998**, *624*, 561.
[3] I. F. Hewaidy, E. Busmann, W. Klemm, *Z. Anorg. Allg. Chem.* **1964**, *328*, 283.
[4] C. Hoch, M. Wendorff, C. Röhr, *Acta Crystallogr.* **2002**, *58 C*, i45.
[5] V. Queneau, S. C. Sevov, *Inorg. Chem.* **1998**, *37*, 1358.
[6] C. Hoch, M. Wendorff, C. Röhr, *Z. Anorg. Allg. Chem.* **2003**, *629*, 2391.
[7] J. D. Corbett, *Struct. Bonding* **1997**, *87*, 157.
[8] H. Schäfer, *Annu. Rev. Mater. Sci* **1985**, *15*, 1.
[9] K. Wade, *J. Chem. Soc. D* **1971**, 792.
[10] K. Wade, *Adv. Inorg. Chem. Radiochem.* **1976**, *18*, 1.
[11] S. Ponou, T. F. Fässler, *Z. Anorg. Allg. Chem.* **2007**, *633*, 393.
[12] V. Queneau, *Angew. Chem.* **1997**, *109*, 1818.
[13] A. Nienhaus, R. Hauptmann, T. F. Fässler, *Angew. Chem.* **2002**, *114*, 3352.
[14] L. Yong, S. D. Hoffmann, T. F. Fässler, *Z. Anorg. Allg. Chem.* **2004**, *630*, 1977.
[15] A. Spiekermann, S. D. Hoffmann, T. F. Fässler, *Angew. Chem.* **2006**, *118*, 3538.
[16] J. M. Goicoechea, S. C. Sevov, *Inorg. Chem.* **2005**, *44*, 2654.
[17] M. Somer, W. Carrillo-Cabrera, E. M. Peters, M. Kaupp, H. G. Von Schnering, *Z. Anorg. Allg. Chem.* **1999**, *625*, 37.
[18] P. A. Edwards, J. D. Corbett, *Inorg. Chem.* **1977**, *16*, 903.
[19] W. Carrillo-Cabrera, R. Cardoso Gil, M. Somer, Ö. Persil, H. G. Von Schnering, *Z. Anorg. Allg. Chem.* **2003**, *629*, 601.
[20] C. Hoch, M. Wendorff, C. Röhr, *J. Alloys Compd.* **2003**, *361*, 206.
[21] A. L. Spek, *PLATON, A Multipurpose Crystallographic Tool, Universität Utrecht* **2006**.
[22] J. D. Corbett, *Chem. Rev.* **1985**, *85*, 383.
[23] M. Somer, W. Carrillo-Cabrera, E. M. Peters, K. Peters, H. G. Von Schnering, *Z. Anorg. Allg. Chem.* **1998**, *624*, 1915.
[24] M. Baitinger, *Dissertation, Technische Universität Darmstadt* **2000**.
[25] T. F. Fässler, *Coord. Chem. Rev.* **2001**, *215*, 347.
[26] P. Alemany, M. Llunell, E. Canadell, *Inorg. Chem.* **2006**, *45*, 7235.
[27] A. Rodriguez-Fortea, E. Canadell, *Inorg. Chem.* **2003**, *42*, 2759.
[28] R. Lam, A. Mar, *Solid State Sci.* **2001**, *3*, 503.
[29] A. V. Mudring, J. D. Corbett, *J. Am. Chem. Soc.* **2004**, *126*, 5277.
[30] S. Bobev, E. D. Bauer, J. D. Thompson, J. L. Sarrao, G. J. Miller, B. Eck, R. Dronskowski, *J. Solid State Chem.* **2004**, *177*, 3545.
[31] F. Zürcher, R. Nesper, S. Hoffmann, T. F. Fässler, *Z. Anorg. Allg. Chem.* **2001**, *627*, 2211.
[32] C. Kronseder, T. F. Fässler, *Angew. Chem.* **1997**, *109*, 2800.
[33] T. F. Fässler, S. Hoffmann, C. Kronseder, *Z. Anorg. Allg. Chem.* **2001**, *627*, 2486.
[34] R. D. Hoffmann, R. Pöttgen, *Z. Kristallogr.* **2001**, *216*, 127.
[35] J. T. Vaughey, G. J. Miller, S. Gravelle, E. A. Leon-Escamilla, J. D. Corbett, *J. Solid State Chem.* **1997**, *133*, 501.
[36] J. Stöhr, H. Schäfer, *Z. Naturforsch.* **1979**, *34B*, 653.
[37] G. Bruzzone, E. Franceschi, F. Merlo, *J. Less -Comm. Met.* **1978**, *60*, 59.
[38] D. A. Hansen, J. F. Smith, *Acta Crystallogr.* **1967**, *22*, 836.
[39] G. Cordier, V. Müller, *Z. Kristallogr.* **1992**, *198*, 281.
[40] Z. C. Dong, J. D. Corbett, Unpublished research.
[41] Z. C. Dong, J. D. Corbett, *J. Am. Chem. Soc.* **1993**, *115*, 11299.
[42] Z. C. Dong, J. D. Corbett, *J. Am. Chem. Soc.* **1995**, *117*, 6447.
[43] S. Kaskel, J. D. Corbett, *Inorg. Chem.* **2000**, *39*, 778.
[44] E. Zintl, W. Dullenkopf, *Z. Phys. Chem.* **1932**, *B 16*, 195.
[45] J. D. Corbett, *Inorg. Chem.* **2000**, *39*, 5178.
[46] G. Cordier, V. Müller, *Z. Naturforsch.* **1993**, *48B*, 1035.

[47] Z. C. Dong, J. D. Corbett, *J. Am. Chem. Soc.* **1994**, *116*, 3429.
[48] E. Zintl, G. Brauer, *Z. Phys. Chem.* **1933**, *B 29*, 245.
[49] K. Frank, K. Schubert, *J. Less -Comm. Met.* **1970**, *20*, 215.
[50] G. Bruzzone, *Ann. Chim. (Rome, Italy)* **1966**, *56*, 1306.
[51] E. Zintl , S. Neumayr, *J. Phys. Chem. Solids* **1970**, *31*, 2653.
[52] A. Iandelli, *Z. Anorg. Allg. Chem.* **1964**, *330*, 221.
[53] D. K. Seo, J. D. Corbett, *J. Am. Chem. Soc.* **2002**, *124*, 415.
[54] J. T. Zhao, J. D. Corbett, *Inorg. Chem.* **1995**, *34*, 378.
[55] S. P. Yatsenko, K. A. Tschuntonow, P. Yarmolyuk, Y. Grin, *J. Less -Comm. Met.* **1983**, *91*, 21.
[56] D. K. Seo, J. D. Corbett, *J. Am. Chem. Soc.* **2001**, *123*, 4512.
[57] G. Cordier, H. Schäfer, M. Stelter, *Z. Anorg. Allg. Chem.* **1986**, *539*, 33.
[58] W. B. Pearson, *The Crystal Chemistry and Physics of Metals and Alloys; Wiley-Interscience, New York* **1972**.
[59] M. T. Klem, J. T. Vaughey, J. G. Harp, J. D. Corbett, *Inorg. Chem.* **2001**, *40*, 7020.
[60] R. Nesper, *Prog. Solid State Chem* **1990**, *20*, 1.
[61] E. A. Leon-Escamilla, J. D. Corbett, *Inorg. Chem.* **2001**, *40*, 1226.
[62] E. A. Leon-Escamilla, J. D. Corbett, *J. Alloys Compd.* **2003**, *356-357*, 59.
[63] T. Björling, D. Noreus, U. Häussermann, *J. Am. Chem. Soc.* **2006**, *128*, 817.

7 Summary

In the course of this work the conducted substitution reactions together with the Zintl-Klemm concept proved to be a prolific strategy for the tailoring of new compounds and the research of induced electronic fluctuations in Zintl ions or the anionic structures of borderline intermetallics. Various strategies were probed:

- Partial substitution of the *p*-block element: Zn for Sn, Bi for Sn, and Tr (Tr = In, Tl) for Sn substitutions.
- Partial substitution of the alkaline-earth metal: Ba for Sr substitution.
- Partial substitution of alkali for the alkaline-earth metal: Na for Sr substitution.

Zn for Sn Substitution in binary Na Stannides The effects of Zn substitution on the Sn-rich intermetallic phase $NaSn_5$ led to the discovery of the new compounds Na_2ZnSn_5, $NaZn_{0.3}Sn_{2.7(1)}$, and $Na_5Zn_{2.28(2)}Sn_{9.72(2)}$ (Chapters 4.2 and 4.3). In all three compounds the average VEC/M (M denotes the atoms forming the anionic substructure) is close to four, which is reflected in their structures that consist of all 4b-atoms arranged in novel networks, which are reminiscent of $NaSn_5$, $NaSn_2$, or diamond. Next to the interesting coloring effect that leads to a different layer packing in Na_2ZnSn_5 (Figure 7.1), the main information provided by these compounds is that Zn, has a closed *d*-shell and can therefore be regarded as a pseudo *p* block metal. LMTO band structure calculations reveal the *d* contributions comprised in a narrow band at approx. –8 eV below the Fermi level and Zn-*p* orbital contributions in the valence band that mix with Sn-*p* states. Additionally, COHP analyses show that Zn–Sn bonding energies are in the range of that for covalent Sn–Sn contacts.

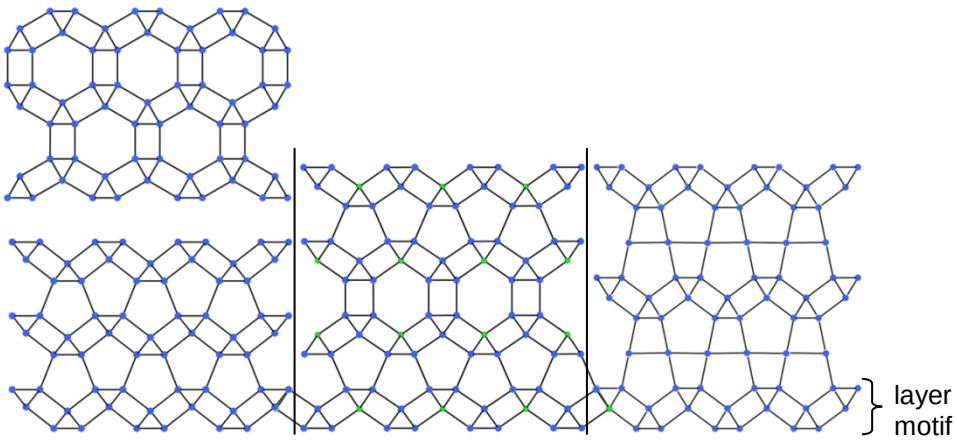

***Figure 7.1*. Different stacking sequences of the layer motif, consisting of 4b-atoms, lead to the phases $NaZn_{0.3}Sn_{2.7(1)}$ (left), Na_2ZnSn_5 (center), and $NaSn_5$ (right). For details see Chapter 4.2.**

When increasing the amount of Zn the VEC/M decreases and at an average value of 3.66 the icosahedral theme starts to form. In $Na_{29}Zn_{24}Sn_{32}$ (Chapter 4.4) icosahedral $\{Zn_8Sn_4\}^{8-}$ units together with covalent motifs of Sn are present. The amount of Sn in this phase is yet high enough to form a covalent $\{Sn_{14}\}$ polyhedron that is novel in Sn chemistry and has no homoatomic precedent (Figure 7.2). The D_{3h} symmetrical body can be derived from a trigonal bipyramid by truncating the three vertices of the basal plane. Disorder of Sn atoms at this enneahedron can be treated with a split model which results in a pseudorotation of the cluster. The consequent interconnection within the network allows the structure to tune its electron demand to 29. Extended-Hückel calculations on two models containing the two different $\{Sn_{14}\}$ isomers show the semiconducting property of the compound.

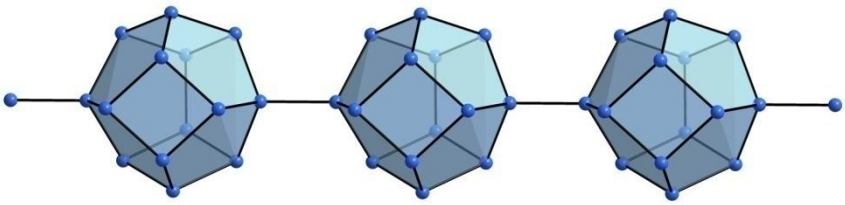

***Figure 7.2*. Linear cluster chain of $\{Sn_{14}\}$ enneahedra. For details see Chapter 4.4.**

In the next three Zn-richer phases $Na_{16}Zn_{13.54}Sn_{13.47(5)}$, $Na_{22}Zn_{20}Sn_{19(1)}$, and $Na_{34}Zn_{65}Sn_{40(1)}$ (Chapters 4.5 and 4.6) the average VEC/M is further lowered to 3.59, 3.54, and 3.08, respectively. These values are low enough to force the formation of structure motifs that can exclusively be found in the intermetallic triel chemistry and in fact, the balanced (in terms of Zn/Sn ratio) compound $Na_{16}Zn_{13.54}Sn_{13.47(5)}$ crystallizes in a new structure type which is composed of only three-member rings, and the two latter compounds are isostructural with $Na_{22}Ga_{39}$ and $K_4Na_{13}Ga_{49.57}$, respectively. The structures are realized without the participation of a triel element emphasizing the dominant electronic factor. $Na_{22}Zn_{20}Sn_{19(1)}$ contains a 15-atom spacer which is remarkable in terms of the combination of multicenter and covalently bonded atoms in one polyhedron. The low VEC/M in $Na_{34}Zn_{65}Sn_{40(1)}$ is reflected in the heavy clustering of the structure: Individual icosahedra condensate forming triply fused icosahedra. As shown in Figure 7.3 the obtained cluster compounds share a common feature: Kagomé nets of icosahedra containing other structure motifs as ‘guests’.

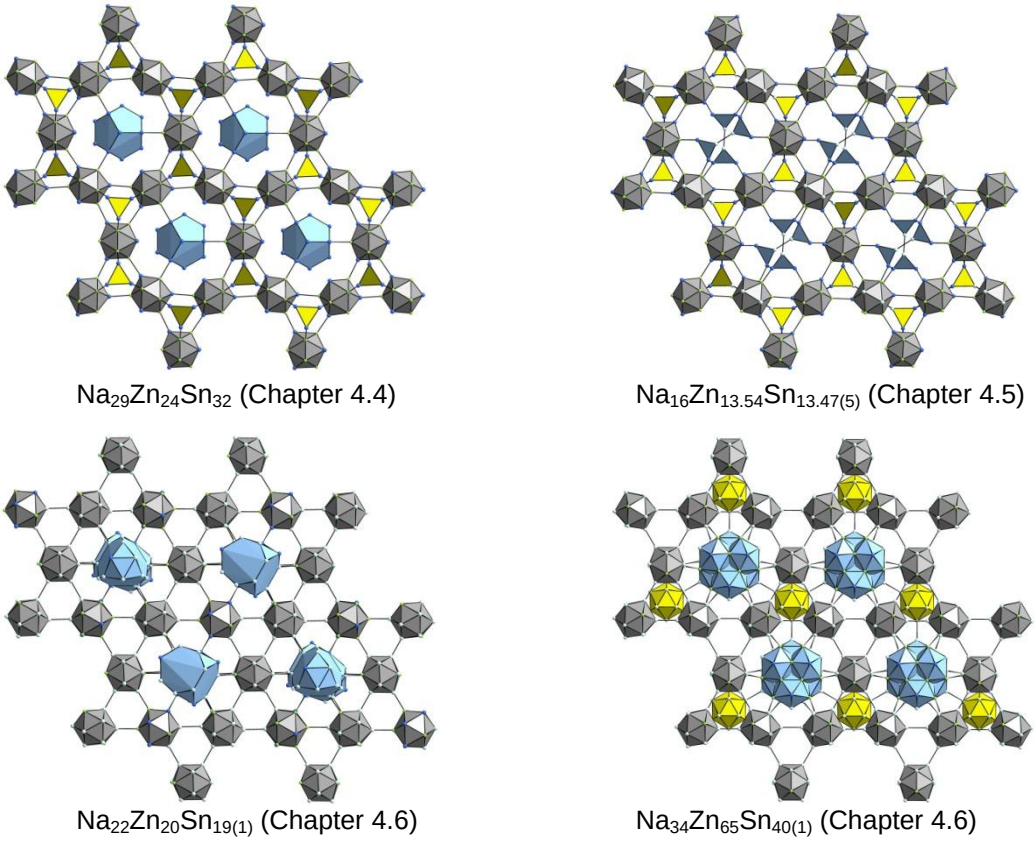

***Figure 7.3*. Cluster representation of selected compounds, reported in this work, featuring Kagomé layers of icosahedra (gray) made of Zn and Sn. In the hexagonal and trigonal channels other clusters are embedded (blue and yellow). For details see Chapters 4.4 to 4.6.**

Finally, experiments on the highly reduced Na-rich side of the phase system led to the discovery of Na_6ZnSn_2 ($Na_{4.23}K_{1.77(1)}ZnSn_2$) and $Na_{20}Zn_8Sn_{11}$ (Chapters 4.7 and 4.8). The VEC/M is increased to 5.33 and 4.21 again, respectively. In contrast to the Sn richer compounds here the electrons are provided mainly by the electropositive Na atoms. Therefore highly charged and isolated anions are formed. The linear anion $\{ZnSn_2\}^{6-}$ is present in those phases and contains 16 valence electrons. Band structure calculations reveal high bonding energies between Zn and Sn that are significantly higher than normal covalent interactions that were found in the Sn rich network structures with 4b-atoms. The 16 VE of this unit suggest different resonance formulae from which one is an allene like cumulated double bond system.

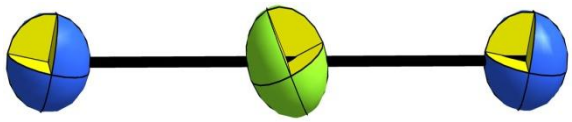

***Figure 7.4.* Anisotropic representation of the linear 16 valence electron anion $\{ZnSn_2\}^{6-}$ found in Na_6ZnSn_2, $Na_{4.23}K_{1.77(1)}ZnSn_2$, and $Na_{20}Zn_8Sn_{11}$. Sn (blue) and Zn (green). For details see Chapter 4.7.**

The bonding situation was evaluated by Hartree-Fock calculations with the Gaussian wavefunction. The resulting NBO and AIM charge assignements and plots of the ELF do not lead to a uniform bonding picture. Whereas the former two methods indicate formulations that involve ~ Zn^{+}, which points towards a two bonded Zn^{0}, the all electron ELF shows a ring shaped attractor for each Zn–Sn bond with high variances that indicate delocalization. The molecular orbital diagram corresponds well with the one of CO_2, but with very low contributions from the Zn-*p* orbitals to the *π*-molecular orbital (HOMO). $Na_{4.23}K_{1.77(1)}ZnSn_2$, was obtained by trying to synthesize the K analogue 'K_6ZnSn_2', which was not possible up to now. In this phase the 16 VE unit is slightly bent, which is likely caused by the many directional and non directional interactions in the neat solid.

Additional icosahedra are present in $Na_{20}Zn_8Sn_{11}$. This relatively high reduced compound contains layers of similar linear $\{ZnSn_2\}^{6-}$ units and isolated layers of eight-fold *exo*-bonded icosahedra rather than the 3D interconnected icosahedra in the less reduced ternaries. Therefore it can be understood as an interesting intergrowth between electron precise Zintl and electron deficient deltahedral layers.

Ba for Sr Substitution in Sr_2Bi_3 The puzzling bonding situation in the helical Bi substructure of Sr_2Bi_3 was clarified by the evaluation of five crystal structures (Chapter 5.1). They were obtained by successive Ba for Sr substitution, which led to the solid solution series $Sr_{2-x}Ba_xBi_3$ ($0 < x < 1.3$). In Sr_2Bi_3 three kinds of Bi–Bi bonds, from which two are in the range of covalent Bi–Bi bonds (intraspiral) and one is significantly longer (interspiral), are present. Besides showing the expected increase in lattice constants, the Bi substructure reacts to the presence of the bigger congener Ba by elongation of the long interspiral contact, whereas the remaining two Bi–Bi bonds almost remain unchanged in length. Band structure calculations of Sr_2Bi_3 and the hypothetical phase 'Ba_2Bi_3' revealed the metallic nature of the compounds and the beginning of a gap opening at an energy that corresponds to one electron less per formula unit. This is consistent with an all two-bonded Bi substructure and, using the Zintl concept, to the ionic formula splitting $(Sr^{2+})_2[(2b\text{-}Bi^{1-})_3]$ plus one extra electron. The metallic nature of this compound is consistent with the measured superconductive transitions of different samples and the presence of flat and steep bands around the Fermi level. The critical temperatures at ~ 4.4 K show little dependency on the composition but changes in diamagnetic shielding.

Future work should include substitutions using the smaller Ca atom in order to investigate effects of possible distance shortening and the removal of the itinerant electron may be accessed by substitution with alkali metals or tetrel elements.

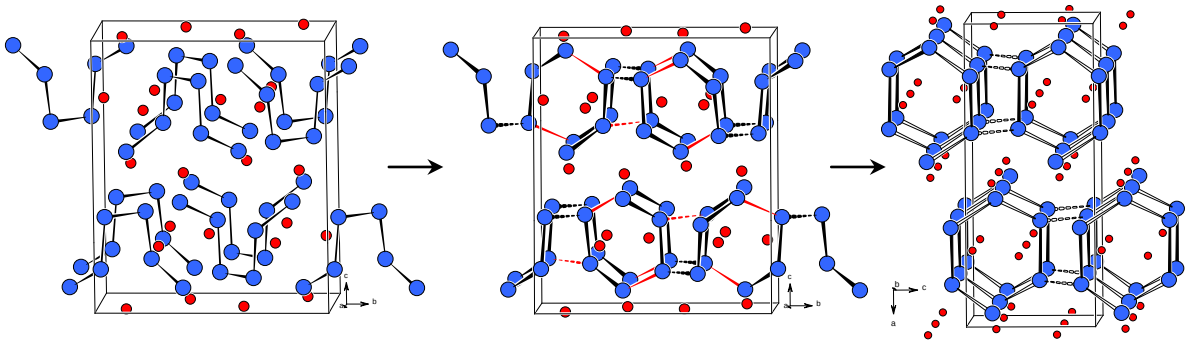

***Figure 7.5*. The Bi lattice of Sr_2Bi_3 (right) can be derived from the Sb sublattice of Sr_2Sb_3 (left) by bond breaking and formation (center). Sb/Bi (blue), Sr (red). For details see Chapter 5.1.**

Na for Sr Substitution in Sr_3Sn_5 While studying the size effect of the cation experiments with Sr_3Sn_5 and Na led to the discovery of Na_2SrSn_4 (Chapter 5.4). Due to the presence of two different kinds of cations the lattice packing evolves in a new covalent Sn substructure featuring condensed Sn hexagons, which are arranged to form isolated 1D tube-like units (Figure 7.6). However the unusual coordination of Sn2 atoms and long, but non negligible Sn–Sn (3.311 Å) interactions demanded the introduction of a 2*c*-1*e* bond, which can be understood in terms of a fractional (half) bond. Similar situations are found in K_6Pb_5 and K_2SnBi. However, band structure calculations show a finite DOS at the Fermi level and again, substantial cation–anion bonding interactions have to be considered that help to stabilize the structure of this polar intermetallic compound.

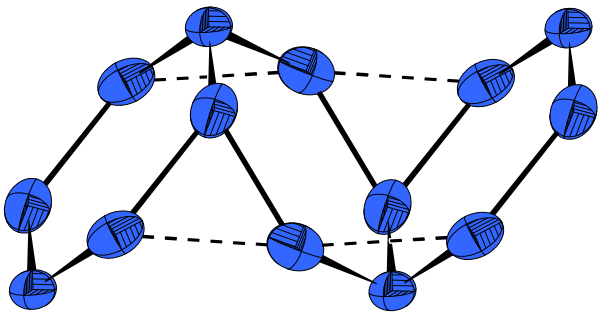

***Figure 7.6*. Anisotropic representation of the Sn substructure of Na_2SrSn_4. Sn (blue). For details see Chapter 5.4.**

Bi for Sn and Tl for Sn Substitution in Sr_3Sn_5 Substitutions in the anionic substructure of Sr_3Sn_5 were carried out with electron richer Bi and electron poorer Tl or In (Chapters 5.2 and 5.3). With Bi the phase $Sr_3Sn_{3.36}Bi_{1.64(3)}$ was obtained (Figure 7.7, right). It contains corrugated layers of weakly interconnected bodyless butterfly shaped {M_4} units that are separated by layers of $^{3}_{\infty}$[$Sr_{6/2}Bi$] octahedral frameworks. Band structure calculations for the hypothetical phase 'Sr_3Sn_4Bi' reveal that the phase is electron deficient. Further substitution leads to the charge balanced end member '$Sr_3(Sn_3Bi)Bi$'. The latter would contain the unit $\{Sn_3Bi\}^{3-}$, which is isoelectronic to $\{Sn_4\}^{4-}$ and should thus form discrete tetrahedral units or an arsenic like layer. Attempts to attain this situation by increasing the Bi content were unsuccessful so far. Fat band analysis showed that the electron deficiency is also associated with the [$Sr_{6/2}Bi$] substructure. The formation of the charge balanced Zintl phase is also thwarted by substantial Sr–Bi interactions, meaning electron removal from the network and 'trapping' the anions as bodyless butterfly units. Substitution reactions in Sr_3Sn_5 (Pu_3Pd_5-type) with electron poorer Tl and In on the one hand led to the phases $Sr_3Sn_{5-x}Tl_x$ (Figure 7.7, left) which contain square pyramidal $\{Sn_{4-x}Tl_{1+x}\}^{6-}$ (x = 0.78, 1,14) clusters (Tm_3Ga_5-type) and on the other hand to the new binaries Ae_3Tl_5 (Ae = Ca, Sr; Pu_3Pd_5-type; Chapter 6.3). Both structure types feature similar square pyramidal clusters that have weak intercluster interactions, the only difference is the orientation of the cluster chains to each other.

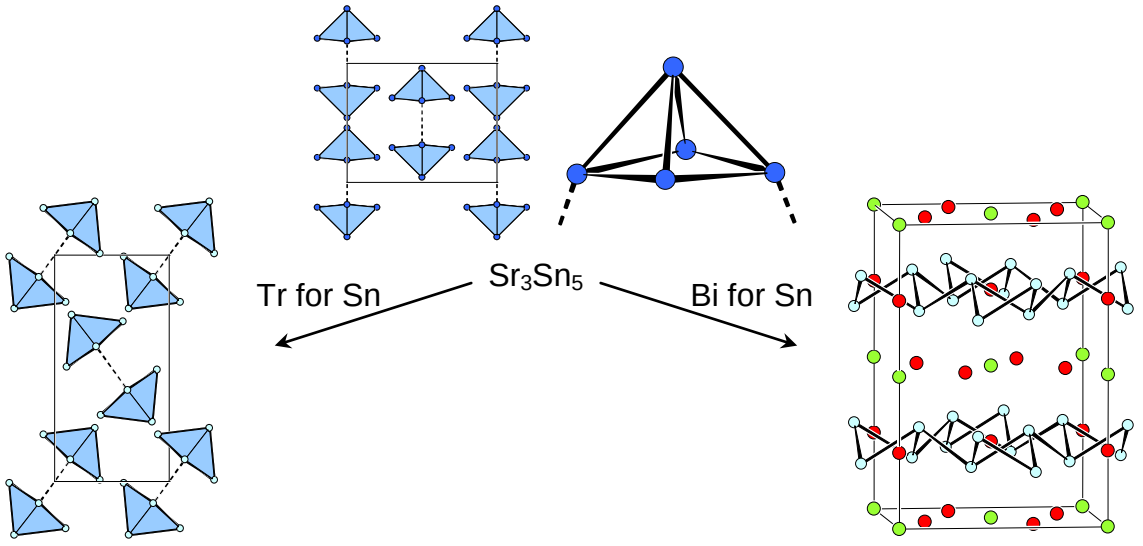

Figure 7.7. **Substitution effects on the Zintl ion $\{Sn_5\}^{6-}$ in Sr_3Sn_5 with Tr (left) and Bi (right). Sn (blue), M = Sn / Tl or Sn/Bi (teal), Bi (green), Sr (red). For details see Chapters 5.2 and 5.3.**

Compared to Sr_3Sn_5, in the phases Ae_3Tl_5 significantly more intercluster and cation-anion interactions help to stabilize the structure, although the clusters are formally five electron deficient, when regarded as *arachno*-type. This example shows the great electronic flexibility of this structure type. Interestingly, the substituted phases $Sr_3Sn_{5-x}Tr_x$ ($x \sim 2$) prefer to crystallize in the lower symmetry arrangement. Here, the average cation–anion distances are somewhat shorter than in Sr_3Sn_5 and Sr_3Tl_5 and likely other factors, such as Madelung energy and packing efficiency, are more important.

Binary Phases $K_{70}Sn_{103}$ (Chapter 6.1) was found as a deep brown crystalline phase upon substitution attempts on K_4Sn_9 with Tl. Thallium was chosen due to its known affinity towards the formation of isolated clusters. The phase crystallizes in a rather large orthorhombic unit cell and contains isolated $\{Sn_9\}^{4-}$, $\{Sn_4\}^{4-}$, and $\{Sn_5\}^{2-}$ cluster anions. Whereas the latter cluster was reported before to be isolated only in compounds from solutions, $K_{70}Sn_{103}$ is the first intermetallic solid state compound containing this *closo*-five-atom cluster (Figure 7.8, left). The cluster can be well rationalized according to Wade's rules qualifying $K_{70}Sn_{103}$ as a pure Zintl phase. By hierarchical cluster replacement the structure can be described in terms of the *Laves* phase $MgZn_2$. This discovery emphasizes the great compositional flexibility of the binary potassium stannide cluster compounds.

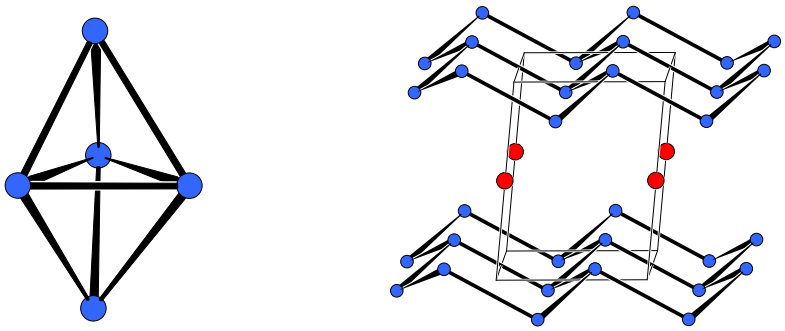

***Figure 7.8. Closo*-$\{Sn_5\}^{2-}$ cluster of $K_{70}Sn_{103}$ (left). Structure of $BaSn_2$ (right). Sn (blue), Ba (red). For details see Chapters 6.1 and 6.2, respectively.**

The simple binary compound $BaSn_2$ (Chapter 6.2) represents a valuable contribution to the binary Ba–Sn phase diagram. This phase was not reported yet and was obtained during the investigation of substitution experiments with Na for Ba in Ba_3Sn_5. However, in the course of this work $BaSn_2$ was only obtained in the presence of $BaSn_3$.

Thermal analysis indicates the corresponding melting points to be very close to each other, which hampers the synthesis of a pure phase. The compound contains 2D layers of 3b-Sn atoms (Figure 7.8, right), which are reminiscent of metallic arsenic. Although the phase satisfies the Zintl concept the calculated band structure predicts the phase to be a weak metallic conductor.

All results of the experiments performed in the different systems allow one to draw several final conclusions:

- The ternary compounds in the system Na–Zn–Sn obtained from partial Zn for Sn substitutions show narrow homogeneity ranges. This means that the structures are highly dependent on the adjusted VEC.
- A similar dependency can be observed for the partial Bi for Sn and partial Tr (Tr = In, Tl) for Sn substitutions, with slightly broader homogeneity ranges.
- The partial Ba for Sr substitutions shows a significant phase width. This is reflected in the formation of mixed crystals with Ba even exceeding the Sr content.
- The partial Na for Sr substitution does not lead to any mixed occupied positions and results in a completely new structure.
- The results of LMTO band structure calculations revealed the alkaline-earth metal intermetallic phases to be rather metallic compared to the alkali metal compounds.

Outlook The results of this thesis reflect the many factors (adding up to the relatively low heats of formation) that have to be considered when trying to explain intermetallic solid state structures. The dominating factor in Zintl phases is the number of valence electrons. Electronic factors are also the driving force for the formation of extended cluster networks. In polar intermetallics or borderline intermetallics, especially in the presence of more polarizing alkaline earth metals, other factors, such as the often underestimated cation–anion interactions, packing efficiency (size), and Madelung energy, which determine the chemical potentials, become more and more important. These can even overwhelm the electronic factor and lead to violations of the Zintl concept.

8 Appendix

This chapter includes tables with selected interatomic distances for all compounds reported in this thesis. Additionally it contains the atomic coordinates, equivalent, and anisotropic thermal displacement parameters for the compound $K_{70}Sn_{103}$.

***Table 8.1*: Interatomic distances (≤ 4 Å) in Na_2ZnSn_5 and $NaZn_{0.3}Sn_{2.7(1)}$ (standard deviation in parentheses).**

Atom pair		*d* / Å	Atom pair		*d* / Å	Atom pair		*d* / Å
				Na_2ZnSn_5 (1)				
Sn1	Zn	2.742(1)	Sn1	Na	3.886(9)	Na	Sn1	3.314(7)
	Sn2	2.813(7)	Sn2	Sn1	2.813(1)×4		Sn1	3.490(7)
	Sn1	2.908(1)		Na	3.525(7)×4		Sn1	3.520(7)
	Sn1	2.909(1)	Zn	Sn1	2.742(1)×4		Sn2	3.525(7)
	Na	3.10(1)		Na	3.18(1)×4		Zn	3.57(1)
	Na	3.19(1)		Na	3.57(1)×4		Sn1	3.687(8)
	Na	3.314(7)	Na	Na	0.90(2)[a]		Na	3.774(7)×2
	Na	3.490(7)		Sn1	3.10(1)		Sn1	3.793(7)
	Na	3.520(7)		Zn	3.18(1)		Sn1	3.886(9)
	Na	3.687(8)		Sn1	3.19(1)			
	Na	3.793(7)		Na	3.29(2)			
				$NaZn_{0.3}Sn_{2.7(1)}$ (2)				
M1	M2	2.809(1)×4	M2	Na_a	3.09(4)	Na_a	Na_a	3.34(7)
	M2	2.835(1)×3		Na_b	3.10(1)		M2	3.40(2)×2
	Na_b*	3.09(1)×2		Na_a	3.16(3)		M2	3.41(4)×2
	Na_a*	3.26(2)×2		Na_a	3.40(2)	Na_b	Na_b	1.38(6)*
M2	M1	2.809(1)×2	Na_a	Na_a	0.69(9)*		Na_b	2.98(5)
	M2	2.810(1)×2		M2	3.09(4)×2		M1	3.09(1)
	M2	2.834(1)×2		M2	3.19(3)×2		M2	3.10(1)×2
	M1	2.835(1)		M1	3.26(2)×2		M2	3.41(2)
							M2	3.42(1)×2
							M1	3.48(2)×2

*) split position

***Table 8.2*: Interatomic distances (≤ 4 Å) in $Na_5Zn_{2.28}Sn_{9.72(2)}$ (standard deviation in parentheses).**

Atom pair		*d* / Å	Atom pair		*d* / Å	Atom pair		*d* / Å
Sn1	Zn1	2.840(1)	Sn4	Zn1	2.723(1)	Na2	Zn1	3.128(5)
	Sn4	2.868(1)		M	2.838(1)		Sn1	3.138(5)
	M	2.907(1)		Sn2	2.865(1)		Sn3	3.269(5)
Sn2	Zn1	2.805(1)		Sn1	2.868(1)	Na2	M	3.300(6)
	Sn3	2.863(1)	Zn1	Sn3	2.717(1)		Sn4	3.320(6)
	Sn4	2.865(1)		Sn4	2.723(1)		Zn1	3.346(5)
	Sn2	2.986(1)		Sn2	2.805(1)		M	3.352(5)
M	Sn4	2.834(1)		Sn1	2.840(1)		Sn2	3.455(5)
	Sn3	2.841(1)	Na1	Zn1	3.116(5)		M	3.627(6)
	Sn1	2.907(1)		Sn1	3.126(5)	Na3	Zn1	3.206(3)×2
	M	2.969(1)		Sn2	3.251(5)		Sn1	3.400(3)×2
Sn3	Zn1	2.717(1)		Sn4	3.293(5)		Na2	3.428(7)×2
Sn3	M	2.841(1)		Sn2	3.317(5)		Na2	3.450(7)×2
	Sn1	2.877(1)		Sn3	3.355(5)		Sn1	3.489(1)×2
	Sn2	2.863(1)		Sn1	3.406(5)		Sn4	3.493(1)×2
				Sn2	3.521(5)			
				M	3.692(5)			

***Table 8.3*: Interatomic distances (≤ 4 Å) in $Na_{29}Zn_{24}Sn_{32}$ (standard deviation in parentheses).**

Atom pair		*d* / Å	Atom pair		*d* / Å	Atom pair		*d* / Å
Sn1	Zn3	2.829(1)×2	Sn6b	Sn6b	2.746(20)	Na2	Sn6a	3.103(3)
	Sn1	3.018(1)×2		Sn3	2.918(9)		Sn3	3.186(3)
	Na5	3.329(4)		Na5	3.080(11)		Zn3	3.195(3)
	Na2	3.363(3)×2		Sn5	3.209(6)×2		Sn2	3.242(3)
	Na1	3.384(4)×2		Na2	3.342(5)×2		Zn1	3.320(3)
	Na2	3.430(3)×2		Na6	3.641(9)		Zn2	3.338(3)
	Na4	3.449(4)	Zn1	Zn3	2.723(1)×2		Sn6b	3.342(6)
Sn2	Zn2	2.724(1)		Sn2	2.818(1)×2		Sn1	3.363(3)
	Zn2	2.729(1)		Zn1	2.891(2)		Zn3	3.386(3)
	Zn1	2.818(1)×2		Sn5	2.914(1)		Na1	3.423(3)
	Zn3	2.833(1)×2		Na4	3.300(1)		Sn1	3.430(3)
	Na2	3.242(3)×2		Na2	3.320(3)×2		Na5	3.563(3)
	Na1	3.297(3)×2		Na3	3.390(4)×2	Na3	Sn5	3.227(3)×2
	Na3	3.313(5)	Zn2	Sn2	2.724(1)		Sn2	3.313(5)
Sn3	Zn2	2.788(1)×2		Sn2	2.729(1)		Sn3	3.346(4)×2
	Zn3	2.856(1)×2		Sn3	2.788(1)×2		Na3	3.373(9)
	Sn6b	2.918(9)		Zn3	2.832(1)×2		Zn1	3.390(4)×2
	Sn3	3.038(1)		Na1	3.271(3)×2		Zn2	3.487(5)
	Na2	3.186(3)×2		Na2	3.338(3)×2		Na2	3.610(4)×2
	Na5	3.250(1)		Na3	3.487(5)		Na3	3.821(9)
	Na3	3.346(4)×2	Zn3	Zn3	2.622(2)	Na4	Zn1	3.300(1)×2
Sn4	Sn4	2.884(2)		Zn1	2.723(1)		Zn3	3.343(4)×4
	Sn5	2.993(1)×3		Sn1	2.829(1)		Sn1	3.449(4)×2
	Na6	3.289(1)		Zn2	2.832(1)		Sn6a	3.574(6)×2
Sn5	Sn6a	2.889(1)×2		Sn2	2.833(1)		Na2	3.596(3)×2
	Zn1	2.914(1)		Sn3	2.856(1)	Na5	Sn6b	3.08(1)×2
	Sn4	2.993(1)		Na2	3.195(3)		Sn3	3.250(1)×2
	Sn6b	3.209(6)×2		Na1	3.268(1)		Sn1	3.329(4)×2
	Na3	3.227(3)×2		Na4	3.343(4)		Zn3	3.343(4)×4
Sn5	Na6	3.502(1)	Zn3	Na5	3.343(4)		Sn6a	3.390(6)×2
	Na4	3.678(6)		Na2	3.386(3)	Na6	Sn4	3.289(1)×2
	Na2	3.720(3)×2	Na1	Zn3	3.268(1)×3		Sn6a	3.359(1)×6
Sn6a	Sn6a	2.825(2)		Zn2	3.271(3)×3		Sn5	3.502(1)×4
	Sn5	2.889(1)×2		Sn2	3.297(3)×3			
	Na2	3.103(3)×2		Sn1	3.384(4)×3			
	Na6	3.359(1)						
	Na5	3.390(6)						
	Na4	3.574(6)						

***Table 8.4*: Interatomic distances (≤ 4 Å) in $Na_{16}Zn_{13.54}Sn_{13.47(5)}$ (standard deviation in parentheses).**

Atom pair		*d* / Å	Atom pair		*d* / Å	Atom pair		*d* / Å
Sn1	Zn3	2.730(1)	M8	Zn6	2.768(1)	Zn5	Zn1	2.644(1)
	Zn7	2.745(1)		Zn7	2.777(1)		Zn4	2.699(1)
	Zn4	2.783(1)×2		M9	2.780(1)		Zn2	2.769(1)
	Zn1	2.785(1)×2		M8	2.795(1)×2		Sn2	2.813(1)
	Na3	3.226(3)×2		Sn4	2.882(1)		Sn6	2.832(1)
	Na2	3.229(3)×2		Zn6	2.906(1)		Sn3	2.929(1)
	Na1	3.241(4)		Na5	3.205(3)		Na6	3.158(3)
Sn2	Zn3	2.774(2)		Na5	3.235(3)		Na6	3.229(3)
	Zn4	2.780(1)×2		Na2	3.287(3)		Na2	3.247(3)
	Zn2	2.807(1)		Na3	3.298(3)		Na4	3.407(4)
	Zn5	2.813(1)×2	M9	M8	2.780(1)×3		Na10	3.472(4)
	Na2	3.257(3)×2		Sn6	2.978(1)×2	Zn6	Zn7	2.658(1)
	Na4	3.292(4)×2		Na2	3.318(3)×2		M8	2.768(1)×2

Sn2	Na9	3.417(5)	M9	Na3	3.333(3)×2	Zn6	Zn6	2.787(2)
Sn3	Zn2	2.845(1)		Na5	3.386(3)×2		Sn4	2.842(1)
	Zn3	2.856(1)	M10	M10	2.602(2)×2		Sn7	2.853(1)
	Zn1	2.859(1)		M10	2.809(2)×2		M8	2.906(1)
	Zn5	2.929(1)		Sn5	2.889(1)		Na3	3.217(3)
	Sn3	3.016(1)		Sn7	2.892(1)		Na1	3.248(4)
	Na10	3.248(4)		Na1	3.127(4)		Na5	3.270(1)
	Na6	3.266(3)		Na8	3.274(5)		Na10	3.428(4)
	Na4	3.298(3)		Na7	3.326(4)	Zn7	Zn6	2.658(1)×2
	Na8	3.441(5)		Na9	3.351(5)		Sn1	2.745(1)
	Na7	3.454(4)		Na7	3.429(4)		M8	2.777(1)×4
	Na9	3.547(5)	Zn1	Zn5	2.644(1)		Sn4	2.930(2)
Sn4	Zn2	2.729(1)		Zn4	2.695(1)		Na1	3.209(5)
	Zn6	2.842(1)×2		Sn6	2.774(1)		Na3	3.243(3)×2
	M8	2.882(1)×3		Sn1	2.785(1)		Na2	3.330(3)
	Zn7	2.930(2)		Zn3	2.813(1)	Na1	M10	3.127(4)×2
	Na10	3.308(4)×2		Sn3	2.859(1)		M10	3.128(4)×2
	Na8	3.347(6)		Na6	3.217(3)		Zn7	3.209(5)
	Na2	3.375(3)		Na6	3.246(3)		Zn4	3.214(4)×3
Sn5	Zn4	2.726(1)		Na3	3.278(3)		Zn6	3.248(4)×2
	M10	2.889(1)		Na2	3.360(3)	Na2	Sn5	3.391(3)×2
	Sn7	3.014(1)		Na4	3.381(4)		Sn1	3.229(3)
	Na6	3.149(3)	Zn2	Sn4	2.729(1)		Zn5	3.247(3)
	Na7	3.207(4)		Zn5	2.769(1)×2		Sn2	3.257(3)
	Na7	3.317(4)		Sn2	2.807(1)		Sn6	3.271(3)
	Na3	3.321(3)		Sn3	2.845(1)		M8	3.287(3)×2
	Na4	3.333(4)		Sn3	2.845(1)		Zn2	3.294(3)
	Na1	3.391(3)		Na2	3.294(3)×2		M9	3.319(3)×2
	Na9	3.395(3)		Na10	3.433(4)×2		Zn7	3.330(3)
Sn6	Zn1	2.774(1)		Na8	3.614(5)		Zn3	3.344(3)
	Zn5	2.832(1)	Zn3	Sn1	2.730(1)		Zn1	3.360(3)
	M9	2.978(1)		Sn2	2.774(2)	Na3	Zn4	3.183(3)
	Sn6	3.069(1)		Zn1	2.813(1)×2		Zn6	3.217(3)
	Na2	3.271(3)		Sn3	2.856(1)×2		Sn1	3.226(3)
	Na3	3.276(3)		Na4	3.279(4)×2		Zn7	3.243(3)
	Na6	3.336(3)		Na2	3.344(3)×2		Sn7	3.246(3)
	Na6	3.351(3)		Na9	3.483(5)		Sn6	3.276(3)
	Na2	3.373(3)	Zn4	Zn1	2.695(1)		Zn1	3.278(3)
	Na4	3.418(4)		Zn5	2.699(1)		M8	3.298(3)×2
	Na4	3.491(4)		Sn5	2.726(1)		Sn5	3.320(3)
Sn7	Zn6	2.853(1)		Sn2	2.780(1)		M9	3.333(3)
	M10	2.892(1)		Sn1	2.783(1)	Na8	M10	3.274(5)×3
	Sn5	3.014(1)		Zn4	2.845(2)		Sn4	3.347(6)
	Sn7	3.077(1)		Na6	3.141(3)		Sn3	3.441(5)×2
	Na5	3.232(5)		Na3	3.183(3)		Zn6	3.443(5)×2
	Na3	3.246(3)		Na1	3.214(4)		Zn2	3.614(5)
	Na7	3.357(4)		Na4	3.408(4)		Na10	3.656(5)×2
	Na10	3.505(4)		Na9	3.502(5)	Na9	M10	3.351(5)×4
	Na1	3.561(2)	Na6	Zn4	3.141(3)		Sn5	3.395(3)×2
	Na8	3.686(3)		Sn5	3.149(3)		Sn2	3.417(5)
Na4	Zn3	3.279(4)		Zn5	3.158(3)		Zn3	3.483(5)
	Sn2	3.292(4)		Zn1	3.217(3)		Zn4	3.502(5)×2
	Sn3	3.298(3)		Zn5	3.229(3)		Sn3	3.547(5)×2
	Sn5	3.333(4)		Zn1	3.246(3)	Na10	Sn3	3.248(4)
	Zn1	3.381(4)		Sn3	3.266(3)		Sn4	3.308(4)
	Zn5	3.407(4)		Sn6	3.336(3)		M8	3.387(4)
	Zn4	3.408(4)		Sn6	3.351(3)		Zn6	3.428(4)
	Sn6	3.417(4)		Na6	3.496(6)		Zn2	3.433(4)
	Sn6	3.491(4)		Na4	3.546(5)		Zn5	3.472(4)
	Na2	3.509(5)		Na3	3.564(5)		M9	3.487(4)

Na4	Na6	3.546(5)	Na7	Sn5	3.207(4)	Na10	Sn7	3.505(4)
	Na4	3.567(7)		Sn5	3.317(4)		Sn6	3.508(4)
Na5	M8	3.205(3)×3		M10	3.326(4)×2		Na5	3.523(4)
	Sn7	3.232(5)×2		Sn7	3.358(4)			
	M8	3.234(3)×4		M10	3.429(4)×2			
	Zn6	3.270(1)		Sn3	3.454(4)			
	Zn6	3.270(1)		Na7	3.582(8)			
				Na4	3.843(5)			
				Na10	3.844(5)			
				Na8	3.866(5)			

***Table 8.5*: Interatomic distances (≤ 4 Å) in $Na_{22}Zn_{20}Sn_{19(1)}$ (standard deviation in parentheses).**

Atom pair		*d* / Å	Atom pair		*d* / Å	Atom pair		*d* / Å
M1	Zn17	2.660(1)	M9	M6	2.670(1)×2	Sn17	Zn17	2.866(1)
	M4	2.760(1)		M5	2.757(1)		Zn18	2.875(1)
	M8	2.845(1)		M6	2.795(1)×2		M2	2.899(1)
	Zn16	2.848(1)		Sn16	2.878(1)		Zn15	2.951(1)
	M3	2.903(1)		Na1	3.240(3)		Sn18	2.976(1)
	M7	2.938(1)		Na5	3.341(3)		Na15	3.286(4)
	Na3	3.222(2)		Na11	3.346(3)		Na13	3.374(3)
	Na9	3.243(2)		Na15	3.365(3)		Na12	3.407(3)
M2	M3	2.701(1)		Na8	3.428(3)		Na4	3.419(3)
	Zn14	2.751(1)	M10	Sn11	2.749(1)		Na11	3.467(3)
	Zn18	2.770(1)		M5	2.793(1)×3		Na5	3.535(3)
	Zn15	2.779(1)		Na14	3.048(4)	Sn18	Zn17	2.905(1)×2
	M2	2.785(1)×2		Na10	3.163(5)		Zn15	2.947(1)
	Sn17	2.899(1)		Na13	3.365(3)×2		Sn17	2.976(1)×2
	Na1	3.221(3)		Na15	3.447(3)×2		Na8	3.239(5)
	Na2	3.285(3)	M11	M10	2.749(1)		Na9	3.296(4)
	Na3	3.319(4)		M12	2.777(1)×4		Na5	3.438(3)×2
	Na4	3.394(3)		Na6	3.093(4)		Na11	3.613(3)×2
M3	M2	2.701(1)		Na10	3.351(5)	Zn14	Sn16	2.720(1)
	Zn16	2.724(1)		Na12	3.383(3)×2		Sn15	2.744(1)
	M7	2.744(1)×2		Na15	3.388(3)×2		M2	2.751(1)
	M4	2.851(1)×2	M12	M11	2.777(1)×2		M2	2.752(1)×2
	M8	2.886(1)		Zn16	2.805(1)		Zn18	2.809(1)×2
	M1	2.903(1)		Sn14	3.045(1)		Na2	3.210(4)
	Na3	3.249(2)		M12	3.156(1)×2		Na1	3.291(3)×2
M4	M5	2.719(1)×2		Na13	3.299(3)		Na11	3.557(3)
	M1	2.760(1)		Na14	3.306(4)	Zn15	M2	2.779(1)×4
M4	M7	2.831(1)	M12	Na4	3.320(3)	Zn15	Sn15	2.811(1)
	M8	2.832(1)×2		Na15	3.441(3)		Sn18	2.947(1)
	M3	2.851(1)×3		Na10	3.449(4)		Sn17	2.951(1)×2
M5	M4	2.719(1)×2		Na12	3.543(3)		Na3	3.286(4)
	M9	2.757(1)	M13	M7	2.808(1)		Na4	3.372(3)×2
	M10	2.793(1)		Sn6	2.835(1)		Na11	3.462(3)
	Sn16	3.093(1)		M13	2.953(1)×2	Zn16	M3	2.724(1)
	M5	3.157(1)×2		Sn14	3.176(1)		M8	2.789(1)×2
	Na5	3.301(3)		Na6	3.340(4)		M12	2.805(1)×2
	Na2	3.325(3)		Na9	3.387(4)		M1	2.848(1)
	Na15	3.333(3)		Na8	3.407(4)		M7	2.853(1)×2
M6	M9	2.670(1)×2		Na12	3.412(3)		M4	2.881(1)
	M9	2.795(1)×2		Na5	3.420(3)	Zn17	M1	2.660(1)×2
	M13	2.835(1)	Sn14	Zn18	2.823(1)		Zn18	2.789(1)
	Sn14	2.916(1)		M6	2.916(1)		Zn17	2.798(2)
	Na1	3.151(3)		M12	3.045(1)		Sn15	2.848(1)
	Na15	3.323(3)		M13	3.176(1)		Sn17	2.866(1)
	Na5	3.326(3)		Na10	3.343(2)		Sn18	2.905(1)

M6	Na8	3.349(2)	Sn14	Na1	3.397(3)	Zn17	Na3	3.250(4)
	Na11	3.425(3)		Na4	3.400(3)		Na9	3.310(4)
M7	M3	2.744(1)×2		Na12	3.412(3)		Na4	3.386(3)
	M8	2.769(1)		Na13	3.417(3)		Na13	3.395(3)
	M13	2.808(1)	Sn15	Zn14	2.744(1)		Na5	3.507(3)
	M4	2.831(1)		Zn15	2.811(1)	Zn18	M2	2.770(1)
	Zn16	2.853(1)		Zn18	2.846(1)×2		Zn17	2.789(1)
	M1	2.938(1)		Zn17	2.848(1)×2		Zn14	2.809(1)
	Na6	3.176(2)		Na3	3.207(4)		Sn14	2.823(1)
M8	M8	2.674(1)×2		Na4	3.322(3)×2		Sn15	2.846(1)
	M7	2.769(1)		Na11	3.454(3)×2		Sn17	2.875(1)
	Zn16	2.789(1)	Sn16	Zn14	2.720(1)		Na1	3.222(3)
	M4	2.832(1)×2		M9	2.878(1)×3		Na4	3.316(3)
	M4	2.832(1)		M5	3.093(1)×3		Na13	3.453(3)
	M3	2.886(1)		Na11	3.307(3)×2		Na12	3.502(3)
	Na3	3.259(4)		Na8	3.327(5)		Na11	3.503(3)
Na1	M6	3.151(3)×2	Na8	Na16	3.152(9)	Na12	M7	3.325(3)×2
	M2	3.221(3)		Sn18	3.239(5)		M11	3.383(3)×2
	Zn18	3.222(3)		Sn16	3.327(5)		Sn17	3.407(3)
	M9	3.240(3)		M6	3.349(2)×4		M13	3.412(3)×2
	M7	3.276(3)×2		M13	3.407(4)×4		Sn14	3.412(3)
	M4	3.286(3)×2		M9	3.428(3)		M3	3.422(3)
	Zn14	3.291(3)	Na9	M1	3.243(2)×4		Zn16	3.441(3)
Na2	M4	3.195(2)×4		M7	3.295(2)×4		Zn18	3.502(3)
	Zn14	3.210(4)		Sn18	3.296(4)	Na13	M12	3.299(3)×2
	M2	3.285(3)×3		Zn17	3.310(4)×2		M1	3.347(3)×2
	M8	3.321(4)		M8	3.356(4)		M10	3.365(3)×2
	M8	3.322(4)	Na10	M10	3.163(5)×2		Sn17	3.374(3)
Na3	Sn15	3.207(4)		Sn14	3.343(2)×2		M5	3.382(3)×2
	M1	3.222(2)×4		M11	3.350(5)×2		Zn17	3.395(3)
	M3	3.249(2)×4		M12	3.449(4)×3		Zn16	3.403(3)
	Zn17	3.250(4)×2		M13	3.453(4)		Sn14	3.417(3)
	M8	3.259(4)	Na11	Sn16	3.307(3)	Na14	M10	3.048(4)×2
Na4	M3	3.261(3)×2		M9	3.346(3)		Zn16	3.204(4)×2
	Zn16	3.273(3)		M6	3.425(3)×2		M12	3.306(4)×4
	Zn18	3.316(3)		M6	3.425(3)		M8	3.312(4)×4
	M12	3.320(3)×2		Sn15	3.454(3)	Na15	Na16	3.185(6)
	Sn15	3.322(3)		Zn15	3.462(3)		Sn17	3.286(4)
	Zn15	3.372(3)		Sn17	3.467(3)		M6	3.323(3)
	M1	3.386(3)×2		Zn18	3.503(3)		M5	3.333(3)×2
	M2	3.394(3)		Sn14	3.521(3)		M9	3.365(3)
Na5	M5	3.302(3)×2		Na4	3.522(4)		M9	3.365(3)
	M6	3.326(3)		Zn14	3.557(3)		M11	3.388(3)×2
	M6	3.326(3)	Na6	M11	3.093(4)×2			
	M9	3.341(3)×2		M7	3.176(2)×3			
	M9	3.341(3)		M7	3.176(2)			
	M1	3.388(3)		M7	3.176(2)			
	M13	3.420(3)×2		M8	3.316(4)×3			
	M4	3.425(3)×2		M13	3.340(4)			

***Table 8.6*: Interatomic distances (≤ 4 Å) in $Na_{34}Zn_{65}Sn_{40(1)}$ (standard deviation in parentheses).**

Atom pair		*d* / Å	Atom pair		*d* / Å	Atom pair		*d* / Å
Sn1	Zn12	2.694(1)×2	M9	M8	2.652(1)×3	Zn15	Zn15	2.527(3)
	Zn14	2.700(3)		M2	2.685(2)		Zn12	2.682(3)
	M7	2.877(2)		Zn15	2.722(2)×2		M9	2.722(2)
	Zn15	3.000(2)×2		Zn12	2.786(3)		M7	2.901(2)
	Na1	3.175(6)×2		Zn13	2.824(2)×2		M8	2.986(2)

Sn1	Na6	3.58(1)	M9	Na5	3.34(1)	Zn15	Sn1	3.000(2)
	Na5	3.691(8)×2	M10	M8	2.670(2)×2		Zn15	3.062(3)
M2	Zn12	2.645(3)×3		M10	2.696(3)×2		Na1	3.165(6)
	M9	2.685(2)×5		M11	2.765(2)×2		Na1	3.170(6)
	Zn13	2.691(4)×3		M3	2.830(2)	Na1	Zn15	3.165(6)
M3	M6	2.696(2)		Zn14	2.851(2)		M8	3.170(6)×2
	M10	2.830(2)×3		M11	3.026(2)×2		Zn15	3.170(6)
	Zn14	2.847(3)		Na1	3.256(6)		Sn1	3.175(6)
	M11	2.943(2)×3	M11	Zn14	2.699(2)		M10	3.256(6)
	Na2	3.293(4)		M10	2.765(2)×2		Zn14	3.266(6)
Sn4	Zn13	2.677(3)×6		M11	2.834(3)×2		M5	3.271(6)×2
M5	M7	2.657(2)		M3	2.943(2)		M5	3.284(6)
	M6	2.764(2)×4		M10	3.026(2)×2	Na2	M8	3.232(7)×4
	M5	2.779(2)×4		M11	3.031(3)×2		M6	3.273(8)×3
	M6	2.845(3)		Na2	3.276(8)		M11	3.276(8)×3
M6	M3	2.696(2)	Zn12	M2	2.645(3)	Na3	M6	3.32(1)×5
	M6	2.707(3)×4		Zn15	2.682(3)×2		M11	3.335(7)×6
	M5	2.764(2)×4		Sn1	2.694(1)×2	Na4	Zn13	3.23(1)
	M5	2.845(3)		Zn12	2.783(4)×2		M9	3.49(1)
M7	M5	2.657(2)		M9	2.786(3)×2		M8	3.536(7)×3
	M8	2.838(2)×2		Na5	3.28(1)		M8	3.624(9)×4
	Sn1	2.877(2)		Na6	3.62(2)		M10	3.655(6)
	Zn15	2.901(2)×2	Zn13	Sn4	2.677(3)	Na5	Zn12	3.28(1)
	Na1	3.287(6)×2		M2	2.691(4)		M9	3.34(1)×2
	Na1	3.314(6)		M8	2.694(3)×3		Zn15	3.41(1)×2
M8	M9	2.652(1)		M9	2.824(2)×3		Zn15	3.45(1)×2
	M10	2.670(2)		Zn13	2.912(5)		M11	3.60(1)×4
	Zn13	2.694(3)	Zn14	M11	2.699(2)×4		Sn1	3.691(8)
	M7	2.838(2)		Sn1	2.700(3)	Na6	Sn1	3.58(1)×3
	Zn15	2.986(2)		M3	2.847(3)		Zn12	3.62(2)×3
	M8	3.106(2)×2		M10	2.851(2)×3		M11	3.70(1)×6
	Na1	3.170(6)		Na1	3.266(6)			
	Na2	3.232(7)						

***Table 8.7*: Interatomic distances (≤ 4 Å) in Na_6ZnSn_2 and $Na_{4.23}K_{1.77(1)}ZnSn_2$ (standard deviation in parentheses).**

Atom pair		*d* / Å	Atom pair		*d* / Å	Atom pair		*d* / Å
				Na_6ZnSn_2 (1)				
Sn	Zn	2.561(1)	Na1	Sn	3.255(2)	Na2	Zn	3.450(2)×2
	Na3	3.157(3)		Na2	3.260(3)		Na1	3.459(4)
	Na1	3.255(2)		Sn	3.280(1)×2		Sn	3.511(2)
	Na1	3.280(1)×2		Na3	3.414(2)×2	Na3	Sn	3.157(3)
	Na2	3.309(1)×2		Na2	3.459(4)		Na2	3.214(4)
	Na3	3.507(2)×2		Na3	3.630(3)		Na1	3.414(2)×2
	Na2	3.511(2)	Na2	Zn	3.110(2)		Sn	3.507(2)×2
	Na3	3.723(3)		Na2	3.205(2)×2		Na1	3.630(3)
Zn	Sn	2.561(1)×2		Na3	3.214(4)		Na3	3.667(5)×3
	Na2	3.110(2)×2		Na1	3.260(3)		Sn	3.723(3)
	Na2	3.450(2)×4		Sn	3.309(1)×2			
				$Na_{4.23}K_{1.77(1)}ZnSn_2$ (2)				
Sn1	Zn	2.582(1)	A	Na2	3.640(2)	Na4	Sn2	3.300(2)
	Na3	3.280(2)		Na2	3.692(3)		Sn2	3.369(2)
	Na2	3.317(2)		K2	3.717(2)		Na5	3.394(3)
	Na4	3.397(2)		Sn2	3.728(1)		Sn1	3.397(2)
	Na3	3.422(2)		Na2	3.737(2)		Na3	3.406(3)
	Na2	3.478(2)		Sn1	3.814(2)		Na3	3.466(3)
	A	3.612(1)		Na3	3.843(2)		Na5	3.620(3)
	K2	3.646(1)		Na5	3.913(3)		A	3.636(3)×2

Sn1	Na5	3.729(2)	A	Zn	3.955(1)	Na4	K2	3.664(3)
	A	3.814(1)	Na2	Zn	3.199(2)		Na4	3.973(4)
	K2	3.981(1)		Sn1	3.317(2)		Na3	4.176(3)
Sn2	Zn	2.556(1)		Na3	3.454(3)	Na5	Zn	3.065(2)
	Na5	3.285(2)		Sn1	3.478(2)		Sn2	3.285(2)
	Na4	3.300(2)		Sn2	3.482(2)		Na3	3.352(3)
	Na3	3.328(2)		Zn	3.593(2)		Sn2	3.393(2)
	Na4	3.369(2)		A	3.640(2)×2		Na4	3.394(3)
	Na5	3.393(2)		A	3.692(3)×2		Na5	3.549(5)
	Na2	3.482(2)		A	3.737(2)×2		Na4	3.620(3)
	A	3.634(1)×2	Na3	Zn	3.117(2)		Na3	3.661(3)
	A	3.728(1)×2		Sn1	3.280(2)		Sn1	3.729(2)
	K2	3.933(1)		Sn2	3.328(2)	K2	Zn	3.401(1)
Zn	Sn2	2.556(1)		Na5	3.352(3)		Na3	3.604(3)
	Sn1	2.582(1)		Na4	3.406(3)		Sn1	3.646(1)
	Na5	3.065(2)		Sn1	3.422(2)		Na4	3.664(3)
	Na3	3.117(2)		Na2	3.454(3)		A	3.717(2)×2
	Na2	3.199(2)		Na4	3.466(3)		Na5	3.771(3)
	K2	3.401(1)		K2	3.604(3)		Na2	3.824(2)
	Na2	3.593(2)		Na5	3.661(3)		Na2	3.845(3)
	A	3.955(1)		A	3.843(2)		K2	3.912(3)
A	Sn1	3.612(1)		K2	3.771(3)		Sn2	3.933(1)
	Sn2	3.634(1)		A	3.913(3)×2		Sn1	3.981(1)
	Na4	3.636(3)						

***Table 8.8*: Interatomic distances (≤ 4 Å) in $Na_{20}Zn_8Sn_{11}$ (standard deviation in parentheses).**

Atom pair		*d* / Å	Atom pair		*d* / Å	Atom pair		*d* / Å
Sn1	Zn2	2.799(1)	Zn1	Sn4	2.687(1)	Na3	Sn5	3.327(4)
	Zn3	2.802(1)		M	2.774(1)×2		Sn2	3.333(4)
	M	2.886(1)		Zn3	2.811(2)		Zn1	3.370(4)
	Na2	3.294(4)		Sn3	2.882(1)		Sn4	3.406(4)
	Na5	3.360(4)		Sn2	2.930(1)		Sn1	3.415(4)
	Na6	3.365(4)		M	2.952(1)		Na10	3.457(7)
	Na1	3.375(4)		Na2	3.222(4)		Na7	3.475(6)
	Na4	3.405(5)		Na1	3.263(4)		Na5	3.492(6)
	Na3	3.415(4)		Na7	3.270(5)		M	3.514(4)
	Na4	3.449(5)		Na6	3.305(4)		Na6	3.538(6)
	Na2	3.516(4)	Zn2	Zn2	2.763(2)		Na1	3.597(6)
Sn2	Zn3	2.860(1)		Sn1	2.799(1)	Na4	Sn3	3.200(4)
	Zn2	2.866(1)		Sn3	2.815(1)		Sn2	3.245(4)
	M	2.890(1)		Zn3	2.815(2)		Zn3	3.269(5)
	Zn1	2.930(1)		Sn2	2.866(1)		Zn2	3.289(4)
	Sn3	2.959(1)		Sn3	2.878(1		Zn3	3.302(4)
	Na4	3.245(4)		Na1	3.276(4)		M	3.341(4)×2
	Na2	3.256(4)		Na1	3.283(4)		Sn1	3.405(5)
	Na3	3.333(4)		Na4	3.289(5)		Sn1	3.449(5)
	Na5	3.363(5)		Na2	3.317(4)		Na2	3.535(6)
	Na9	3.427(5)		Na5	3.450(4)		Na1	3.551(6)
	Na7	3.442(5)	Zn3	Sn1	2.802(1)		Na2	3.568(6)
Sn3	Zn3	2.813(1)		M	2.804(1)×2	Na5	Sn5	3.274(4)
	Zn2	2.815(1)		Zn1	2.811(2)		Zn4	3.303(4)
	Zn2	2.878(1)		Sn3	2.813(1)		Sn3	3.356(4)
	Zn1	2.882(1)		Zn2	2.815(2)		Sn1	3.360(4)
	Sn2	2.959(1)		Sn2	2.860(1)		Sn2	3.363(5)
	Na4	3.200(4)		Na4	3.269(5)		Na8	3.429(6)
	Na1	3.231(4)		Na2	3.276(4)		Zn2	3.450(4)
	Na6	3.335(4)		Na2	3.294(4)		Na9	3.459(7)
	Na5	3.356(4)		Na4	3.302(4)		Na3	3.492(6)

Sn3	Na8	3.398(5)	Zn3	Na6	3.421(4)	Na5	Na6	3.530(6)
	Na7	3.433(5)	Zn4	Sn5	2.547(1)×2		Na1	3.588(6)
Sn4	Zn1	2.687(1)		Na10	3.109(9)×2		Na2	3.666(6)
	Na10	2.971(6)		Na5	3.303(4)×2	Na6	Zn1	3.305(4)
	Na10	2.980(6)		Na6	3.636(4)×2		Sn5	3.321(4)
	Na1	3.221(4)		Na3	3.638(4)×2		Sn3	3.335(4)
	Na2	3.226(4)	Na1	Sn4	3.221(4)×2		Sn1	3.365(4)
	Na8	3.342(5)		M	3.234(4)		Sn4	3.396(4)
	Na9	3.346(5)		Zn1	3.263(4)		Zn3	3.421(4)
	Na7	3.370(5)		Zn2	3.276(4)		Na10	3.441(7)
	Na6	3.396(4)		Zn2	3.283(4)		Na7	3.479(6)
	Na3	3.406(4)		M	3.306(4)×2		Na5	3.530(6)
Sn5	Zn4	2.547(1)		Sn1	3.375(4)		Na3	3.538(6)
	Na7	3.259(4)		Sn1	3.531(4)		Na2	3.617(6)
	Na5	3.274(4)		Na4	3.551(6)		Zn4	3.636(4)
	Na9	3.298(5)	Na2	Zn1	3.222(4)	Na7	Sn5	3.259(4)
	Na8	3.307(5)		Sn4	3.226(4)		Zn1	3.270(5)
	Na6	3.321(4)		M	3.237(4)		Sn4	3.370(5)
	Na3	3.327(4)		Sn2	3.256(4)		Sn3	3.433(5)
	Na9	3.489(5)		Zn3	3.276(4)		Sn2	3.442(5)
	Na8	3.520(5)		Sn1	3.294(4)		Na3	3.475(6)
M	M	2.756(2)×2		Zn3	3.294(4)		Na6	3.479(6)
	Zn1	2.774(1)		Zn2	3.317(4)		Na8	3.552(7)
	Zn3	2.804(1)		Sn1	3.516(4)		Na9	3.584(6)
M	Sn1	2.886(1)	Na2	Na4	3.535(6)	Na7	Na10	3.626(7)
	Sn2	2.890(1)		Na4	3.568(6)		Na10	3.654(8)
	Zn1	2.952(1)	Na9	Sn5	3.298(5)		Na8	3.704(7)
	Na1	3.234(4)		Sn4	3.346(5)	Na10	Sn4	2.971(6)
	Na2	3.237(4)		Sn2	3.427(5)		Sn4	2.980(6)
	Na1	3.306(4)		Na5	3.459(7)		Na10	3.10(2)
	Na4	3.341(4)		Sn5	3.489(5)		Zn4	3.109(9)
	Na3	3.514(4)		Na10	3.497(7)		Na6	3.441(7)
Na8	Sn5	3.307(5)		Na8	3.547(6)		Na3	3.457(7)
	Sn4	3.342(5)		Na7	3.584(6)		Na8	3.470(7)
	Sn3	3.398(5)		Na7	3.704(7)		Na9	3.497(7)
	Na5	3.429(6)		Na3	3.803(7)		Na7	3.626(7)
	Na10	3.470(7)		Na2	3.875(6)		Na7	3.654(8)
	Sn5	3.520(5)		Na9	3.930(9)			
	Na9	3.547(6)						
	Na7	3.552(7)						
	Na7	3.704(7)						
	Na6	3.783(6)						
	Na1	3.857(6)						
	Na8	3.93(1)						

***Table 8.9*: Interatomic distances (≤ 4 Å, *l* Å) in $Sr_{2-x}Ba_xBi_3$ (x = 0, 0.45, 0.86, 1.08, 1.28) and bond length differences (standard deviation in parentheses).**

Atom pair		x = 0	0.45	0.86	1.08	1.28	*d*(x = 1.28) – *d*(x = 0)
Sr1	Bi1×2	3.440(1)	3.469(1)	3.506(1)	3.506(2)	3.515(1)	0.07
	Bi2×2	3.519(1)	3.562(2)	3.604(1)	3.612(2)	3.617(2)	0.10
	Bi1×2	3.521(3)	3.545(1)	3.574(1)	3.569(3)	3.577(3)	0.06
	Bi1×2	3.787(3)	3.808(1)	3.835(1)	3.849(3)	3.853(3)	0.06
Sr2	Bi1×2	3.409(2)	3.424(1)	3.454(1)	3.457(2)	3.462(2)	0.05
	Bi1×2	3.479(2)	3.498(1)	3.526(1)	3.532(2)	3.541(2)	0.06
	Bi2×2	3.481(1)	3.499(1)	3.527(1)	3.533(1)	3.540(1)	0.06
Sr2	Bi2×2	3.575(1)	3.584(1)	3.611(1)	3.613(1)	3.621(1)	0.05

Bi1	Bi1	3.132(1)	3.142(1)	3.154(1)	3.145(2)	3.142(2)	0.01
Bi1	Bi2	3.310(1)	3.319(1)	3.336(1)	3.337(2)	3.339(1)	0.03
	Bi1	3.392(1)	3.454(1)	3.523(1)	3.537(2)	3.557(2)	0.17
	Sr2	3.409(2)	3.424(1)	3.454(1)	3.457(2)	3.462(2)	0.05
	Sr1	3.440(1)	3.469(1)	3.506(1)	3.506(2)	3.515(1)	0.07
	Sr2	3.479(2)	3.498(1)	3.526(1)	3.532(2)	3.541(2)	0.06
	Sr1	3.521(3)	3.545(1)	3.574(1)	3.579(3)	3.577(3)	0.06
	Sr1	3.787(3)	3.808(1)	3.835(1)	3.849(3)	3.853(3)	0.06
	Bi2	3.902(1)	3.915(1)	3.952(1)	3.959(2)	3.971(2)	0.07
Bi2	Bi1×2	3.310(1)	3.319(1)	3.336(1)	3.337(2)	3.339(1)	0.03
	Sr2×2	3.481(1)	3.499(1)	3.527(1)	3.533(1)	3.540(1)	0.06
	Sr1×2	3.519(1)	3.562(1)	3.604(1)	3.612(2)	3.617(2)	0.10
	Sr2×2	3.575(1)	3.584(1)	3.611(1)	3.613(1)	3.621(1)	0.05
	Bi1×2	3.902(1)	3.915(1)	3.952(1)	3.959(2)	3.971(2)	0.07

***Table 8.10*: Interatomic distances (≤ 4 Å) in $Sr_3Sn_{3.36}Bi_{1.64(3)}$ and $Sr_{11}Sn_{12}Bi_4$ (standard deviation in parentheses).**

Atom pair		*d* / Å	Atom pair		*d* / Å	Atom pair		*d* / Å
M	M	2.998(1)×2	Sr1	Bi2	3.357(1)×2	Sr2	Bi2	3.215(1)×2
	M	3.177(1)		M	3.463(1)×2		M	3.546(1)×8
Bi2	Sr2	3.215(1)×2		M	3.654(1)×3			
	Sr1	3.357(1)×4						

***Table 8.11*: Interatomic distances (≤ 4 Å) in $Sr_3Sn_{3.22}Tl_{1.78(5)}$, $Sr_3Sn_{2.86}Tl_{2.14(5)}$, and $Sr_3Sn_{3.8}In_{1.2(3)}$ (standard deviation in parentheses).**

Atom pair		*d* / Å	Atom pair		*d* / Å	Atom pair		*d* / Å
					$Sr_3Sn_{3.22}Tl_{1.78(5)}$ (1)			
M1	M3	3.023(1)	M2	Sr2	3.418(1)×2	M4	Sr1	3.266(1)
	M2	3.059(1)		Sr1	3.531(1)		Sr2	3.496(1)×2
	M4	3.196(1)		Sr2	3.694(1)×2		Sr2	3.540(1)
	Sr1	3.338(1)		Sr1	3.715(2)	Sr1	M4	3.266(1)
	M1	3.429(1)*	M3	M1	3.023(1)×3		M1	3.338(1)×2
	Sr2	3.491(1)		M4	3.092(1)		M3	3.400(1)×2
	Sr2	3.504(1)		Sr1	3.400(1)		M2	3.531(1)×2
	Sr1	3.608(1)		Sr2	3.419(1)×2		M1	3.608(1)×2
	Sr2	3.625(1)		Sr2	3.686(1)×2	Sr2	M2	3.418(1)×4
M2	M1	3.059(1)×3		Sr1	3.791(1)		M1	3.491(1)×2
	M4	3.114(1)	M4	M3	3.092(1)		M4	3.496(1)×2
				M2	3.114(1)		M1	3.504(1)
				M1	3.196(1)×3		M4	3.540(1)
					$Sr_3Sn_{2.86}Tl_{2.14(5)}$ (2)			
M1	M3	3.020(1)	M3	M1	3.020(1)×3	Sr1	M4	3.264(2)
	M2	3.077(1)		M4	3.081(2)		M1	3.354(1)×2
	M4	3.212(1)		Sr1	3.388(2)		M3	3.388(2)×2
	Sr1	3.355(1)		Sr2	3.413(1)×2		M2	3.530(2)×2
	M1	3.451(1)*		Sr2	3.713(1)×2		M1	3.603(2)×2
	Sr2	3.492(1)		Sr1	3.751(2)	Sr2	M3	3.413(1)×2
	Sr2	3.497(2)	M4	M3	3.081(2)		M2	3.435(1)×2
	Sr2	3.594(1)		M2	3.155(1)		M1	3.492(1)
	Sr1	3.603(2)		M1	3.212(1)×3		M1	3.497(2)×2
M2	M1	3.077(1)×3		Sr1	3.264(2)		M4	3.510(1)×2
	M4	3.155(1)		Sr2	3.510(1)×2		M4	3.538(1)
	Sr2	3.435(1)×2		Sr2	3.538(1)			
	Sr1	3.529(2)						

M2	Sr2	3.683(1)×2						
	Sr1	3.733(2)						

$Sr_3Sn_{3.8}In_{1.2(3)}$ (3)

M1	Sn2	2.978(1)	Sn2	M1	2.978(1)×3	Sr1	M4	3.295(1)
	Sn3	2.997(1)		M4	3.014(1)		M1	3.344(1)×2
	M4	3.149(1)		Sr1	3.404(1)		Sn2	3.404(1)
	M1	3.306(1)*		Sr2	3.431(1)×2		Sn3	3.511(1)
	Sr1	3.344(1)		Sr2	3.660(1)×2		M1	3.575(1)×4
	Sr2	3.519(1)×2		Sr1	3.821(1)	Sr2	Sn3	3.416(1)
	Sr1	3.575(1)	Sn3	M1	2.997(1)×3		Sn2	3.431(1)
	Sr2	3.638(1)		M4	3.008(1)		M4	3.484(1)×2
	Sr2	3.673(1)		Sr2	3.416(1)×2		M1	3.519(1)×4
M4	Sn3	3.008(1)		Sr1	3.511(1)		M4	3.520(1)×2
	Sn2	3.014(1)		Sr2	3.681(1)×2		M1	3.638(1)×2
	M1	3.149(1)×3		Sr1	3.710(1)			
	Sr1	3.295(1)						
	Sr2	3.484(1)×2						
	Sr2	3.520(1)×2						

*) intercluster

***Table 8.12*: Interatomic distances (≤ 4 Å) in Na_2SrSn_4 (standard deviation in parentheses).**

Atom pair		*d* / Å	Atom pair		*d* / Å	Atom pair		*d* / Å
Sn1	Sn1	2.909(4)	Sn2	Na	3.27(1)	Na	Sn1	3.15(1)
	Sn2	2.918(3)×2		Sn2	3.311(3)×2		Sn2	3.18(1)
	Na	3.154(11)		Na	3.45(1)		Sn2	3.26(1)
	Sr1	3.539(3)		Sr	3.515(2)		Sn2	3.27(1)
	Sr1	3.601(2)		Sr	3.711(2)		Sn2	3.45(1)
	Na	3.64(1)	Sr1	Sn2	3.515(2)×2		Na	3.546(8)×2
	Sr	3.676(3)		Sn1	3.539(3)×2		Sn1	3.64(1)
	Sr	3.714(3)		Sn1	3.601(2)×2		Na	3.81(1)×2
Sn2	Sn1	2.918(3)×2		Sn1	3.676(3)×2		Na	3.89(2)
	Na	3.18(1)		Sn2	3.711(2)×2			
	Na	3.26(1)		Sn1	3.714(3)×2			

***Table 8.13*: Atomic coordinates and equivalent isotropic displacement parameters for $K_{70}Sn_{103}$.**

Atom	site	*x*	*y*	*z*	U_{eq}	Atom	site	×	*y*	*z*	U_{eq} / Å^2
Sn1A	8*c*	0.0372(1)	–0.3670(1)	0.2292(1)	0.039(1)	Sn1J	8*c*	0.0456(1)	–0.1666(1)	0.2611(1)	0.068(1)
Sn2A	8*c*	0.1072(1)	–0.4456(1)	0.2125(1)	0.056(1)	Sn2J	8*c*	–0.0401(1)	–0.0991(1)	0.2655(1)	0.068(1)
Sn3A	8*c*	–0.0116(1)	–0.4406(1)	0.2072(1)	0.055(1)	Sn3J	8*c*	–0.0365(1)	–0.1549(1)	0.2340(1)	0.072(1)
Sn4A	8*c*	–0.0315(1)	–0.3513(1)	0.1914(1)	0.051(1)	Sn4J	8*c*	0.0442(1)	–0.0855(1)	0.2394(1)	0.059(1)
Sn5A	8*c*	0.1501(1)	–0.3536(1)	0.2111(1)	0.064(1)	Sn1K	8*c*	–0.5258(2)	–0.4282(1)	0.0829(1)	0.083(1)
Sn6A	8*c*	0.0603(1)	–0.2912(1)	0.2026(1)	0.062(1)	Sn2K	8*c*	–0.4809(2)	–0.3612(1)	0.1061(1)	0.091(1)
Sn7A	8*c*	0.0753(1)	–0.3364(1)	0.1689(1)	0.065(1)	Sn3K	8*c*	–0.4465(2)	–0.3610(1)	0.0703(1)	0.090(1)
Sn8A	8*c*	0.0317(2)	–0.4287(1)	0.1716(1)	0.082(1)	Sn4K	8*c*	–0.5558(2)	–0.3327(1)	0.0795(1)	0.096(1)
Sn9A	8*c*	0.1487(2)	–0.4103(2)	0.1785(1)	0.092(1)	Sn1L	8*c*	–0.2337(1)	–0.2400(1)	0.1993(1)	0.058(1)
Sn1B	8*c*	–0.6458(1)	–0.0883(1)	0.0123(1)	0.069(1)	Sn2L	8*c*	–0.1614(1)	–0.2718(1)	0.2266(1)	0.060(1)
Sn2B	8*c*	–0.5905(1)	–0.0533(1)	0.0448(1)	0.059(1)	Sn3L	8*c*	–0.2564(1)	–0.2173(1)	0.2355(1)	0.060(1)
Sn3B	8*c*	–0.5763(2)	–0.1598(1)	–0.0029(1)	0.078(1)	Sn4L	8*c*	–0.2702(1)	–0.3108(1)	0.2236(1)	0.064(1)
Sn4B	8*c*	–0.5751(2)	–0.2112(1)	0.0295(1)	0.076(1)	Sn1M	8*c*	–0.2255(1)	–0.4626(1)	0.2084(1)	0.064(1)
Sn5B	8*c*	–0.6489(1)	–0.1422(1)	0.0446(1)	0.058(1)	Sn2M	8*c*	–0.3247(1)	–0.5074(1)	0.2220(1)	0.057(1)
Sn6B	8*c*	–0.4735(1)	–0.1583(1)	0.0191(1)	0.057(1)	Sn3M	8*c*	–0.2284(1)	–0.4890(1)	0.2445(1)	0.072(1)
Sn7B	8*c*	–0.5286(1)	–0.1472(1)	0.0563(1)	0.065(1)	Sn4M	8*c*	–0.2258(1)	–0.5583(1)	0.2183(1)	0.080(1)
Sn8B	8*c*	–0.4741(1)	–0.0709(1)	0.0379(1)	0.076(1)	Sn1N	8*c*	–0.2201(1)	–0.6476(1)	0.3283(1)	0.057(1)
Sn9B	8*c*	–0.5295(1)	–0.0679(1)	0.0040(1)	0.071(1)	Sn2N	8*c*	–0.2196(1)	–0.5833(1)	0.2992(1)	0.058(1)
Sn1C	8*c*	–0.6104(1)	–0.4357(1)	0.1821(1)	0.049(1)	Sn3N	8*c*	–0.2389(1)	–0.6800(1)	0.2929(1)	0.058(1)
Sn2C	8*c*	–0.4872(1)	–0.3904(1)	0.1745(1)	0.059(1)	Sn4N	8*c*	–0.3229(1)	–0.6252(1)	0.3103(1)	0.059(1)
Sn3C	8*c*	–0.6028(1)	–0.3884(1)	0.2216(1)	0.055(1)	Sn1O	8*c*	–0.2869(1)	–0.4545(1)	0.3838(1)	0.062(1)
Sn4C	8*c*	–0.6650(1)	–0.3483(1)	0.1915(1)	0.059(1)	Sn2O	8*c*	–0.2337(1)	–0.5145(1)	0.4097(1)	0.068(1)
Sn5C	8*c*	–0.5901(1)	–0.3504(1)	0.1616(1)	0.061(1)	Sn3O	8*c*	–0.1876(1)	–0.5034(1)	0.3747(1)	0.066(1)
Sn6C	8*c*	–0.5857(1)	–0.2926(1)	0.2113(1)	0.062(1)	Sn4O	8*c*	–0.2915(1)	–0.5512(1)	0.3803(1)	0.071(1)
Sn7C	8*c*	–0.5135(1)	–0.2941(1)	0.1815(1)	0.064(1)	Sn1P	8*c*	–0.2891(1)	–0.7102(1)	0.3951(1)	0.062(1)
Sn8C	8*c*	–0.4810(1)	–0.3467(1)	0.2142(1)	0.060(1)	Sn2P	8*c*	–0.2457(1)	–0.7543(1)	0.3641(1)	0.062(1)
Sn9C	8*c*	–0.5125(2)	–0.4413(1)	0.2056(1)	0.075(1)	Sn3P	8*c*	–0.2568(1)	–0.8059(1)	0.3966(1)	0.061(1)
Sn1D	8*c*	–0.3946(1)	–0.1954(1)	0.1231(1)	0.060(1)	Sn4P	8*c*	–0.1740(1)	–0.7354(1)	0.3937(1)	0.066(1)
Sn2D	8*c*	–0.4299(1)	–0.0444(1)	0.1365(1)	0.067(1)	Sn1Q	8*c*	0.0345	–0.8348(1)	0.4006(1)	0.071(1)
Sn3D	8*c*	–0.3317(1)	–0.1176(1)	0.1435(1)	0.061(1)	Sn2Q	8*c*	–0.0464(1)	–0.8452(1)	0.4276(1)	0.063(1)
Sn4D	8*c*	–0.4178(2)	–0.0907(1)	0.1704(1)	0.072(1)	Sn3Q	8*c*	0.0552(1)	–0.8992(1)	0.4285(1)	0.075(1)
Sn5D	8*c*	–0.4062(1)	–0.1871(1)	0.1616(1)	0.061(1)	Sn4Q	8*c*	–0.0282(1)	–0.9190(1)	0.4033(1)	0.073(1)
Sn6D	8*c*	–0.5232(2)	–0.0981(1)	0.1525(1)	0.080(1)	Sn1R	8*c*	–0.2271(1)	–0.3244(1)	0.4791(1)	0.067(1)
Sn7D	8*c*	–0.3851(2)	–0.1020(1)	0.1088(1)	0.084(1)	Sn2R	8*c*	–0.2249(1)	–0.3819(1)	0.4485(1)	0.063(1)
Sn8D	8*c*	–0.5081(1)	–0.1918(1)	0.1409(1)	0.085(1)	Sn3R	8*c*	–0.2098(2)	–0.4229(1)	0.4824(1)	0.072(1)
Sn9D	8*c*	–0.5014(2)	–0.1161(1)	0.1159(1)	0.083(1)	Sn4R	8*c*	–0.3177(1)	–0.3879(1)	0.4724(1)	0.074(1)
Sn1E	8*c*	0.1311(3)	–0.5519(2)	0.3511(1)	0.207(4)	K1	8*c*	–0.4808(7)	–0.0288(5)	0.0826(2)	0.115(5)
Sn2E	8*c*	0.0028(1)	–0.6312(1)	0.3331(1)	0.070(1)	K2	8*c*	–0.3637(5)	–0.1229(4)	0.0603(2)	0.093(4)
Sn3E	8*c*	0.0707(3)	–0.5565(1)	0.3837(1)	0.129(2)	K3	8*c*	0.2431(6)	–1.0254(5)	0.3810(2)	0.106(4)
Sn4E	8*c*	0.1579(2)	–0.6364(1)	0.3705(1)	0.087(1)	K4	8*c*	0.1869(5)	–0.8735(5)	0.4121(2)	0.115(5)
Sn5E	8*c*	0.0196(3)	–0.5423(1)	0.3491(1)	0.166(3)	K5	8*c*	–0.2265(5)	0.0391(4)	0.0045(1)	0.078(3)
Sn6E	8*c*	0.1233(2)	–0.6336(2)	0.3323(1)	0.110(2)	K6	8*c*	0.1510(6)	–0.8985(5)	0.4637(2)	0.110(5)
Sn7E	8*c*	0.0561(2)	–0.6990(1)	0.3565(1)	0.086(1)	K7	8*c*	–0.3765(5)	–0.0367(4)	0.0040(1)	0.087(3)
Sn8E	8*c*	–0.0335(1)	–0.6210(2)	0.3692(1)	0.085(1)	K8	8*c*	–0.3764(5)	–0.4589(4)	0.0900(1)	0.090(3)
Sn9E	8*c*	0.0602(2)	–0.6512(2)	0.3901(1)	0.120(2)	K9	8*c*	–0.2597(6)	–0.1605(5)	0.0967(2)	0.107(4)
Sn1F	8*c*	–0.0371(4)	–0.6006(3)	0.5031(1)	0.219(5)	K10	8*c*	–0.0971(6)	–0.1116(5)	0.0679(2)	0.111(4)
Sn2F	8*c*	0.0369(2)	–0.6247(2)	0.4748(1)	0.141(2)	K11	8*c*	–0.3243(5)	–0.3575(4)	0.0456(2)	0.092(4)
Sn3F	8*c*	–0.0378(2)	–0.7008(1)	0.4952(1)	0.098(1)	K12	8*c*	–0.0424(6)	0.0432(4)	0.0428(2)	0.119(5)
Sn4F	8*c*	–0.0138(2)	–0.6987(1)	0.4578(1)	0.099(1)	K13	8*c*	–0.0905(5)	–0.0327(5)	0.0023(2)	0.103(4)
Sn5F	8*c*	–0.1392(2)	–0.6452(2)	0.4997(1)	0.103(1)	K14	8*c*	–0.3475(5)	–0.7368(4)	0.3273(2)	0.083(3)
Sn6F	8*c*	–0.1344(2)	–0.6914(1)	0.4638(1)	0.075(1)	K15	8*c*	–0.0633(5)	–0.0450(4)	0.3087(1)	0.079(3)
Sn7F	8*c*	–0.1523(2)	–0.5897(1)	0.4679(1)	0.077(1)	K16	8*c*	–0.2241(5)	–0.3000(4)	0.2693(1)	0.084(3)
Sn8F	8*c*	–0.0658(2)	–0.6167(1)	0.4426(1)	0.081(1)	K17	8*c*	–0.0611(5)	–0.4434(4)	0.3677(1)	0.086(3)
Sn9F	8*c*	–0.0399(3)	–0.5526(2)	0.4706(1)	0.200(4)	K18	8*c*	–0.1005(6)	–0.7210(4)	0.3492(2)	0.103(4)
Sn1G	8*c*	–0.3400(1)	0.0006(1)	0.0769(1)	0.064(1)	K19	8*c*	–0.0328(4)	–0.2736(4)	0.2457(1)	0.069(3)
Sn2G	8*c*	–0.2916(1)	–0.0202(1)	0.0407(1)	0.075(1)	K20	8*c*	–0.1134(5)	–0.4690(4)	0.1745(1)	0.085(3)
Sn3G	8*c*	–0.2308(1)	–0.0517(1)	0.0716(1)	0.070(1)	K21	8*c*	–0.0200(5)	–0.1758(4)	0.3052(2)	0.087(3)
Sn4G	8*c*	–0.1716(1)	–0.0107(2)	0.0439(1)	0.092(1)	K22	8*c*	–0.2171(5)	–0.6363(4)	0.4268(1)	0.080(3)
Sn5G	8*c*	–0.2418(2)	0.0474(1)	0.0635(1)	0.116(2)	K23	8*c*	–0.0709(5)	–0.2303(4)	0.1931(1)	0.079(3)
Sn1H	8*c*	–0.2212(2)	0.0977(1)	0.1200(1)	0.081(1)	K24	8*c*	–0.1282(4)	–0.5091(3)	0.2775(1)	0.071(3)
Sn2H	8*c*	–0.3056(2)	0.1522(2)	0.1368(1)	0.130(2)	K25	8*c*	–0.3445(4)	–0.6439(3)	0.3586(1)	0.067(3)
Sn3H	8*c*	–0.2656(2)	0.0665(2)	0.1522(1)	0.116(2)	K26	8*c*	–0.4239(5)	–0.4906(4)	0.3680(1)	0.079(3)
Sn4H	8*c*	–0.1976(2)	0.1469(1)	0.1521(1)	0.090(1)	K27	8*c*	–0.1224(5)	–0.8461(4)	0.3801(2)	0.088(3)
Sn1I	8*c*	–0.1966(2)	–0.1971(2)	0.0569(1)	0.123(2)	K28	8*c*	–0.1200(5)	–0.5529(4)	0.3346(1)	0.078(3)
Sn2I	8*c*	–0.3128(2)	–0.2309(2)	0.0549(1)	0.116(2)	K29	8*c*	–0.1878(4)	–0.6299(3)	0.3733(1)	0.067(3)
Sn3I	8*c*	–0.2239(2)	–0.2738(2)	0.0350(1)	0.122(2)	K30	8*c*	–0.0626(5)	0.1973(3)	0.1428(1)	0.078(3)
Sn4I	8*c*	–0.2290(2)	–0.2787(2)	0.0719(1)	0.139(2)	K31	8*c*	–0.2699(5)	–0.8805(4)	0.3521(1)	0.077(3)

K32	8*c*	–0.3936(4)	–0.7850(4)	0.3780(1)	0.072(3)	K52	8*c*	–0.4483(6)	–0.2699(5)	0.0396(2)	0.112(4)
K33	8*c*	–0.2464(5)	–0.4433(4)	0.2901(2)	0.085(3)	K53	8*c*	–0.0521(5)	–0.3240(5)	0.1450(2)	0.097(4)
K34	8*c*	0.0869(4)	–0.0409(4)	0.2804(1)	0.074(3)	K54	8*c*	–0.1786(5)	–0.7905(4)	0.4379(2)	0.086(3)
K35	8*c*	–0.2052(5)	–0.7779(4)	0.3193(1)	0.078(3)	K55	8*c*	–0.2753(5)	–0.5125(4)	0.4560(1)	0.081(3)
K36	8*c*	–0.0474(5)	–0.0539(4)	0.2020(2)	0.079(3)	K56	8*c*	–0.2510(6)	–0.5488(5)	0.1743(1)	0.094(4)
K37	8*c*	–0.1166(5)	–0.2183(5)	0.0105(2)	0.097(4)	K57	8*c*	–0.0534(6)	–0.8172(4)	0.4727(2)	0.100(4)
K38	8*c*	–0.0885(4)	–0.6633(4)	0.2956(1)	0.073(3)	K58	8*c*	–0.0381(5)	0.0174(4)	0.2473(1)	0.076(3)
K39	8*c*	–0.3341(6)	–0.4011(4)	0.2421(2)	0.106(4)	K59	8*c*	0.1221(6)	–0.2628(5)	0.2468(3)	0.147(7)
K40	8*c*	–0.4054(5)	–0.4374(4)	0.1382(2)	0.096(4)	K60	8*c*	–0.2283(5)	–0.3043(4)	–0.0114(2)	0.096(4)
K41	8*c*	–0.0700(6)	–0.5449(4)	0.4035(2)	0.101(4)	K61	8*c*	–0.1754(4)	–0.0551(4)	0.2677(1)	0.073(3)
K42	8*c*	0.0825(5)	–0.7836(5)	0.4437(2)	0.104(4)	K62	8*c*	–0.2499(7)	0.2753(6)	0.1543(2)	0.130(6)
K43	8*c*	–0.1677(4)	–0.1386(3)	0.2156(2)	0.074(3)	K63	8*c*	–0.1921(5)	–0.3503(4)	0.1863(1)	0.078(3)
K44	8*c*	–0.1328(4)	–0.3918(3)	0.2325(1)	0.070(3)	K64	8*c*	–0.4160(6)	–0.8511(5)	0.4656(2)	0.116(5)
K45	8*c*	–0.1394(5)	–0.2541(4)	0.1074(2)	0.109(5)	K65	8*c*	–0.1649(6)	–0.7843(6)	0.5078(2)	0.130(6)
K46	8*c*	–0.1709(4)	–0.4020(3)	0.4060(1)	0.067(3)	K66	8*c*	–0.1557(5)	–0.6581(4)	0.2046(1)	0.083(3)
K47	8*c*	–0.3366(5)	–0.7642(4)	0.4356(1)	0.076(3)	K67	8*c*	–0.1620(6)	0.1936(5)	0.1011(2)	0.124(5)
K48	8*c*	–0.0319(7)	–0.9447(5)	0.4601(2)	0.117(5)	K68	8*c*	–0.1399(4)	–0.1895(3)	0.2665(1)	0.063(3)
K49	8*c*	–0.2805(5)	–0.5214(4)	0.3358(1)	0.087(3)	K69	8*c*	–0.1305(5)	–0.4801(4)	0.4448(1)	0.079(3)
K50	8*c*	–0.0410(5)	–0.7231(4)	0.4104(2)	0.094(4)	K70	8*c*	–0.1854(4)	–0.6222(3)	0.2548(1)	0.062(3)
K51	8*c*	–0.1342(5)	0.2116(5)	0.1890(2)	0.095(4)						

***Table 8*.14: Anisotropic thermal displacement parameters (*I* Å^2) for $K_{70}Sn_{103}$.**

Atom	U_{11}	U_{22}	U_{33}	U_{23}	U_{13}	U_{12}	Atom	U_{11}	U_{22}	U_{33}	U_{23}	U_{13}	U_{12}
Sn1A	0.041(2)	0.030(1)	0.045(1)	–0.008(1)	0	0	Sn8E	0.055(2)	0.130(3)	0.071(2)	–0.025(2)	0.011(2)	–0.012(2)
Sn2A	0.052(2)	0.046(2)	0.070(2)	0.007(1)	–0.006(2)	–0.002(1)	Sn9E	0.191(5)	0.107(3)	0.063(2)	0.016(2)	0.018(3)	0.036(3)
Sn3A	0.051(2)	0.051(2)	0.062(2)	0.004(1)	–0.001(1)	–0.006(1)	Sn1F	0.269(8)	0.310(10)	0.077(3)	–0.043(4)	0.025(4)	–0.214(8)
Sn4A	0.051(2)	0.045(2)	0.056(2)	0.005(1)	–0.005(1)	0	Sn2F	0.066(3)	0.133(4)	0.223(6)	–0.071(4)	0.015(3)	–0.002(3)
Sn5A	0.049(2)	0.048(2)	0.094(2)	0	–0.004(2)	–0.002(1)	Sn3F	0.120(3)	0.083(3)	0.091(3)	0.023(2)	0.012(2)	0.017(2)
Sn6A	0.065(2)	0.044(2)	0.078(2)	–0.003(2)	–0.009(2)	0.002(2)	Sn4F	0.102(3)	0.082(3)	0.114(3)	–0.017(2)	0.007(2)	0.027(2)
Sn7A	0.077(2)	0.059(2)	0.059(2)	0.014(2)	0.004(2)	–0.006(2)	Sn5F	0.094(3)	0.145(4)	0.070(2)	0.021(2)	0.023(2)	0.019(3)
Sn8A	0.104(3)	0.075(2)	0.067(2)	–0.021(2)	0.023(2)	–0.032(2)	Sn6F	0.077(2)	0.056(2)	0.093(2)	–0.009(2)	–0.010(2)	–0.010(2)
Sn9A	0.082(3)	0.136(2)	0.058(2)	0.004(2)	0.013(2)	0.054(2)	Sn7F	0.084(2)	0.076(2)	0.071(2)	0.009(2)	0.009(2)	0.028(2)
Sn1B	0.058(2)	0.093(2)	0.057(2)	0.012(2)	–0.001(2)	0.020(2)	Sn8F	0.083(2)	0.110(3)	0.049(2)	0.021(2)	0.005(2)	0.019(2)
Sn2B	0.044(2)	0.055(2)	0.077(2)	–0.017(2)	–0.003(2)	0.003(1)	Sn9F	0.191(6)	0.052(3)	0.350(10)	0.023(4)	–0.188(7)	–0.020(3)
Sn3B	0.089(3)	0.073(2)	0.073(2)	–0.014(2)	–0.023(2)	0.014(2)	Sn1G	0.082(2)	0.050(2)	0.061(2)	0.014(1)	0.036(2)	0.017(2)
Sn4B	0.076(2)	0.055(2)	0.097(2)	0.003(2)	0.019(2)	0	Sn2G	0.067(2)	0.098(3)	0.059(2)	0.004(2)	–0.011(2)	–0.009(2)
Sn5B	0.054(2)	0.069(2)	0.052(2)	0.005(1)	0.007(1)	0.002(2)	Sn3G	0.085(2)	0.066(2)	0.059(2)	0.013(2)	0.004(2)	0.012(2)
Sn6B	0.051(2)	0.067(2)	0.052(2)	0.004(1)	0.006(1)	0.009(2)	Sn4G	0.061(2)	0.136(3)	0.079(2)	0.036(2)	–0.002(2)	–0.014(2)
Sn7B	0.055(2)	0.091(2)	0.048(2)	0.011(2)	0.004(2)	0.010(2)	Sn5G	0.122(4)	0.056(2)	0.169(4)	–0.009(3)	–0.057(3)	0.012(2)
Sn8B	0.061(2)	0.089(3)	0.078(2)	–0.014(2)	–0.002(2)	–0.011(2)	Sn1H	0.086(3)	0.094(3)	0.061(2)	0.010(2)	0.022(2)	0.025(2)
Sn9B	0.056(2)	0.081(2)	0.075(2)	0.027(2)	–0.008(2)	–0.009(2)	Sn2H	0.095(3)	0.162(5)	0.133(4)	–0.073(3)	–0.048(3)	0.062(3)
Sn1C	0.066(2)	0.035(2)	0.047(2)	0.002(1)	0.008(1)	0	Sn3H	0.168(5)	0.107(3)	0.074(2)	–0.017(2)	0.036(3)	–0.070(3)
Sn2C	0.060(2)	0.059(2)	0.059(2)	0.005(1)	0.014(2)	0.012(2)	Sn4H	0.062(2)	0.088(3)	0.118(3)	–0.010(2)	–0.024(2)	–0.008(2)
Sn3C	0.063(2)	0.052(2)	0.050(2)	0.006(1)	0.009(1)	0.002(1)	Sn1I	0.151(4)	0.085(3)	0.133(5)	–0.029(3)	0.045(3)	–0.048(3)
Sn4C	0.054(2)	0.064(2)	0.060(2)	–0.004(1)	0.002(1)	0.006(2)	Sn2I	0.093(3)	0.146(4)	0.111(3)	–0.040(3)	–0.029(3)	0.045(3)
Sn5C	0.067(2)	0.067(2)	0.050(2)	0.009(1)	0	0	Sn3I	0.087(3)	0.157(4)	0.120(3)	–0.074(3)	0.011(3)	–0.009(3)
Sn6C	0.061(2)	0.056(2)	0.069(2)	–0.012(2)	0.007(2)	0	Sn4I	0.094(3)	0.217(6)	0.106(3)	0.086(4)	–0.007(3)	–0.004(3)
Sn7C	0.068(2)	0.054(2)	0.070(2)	0.005(2)	0.011(2)	–0.005(2)	Sn1J	0.064(2)	0.060(2)	0.082(2)	0.010(2)	–0.007(2)	0.011(2)
Sn8C	0.050(2)	0.071(2)	0.057(2)	0	0.003(1)	0	Sn2J	0.064(2)	0.058(2)	0.083(2)	–0.005(2)	0.028(2)	0.004(2)
Sn9C	0.079(2)	0.064(2)	0.082(2)	0.025(2)	0.014(2)	0.022(2)	Sn3J	0.075(2)	0.083(2)	0.058(2)	0.002(2)	–0.011(2)	–0.028(2)
Sn1D	0.078(2)	0.047(2)	0.055(2)	–0.010(1)	0.013(2)	0	Sn4J	0.056(2)	0.056(2)	0.064(2)	0.003(1)	0.010(2)	–0.011(2)
Sn2D	0.081(2)	0.048(2)	0.071(2)	0.008(2)	–0.004(2)	0	Sn1K	0.084(3)	0.060(2)	0.105(3)	–0.021(2)	0.035(2)	–0.017(2)
Sn3D	0.060(2)	0.054(2)	0.071(2)	0.012(2)	–0.002(2)	–0.004(2)	Sn2K	0.117(3)	0.102(3)	0.054(2)	0.004(2)	–0.012(2)	–0.032(2)
Sn4D	0.100(3)	0.061(2)	0.057(2)	–0.008(2)	–0.010(2)	0.011(2)	Sn3K	0.081(3)	0.082(3)	0.106(3)	0.004(2)	0.039(2)	–0.004(2)
Sn5D	0.079(2)	0.050(2)	0.053(2)	0.004(1)	–0.010(2)	0	Sn4K	0.077(3)	0.093(3)	0.119(3)	0.026(2)	–0.014(2)	0.014(2)
Sn6D	0.075(2)	0.088(3)	0.078(2)	–0.018(2)	0.017(2)	–0.011(2)	Sn1L	0.068(2)	0.056(2)	0.049(2)	0	0	0
Sn7D	0.088(3)	0.099(3)	0.064(2)	0.022(2)	0.018(2)	0.023(2)	Sn2L	0.049(2)	0.065(2)	0.065(2)	0.001(2)	–0.003(1)	0.004(2)
Sn8D	0.062(2)	0.061(2)	0.132(3)	0.004(2)	–0.018(2)	–0.004(2)	Sn3L	0.068(2)	0.057(2)	0.055(2)	–0.004(1)	0.007(2)	0.010(2)
Sn9D	0.076(2)	0.110(3)	0.064(2)	0.008(2)	–0.019(2)	–0.008(2)	Sn4L	0.066(2)	0.061(2)	0.066(2)	0.005(2)	0	–0.016(2)
Sn1E	0.161(5)	0.086(3)	0.37(1)	–0.030(5)	0.168(7)	–0.016(3)	Sn1M	0.068(2)	0.069(2)	0.056(2)	0.011(2)	0	–0.015(2)
Sn2E	0.068(2)	0.089(2)	0.053(2)	–0.003(2)	–0.010(2)	0.014(2)	Sn2M	0.045(2)	0.062(2)	0.065(2)	0.002(2)	–0.003(1)	0
Sn3E	0.257(7)	0.067(3)	0.063(2)	–0.017(2)	–0.013(3)	–0.016(3)	Sn3M	0.073(2)	0.096(3)	0.048(2)	0.004(2)	–0.008(2)	–0.026(2)
Sn4E	0.078(2)	0.087(3)	0.096(3)	0	–0.022(2)	0.008(2)	Sn4M	0.064(2)	0.055(2)	0.122(3)	–0.013(2)	–0.009(2)	0.009(2)
Sn5E	0.167(5)	0.048(2)	0.283(7)	0.008(3)	–0.151(5)	–0.010(3)	Sn1N	0.064(2)	0.060(2)	0.047(2)	0.003(1)	–0.009(1)	0
Sn6E	0.066(2)	0.207(5)	0.057(2)	–0.028(3)	0.013(2)	–0.027(3)	Sn2N	0.065(2)	0.054(2)	0.055(2)	0.005(1)	0	–0.009(2)
Sn7E	0.134(3)	0.047(2)	0.077(2)	–0.005(2)	–0.050(2)	0.007(2)	Sn3N	0.068(2)	0.053(2)	0.054(2)	–0.010(1)	0	0

Atom	U_{11}	U_{22}	U_{33}	U_{23}	U_{13}	U_{12}	Atom	U_{11}	U_{22}	U_{33}	U_{23}	U_{13}	U_{12}
Sn4N	0.049(2)	0.066(2)	0.062(2)	0.003(2)	0.004(1)	0.002(2)	K27	0.084(8)	0.069(7)	0.112(9)	0.011(6)	–0.006(7)	0.009(6)
Sn1O	0.069(2)	0.052(2)	0.066(2)	0.006(1)	–0.001(2)	0.007(2)	K28	0.074(7)	0.070(7)	0.090(8)	–0.003(6)	–0.011(6)	0
Sn2O	0.085(2)	0.069(2)	0.050(2)	0.008(2)	–0.008(2)	0	K29	0.067(7)	0.069(7)	0.066(6)	0.008(5)	0.002(5)	–0.004(5)
Sn3O	0.056(2)	0.069(2)	0.072(2)	–0.006(2)	0.010(2)	–0.005(2)	K30	0.114(9)	0.057(6)	0.062(6)	0.004(5)	0.014(6)	0.006(6)
Sn4O	0.065(2)	0.061(2)	0.088(2)	–0.018(2)	0	–0.011(2)	K31	0.078(7)	0.083(8)	0.070(7)	0.007(6)	–0.005(6)	0.009(6)
Sn1P	0.069(2)	0.054(2)	0.064(2)	–0.007(1)	0.007(2)	0	K32	0.063(6)	0.087(7)	0.065(6)	–0.010(5)	–0.007(5)	–0.004(6)
Sn2P	0.074(2)	0.065(2)	0.045(2)	–0.003(1)	0	–0.004(2)	K33	0.069(7)	0.084(8)	0.103(8)	–0.017(7)	–0.005(6)	0
Sn3P	0.066(2)	0.051(2)	0.065(2)	0.012(1)	0	–0.010(2)	K34	0.063(7)	0.080(7)	0.078(7)	–0.018(6)	–0.003(5)	0.014(6)
Sn4P	0.057(2)	0.065(2)	0.075(2)	0.010(2)	–0.015(2)	–0.010(2)	K35	0.077(7)	0.082(8)	0.076(7)	0	0.010(6)	0.018(6)
Sn1Q	0.085(2)	0.058(2)	0.069(2)	0.010(2)	0.024(2)	–0.006(2)	K36	0.072(7)	0.069(7)	0.096(8)	–0.012(6)	0	0
Sn2Q	0.055(2)	0.072(2)	0.064(2)	–0.014(2)	0.011(2)	0	K37	0.088(9)	0.102(9)	0.102(9)	–0.004(7)	–0.007(7)	0
Sn3Q	0.062(2)	0.095(3)	0.067(2)	0.011(2)	–0.010(2)	0	K38	0.065(7)	0.075(7)	0.080(7)	0.006(6)	0	0
Sn4Q	0.069(2)	0.063(2)	0.087(2)	–0.023(2)	–0.009(2)	–0.003(2)	K39	0.15(1)	0.057(7)	0.11(1)	–0.012(6)	0.048(9)	–0.020(7)
Sn1R	0.078(2)	0.057(2)	0.066(2)	–0.010(2)	0.004(2)	–0.003(2)	K40	0.100(9)	0.074(8)	0.114(9)	–0.017(7)	0.035(8)	–0.013(7)
Sn2R	0.069(2)	0.073(2)	0.046(2)	–0.001(1)	0.005(1)	0.012(2)	K41	0.15(1)	0.077(8)	0.076(7)	–0.001(6)	–0.017(8)	0.003(8)
Sn3R	0.091(3)	0.066(2)	0.060(2)	0.005(2)	–0.017(2)	0.015(2)	K42	0.072(8)	0.11(1)	0.13(1)	–0.051(8)	–0.007(7)	0.009(7)
Sn4R	0.053(2)	0.088(2)	0.079(2)	–0.005(2)	0.009(2)	–0.003(2)	K43	0.064(7)	0.059(6)	0.097(8)	0.008(6)	0.008(6)	0
K1	0.13(1)	0.11(1)	0.11(1)	–0.013(8)	–0.018(9)	0.033(9)	K44	0.078(7)	0.060(6)	0.072(6)	0	–0.006(5)	–0.009(5)
K2	0.091(9)	0.098(9)	0.091(8)	0.017(7)	–0.005(7)	–0.006(7)	K45	0.086(9)	0.089(9)	0.15(1)	–0.049(8)	–0.019(8)	0.019(7)
K3	0.14(1)	0.093(9)	0.084(8)	0.005(7)	–0.008(8)	–0.034(8)	K46	0.079(7)	0.059(6)	0.064(6)	–0.002(5)	–0.006(5)	0.007(5)
K4	0.081(9)	0.090(9)	0.17(1)	0.036(9)	0.040(9)	0.014(7)	K47	0.083(8)	0.076(7)	0.070(7)	–0.007(5)	0.007(6)	–0.010(6)
K5	0.077(7)	0.090(8)	0.066(6)	0.013(6)	0.002(5)	0.007(6)	K48	0.16(1)	0.1(1)	0.095(9)	0.010(7)	0.024(9)	–0.029(9)
K6	0.11(1)	0.15 (1)	0.070(7)	–0.017(8)	–0.014(7)	0.050(9)	K49	0.104(9)	0.084(8)	0.074(7)	–0.013(6)	–0.003(6)	0.018(7)
K7	0.079(8)	0.111(9)	0.071(7)	–0.003(6)	–0.010(6)	–0.015(7)	K50	0.078(8)	0.085(8)	0.12(1)	–0.010(7)	–0.029(7)	0.006(6)
K8	0.087(8)	0.113(9)	0.071(7)	–0.001(7)	0.002(6)	0	K51	0.069(7)	0.12(1)	0.096(8)	0.008(7)	0.015(6)	0.011(7)
K9	0.10(1)	0.122(11)	0.099(9)	–0.009(8)	0.008(7)	0.039(8)	K52	0.105(10)	0.12(1)	0.12(1)	0.034(8)	–0.003(8)	0.017(8)
K10	0.10(1)	0.11(1)	0.12(1)	–0.005(8)	–0.013(8)	0.009(8)	K54	0.068(7)	0.104(9)	0.086(8)	0.014(7)	–0.002(6)	–0.012(6)
K11	0.076(8)	0.103(9)	0.097(8)	0	0.012(6)	–0.001(7)	K55	0.072(7)	0.104(9)	0.066(7)	0	0.004(5)	–0.010(6)
K12	0.086(9)	0.17(2)	0.096(9)	–0.027(9)	–0.005(7)	–0.023(9)	K56	0.103(9)	0.11(1)	0.068(7)	–0.002(7)	–0.008(7)	–0.005(8)
K13	0.072(8)	0.14(1)	0.101(9)	–0.027(8)	–0.024(7)	0.018(8)	K57	0.14(1)	0.083(8)	0.076(7)	0.002(6)	–0.016(7)	–0.019(8)
K14	0.097(8)	0.062(7)	0.091(8)	–0.003(6)	–0.017(7)	–0.006(6)	K58	0.090(8)	0.078(7)	0.061(6)	–0.004(5)	0.005(6)	0.023(6)
K15	0.088(8)	0.075(7)	0.075(7)	0.019(6)	–0.007(6)	0	K59	0.078(9)	0.14(1)	0.23(2)	–0.10(1)	–0.07(1)	0.045(9)
K16	0.069(7)	0.114(9)	0.069(7)	0.017(6)	–0.004(6)	–0.011(7)	K60	0.103(9)	0.089(9)	0.095(8)	–0.010(7)	0.003(7)	0.014(7)
K17	0.092(8)	0.088(8)	0.078(7)	0.018(6)	–0.009(6)	–0.015(7)	K61	0.063(7)	0.081(7)	0.075(7)	0.017(6)	0.008(5)	0.013(6)
K18	0.099(9)	0.076(8)	0.134(7)	–0.011(7)	0.031(8)	–0.002(7)	K62	0.14(1)	0.17 (2)	0.082(9)	0.051(9)	–0.025(8)	–0.06(1)
K19	0.063(6)	0.073(7)	0.072(7)	–0.004(5)	0.002(5)	–0.002(5)	K63	0.097(8)	0.066(7)	0.073(7)	–0.016(5)	0.005(6)	0.009(6)
K20	0.084(8)	0.094(8)	0.077(7)	–0.013(6)	–0.013(6)	0.015(7)	K64	0.092(9)	0.10(1)	0.16(1)	0.033(9)	0.003(9)	–0.002(8)
K21	0.100(9)	0.065(7)	0.096(8)	0.017(6)	–0.009(7)	–0.009(6)	K65	0.11(1)	0.15(1)	0.14(1)	–0.05(1)	–0.046(9)	0.04(1)
K22	0.088(8)	0.077(7)	0.076(7)	–0.005(6)	–0.004(6)	–0.007(6)	K66	0.089(8)	0.081(8)	0.078(7)	–0.006(6)	0.022(6)	–0.008(6)
K23	0.073(7)	0.072(7)	0.091(8)	0.003(6)	0.017(6)	0.009(6)	K67	0.11(1)	0.087(9)	0.17(1)	–0.015(9)	–0.05(1)	0.015(8)
K24	0.071(7)	0.052(6)	0.089(7)	–0.012(5)	0.008(6)	0	K68	0.067(7)	0.056(6)	0.067(6)	–0.005(5)	0.007(5)	–0.008(5)
K25	0.077(7)	0.062(6)	0.063(6)	–0.006(5)	0	–0.003(5)	K69	0.077(7)	0.078(7)	0.082(7)	0.005(6)	0.007(6)	0.016(6)
K26	0.079(7)	0.074(7)	0.083(7)	–0.018(6)	–0.007(6)	0.007(6)	K70	0.069(7)	0.063(6)	0.055(6)	–0.012(5)	–0.003(5)	–0.009(5)

***Table 8.15*: Interatomic distances (≤ 4 Å) in $K_{70}Sn_{103}$ (standard deviation in parentheses).**

Atom pair		*d* / Å	Atom pair		*d* / Å	Atom pair		*d* / Å	Atom pair		*d* / Å
Sn1A	Sn3A	3.013(4)	Sn5A	K35	3.52(1)	Sn1B	Sn5B	2.967(4)	Sn6B	Sn3B	3.037(4)
	Sn6A	3.097(4)		K33	3.67(1)		Sn9B	2.981(5)		Sn4B	3.048(5)
	Sn5A	3.124(4)		K16	3.78(1)		Sn2B	3.035(4)		Sn7B	3.191(4)
	Sn2A	3.168(4)		K39	3.90(1)		K5	3.69(1)		Sn9B	3.229(4)
	K19	3.49(1)		K59	3.92(1)		K60	3.77(1)		K57	3.72(1)
	K58	3.88(1)	Sn6A	Sn5A	2.946(4)		K66	3.78(1)		K52	3.72(1)
	K59	3.96(1)		Sn7A	2.955(4)		K55	3.84(1)		K65	3.89(1)
	K39	3.98(1)		Sn4A	2.996(4)		K7	3.95(1)	Sn7B	Sn8B	2.986(5)
Sn2A	Sn5A	2.924(4)		Sn1A	3.097(4)	Sn2B	Sn8B	2.946(4)		Sn4B	3.029(5)
	Sn3A	2.940(4)		K23	3.76(1)		Sn5B	2.999(4)		Sn5B	3.082(4)
	Sn9A	3.000(5)		K59	3.83(2)		Sn1B	3.035(4)		Sn6B	3.191(4)
	Sn1A	3.168(4)		K38	3.86(1)		Sn7B	3.292(4)		Sn2B	3.292(4)
	K15	3.54(1)		K35	3.95(1)		K5	3.50(1)	Sn8B	Sn2B	2.946(4)
	K33	3.59(1)	Sn7A	Sn9A	2.930(5)		K48	3.55(1)		Sn9B	2.954(5)
	K58	3.71(1)		Sn8A	2.945(5)	Sn3B	Sn4B	2.935(5)		Sn6B	2.972(5)
	K61	3.96(1)		Sn6A	2.955(4)		Sn1B	2.961(5)		Sn7B	2.986(5)
Sn3A	Sn2A	2.940(4)		Sn4A	3.175(4)		Sn9B	3.002(5)		K2	3.56(1)
	Sn4A	2.954(4)		K53	3.64(1)		Sn6B	3.037(4)		K1	3.68(1)
	Sn8A	2.968(4)		K35	3.73(1)		K66	3.60(1)		K7	3.69(1)
	Sn1A	3.013(4)		K18	3.75(1)		K57	3.75(1)	Sn9B	Sn8B	2.954(5)
	K34	3.63(1)		K27	3.96(1)		K33	3.79(1)		Sn1B	2.981(5)
	K20	3.65(1)	Sn8A	Sn7A	2.945(5)	Sn4B	Sn3B	2.935(5)		Sn3B	3.002(5)
	K15	3.80(1)		Sn9A	2.963(6)		Sn5B	2.968(5)		Sn6B	3.229(4)
	K44	3.83(1)		Sn3A	2.968(4)		Sn7B	3.029(5)		K486	3.72(2)
	K58	3.92(1)		Sn4A	3.163(5)		Sn6B	3.048(5)		K7	3.86(1)
Sn4A	Sn3A	2.954(4		K26	3.73(1)		K52	3.64(1)		K7	3.91(1)
	Sn6A	2.996(4)		K20	3.75(1)		K47	3.79(1)	Sn1C	Sn4C	3.005(4)
	Sn8A	3.163(5)		K15	3.85(1)		K37	3.87(1)		Sn9C	3.010(5)
	Sn7A	3.175(4)	Sn9A	Sn7A	2.930(5)	Sn5B	Sn1B	2.967(4)		Sn5C	3.028(4)
	K53	3.71(1)		Sn8A	2.963(6)		Sn4B	2.968(5)		K28	3.72(1)
	K23	3.72(1)		Sn2A	3.000(5)		Sn2B	2.999(4)		K24	3.83(1)
	K63	3.95(1)		Sn5A	3.023(5)		Sn7B	3.082(4)		K33	3.96(1)
Sn5A	Sn2A	2.924(4)		K33	3.66(1)		K60	3.59(1)	Sn2C	Sn9C	2.905(4)
	Sn6A	2.946(4)		K49	3.89(1)		K47	3.94(1)		Sn5C	2.957(4)
	Sn9A	3.023(5)		K31	3.90(1)		K22	3.96(1)		Sn7C	2.976(4)
	Sn1A	3.124(4)	Sn1B	Sn3B	2.961(5)	Sn6B	Sn8B	2.972(5)		K40	3.72(1)
Sn2C	Sn8E	3.086(7)	Sn7C	Sn6C	2.906(4)	Sn3D	Sn1D	3.192(4)	Sn8D	Sn5D	2.968(5)
	K28	3.61(1)		Sn5C	2.943(5)		Sn2D	3.284(4)		Sn1D	3.099(5)
	K40	3.743(1)		Sn2C	2.976(4)		K56	3.73(1)		K30	3.72(1)
	K17	3.82(1)		Sn8C	3.076(4)		K33	3.80(1)		K25	3.88(1)
Sn3C	Sn9C	2.976(4)		K21	3.66(1)	Sn4D	Sn6D	2.932(5)	Sn9D	Sn7D	2.927(5)
	Sn6C	2.980(4)		K51	3.67(1)		Sn5D	2.953(4)		Sn6D	2.929(5)
	Sn4C	3.022(4)		K14	3.86(1)		Sn2D	2.971(4)		Sn8D	2.964(5)
	Sn8C	3.277(4)	Sn8C	Sn9C	2.983(5)		Sn3D	3.061(5)		Sn2D	3.180(5)
	K44	3.62(1)		Sn6C	3.033(4)		K20	3.70(1)		K1	3.69(2)
	K24	3.63(1)		Sn7C	3.076(4)		K66	3.77(1)	Sn1E	Sn5E	2.747(9)
	K33	3.98(1)		Sn3C	3.277(4)	Sn5D	Sn4D	2.953(4)		Sn6E	2.832(8)
Sn4C	Sn5C	2.952(4)		K51	3.84(1)		Sn8D	2.968(5)		Sn3E	2.926(9)
	Sn6C	2.972(4)		K19	3.99(1)		Sn1D	2.998(4)		Sn4E	2.990(9)
	Sn1C	3.005(4)	Sn9C	Sn2C	2.905(4)		Sn3D	3.087(4)		K56	3.49(1)
	Sn3C	3.022(4)		Sn3C	2.976(4)		K66	3.75(1)		K40	3.61(1)
	K14	3.62(1)		Sn8C	2.983(5)		K21	3.80(1)		K37	3.93(2)
	K16	3.65(1)		Sn1C	3.010(5)		K30	3.80(1)	Sn2E	Sn8E	2.939(5)
	K33	3.73(1)		K36	3.66(1)		K51	3.81(1)		Sn5E	2.940(6)
	K31	3.85(1)		K58	3.66(1)	Sn6D	Sn9D	2.929(5)		Sn6E	2.951(5)

Sn4C	K35	3.89(1)	Sn9C	K24	3.71(1)	Sn6D	Sn4D	2.932(5)	Sn2E	Sn7E	3.003(5)
Sn5C	Sn7C	2.943(5)	Sn1D	Sn7D	2.991(5)		Sn8D	2.945(5)		K36	3.72(1)
	Sn4C	2.952(4)		Sn5D	2.998(4)		Sn2D	3.047(5)		K38	3.78(1)
	Sn2C	2.957(4)		Sn8D	3.099(5)		K15	3.53(1)		K28	3.80(1)
	Sn1C	3.028(4)		Sn3D	3.192(4)		K25	3.62(1)		K18	3.88(1)
	K17	3.64(1)		K30	3.68(1)		K26	3.79(1)		K23	3.94(1)
	K32	3.65(1)		K67	3.96(1)		K21	4.00(1)	Sn3E	Sn9E	2.862(6)
	K31	3.70(1)	Sn2D	Sn7D	2.948(5)	Sn7D	Sn9D	2.927(5)		Sn1E	2.926(9)
	K14	3.80(1)		Sn4D	2.971(4)		Sn2D	2.948(5)		Sn5E	2.982(7)
Sn6C	Sn7C	2.906(4)		Sn6D	3.047(5)		Sn1D	2.991(5)		K8	3.77(1)
	Sn4C	2.972(4)		Sn9D	3.180(5)		Sn3D	3.019(5)		K41	3.78(2)
	Sn3C	2.980(4)		Sn3D	3.284(4)		K9	3.65(1)		K40	3.96(1)
	Sn8C	3.033(4)		K20	3.84(1)		K1	3.78(1)	Sn4E	Sn9E	2.865(7)
	K19	3.61(1)		K26	3.93(1)		K2	3.84(1)		Sn1E	2.990(9)
	K16	3.71(1)	Sn3D	Sn7D	3.019(5)		K33	3.95(1)		Sn6E	3.071(5)
	K68	3.75(1)		Sn4D	3.061(5)	Sn8D	Sn6D	2.945(5)		Sn7E	3.288(5)
	K14	3.78(1)		Sn5D	3.087(4)		Sn9D	2.964(5)		K9	3.63(2)
Sn4E	K45	3.91(1)	Sn1F	K13	3.74(1)		Sn6F	3.065(5)		Sn1G	3.115(5)
	K62	3.95(2)	Sn2F	Sn4F	2.843(7)		K58	3.68(1)		K10	3.74(2)
Sn5E	Sn1E	2.747(9)		Sn9F	2.863(8)		K69	3.75(1)		K33	3.80(1)
	Sn2E	2.940(6)		Sn1F	2.931(9)		K22	3.81(1)		K9	3.83(2)
Sn6E	Sn1E	2.832(8)		K13	3.51(2)		K55	3.89(1)		K2	3.98(1)
	Sn2E	2.951(5)		K37	3.58(1)	Sn8F	Sn9F	2.950(8)	Sn4G	Sn3G	2.854(5)
	Sn4E	3.071(5)		K10	3.63(2)		Sn4F	2.984(5)		Sn5G	2.866(7)
	Sn7E	3.159(6)	Sn3F	Sn4F	2.950(6)		Sn7F	2.989(5)		Sn2G	2.959(5)
	K23	3.70(1)		Sn5F	2.998(6)		Sn6F	3.225(5)		K12	3.54(1)
	K43	3.86(1)		Sn1F	3.04(1)		K41	3.70(1)		K5	3.64(1)
Sn7E	Sn9E	2.958(5)		K52	3.55(2)		K22	3.94(1)		K13	3.83(1)
	Sn2E	3.003(5)		K37	3.84(1)	Sn9F	Sn2F	2.863(8)		K10	3.96(2)
	Sn6E	3.159(6)		K57	3.88(1)		Sn1F	2.89(1)	Sn5G	Sn4G	2.866(7)
	Sn4E	3.288(5)	Sn4F	Sn2F	2.843(7)		Sn8F	2.950(8)		Sn2G	2.931(5)
	K53	3.71(2)		Sn3F	2.950(6)		Sn7F	2.969(7)		Sn1G	2.963(6)
	K45	3.82(1)		Sn8F	2.984(5)		K12	3.6(2)		Sn3G	3.016(5)
	K18	3.93(2)		Sn6F	2.995(6)		K69	3.68(1)		K43	3.48(2)
	K23	3.96(1)		K42	3.62(1)		K138	3.73(2)		K11	3.53(1)
Sn8E	Sn2E	2.939(5)		K50	3.79(1)		K13	3.86(1)		K80	3.55(1)
	Sn9E	2.947(6)		K57	3.82(1)	Sn1G	Sn5G	2.963(6)		K63	3.72(1)
	Sn5E	3.086(7)	Sn5F	Sn1F	2.840(8)		Sn2G	3.095(4)	Sn1H	Sn3H	2.873(5)
	K41	3.60(1)		Sn7F	2.973(5)		Sn3G	3.115(5)		Sn2H	2.927(5)
	K18	3.73(1)		Sn3F	2.998(6)		K1	3.58(2)		Sn4H	2.938(5)
	K29	3.80(1)		Sn6F	3.095(5)		K43	3.89(1)		K43	3.46(1)
	K28	3.96(1)		K11	3.66(1)		K33	3.91(1)		K67	3.51(2)
Sn9E	Sn3E	2.862(6)		K60	3.67(2)		K2	3.92(1)		K40	3.56(1)
	Sn4E	2.865(7)		K58	3.82(1)	Sn2G	Sn5G	2.931(5)		K80	3.73(1)
	Sn8E	2.947(6)	Sn6F	Sn4F	2.995(6)		Sn4G	2.959(5)		K33	3.75(1)
	Sn7E	2.958(5)		Sn7F	3.065(5)		Sn3G	2.960(5)	Sn2H	Sn4H	2.901(5)
	K10	3.57(2)		Sn5F	3.095(5)		Sn1G	3.095(4)		Sn1H	2.927(5)
	K45	3.62(1)		Sn8F	3.225(5)		K7	3.56(1)		Sn3H	2.972(8)
	K50	3.63(2)		K54	3.72(1)		K5	3.67(1)		K53	3.61(1)
Sn1F	Sn5F	2.840(8)		K22	3.87(1)		K2	3.83(1)		K63	3.83(1)
	Sn9F	2.89(1)		K60	3.87(1)		K63	3.88(2)		K45	3.83(2)
	Sn2F	2.931(9)	Sn7F	Sn9F	2.969(7)	Sn3G	Sn4G	2.854(5)		K43	3.86(2)
	Sn3F	3.04(1)		Sn5F	2.973(5)		Sn2G	2.960(5)	Sn3H	Sn1H	2.873(5)
Sn3H	Sn2H	2.972(8)		K45	3.59(1)		K38	3.72(1)		K63	3.57(1)
	K20	3.58(1)		K67	3.59(2)		K36	3.78(1)		K51	3.63(1)
	K33	3.75(1)		K42	3.78(1)	Sn1K	Sn2K	2.891(5)		K43	3.64(1)
	K63	3.75(1)		K11	3.88(1)		Sn4K	2.939(5)		K66	3.66(1)

Sn3H	K56	3.843(14)	Sn1J	Sn2J	2.918(4)	Sn1K	Sn3K	2.947(5)	Sn2L	Sn1L	2.908(4)
Sn4H	Sn2H	2.901(5)		Sn3J	2.919(5)		K12	3.62(1)		Sn4L	2.912(4)
	Sn3H	2.906(5)		Sn4J	2.931(4)		K69	3.68(1)		Sn3L	2.913(4)
	Sn1H	2.938(5)		K59	3.58(1)		K46	3.73(1)		K19	3.47(1)
	K30	3.70(1)		K21	3.78(1)		K41	3.77(1)		K23	3.62(1)
	K40	3.71(1)		K66	3.79(1)		K8	3.81(1)		K44	3.66(1)
	K51	3.77(1)		K70	3.87(1)		K17	3.94(1)		K16	3.73(1)
	K63	3.78(1)		K19	3.90(1)	Sn2K	Sn4K	2.878(5)		K63	3.96(1)
Sn1I	Sn4I	2.796(7)	Sn2J	Sn4J	2.909(4)		Sn3K	2.890(5)		K68	3.96(1)
	Sn3I	2.907(6)		Sn1J	2.918(4)		Sn1K	2.891(5)	Sn3L	Sn2L	2.913(4)
	Sn2I	3.019(7)		Sn3J	2.939(5)		K30	3.49(1)		Sn1L	2.925(4)
	K9	3.61(1)		K61	3.56(1)		K17	3.73(1)		Sn4L	2.940(4)
	K10	3.62(2)		K68	3.63(1)		K40	3.83(2)		K70	3.496(9)
	K42	3.79(2)		K58	3.73(1)		K67	3.87(2)		K43	3.54(1)
Sn2I	Sn4I	2.818(6)		K34	3.74(1)	Sn3K	Sn2K	2.890(5)		K59	3.54(1)
	Sn3I	2.953(6)		K15	3.75(1)		Sn4K	2.892(6)		K66	3.66(1)
	Sn1I	3.019(7)		K21	3.86(1)		Sn1K	2.947(5)		K16	3.67(1)
	K2	3.46(1)	Sn3J	Sn4J	2.884(4)		K11	3.55(1)		K68	3.81(1)
	K52	3.71(2)		Sn1J	2.919(5)		K12	3.56(2)	Sn4L	Sn2L	2.912(4)
	K65	3.71(2)		Sn2J	2.939(5)		K52	3.60(1)		Sn3L	2.940(4)
	K11	3.84(1)		K43	3.55(1)		K8	3.70(1)		Sn1L	2.951(4)
Sn3I	Sn4I	2.855(7)		K19	3.64(1)		K67	3.92(2)		K39	3.41(1)
	Sn1I	2.907(6)		K68	3.71(1)	Sn4K	Sn2K	2.878(5)		K51	3.61(1)
	Sn2I	2.953(6)		K38	3.83(1)		Sn3K	2.892(6)		K63	3.65(1)
	K11	3.59(1)		K36	3.89(1)		Sn1K	2.939(5)		K16	3.72(1)
	K37	3.63(1)		K23	3.96(1)		K47	3.53(1)		K59	3.77(2)
	K60	3.70(1)	Sn4J	Sn3J	2.884(4)		K64	3.60(2)	Sn1M	Sn3M	2.898(4)
	K42	3.84(1)		Sn2J	2.909(4)		K46	3.66(1)		Sn4M	2.939(5)
	K65	3.85(2)		Sn1J	2.931(4)		K32	3.78(1)		Sn2M	2.960(4)
Sn4I	Sn1I	2.796(7)		K24	3.33(1)	Sn1L	Sn2L	2.908(4)		K44	3.61(1)
	Sn2I	2.818(6)		K34	3.58(1)		Sn3L	2.925(4)		K56	3.72(1)
	Sn3I	2.855(7)		K70	3.65(1)		Sn4L	2.951(4)		K20	3.80(1)
Sn2M	Sn4M	2.867(4)		K49	3.69(1)		K17	3.61(1)	Sn4P	Sn3P	2.918(4)
	Sn1M	2.960(4)		K70	3.712(9)		K29	3.75(1)		Sn1P	2.919(5)
	Sn3M	2.977(4)		K28	3.78(1)		K28	3.80(1)		Sn2P	2.940(4)
	K39	3.52(1)		K38	4.00(1)		K49	3.80(1)		K50	3.52(1)
	K36	3.76(1)	Sn3N	Sn1N	2.932(4)		K41	3.84(1)		K29	3.52(1)
	K61	3.80(1)		Sn4N	2.943(4)		K46	3.88(1)		K27	3.67(1)
	K43	3.93(1)		Sn2N	2.946(4)	Sn4O	Sn1O	2.881(5)		K54	3.79(1)
	K58	3.95(1)		K68	3.61(1)		Sn2O	2.886(5)		K18	3.91(1)
Sn3M	Sn4M	2.885(5)		K35	3.64(1)		Sn3O	2.944(5)	Sn1Q	Sn2Q	2.890(4)
	Sn1M	2.898(4)		K70	3.65(1)		K25	3.47(1)		Sn3Q	2.921(5)
	Sn2M	2.977(4)		K38	3.72(1)		K29	3.41(1)		Sn4Q	2.938(5)
	K61	3.55(1)	Sn4N	Sn3N	2.943(4)	Sn4O	K49	3.56(1)		K45	3.56(1)
	K24	3.59(1)		Sn2N	2.945(4)		K26	3.83(1)		K53	3.57(1)
	K39	3.68(2)		Sn1N	2.951(4)	Sn1P	Sn4P	2.919(5)		K42	3.84(1)
	K33	3.80(1)		K14	3.61(1)		Sn2P	2.934(4)		K50	3.87(1)
	K44	3.83(1)		K15	3.66(1)		Sn3P	2.949(4)	Sn2Q	Sn1Q	2.890(4)
Sn4M	Sn2M	2.867(4)		K49	3.80(1)		K32	3.63(1)		Sn4Q	2.916(4)
	Sn3M	2.885(5)		K25	3.81(1)		K25	3.69(1)		Sn3Q	2.957(5)
	Sn1M	2.939(5)		K61	3.89(1)		K47	3.70(1)		K57	3.58(1)
	K34	3.44(1)		K68	3.99(1)		K22	3.72(1)		K54	3.71(1)
	K56	3.47(1)	Sn1O	Sn4O	2.881(5)		K29	3.83(1)		K42	3.85(1)
	K43	3.54(1)		Sn3O	2.917(4)	Sn2P	Sn1P	2.934(4)		K50	3.86(1)
	K70	3.54(1)		Sn2O	2.978(4)		Sn4P	2.940(4)		K48	3.89(1)
	K66	3.58(1)		K31	3.57(1)		Sn3P	2.953(4)	Sn3Q	Sn4Q	2.881(5)
Sn1N	Sn3N	2.932(4)		K46	3.67(1)		K35	3.66(1)		Sn1Q	2.921(5)

Sn1N	Sn2N	2.947(4)	Sn1O	K26	3.72(1)	Sn2P	K14	3.82(1)	Sn3Q	Sn2Q	2.957(5)
	Sn4N	2.951(4)		K27	3.92(1)		K18	3.86(1)		K48	3.51(1)
	K29	3.61(1)	Sn2O	Sn4O	2.886(5)		K32	3.89(1)		K4	3.54(1)
	K28	3.76(1)		Sn3O	2.951(4)		K31	3.90(1)		K6	3.59(1)
	K25	3.85(1)		Sn1O	2.978(4)	Sn3P	Sn4P	2.918(4)		K42	3.69(1)
	K35	3.94(1)		K46	3.68(1)		Sn1P	2.949(4)	Sn4Q	Sn3Q	2.881(5)
	K18	3.99(2)		K55	3.72(1)		Sn2P	2.953(4)		Sn2Q	2.916(4)
Sn2N	Sn4N	2.945(4)		K69	3.84(1)		K46	3.43(1)		Sn1Q	2.938(5)
	Sn3N	2.946(4)		K22	3.87(1)		K32	3.70(1)		K1	3.62(1)
	Sn1N	2.947(4)	Sn3O	Sn1O	2.917(4)		K27	3.72(1)		K27	3.64(1)
	K24	3.56(1)		Sn4O	2.944(5)		K54	3.75(1)		K26	3.65(1)
	Sn4R	2.955(5)		Sn1G	3.92(1)		Sn3E	3.77(1)		Sn2P	3.82(1)
	Sn3R	2.962(5)		K9	3.95(2)		Sn1K	3.81(1)		Sn7C	3.86(1)
	K65	3.65(1)		Sn3G	3.98(1)		K40	3.84(2)	K15	Sn6D	3.53(1)
	K64	3.74(2)	K3	Sn3H	3.75(1)	K9	Sn1I	3.61(1)		Sn2A	3.54(1)
	K37	3.85(1)		Sn1H	3.75(1)		Sn4E	3.63(2)		Sn4N	3.66(1)
	K60	3.89(1)		Sn3G	3.80(1)		Sn7D	3.65(1)		Sn2J	3.75(1)
Sn2R	Sn3R	2.906(4)		Sn3D	3.80(1)		Sn3G	3.83(2)		Sn3A	3.80(1)
	Sn1R	2.915(4)		Sn1G	3.91(1)		K2	3.95(2)		Sn8A	3.85(1)
	Sn4R	2.933(4)		Sn1E	3.93(2)	K10	Sn9E	3.57(2)	K16	Sn4C	3.65(1)
	K46	3.59(1)		Sn7D	3.95(1)		Sn1I	3.62(2)		Sn3L	3.67(1)
	K54	3.69(1)	K4	Sn4I	3.24(2)		Sn2F	3.63(2)		Sn6C	3.71(1)
	K69	3.73(1)		Sn1H	3.46(1)		Sn3G	3.74(2)		Sn4L	3.72(1)
	K64	3.80(2)		Sn5G	3.48(2)		Sn4G	3.96(2)		Sn2L	3.73(1)
	K47	3.93(1)		Sn3Q	3.54(1)	K11	Sn5G	3.53(1)		Sn5A	3.78(1)
Sn3R	Sn2R	2.906(4)		Sn2H	3.86(2)		Sn3K	3.55(1)		K68	3.87(2)
	Sn4R	2.940(5)		Sn1G	3.89(1)		Sn3I	3.59(1)	K17	Sn3O	3.61(1)
	Sn1R	2.962(5)	K5	Sn4G	3.64(1)		Sn5F	3.66(1)		Sn5C	3.64(1)
	K13	3.56(1)		Sn2G	3.67(1)		Sn2I	3.84(1)		Sn2K	3.73(1)
	K55	3.71(1)		Sn7F	3.68(1)		Sn4I	3.88(1)		Sn5E	3.82(1)
	K58	3.87(1)		Sn1B	3.69(1)	K12	Sn1F	3.51(1)		K40	3.84(2)
	K69	3.88(1)		Sn5F	3.82(1)		Sn4G	3.54(1)		Sn1K	3.94(1)
	K64	3.96(2)		Sn3R	3.87(1)		Sn3K	3.56(2)	K18	Sn8E	3.73(1)
Sn4R	Sn2R	2.933(4)		K13	3.96(2)		Sn1K	3.62(1)		Sn7A	3.75(1)
	Sn3R	2.940(5)	K6	Sn3Q	3.59(1)		Sn9F	3.63(2)		K35	3.84(2)
	Sn1R	2.955(5)		Sn3B	3.60(1)	K13	Sn2F	3.51(2)		Sn2P	3.86(1)
	K78	3.61(1)		Sn5G	3.72(1)		Sn3R	3.56(1)		Sn2E	3.88(1)
	K57	3.79(1)		Sn1B	3.78(1)		Sn9F	3.73(2)		Sn4P	3.91(1)
	K54	3.93(1)	K6	Sn2G	3.89(2)	K13	Sn1F	3.74(1)	K18	K29	3.92(2)
K1	Sn1G	3.58(2)	K7	Sn2G	3.56(1)		Sn4G	3.83(1)		Sn7E	3.93(2)
	Sn4Q	3.62(1)		Sn4R	3.61(1)		Sn9F	3.86(1)		Sn1N	3.99(2)
	Sn8B	3.68(1)		Sn8B	3.69(1)		K5	3.96(2)	K19	Sn2L	3.48(1)
	Sn9D	3.69(2)		Sn9B	3.86(1)	K14	Sn4N	3.61(1)		Sn1A	3.49(1)
	Sn7D	3.78(1)		Sn9B	3.91(1)		Sn4C	3.63(1)		Sn6C	3.61(1)
K2	Sn2I	3.46(1)		Sn1B	3.95(1)		K25	3.67(2)		Sn3J	3.64(1)
	Sn8B	3.56(1)	K8	Sn5G	3.55(1)		K35	3.74(2)		K59	3.80(2)
	Sn2G	3.83(1)		Sn3K	3.70(1)		Sn6C	3.78(1)		Sn1J	3.90(1)
	Sn8C	3.99(1)		Sn1N	3.85(1)		Sn4C	3.85(1)		Sn3B	3.79(1)
K20	Sn3H	3.58(1)		Sn8D	3.88(1)		Sn9A	3.90(1)		Sn3F	3.84(1)
	Sn3A	3.65(1)	K26	Sn4Q	3.65(1)		Sn2P	3.90(1)		Sn1R4	3.85(1)
	Sn4D	3.70(1)		Sn1O	3.72(1)	K32	Sn1P	3.63(1)		Sn4B	3.87(1)
	Sn8A	3.75(1)		Sn8A	3.73(1)		Sn5C	3.65(1)	K38	Sn4J	3.72(1)
	Sn1M	3.80(1)		Sn6D	3.79(1)		Sn3P	3.70(1)		Sn3N	3.72(1)
	Sn2D	3.84(1)		Sn4O	3.83(1)		Sn4K	3.78(1)		Sn2E	3.78(1)
K21	Sn7C	3.66(1)		Sn2D	3.93(1)		Sn2P	3.89(1)		Sn3J	3.83(1)
	Sn1J	3.78(1)	K27	Sn4Q	3.64(1)		Sn8D	3.94(1)		Sn6A	3.86(1)
	Sn5D	3.80(1)		Sn4P	3.67(1)	K33	Sn2A	3.59(1)		Sn2N	4.00(1)

K21	Sn2J	3.86(1)	K27	Sn3P	3.72(1)	K33	K24	3.62(2)	K39	Sn4L	3.41(1)
	Sn6D	4.00(1)		Sn1O	3.92(1)		Sn9A	3.66(1)		Sn2M	3.52(1)
K22	Sn1P	3.72(1)		Sn7A	3.96(1)		Sn5A	3.67(1)		Sn3M	3.68(2)
	Sn7F	3.81(1)	K28	Sn5E	3.61(1)		Sn4C	3.73(1)		Sn5A	3.91(1)
	Sn2O	3.87(1)		Sn1C	3.72(1)		Sn3M	3.80(1)		K581	3.97(2)
	Sn6F	3.87(1)		Sn1N	3.76(1)		Sn1C	3.96(1)		Sn1A	3.98(1)
	Sn8F	3.94(1)		Sn2N	3.78(1)		Sn3C	3.98(1)	K40	Sn1H	3.56(1)
	Sn5B	3.96(1)		Sn2E	3.80(1)	K34	Sn4M	3.44(1)		Sn1E	3.61(1)
K23	Sn2L	3.62(1)		Sn3O	3.80(1)		Sn4J	3.58(1)		Sn4H	3.71(1)
	Sn6E	3.70(1)		Sn8E	3.96(1)		Sn3A	3.63(1)		Sn2C	3.72(1)
	Sn4A	3.72(1)	K29	Sn4O	3.49(1)		Sn2J	3.74(1)		Sn5E	3.74(1)
	Sn6A	3.76(1)		Sn4P	3.52(1)	K35	Sn5A	3.52(1)		Sn2K	3.83(2)
	Sn2E	3.94(1)		Sn1N	3.6(1)		Sn3N	3.64(1)		K17	3.84(2)
	Sn7E	3.96(1)		Sn3O	3.75(1)		Sn2P	3.66(1)		K8	3.84(2)
	Sn3J	3.96(1)		Sn8E	3.80(1)		Sn7A	3.73(1)		Sn3E	3.96(1)
K24	Sn4J	3.33(1)		Sn1P	3.83(1)		K14	3.74(2)	K41	Sn8E	3.60(1)
	Sn2N	3.56(1)		K18	3.92(2)		K18	3.84(2)		Sn8F	3.70(1)
	Sn3M	3.59(1)	K30	Sn2K	3.49(1)		Sn4C	3.89(1)		Sn1K	3.77(1)
	K33	3.62(1)		Sn7C	3.53(1)		Sn1N	3.94(1)		Sn3E	3.78(2)
	Sn3C	3.63(1)		Sn1D	3.68(1)		Sn6A	3.95(1)		Sn3O	3.84(1)
	Sn9C	3.71(1)		Sn4H	3.70(1)	K36	Sn9C	3.66(1)	K42	Sn4F	3.62(1)
	Sn1C	3.83(1)		Sn8D	3.72(1)		Sn2E	3.72(1)		Sn3Q	3.69(1)
K25	Sn4O	3.47(1)		Sn2C	3.77(1)		Sn2M	3.76(1)		Sn4I	3.78(1)
	Sn6D	3.62(1)		Sn5D	3.80(1)		Sn4J	3.77(1)		Sn1I	3.79(2)
	K14	3.67(2)		K51	4.00(2)		Sn3J	3.89(1)		Sn3I	3.84(1)
	Sn1P	3.69(1)	K31	Sn1O	3.578(1)	K37	Sn2F	3.58(1)		Sn1Q	3.84(1)
K43	Sn4M	3.54(1)		K57	3.94(2)		Sn2O	3.72(1)		Sn1R	3.89(1)
	Sn3L	3.54(1)	K49	Sn4O	3.56(1)		K69	3.77(2)		K65	3.99(2)
	Sn3J	3.55(1)		Sn2N	3.69(1)		Sn1B	3.84(1)	K61	Sn3M	3.55(1)
	Sn1L	3.64(1)		Sn4N	3.80(1)		Sn7F	3.89(1)		Sn2J	3.56(1)
	Sn6E	3.86(1)		Sn3O	3.80(1)	K56	Sn4M	3.47(1)		Sn2N	3.64(1)
	Sn2M	3.93(1)		Sn9A	3.89(1)		Sn1E	3.49(1)		Sn2M	3.80(1)
K44	Sn1M	3.61(1)	K50	Sn4P	3.52(1)		Sn1M	3.72(1)		Sn4N	3.89(1)
	Sn3C	3.62(1)		Sn9E	3.63(2)		Sn3D	3.73(1)		Sn2A	3.96(1)
	Sn2L	3.66(1)		Sn4F	3.79(1)		Sn3H	3.84(1)	K62	Sn1L	3.53(1)
	Sn3M	3.83(1)		Sn2Q	3.86(1)	K57	Sn2Q	3.58(1)		Sn3D	3.85(2)
	Sn3A	3.83(1)		Sn1Q	3.87(1)		Sn6B	3.72(1)		Sn4E	3.95(2)
K45	Sn1Q	3.56(1)	K51	Sn4L	3.61(1)		Sn3B	3.75(1)	K63	Sn1L	3.57(1)
	Sn4I	3.59(1)		Sn1L	3.63(1)		Sn4R	3.79(1)		Sn4L	3.65(1)
	Sn9E	3.62(1)		Sn7C	3.67(1)		Sn4F	3.82(1)		Sn3H	3.75(1)
	Sn7E	3.82(1)		Sn4H	3.77(1)		Sn3F	3.88(1)		Sn4H	3.78(1)
	Sn2H	3.83(1)		Sn5D	3.81(1)		K48	3.94(2)		Sn2H	3.83(1)
	Sn4E	3.91(1)		Sn8C	3.84(1)		K65	3.97(2)		Sn1M	3.83(1)
K46	Sn3P	3.43(1)		K30	4.00(2)	K58	Sn9C	3.66(1)		Sn4A	3.95(1)
	Sn2R	3.59(1)	K52	Sn3F	3.55(2)		Sn4J	3.70(1)		Sn2L	3.96(1)
	Sn4K	3.66(1)		Sn3K	3.601)		Sn2A	3.71(1)	K64	Sn4K	3.60(2)
	Sn1O	3.67(1)		Sn4B	3.64(1)		Sn2J	3.73(1)		Sn1R	3.74(2)
	Sn2O	3.68(1)		Sn2I	3.71(2)		Sn1A	3.88(1)		Sn2R	3.80(2)
	Sn1K	3.73(1)		Sn6B	3.72(1)		Sn3A	3.93(1)		Sn3R	3.96(1)
	Sn3O	3.88(1)	K53	Sn1Q	3.57(1)		Sn2M	3.95(1)		K47	3.97(2)
	K69	3.91(1)		Sn2H	3.61(1)		K39	3.97(2)	K65	Sn1R	3.65(1)
K47	Sn4K	3.53(1)		Sn7A	3.64(1)	K59	Sn3L	3.54(1)		Sn2I	3.71(2)
	Sn1P	3.70(1)		Sn4A	3.71(1)		Sn1J	3.59(1)		Sn3I	3.85(2)
	Sn4B	3.79(1)		Sn7E	3.71(1)		Sn4L	3.77(2)		Sn6B	3.89(1)
	Sn3P	3.80(1)	K54	Sn2R	3.69(1)		K19	3.80(2)		K57	3.97(2)
	Sn2R	3.93(1)		Sn2Q	3.71(1)		Sn6A	3.83(2)		K60	3.99(2)
	Sn5B	3.94(1)		Sn6F	3.72(1)		Sn5A	3.92(1)	K66	Sn4M	3.58(1)

K47	K54	3.95(2)	K54	Sn3P	3.75(1)	K59	Sn1A	3.96(1)	K66	Sn1L	3.66(1)
	K64	3.97(2)		Sn4P	3.79(1)	K60	Sn5B	3.59(1)		Sn3L	3.66(1)
K48	Sn3Q	3.51(1)		Sn4R	3.93(1)		Sn5F	3.67(1)		Sn5D	3.75(1)
	Sn2B	3.55(1)		K47	3.95(2)		Sn3I	3.70(1)		Sn4D	3.77(1)
	Sn9B	3.72(2)	K55	Sn2B	3.50(1)		Sn1B	3.77(1)		Sn1J	3.79(1)
	Sn4I	3.59(2)	K68	K19	3.96(1)	K69	K46	3.91(1)			
	Sn2K	3.87(2)		Sn2L	3.96(1)	K70	Sn3L	3.496(9)			
	Sn3K	3.92(2)		Sn4N	3.99(1)		Sn4M	3.54(1)			
	Sn1D	3.96(1)	K69	Sn1K	3.68(1)		Sn4J	3.65(1)			
K68	Sn3N	3.61(1)		Sn9F	3.68(1)		Sn3N	3.65(1)			
	Sn2J	3.63(1)		Sn2R	3.73(1)		Sn2N	3.712(9)			
	Sn3J	3.71(1)		Sn7F	3.75(1)		Sn1J	3.87(1)			
	Sn6C	3.75(1)		K55	3.77(2)						
	Sn3L	3.81(1)		Sn2O	3.84(1)						
	K16	3.88(2)		Sn3R	3.88(1)						

Table *8.16*: Interatomic distances (≤ 4 Å) in $BaSn_2$ (standard deviation in parentheses).

Atom pair		*d* / Å	Atom pair		*d* / Å
Ba	Sn	3.473(2)×6	Sn	Sn	2.919(1)×3
	Ba	4.652(2)×4		Ba	3.473(2)×3

***Table 8.17*: Interatomic distances (≤ 4 Å) in Ca_3Tl_5 and Sr_3Tl_5 (standard deviation in parentheses).**

Atom pair		*d* / Å	Atom pair		*d* / Å	Atom pair		*d* / Å
					Ca_3Tl_5 (1)			
Tl1	Tl2	3.157(1)×2	Tl2	Ca1	3.279(4)	Ca1	Tl1	3.203(3)×2
	Ca1	3.203(3)		Ca2	3.387(2)×2		Tl3	3.263(9)
	Ca1	3.323(6)		Tl3	3.427(1)		Tl2	3.279(4)×2
	Ca2	3.330(4)×2		Ca2	3.457(1)×3		Tl1	3.323(6)×2
	Ca2	3.409(5)×2	Tl3	Tl2	3.246(2)×2		Tl2	3.477(6)×2
	Tl3	3.492(2)		Ca1	3.263(9)	Ca2	Tl1	3.330(4)×2
	Tl1	3.499(2)*		Tl2	3.427(2)×2*		Tl2	3.387(2)×2
Tl2	Tl1	3.157(1)×2	Tl3	Ca2	3.447(3)×4	Ca2	Tl1	3.409(5)×2
	Tl3	3.247(2)		Tl1	3.492(2)×2		Tl3	3.447(3)×2
							Tl2	3.457(1)×2
					Sr_3Tl_5 (2)			
Tl1	Tl2	3.107(2)×2	Tl2	Sr1	3.413(3)	Sr1	Tl3	3.324(6)
	Sr1	3.355(3)		Sr2	3.495(2)×2		Tl1	3.355(3)×2
	Tl3	3.447(3)		Sr2	3.627(2)×2		Tl2	3.413(3)×2
	Sr2	3.480(3)×3		Sr1	3.670(5)		Tl1	3.481(4)×2
	Tl1	3.560(4)*		Tl3	3.681(2)		Tl2	3.670(5)×2
	Sr2	3.566(3)×2	Tl3	Tl2	3.227(3)×2	Sr2	Tl1	3.480(3)×2
Tl2	Tl1	3.107(2)×2		Sr1	3.324(6)		Tl2	3.495(2)×2
	Tl3	3.227(3)		Tl1	3.447(3)×2		Tl3	3.521(3)×2
				Sr2	3.521(3)×4		Tl1	3.566(3)×2
				Tl2	3.681(2)×2		Tl2	3.627(2)×2

*) intercluster